

**Zu Gast bei den Polyoxometallaten: Entwicklung
und katalytische Anwendung**

vorgelegt von

Jan-Christian Raabe

Institut für Technische und Makromolekulare Chemie

Universität Hamburg

als an der Universität eingereichte Dissertation

zur Erlangung des Grades

Doktor rerum naturalium

im Jahr **2024**

Gutachter:

1. Prof. Dr.-Ing. Jakob Albert
2. Prof. Dr. Michael Steiger

Tag der Disputation: 06.09.2024

Prüfer:

1. Prof. Dr.-Ing. Jakob Albert
2. Prof. Dr. Lisa Vondung
3. Prof. Dr. Wolfgang Maison

Datum der Druckfreigabe: 06.09.2024

URN: urn:nbn:de:gbv:18-ediss-121126

Die praktischen Arbeiten der vorliegenden Dissertation wurden im Zeitraum vom 01.12.2020 bis zum 30.11.2023 in der Arbeitsgruppe von Herrn Prof. Dr.-Ing. Jakob Albert am Institut für Technische und Makromolekulare Chemie der Universität Hamburg durchgeführt.

*„Forschung nennt man das Bestreben, den Nachlass der
Götter zu sichten“*

Thom Renzie

Publikationsliste

ORCID: [0000-0002-8240-1355](https://orcid.org/0000-0002-8240-1355)

<https://orcid.org/0000-0002-8240-1355>

Web of Science ResearcherID: [IWU-8465-2023](https://www.webofscience.com/wos/author/record/IWU-8465-2023)

<https://www.webofscience.com/wos/author/record/IWU-8465-2023>

H-Index (nach [ResearchGate](https://www.researchgate.net/)): 5 (Stand: 23.09.2024)

<https://www.researchgate.net/profile/Jan-Christian-Raabe>

SciProfiles: <https://sciprofiles.com/profile/jan-christian-raabe>

Publikationen in wissenschaftlichen Journalen

Total: 10

Erstautorenschaften: 7

Co-Autorenschaften: 3

- J.-C. Raabe, T. Esser, M. J. Poller, J. Albert, *Catal. Today* **2024**, *441*, 114899. <https://doi.org/10.1016/j.cattod.2024.114899>
- J.-C. Raabe, L. Hombach, M. J. Poller, A. Collauto, M. M. Roessler, A. Vorholt, A. K. Beine, J. Albert, *ChemCatChem* **2024**, e202400395. <https://doi.org/10.1002/cctc.202400395>
- S. D. Mürtz, J.-C. Raabe, M. J. Poller, R. Palkovits, J. Albert, N. Kurig, *ChemCatChem* **2024**, e202301632. <https://doi.org/10.1002/cctc.202301632>
- J.-C. Raabe, F. Jameel, M. Stein, J. Albert, M. J. Poller, *Dalton Trans.* **2024**, *53*, 454-466. <https://doi.org/10.1039/D3DT03883A>
- T. Esser, A. Wassenberg, J.-C. Raabe, D. Voß, J. Albert, *ACS Sustainable Chem. Eng.* **2024**, *12*, 543-560. <https://pubs.acs.org/doi/10.1021/acssuschemeng.3c06539>
- J.-C. Raabe, T. Esser, F. Jameel, M. Stein, J. Albert, M. J. Poller, *Inorg. Chem. Front.* **2023**, *10*, 4854-4868. <https://doi.org/10.1039/D3QI00937H>
- J.-C. Raabe, M. J. Poller, D. Voß, J. Albert, *ChemSusChem* **2023**, *16*, e202300072. <https://doi.org/10.1002/cssc.202300072>
- J.-C. Raabe, J. Aceituno Cruz, J. Albert, M. J. Poller, *Inorganics* **2023**, *11*, 138. <https://doi.org/10.3390/inorganics11040138>
- M. J. Poller, S. Bönisch, B. Bertleff, J.-C. Raabe, A. Görling, J. Albert, *Chem. Eng. Sci.* **2022**, *264*, 118143. <https://doi.org/10.1016/j.ces.2022.118143>
- J.-C. Raabe, J. Albert, M. J. Poller, *Chem. – A Eur. J.* **2022**, *28*, e202201084. <https://doi.org/10.1002/chem.202201084>

Konferenzbeiträge

Präsentierender Autor:

- 06/2024: “*The role of main-group elements in polyoxometalates: incorporation of main-group elements in the hetero- and addenda-element position*“ – Vortrag auf der CSC 2024 - 107th Canadian Chemistry Conference in Winnipeg (Kanada).
- 10/2023: “*H₈[PV₅Mo₇O₄₀] (HPA-5): “Single-Crystal Structure Analysis of V(V) Substituted Phosphomolybdates*” – Poster und Vortrag auf dem 10th Anniversary Meeting of the Young Crystallographers in Hamburg (Deutschland).
- 09/2023: “*Tuning the RedOx-properties of phosphomolybdate-polyoxometalates by incorporation of manganese(II)*” – Poster auf der 6th EuChemS Inorganic Chemistry Conference in Wien (Österreich).
- 8/2023: „*Synthesis, characterization and purification of tailor-made polyoxometalate (POM) catalysts for catalytic applications via the lacunary anion [PMo₉O₃₄]⁹⁻*“ – Vortrag auf dem 15th European Congress on Catalysis (EuropaCat 2023) in Prag (Tschechische Republik).

Co-Autor:

- 06/2024: “*Synthesis and characterisation of transition-metal substituted polyoxometalates for catalytic applications*” – Vortrag auf der CSC 2024 - 107th Canadian Chemistry Conference in Winnipeg (Kanada).
- 05/2024: „*Transition-metal substituted polyoxometalates as soluble redox mediators in electrocatalytic biomass conversion*“ – Vortrag auf dem Annual Meeting on Reaction Engineering and Electrochemical Processes 2024 in Würzburg (Deutschland).
- 10/2023: “*Crystallography of the Keggin Polyoxometalate Structure: [PMo₉O₃₄]⁹⁻ vs. [PV₃Mo₉O₄₀]⁶⁻*“ – Poster und Vortrag auf dem 10th Anniversary Meeting of the Young Crystallographers in Hamburg (Deutschland).
- 09/2023: “*Synthesis and characterisation of transition-metal substituted Keggin-type polyoxometalates*” – Poster auf der 6th EuChemS Inorganic Chemistry Conference in Wien (Österreich).
- 08/2023: „*Revealing activating and deactivating effects of carboxylic acids on polyoxometalate-catalysed three-phase liquid-liquid-gas reactions using theoretical and*

analytical tools” – Vortrag auf dem 15th European Congress on Catalysis (EuropaCat 2023) in Prag (Tschechische Republik).

- 08/2023: „*Spectroscopic Characterisation of Keggin-type Polyoxometalate Catalysts*” – Poster auf dem 15th European Congress on Catalysis (EuropaCat 2023) in Prag (Tschechische Republik).
- 06/2023: “*Synthesis and characterisation of metal substituted polyoxometalates for catalytic applications*” – Poster auf der CSC 2023 - 106th Canadian Chemistry Conference in Vancouver (Kanada).
- 06/2022: „*Synthesis of Transition-Metal substituted Polyoxometalates for Applications in RedOx-Catalysis*“ – Poster auf dem 55th Annual Meeting of German Catalysts in Weimar (Deutschland).
- 02/2022: „*Tuning the RedOx-Activity of Polyoxometalate Catalysts by Transition-Metal Substitution*“ – Poster auf 30th ATC Industrial Inorganic Chemistry in Frankfurt (Deutschland).

Posterbeiträge

- Maximilian J. Poller, Jan-Christian Raabe, Jakob Albert: *Tuning the RedOx-Activity of Polyoxometalate Catalysts by Transition-Metal Substitution.*
- Maximilian J. Poller, Jan-Christian Raabe, Jakob Albert: *Synthesis of Transition-Metal substituted Polyoxometalates for Applications in RedOx-Catalysis.*
- Jan-Christian Raabe, Jakob Albert, Maximilian J. Poller: *H₈[PV₅Mo₇O₄₀] – HPA-5 a POM based catalyst with modern applications in green chemical processes.*
- Jan-Christian Raabe, Jan-Dominik Krüger, Maximilian J. Poller, Jakob Albert: *Unique polyoxometalates for acid and redox catalysis – synthesis and modification.*
- Maximilian J. Poller, Jan-Christian Raabe, Jakob Albert: *Synthesis and characterisation of transition-metal substituted polyoxometalates for catalytic applications.*
- Jan-Christian Raabe, Maximilian J. Poller, Jakob Albert: *Tuning the RedOx-properties of phosphomolybdate- Polyoxometalates by incorporation of Manganese(II).*
- Maximilian J. Poller, Jan-Christian Raabe, Tobias Esser, Jakob Albert: *Synthesis and Characterisation of transition-metal substituted Keggin-type Polyoxometalates.*
- Maximilian J. Poller, Jan-Christian Raabe, Jan-Dominik Krüger, Jakob Albert: *Spectroscopic Characterization of Keggin-type Polyoxometalate Catalysts.*

-
- Jan-Christian Raabe, Zainab Yusufzadeh, Jakob Albert, Maximilian J. Poller: *H₈[PV₅Mo₇O₄₀] (HPA-5): Single-Crystal Structure Analysis of V(V) Substituted Phosphomolybdates.*
 - Zainab Yusufzadeh, Jan-Christian Raabe, Jakob Albert, Maximilian J. Poller: *Crystallography of the Keggin Polyoxometalate Structure: [PMo₉O₃₄]⁹⁻ vs. [PV₃Mo₉O₄₀]⁶⁻.*
 - Jan-Dominik Krüger, Jan-Christian Raabe, Maximilian J. Poller, Jakob Albert: *Unique polyoxometalates for acid and redox catalysis – synthesis and modification.*

Inhaltsverzeichnis

Publikationsliste	i
Abkürzungsverzeichnis	iv
Verbindungsverzeichnis	vii
1 Zusammenfassung	1
2 Abstract	5
3 Einleitung	9
3.1 Polyoxometallate	9
3.1.1 Grundlagen	9
3.1.2 Strukturtypen	11
3.1.3 Synthesemethoden für Polyoxometallate	16
3.1.4 Übergangsmetallsubstituierte Polyoxometallate	21
3.2 Anwendungen für Polyoxometallate	23
3.2.1 Oxidative und Säurekatalyse mit Polyoxometallaten	24
3.2.2 Reduktive Katalyse mit Polyoxometallaten	28
3.3 Charakterisierung von Polyoxometallaten	33
4 Zielsetzung und Problemstellung der Arbeit	36
5 Kumulativer Teil der Dissertation/Synopsis	40
5.1 Synthese, Charakterisierung und Reinigung maßgeschneiderter Keggin- Phosphormolybdatstrukturen	41
5.2 Synthese und Charakterisierung von Mn(II)/V(V) gemischt substituierten Phosphormolybdaten	44
5.3 Vergleichende spektroskopische und elektrochemische Studie über V(V) substituierte Keggin-Typ Phosphormolybdate und -wolframate	46
5.4 Synthese und Anwendung Co(II) substituierter Keggin-Phosphormolybdat- strukturen in der homogenkatalysierten Hydroformylierung	48
5.5 Einfluss des Heteroelementes auf die Polyoxometallat-Strukturtypbildung	51

5.6	Synthese, Charakterisierung und katalytische Anwendungen V(V) substituierter Anderson-Evans Polyoxometallate für die oxidative Umsetzung von Monofuranderivaten	54
6	Diskussion	57
7	Literaturliste	76
	Anhang	viii
	Gefahrstoffliste	viii
	Online verfügbare „supporting information“	xv
	Verwendete Methoden und Software	xvi
	Bilderanhang	xxviii
	Danksagung	xxxviii
	Lebenslauf	xl
	Eidesstattliche Versicherung	xliii

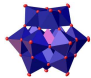


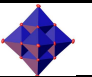
Abkürzungsverzeichnis

AAS	Atomabsorptionsspektrometrie
CAS-RN	Aus dem Englischen: <i>chemical abstracts service registry number</i>
Co-Acetat	Cobalt-(II)-acetat
CV	Cyclovoltammetrie
D1	Aus dem Englischen: <i>Delay</i>
DFT	Dichtefunktionaltheorie
ECODS	Aus dem Englischen: <i>Extraction-coupled oxidative desulfurization</i>
EDX	Aus dem Englischen: <i>energy-dispersive X-ray spectroscopy</i>
F-AAS	Flammen-Atomabsorptionsspektrometrie
FA	Ameisensäure (im Englischen: <i>formic acid</i>)
GC	Gaschromatographie
GC-TCD	Aus dem Englischen: <i>thermal conductivity detector</i> Gaschromatographie (mit Wärmeleitfähigkeitsdetektor)
GHS	Aus dem Englischen: <i>Globally Harmonized System of Classification and Labelling of Chemicals</i>
HMF	5-(Hydroxymethyl)furfural
HPA	Heteropolyanion/Heteropolysäure (im Englischen: <i>heteropolyacid</i>)
HPA-5	Heteropolysäure-5 $\text{H}_8[\text{PV}_5\text{Mo}_7\text{O}_{40}]$
HPLC	Aus dem Englischen: <i>high-performance liquid chromatography</i>
HyFo	Hydroformylierung
ICP-OES	Aus dem Englischen: <i>Inductively Coupled Plasma Optical Emission spectroscopy</i>

IPA	Isopolyanion/Isopolysäure (im Englischen: <i>isopolyacid</i>)
IR	Infrarot
IUPAC	Aus dem Englischen: <i>International Union of Pure and Applied Chemistry</i>
KMR	kanzerogen, mutagen, reproduktionstoxisch
LMCT	Aus dem Englischen: <i>ligand to metal charge-transfer</i>
LPO	Aus dem Englischen: <i>low-pressure-Oxoverfahren</i>
MO	Molekülorbital
MPI	Max-Planck-Institut
MS	Maleinsäure
Na-TPPTS	Natriumtriphenylphosphintrisulfonat
NMR	Aus dem Englischen: <i>Nuclear magnetic resonance</i> , im Deutschen: Kernresonanzspektroskopie
NPD	Aus dem Englischen: <i>Non-positive definite</i>
NS	Aus dem Englischen: <i>Number of Scans</i>
O1	Aus dem Englischen: <i>Transmitter Frequency Offset</i> für Kanal F1
ODS	Aus dem Englischen: <i>oxidative desulfurization</i>
OxFA	Oxidative Ameisensäuregewinnung aus Biomasse
pH	Negativer dekadischer Logarithmus der Wasserstoffionenkonzentration: $\text{pH} = -\log(c(\text{H}_3\text{O}^+))$
POM	Polyoxometallat
PSE	Periodensystem der Elemente
RedOx	Reduktion/Oxidation
SW	Aus dem Englischen: <i>Spectral Width</i>
SWV	Square-Wave-Voltammetrie

TD	Aus dem Englischen: <i>Time Domain Data Size</i>
TGA	Thermogravimetrische Analyse
TMSPOM	Aus dem Englischen: <i>transition-metal-substituted polyoxometalate</i>
TMS-systems	Aus dem Englischen: <i>temperature dependant multicomponent solvent systems</i>
UV-Vis	Aus dem Englischen: <i>Ultraviolet-visible</i>
XRD	Aus dem Englischen: <i>X-ray diffraction</i>
• p-XRD	• Pulver-XRD
• sc-XRD	• Aus dem Englischen: <i>single-crystal-XRD</i>

Verbindungsverzeichnis

Keggin 		Anderson-Evans 	
HPMo	$H_3[PMo_{12}O_{40}]$	NaTeV _x W	$Na_{6+x}[TeV_xW_{6-x}O_{24}]$
HPV _x Mo	$H_{3+x}[PV_xMo_{12-x}O_{40}]$	NaTeV _x Mo	$Na_{6+x}[TeV_xMo_{6-x}O_{24}]$
HPW	$H_3[PW_{12}O_{40}]$	NaSbW	$Na_7[SbW_6O_{24}]$
NaPV _x W	$Na_{3+x}[PV_xW_{12-x}O_{40}]$	Lacunary 	
HPV _x Mn _y Mo	$H_{3+x+4y}[PV_xMn_yMo_{12-x-y}O_{40}]$	Na ₉ [PMo ₉ O ₃₄]	Na ₉ [PMo ₉ O ₃₄]
HPCo _x Mo	$H_{3+4x}[PCo_xMo_{12-x}O_{40}]$	Na ₉ [PW ₉ O ₃₄]	Na ₉ [PW ₉ O ₃₄]
NaPW _x Mo	$Na_3[PW_xMo_{12-x}O_{40}]$	Na ₉ [AsW ₉ O ₃₄]	Na ₉ [AsW ₉ O ₃₄]
NaPNb _x Mo	$Na_{3+x}[PNb_xMo_{12-x}O_{40}]$	Sonstige POMs	
NaPV _x Nb _y Mo	$Na_{3+x+y}[PV_xNb_yMo_{12-x-y}O_{40}]$	Na ₈ [W ₁₂ O ₄₀]	
NaPFeMo	$Na_6[PFeMo_{11}O_{40}]$	Na ₁₂ [P ₄ W ₁₄ O ₅₈]	
NaPCoMo	$Na_7[PCoMo_{11}O_{40}]$		
NaPNiMo	$Na_7[PNiMo_{11}O_{40}]$		
<i>n</i> Bu ₄ NPCu ₂ Mo	$(nBu_4N)_{11}[PCu_2Mo_{10}O_{40}]$		
NaPZnMo	$Na_7[PZnMo_{11}O_{40}]$		
Lindqvist 			
KNb	$K_8[Nb_6O_{19}]$		

1 Zusammenfassung

Bei den Polyoxometallaten (POMs) handelt es sich um anorganische, polyanionische Clusterverbindungen, die aus ecken- und kantenverknüpften Oktaedern bestehen. In der Koordinationschemie nehmen POMs eine zentrale Stellung ein, da es sich um sogenannte Oxometallkomplexe handelt, die eine hohe Stabilität bzw. Löslichkeit im wässrigen Medium aufweisen und in sauren Medien synthetisiert werden. In dieser Eigenschaft sind die POMs den klassischen metallorganischen Koordinationsverbindungen überlegen, die sich unter Einfluss von Wasser zersetzen würden. Daher können POMs als Katalysatoren in wässrigen Reaktionsmedien eingesetzt werden, wodurch auf schädliche, organische Lösungsmittel verzichtet werden kann. Ein weiterer Vorteil besteht darin, dass POMs leicht aus den entsprechenden Metallatprecursoren der fünften (Vanadium) und sechsten Gruppe (Molybdän und Wolfram) aus dem Periodensystem (PSE) synthetisiert werden können. Somit stellen POMs ideale Kandidaten für die Entwicklung und die Zukunft grüner und nachhaltiger Prozesse dar. Bevor jedoch mit einem POM eine katalytische Anwendung geplant werden kann, muss erstmal ein robustes und reproduzierbares Synthesekonzept erarbeitet werden, mit dem der POM-Katalysator von Interesse synthetisiert werden kann. Hierfür wurden im Rahmen dieser Arbeit verschiedene Fragestellungen untersucht, die für ein Verständnis der POM-Chemie und für eine gezielte Syntheseplanung von zentraler Bedeutung sind. Generell sind für die POM-Synthesen das Lacunary- und das *self-assembly*-Konzept von zentraler Bedeutung, auf denen die Synthesen und Untersuchungen dieser Arbeit basieren.

In der POM-Chemie ist es üblich, die Elemente, die in einer POM-Struktur verschiedene Positionen einnehmen können, durch Fremdelemente zu substituieren. Das Ziel besteht darin, sich die Eigenschaften des Substitutionselementes zu Nutzen zu machen, so zum Beispiel in der homogenen RedOx-Katalyse. Dabei werden Hauptgruppenelemente zur Substitution des Heteroelementes in Heteropolyanion (HPA)-Strukturen verwendet und Übergangselemente zur Substitution der Gerüstelemente. Auch wenn das Lacunary-Konzept bereits erforscht wurde, ist es weitestgehend unbekannt in Bezug auf die Synthese verschiedener Phosphormolybdate. Dies lässt sich durch die weitverbreitete Annahme erklären, dass das $[\text{PMo}_9\text{O}_{34}]^{9-}$ Anion zu instabil wäre und nur durch organische Kationen in organischen Medien stabilisiert werden könne. Das Lacunary-Konzept mit dem Anion $[\text{PMo}_9\text{O}_{34}]^{9-}$ konnte jedoch im Rahmen dieser Arbeit erfolgreich auf die wässrige Synthesechemie erweitert werden. Hierfür wurde das Lacunary-Anion *in-situ* generiert und durch Zugabe von Precursoren eines Fremdelementes zum *transition-*

metal-substituted polyoxometalate (TMSPOM) umgesetzt. So konnten zahlreiche TMSPOMs, die mit verschiedenen Übergangselementen substituiert wurden und die auf Basis vom Phosphormolybdat beruhen, synthetisiert werden. Limitierungen ergaben sich unter Verwendung der späten Übergangselemente Kupfer-(II) und Zink-(II) und den Hauptgruppenelementen Indium-(III) und Zinn-(IV).

Mit dem *self-assembly* Ansatz konnten die Elemente V(V), Mn(II) und Co(II) in die Phosphormolybdatstruktur eingebaut werden. Dabei konnte gezeigt werden, dass der maximale Substitutionsgrad stark abhängig von der Oxidationsstufe des entsprechenden Übergangselementes ist. Das *self-assembly* Synthesekonzept konnte auch angewendet werden, um V(V) substituierte Anderson-Evans-POMs auf Basis der Molybdo- und Wolframatotellurate zu synthetisieren. Auch wenn die Übergangsmetallsubstitution in Anderson-Evans-Strukturen nach dem Stand der Literatur noch keine signifikante Rolle spielt, konnten mit der vorliegenden Arbeit die ersten Methoden entwickelt werden, um in Zukunft weitere Übergangsmetallsubstituierte TMSPOMs auf Basis des Anderson-Evans Strukturtyps zu synthetisieren. Diese Erkenntnisse sind insbesondere für die homogene RedOx-Katalyse interessant, da somit neuartige Struktur-motive für die Katalyse bereitstehen.

Wenn entsprechende, alkalimetallhaltige Precursoren für die POM-Synthese eingesetzt werden, bilden sich Alkalihalogenide als Nebenprodukte. Hierfür wurde ein effizientes *downstream* Dialyseverfahren basierend auf einer Nanofiltration an einer nanoporösen Membran etabliert. Mit diesem Konzept konnte der POM effizient unter Wahrung einer hohen Ausbeute nach vier Zyklen der Diafiltration entsalzt werden. Somit kann auf die weniger effizienten Reinigungsverfahren, wie die Kristallisation oder die Etherat-Methode verzichtet werden, die mit einem hohen Ausbeuteverlust und einem teilweise niedrigen Reinigungserfolg einhergehen.

Alle TMSPOMs wurden mit diversen spektroskopischen, elektrochemischen und kristallographischen Methoden charakterisiert, wobei gezeigt werden konnte, dass die jeweiligen Substitutionselemente einen signifikanten Einfluss auf die spektroskopischen und insbesondere elektrochemischen Eigenschaften der TMSPOMs nahmen. Durch den Einbau verschiedener RedOx-aktiver Elemente konnte gezeigt werden, dass eine gezielte Beeinflussung der RedOx-Potentiale möglich ist, was ein erster Schritt in Richtung der Synthese maßgeschneiderter TMSPOMs für eine konkrete katalytische Anwendung darstellt. Durch die detaillierte Charakterisierung der TMSPOM-Materialien wurden vertiefte Einblicke in die Festkörper- und Lösungsanalytik

der Materialien erlangt, die die Grundlagen für eine Anwendung der TMSPOMs in der homogenen RedOx-Katalyse darstellen.

In der POM-Chemie ist es ebenfalls gängige Praxis, verschiedene Heteroelemente für die Synthese unterschiedlicher HPA-Strukturen einzusetzen. Es ist bekannt, dass verschiedene Heteroelemente an der Bildung verschiedener HPA-Struktur motive beteiligt sind, jedoch fehlt eine systematische Untersuchung in Bezug auf diese Beobachtung. In dieser Arbeit wurde der Einfluss verschiedener Gruppe 15 Elemente auf die POM-Bildung bei zwei pH-Werten (1 und 5) analysiert. Unter Zuhilfenahme von computergestützten Simulationen mittels Dichtefunktionaltheorie (DFT) und Kristallographie konnte der Einfluss des jeweiligen Heteroelementes auf die sich ausbildenden Strukturtypen analysiert werden. Alle DFT-Simulationen wurden dabei in der Forschungsgruppe von Prof. Dr. Matthias Stein am Max-Planck-Institut für Dynamik komplexer technischer Systeme (MPI) von Froze Jameel und Matthias Stein durchgeführt. Mittels DFT wurde die Thermodynamik der Bildung verschiedener Koordinationsgeometrien mit den verschiedenen Heteroelementen in Bezug auf die Keggin- (tetraedrisch) und Anderson-Evans-Struktur (oktaedrisch) simuliert. Es wurde der Trend gefunden, dass leichte Elemente, wie das Phosphor (P), die Ausbildung von Keggin-Strukturen fördern, während schwerere Elemente, wie das Antimon (Sb), die Bildung einer Anderson-Evans-Struktur begünstigen. Auch der Einfluss der weniger erforschten Periode vier Elemente, wie der vom Arsen (As), konnte analysiert werden. Es zeigte sich, dass bedingt durch die Größe des As-Atoms die Ausbildung einer Keggin-Struktur erschwert wurde und die Bildung einer Anderson-Evans-Struktur nicht möglich war. Stattdessen wurden mit As offene Struktur motive auf Basis des $[\text{AsW}_9\text{O}_{34}]^{9-}$ Anions gebildet, um die erhöhte, strukturelle Spannung, die durch den AsO_4^{3-} Tetraeder resultiert, auszugleichen. Die so gesammelten Erkenntnisse tragen dazu bei, die POM-Strukturtypbildung in Abhängigkeit des jeweiligen Heteroelementes besser zu verstehen.

Einige der hergestellten TMSPOMs konnten erfolgreich in verschiedenen katalytischen Anwendungen eingesetzt werden. So zeigte sich, dass eine Hydroformylierung (HyFo) von 1-Hexen unter Verwendung Co(II) substituierter Phosphormolybdate möglich war. Die so erzielten Ergebnisse sind daher von besonderer Bedeutung, da in der Literatur TMSPOMs für die HyFo bislang keine Rolle spielen, insbesondere solche nicht, in denen das katalytisch aktive Element in der Gerüstmetallposition des POMs integriert wurde. Damit eröffnet sich für die HyFo-Katalysatoren eine neue Substanzklasse, deren katalytischer Einfluss es noch zu erforschen gilt. Der katalytische Einfluss der V(V) substituierten Anderson-Evans-POMs konnte anhand der Oxida-

tion von Monofuranderivaten untersucht werden. Es zeigte sich, dass eine Oxidation der Monofuranderivate zu Plattformchemikalien wie Ameisensäure (*formic acid*, FA) und Maleinsäure (MS) an den C₁-funktionalisierten Derivaten (wie Furfural) möglich ist. Die katalytische Umsetzung weniger funktionalisierter Derivate (Furanon und 2-Methylfuran) war erschwert, da dem POM-Katalysator keine funktionellen Gruppen zum Angriff zur Verfügung stehen. Diese sogenannten „Struktur-Eigenschaftsbeziehungen“ erweitern das Verständnis in Bezug auf die oxidative Umsetzung komplexerer Biopolymere (wie den Huminen), deren Zusammensetzung auf Basis von Monofuranderivaten beruhen.

Mit denen im Rahmen dieser Arbeit gesammelten Erkenntnissen über die POM-Bildung und die Entwicklung neuartiger Synthese- und Reinigungskonzepte für TMSPOMs, wurde ein Fundament aufgebaut, mit denen zahlreiche, neuartige TMSPOMs erfolgreich und reproduzierbar synthetisiert und hinterher gereinigt werden können. Die hier gesammelten Ergebnisse stellen auch die Grundlage für spätere katalytische Anwendungen dar. Insbesondere durch den Einbau verschiedener Übergangselemente in verschiedene POM-Strukturen bekommt der resultierende TMSPOMs neuartige Eigenschaften, die sich insbesondere auf die RedOx-Potentiale auswirken, sodass in Zukunft maßgeschneiderte TMSPOMs für eine konkrete katalytische Anwendung hergestellt werden können. Somit sind die hier gesammelten Ergebnisse nicht nur vom akademischen Interesse her nützlich, sondern helfen auch dabei katalytische Probleme und damit die Herausforderungen im 21. Jahrhundert effizient anzugehen.

2 Abstract

Polyoxometalates (POMs) are inorganic, polyanionic cluster compounds consisting of corner- and edge-linked octahedra. POMs play a fundamental role in coordination chemistry, as they are so-called „oxometal“ complexes that are highly stable, soluble in aqueous medium and are synthesized in acidic media. In this property, POMs are superior to classic organometallic coordination compounds, which would decompose under the influence of water. POMs can therefore be used as catalysts in aqueous reaction media, so that harmful organic solvents can be avoided. A further advantage is that POMs can be easily synthesized from the corresponding metallate precursors of the fifth (vanadium) and sixth group (molybdenum and tungsten) from the periodic table of elements. POMs are therefore ideal candidates for the development and future of green and sustainable processes. Before planning a catalytic application using a POM, a robust and reproducible synthesis concept must first be developed for synthesizing the POM of interest. For this purpose, different research questions were investigated in this work, which are of fundamental importance for an understanding of POM chemistry and for target-oriented synthesis planning. In general, the lacunary and *self-assembly* concepts are of great interest for POM syntheses, on which the syntheses and investigations in this work are based.

In POM chemistry, it is common to substitute elements, that can occupy different positions in a POM structure with foreign elements. The aim is to utilize the properties of the substitution element, for example in the field of homogeneous RedOx catalysis. Main-group elements are used to substitute the heteroelement in heteropolyanion (HPA) structures and transition-elements are used to substitute the framework elements. The lacunary concept has already been explored, but it is still widely unknown for the synthesis of various phosphomolybdates. This can be explained by the widely accepted assumption that the $[\text{PMo}_9\text{O}_{34}]^{9-}$ anion is too labile and can only be stabilized by organic cations in organic media. However, the lacunary concept with the anion $[\text{PMo}_9\text{O}_{34}]^{9-}$ was successfully extended to aqueous synthesis chemistry in this work. Herefore, the lacunary anion was synthesized *in situ* and converted to transition-metal-substituted polyoxometalates (TMSPOM) by adding precursors of a foreign element. In this way, different TMSPOMs, substituted with various transition-elements based on phosphomolybdate, could be synthesized. Limitations were found using the late transition-elements Cu(II) and Zn(II) and the main-group elements In(III) and Sn(IV).

Using the *self-assembly* approach, the elements V(V), Mn(II) and Co(II) could be incorporated into the phosphomolybdate structure. It was shown that the maximum degree of substitution is strongly dependent on the oxidation state of the corresponding transition-element. The *self-assembly* synthesis concept could also be applied to synthesize V(V) substituted Anderson-Evans POMs based on the molybdo- and tungstatotellurates. Despite transition-metal substitution in Anderson-Evans structures is still not playing a significant role according to the state of the art, the present work has provided the first methods to synthesize further TMSPOMs based on the Anderson-Evans structure type in the future. These findings are of particular interest for homogeneous RedOx catalysis, as novel structural motifs are available for catalysis.

If alkali metal containing precursors are used during POM synthesis, alkali halides will be formed as by-products. So, an efficient downstream dialysis process based on nanofiltration on a nanoporous membrane was established. Using this concept, the POM could be efficiently desalted while maintaining a high yield after four cycles of diafiltration. This means that less efficient purification methods such as crystallization or the etherate method, which are often accompanied by a high yield loss and sometimes low purification success, are no longer necessary.

All TMSPOMs were characterized using a wide range of spectroscopic, electrochemical and crystallographic methods and it was shown that the respective substitution elements had a significant influence on the spectroscopic and especially electrochemical properties of the TMSPOMs. By incorporating various RedOx-active elements, it could be shown that a targeted influence on the RedOx potentials is possible, which represents a first step towards the synthesis of tailor-made TMSPOMs for a specific catalytic application. Due to the detailed characterization of the TMSPOM-materials deep insights into the solid-state and solution behavior were obtained, which are of great importance for an application of the TMSPOM in the homogeneous RedOx catalysis.

In POM chemistry, it is also common to use different heteroelements for the synthesis of different HPA structures. It is generally known that different heteroelements are involved in the formation of different HPA structural motifs, but a systematic study regarding this observation is still missing. In this work, the influence of different group 15 elements on POM formation at two pH values (1 and 5) was analyzed. With the help of computer-supported simulations by using density functional theory (DFT) and crystallography, the influence of the respective heteroelement on the forming structure types was analyzed. All DFT simulations were done by

Froze Jameel and Matthias Stein in the research group of Prof. Dr. Matthias Stein at the Max-Planck-Institute for Dynamics of Complex Technical Systems (MPI). DFT was used to calculate the thermodynamics of the formation for different coordination geometries with the various heteroelements in relation to the Keggin- (tetrahedral) and Anderson-Evans (octahedral) structure. The trend was found that light elements, such as phosphorous (P), favor the formation of Keggin-type structures, while heavier elements, such as antimony (Sb), favor the formation of an Anderson-Evans structure-type. The influence of the less explored period four elements, such as arsenic (As), was also analyzed. It was found that due to the size of the As atom, the formation of a Keggin structure was more difficult and the formation of an Anderson-Evans structure was not possible. Instead, open structural motifs based on the $[\text{AsW}_9\text{O}_{34}]^{9-}$ anion were formed with As in order to compensate the increased structural tension resulting from the AsO_4^{3-} tetrahedron. The knowledge gained in this way contributes to a better understanding of the POM structure-type formation depending on the respective heteroelement.

Some of the synthesized TMSPOMs were successfully used in various catalytic applications. It was shown that hydroformylation (HyFo) of 1-hexene was possible using Co(II) substituted phosphomolybdates. The results obtained in this way are of great importance, as TMSPOMs have not played a major role in HyFo in the literature to date, especially not those in which the catalytically active element was incorporated into the framework metal position of a POM. This opens up a new substance class for HyFo catalysts, of which the catalytic influence still needs to be investigated. The catalytic influence of the V(V) substituted Anderson-Evans POMs was analyzed on the oxidation of monofuran derivatives. It was shown that oxidation of the monofuran derivatives to platform chemicals such as formic acid (FA) and maleic acid (MS) is possible based on the C_1 -functionalized derivatives (like furfural). The catalytic conversion of less functionalized derivatives (furanone and 2-methylfuran) was more difficult, because there are no functional groups available for the attack of the POM catalyst. These so-called „structure-property relationships“ expand the understanding of the oxidative conversion of more complex biopolymers (such as humins), the composition of which is based on monofuran derivatives.

With the knowledge gained in this work on the POM formation and the development of novel synthesis and purification concepts for TMSPOMs, a fundament has been built up, with which numerous, novel TMSPOMs can be successfully and reproducibly synthesized and successfully purified. The results obtained also form the basis for later catalytic applications. In particular, the incorporation of various transition-elements into different POM structures gives the resul-

ting TMSPOMs novel properties, which have a particular effect on the RedOx potentials, so that customized TMSPOMs can be produced for a specific catalytic application in the future. Therefore, the collected results are not only useful from an academic point of view, but also help to efficiently adress catalytic problems and thus the challenges of the 21st century.

3 Einleitung

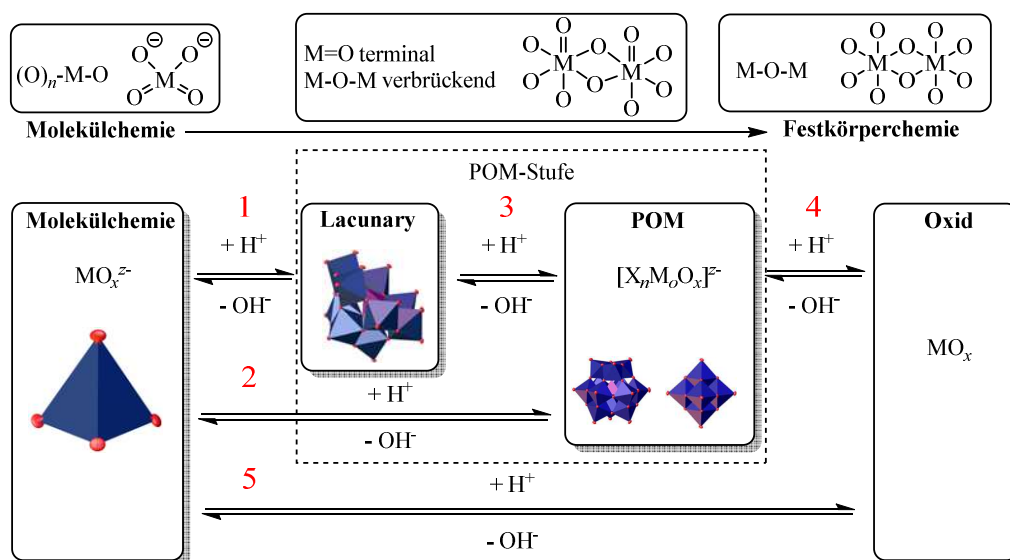
3.1 Polyoxometallate

3.1.1 Grundlagen

Polyoxometallate (POMs) sind eine Gruppe von anorganischen, polyanionischen Clusterverbindungen, die vorwiegend mit Elementen der fünften (Vanadium V, Niob Nb und Tantal Ta) und sechsten Gruppe (Molybdän Mo und Wolfram W) aus dem Periodensystem (PSE, Periodensystem der Elemente), jeweils in ihrer höchsten Oxidationsstufe, gebildet werden.^[1] Koordinationsschemisch handelt es sich bei POMs um Oxometallkomplexe, in denen der Oxoligand zwei Metalle M verbrückend M-O-M oder terminal M=O koordiniert (Abbildung 1). In den POMs werden definierte Metall-Sauerstoffpolyeder MO_x gebildet, bei denen es sich meistens um Oktaeder MO_6 handelt, die über gemeinsame Ecken und Kanten miteinander verknüpft sind. Eine Verknüpfung der Oktaeder über gemeinsame Flächen kommt in der POM-Chemie eine untergeordnete Rolle zu, da sich die stark positiv geladenen Metallionen in ihren höchsten Oxidationsstufen durch die räumliche Nähe zu stark abstoßen.^[2,3] Die MO_x Einheiten können sich in der POM-Chemie mit Heteroatom- (X) Polyedern XO_x verknüpfen, die sich meistens im Zentrum der POM-Struktur anordnen.^[4-6] Bei den Heteroelementen handelt es sich hauptsächlich um Hauptgruppenelemente aus dem PSE, wobei Phosphor P die bedeutendste Rolle zukommt. Weitere bekannte Heteroelemente stellen Arsen As^[7], Silizium Si^[8-11] und auch Tellur Te dar.^[12] POMs mit Heteroelementen werden als Heteropolyanionen oder Heteropolysäuren – im Englischen *heteropolyacids* - (HPAs) bezeichnet, während POMs ohne Heteroelemente Isopolyanionen oder Isopolysäuren – im Englischen *isopolyacids* – (IPAs) genannt werden.^[5,13] POMs zeichnen sich durch ihre enorme molekulare Größe (teilweise ein oder mehrere Nanometer) und durch ihre stark anionischen Ladungen aus. Es sind POM-Strukturen bekannt, die teilweise aus mehr als 300 Atomen aufgebaut sind und die Größendimensionen von Proteinen annehmen.^[14-16] Historisch dauerte es jedoch bis zum Jahr 1991, als durch Pope und Müller^[17] das Potential der POMs für die Herstellung maßgeschneiderter Materialien erkannt wurde, wodurch sich die POM Chemie zu einem interdisziplinären Forschungsgebiet entwickelte mit zahlreichen Anwendungen in der Katalyse und Biomedizin.^[18-20]

Thematisch lassen sich POMs in der anorganischen Strukturchemie zwischen der klassischen Molekülchemie (meist lösliche, kleine, definierte und aus wenigen Atomen bestehende Mole-

küle) und der Festkörperchemie, den Metalloxiden (meist unlösliche, teilweise undefinierte und aus annähernd unendlich vielen Atomen bestehende Metall-Sauerstoff Verbände, dominiert durch unendlich viele M-O-M Bindungen) einordnen (Abbildung 1). Formal gehören POMs demnach zu den Metalloxiden, jedoch wird die POM-Chemie zur klassischen Molekülchemie gezählt, da es sich bei POMs um Moleküle mit definierter Struktur und einer definierten Anzahl an Atomen handelt, die zudem meist eine sehr hohe Wasserlöslichkeit aufweisen.^[21]



Beispiele:

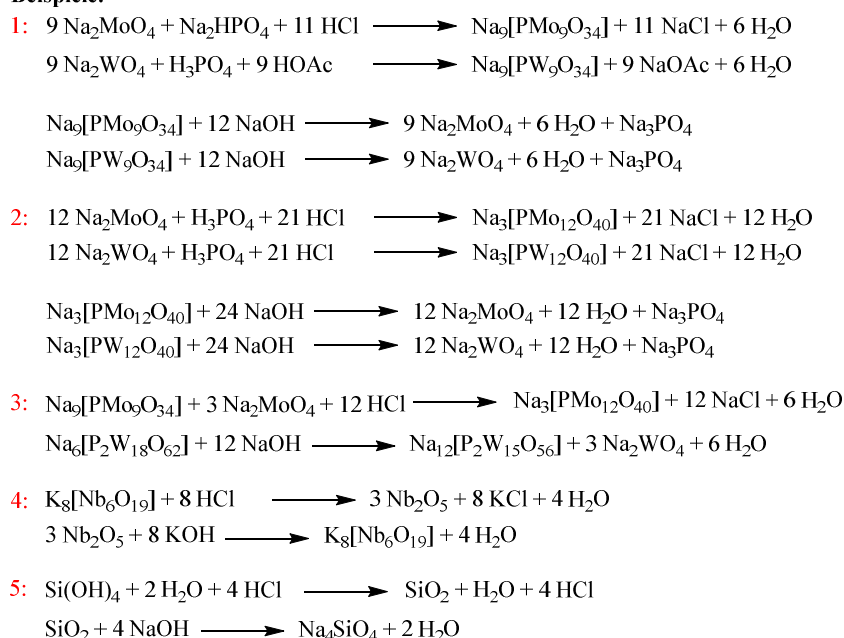


Abb. 1: Einordnung des Themengebietes der POM-Chemie zwischen den Gebieten der Molekül- und Festkörperchemie in der anorganischen Chemie.^[21]

Für die Schritte 1 bis 5 in Abbildung 1 gibt es in der Molekül- und Festkörperchemie zahlreiche Beispielreaktionen:

1 bis 3: Formal können aus molekularen Vorläuferverbindungen wie dem Molybdat MoO_4^{2-} oder dem Wolframat WO_4^{2-} (allgemein Metallationen MO_4^{2-}) POMs oder Lacunary-Strukturen durch Ansäuern wässriger Lösungen gebildet werden.^[21,22] Eine Rückreaktion zu den molekularen Vorläuferverbindungen kann im basischen Medium induziert werden.^[22,23] Eine Sonderstellung nimmt hierbei die kontrolliert basische Behandlung von definierten POM-Strukturen ein, wobei sich die POM-Struktur hierbei nicht vollständig zu den Metallaten zersetzt.^[23–25] Stattdessen lassen sich selektiv nur einzelne MO_4^{2-} Anionen entfernen, wodurch vakante, lacunäre POM-Strukturen gebildet werden.^[23] Das bedeutet, dass POMs kinetisch stabil sind und sich bei hinreichend basischen pH-Werten zunächst zu Lacunary-Strukturen umwandeln, die sich bei noch basischeren pH-Werten zu den MO_4^{2-} Anionen zersetzen.^[26] Im sauren pH-Medium lässt sich umgekehrt aus der lacunären POM-Struktur die intakte POM-Struktur durch Zugabe von weiteren MO_4^{2-} Ionen regenerieren.^[27]

4: Seltener hingegen ist der Fall, bei dem aus einem Metalloxid eine POM-Struktur im basischen Medium gebildet werden kann. Als Beispiele lassen sich die basischen Schmelzsynthesen nennen, bei denen Diniob- und Ditantalpentoxid (Nb_2O_5 und Ta_2O_5) mit Kaliumhydroxid KOH zu den Hexametallaten, dem Hexaniobat $[\text{Nb}_6\text{O}_{19}]^{8-}$ und Hexatantalat $[\text{Ta}_2\text{O}_{19}]^{8-}$ umgesetzt werden können. Häufiger hingegen sind die Fälle bekannt, in denen POM-Strukturen durch stetiges Ansäuern zu Oxiden umgesetzt werden. Als prominentes Beispiel lässt sich die saure Ausfällung von Nb_2O_5 aus Lösungen von $[\text{Nb}_6\text{O}_{19}]^{8-}$ aufführen.^[28]

5: Auch direkte Übergänge zwischen den molekularen Vorläuferverbindungen und den Oxiden, sind bekannt. So lassen sich aus Kieselsäuren H_4SiO_4 im sauren Reaktionsmedium Siliziumdioxid SiO_2 bilden, welches im basischen Medium die Kieselsäuren zurückbildet.^[22] Auch aus WO_4^{2-} können Wolfram-(VI)-oxide durch Ansäuern mit Mineralsäuren (Salzsäure) gebildet werden.^[29]

3.1.2 Strukturtypen

Durch die verschiedenen Möglichkeiten die MO_x und XO_x Polyeder miteinander zu verknüpfen, resultiert eine enorme, strukturelle Vielfalt an POMs. Der bekannteste Strukturtypvertreter stellt die Keggin-Struktur mit der allgemeinen Summenformel $[\text{XM}_{12}\text{O}_{40}]^{n-}$ dar, wobei der Keggin-Typ durch die Anwesenheit eines Heteroatoms zu den HPA-Strukturen gerechnet wird.^[1,30] Die erste erfolgreiche Synthese eines Keggin-Anions erfolgte 1826 durch Berzelius, wobei es sich dabei um das Phosphormolybdat Anion $[\text{PMo}_{12}\text{O}_{40}]^{3-}$ handelte.^[31] Im Jahr 1864 wurde erfolg-

reich durch Marignac das Silikowolframat Anion $[\text{SiW}_{12}\text{O}_{40}]^{4-}$ dargestellt.^[32] Eine genaue Vorstellung über die strukturchemischen Eigenschaften der neu isolierten Verbindungen bestand zu diesem Zeitpunkt allerdings noch nicht. Erst mit den Arbeiten von Rosenheim und Liebknecht^[33] am Anfang des 20. Jahrhunderts, begannen die ersten Versuche zur systematischen Charakterisierung und zur strukturellen Aufklärung dieser neuartigen Verbindungen.^[34] So wurden die ersten Hypothesen aufgestellt, dass es sich bei diesen Verbindungen um polyanionische Cluster handeln könnte, dessen Polyeder über gemeinsame Ecken und Kanten verknüpft sein könnten.^[35,36] Erst im Jahr 1934 wurde zum ersten Mal die Struktur des Phosphorwolframat-Anions $[\text{PW}_{12}\text{O}_{40}]^{3-}$ durch den Namensgeber James Keggin diskutiert, wobei es sich bei dieser Verbindung um das Wolframanalogon des Phosphormolybdat-Anions handelt.^[37] Insbesondere trugen moderne Röntgenbeugungsexperimente dazu bei, dass der molekulare Aufbau des Keggin-Strukturtyps mittlerweile als vollständig aufgeklärt gilt.^[38,39] Strukturell verknüpfen sich in der Keggin-Struktur die zwölf MO_6 Oktaeder um einen zentralen XO_4 Tetraeder, wobei jedes der vier Sauerstoffatome, die das zentrale Heteroatom X koordinieren, Teil einer M_3O_{13} Triade sind (Abbildung 2).^[38]

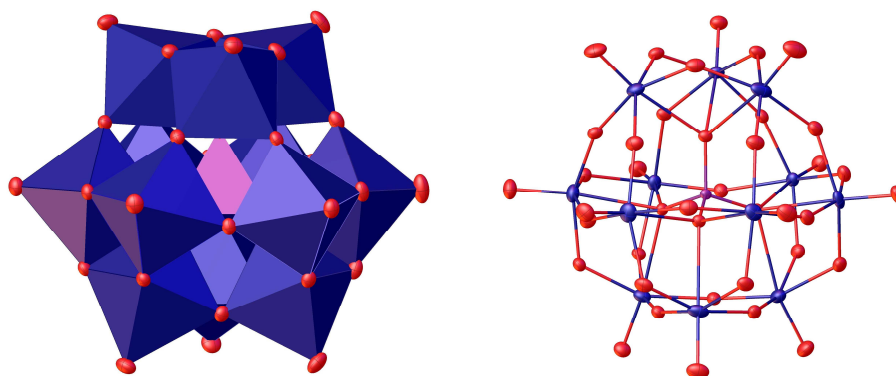


Abb. 2: Schematische Darstellung einer Keggin-Typ POM-Struktur. Polyederdarstellung (links) und atomistische Darstellung (rechts). Farbcode: O-Atome (rot), Metalle (blau) und Heteroelement (violett).

Auffällig in den Einkristallstrukturdaten ist, dass die Bindungslängen der Sauerstoff-Metallbindungen M-O (2.4 \AA) aller Sauerstoffatome, die an das Heteroelement gebunden sind, signifikant größer als die erwarteten Werte für M-O Bindungen sind.^[38,39] Dies unterstreicht den dativen Bindungscharakter, mit dem der XO_4 Tetraeder an die insgesamt zwölf Metalle koordiniert. Die Bindungslängen der übrigen Metall-Oxo-Bindungen liegen in den erwarteten Größenordnungen (1.9 \AA), lediglich die Bindungslängen der terminalen Oxoliganden (1.7 \AA) sind signifikant verkürzt. Diese Beobachtung lässt sich auf den Doppelbindungscharakter des terminal koordinierenden Oxoliganden $\text{M}=\text{O}$ zurückführen.^[38] Grundlage für die Berechnung der erwarteten

ten Bindungslängen stellen hierbei die Summen der kovalenten Radien dar.^[40] Ähnliche Trends wurden auch bei anderen POM-Strukturtypen beobachtet. Abbildung 2 zeigt schematisch den Aufbau einer typischen Keggin-Struktur sowohl in der atomistischen als auch in der gebräuchlicheren Polyederdarstellung.

Eine weitere bekannte HPA-Struktur stellt die Wells-Dawson-Struktur mit der allgemeinen Summenformel $[P_2M_{18}O_{62}]^{n-}$ dar.^[1] Der erste Wells-Dawson-Cluster war die Verbindung $K_6[P_2W_{18}O_{62}]$, das durch Kehrman 1894^[41] erstmals synthetisiert wurde und zum damaligen Zeitpunkt die empirische Summenformel $3 K_2O \cdot P_2O_5 \cdot 18 WO_3 \cdot 14 H_2O$ trug, die durch Rosenheim und Jaenicke 1917^[42] bestätigt wurde.^[43] Die tatsächliche dreidimensionale Struktur wurde zunächst durch Wells vorgeschlagen^[44] und im Jahr 1953 durch Dawson erstmals am Beispiel des 18-Wolframato-phosphat Anions $[P_2W_{18}O_{62}]^{6-}$ durch Einkristallstrukturanalyse vorgestellt, wobei die Verbindung hierfür ebenfalls als Kaliumsalz $K_6[P_2W_{18}O_{62}] \cdot 14 H_2O$ isoliert wurde.^[43,45,46]

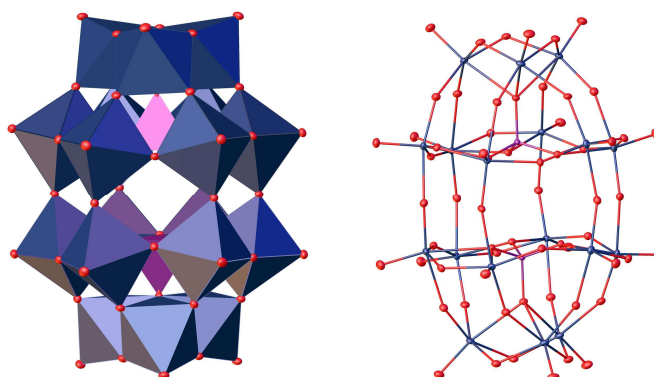


Abb. 3: Schematische Darstellung einer Wells-Dawson-Typ-POM-Struktur. Polyederdarstellung (links) und atomistische Darstellung (rechts). Farbcode: O-Atome (rot), Metalle (blau) und Heteroelement (violett).

Formal handelt es sich bei der Wells-Dawson-Struktur um ein Dimer der Anionen $[PM_9O_{34}]^{9-}$, wobei das Strukturmotiv zwei zentrale XO_4 Tetraeder enthält, die je eine M_3O_{13} Triadenkappe und einen M_6O_{14} Gürtel durch MO_6 Oktaedereckenverknüpfung koordinieren.^[1] Der klassische Aufbau einer Wells-Dawson-Struktur ist dabei in Abbildung 3 in der atomistischen und in der Polyederdarstellung veranschaulicht und ist dabei formal der Keggin-Struktur ähnlich.

POMs sind dafür bekannt, zahlreiche dreidimensionale Struktur motive anzunehmen. Allerdings existieren auch planare Vertreter dieser Substanzklasse, wie die Anderson-Evans-Struktur mit der allgemeinen Summenformel $[XM_6O_{24}]^{n-}$.^[1,47-50] Hierbei kommt für das Heteroelement X z. B. das Hauptgruppenelement Te in Frage.^[12,49] Somit gehört der Anderson-Evans-Typ eben-

falls zu den HPA-Strukturen, wobei das Heteroelement hier oktaedrisch im Zentrum der Struktur durch sechs Oxoliganden koordiniert wird. In der zeitlichen Entwicklung der POM-Chemie wurde zunächst die planare Geometrie durch Anderson 1937 postuliert^[51] und 1948 durch Einkristallstrukturanalyse von Evans am Beispiel von den Molybdotelluraten $[\text{TeMo}_6\text{O}_{24}]^{6-}$, die als Ammonium- und Kaliumsalze isoliert wurden, verifiziert.^[52] In einer typischen Anderson-Evans-Struktur, wie in Abbildung 4 gezeigt, ist jedes der sechs Sauerstoffatome des zentralen XO_6 Oktaeders Teil eines weiteren MO_6 Oktaeders, wodurch sich die insgesamt sieben Oktaeder über gemeinsame Kanten zu dem typischen hexagonalen Arrangement verknüpfen.^[12]

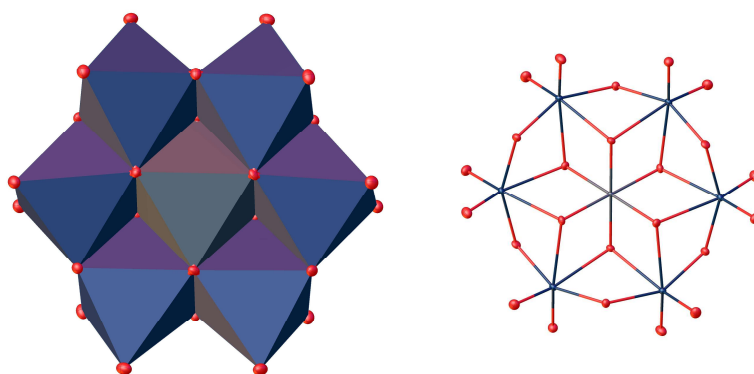


Abb. 4: Schematische Darstellung einer Anderson-Evans-Typ-POM-Struktur. Polyederdarstellung (links) und atomistische Darstellung (rechts). Farbcode: O-Atome (rot), Metalle (blau) und Heteroelement (grau).

Mittlerweile wurden auch Anderson-Evans-Strukturen hergestellt, in denen Übergangsmetalle die Rolle des Heteroatoms übernehmen. So wurden bereits erfolgreich Anionen der Typen $[\text{CrMo}_6\text{O}_{24}]^{6-}$ und $[\text{MnW}_6\text{O}_{24}]^{8-}$ synthetisiert.^[53,54] Ein besonderes Resultat im Bereich der Anderson-Evans-Forschung stellt das Polyiodobismutat $[\text{Bi}_7\text{I}_{24}]^{3-}$ dar, ein Anderson-Evans-Anion, in dem die Gerüstelementposition das Hauptgruppenelement Bismut besetzt und die Oxo-Liganden durch Iodliganden ersetzt wurden.^[55]

Die Lindqvist-Struktur stellt einen bekannten Vertreter der IPA-Strukturen mit der allgemeinen Summenformel $[\text{M}_6\text{O}_{19}]^{n-}$ dar und wird daher auch als Hexametallat-Anion bezeichnet.^[13,56] Benannt wurde die POM-Struktur dabei nach dem schwedischen Chemiker Fritz Ingvar Lindqvist, der 1950 schwerpunktmäßig auf dem Gebiet der Isopolymolybdate im Rahmen seiner Dissertation forschte und unter anderem POMs auf Hexametallatbasis analysierte.^[57] 1953 wurde durch Lindqvist die Lindqvist-Struktur für das Anionen $[\text{Nb}_6\text{O}_{19}]^{8-}$ bestätigt. Ein Jahr darauf (1954) folgte in einer Kooperation mit Aronsson der Beweis für das analoge $[\text{Ta}_6\text{O}_{19}]^{8-}$ Anion.^[58] Dabei kann die Lindqvist-Struktur sowohl von Gruppe 5 als auch von

Gruppe 6 Elementen in ihren jeweils höchsten Oxidationsstufen gebildet werden.^[59] Alle sechs MO_6 Oktaeder sind dabei über gemeinsame Kanten und Ecken miteinander zu einem größeren Oktaeder verknüpft, wobei sich die Oktaeder um einen zentralen, sechsfach oktaedrisch koordinierten Oxoliganden $\mu_6\text{-O}$ anordnen. Jedes der sechs Metallatome trägt einen terminal koordinierenden Oxoliganden M=O , der die Ecken des Hexametallatoktaeders besetzt.^[58] Die Lindqvist POMs der Gruppe 6 ($\text{M} = \text{Mo}$ und W) wurden als Clathrat-(Einschluss-)verbindungen, basierend auf dem Wirt/Gast Konzept, definiert, wobei der $\mu_6\text{-O}$ Oxoligand (Gast) die volle sechsfache, anionische Ladung trägt und die Metalloxidschale (Wirt) als elektroneutral angesehen wurde.^[58,60] Diese Annahme wurde dadurch gestützt, dass durch kristallographische Analyse festgestellt wurde, dass die Bindungen der Metalle zum $\mu_6\text{-O}$ Oxoliganden deutlich verlängert sind als im Vergleich zu den Metall-Metall verbrückenden Oxoliganden $\mu_2\text{-O}$.^[58,60,61] Durch Rechnungen auf Basis der Dichtefunktionaltheorie (DFT) wurde gezeigt, dass der Cluster $\{\text{M}_6\text{O}_{18}\}$ ohne den $\mu_6\text{-O}$ Liganden eine erhöhte Stabilität aufweist, was die Rolle des Wirtes vom $\{\text{M}_6\text{O}_{18}\}$ Cluster bezogen auf die Wirt/Gast These stützt.^[58,62]

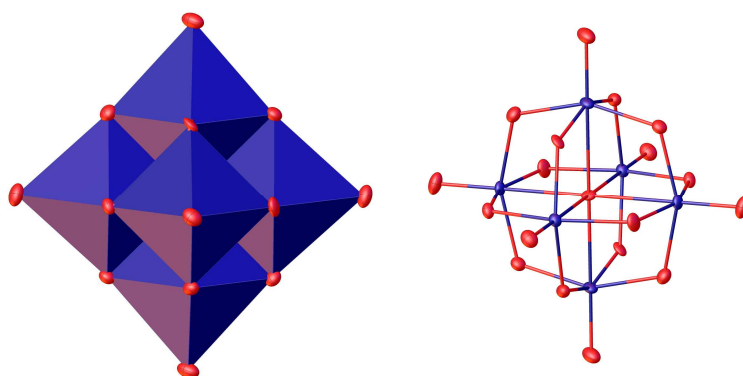


Abb. 5: Schematische Darstellung einer Lindqvist-Typ-POM-Struktur. Polyederdarstellung (links) und atomistische Darstellung (rechts). Farbcode: O-Atome (rot) und Metalle (blau).

Der molekulare Aufbau einer typischen Hexametallat Lindqvist-Struktur ist in Abbildung 5 schematisch in beiden gebräuchlichen Darstellungsweisen gezeigt.^[1]

Eine besondere Stellung unter den Lindqvist-Anionen nehmen die Verbindungen der Typen $[\text{Nb}_6\text{O}_{19}]^{8-}$ und $[\text{Ta}_6\text{O}_{19}]^{8-}$ ein, die in den meisten Fällen als Kaliumsalze isoliert werden.^[56,63,64] Im Gegensatz zu den meisten anderen Lindqvist-Strukturen entfalten diese Anionen ihre Stabilität im basischen Medium, während diese sich im sauren Medium zu Niob-/Tantal-(V)-oxid zersetzen.^[22] Jedoch können diese Anionen im sauren Medium unter Zugabe von Wasserstoffperoxid stabilisiert werden, was von synthetischem Nutzen ist.^[65]

Unter den Strukturtypen nehmen Lacunary-POM-Strukturen eine Sonderstellung ein, da es sich nicht um einen eigenständigen POM-Strukturtyp handelt. Formal leiten sich Lacunary-Strukturen von einem beliebigen POM-Strukturtyp ab (in der Regel Keggin oder Wells-Dawson), bei dem ein oder mehrere MO_x Polyeder im Strukturverband fehlen.^[66–69] Durch die so entstehenden Vakanzen erweisen sich Lacunary-Strukturen als besonders reaktiv gegenüber sich selbst oder gegenüber fremden Metallionen.^[70] So ist zum Beispiel eine Dimerisierung des Keggin-Lacunary-Anions $[\text{PMo}_9\text{O}_{34}]^{9-}$ zur Wells-Dawson-Struktur $[\text{PMo}_{18}\text{O}_{62}]^{6-}$ bekannt.^[70]

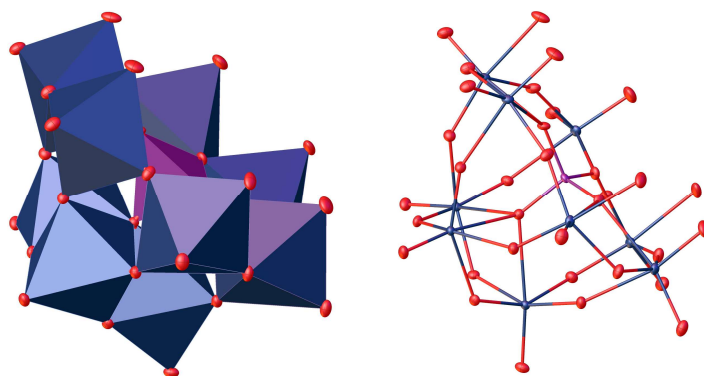


Abb. 6: Exemplarische, schematische Darstellung einer Keggin-Lacunary-POM-Struktur. Polyederdarstellung (links) und atomistische Darstellung (rechts). Farbcode: O-Atome (rot), Metalle (blau) und Heteroelement (violett).

Bekannte, lacunäre Struktur motive stellen Keggin basierte Vertreter wie die Anionen $[\text{PM}_{11}\text{O}_{39}]^{7-}$ bzw. $[\text{PM}_9\text{O}_{34}]^{9-}$ oder Wells-Dawson basierte Anionen wie $[\text{P}_2\text{M}_{17}\text{O}_{61}]^{10-}$ bzw. $[\text{P}_2\text{M}_{15}\text{O}_{54}]^{8-}$ dar.^[71–73] In der Regel liegt die Anzahl der sich ausbildenden Vakanzen zwischen eins und drei. Ein Beispiel für eine Keggin basierte, lacunäre Struktur mit drei Vakanzen ist in Abbildung 6 dargestellt.

3.1.3 Synthesemethoden für Polyoxometallate

Eine Möglichkeit zur Synthese einer POM-Struktur besteht darin, diese aus geeigneten Vorläuferverbindungen (Precursorsubstanzen) zu synthetisieren. Als geeignete Precursoren für die Gerüstmetalle werden meistens die Anionen MoO_4^{2-} oder WO_4^{2-} eingesetzt, die im sauren Medium zu POM-Strukturen oligomerisieren (Abbildung 7). Für molybdänbasierte POM-Strukturen kann ebenfalls auf das Molybdän-(VI)-oxid MoO_3 zurückgegriffen werden, das sich im basischen oder im phosphorsauren Medium löst.^[74–76] Für die Heteroatome werden als Precursoren meistens die aus dem betreffenden Element entsprungene Mineralsäuren wie z. B. das Phosphat PO_4^{3-} , Metasilikat SiO_3^{2-} oder Tellursäure $\text{Te}(\text{OH})_6$ eingesetzt.^[9,74,77] Diese Methode wird

als *self-assembly* Prozess bezeichnet, was bedeutet, dass sich die protonierten Precursoren, getrieben durch thermodynamische Triebkräfte, von selbst zur POM-Struktur anordnen.^[78–80] Hierfür werden die Precursoren in der richtigen Stöchiometrie vereint und zur Reaktion gebracht. Wichtige Parameter zur Synthesesteuerung stellen dabei die Reaktionstemperatur und der pH-Wert dar. Insbesondere kommt der letztgenannten „Stellschraube“ die wichtigste Bedeutung zu, da sich der Strukturtyp in Abhängigkeit des pH-Wertes umwandeln kann.^[81,82] Der *self-assembly* Prozess erweist sich als äußerst robustes Synthesekonzept, wobei auch *self-assembly* Prozesse bekannt sind, die sich als besonders widerstandsfähig gegenüber Temperatur- und pH-Fluktuationen erweisen.^[74–76] Werden Fremdmethylprecursoren in definierter Stöchiometrie der Reaktionsmischung hinzugegeben, die bereits eine definierte Menge an Gerüstmetallprecursoren enthält, können übergangsmetallsubstituierte POMs, sogenannte TMSPOMs (aus dem Englischen *transition-metal-substituted* POMs) mit teilweise hohen Substitutionsgraden synthetisiert werden (Abbildung 7).^[67,83,84]

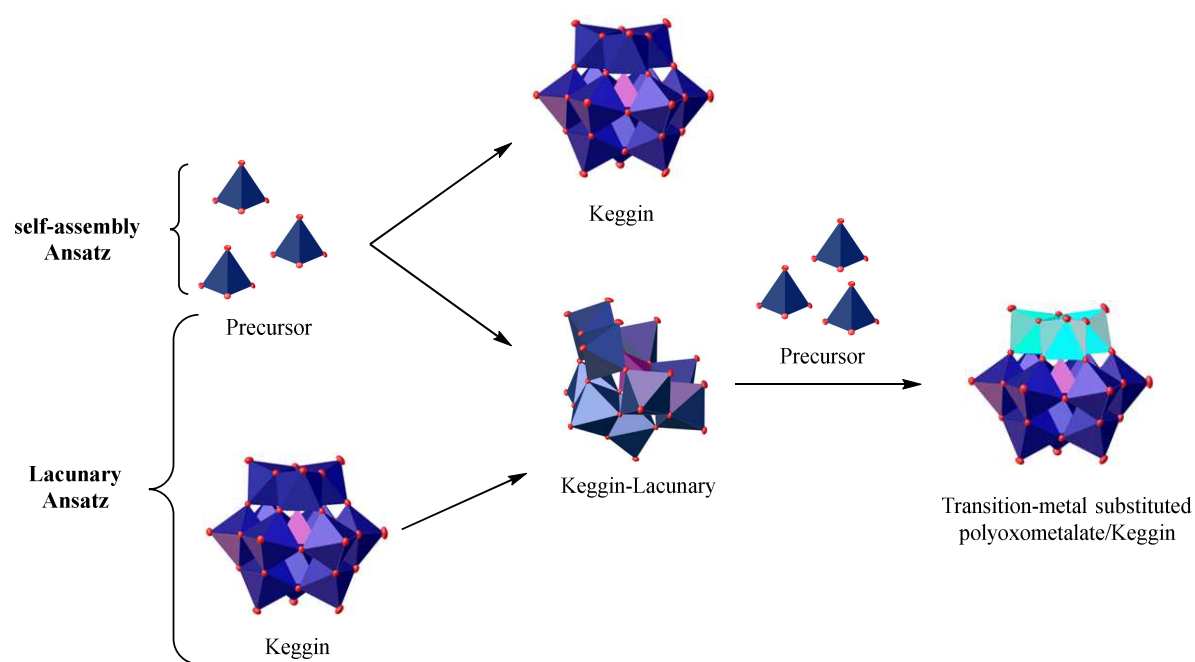


Abb. 7: Zusammenfassung beider Methoden zur Darstellung von (TMS)POMs. Im *self-assembly* Ansatz werden alle Precursorsubstanzen in definierter Stöchiometrie vereint und umgesetzt. Beim Lacunary-Ansatz wird die benötigte Lacunary-Struktur zunächst aus einer bestehenden POM-Struktur oder durch den *self-assembly* Ansatz aufgebaut. Dem Lacunary-Anion werden Fremdmethyl-Precursor hinzugefügt, die die vakanten Positionen füllen und die TMSPOM-Struktur ausbilden.

TMSPOMs können auch aus einer bereits bestehenden, häufig kommerziell erhältlichen, unsubstituierten POM-Spezies synthetisiert werden. Hierfür wird die kommerziell erhältliche

POM-Spezies (z. B. $H_3[PM_{12}O_{40}]$ mit $M = Mo$ oder W) definierten, basischen pH-Werten ausgesetzt, bei denen die MO_6 Oktaeder durch Hydroxid-Anionen aus dem POM-Verband ausgebaut werden, sodass Lacunary-POM-Strukturen mit einer definierten Anzahl an Vakanzen gebildet werden.^[85] Die Lacunary-Strukturen können jedoch auch direkt aus Precursorsubstanzen durch einen *self-assembly* Prozess erzeugt werden.^[86,87] Eine Lacunary-Struktur muss dabei nicht zwangsläufig gereinigt und isoliert werden, sondern kann auch *in-situ* erzeugt und weiterverarbeitet werden. Werden der Lacunary-Struktur Precursorsubstanzen eines Übergangselementes zugegeben, werden die vakanten Positionen stückweise mit Übergangsmetallen aufgefüllt, sodass eine TMSPOM-Struktur entsteht, wie in Abbildung 7 gezeigt.^[88,89]

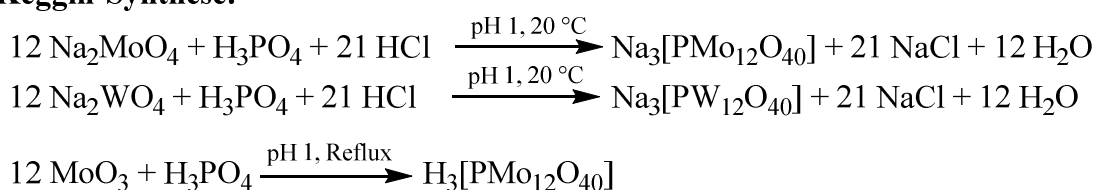
Gegenüber dem *self-assembly* Prozess zeigt der Lacunary Ansatz einige Nachteile auf. Eine Lacunary-Struktur ist häufig nur in einem definierten, schmalen pH-Fenster stabil.^[89] Zudem ist der maximale Substitutionsgrad, der mit einem Fremdelement erzielt werden kann, gleich der Anzahl an Vakanzen (in der Regel zwischen 1 und 3), sodass der Substitutionsgrad meist stark limitiert ist. Eine Zusammenfassung beider Methoden ist in Abbildung 7 dargestellt.^[5,90]

Keggin-Strukturen auf Wolfram- und Molybdänbasis können grundsätzlich durch das stetige Ansäuern wässriger WO_4^{2-} und MoO_4^{2-} Lösungen in Anwesenheit von Phosphatanionen (PO_4^{3-}) auf pH 1 gewonnen werden, wobei das PO_4^{3-} als Templat fungiert, um das sich die Metallat-anionen zur Keggin-Struktur verknüpfen.^[8,86,91] Mögliche Syntheseschemata hierzu sind in Abbildung 8 gezeigt. Die Keggin-Anionen werden als Phosphormolybdate bzw. -wolframate bezeichnet und werden hierbei als Natriumsalze gewonnen.^[92,93] Ein alternativer Syntheseweg zum Keggin-Phosphormolybdat besteht darin, MoO_3 in Phosphorsäure unter Refluxieren zu lösen.^[75,92,94] Im Gegensatz zu dem erst genannten Ansatz, wird hierbei das Phosphormolybdat als freie POM-Säure isoliert, da keine alkalihaltigen Vorläuferverbindungen in der Syntheseprozedur eingesetzt werden.^[92] Jedoch kann das Wolframanalogon auf Basis dieser Syntheseroute (ausgehend von WO_3) nicht erhalten werden. Synthesekonzepte für die Phosphorwolframatstrukturen basieren daher ausschließlich auf *self-assembly* Prozessen auf Basis von WO_4^{2-} .^[26,95] Aus den Natriumsalzen der Keggin-Molybdate/Wolframate kann jedoch auch die POM-Säure isoliert werden, indem wässrige, saure POM-Lösungen mit Diethylether extrahiert werden (Etherat-Methode).^[96] Es findet hierbei eine Komplexierung des POMs zu einem Etheratkomplex statt, wobei die Alkali-/Natriumionen in der wässrigen Phase verbleiben und die zusätzlichen Protonen die Rolle der Gegenionen übernehmen. Der POM Etheratkomplex bildet dabei eine

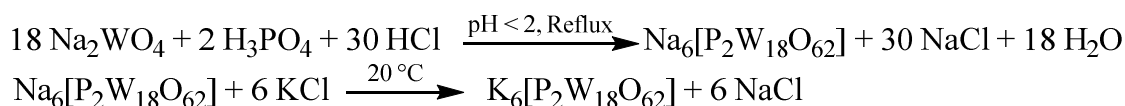
separate Phase, die sich aufgrund der erhöhten Dichte ($> 1 \text{ g/cm}^3$) unter der wässrigen Phase absetzt. Eine Isolation der POM-Säure ist dann durch Eindampfen des Ethers möglich.^[96,97]

Die Synthese der Wells-Dawson-Struktur erfolgt dabei nach der Originalvorschrift (Finke, Mbomekalle und Contant), indem eine mit Salzsäure angesäuerte WO_4^{2-} Lösung unter Zugabe von PO_4^{3-} für 24 Stunden refluxiert wird.^[25,45,98] Um die Verbindung als Kaliumsalz zu isolieren, findet ein Kationenaustausch in wässriger Lösung durch Zugabe von Kaliumchlorid statt. Die Verbindung wird dabei in das schwerer lösliche Kaliumsalz überführt, das durch Kristallisation aus der Reaktionsmischung leichter als das Natriumsalz isoliert werden kann (siehe Abbildung 8).^[45] Auch die Synthese der molybdänanalogen Wells-Dawson-Struktur wurde in der Literatur beschrieben. Hier gelingt eine Synthese ausgehend von MoO_4^{2-} und PO_4^{3-} unter stetigem Ansäuern mit Schwefelsäure und längerem Refluxieren der Reaktionslösung. Jedoch sind die Molybdate weniger stabil und somit auch weniger erforscht.^[99–101]

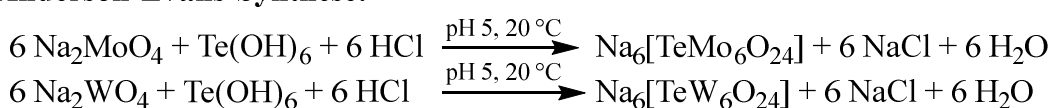
Keggin-Synthese:



Wells-Dawson-Synthese:



Anderson-Evans-Synthese:



Lindqvist-Synthese:

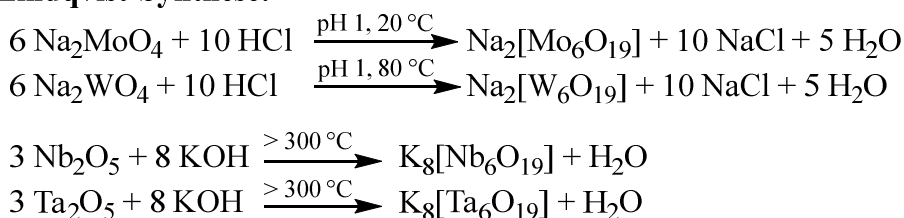


Abb. 8: Übersicht möglicher Synthesewege für ausgewählte POM-Strukturtypen.

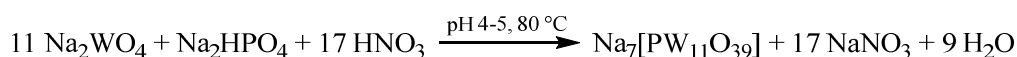
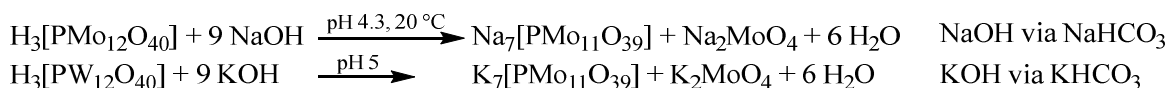
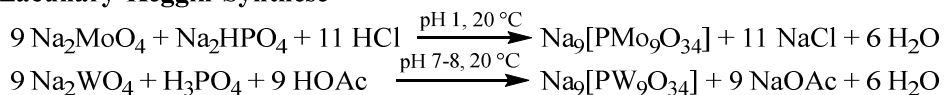
Anderson-Evans-Strukturen können sowohl auf Wolfram- als auch auf Molybdänbasis hergestellt werden. Nach der Originalvorschrift basiert die Anderson-Evans-Synthese auf der Chemie

der Tellurate. Hier gelingt eine Synthese durch stetiges Ansäuern von WO_4^{2-} bzw. MoO_4^{2-} in Gegenwart von Tellursäure $\text{Te}(\text{OH})_6$ auf pH Werte von 5. Die Anderson-Evans Anionen werden dabei als Natriumsalze erhalten (siehe Abbildung 8).^[12,102]

In typischen Prozeduren zur Synthese von Lindqvist POM Anionen werden die WO_4^{2-} oder MoO_4^{2-} Vorläuferverbindungen bei erhöhten Temperaturen stetig angesäuert.^[25,103–107] Für die verschiedenartigen Lindqvist-Strukturen sind dabei unterschiedliche pH-Werte optimal. Die Lindqvist-Strukturen können dabei abhängig von der angestrebten Anwendung als Alkalisalze, aber auch mit organischen Kationen modifiziert, isoliert werden (siehe Abbildung 8).^[104,107]

Eine Sonderstellung nehmen wiederum die Lindqvist-Anionen $[\text{Nb}_6\text{O}_{19}]^{8-}$ und $[\text{Ta}_6\text{O}_{19}]^{8-}$ ein, die im Gegensatz zu den molybdän- bzw. wolframbasierten Strukturen nur im basischen Medium synthetisiert werden können. In einer klassischen Syntheseprozedur werden die entsprechenden Metalloxide Nb_2O_5 und Ta_2O_5 in einem Schmelztiegel mit einem Überschuss an KOH geschmolzen. Das entsprechende Hexametallat-Anion bildet sich dabei in der KOH-Schmelze. Die Syntheseschemata für die ausgewählten POM-Strukturtypen sind in Abbildung 8 zusammengefasst.^[56,65,108,109]

Lacunary-Keggin-Synthese



Lacunary-Wells-Dawson-Synthese:

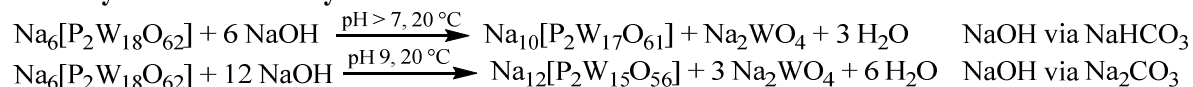


Abb. 9: Synthesemethoden für POM-Lacunary-Strukturen. Die Synthesen können dabei aus verschiedenen Metallat-Vorläuferverbindungen im sauren- oder aus einer bestehenden POM-Struktur im basischen Reaktionsmedium erfolgen.

Eine weitere Sonderstellung in der POM-Synthese stellen Lacunary-Strukturen dar, wie in Abbildung 9 gezeigt. Die Synthese kann dabei ausgehend von einer intakten POM-Struktur im basischen Reaktionsmedium erfolgen. Dabei werden einzelne Metallat-Anionen aus dem Strukturverband ausgebaut und eine Lacunary-POM-Struktur mit definierter Anzahl an Vakanzen gebildet.^[23,26] Geeignete Basen zur Einstellung der erforderlichen pH-Werte stellen Hydrogencar-

bonate oder Carbonate dar, die im wässrigen Reaktionsmedium Hydroxid-Anionen freisetzen. Die Alternative besteht darin, die Lacunary-Struktur direkt aus den MO_4^{2-} Precursoren aufzubauen (*self-assembly*), indem diese bei definierten pH-Werten umgesetzt werden. Keggin-Lacunary-Strukturen können dabei auf beiden Wegen generiert werden, wobei die dreifach lacunären Phosphorwolframat und -molybdat-Strukturen durch einen *self-assembly* Ansatz aus den Metallatvorläufern aufgebaut werden.^[71,86,87] Die einfachen Lacunary-Anionen $[\text{PW}_{11}\text{O}_{39}]^{7-}$ und $[\text{PMo}_{11}\text{O}_{39}]^{7-}$ können sowohl aus den intakten Keggin-Strukturen im basischen Medium, als auch durch *self-assembly* Synthesen generiert werden (Abbildung 9).^[23,24,26,69,110,111]

Für die Synthese von Wells-Dawson-Lacunary-Strukturen sind nur Synthesen aus der intakten Wells-Dawson-Struktur bekannt (Abbildung 9). Das einfach lacunäre Wells-Dawson-Anion $[\text{P}_2\text{W}_{17}\text{O}_{61}]^{10-}$ kann durch stetige Zugabe von Hydrogencarbonat zu einer $[\text{P}_2\text{W}_{18}\text{O}_{62}]^{6-}$ Lösung erzeugt werden, während das dreifach lacunäre Anion $[\text{P}_2\text{W}_{15}\text{O}_{56}]^{12-}$ durch Zugabe von Carbonat generiert wird.^[25,73,98,112–114] Durch die stetige Zugabe der entsprechenden Basen lassen sich die pH-Werte präzise kontrollieren, wodurch eine Zersetzung der Wells-Dawson-Struktur zu WO_4^{2-} unterdrückt wird. Durch Contant und Ciabrini^[115] wurde 1977 zum ersten Mal die Synthese eines Hexalacunary-Wells-Dawson Anion $[\text{H}_2\text{P}_2\text{W}_{12}\text{O}_{48}]^{12-}$ beschrieben. Das Anion wurde dabei aus der intakten Wells-Dawson $[\text{P}_2\text{W}_{18}\text{O}_{62}]^{6-}$ Struktur in Anwesenheit der Basen Tris(hydroxymethyl)aminomethan und Ammoniumcarbonat hergestellt.^[115–117]

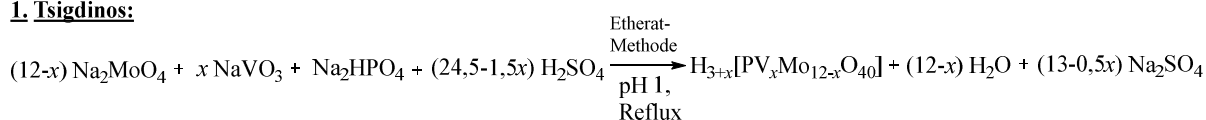
3.1.4 Übergangsmetallsubstituierte Polyoxometallate

Eine Möglichkeit in der synthetischen POM-Chemie besteht darin, neben der Variation der Heteroelemente in HPA-Strukturen, die Gerüstmetallpositionen/addenda-Metalle (Mo- oder W-Positionen) durch Fremdübergangsmetalle zu substituieren.^[118,119] Solche übergangsmetallsubstituierten POMs werden dann als TMSPOMs bezeichnet.^[67,83,84] Bekannte TMSPOMs stellen die Vanadium(V) substituierten Keggin-Phosphormolybdate $\text{H}_{3+x}[\text{PV}_x\text{Mo}_{12-x}\text{O}_{40}]$ dar, die zunächst durch Odyakov und Zhizhina dargestellt wurden.^[74,75,94] Das Konzept der TMSPOMs ist nicht nur auf den Keggin-Strukturtyp limitiert, sondern wurde auch für Wells-Dawson- und Lindqvist-Strukturen angewendet, wodurch unter anderem POM-Strukturen der Typen $\text{K}_{6+x}[\text{P}_2\text{V}_x\text{W}_{18-x}\text{O}_{62}]$ und $\text{K}_{2+x}[\text{V}_x\text{W}_{6-x}\text{O}_{19}]$ hervorgingen.^[7,68,73,103,120–123]

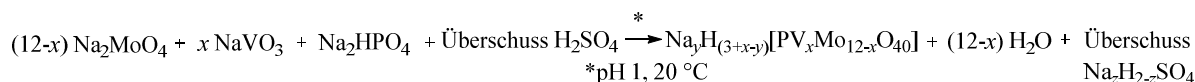
Für die Synthese von Keggin-Typ TMSPOMs eignen sich *self-assembly* Ansätze^[74–76,94,124] aber auch diverse Lacunary Ansätze wurden bereits etabliert.^[71] In der zeitlichen Entwicklung der

POM-Chemie wurden zunächst V(V) substituierte Phosphormolybdatstrukturen in ihrer Säureform durch Tsigdinos und Hallada^[125] synthetisiert, indem Salze von MoO_4^{2-} , VO_3^- und PO_4^{3-} in der angestrebten Stöchiometrie vereint und durch gezielte Einstellung der pH-Werte zur Reaktion gebracht wurden. Die POM-Säuren wurden anschließend durch die Etherat-Methode aus der Reaktionsmischung isoliert. Jedoch konnten keine Substitutionsgrade x größer als drei mit dieser Methode erreicht werden.^[125] Durch Grate^[126] wurden 1996 die V(V) substituierten Phosphormolybdate als gemischte Säuren und Salze isoliert, indem die Anionen MoO_4^{2-} , PO_4^{3-} und VO_3^- mit einem Überschuss an Schwefelsäure umgesetzt wurden.^[126] Optimiert wurde das Verfahren anschließend durch Odyakov *et al.*^[94] Hierbei gelang im Gegensatz zu den anderen Methoden eine Synthese direkt aus den Metalloxiden MoO_3 und Divanadiumpentoxid V_2O_5 . Es sind keine weiteren Reinigungsschritte notwendig, da das POM als POM-Säure isoliert werden kann und keine störenden Alkalisalze gebildet werden (Abbildung 10).

1. Tsigdinos:



2. Grate



3. Odyakov:

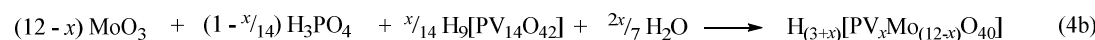
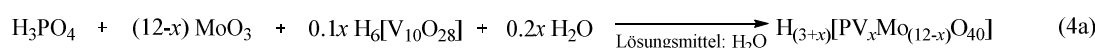
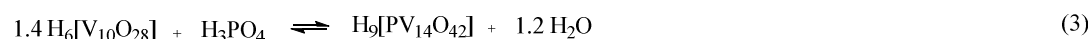
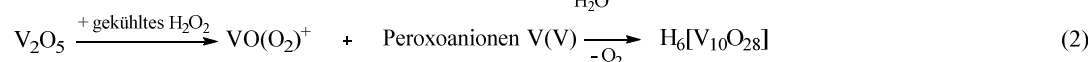
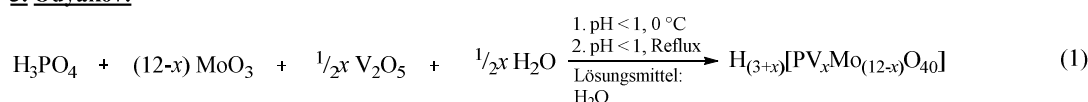


Abb. 10: (Zeitliche) Entwicklung der Synthesekonzepte für V(V) substituierte Keggin-Typ-Phosphormolybdat-Strukturen.^[74,94,125,126]

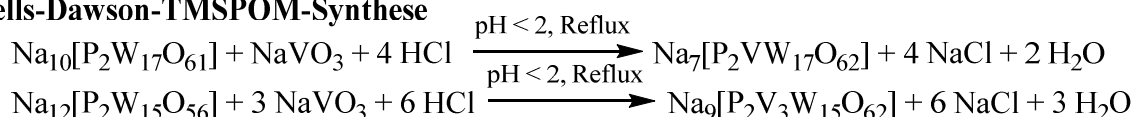
Während der Syntheseprozedur nach Odyakov *et al.*^[94] wird zunächst das V_2O_5 in wässriger, gekühlter Wasserstoffperoxid-Lösung gelöst, wodurch sich V(V) Peroxokomplexe $\text{VO}(\text{O}_2)^+$ bilden, die sich unter Sauerstofffreisetzung zur Spezies $\text{H}_6[\text{V}_{10}\text{O}_{28}]$ umsetzen. Zur Stabilisierung des temperaturempfindlichen $\text{H}_6[\text{V}_{10}\text{O}_{28}]$ wird der Lösung PO_4^{3-} zugesetzt, wodurch sich die finale V(V) Vorläuferverbindung $\text{H}_9[\text{PV}_{14}\text{O}_{42}]$ bildet. Parallel wird MoO_3 in wässriger, verdünnter Phosphorsäure-Lösung gelöst und anschließend mit der vorbereiteten $\text{H}_9[\text{PV}_{14}\text{O}_{42}]$ -Lösung vereint, um die finale V(V) substituierte Keggin-Phosphormolybdatstruktur zu bilden. Der

Vorteil gegenüber den anderen Synthesemethoden besteht darin, dass der gewünschte Substitutionsgrad durch die Wahl des richtigen stöchiometrischen Verhältnisses P:V:Mo eingestellt werden kann. Es können alle Substitutionsgrade zwischen eins und sechs erhalten werden, wobei jeder TMSPOM in der Säureform erhalten wird.^[74,94] Die zeitliche Entwicklung der Synthese V(V) substituierter Keggin-TMSPOMs ist in Abbildung 10 schematisch zusammengefasst.

Übergangsmetallsubstituierte Wells-Dawson-Vertreter können nur aus den Lacunary Strukturen $K_{10}[P_2W_{17}O_{61}]$ und $K_{12}[P_2W_{15}O_{56}]$ synthetisiert werden.^[114,127,128] Der maximal mögliche Substitutionsgrad ist hierbei gleich der Anzahl der Fehlstellen in der Lacunary-Struktur.^[7,45,73,98,112,120,122,129–131] Die Übergangsmetallsubstitution in Anderson-Evans- und Lindqvist-Strukturen spielt nach dem jetzigen Stand der Literatur nur für die Lindqvist-Struktur eine signifikante Rolle, wobei auch die substituierten Lindqvist-Strukturen nur über *self-assembly* Syntheseansätze dargestellt werden können.^[103] Lacunary-basierte Syntheseansätze spielen sowohl für die Anderson-Evans-Struktur als auch für die Lindqvist-Struktur derzeit keine Rolle.

Die Synthese von TMSPOMs auf Basis des Lindqvist-Typs begann bereits in den frühen 70er Jahren. So wurden zunächst Strukturen der Typen $[V_xW_{6-x}O_{19}]^{(2+n)-}$ analysiert.^[132,133] Das Interesse an der Synthese und Charakterisierung der entsprechenden Mo-Analoga der Typen $[V_xMo_{6-x}O_{19}]^{(2+n)-}$ begann erst deutlich später.^[107] Abbildung 11 fasst einige typische Syntheschemata zusammen, die angewendet werden, um TMSPOMs auf Basis vom Wells-Dawson- und Lindqvist-Typ herzustellen.

Wells-Dawson-TMSPOM-Synthese



Lindqvist-TMSPOM-Synthese

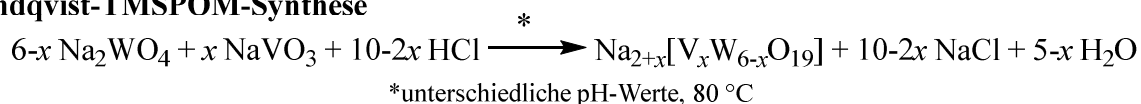


Abb. 11: Synthese V(V) substituierter Wells-Dawson- und Lindqvist-Typ TMSPOMs.

3.2 Anwendungen für Polyoxometallate

Da sich die addenda Elemente der POM-Struktur in ihren jeweils höchsten Oxidationsstufen befinden, sind POMs dazu befähigt ein oder mehrere Elektronen aufzunehmen oder abzugeben, ohne sich dabei strukturell zu verändern. Dies ermöglicht es den POMs als Oxidationsmittel zu fungieren, wodurch POMs unter anderem als homogene RedOx-Katalysatoren eingesetzt wer-

den können.^[3,134–139] Das allgemeine RedOx-Schema für eine POM-Struktur am Beispiel des Keggin-Typs ist in Abbildung 12 visualisiert. Hierbei liegt der POM-Katalysator zunächst in seiner voll oxidierten Form HPA_{ox} vor und wird durch das Substrat, das in seiner reduzierten Form $\text{Substrate}_{\text{red}}$ vorliegt, reduziert, wodurch sich eine sogenannte reduzierte POM-Struktur HPA_{red} ausbildet. Das Substrat wird oxidiert und wechselt dabei in seine oxidierte Form $\text{Substrate}_{\text{ox}}$ über (Substratoxidationsschritt). Durch molekularen Sauerstoff wird die reduzierte HPA-Struktur anschließend erneut zur Spezies HPA_{ox} oxidiert (Reoxidation), wobei ein Molekül Wasser gebildet wird. Generell zeigt sich, dass im Katalysezyklus der Substratoxidationsschritt der langsamste und damit geschwindigkeitsbestimmende Reaktionsschritt ist.^[140]

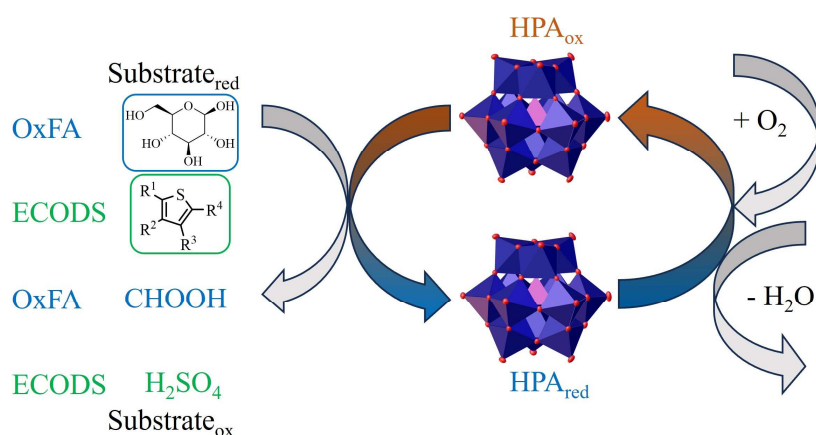


Abb. 12: Allgemeines Schema eines RedOx Katalysezyklus für eine Keggin-POM HPA-Struktur. Durch das Substrat im reduzierten Zustand ($\text{Substrate}_{\text{red}}$), wird die HPA-Struktur in ihrer oxidierten Form HPA_{ox} reduziert, wodurch das Substrat in die jeweils oxidierte Form überwechselt ($\text{Substrate}_{\text{ox}}$) und der POM sich in die reduzierte Spezies HPA_{red} umwandelt. Durch molekularen Sauerstoff wird die reduzierte HPA-Spezies wieder in die oxidierte Spezies umgewandelt und Wasser gebildet (Katalysator-Reoxidation).

3.2.1 Oxidative und Säurekatalyse mit Polyoxometallaten

Die bereits zu POMs publizierten homogenen, RedOx katalytischen Anwendungen reichen dabei von der katalytischen Umsetzung von Biomasse zu Ameisensäure (FA, *formic acid*) (OxFA-Prozess),^[103,140,149–155,141–148] über die oxidative, katalytische Entschwefelung von Kraftstoffen (*extrac-tion-coupled oxidative desulfurization*, ECODS),^[156–161] bis hin zur katalytischen Umsetzung von Ligninen.^[162,163,172–181,164,182,165–171]

Im Bereich der katalytischen Umsetzung von Biomasse werden sich sowohl die sauren als auch die RedOx-Eigenschaften einer Keggin-Typ HPA-Struktur zu Nutze gemacht. Es wird daher auch von einer bifunktionellen Katalyse gesprochen. Ein berühmter Katalysator hierfür stellt

die Verbindung $H_8[PV_5Mo_7O_{40}]$ (genannt HPV₅Mo oder HPA-5, wobei die „5“ die Anzahl der durch V(V) substituierten Mo(VI) Positionen angibt) dar.^[142]

Die POM-Säuren, wie das HPA-5, sind 10- bis 1000-mal saurer und damit katalytisch aktiver als die klassischen Mineralsäuren, wodurch Reaktionsführungen bei niedrigeren Temperaturen und Katalysatorkonzentrationen ermöglicht werden. Weiterhin lassen sich klassische, durch Mineralsäuren induzierte, unerwünschte Nebenreaktionen wie die Substratsulfonierung, -nitrierung und -chlorierung unter Einsatz der POM-Säuren vermeiden.^[138,139] So wurden Anwendungen für POM katalysierte Veresterungen (Veresterung von FA mit 1-Hexanol oder 1-Heptanol) beschrieben. Auch Anwendungen, die eine präzise Kombination aus RedOx und Säurekatalyse erfordern wurden bereits publiziert, wie z. B. die RedOx katalytische Umsetzung von Glucose im methanolischen Medium zu FA und die darauffolgende säurekatalysierte Veresterung der FA mit Methanol zu Methylformiat.^[144,152]

Eine weitere Klasse der katalytischen Anwendungen in diesem Themenbereich basiert auf der säurekatalysierten Dehydratisierung von biomassebasierten Substraten mit anschließender Oxidation der resultierenden Substratfragmente. Als Beispiel sei die HPA-5 katalysierte Hydrolyse von Cellulose zu Glucose und die darauffolgende RedOx katalysierte Oxidation der Glucose zu FA und Levulinsäure genannt. Jedoch wird der Erfolg diese Reaktion von der unerwünschten Huminbildung eingeschränkt. Bei den Huminen handelt es sich um unlösliche Biopolymere, die sich bevorzugt aus C₆-Zuckern wie Glucose bilden. Mechanistisch wird hierbei die Glucose zunächst säurekatalytisch zu 5-(Hydroxymethyl)furfural (HMF) umgesetzt, das anschließend durch eine komplexe Reaktionsabfolge zu Huminen polymerisiert (Abbildung 13).^[145,183]

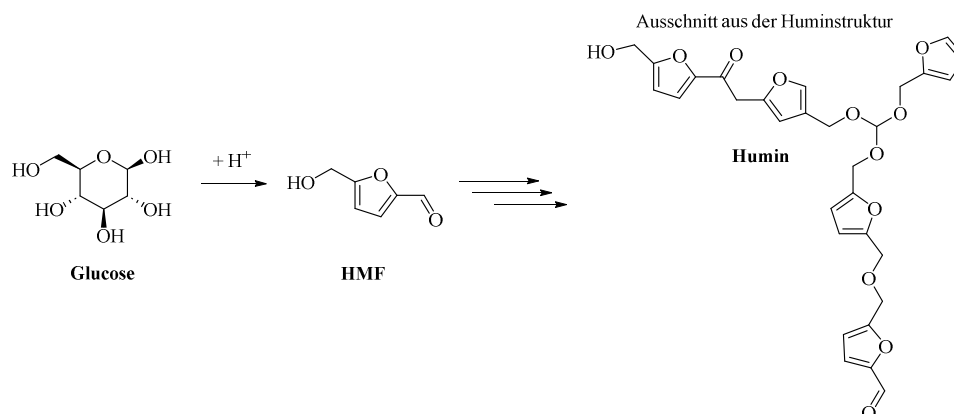


Abb. 13: Säurekatalysierte Umwandlung von Glucose zu HMF und anschließende Polymerisation von HMF über eine komplexe Reaktionsabfolge zu Huminen (postulierter Ausschnitt aus einer möglichen Huminstruktur).^[145]

Da sich Humine nicht zerstörungsfrei lösen lassen und sich aus den Reaktionslösungen als dunkle Feststoffe abscheiden, lassen sich die Massenbilanzen nicht schließen und die Ausbeuten an Wertprodukten wie FA oder Levulinsäure verringern sich. Daher stellt sich aus katalytischer und reaktionstechnischer Sicht die Frage, inwiefern es möglich ist, Humine katalytisch zu Wertprodukten wie FA oder Levulinsäure umzusetzen, anstatt die Humine zu entsorgen. Von Maerten *et al.*^[145] wurde hierzu 2017 bereits eine Studie präsentiert, in der unter HPA-5 Katalyse Humine erfolgreich umgesetzt wurden. Jedoch zeigten sich äußerst geringe Selektivitäten für FA und andere kurzkettige, organische Carbonsäuren, da Kohlenstoffdioxid CO₂ zu 63.7 % als Hauptprodukt gebildet wurde.^[145] Für eine effizientere Huminumsetzung erweist es sich daher als erforderlich ein präzises Zusammenspiel zwischen der Säurekomponente, die für die Huminhydrolyse zuständig ist und der RedOx-Komponente, die für die Huminfragmentoxidation notwendig ist, zu erreichen.

Eine andere Anwendung, die auf der POM-Oxidationskatalyse basiert, stellt der OxFA-Prozess dar. Der OxFA-Prozess bezeichnet eine effiziente Technologie, mit der biomassebasierte Substrate selektiv zu FA umgesetzt werden können.^[142,153,184] FA zählt nicht nur als wertvolle Plattformchemikalie, sondern erweist sich auch als Wasserstoffspeichermolekül, da FA formal aus je einem Molekül CO₂ und H₂ besteht.^[185,186] Für die katalytische Umsetzung von Glucose zu FA wurde mit POM-Katalysatoren der Typen H_{3+x}[PV_xMo_{12-x}O₄₀] gezeigt, dass die katalytische Aktivität mit dem Substitutionsgrad x stetig zunimmt. So erweisen sich die POMs mit $x = 0$ und 1 als wenig effizient, da die katalytische Aktivität zu gering ist und sich auch die Reoxidationsgeschwindigkeiten mit molekularem Sauerstoff als äußerst langsam herausstellen. POMs mit höheren Substitutionsgraden erweisen sich dagegen unter den erforderlichen Prozessbedingungen als schnell reoxidierbar. Die höchste Selektivität zur FA wurde dabei für die POM-Katalysatoren mit $x = 5$ und 6 gefunden, jedoch zeigte sich für $x = 6$ keine ausreichende Katalysatorstabilität, sodass die Wahl auf $x = 5$ und damit auf HPA-5 fiel. Die höhere katalytische Aktivität mit zunehmendem x lässt sich auch mit der erhöhten Konzentration von Pervanadylkationen VO₂⁺ in wässriger Lösung in Einklang bringen, die sich durch Dissoziation der V(V) haltigen TMSPOMs im wässrigen, sauren Reaktionsmedium nach dem verallgemeinerten Reaktionsschema HPV₅Mo → HPV_{5-x}Mo + x VO₂⁺ bilden.^[142]

Zur Optimierung des OxFA-Prozesses wurde ein *in-situ* Extraktionskonzept in einer zweiphasigen Wasser/Organik-Mischung entwickelt, wobei langkettige, organische Alkohole wie 1-Hexanol und 1-Heptanol als Extraktionsmittel fungieren. Nach der Reaktion wurde hierbei ein

zweiphasiges, ternäres Reaktionsgemisch aus Wasser, dem organischen Lösungsmittel und FA erhalten. HPA-5 als POM-Säure katalysiert zwar auch die Veresterung der FA mit den organischen Alkoholen, jedoch findet die säurekatalysierte Esterspaltung zeitgleich im darauffolgenden Reaktivdestillationsschritt statt, wobei die FA anschließend im Destillat zurückgewonnen werden kann.^[144] Die zweiphasige Reaktionsführung des OxFA-Prozesses ist in Abbildung 14 schematisch dargestellt.

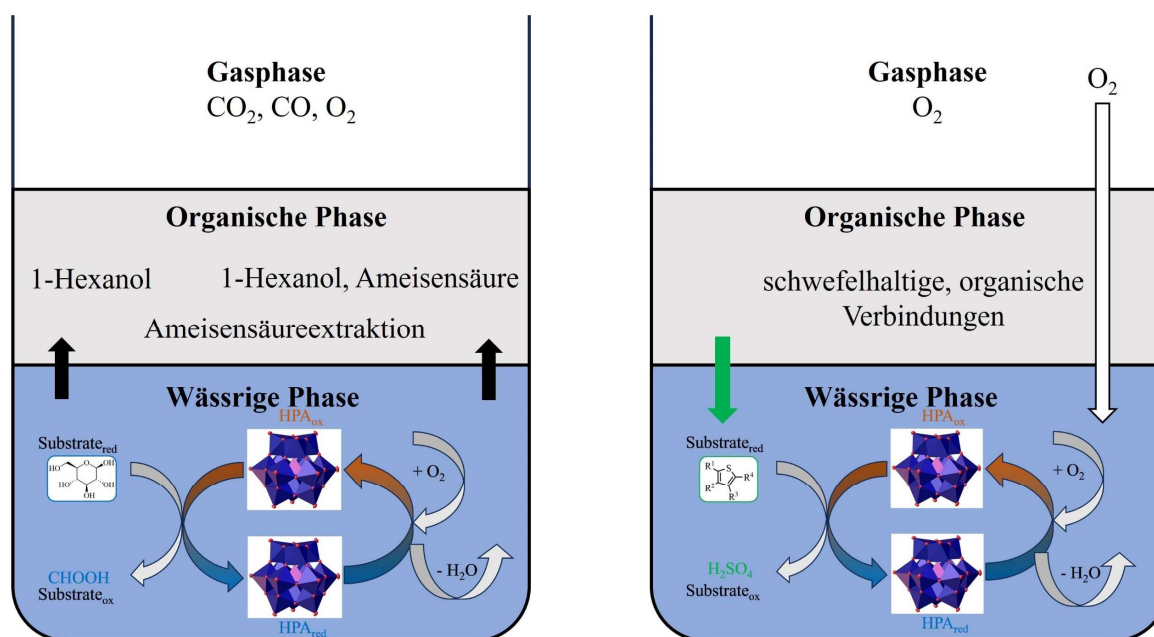


Abb. 14: Schematische Darstellung der zweiphasigen Reaktionsführungen des OxFA-Prozesses (links) und des ECODS-Prozesses (rechts). In beiden Prozessen besteht die wässrige Phase aus dem POM-Katalysator (Katalysatorphase). Beim OxFA-Prozess wird z. B. aus Glucose FA gebildet, die während der Reaktion von dem Alkohol 1-Hexanol in die organische Phase extrahiert wird (*in-situ* Extraktion). In der Gasphase befindet sich der Hochdrucksauerstoff und es reichern sich die gasförmigen Produkte CO₂ und CO an.^[144] Beim ECODS-Prozess werden die organischen Schwefelverbindungen aus der organischen Phase zunächst in die wässrige Phase überführt und dort zu wasserlöslichen Produkten wie z. B. Schwefelsäure umgesetzt, die nach der Reaktion in der wässrigen Katalysatorphase verbleiben. Die Gasphase besteht dabei aus Sauerstoff, der zur Reoxidation des POM-Katalysators benötigt wird.^[156]

Eine zweite oxidative Anwendung von POMs liegt im ECODS Prozess, einem katalytischen, oxidativen Entschwefelungsprozess von Kraftstoffen. Die Anwendung fällt in das Gebiet der *oxidative desulfurization* (ODS), wobei das Verfahren, ähnlich wie der OxFA-Prozess, weiterentwickelt und mit einer *in-situ* Extraktion gekoppelt wurde. Die organische Phase bilden dabei der Kraftstoff und die im Kraftstoff enthaltenen organischen Schwefelverbindungen (wie z. B. Schwefelheterocyclen), während die wässrige Phase zunächst nur den POM-Katalysator (das

HPA-5) enthält. Während der Reaktionsführung werden die organischen Schwefelverbindungen in die wässrige Katalysatorphase überführt und dort umgesetzt. Als Produkte werden beim ECODS-Prozess im Wesentlichen nur wasserlösliche Produkte wie z. B. Schwefelsäure gebildet, die sich in der wässrigen Katalysatorphase anreichern. Der ECODS-Prozess erweist sich dabei als sehr effektiv, um aromatische Schwefelverbindungen, wie Benzo- und Dibenzothio- phene nur mit Sauerstoff als Oxidationsmittel über 2-Sulfobenzoessäure und Solfoessigsäure als Zwischenprodukte zu Sulfaten umzuwandeln. Jedoch stellt sich die Herausforderung, den Katalysator nach der Umsetzung zurückzugewinnen, da sich in der wässrigen Katalysatorphase auch die Umsetzungsprodukte anreichern.^[156] Auch die zweiphasige Reaktionsführung des ECODS Prozesses ist in Abbildung 14 schematisch präsentiert.

3.2.2 Reduktive Katalyse mit Polyoxometallaten

3.2.2.1 Hydroformylierung

Die Hydroformylierung (HyFo), auch Oxosynthese oder Roelen-Reaktion, ist eine nach Otto Roelen (1938) vom Kaiser-Wilhelm-Institut in Mülheim an der Ruhr benannte Reaktion. Es handelt sich dabei um die katalytische Umsetzung eines Alkens mit Synthesegas (Mischung aus CO und H₂) zu Aldehyden, wie in Abbildung 15 gezeigt. Entdeckt wurde die Reaktion 1938 von Otto Roelen, der beim Studium der Fischer-Tropsch-Synthese entdeckte, dass Ethylen an einem auf ThO₂ und SiO₂ abgeschiedenen Cobaltkatalysator durch Synthesegaseinwirkung zu Propanal umgesetzt wurde.^[187,188] Die Addition des Carbonylliganden kann dabei am Alken sowohl in 1- als auch in 2-Position erfolgen, sodass eine Konkurrenz zwischen der Bildung der *n*- und *iso*-Aldehyde besteht. Katalysiert wird die HyFo im Wesentlichen durch cobalt- (Co) und rhodium-(Rh)-haltige Carbonylkomplexe.^[188,189]

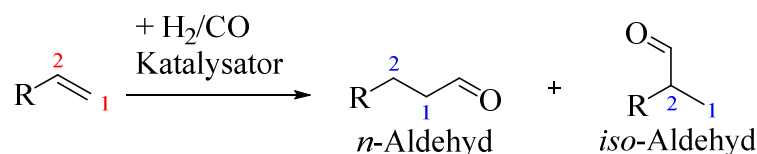


Abb. 15: Katalytische Umsetzung eines Alkens mit Synthesegas zu *n*- und *iso*-Aldehyden.

Die verwendeten HyFo-Katalysatoren werden hinsichtlich ihrer historischen Entwicklung in verschiedene Generationen unterteilt. In die erste Katalysatorgeneration fallen einfache Cobaltcarbonyle wie das [CoH(CO)₄]. Jedoch werden zur Reaktionsführung drastische Reaktionsbedingungen benötigt, unter anderem 180 °C Reaktionstemperatur und 200 bis 350 bar Synthese-

gasdruck. Hierbei wurden *n/iso*-Verhältnisse von 80/20 erzielt.^[189–191] In die zweite Generation fallen phosphinligandmodifizierte Cobaltcarbonylkomplexe wie das $[\text{CoH}(\text{CO})_3\text{PBU}_3]$, das in den 60er Jahren durch die Firma Shell entwickelt wurde.^[192,193] Durch die Modifizierung mit den Phosphinliganden werden nur noch Synthesegasdrücke von ungefähr 100 bar benötigt und das *n/iso*-Verhältnis wurde auf 88/12 optimiert. Jedoch wurde der Erfolg dadurch überschattet, dass eine Folgehydrierung der Aldehyde zu den Alkoholen beobachtet wurde, die eine bedeutende Nebenreaktion in der HyFo darstellt.^[189] Mit der Entdeckung, dass auch das Element Rhodium katalytisch aktiv ist, wurde die dritte Katalysatorgeneration geboren. Es handelt sich dabei um phosphinhaltige Rhodiumcarbonylkomplexe, die die HyFo bei Synthesegasdrücken von nur 15 bis 20 bar ermöglichen, wobei der Name *low-pressure-Oxoverfahren*, LPO populär wurde.^[189,194,195] Die erste Anlage hierzu wurde 1974 in Bishop, Texas durch die Firma Celanese in Betrieb genommen.^[189] In den 80er Jahren wurde die vierte Katalysatorgeneration geboren, bei denen die Phosphinliganden, die das Rhodium koordinieren, mit Sulfonatgruppen modifiziert wurden, um die Wasserlöslichkeit der Rhodiumcarbonylkomplexe zu gewährleisten. Ein berühmter Phosphinligand stellt das Natriumtriphenylphosphintrisulfonat (Na-TPPTS) dar, das im sogenannten Ruhrchemie-Rhône-Poulenc-Prozess seit den 80er Jahren eingesetzt wird.^[196] Durch die Katalysatoren der vierten Generation werden biphasige Reaktionsführungen ermöglicht, wodurch der Katalysator, der sich in der wässrigen Phase befindet, leicht von der organischen Produktphase in seiner aktiven Form separiert und recycelt werden kann.^[189]

Optimiert wurde dieses Konzept durch Einführung der sogenannten *temperature dependant multi-component solvent systems* (TMS-systems).^[197] Hierbei werden zwei Lösungsmittel verwendet, die sich bei Raumtemperatur nicht miteinander mischen, z. B. Wasser und 1-Butanol.^[197] Da die sogenannte Mischungslücke mit zunehmender Temperatur abnimmt, wird eine Mischbarkeit beider Lösungsmittel bei erhöhten Temperaturen, idealerweise bei Prozessbedingungen, gewährleistet. Somit liegen während der HyFo homogene Prozessbedingungen ohne Massentransportprobleme vor, die resultieren würden, wenn die Reaktion auch unter Prozessbedingungen zweiphasig ablaufen würde. Ein solches System wird auch als thermomorphisch bezeichnet. Im Anschluss an die Reaktion, wird das System wieder gekühlt, wodurch sich beide Phasen entmischen (Abbildung 16). Somit gelingt eine einfache Trennung der Reaktionsprodukte von der Katalysatorphase. Der Katalysator kann so effektiv entweder zurückgewonnen oder wiederverwendet werden.^[197] Eine Zusammenfassung ausgewählter HyFo-Katalysatoren, sortiert nach den jeweiligen Katalysatorgenerationen ist in Abbildung 17 zusammengestellt.^[188]

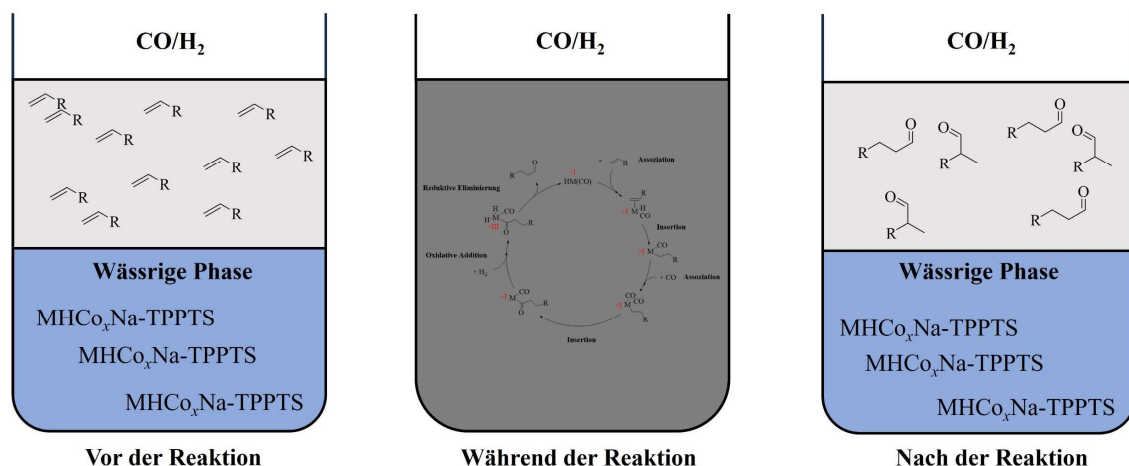


Abb. 16: Biphasige HyFo in einem thermomorphischen Lösungsmittelsystem.

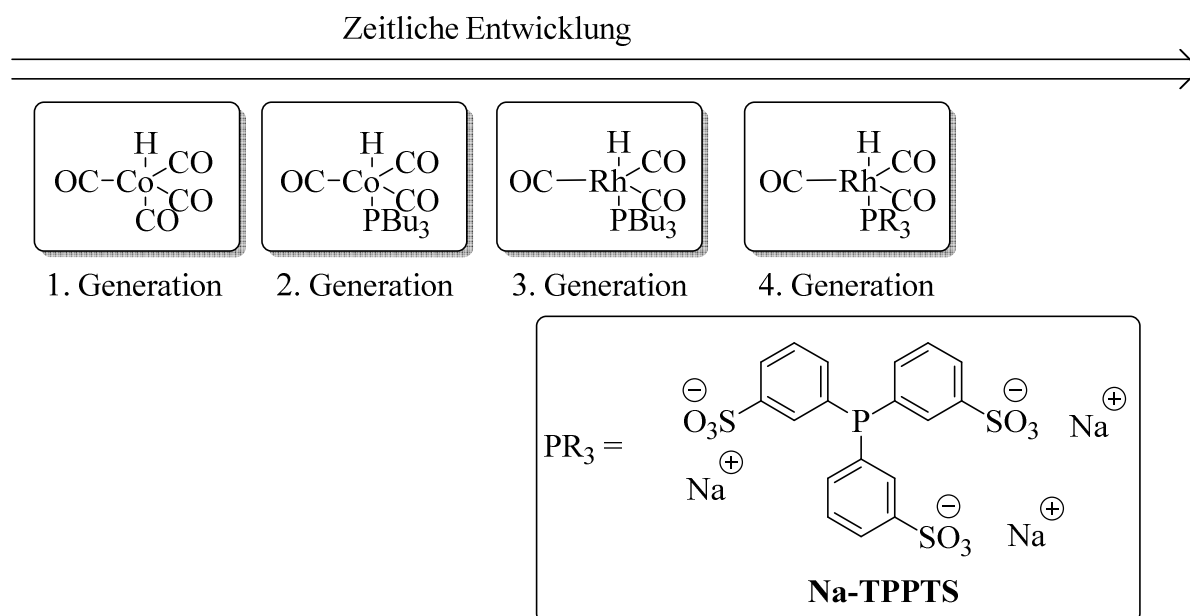


Abb. 17: Zeitliche Entwicklung der HyFo-Katalysatoren und Unterteilung in verschiedene Katalysatorgenerationen.

Der Mechanismus der klassischen cobalt- oder rhodiumkatalysierten HyFo ist in Abbildung 18 demonstriert und besteht aus insgesamt sechs wesentlichen Elementarschritten.^[189] Zunächst liegt eine allgemeine katalytisch aktive Spezies vor, bei der es sich um einen Hydrido-Carbonyl-Metallkomplex $MHCO$ handelt, wobei M den Platzhalter für Cobalt Co und Rhodium Rh freihält. Das Metallzentrum liegt dabei für gewöhnlich in der Oxidationsstufe +I vor. Im ersten Elementarschritt wird das Alken an das Metallzentrum koordiniert, wobei dieser Elementarschritt als Assoziation bezeichnet wird.^[189] Hierbei erhält das Metallzentrum einen weiteren Ligan-

den, die Oxidationsstufe bleibt unverändert (+I) und die Valenzelektronenzahl des Metalls wird um zwei erhöht.^[198] Im zweiten Schritt wird das koordinierte Alken in die Metall-Hydrido-Bindung inseriert, wobei ein Metall-Alkylkomplex resultiert. Es wird auch von einer Olefin- oder Alken-Insertion gesprochen.^[189] Hierdurch reduziert sich die Koordinationsumgebung des Metallzentrums um eins, die Oxidationsstufe bleibt unverändert (+I) und die Valenzelektronenzahl des Metalls reduziert sich um zwei. Insertionen verlaufen als *syn*-Addition ab, wobei hierfür das Alken und der Hydridoligand *cis*-ständig zueinander orientiert sein sollten.^[198] Somit wird Platz für die Koordination eines neuen CO-Liganden geschaffen, der durch eine Assoziationsreaktion an das Metallzentrum koordiniert wird (dritter Schritt).^[189] Im vierten Schritt, der Insertion, wird der CO-Ligand in die Metall-Alkylbindung inseriert, wodurch sich ein Acyl-carbonyl-Metallkomplex bildet.^[189] Die Koordinationszahl verringert sich dabei um eins, während die Oxidationsstufe konstant (+I) bleibt und sich die Valenzelektronenzahl um zwei reduziert.^[198] Mittels ¹³C-Isotopenmarkierung wurde gezeigt, dass solche Insertionen unter Wanderung eines Alkyliganden an das C-Atom eines *cis*-ständigen CO-Liganden verlaufen und werden daher auch als migratorische Insertionen oder 1,1-Insertionen bezeichnet.^[198–200] Im fünften Elementarschritt, der oxidativen Addition wird ein H₂-Molekül addiert.^[189] Hierbei erhöht sich die Koordinationszahl, die Oxidationsstufe und die Valenzelektronenzahl des Metallzentrums um jeweils zwei.^[198] Somit liegt das Metallzentrum in der Oxidationsstufe +III vor. Da im vorherigen Schritt die Valenzelektronenzahl um zwei reduziert wurde, lag ein koordinativ und elektronisch ungesättigter Metallkomplex vor. Co(I) als d⁸-Ion verfügte daher auch über genug Elektronen um zu Co(III) (d⁶) überzugehen, was eine weitere Voraussetzung für den Erfolg einer oxidativen Addition ist. Mechanistisch können oxidative Additionen radikalisch, ionisch oder synchron, als konzertierter Mechanismus ablaufen.^[198] Im sechsten und letzten Elementarschritt, der reduktiven Eliminierung, kommt es zur Freisetzung des Aldehyds unter Regenerierung der katalytisch aktiven Hydrido-Metall-Spezies, die einen neuen Zyklus durchlaufen kann.^[189] Die Koordinationsumgebung, die Oxidationsstufe und die Valenzelektronenzahl wird um je zwei reduziert, sodass der Metallkatalysator wieder in der ursprünglichen Oxidationsstufe +I vorliegt. Reduktive Eliminierungen verlaufen mechanistisch als Umkehrreaktion zur oxidativen Addition.^[198]

Die Bedeutung der HyFo liegt darin, dass die Aldehyde durch die Oxidationsstufe +II des Kohlenstoff-Atoms eine besondere Stellung in der organischen Chemie einnehmen (Abbildung 19). So können Aldehyde eine reichhaltige Folgechemie eingehen, entweder in der katalytischen Reduktion (Hydrierung) zu Alkoholen (Oxidationsstufe Kohlenstoff +I), der katalytischen Oxi-

dation zu Carbonsäuren (Oxidationsstufe Kohlenstoff +III) oder der katalytischen Aldolreaktion. Auch in der Arzneimittelsynthese spielt die HyFo eine Rolle, unter anderem in der Herstellung von Ibuprofen.^[189]

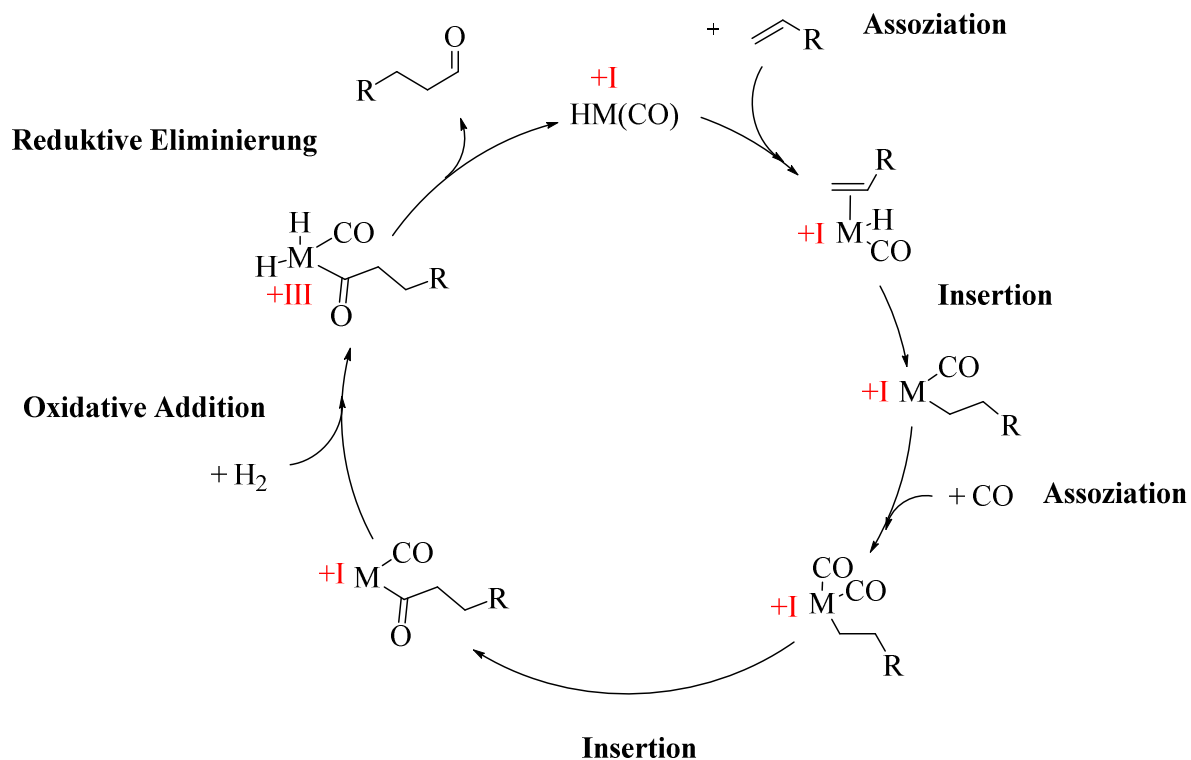


Abb. 18: Homogenkatalysierter Reaktionsmechanismus und dessen Elementarschritte der HyFo unter Einsatz von Co- oder Rh-haltigen Hydrido-Carbonylkomplexen.

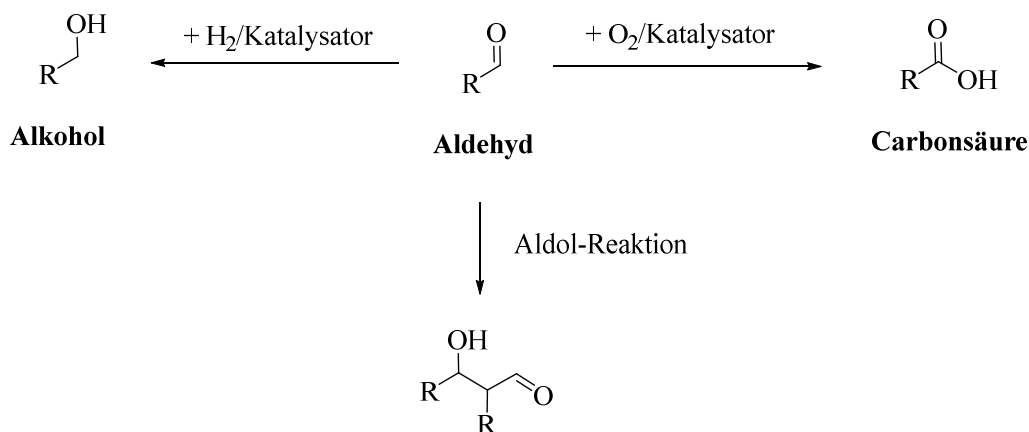


Abb. 19: Ausschnitt aus den möglichen, katalytischen Folgeprozessen der HyFo-Produkte.

3.2.2.2 Hydroformylierung mit Polyoxometallaten

POMs in der HyFo spielen bislang keine signifikante Rolle, jedoch sind sogenannte POM-Hybridverbindungen bekannt, die aus einem POM Anion $[\text{XM}_{12}\text{O}_{40}]^{n-}$ (mit $\text{X} = \text{P}, \text{Si}$ und $\text{M} = \text{Mo}, \text{W}$) und einem organometallischen Kation mit der chemischen Zusammensetzung $[(\text{Ph}_3\text{P})_2\text{Rh}(\text{CO})(\text{CH}_3\text{CN})]^+$ bestehen. Die HyFo wurde dabei an verschiedenen Hexen Substraten durchgeführt. Dabei wurden die Produkte Heptanal, 2-Methylhexanal und 2-Ethylpentanal gefunden, wobei mit dem Katalysator $[(\text{Ph}_3\text{P})_2\text{Rh}(\text{CO})]_4[\text{PVMo}_{11}\text{O}_{40}]$ für 1-Hexen hauptsächlich das *n*-Aldehyd (*n*-Heptanal), als Hauptprodukt (64 %) erhalten wurde.^[201]

Eine weitere Anwendung, in der POMs in HyFo-Experimenten eingesetzt wurden, beruht darauf, dass unter anderem der Katalysator $[\text{RhH}(\text{CO})(\text{PPh}_3)_3]$ auf Keggin-POMs wie dem $\text{H}_3[\text{PW}_{12}\text{O}_{40}]$ immobilisiert wurde. Dabei koordiniert das POM-Anion über die Oxoliganden an das Rhodiumzentralatom, wobei der POM als weiterer Ligand fungiert, der insgesamt schwächer als das CO koordiniert. In den HyFo-Experimenten an 1-Okten, mit immobilisierten $[\text{RhH}(\text{CO})(\text{PPh}_3)_3]$, konnten 41 % des *n*-Aldehyds erhalten werden, wenn das Substrat zu Rh-Verhältnis minimiert wurde.^[202]

Auch in der Einatomkatalyse spielen POMs bereits eine Bedeutung, wobei der Keggin-Typ POM $[\text{PW}_{12}\text{O}_{40}]^{3-}$ einem Kationenaustausch mit Rh^{3+} Kationen unterzogen wurde. Der Katalysator wurde anschließend durch Alkalimetallionen (K^+ , Rb^+ und Cs^+) aus der Lösung präzipitiert. Die so erhaltenen Katalysatorpartikel wurden anschließend in der HyFo von Styrol analysiert. Es konnten dabei Ausbeuten des *n*-Aldehyds von bis zu 25.99 % erhalten werden.^[203]

3.3 Charakterisierung von Polyoxometallaten

Zunächst wird ein Konzept benötigt, mit dem eine POM-Struktur im Hinblick auf verschiedene Fragestellungen charakterisiert werden kann. Hierfür lassen sich folgende Methoden etablieren, die sich in die unten beschriebenen Kategorien unterteilen lassen:

1. **Zusammensetzung:** Die Zusammensetzung eines POMs besteht zum einen aus der elementaren Zusammensetzung, die insbesondere für TMSPOMs eine fundamentale Rolle spielt, da hier definierte Stöchiometrien für die beteiligten Elemente angestrebt werden. Zum anderen besteht die POM-Zusammensetzung aus dem Hydratwasseranteil, der einen signifikanten Anteil in einem POM-Material ausmacht.

- **Elementaranalyse:** Die Elementaranalyse stellt eine bedeutende Methode dar, die stöchiometrische Zusammensetzung eines POM-Materials aufzuklären. Hierfür eignen sich die nasschemischen Methoden *Inductively Coupled Plasma Optical Emission spectroscopy* (ICP-OES) und Flammen-Atomabsorptionsspektrometrie (F-AAS, häufig auch nur AAS). Als Messergebnis werden zunächst Konzentrationen der beteiligten Elemente in einer wässrigen Lösung bekannter Konzentration erhalten, aus denen letztendlich die Massenprozentwerte errechnet werden können, die zur Berechnung der stöchiometrischen Verhältnisse dienen. Im Vergleich der errechneten stöchiometrischen Verhältnisse mit den Sollwerten kann die Stöchiometrie des Materials verifiziert werden.^[204,205]
 - **Thermogravimetrische Analyse (TGA):** Die TGA stellt eine Methode dar, bei der eine Probe mit einer definierten Heizrate auf eine vorher definierte Temperatur geheizt wird. Das Hydratwasser verdampft, wodurch die Probe stetig an Masse verliert. Aus dem Massenverlust lässt sich daher der Hydratwasseranteil eines POM-Materials berechnen.^[206,207]
2. **Feststoffanalytik:** Durch die Feststoffanalytik kann der POM-Strukturtyp verifiziert und die erfolgreiche Elementsubstitution in einem TMSPOM im Vergleich zu der jeweils unsubstituierten POM-Spezies bestätigt werden. Hierzu eignen sich folgende Methoden:
- **Schwingungsspektroskopie:** Zur Schwingungsspektroskopie zählen die Infrarot- (IR) und Raman-Spektroskopie. Aus den charakteristischen Schwingungsbanden kann ein POM-Strukturtyp identifiziert werden. Im Vergleich zu einer unsubstituierten POM-Spezies können durch Bandenverschiebungen/Banden-Shifts in TMSPOMs Hinweise auf eine erfolgreiche Elementsubstitution abgeleitet werden, die ein Resultat der unterschiedlichen Massen von Substitutions- und Gerüstelement sind.^[30,208,209]
 - **Kristallographie:** Das bedeutendste kristallographische Verfahren stellt die Röntgenbeugung (*X-ray diffraction*, XRD) dar, wobei der Feststoff als Einkristall mit der Einkristall- (*single-crystal*) und als Pulver mit der Pulver-Röntgenbeugung (sc- und p-XRD) analysiert werden kann. Aus den sc-XRD-Daten ist neben der Identifizierung des POM-Strukturtyps eine detaillierte Festkörperanalytik möglich.^[210,211,220,212–219] So können Informationen über Bindungslängen, -winkel und über die Packung der einzelnen POM-Anionen und der jeweiligen Kationen abgeleitet werden. Eventuell zu beobachtende Verzerrungen im POM-Strukturtyp sind direkte Auswirkungen eines Substitutionselementes, das in den Strukturtyp integriert wurde.

3. Lösungsanalytik: Durch die Analytik eines POMs in Lösung werden Dissoziationsgleichgewichte und Isomerenverteilungen der jeweiligen POM-Struktur erkannt und unter anderem RedOx-Potentiale identifiziert. Es sind folgende Methoden von Bedeutung:

- *Nuclear magnetic resonance-* (NMR-) Spektroskopie: Insbesondere die Isotope ^{31}P und ^{51}V sind häufig in der POM-Chemie vorkommende Kerne, sodass eine NMR-Untersuchung dieser Kerne sinnvolle Informationen liefert. Aus den Spektren werden Signale bei verschiedenen chemischen Verschiebungen erhalten, die Hinweise über Isomerenverteilungen und Dissoziationsgleichgewichte des POMs in Lösung generieren.^[221–225]
- *Ultraviolet-visible-* (UV-Vis-) Spektroskopie: In den UV-Vis-Spektren von POMs werden sogenannte *ligand to metal charge-transfer-* (LMCT-) Banden beobachtet, die formal einer Übertragung eines Elektrons vom Oxoliganden zum Metallatom entsprechen. Die Banden liegen bei unterschiedlichen Wellenlängen und können zur Bestimmung von Extinktionskoeffizienten nach dem Lambert-Beer'schen Gesetz genutzt werden.^[226–231]
- Elektrochemie: Zur Bestimmung von RedOx-Potentialen, die insbesondere für die RedOx-katalytischen Anwendungen interessant sind, eignen sich elektrochemische Messungen. Die wichtigsten Methoden stellen die Cyclovoltammetrie (CV) und die Square-Wave-Voltammetrie (SWV) dar. Als Messergebnisse werden Potentiale erhalten, die gegen eine Referenzelektrode im Rahmen einer Dreielektrodenanordnung gemessen werden (z. B. Ag/Ag⁺). Im Vergleich eines TMSPOM mit dem unsubstituierten Vertreter aus der jeweiligen Strukturreihe, können Unterschiede in den Voltammogrammen aufgezeigt werden, die Schlüsse über den Einfluss des Substitutionselementes auf die RedOx-Potentiale des TMSPOMs zulassen.^[232,233,242,234–241]

Mit den aufgeführten Methoden können neuartige (TMS)POM-Strukturen effizient analysiert werden. So können in die jeweiligen Strukturen tiefe Einblicke erlangt werden, die als ideale Basis zur Charakterisierung neuer, maßgeschneiderter TMSPOM-Strukturen fungieren.

4 Zielsetzung und Problemstellung der Arbeit

Die Anwendung von POMs reicht von der homogenen RedOx-Katalyse, über die Biomedizin bis hin zur Elektrokatalyse. Insbesondere im Bereich der homogenen Katalyse erweisen sich POMs als ideale und robuste Kandidaten wie z. B. in der katalytischen Umsetzung von Biomasse zu FA oder zu anderen industriellen Wertprodukten. Somit leisten POMs einen Beitrag im Bereich der nachhaltigen/grünen Chemie. Hinzu kommt, dass POMs im Vergleich zu anderen metallorganischen Katalysatorsystemen leicht zu synthetisieren sind und sich als robust gegenüber Luftsauerstoff und Wasser erweisen. Die spezifische Elementsubstitution in POMs mit verschiedenen RedOx aktiven Elementen stellt die Basis für die Entwicklung neuer Katalysatorsysteme und dem Verständnis der POM-Chemie dar. Somit erweist sich die Forschung an POMs nicht nur für das akademische Interesse von Nutzen, sondern hilft auch der gesamten Menschheit dabei die Probleme im 21. Jahrhundert effizient anzugehen. Auch wenn das Forschungsgebiet der POMs bereits ein älteres Teilgebiet in der anorganischen Chemie ist, lassen sich noch diverse offene Fragestellungen definieren.

Bevor ein POM in der Katalyse eingesetzt werden kann, muss zunächst ein robustes und reproduzierbares Synthesekonzept erarbeitet werden. Somit stellt die POM-Synthese das zentrale Fundament dar, auf dem die katalytischen Anwendungen im nächsten Schritt aufbauen können. Daher wurden für das Dissertationsprojekt folgende Fragestellungen definiert:

- 1. Erweiterung des Synthesekonzeptes der V(V) substituierten Phosphormolybdate auf andere Übergangsmetalle:** Die Substitution verschiedener addenda Elemente in POM-Strukturen durch V(V) stellt ein seit dem Ende der 60er Jahre praktiziertes Synthesekonzept dar. Jedoch sind insbesondere für die Phosphormolybdatstrukturen kaum Studien bekannt, in denen das Konzept der Übergangsmetallsubstitution auf andere Übergangsmetalle erweitert wurde. Aus katalytischer Sicht sind jedoch auch andere Metalle außer V(V) interessant. So zeigen insbesondere die frühen Übergangsmetalle faszinierende RedOx-Eigenschaften, die sich in der Katalyse zu Nutzen gemacht werden können. Hierbei bieten sich die Metalle Mangan Mn mit seinen zahlreichen Oxidationsstufen von +I bis +VII, Eisen Fe mit dem RedOx-Paar Fe(II)/Fe(III), Cobalt Co mit den Paaren Co(III)/Co(II)/Co(I) und Nickel mit seinem RedOx-Paar Ni(II)/Ni(I) an.^[22]

Das Keggin-Typ Lacunary Anion $[\text{PMo}_9\text{O}_{34}]^{9-}$ stellt eine seit den 70er Jahren bekannte Struktur dar, jedoch existieren kaum Studien, die sich mit dem gezielten synthetischen Nut-

zen dieser Struktur, vor allem im wässrigen Medium, beschäftigen.^[87] Im Gegensatz dazu existieren bereits verschiedene Studien, die das analoge Keggin-Lacunary Anion $[\text{PW}_9\text{O}_{34}]^{9-}$ nutzen, um verschiedene Übergangsmetalle in die Keggin-Struktur einzubauen.^[27] Daher stellt sich für diese Arbeit die Frage, inwiefern es möglich ist, das Lacunary-Anion $[\text{PMo}_9\text{O}_{34}]^{9-}$ zu nutzen, um weitere Übergangsmetalle in die Keggin-Struktur einzubauen. Laut dem Stand der Literatur ist bereits der V(V) Einbau in das $[\text{PMo}_9\text{O}_{34}]^{9-}$ Anion bekannt, das bereits zuvor mit organischen Liganden modifiziert wurde.^[88] Chemisch gesehen handelt es sich dabei um eine nasschemische Synthese des Anions $[\text{PV}_3\text{Mo}_9\text{O}_{40}]^{6-}$ im organischen Medium. Für die nachfolgenden katalytischen Anwendungen der POMs ist allerdings eine Reaktionsführung im wässrigen Medium erstrebenswert, sodass die organisch modifizierten POMs für die RedOx-Katalyse nicht tauglich sind. Daher stellt sich die Frage, inwiefern es möglich ist, die Chemie des $[\text{PMo}_9\text{O}_{34}]^{9-}$ Anions auf das wässrige Reaktionsmedium zu erweitern.

- 2. Einfluss der verschiedenen Substitutionselemente auf die RedOx-Potentiale der POMs:** Insbesondere für die späteren RedOx katalytischen Anwendungen ist es von zentraler Bedeutung, den Einfluss des entsprechenden Substitutionselementes auf die RedOx-Eigenschaften der finalen POM-Struktur zu kennen. Somit ist es von fundamentaler Bedeutung, ob gegebenenfalls eine gezielte Steuerung der elektrochemischen Potentiale möglich ist. Die effizienteste Möglichkeit zur Bestimmung von RedOx-Potentialen in der analytischen Chemie, stellt die Anwendung elektrochemischer Messmethoden wie die CV und die SWV dar. Aus den Daten können Trends abgeleitet werden, mit denen die Auswirkungen des Substitutionselementes auf die RedOx-Potentiale im Vergleich zur jeweiligen unsubstituierten Spezies des jeweiligen POM-Strukturtyps beurteilt werden können. Die Beantwortung der genannten Fragestellungen ebnet das Fundament für die Synthese maßgeschneiderter TMSPOMs für eine spezielle RedOx katalytische Anwendung.
- 3. Entwicklung eines effektiven Entsalzungsprozesses als Reinigungskonzept für TMSPOMs:** Auch wenn aus katalytischer Sicht die POMs im Idealfall als POM-Säuren eingesetzt werden sollen, um die säure- und RedOx-katalytischen Eigenschaften in der Katalyse zu kombinieren, werden in den meisten Fällen die POMs als POM-Alkalisalze (z. B. $\text{Na}_{3+x}[\text{PV}_x\text{Mo}_{12-x}\text{O}_{40}]$) isoliert. Diese Beobachtung ist darauf zurückzuführen, dass in der POM-Synthese häufig alkalimetallhaltige Precursoren (Na_2MoO_4 oder NaVO_3) eingesetzt werden. Erschwerend kommt hinzu, dass es durch die präzise Justierung des pH-Wertes zur unerwünschten Alkalisalzbildung (Natrium- und/oder Kaliumchlorid) kommt. Eine Separation

tion des Alkalisalzes vom POM ist nicht ohne weiteres möglich, da sowohl das Alkalisalz als auch das POM-Alkalisalz eine hohe Wasserlöslichkeit aufweisen. In der Literatur werden Umkristallisationen und extraktive Verfahren als Problemlösungsstrategien vorgestellt. Jedoch gehen beide Methoden mit erheblichen Ausbeuteverlusten einher und insbesondere bei Kristallisationsansätzen zeigt sich, dass das Alkalisalz und das POM-Alkalisalz häufig co-kristallisieren, was den Reinigungserfolg drastisch schmälert. Die Etheratmethode scheidet zudem insbesondere bei TMSPOMs und erweist sich meist nur bei unsubstituierten Keggin-Typ-POM Vertretern als zielführend. Die hier dargestellte Problematik unterstreicht, dass es notwendig ist, ein neues Verfahren zur effektiveren Entsalzung von POMs zu entwickeln, mit denen der POM in hoher Ausbeute und Reinheit isoliert werden kann.

4. **Kristallographisches Studium der TMSPOM-Strukturen:** Als klassische Vertreter aus der Molekülchemie eignen sich (TMS)POMs für eine kristallographische Untersuchung dieser Substanzklasse. Klassische Parameter, die es zu untersuchen gilt, sind Bindungslängen und -winkel. Durch Interpretation dieser Daten können unter anderem Aussagen über die vorliegenden Bindungssituationen in der POM-Struktur getroffen werden.
5. **Katalytische Anwendungen für die TMSPOMs:** Ein weiteres Ziel dieser Arbeit besteht darin, für die synthetisierten TMSPOMs Anwendungen in der homogenen Katalyse zu finden. Hierfür werden die POMs in verschiedenen oxidativen und reduktiven katalytischen Anwendungen eingesetzt, um für die synthetisierten TMSPOM-Strukturen spezifische Anwendungen zu finden.
6. **Mechanistische Grundlagen für die Bildung verschiedener POM-Strukturtypen:** Die Bildung einer Keggin-Struktur in wässriger Lösung gilt bereits als verstanden und aufgeklärt. Jedoch zeigt sich, dass die mechanistischen Details, die zur Bildung anderer HPA-Strukturen (wie beispielsweise zur Anderson-Evans-Struktur) führen, nur in Grundzügen verstanden sind. Da die bekanntesten Keggin-Typ POM-Strukturen vorzugsweise mit den Heteroelementen P und Si (Periode 3) gebildet werden, erfolgt eine Anderson-Evans-Bildung mit Elementen wie Te (Gruppe 5). Es wird schnell ersichtlich, dass die Herkunft des betreffenden Heteroelementes aus dem PSE einen signifikanten Einfluss auf die POM-Strukturtypbildung hat. Insbesondere der Einfluss von Gruppe 4 Elementen, wie As, gilt nur als teilweise verstanden. In der Literatur existieren jedoch noch keine fundierten Studien, die systematisch den Einfluss des betreffenden Heteroelementes auf die POM-Strukturtypbildung analysieren. Daher besteht ein Ziel der vorliegenden Arbeit darin, systematisch den Einfluss verschiedener Hauptgruppenheteroelemente auf die POM-Strukturtypbildung zu

analysieren und Trends abzuleiten, die das Verständnis der Bildung weniger trivialer Strukturtypen erweitern.

7. **Übertragung des TMSPOM-Konzeptes auf andere Strukturtypen:** Das Konzept der Übergangsmetallsubstitution in POM-Strukturen spielt nach dem aktuellen Stand der Literatur nur für die Keggin-, Wells-Dawson- und Lindqvist-Struktur eine bedeutende Rolle. Für die Anderson-Evans-Strukturen wurden jedoch noch keine Synthesekonzepte erarbeitet, bei denen die addenda-Elemente durch RedOx aktive Fremdelemente wie V(V) substituiert wurden. Daher besteht ein Ziel dieser Arbeit darin, ein Synthesekonzept zu entwickeln, mit denen TMSPOMs auf Anderson-Evans-Basis synthetisiert werden können.

5 Kumulativer Teil der Dissertation/Synopsis

Das folgende Kapitel enthält die Originalpublikationen, die in *peer-reviewed* Journalen mit einer Erstautorenschaft publiziert wurden.

- Synthese, Charakterisierung und Reinigung maßgeschneiderter Keggin-Phosphormolybdatstrukturen, publiziert in *Inorg. Chem. Front.* **2023**, *10*, 4854–4868 (P1).
- Synthese und Charakterisierung von Mn(II)/V(V) gemischt substituierten Phosphormolybdaten, publiziert in *Chem. Eur. J.* **2022**, *28*, e202201084 (P2).
- Vergleichende spektroskopische und elektrochemische Studie über V(V) substituierte Keggin-Typ Phosphormolybdate und wolframate, publiziert in *Inorganics.* **2023**, *11* (4), 138 (P3).
- Synthese und Anwendung Co(II) substituierter Keggin-Phosphormolybdatstrukturen in der homogenkatalysierten Hydroformylierung, publiziert in *ChemCatChem* **2024**, e202400395 (P4).
- Einfluss des Heteroelementes auf die Polyoxometallat-Strukturtypbildung, publiziert in *Dalton Trans.* **2024**, *53*, 454-466 (P5).
- Synthese, Charakterisierung und katalytische Anwendungen V(V) substituierter Anderson-Evans Polyoxometallate für die oxidative Umsetzung von Monofuranderivaten, publiziert in *Catal. Today* **2024**, *441*, 114899 (P6).

5.1 Synthese, Charakterisierung und Reinigung maßgeschneiderter Keggin-Phosphormolybdatstrukturen

P1

Study on the incorporation of various elements into the Keggin lacunary-type phosphomolybdate $[\text{PMo}_9\text{O}_{34}]^{9-}$ and subsequent purification of the polyoxometalates by nanofiltration

Jan-Christian Raabe, Tobias Esser, Froze Jameel, Matthias Stein, Jakob Albert, Maximilian J. Poller

Raabe, J.-C.; Esser, T.; Jameel, F.; Stein, M.; Albert, J.; Poller, M. J. Study on the Incorporation of Various Elements into the Keggin Lacunary-Type Phosphomolybdate $[\text{PMo}_9\text{O}_{34}]^{9-}$ and Subsequent Purification of the Polyoxometalates by Nanofiltration. *Inorg. Chem. Front.* **2023**, *10* (16), 4854–4868. <https://doi.org/10.1039/D3QI00937H>.

Das Lacunary-Synthesekonzept mit dem $[\text{PMo}_9\text{O}_{34}]^{9-}$ Anion zur Synthese von TMSPOMs konnte erfolgreich auf die wässrige Synthesechemie übertragen werden (P1, *Inorg. Chem. Front.* **2023**, *10*, 4854–4868).^[243] Eine vorherige Isolierung des Lacunary-Anions als organisches Salz ist daher nicht zwingend erforderlich. Hierfür wurde ein Konzept entwickelt, in dem das Anion $[\text{PMo}_9\text{O}_{34}]^{9-}$ *in-situ* erzeugt und ohne Isolierung aus der Reaktionslösung direkt mit weiteren Fremdmetallprecursoren zu TMSPOMs auf Basis des Keggin-Strukturtyps umgesetzt wurde (Abbildung 20). Es wurde gezeigt, dass mit diesem Konzept der Einbau der Übergangselemente W(VI), V(V), Nb(V), Fe(III), Co(II) und Ni(II) vollständig funktioniert. Limitierungen wurden bei den späten Übergangsmetallen Cu(II) und Zn(II) gefunden, deren Einbau in die Keggin-Struktur nicht vollständig gelang. Weitere Limitierungen wurden für die Hauptgruppenelemente In(III) und auch Sn(IV) gefunden, wobei der Einbau von In(III) nur unvollständig gelang, während der Einbau von Sn(IV) unter den gewählten Reaktionsbedingungen scheiterte.^[243] Diese Beobachtung stellt bereits einen ersten signifikanten Unterschied zur Chemie des $[\text{PW}_9\text{O}_{34}]^{9-}$ Anions dar, bei dem Keggin-Anionen der Typen $[\text{PInW}_{11}\text{O}_{40}]^{6-}$ und $[\text{PSnMo}_2\text{W}_9\text{O}_{40}]^{5-}$ bekannt sind.^[244–246] Da das Lacunary Anion $[\text{PMo}_9\text{O}_{34}]^{9-}$ aus natriumhaltigen Precursoren erzeugt wurde und während der Prozedur der pH-Wert präzise justiert werden musste, bildete sich Natriumchlorid als Nebenprodukt, wie aus Abbildung 20 hervorgeht. Um die erhaltenen POMs zu entsalzen, wurde ein effektives *down-stream* Dialyseverfahren basierend auf einer Nanofiltration entwickelt. Es wurde eine effektive Entsalzung des POMs bei gleichzeitiger Bewahrung einer hohen Ausbeute nach vier Zyklen der Diafiltration gewährleistet. Der Chloridgehalt wurde mit Hilfe der *energy-dispersive X-ray spectroscopy* (EDX) auf unter 1 Promille bestimmt, was für eine effektive Entsalzung des POMs spricht. In Abbildung 20 wurde am Beispiel des POMs NaPNb_3Mo gezeigt, dass die Gerüstelemente (hier P, Nb und Mo) effektiv von der nanoporösen Membran zurückgehalten wurden. Dies zeigt, dass die POMs bzw. deren Dissoziationsfragmente die Membran nicht passieren konnten. Wie zu erwarten, nahm die Natrium- und Kaliumionenkonzentration in der Retentatfraktion von Zyklus zu Zyklus stetig ab, da nur die Alkaliionen die Membran passieren konnten. Dabei sank die Alkalimetallkonzentration auf einen Wert nach vier Zyklen, der der Menge an Kationen entsprach, um mit dem sechsfach anionisch geladenen Anion Elektroneutralität zu gewährleisten. Durch Analyse der POMs mit CV und SWV wurde gezeigt, dass sich die RedOx-Potentiale gezielt in Abhängigkeit des Fremdmetalls beeinflussen lassen, was einen ersten Schritt in Richtung der Synthese maßgeschneiderter TMSPOMs darstellt.^[243] In Abbildung 20 sind die wichtigsten Ergebnisse der Studie P1 graphisch zusammengefasst.

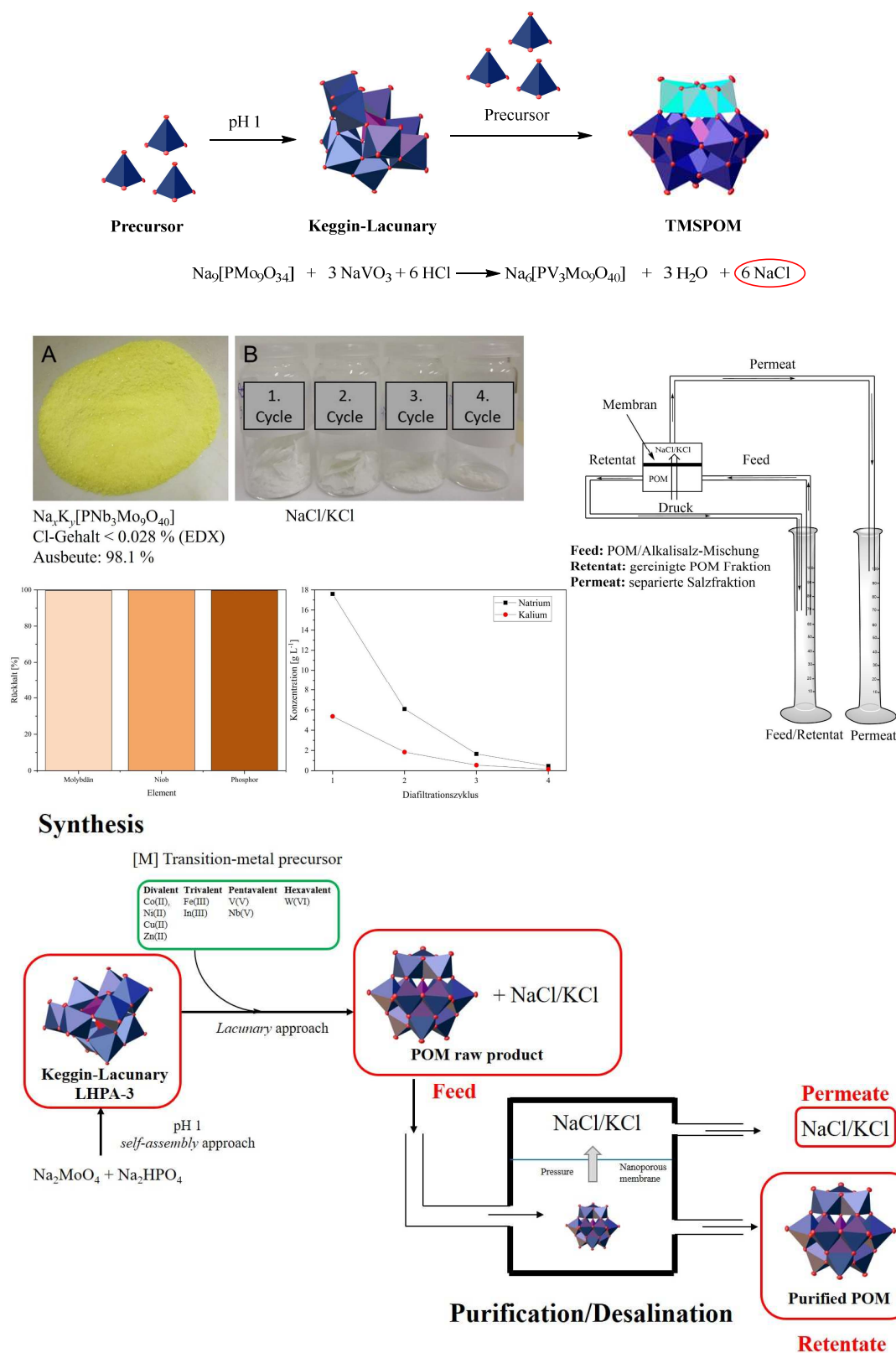


Abb. 20: Synthesekonzept zum Einbau verschiedener Übergangselemente in die *in-situ* erzeugte Keggin-Lacunary-Struktur $[\text{PMo}_9\text{O}_{34}]^{9-}$ (oben), Entsalzungskonzept mit der nanoporösen Membran (Mitte) und *graphical abstract* von P1, *Inorg. Chem. Front.* **2023**, *10*, 4854–4868 (Zusammenspiel aus Synthesansatz und anschließendem Entsalzungskonzept).^[243]

RESEARCH ARTICLE

[View Article Online](#)
[View Journal](#) | [View Issue](#)

 Cite this: *Inorg. Chem. Front.*, 2023, **10**, 4854

Study on the incorporation of various elements into the Keggin lacunary-type phosphomolybdate $[\text{PMo}_9\text{O}_{34}]^{9-}$ and subsequent purification of the polyoxometalates by nanofiltration†

 Jan-Christian Raabe, ^a Tobias Esser, ^a Froze Jameel,^b Matthias Stein, ^b Jakob Albert ^a and Maximilian J. Poller ^{*a}

Transition-metal substituted Keggin-type polyoxometalates (POMs) are of great interest for applications in biomedicine, material science, and catalysis. The synthesis of transition metal-substituted Keggin-type polytungstates *via* the formation of a lacunary structure is well established, in contrast this approach is so far unexplored for Keggin-type polymolybdates. This is because the prevailing doctrine assumes that the lacunary Keggin phosphomolybdate $[\text{PMo}_9\text{O}_{34}]^{9-}$ is too unstable and can only be stabilized with organic ligands such as pyridine in organic solvents. In this work, we present a reliable procedure for the synthesis of the lacunary compound $[\text{PMo}_9\text{O}_{34}]^{9-}$ and its application in a novel *in situ* approach for the synthesis of different metal substituted POMs. The method is based on generating the lacunary species *in situ*, where the metal-substituted POMs are produced by adding another precursor compound. We employed this method to synthesize several new specific element-substituted POMs, which we present with comprehensive characterization. The interpretation of the analytical results was complemented by DFT calculations. For the separation of by-products from synthesis, we employed a novel membrane-based nanofiltration process, that enables superior separation of alkali salts from the POM solution resulting in >99% rejection of the POM components.

 Received 22nd May 2023,
 Accepted 14th July 2023

DOI: 10.1039/d3qi00937h

rsc.li/frontiers-inorganic

Introduction

Polyoxometalates (POMs) are an inorganic substance class of polyanionic metal oxide cluster compounds with defined nanoscale sizes and geometries. In general, there are two main coordination motifs for the oxo ligand: the metal–metal bridging M–O–M and the terminal M=O coordination motif. The history of the development of POMs starts in 1788 with Sheele, who studied the first example of *Molybdenum Blue*. Later in 1826, Berzelius discovered the anion $[\text{PMo}_{12}\text{O}_{40}]^{3-}$ which was isolated as an ammonium salt. One century later in 1934, Keggin presented the first solid-state structure as determined

by X-ray diffraction techniques, of the anion $[\text{PW}_{12}\text{O}_{40}]^{3-}$ which is known as the Keggin-type structure.^{1–3} Today, POMs are in the focus of different research topics ranging from catalysis, biomedicine, nanostructure to photovoltaic applications.^{4,5} Furthermore, there are applications for POMs acting as proton conductors or as motifs to modify perovskite and metal organic framework (MOF) materials to use the resulting compounds in photovoltaic applications.^{1,6–10} Due to their unique properties, an inorganic POM structure can be combined with an organic cation. The resulting hybrid materials are interesting for nanoscience and biobased applications.⁶

The incorporation of different elements, especially transition metals, into the Keggin-type phosphomolybdate POMs (also known as heteropolyanions/heteropolyacids (HPA))^{11–13} is a currently very active area of research.^{14,15} It is an interesting field not only from a synthetic point of view, but also from a catalytic perspective; in fact a major goal of this field is the synthesis of tailor-made catalysts.^{15–17} By substituting the framework metal with redox active transition metals, the redox potentials and thus the redox activity of the POM can be

^aInstitute of Technical and Macromolecular Chemistry, Hamburg University, Bundesstr. 45, 20146 Hamburg, Germany.

E-mail: maximilian.poller@uni-hamburg.de

^bMax Planck Institute for Dynamics of Complex Technical Systems, Molecular Simulations and Design Group, Sandtorstrasse 1, 39106 Magdeburg, Germany

† Electronic supplementary information (ESI) available. CCDC 2205006, 2205007, 2216946 and 2216947. For ESI and crystallographic data in CIF or other electronic format see DOI: <https://doi.org/10.1039/d3qi00937h>



tuned.¹⁵ Various transition metal-substituted phosphomolybdates are mentioned in literature. One of the most prominent examples is $H_8[PV_5Mo_7O_{40}]$ called HPA-5 (HPA for heteropolyacid and “5” representing the number of Mo(VI) positions that are substituted by V(V)) or HPV_5Mo , a POM that has been successfully established as a catalyst for the conversion of biomass to formic acid, as well as for the oxidative desulfurization of fuels.^{18–24} Quantum chemical calculations have shown that the incorporation of the different metals alters the shape of the POMs, where the bond distances between the oxygen atoms and upcoming metal change with respect to their atomic radii.²⁵ These distortions in M–O bonds originate from a pseudo Jahn–Teller vibronic instability at high symmetry configurations.²⁶

There are two possible pathways to synthesize element-substituted Keggin-type POMs: the self-assembly process,^{14,15,27,28} or, alternatively, *via* the formation of a lacunary structure. In the self-assembly process, the precursor compounds are dissolved in water in the targeted stoichiometry and then converted to the desired POM structure. This strategy has been successfully employed for the synthesis of V(V) substituted Keggin phosphomolybdates by Odyakov *et al.* using V_2O_5 as a precursor compound, resulting in structures of the type $H_{3+x}[PV_xMo_{12-x}O_{40}]$

(with $x = 0$ to 6).^{14,27,28} Our own group has successfully improved this method for the synthesis of Mn(II) and mixed Mn(II)–V(V)-substituted Keggin phosphomolybdates.¹⁵

The other possibility is the lacunary route: a lacunary POM is a defect POM structure where one or more MO_6 octahedra have been removed.^{29,30} These vacancies can then be filled with suitable multivalent transition metals, resulting in a redox substituted POM (Fig. 1). This approach has been successfully employed for Keggin and Wells–Dawson tungstates^{31,32} but so far has not successfully been extended to the respective molybdates. This is mainly due to the fact that phosphomolybdates are less stable than the corresponding tungstates. There are some reports of the lacunary phosphomolybdate structures dating back as far as the 1970s,^{33–38} however a detailed study of this compound is still missing.

In the present study, we present a reproducible synthetic procedure and comprehensive characterization for the lacunary Keggin-type phosphomolybdate anion $[PMo_9O_{34}]^{9-}$ (LHPA-3, where “3” represents the number of vacancies). Furthermore, we have thoroughly explored this synthetic opportunity by successfully incorporating various metals of different valence into LHPA-3 (Fig. 1) and characterized the resulting new compounds in detail.

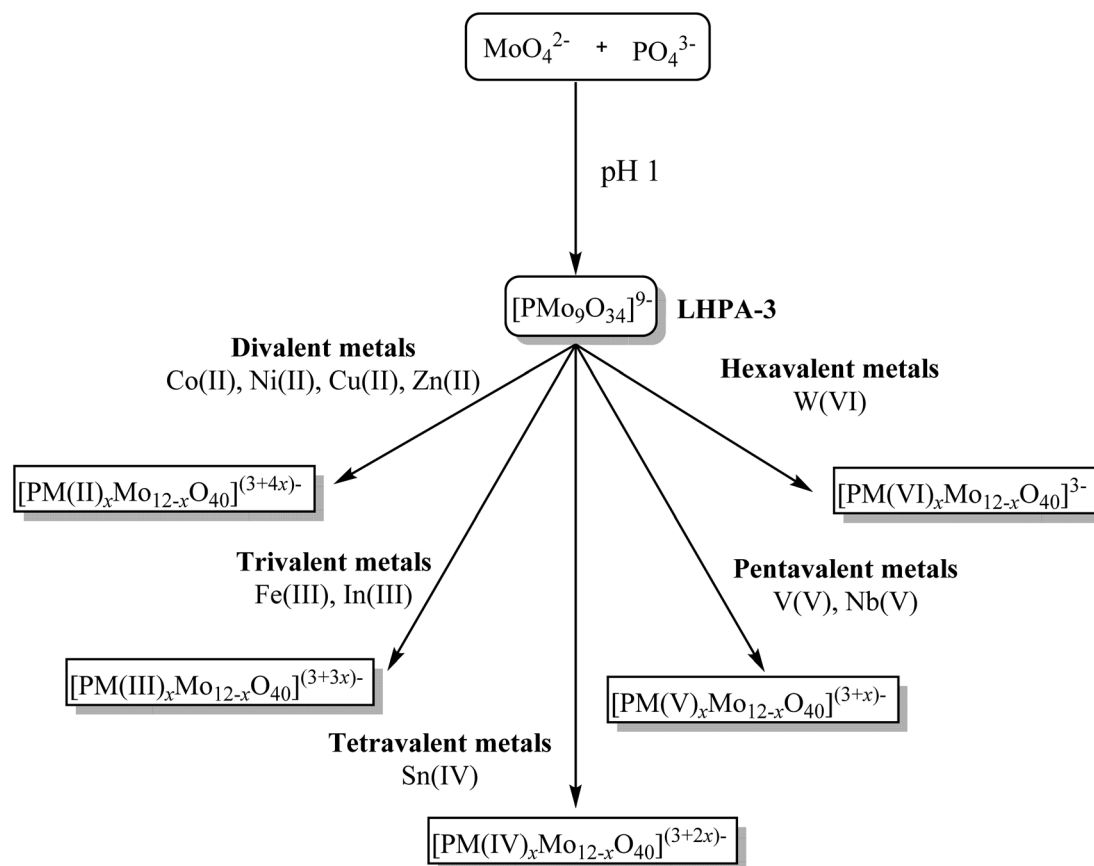


Fig. 1 Lacunary approach used in this work. $[PMo_9O_{34}]^{9-}$ (LHPA-3) as main compound for further substitution by different redox-active metals of various valence.



Previous computational studies have focused on relative stabilities of isomers of Keggin structures,^{39,40} the dimerization of Lindqvist and Keggin structures⁴¹ and spectra of first-row substituted Keggin structures.⁴² Here, the investigation is extended to phosphomolybdate POMs and substitutes thereof. The results from DFT calculations allow to make statements about relative stabilities of metal substitutions and rationalize peak positions in IR and Raman spectra.

A particular challenge in our synthetic procedure was the separation of the products from the counterions of the precursor materials (usually alkali salts). Commonly, this problem is solved by crystallisation or extractive removal of the POM using diethyl ether from the aqueous reaction solution.⁴³ From our experience the diethyl ether purification method does not work for transition-metal substituted POMs with high degrees of substitution or with high charges. Crystallisation is usually time consuming and lowers the yield significantly due to similar solubilities of the POM and the impurities.²⁹ For the here presented study, we have used a membrane process using nanofiltration as a novel approach to solve this problem. Esser *et al.* have already demonstrated that a Keggin-type POM catalyst can be separated from the reaction products using nanofiltration membranes, achieving catalyst rejections of over 99%.⁴⁴ Hereby, the competitiveness of an alternative membrane system with an integrated stirrer in the membrane cell could be demonstrated and showed its potential economic advantages in the enrichment of POMs in the retentate.⁴⁴ In this work, we used the same nanofiltration membrane setup for the efficient removal of accompanying metal salts from the POM solution to isolate the synthesized compounds in high yield and purity.

Results and discussion

Synthesis and characterization of the Lacunary compound

For the synthesis of the Keggin-type lacunary POM LHPA-3, we adapted the procedure described by Himeno *et al.*⁴⁵ An aqueous solution of Na₂MoO₄ and Na₂HPO₄ was acidified using concentrated hydrochloric acid. Upon evaporation of the solvent, the product precipitated in the form of yellow crystals, some of them were suitable for single crystal X-ray diffraction (Fig. 2).

The asymmetric unit of the structure (depicted in the ESI, Fig. S40†) contains three different metal sites, aside from the phosphorus atom and 12 oxygen atoms. The oxygen atoms can be grouped into four categories: oxygens connecting the central P atom to Mo atoms (O_p), bridging oxygen atoms between two Mo atoms (O_b), terminal oxygen atoms bound to a Mo atom (O_t), and oxygen atoms pointing into the lacunary position (O_l), *i.e.* the void which is caused by the missing MoO₆ octahedra.

The comparison of selected structural features of LHPA-3 and the parent compound H₃[PMO₁₂O₄₀] (HPMo) (Table 1) shows a significant contraction of the internal metal oxygen bonds (Mo–O_{p,b}) and an elongation of the bonds to the term-

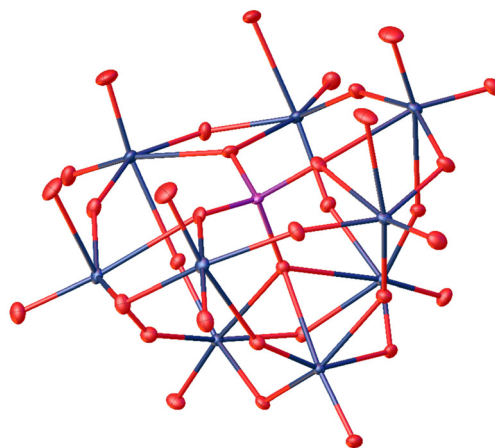


Fig. 2 Solid-state structure of LHPA-3 as determined by single crystal X-ray diffraction. The compound was crystallized in the hexagonal space group $P6_3$ (173). R_1 : 1.85%, wR_2 : 5.38%, R_{int} : 3.28%, GooF: 1.098. Thermal ellipsoids are drawn at 50% probability level. Colour code: purple: phosphorous, blue: molybdenum, and red: oxygen. Hydrogen atoms have not been modelled. The full crystallographic information file (cif) is available through the joint Cambridge Crystallographic Data Centre and Fachinformationszentrum Karlsruhe Access Structures service (deposition number: 2205006†).

Table 1 Selected structural features of LHPA-3 in the solid state, a full overview is provided in the ESI, Table S11†

Bond lengths			
	LHPA-3	HPMo ⁴⁶	Sum of covalent radii ⁴⁷
P–O _p ^a	1.55 Å	1.53 Å	1.74 Å
Mo–O _p ^a	2.36 Å	2.44 Å	2.01 Å
Mo–O _b ^a	1.88 Å	1.92 Å	2.01 Å
Mo–O _t ^a	1.70 Å	1.67 Å	2.01 Å
Mo–O _l	1.71 Å and 2.21 Å (3 each)	n.a.	2.01 Å
Angles			
	LHPA-3	HPMo	Ideal angle
O _p –P–O _p ^a	108.4°	109.5°	109.5°
O _b –Mo–O _t ^a	99.5°	102.1°	90°
O _l –Mo–O _{p,b,t} ^a	97.2° and 82.6° (3 each)	n.a.	90°

^a Average value of multiple bonds of the same type.

inal/lacunary oxygen atoms in LHPA-3. Generally short bond lengths are expected for the terminal (and lacunary) oxygen atoms, corresponding to their double bond character. Noteworthy is, that the oxygen atoms pointing into the lacunary void have very different bond lengths: half of them have very short bonds and are connected to a convex coordinated Mo (O_l–Mo–O_{p,b,t} > 90°), the other half has a very long bond and is connected to a concavely coordinated Mo (O_l–Mo–O_{p,b,t} < 90°). As expected, angles of the polyhedra deviate more strongly from the mathematically ideal angles in LHPA-3 due



Table 2 Elemental analysis and TGA results of LHPA-3

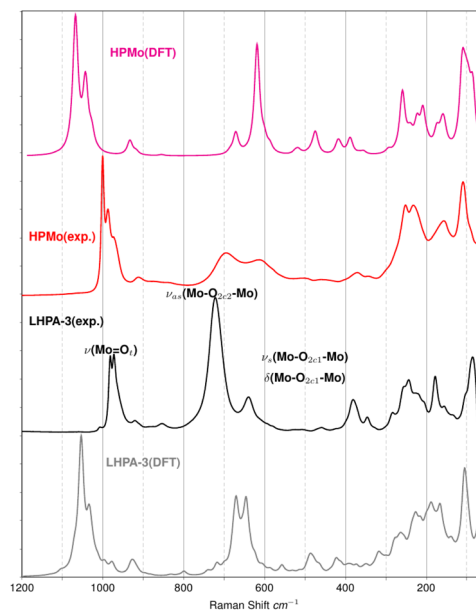
Compound	Targeted molecular composition	Na/K/P/Mo ratio ^a	Hydration water ^b [mol per mol-POM]
LHPA-3	Na ₉ [PMo ₉ O ₃₄]	20.8/0/1.2/9	6

^a P and Mo were determined by ICP-OES, Na and K by AAS, the data were normalized to the target Mo content. ^b The content of hydration water was determined by thermogravimetric analysis (TGA).

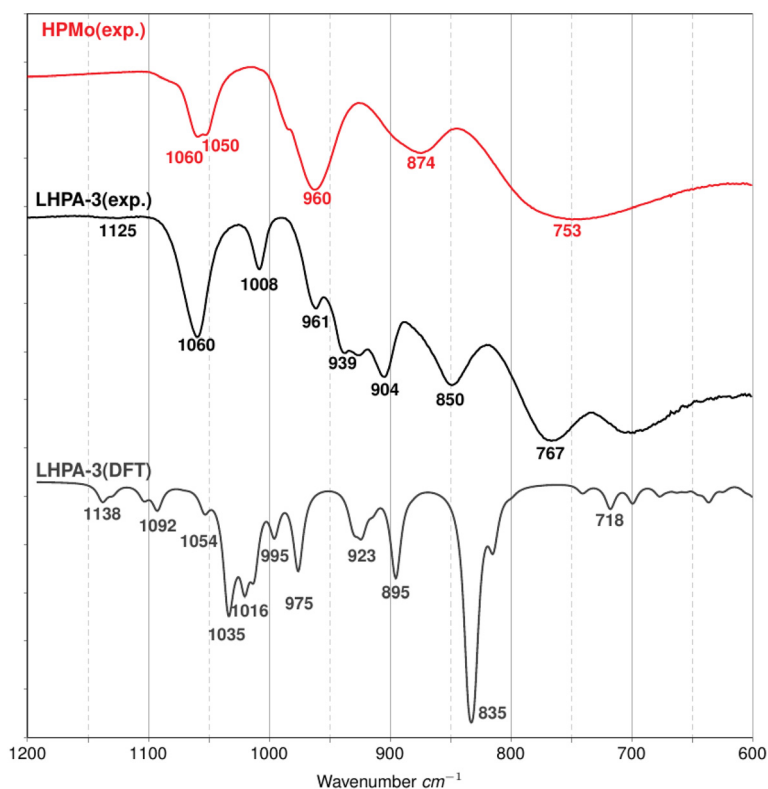
to the loss of the high symmetry present in the full Keggin structure.

The bulk product was further characterized by AAS/ICP-OES and thermogravimetric analysis (TGA) (Table 2).

The analysis confirms the 1 : 9 P : Mo stoichiometry. Using alkali metal containing precursors and adjustment of the pH value using hydrochloric acid, undesirable salt formation is not avoidable. Therefore, the increased sodium content is expected due to the coprecipitation of the sodium chloride. Purification with the nanofiltration membrane was not possible as the conditions in the setup caused LHPA-3 to decompose, possibly forming [P₂Mo₁₈O₆₂]⁶⁻ (*vide infra*). The potassium content was determined, as it is a common impurity in sodium salts, but no potassium was detected. The amount of hydration water of LHPA-3 was determined as 6 mol H₂O per mol LHPA-3.

**Fig. 4** Experimental and calculated Raman spectra of LHPA-3 (in comparison to HPMo).

The material was further analysed with ATR-FT-IR spectroscopy (Fig. 3) and Raman spectroscopy (Fig. 4). In both, the IR- and the Raman spectrum, LHPA-3 exhibits several

**Fig. 3** ATR-FT-IR spectra of LHPA-3 (experimental and calculated) in comparison to HPMo.

additional bands compared to HPMo, corresponding to the loss of symmetry. These additional bands were then assigned by spectral comparison with quantum chemical (DFT) calculations.

Fig. 3 shows the comparison of the experimental IR spectra of both Lacunary and HPMo structures with DFT calculated spectrum of the LHPA-3 lacunary complex. In the IR spectrum of HPMo, characteristic vibrational modes can be seen, which are assigned to the antisymmetric P–O (above 1000 cm^{-1}) and to the terminal Mo=O vibration (above 900 cm^{-1}) modes, as well as two types of Mo–O–Mo vibration modes: $(\text{M–O–M})_{\text{vertex}}$ and $(\text{M–O–M})_{\text{edge}}$ in the range of $800\text{ to }900\text{ cm}^{-1}$ and $600\text{ to }800\text{ cm}^{-1}$.^{15,48,49} LHPA-3 exhibits several additional bands in the range of the terminal Mo=O vibrations. This matches the observation of several different bond lengths for the terminal and lacunary O atoms, identified in the solid-state structure (*vide supra*).

The new peaks in the experimental IR absorption spectrum of LHPA-3 appear at roughly 850 , 904 , 939 , 1008 , and 1125 cm^{-1} compared to the HPMo species. In order to be able to assign these new peaks to specific vibrations, the LHPA-3 lacunary structure was optimized using DFT methods. The results from DFT calculations show that new peaks appear due to the central phosphate group. The broad peak at 1125 cm^{-1} in the experimental spectrum can be split into two small peaks at 1138 and 1092 cm^{-1} and refers to the central P=O bond stretches in DFT optimized LHPA-3. The peaks at 1054 and 1035 cm^{-1} correspond to the symmetric and anti-symmetric terminal Mo=O stretches, respectively, and can be related to the experimental peaks at 1060 cm^{-1} in both LHPA-3 and HPMo complexes. The peak at 1016 cm^{-1} represents the O=P=O asymmetric stretching and the peak at 995 cm^{-1} refers to a symmetric in-plane P=O stretch motion. The peak at 975 cm^{-1} shows an out-of-plane P=O bond vibrational mode. The peaks at 923 and 895 cm^{-1} correspond to symmetric and asymmetric M–O–M distortions along the vertex and finally the strong peak at 835 cm^{-1} in the DFT calculated spectrum of LHPA-3 complex refers to the M–O–M stretch along the edge.

The Raman spectra (Fig. 4) also show a noticeable difference in the bridging Mo–O–Mo vibrational bands ($600\text{ to }800\text{ cm}^{-1}$) between the two molecules and confirms the spectral assignment. Frequently, a fitted scaling factor is applied to the computed spectra in order to improve the agreement with the experiment. For our unscaled theoretical peak positions, a systematic shift of $\sim 50\text{ cm}^{-1}$ is considered satisfying. Furthermore, the comparison of experimental Raman spectra from solid samples with isolated molecules may contribute to the shift. Theoretical means are thus able to provide reliable spectral features in IR and Raman to support the assignment of peak positions from the experiment.

In order to gain further insights into the behaviour of LHPA-3 in solution, the compound was studied using ^{31}P -NMR spectroscopy at pH 1 in comparison with HPMo (Fig. 5).

The ^{31}P -NMR spectrum of LHPA-3 (Fig. 5 bottom) shows a single signal at -3.96 ppm , which is similar to the chemical

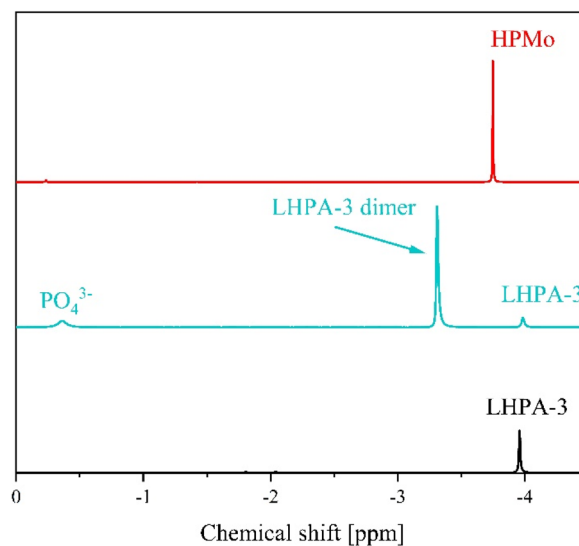


Fig. 5 ^{31}P -NMR spectra of LHPA-3 (bottom) in comparison with HPMo (top) and dimerized LHPA-3/Wells–Dawson phosphomolybdate (middle) in a mixture of 90% H_2O (pH 1, adjusted with HCl) and 10% acetone- d_6 . The spectra were measured at 242.9 MHz, using 85% H_3PO_4 as external standard. The dimerization was induced by heating the solution to $85\text{ }^\circ\text{C}$ for some minutes.

shift of HPMo at -3.75 ppm (Fig. 5 top). This clearly shows that LHPA-3 remains stable in solution (at room temperature) as no impurities or dissociation products are observed. While our here presented results clearly demonstrate that LHPA-3 is sufficiently stable to obtain single crystals and to be used for further synthesis, the notion of the instability of LHPA-3 is not entirely unfounded. Our attempts to work up aqueous solutions of LHPA-3 using a rotary evaporator ($80\text{ }^\circ\text{C}$, *ca.* 200 mbar), resulted in crystals of the mixed sodium/potassium salt of $[\text{P}_2\text{Mo}_{18}\text{O}_{62}]^{6-}$. This compound, which is a Wells–Dawson type phosphomolybdate, is formed by the condensation of two LHPA-3 units, likely induced by the elevated temperature. Since the structure of this anion has been discussed in sufficient detail by Haiyan An *et al.*,⁵⁰ we refrain from further discussion here but provide details in the ESI (Fig. S42 and S43[†]). We have also verified this dimerization of LHPA-3 by briefly heating up an acidic aqueous solution of LHPA-3 to $85\text{ }^\circ\text{C}$ and subsequently performing ^{31}P -NMR spectroscopy (Fig. 5 middle). The resulting spectrum clearly shows an additional peak at -3.31 ppm , which is attributed to the dimerized Wells–Dawson species $[\text{P}_2\text{Mo}_{18}\text{O}_{62}]^{6-}$. This value is close to the literature value of -3.22 ppm .⁵¹ So, this behaviour might have led researchers to conclude that LHPA-3 is not stable enough for further use.

The Gibbs free energy of the formation of LHPA-3 was calculated using quantum chemical (DFT) calculations, where a Wells–Dawson species $[\text{P}_2\text{Mo}_{18}\text{O}_{62}]^{6-}$ is formed from two LHPA-3 monomers and 6 water molecules are released in the process (Fig. 6). In an acidic medium, the terminal oxygen atoms at the vertex are most likely to be protonated. The for-



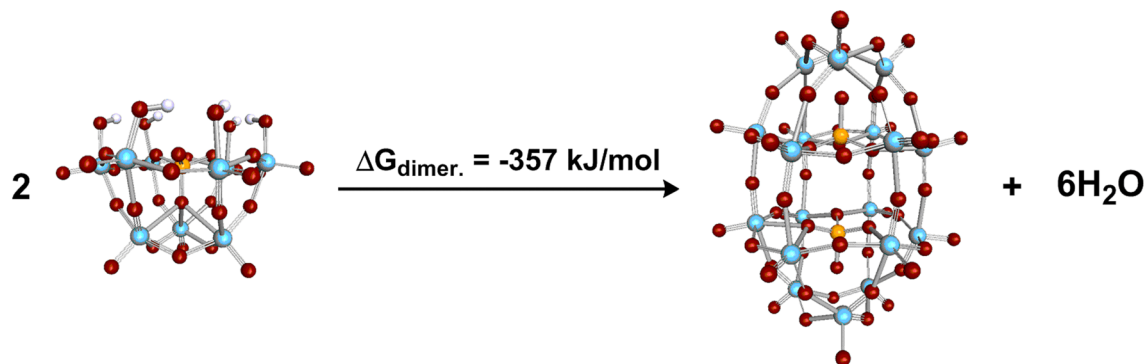


Fig. 6 Calculated dimerization of LHPA-3 in acidic aqueous medium (pH 1) forming a Wells–Dawson species.

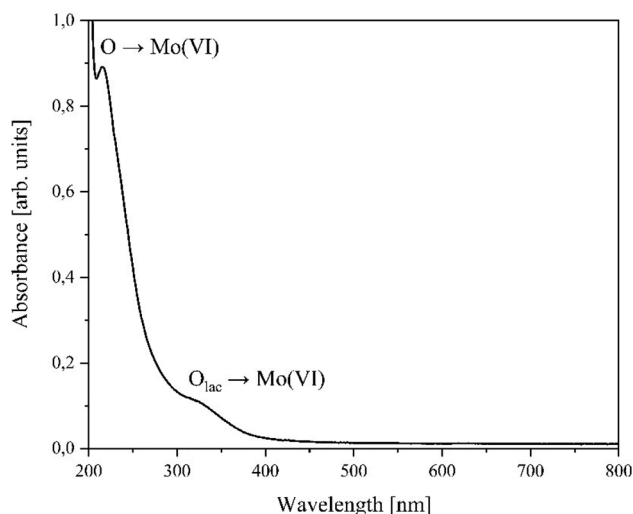


Fig. 7 UV Vis spectrum of LHPA 3 in aqueous, pH 1 solution with the characteristic LMCT bands.

mation of the dimerized Wells–Dawson species is thermodynamically favourable in acidic solution with a change in Gibbs free energy of -357 kJ mol^{-1} using an implicit solvent model.

UV-Vis measurements of the acidic aqueous solution of LHPA-3 (Fig. 7) show two significant peaks: 215 nm and 321 nm. After reaching the maximum from the LMCT peak at 215 nm, the intensity continues to increase towards smaller wavelengths. However, the maximum of the increase is no longer reached in the available measurement range ($>200 \text{ nm}$), which could indicate the presence of another peak below 200 nm.

The observed signals correspond to the $\text{O} \rightarrow \text{Mo}(\text{VI})$ ligand-to-metal-charge-transfer excitations (LMCT) of different oxygen atoms. Since for HPMo the main UV-Vis band has its maximum at 218 nm with no additional peaks at higher wavelengths,¹⁵ it can be concluded that the band at 321 nm belongs to the $\text{O} \rightarrow \text{Mo}(\text{VI})$ LMCT of the lacunary oxygen atoms (O_l).

To complete the characterization of LHPA-3 we have performed electrochemical measurements, in detail cyclic voltammetry (CV) and square-wave voltammetry (SWV). The results are shown in the ESI Table 8 and Fig. S30 and S31.† From the obtained data we see that LHPA-3 undergoes similar redox processes as HPMo. However, the structural changes in LHPA-3 cause a shift of its potentials to higher values.

Application of the lacunary phosphomolybdate for the synthesis of various addenda element substituted Keggin-type POMs

As stated in the introduction, the significance of LHPA-3 lies in its potential as a precursor for the synthesis of POMs with further element substitutions in the metal framework. We therefore investigated this synthetic route by combining LHPA-3 with various metals of different oxidation states, namely: $\text{Co}(\text{II})$, $\text{Ni}(\text{II})$, $\text{Zn}(\text{II})$, $\text{Cu}(\text{II})$, $\text{Fe}(\text{III})$, $\text{In}(\text{III})$, $\text{Sn}(\text{IV})$, $\text{V}(\text{V})$, $\text{Nb}(\text{V})$, and $\text{W}(\text{VI})$. Most of these elements are of interest for catalytic applications due to their redox properties such as $\text{V}(\text{V})/\text{V}(\text{IV})$, $\text{Fe}(\text{III})/\text{Fe}(\text{II})$, $\text{Co}(\text{III})/\text{Co}(\text{II})/\text{Co}(\text{I})$, $\text{Cu}(\text{II})/\text{Cu}(\text{I})$, and $\text{Sn}(\text{IV})/\text{Sn}(\text{II})$.⁵² Other metals were chosen to explore the limits of this synthetic strategy, especially the main group elements In and Sn, as the incorporation of main group elements in POMs, although previously demonstrated, is still in its infancy.^{53,54}

A particular challenge was the choice of a suitable precursor for $\text{Nb}(\text{V})$ as most Nb salts are either not water soluble or precipitate as Nb_2O_5 in aqueous solution. Various studies report potassium hexaniobate $\text{K}_8[\text{Nb}_6\text{O}_{19}]$ (KNb) as a suitable precursor, a Lindqvist-type POM structure that can only be stabilized in strongly alkaline media ($\text{pH} > 12$).^{55–60} Since LHPA-3 is only stable in acidic solutions, KNb was first dissolved in an aqueous hydrogen peroxide solution, which was then acidified.⁶¹ The peroxide prevents the precipitation of Nb_2O_5 , presumably *via* formation of a $\text{Nb}(\text{V})$ peroxo complex, long enough for the $\text{Nb}(\text{V})$ to be incorporated into LHPA-3. A detailed procedure for the synthesis, characterisation, and utilisation of $\text{K}_8[\text{Nb}_6\text{O}_{19}]$ is presented in the ESI (section 1.4).†

In a typical synthesis procedure for these metal incorporations, LHPA-3 was prepared *in situ* and used in aqueous solution, without previous purification. To this solution, suitable



precursors or respective aqueous solutions were added, and the mixture was heated to reflux for 30 minutes. The pH of the mixture was adjusted to approx. 1.5 using hydrochloric acid. For subsequent purification, a nano-filtration membrane setup, which has previously been successfully employed for the recycling of homogenous POM catalysts,⁴⁴ was used. An overview of the synthesised compounds is given in Table 4.

Purification of the newly synthesized POMs by nanofiltration

Since the above-described procedure requires the adjustment of a defined pH value, various alkali salts are present in addition to the POM. For the purification of the POMs, we have developed a nanofiltration method, which succeeds in separating salts and POM from each other.

The nanofiltration system was operated in a modified diafiltration mode. Samples were taken from the permeate of each cycle to determine the salt content and catalyst loss by AAS/ICP-OES analysis. In addition, the permeates were concentrated by rotary evaporation and the resulting salt fractions were combined and analyzed by FT-IR spectroscopy as well as ICP-OES analysis. Fig. 8 shows the evolution of sodium and potassium concentrations over the four diafiltration cycles. There is a clear exponential decrease in the concentrations of sodium and potassium. The sodium concentration in the permeate already decreases from an initial value around 17.6 g L⁻¹ to 6.1 g L⁻¹ within one diafiltration cycle, which corresponds to a decrease by a factor about 3. After the fourth cycle, the sodium concentration in the permeate reaches a value below 0.5 g L⁻¹. The potassium concentration shows a comparable trend.

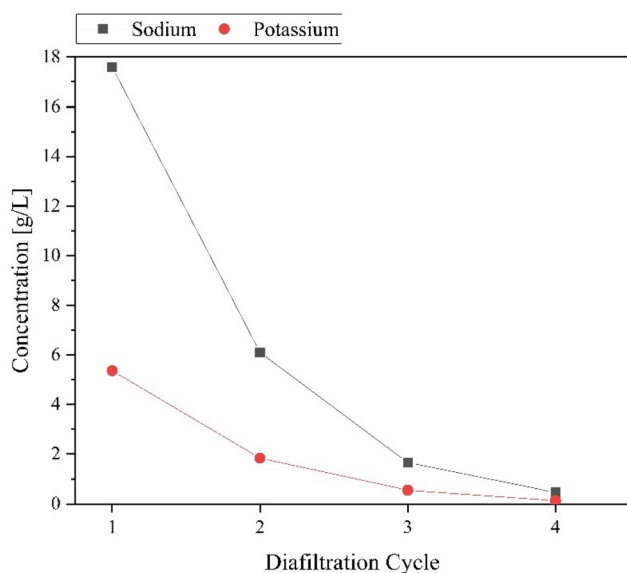


Fig. 8 Development of the sodium and potassium concentrations in the permeate depending on the conducted diafiltration cycles.

AAS measurements of the retentate reveal that there is still a residual sodium concentration of 7.0 g L⁻¹, which corresponds to a difference about 6.5 g L⁻¹, compared to the corresponding permeate. However, for each POM anion, a sufficient number of cations must remain in the retentate. In this exemplarily presented case, the anion is [PNb₃Mo₉O₄₀]⁶⁻, which requires six equivalents of alkali counterions. A visual representation of the decreasing salt concentration from cycle to cycle and the purified yellow POM fraction [PNb₃Mo₉O₄₀]⁶⁻ is shown in Fig. S7.† To finally confirm that the isolated POM is free of chloride (and thus free of the corresponding alkali chloride salts), the POM sample was analyzed for chloride content by energy dispersive X-ray spectroscopy (EDX). As an average value over three measurements, a chloride content of 0.028 wt% was found. Thus, it can be assumed that the corresponding salts were almost completely removed by the nanofiltration process.

In order to minimize losses of the valuable products, a high selectivity is extremely important for the purification process. For this purpose, the permeate samples were analysed by AAS and ICP-OES with regard to their content of the POM components molybdenum, niobium and phosphorous. For each permeate the rejections of these components were determined as described in the corresponding section of the experimental part (ESI†). All catalyst components were rejected virtually to 100%, meaning that almost no POM anion passed the membrane (see Fig. S8†). Furthermore, the permeate sample was analyzed using powder XRD. The powder diffractogram in the ESI (Fig. S9†) shows that the permeate fraction consists mainly of sodium and potassium chloride. Essentially, the potassium content comes from the KNb precursor.

The success of the purification process can be evaluated based on the composition of the POM fraction as target product of the process. For this purpose, the stoichiometric ratios of the individual catalyst components before and after purification are shown in Table 3.

Table 3 Calculated stoichiometries of the catalyst components before and after purification

Entry ^a	Process step	Stoichiometry ^b				
		Mo ^c	Nb ^c	P ^c	Na ^d	K ^d
1	Target value	9.0	3.0	1.0	6.0	
2	Before purification	9.0	2.9	1.1	19.5	4.0
3	After purification	9.0	2.8	1.0	5.1	1.5

^a Experimental conditions: pre-wetted DK-series membrane, ambient temperature, 30 bar transmembrane pressure, 15 ml min⁻¹ flow rate, 1100 rpm stirring speed. ^b Calculated as described in the corresponding section of the experimental part. ^c Determined with ICP-OES. ^d Determined with AAS.

Finally, after synthesis and purification, the elemental composition of all compounds was confirmed by ICP-OES and AAS (Table 4).



Table 4 Overview of POMs synthesized in this project. Green indicates successful synthesis, yellow indicates successful incorporation of the substituting metal but significant deviation from the target stoichiometry, red indicates unsuccessful attempts

Compound	Subst. precursor	Target composition	Measured composition ^a	Hydration water ^b
Divalent metals				
NaPCoMo	Co(OAc) ₂	Na ₇ [PCoMo ₁₁ O ₄₀]	Na _{3.5} [P ₁ Co ₁ Mo ₁₁ O ₄₀]	8
NaPNiMo	Ni(OAc) ₂	Na ₇ [PNiMo ₁₁ O ₄₀]	Na ₄ [P ₁ Ni _{0.9} Mo ₁₁ O ₄₀]	8
ⁿ Bu ₄ NPCu ₂ Mo	CuCl ₂	(ⁿ Bu ₄ N) ₁₁ [PCu ₂ Mo ₁₀ O ₄₀]	Na _{2.2} [P _{1.1} Cu _{0.8} Mo ₁₀ O ₄₀]	—
NaPZnMo	Zn + HCl	Na ₇ [PZnMo ₁₁ O ₄₀]	Na _{3.7} [P _{1.1} Zn _{0.4} Mo ₁₁ O ₄₀]	8
Trivalent metals				
NaPFeMo	FeCl ₃	Na ₆ [PFeMo ₁₁ O ₄₀]	Na _{3.5} [P _{1.1} Fe _{1.1} Mo ₉ O ₄₀]	8
NaPIn ₃ Mo	In(OH) ₃ + HCl	Na ₁₂ [PIn ₃ Mo ₉ O ₄₀]	Na _{1.6} [P ₁ In _{2.5} Mo ₉ O ₄₀]	20
Tetravalent metals				
NaPSnMo	Sn + HCl + H ₂ O ₂	Na ₅ [PSnMo ₁₁ O ₄₀]	Na _{0.1} [P ₁ Sn ₀ Mo ₁₁ O ₄₀]	9
Pentavalent metals				
NaKPNbMo	K ₈ [Nb ₆ O ₁₉]	Na ₄ [PNbMo ₁₁ O ₄₀]	Na ₃ K _{0.5} [P _{0.9} Nb _{1.1} Mo ₁₁ O ₄₀]	6
NaKPNb ₂ Mo	K ₈ [Nb ₆ O ₁₉]	Na ₅ [PNb ₂ Mo ₁₀ O ₄₀]	Na ₄ K _{0.7} [P ₁ Nb _{1.8} Mo ₁₀ O ₄₀]	5
NaKPNb ₃ Mo	K ₈ [Nb ₆ O ₁₉]	Na ₆ [PNb ₃ Mo ₉ O ₄₀]	Na _{4.2} K _{1.4} [P _{0.9} Nb _{2.9} Mo ₉ O ₄₀]	7
NaKPV ₂ NbMo	K ₈ [Nb ₆ O ₁₉]	Na ₆ [PV ₂ NbMo ₉ O ₄₀]	Na _{6.3} K _{0.8} [P _{1.1} V _{2.3} Nb _{1.1} Mo ₉ O ₄₀]	7
NaKPVNb ₂ Mo	Na ₃ VO ₄ K ₈ [Nb ₆ O ₁₉]	Na ₆ [PVNb ₂ Mo ₉ O ₄₀]	Na _{4.1} K _{0.8} [P ₁ V _{0.9} Nb ₂ Mo ₉ O ₄₀]	5
NaPV ₃ Mo	Na ₃ VO ₄	Na ₆ [PV ₃ Mo ₉ O ₄₀]	Na _{5.4} [P ₁ V ₃ Mo ₉ O ₄₀]	8
Hexavalent metals				
NaPW ₃ Mo	Na ₂ WO ₄	Na ₆ [PW ₃ Mo ₉ O ₄₀]	Na _{4.9} [P _{1.1} W ₃ Mo ₉ O ₄₀]	28

^aThe content of the elements (except O) was determined by ICP-OES or AAS. The results were normalized to the targeted Mo content. Residual negative charge is assumed to be compensated by H⁺, as all compounds were obtained from acidic solutions. ^bHydration water was determined by thermogravimetric analysis (TGA).

Based on the results from elemental analysis (Table 4 and ESI section 1.7†) the incorporation of most of guest elements, particularly the penta- and hexavalent metals, was successful. From the obtained ICP-OES data (yellow and red markers), limitations were found for the following elements: Cu(II), Zn(II), In(III) and Sn(IV). The limitations are limited to the late transition metals and to the main group elements, whereas the incorporation of Sn(IV) was not successful.

DFT calculations were performed in order to probe structural changes by substituting one molybdenum atom of HPMo with di- to hexavalent metal atoms (see Fig. 9). The structural changes in the POM structure upon introducing the (di- to hexavalent) metal atoms were characterized based on: (i) metal–oxygen bond lengths and (ii) distance of central phosphorous atom to the newly introduced metal atom.

The metal–oxygen and phosphorus–metal distances remain almost unchanged upon substituting molybdenum with pentavalent vanadium. Due to the increase in the atomic radii, the metal–oxygen distances slightly increase from 1.8 Å to 1.97 Å and 1.99 Å for M–O₁ and M–O₂ upon introduction of niobium into the POM. However, the rest of the structural parameters remains almost unchanged. The similar trend was also found for tungsten substitution, thus suggesting an easy incorporation of penta- and hexavalent metals into the Keggin structure. Exceptions are the incorporation of Cu(II), Zn(II) and In(III), which were only partially successful, and the incorporation of Sn(IV), which was entirely unsuccessful. A reason for this might be that the coordination chemistry of these metal ions is dominated by p-orbitals as opposed to d-orbitals. In(III) (4d¹⁰5s⁰5p⁰) and Sn(IV) (4d¹⁰5s⁰5p⁰) are main-group elements in which the full d-orbitals are generally unavailable for

coordination chemistry. The DFT-optimized mono-substituted Co(II), In(III) and Sn(IV) POM structures show a significant elongation of M–O and P–M bond distances. The large bond distances indicate a weak binding interaction of the newly incorporated metal into the phosphomolybdate complex. M–O bond and P–M bond distances are increasing by 0.2 Å to 0.46 Å and 0.14 Å to 0.57 Å by introducing Co(II), In(III), and Sn(IV), with In(III) showing the largest increase followed by Sn(IV) and Co(II). In comparison to In(III), the introduction of Fe(III) reduces the P–M distance by 0.24 Å (from 3.56 Å to 3.32 Å) compared to HPMo. The possible reason for the reduction might be localization of the unpaired electron on the iron atom. Zn(II) is formally a transition metal, however it also has full d-orbitals (3d¹⁰4s⁰) and has therefore similar coordination propensities as main group elements.

The Cu(II) substituted POM exhibits a highly reactive behaviour: in contact with stainless steel, the solution turned dark blue, indicating reduction of the POM. It might therefore be possible, that a corresponding compound containing two Cu(II) ions is not thermodynamically stable. For this reason, the resulting compound, ⁿBu₄NPCu₂Mo, was not purified with the membrane setup, instead the POM was selectively precipitated from aqueous solution as a tetrabutylammonium (TBA) salt, whereby the other salts remain in solution.

The integrity of the Keggin structure was confirmed by ATR-FT-IR and Raman spectroscopy (Fig. 10 and ESI Fig. S11–S20†). Vibrational spectroscopy of POMs as a method for identifying the structure type is a well-established method and is discussed in literature to a great extent.^{15,48,49,62}

The IR spectra of all compounds exhibit the above described (see Fig. 3), characteristic bands for Keggin structures.



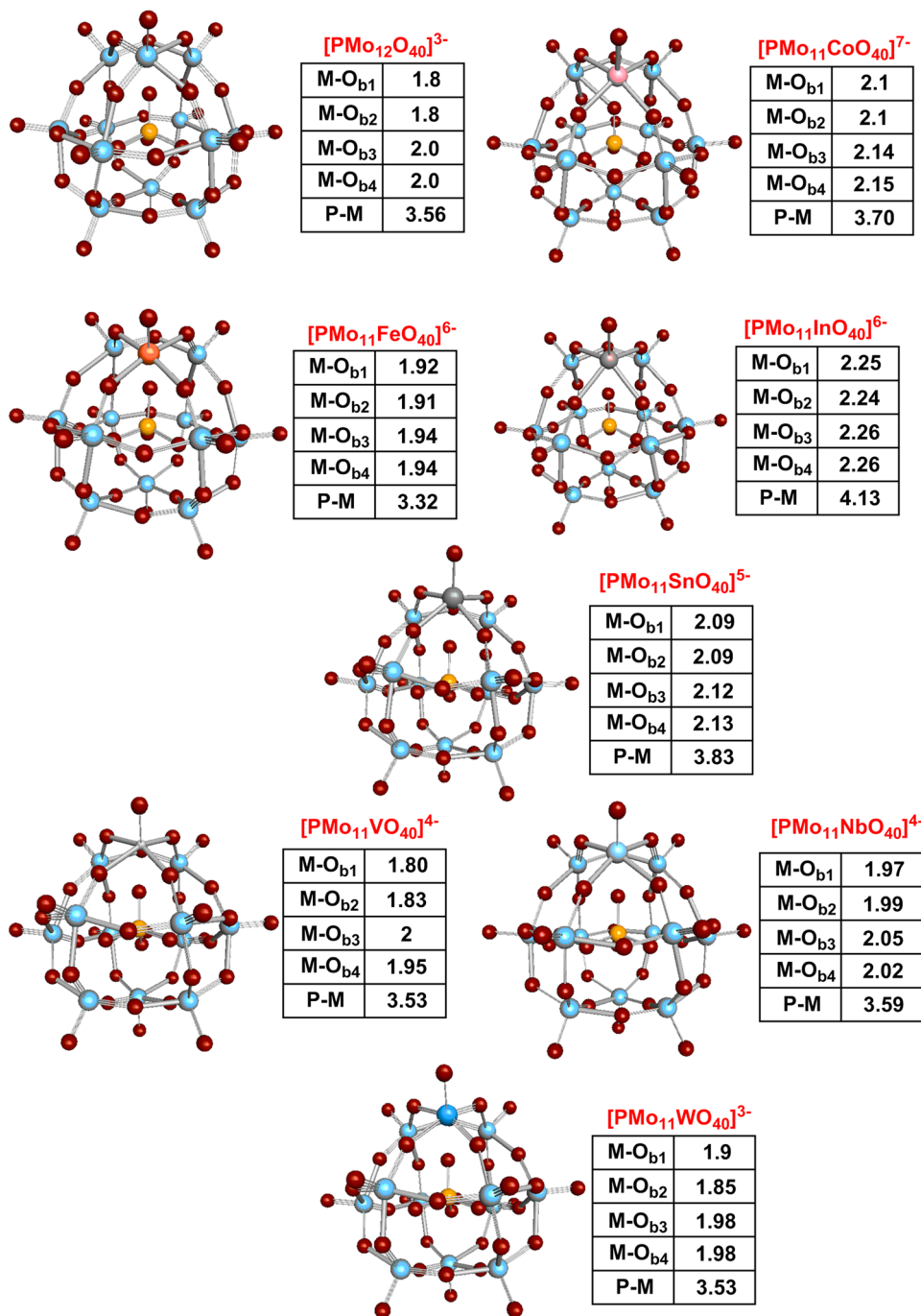


Fig. 9 DFT optimized structures of mono-substituted Keggin phosphomolybdates. Characteristic bond distances for O_t = terminal oxygen, O_b = bridging O, O_p = phosphate O are given.

From previous investigations, it is known, that for POMs, which are substituted with elements of significant lower mass than Mo(vi), the vibration bands are shifting to lower wavenumbers in comparison to the unsubstituted HPMo.^{15,18,48,49} This trend is observed for the substitution with Co(II), Ni(II), Cu(II), Zn(II), Fe(III) and V(V). Interestingly, although Nb and Mo have a similar mass, the vibration bands of the Nb(V) substituted POMs show the same trend indicating that the charge/oxidation state of the metal ion also plays a role (Table 5 and ESI Table 5†).

In contrast, a shift to higher wavenumbers occurs for POMs that are substituted with elements of significant higher mass. This is observed for NaPW₃Mo (Table 5 and Table 5 ESI†), the higher mass of W(VI) leads to shoulder formation of the P-O band (see ESI Fig. S19 and S20†).

The Raman spectra of the substituted POMs also exhibit significant differences in comparison with the unsubstituted HPMo, indicating the successful incorporation of the elements.



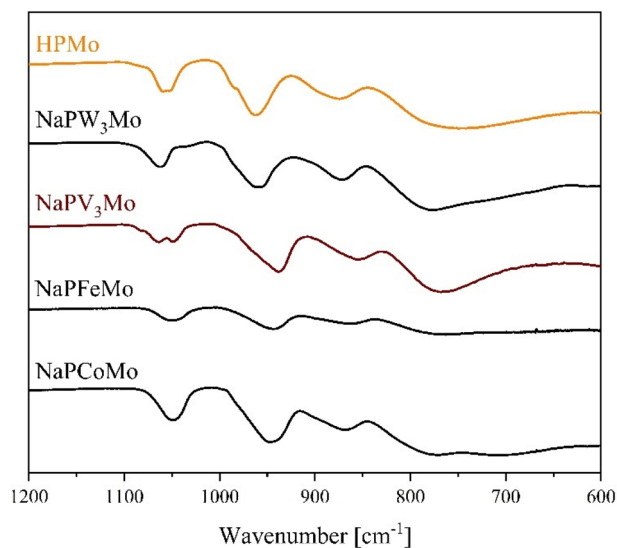


Fig. 10 ATR-FT-IR spectra of selected POMs, substituted with di-, tri-, penta- and hexavalent metals.

Table 5 Assignment of the FT-IR peaks of each POM to the corresponding vibration modes

POM	P-O	M=O _t	(M-O-M) _{vertex}	(M-O-M) _{edge}
HPMo ¹⁵	1059	962	877	744
NaPCoMo	1049	946	869	772, 707
NaPNiMo	1047	942	869	783
ⁿ Bu ₄ NPCu ₂ Mo	1077, 1055	935	864	777
NaPZnMo	1075, 1060, 1045	939	900	775
NaPFeMo	1051	945	864	766
NaPin ₃ Mo	1058	956	867	770
NaKPNbMo	1058, 1034	944	859	741
NaKPNb ₂ Mo	1049	947	856	757
NaKPNb ₃ Mo	1047	944	857	760
NaKPV ₂ NbMo	1045	942	847	750
NaKPVNb ₂ Mo	1048	944	859	762
NaPV ₃ Mo	1064, 1048	937	846	758
NaPW ₃ Mo	1062	959	872	777

In order to elucidate the structural influence of the metal substitution, a crystal of NaPV₃Mo was analysed with single-crystal X-ray diffraction (Fig. 11, crystallographic information file is available through the CCDC under the deposition number 2205007†).

The compound crystallized in the tetragonal space group $P4_21c$ (114) and conforms to the typical Keggin structure type. The asymmetric unit contains a quarter of the molecule with three distinct metal sites, which are all partially occupied by V and Mo, therefore a substitution pattern cannot be recognised. For each Keggin unit, four Na atoms are found, the remaining charge is presumably compensated by H⁺, which was not modelled. The closest distance between the counter ions and the POM is to two of the bridging O atoms. Since the distance is significantly larger than the sum of the respective covalent radii (Table 6), this interaction can be considered purely ionic with no covalent/dative bond character.

The bond lengths within the POM molecule are mostly similar to the bond lengths of the unsubstituted HPMo,⁴⁶ with

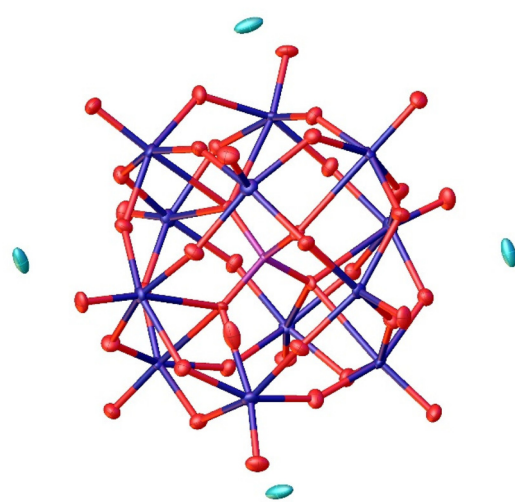


Fig. 11 Solid-state structure of NaPV₃Mo determined by single crystal X-ray diffraction. The compound crystallizes in the tetragonal space group $P4_21c$ (114). Hydrogen atoms have not been modelled. R_1 : 3.03%, wR_2 : 7.84%, R_{int} : 4.49%, GooF: 1.089. Color code: turquoise: sodium, purple: phosphorous, blue: molybdenum, and red: oxygen.

Table 6 Selected structural properties of NaPV₃Mo

	Bond lengths		
	NaPV ₃ Mo	H ₃ PMo ₁₂ O ₄₀ ⁴⁶	Sum of covalent radii ⁴⁷
P-O _p	1.54 Å	1.53 Å	1.74 Å
M-O _p ^a	2.29 Å	2.44 Å	2.01 Å (Mo-O), 1.97 Å (V-O), 2.00 Å (weighted average ^b)
M-O _b ^a	1.91 Å	1.92 Å	
M-O _t ^a	1.66 Å	1.67 Å	
Na-O _b ^a	3.00 Å	n.a.	2.18 Å
Angles			
	NaPV ₃ Mo	H ₃ PMo ₁₂ O ₄₀ ⁴⁶	Ideal angle
O _p -P-O _p ^a	109.5°	109.5°	109.5°
M-O _b -M ^a	123.4°/149.7°	125.7°/151.7°	90°/n.a.
O _t -M-O _b ^a	101.1°	102.1°	90°

^a Average value of multiple bonds/angles of the same type.

$$^b = \frac{3 \cdot (r_V + r_O) + 9 \cdot (r_{Mo} + r_O)}{12}$$

the exception of the bond between the metals and the phosphate oxygen atoms, which is significantly shorter in NaPV₃Mo although it still exceeds the sum of the respective covalent radii (Table 6). Among the bridging O atoms, two groups can be distinguished: three atoms with an average M-O-M angle of 123.4° connection, two edge-sharing MO₆ octahedra, and three other atoms with an average angle of 149.7° connecting corner-sharing MO₆ octahedra. These values are slightly lower than in HPMo.⁴⁶

Since the primary intended application for transition metal substituted POMs is homogeneous catalysis in aqueous solution, we further studied the newly synthesized compounds in



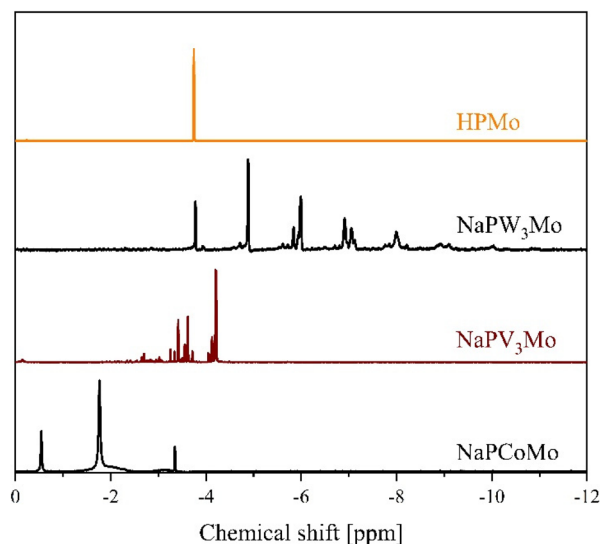


Fig. 12 ^{31}P -NMR spectra of selected POMs substituted with di-, penta- and hexavalent elements in a mixture of 90% H_2O (pH 1) and 10% D_2O . The spectra were measured at 242.9 MHz, 85% H_3PO_4 was used as external standard.

solution. For this purpose, we measured ^{31}P - and, where applicable, ^{51}V -NMR spectra, of the POMs. Fig. 12 shows the ^{31}P -NMR data of selected POMs, substituted with di-, penta- and hexavalent metals in comparison with HPMo. The ^{31}P data of NaFeMo are only shown in the ESI in Fig. S24,† because this spectrum shows no peaks, due to the strong paramagnetism of $\text{Fe}(\text{III})$. $\text{Co}(\text{II})$ is also a paramagnetic nucleus, so the ^{31}P signals are broadened in comparison to HPMo as shown in Fig. 12. Although the NMR samples were prepared of pure compounds, a complex pattern of signals is observed.

This is caused by two phenomena: the pH depended dissociation of the POMs and the isomerism (positional isomerism caused by the substitution as well as the intrinsic α/β isomerism of the Keggin structure).^{63–65} The dissociation, especially of substituted Keggin POMs has been described previously by several research groups.^{63,64} In aqueous solution, dissociation equilibria such as the ones shown in Fig. 13 cause multiple signals in the NMR spectra and lead to positional isomerisation.

In an unsubstituted POM like HPMo, all metal positions are equivalent, therefore only one signal is observed in the ^{31}P -NMR spectrum (ESI Fig. S20–S24†).^{63–67} However, as soon as a metal atom is substituted, the metal sites are not all equivalent anymore. Therefore, a second substitution can lead to several positional isomers with different substitution patterns.

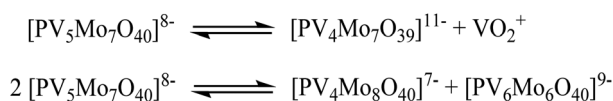


Fig. 13 Examples of possible dissociation equilibria POMs undergo in aqueous solution.

The number of such isomers increases drastically with the degree of substitution. While a substitution degree of two leads to only five isomers, the substitution of three metal atoms in the Keggin structure results in 13 possible isomers.⁶⁵ Furthermore, there are different isomers for a Keggin-structure, most importantly the α and the β isomer. The β isomer is significantly less stable than the corresponding α isomer, so the peaks corresponding to the β isomer have a comparatively low intensity.⁶²

As a result, the recorded spectra show a multitude of signals which are difficult to assign. In the recorded NMR-spectra (Fig. 12 and ESI Fig. S21–S25†) we find the above described phenomena confirmed in the fact that a multitude of signals is observed for all investigated compounds.

For catalytic applications of the POMs, the HOMO–LUMO gap (HOMO = highest occupied molecular orbital, LUMO = lowest unoccupied molecular orbital) is a relevant molecular property. To investigate this, UV-Vis spectra of all compounds were measured in aqueous solution (Fig. S26S29 ESI†). For the unsubstituted HPMo only one maximum is observed at a very low wavelength (218 nm), which can be assigned to the $\text{O} \rightarrow \text{Mo}(\text{VI})\text{O}_6$ LMCT (see ESI Table 7†).¹⁵ Most of the transition-metal substituted POMs, however, show an additional smaller maximum at slightly higher wavelengths (280–350 nm, Fig. 14). This second band can be attributed to the LMCT from oxygen to the substituted transition element. Excitations from lower metal d orbitals to higher metal d orbitals are not expected to be visible, since they are known to be 1000 times less intense than LMCT transitions.⁶⁸

The data in Fig. 14 show the $\text{O} \rightarrow \text{Mo}(\text{VI})\text{O}_6$ LMCT above 200 nm and the different transition metal LMCT bands about 300 nm for all elements investigated in this work, indicating that the latter transition requires less energy. The LMCTs for $\text{Nb}(\text{V})$ tend to be found in the 297 to 300 nm range, while the additional incorporation of vanadium causes the LMCT bands

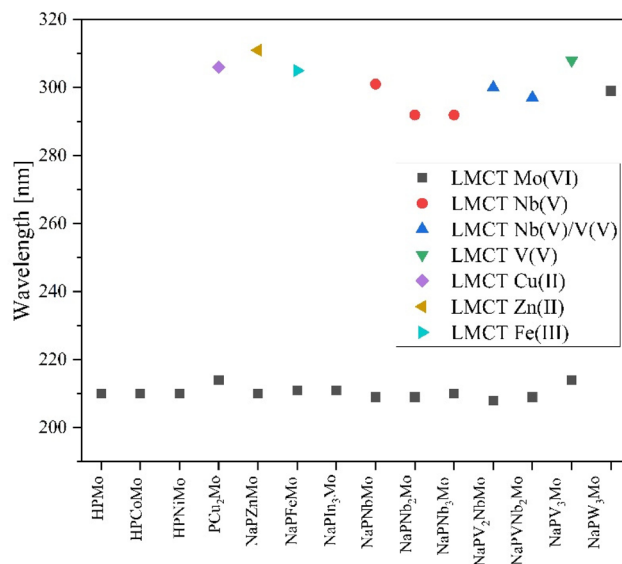


Fig. 14 LMCT positions of the metal-substituted POMs.



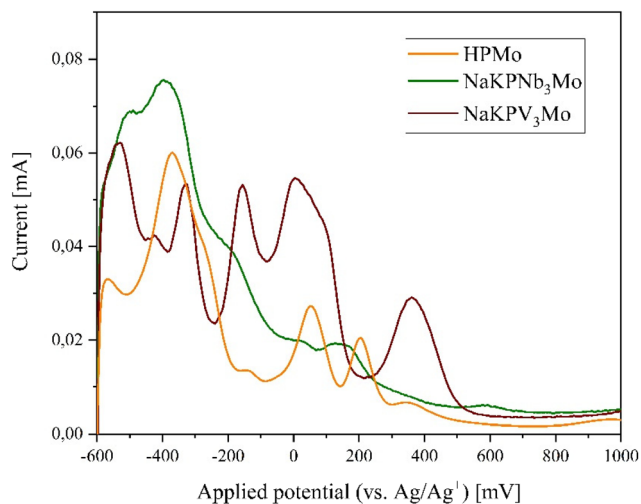


Fig. 15 Comparison between the SWV measurements of the three-fold substituted POMs with V(v) and Nb(v) in comparison to HPMo (concentration 1 mmol L⁻¹, scan rate 5 mV s⁻¹ (SWV) and pH 1). Hydrochloric acid was used as supporting electrolyte.

to shift to higher wavelengths. For NaPV₃Mo, the LMCT for the V(v) reaches 308 nm and for the V(v) and Nb(v) mixed substituted POMs the LMCT for Nb(v) and V(v) are overlapping and cannot be distinguished from each other. It is known from literature that the V(v) LMCT protrudes into the visible region: this is the reason for the colours of POMs.^{15,62,69} With increasing substitution of vanadium, the V(v) LMCT increases while the Mo(vi) LMCT decreases, leading to a darker color.¹⁵ Theoretically, the LMCT bands contain two LMCTs. The LMCT at smaller wavelengths is assigned to the transition from the terminal oxygen atom to the metal V=O_t and the LMCT at longer wavelengths is assigned to the transition from the metal-bridging oxygen atoms V-O_b/V-O_c to the metal. This effect is often not resolved but may manifest itself by the formation of a shoulder at higher wavelengths.^{15,69,70}

For applications in oxidation catalysis, the redox potentials of the transition-metal substituted POMs are of great importance. Therefore, the redox potentials of the synthesized POMs were measured using cyclic voltammetry (CV) and square-wave voltammetry (SWV). Exemplary the data are shown in Fig. 15 for the three-fold substituted POMs with Nb(v) as well as V(v) in comparison with the unsubstituted HPMo. Electrochemical data of the other POMs are provided in the ESI (see ESI Fig. S30–S39 and Tables 8–10†).

It is known from previous reports, that phosphomolybdates show several two-electron redox processes that can be tuned by incorporating different elements into the Keggin structure.^{15,71,72} The SWV data of the POMs containing Co(II), Ni(II), Cu(II), and Fe(III) (ESI Fig. S33 and S35†) show that these elements cause a shift of the redox potentials to higher potentials in comparison to HPMo. For ¹⁸Bu₄NPCu₂Mo (measured in acetonitrile) there are two peak potentials which are not observed for HPMo at 615 mV and 790 mV. These peak potentials might correspond to a redox process of Cu(II) to Cu(I).

Comparing NaPV₃Mo and NaKPNb₃Mo, the former shows a pronounced redox activity while the latter seems to be redox inactive. The V(v) substituted POMs show that the V(v) lowers the peak potentials in comparison to HPMo.¹⁵ For the Nb(v)-substituted POMs, the following trend is observed: by incorporating one Nb(v), the peak potentials seem to shift initially to lower potential values, while by multiple substitution with Nb(v) the potentials partially shift back to higher values (ESI Table 10†). For the Nb(v)/V(v) mixed substituted POMs, some peak potentials are shifted to lower potentials in comparison to the pure Nb(v) substituted POMs. NaPW₃Mo shows extremely low redox activity in the electrochemical measurements as it was also observed for the Nb(v) containing POMs.

Through the collected electrochemical results, it is shown, as also indicated in our previously published study, that the redox potentials – and thus also the electronic structure – of the POM can be specifically tuned by the incorporation of different metals.¹⁵ This represents an essential step forward for the synthesis of tailor-made POM catalysts and a preliminary assessment which POM catalysts might be suitable for redox catalysis.

Materials and methods

Detailed experimental procedures as well as information on the materials and devices used is provided in the ESI.†

Computational details plus Cartesian coordinates of all structures can be found in the ESI.†

Conclusion

In this work, we show that the lacunary compound LHPA-3 is more stable and potentially applicable than anticipated and described in the literature. The LHPA-3 complex was characterized using various experimental spectroscopic techniques and the previously not annotated spectral peaks were assigned from quantum chemical calculations. Furthermore, DFT calculations show that in acidic medium the formation of a dimerized Wells–Dawson species is thermodynamically feasible. Using our novel *in situ* approach, in which LHPA-3 is formed and directly reacted by addition of other elemental precursors, a variety of element-substituted phosphomolybdates can be formed. In order to purify these compounds, we applied a novel approach using a nanofiltration membrane process, which is superior to (re-)crystallisation or extraction with diethyl ether, because it results in high purity products with no significant loss of yield. Using this synthetic approach and purification method, we successfully produced Keggin-type POMs containing Co(II), Ni(II), Zn(II), Cu(II), Fe(III), In(III), V(v), Nb(v), and W(vi). Quantum chemical calculations showed that incorporation of these metals significantly affects the structural properties of Keggin-type POMs. These new compounds were comprehensively characterised by various spectroscopic and electrochemical methods and it was found that the incor-



poration of these elements has a significant influence on the molecular properties (*i.e.* the redox potential) of the POM. Overall, our findings represent a major step forward in the development of tailor-made functional POMs for catalytic applications.

Conflicts of interest

There are no conflicts to declare.

Acknowledgements

We would like to thank the analytical service teams of the Chemistry Department at Hamburg University: Dr. Dirk Eifler and his team for elemental analysis, Dr. Frank Hoffmann for his assistance in refining our crystallographic data sets and his co-worker, Mrs. Isabelle Nevoigt for data collection of the single crystals and the powder XRD samples, and Mrs. Ute Gralla for Raman measurements. Our thanks also go to the research group of Prof. Dr. Peter Burger, in particular to Mr. Thomas Marx for lending the equipment and assisting with electrochemical measurements. Prof. Dr. Matthias Stein and Froze Jameel are grateful to the Max Planck Society of the Advancement of Science for financial support. This work is part of the Research Initiative “SmartProSys: Intelligent Process Systems for the Sustainable Production of Chemicals” funded by the Ministry for Science, Energy, Climate Protection and the Environment of the State of Saxony-Anhalt.

References

- 1 Y. Wei, Polyoxometalates: An interdisciplinary journal focused on all aspects of polyoxometalates, *Polyoxometalates*, 2022, **1**, 9140014.
- 2 J. J. Berzelius, Beitrag zur näheren Kenntnis des Molybdäns, *Ann. Phys.*, 1826, **82**, 369–392.
- 3 J. F. Keggin, Structure of the Molecule of 12-Phosphotungstic Acid, *Nature*, 1933, **131**, 908–909.
- 4 X. Huang, W. Cui, S. Liu, G. Liu, Y. Zhang, Z. Zhang, G. Shen, Z. Li, J. Wang and Y. Chen, One-step assembly of Pd-Keggin-polyoxometalates for catalytic benzothiadiazole generation and derived cell-imaging probe application, *Chin. Chem. Lett.*, 2023, **34**, 107692.
- 5 Y. Ma, F. Gao, W. Xiao, N. Li, S. Li, B. Yu and X. Chen, Two transition-metal-modified Nb/W mixed-addendum polyoxometalates for visible-light-mediated aerobic benzylic C–H oxidations, *Chin. Chem. Lett.*, 2022, **33**, 4395–4399.
- 6 B. Li and L. Wu, Perspective of polyoxometalate complexes on flexible assembly and integrated potentials, *Polyoxometalates*, 2023, **2**, 9140016.
- 7 Y. Wang, Y. Lu, W. Zhang, T. Dang, Y. Yang, X. Bai and S. Liu, Construction of hydrogel composites with superior proton conduction and flexibility using a new POM-based inorganic–organic hybrid, *Polyoxometalates*, 2022, **1**, 9140005.
- 8 H. Li, H. Pan, Y. Fan, Y. Bai and D. Dang, Syntheses, crystal structures, and properties of four polyoxometalate-based metal–organic frameworks based on Ag(I) and 4,4'-dipyridine-N,N'-dioxide, *Polyoxometalates*, 2022, **1**, 9140007.
- 9 S. Duan, X. Xu, W. Chen, J. Zhi and F. Li, Grain boundaries passivation of high efficiency and stable perovskite photo-detector by polyoxometalate-based composite SiW 11 @ZIF-8, *Polyoxometalates*, 2022, **1**, 9140003.
- 10 Z. Xia, L. Wang, Q. Zhang, F. Li and L. Xu, Fast degradation of phenol over porphyrin-polyoxometalate composite photocatalysts under visible light, *Polyoxometalates*, 2022, **1**, 9140001.
- 11 M. T. Pope and A. Müller, Polyoxometalate Chemistry: An Old Field with New Dimensions in Several Disciplines, *Angew. Chem., Int. Ed. Engl.*, 1991, **30**, 34–48.
- 12 M. T. Pope and A. Müller, *Polyoxometalate Chemistry From Topology via Self-Assembly to Applications*, Kluwer Academic Publishers, New York, Boston, Dordrecht, London, Moscow, 2002.
- 13 R. Dehghani, S. Aber and F. Mahdizadeh, Polyoxometalates and Their Composites as Photocatalysts for Organic Pollutants Degradation in Aqueous Media—A Review, *Clean: Soil, Air, Water*, 2018, **46**, 1800413.
- 14 V. F. Odyakov and E. G. Zhizhina, New process for preparing aqueous solutions of Mo-V-phosphoric heteropoly acids, *Russ. J. Inorg. Chem.*, 2009, **54**, 361–367.
- 15 J.-C. Raabe, J. Albert and M. J. Poller, Spectroscopic, Crystallographic, and Electrochemical Study of Different Manganese(II)-Substituted Keggin-Type Phosphomolybdates, *Chem. – Eur. J.*, 2022, **28**, 1–12.
- 16 J. Albert, M. Mendt, M. Mozer and D. Voß, Explaining the role of vanadium in homogeneous glucose transformation reactions using NMR and EPR spectroscopy, *Appl. Catal., A*, 2019, **570**, 262–270.
- 17 S. Pathan and A. Patel, Transition-Metal-Substituted Phosphomolybdates: Catalytic and Kinetic Study for Liquid-Phase Oxidation of Styrene, *Ind. Eng. Chem. Res.*, 2013, **52**, 11913–11919.
- 18 J. Albert, D. Lüders, A. Bösmann, D. M. Guldi and P. Wasserscheid, Spectroscopic and electrochemical characterization of heteropoly acids for their optimized application in selective biomass oxidation to formic acid, *Green Chem.*, 2014, **16**, 226–237.
- 19 J. Reichert, B. Brunner, A. Jess, P. Wasserscheid and J. Albert, Biomass oxidation to formic acid in aqueous media using polyoxometalate catalysts – boosting FA selectivity by *in situ* extraction, *Energy Environ. Sci.*, 2015, **8**, 2985–2990.
- 20 P. Preuster and J. Albert, *Energy Technol.*, 2018, **6**, 501–509.
- 21 J. Claußnitzer, B. Bertleff, W. Korth, J. Albert, P. Wasserscheid and A. Jess, Kinetics of Triphase Extractive Oxidative Desulfurization of Benzothiophene with Molecular Oxygen Catalyzed by HPA-5, *Chem. Eng. Technol.*, 2020, **43**, 465–475.
- 22 B. Bertleff, J. Claußnitzer, W. Korth, P. Wasserscheid, A. Jess and J. Albert, Extraction Coupled Oxidative Desulfurization



- of Fuels to Sulfate and Water-Soluble Sulfur Compounds Using Polyoxometalate Catalysts and Molecular Oxygen, *ACS Sustainable Chem. Eng.*, 2017, **5**, 4110–4118.
- 23 J.-C. Raabe, M. Poller, D. Voß and J. Albert, H8 [PV5Mo7O40] (HPA-5) – a unique polyoxometalate for acid and RedOx catalysis: synthesis, characterization, and modern applications in green chemical processes, *ChemSusChem*, 2023, 2013–2015.
- 24 M. J. Poller, S. Bönisch, B. Bertleff, J.-C. Raabe, A. Göring and J. Albert, Elucidating activating and deactivating effects of carboxylic acids on polyoxometalate-catalysed three-phase liquid-liquid-gas reactions, *Chem. Eng. Sci.*, 2022, **264**, 118143.
- 25 F. Steffler, G. F. De Lima and H. A. Duarte, The effect of the heteroatom (X=P, As, Si and Ge) on the geometrical and electronic properties of α -Keggin polyoxometalates (M=Mo, W and Nb) – A DFT investigation, *J. Mol. Struct.*, 2020, **1213**, 128159.
- 26 L. Yan, X. López, J. J. Carbó, R. Sniatynsky, D. C. Duncan and J. M. Poblet, On the Origin of Alternating Bond Distortions and the Emergence of Chirality in Polyoxometalate Anions, *J. Am. Chem. Soc.*, 2008, **130**, 8223–8233.
- 27 V. F. Odyakov, E. G. Zhizhina and R. I. Maksimovskaya, Synthesis of molybdovanadophosphoric heteropoly acid solutions having modified composition, *Appl. Catal., A*, 2008, **342**, 126–130.
- 28 V. F. Odyakov and E. G. Zhizhina, A novel method of the synthesis of molybdovanadophosphoric heteropoly acid solutions, *React. Kinet. Catal. Lett.*, 2008, **95**, 21–28.
- 29 M. Abbessi, R. Contant, R. Thouvenot and G. Hervé, Dawson Type Heteropolyanions. 1. Multinuclear (31P, 51 V, 183 W) NMR Structural Investigations of Octadeca(molybdotungstovanado)diphosphates α -1,2,3-[P2MM'2W15O62]n- (M, M' = Mo, V, W): Syntheses of New Related Compounds, *Inorg. Chem.*, 1991, **30**, 1695–1702.
- 30 A. Patel, N. Narkhede, S. Singh and S. Pathan, Keggin-type lacunary and transition metal substituted polyoxometalates as heterogeneous catalysts: A recent progress, *Catal. Rev. - Sci. Eng.*, 2016, **58**, 337–370.
- 31 P. A. Abramov, A. A. Shmakova, M. Haouas, G. Fink, E. Cadot and M. N. Sokolov, Self-assembly of [PNbxW12-xO40]n- Keggin anions—a simple way to mixed Nb-W polyoxometalates, *New J. Chem.*, 2016, **41**, 256–262.
- 32 D. K. Lyon, W. K. Miller, T. Novet, P. J. Domaille, E. Evitt, D. C. Johnson and R. G. Finke, Highly Oxidation Resistant Inorganic-Porphyrin Analogue Polyoxometalate Oxidation Catalysts. 1. The Synthesis and Characterization of Aqueous-Soluble Potassium Salts of α 2-P2W17O61(Mn+OH2)(n-10) and Organic Solvent Soluble Tetra-n-butylammonium Salts of, *J. Am. Chem. Soc.*, 1991, **113**, 7209–7221.
- 33 H. D'Amour, Vergleich der Heteropolyanionen [PMo9O31(H2O)3]3-, [P2Mo18O62]6- und [P2W18O62]6-, *Acta Crystallogr., Sect. B: Struct. Crystallogr. Cryst. Chem.*, 1976, **32**, 729–740.
- 34 C. Marchal-Roch, E. Ayrault, L. Lisnard, J. Marrot, F.-X. Liu and F. Sécheresse, Dimerization in Acetonitrile of [H6PMo9O34]3- into [P2Mo18O62]6-: Structural Characterization of the Tetrabutyl Ammonium Salt, *J. Cluster Sci.*, 2006, **17**, 283–290.
- 35 C. Li, A. Jimbo, K. Yamaguchi and K. Suzuki, A protecting group strategy to access stable lacunary polyoxomolybdates for introducing multinuclear metal clusters, *Chem. Sci.*, 2021, **12**, 1240–1244.
- 36 C. Li, K. Yamaguchi and K. Suzuki, Synthesis of a phosphomolybdate with a tetranuclear vanadium core by installing vanadium atoms in a lacunary template using the protecting group strategy, *Chem. Commun.*, 2021, **57**, 7882–7885.
- 37 K. Suzuki, N. Mizuno and K. Yamaguchi, New Strategy for Precise Synthesis of Polyoxometalate Catalysts with Designed Active Sites, *J. Jpn. Pet. Inst.*, 2020, **63**, 258–266.
- 38 C. Li, K. Yamaguchi and K. Suzuki, Ligand-Directed Approach in Polyoxometalate Synthesis: Formation of a New Divacant Lacunary Polyoxomolybdate [γ -PMo 10 O 36] 7-, *Angew. Chem.*, 2021, **133**, 7036–7040.
- 39 X. López, J. M. Maestre, C. Bo and J.-M. Poblet, Electronic Properties of Polyoxometalates: A DFT Study of α/β -[XM 12 O 40] n - Relative Stability (M = W, Mo and X a Main Group Element), *J. Am. Chem. Soc.*, 2001, **123**, 9571–9576.
- 40 P. Miró, J. M. Poblet, J. B. Ávalos and C. Bo, Towards a computational treatment of polyoxometalates in solution using QM methods and explicit solvent molecules, *Can. J. Chem.*, 2009, **87**, 1296–1301.
- 41 X. López, I. A. Weinstock, C. Bo, J. P. Sarasa and J. M. Poblet, Structural Evolution in Polyoxometalates: A DFT Study of Dimerization Processes in Lindqvist and Keggin Cluster Anions, *Inorg. Chem.*, 2006, **45**, 6467–6473.
- 42 S. Mir, B. Yadollahi and R. Omidyan, Theoretical comparative survey on the structure and electronic properties of first row transition metal substituted Keggin type polyoxometalates, *J. Solid State Chem.*, 2022, **305**, 122667.
- 43 J. M. Brégeault, M. Vennat, S. Laurent, J. Y. Piquemal, Y. Mahha, E. Briot, P. C. Bakala, A. Atlamsani and R. Thouvenot, From polyoxometalates to polyoxoperoxometalates and back again; potential applications, *J. Mol. Catal. A: Chem.*, 2006, **250**, 177–189.
- 44 T. Esser, M. Huber, D. Voß and J. Albert, Development of an efficient downstream process for product separation and catalyst recycling of a homogeneous polyoxometalate catalyst by means of nanofiltration membranes and design of experiments, *Chem. Eng. Res. Des.*, 2022, **185**, 37–50.
- 45 S. Himeno, M. Hashimoto and T. Ueda, Formation and conversion of molybdophosphate and -arsenate complexes in aqueous solution, *Inorg. Chim. Acta*, 1999, **284**, 237–245.
- 46 M.-X. Xu, S. Lin, L.-M. Xu and S.-L. Zhen, Crystal structure and properties of H 3 [PMo 12 O 40] · 3C 2 H 6 O, *Transition Met. Chem.*, 2004, **29**, 332–335.
- 47 P. Pyykkö and M. Atsumi, Molecular Single-Bond Covalent Radii for Elements 1–118, *Chem. – Eur. J.*, 2009, **15**, 186–197.
- 48 J. K. Lee, J. Melsheimer, S. Berndt, G. Mestl, R. Schlögl and K. Köhler, Transient responses of the local electronic and geometric structures of vanado-molybdo-phosphate catalysts H3+nPvNMo12-nO40 in selective oxidation, *Appl. Catal., A*, 2001, **214**, 125–148.



- 49 A. J. Bridgeman, Computational Study of the Vibrational Spectra of α - and β -Keggin Polyoxometalates, *Chem. – Eur. J.*, 2004, **10**, 2935–2941.
- 50 H. An, T. Xu, X. Liu and C. Jia, A series of new hybrid compounds constructed from Dawson-type phosphomolybdates and metal–organic coordination complexes, *J. Coord. Chem.*, 2010, **63**, 3028–3041.
- 51 L. E. Briand, G. M. Valle and H. J. Thomas, Stability of the phospho-molybdic Dawson-type ion P₂Mo₁₈O₆₂– in aqueous media, *J. Mater. Chem.*, 2002, **12**, 299–304.
- 52 A. F. Holleman, E. und Nils Wiberg and G. Fischer, *Lehrbuch der Anorganischen Chemie*, Berlin, New York, 2009.
- 53 X. Wu, T. Huang, Q. Wu and L. Xu, Synthesis and conductive performance of indium-substituted ternary heteropoly acids with Keggin structures, *Dalton Trans.*, 2015, **45**, 271–275.
- 54 E. Rafiee, I. M. Baltork, S. Tangestaninejad, A. Azad and S. Moinee, Tin(II) Polyoxometalate as an Efficient Catalyst for the Selective Oxidation of Sulfides to Sulfoxides, *Z. Naturforsch., B: J. Chem. Sci.*, 2006, **61**, 601–606.
- 55 F. W. Smith, *The Ion-Exchange Behaviour of Niobate and Tantalate in Alkaline Solution*, University of Cape Town, 1967.
- 56 V. G. Maiorov, A. I. Nikolaev, V. K. Kopkov, V. Y. Kuznetsov and N. L. Mikhailova, Preparation of Alkaline Solutions of Niobium(V), *Russ. J. Appl. Chem.*, 2011, **84**, 1137–1140.
- 57 M. Nyman, T. M. Alam, F. Bonhomme, M. A. Rodriguez, C. S. Frazer and M. E. Welk, Solid-state structures and solution behavior of alkali salts of the [Nb₆O₁₉]⁸⁻ Lindqvist ion, *J. Cluster Sci.*, 2006, **17**, 197–219.
- 58 M. Nyman, F. Bonhomme, T. M. Alam, M. A. Rodriguez, B. R. Cherry, J. L. Krumhansi, T. M. Nenoff and A. M. Sattler, A General Synthetic Procedure for Heteropolyniobates, *Science*, 2002, **297**, 996–998.
- 59 D. J. Sures, P. I. Molina, P. Miró, L. N. Zakharov and M. Nyman, Cesium salts of niobo-tungstate isopolyanions with intermediate group V-group VI character, *New J. Chem.*, 2016, **40**, 928–936.
- 60 D. J. Sures, S. K. Sahu, P. I. Molina, A. Navrotsky and M. Nyman, Distinctive Interactions of Cesium and Hexaniobate in Water, *ChemistrySelect*, 2016, **1**, 1858–1862.
- 61 M. Dabbabi and M. Boyer, Syntheses et propriétés d'hexaniobo(V)-tungstates(VI), *J. Inorg. Nucl. Chem.*, 1976, **38**, 1011–1014.
- 62 J.-C. Raabe, J. Aceituno Cruz, J. Albert and M. J. Poller, Comparative Spectroscopic and Electrochemical Study of V(V)-Substituted Keggin-Type Phosphomolybdates and -Tungstates, *Inorganics*, 2023, **11**, 138.
- 63 L. Pettersson, I. Andersson, J. H. Grate and A. Selling, Multicomponent Polyanions. 46. Characterization of the Isomeric Keggin Decamolybdoivanadophosphate Ions In Aqueous Solution by ³¹P and ⁵¹V NMR, *Inorg. Chem.*, 1994, **33**, 982–993.
- 64 D. V. Evtuguin, C. Pascoal Neto, J. Rocha and J. D. Pedrosa de Jesus, Oxidative delignification in the presence of molybdovanadophosphate heteropolyanions: mechanism and kinetic studies, *Appl. Catal., A*, 1998, **167**, 123–139.
- 65 M. T. Pope and T. F. Scully, Geometrical Isomerism Arising from Partial Substitution of Metal Atoms in Isopoly and Heteropoly Complexes. Possibilities for the Keggin Structure, *Inorg. Chem.*, 1975, **14**, 953–954.
- 66 K. Lee, G. Pozarnsky, O. Zarembowitch and A. McCormick, ⁵¹V NMR of homogeneous multicomponent vanadium oxide solutions, *Chem. Eng. J. Biochem. Eng. J.*, 1996, **64**, 215–223.
- 67 A. Selling, I. Andersson, J. H. Grate and L. Pettersson, A Potentiometric and (³¹P,⁵¹V) NMR Study of the Aqueous Molybdovanadophosphate System, *Eur. J. Inorg. Chem.*, 2000, **2000**, 1509–1521.
- 68 B. Weber, *Koordinationschemie*, Springer Berlin Heidelberg, Berlin, Heidelberg, 2014, vol. 7.
- 69 N. K. K. Raj, A. V. Ramaswamy and P. Manikandan, Oxidation of norbornene over vanadium-substituted phosphomolybdic acid catalysts and spectroscopic investigations, *J. Mol. Catal. A: Chem.*, 2005, **227**, 37–45.
- 70 H. Salavati and N. Rasouli, Synthesis and characterization of supported heteropolymolybdate nanoparticles between silicate layers of Bentonite with enhanced catalytic activity for epoxidation of alkenes, *Mater. Res. Bull.*, 2011, **46**, 1853–1859.
- 71 D. Y. Hwang, Y. S. Ha and S. Kim, Electrode-Assisted Wacker Process: Phosphomolybdate-Mediated Oxidation of 1-Butene to Methyl Ethyl Ketone, *Bull. Korean Chem. Soc.*, 2001, **22**, 441–442.
- 72 M. Sadakane and E. Steckhan, Electrochemical Properties of Polyoxometalates as Electrocatalysts, *Chem. Rev.*, 1998, **98**, 219–237.



5.2 Synthese und Charakterisierung von Mn(II)/V(V) gemischt substituierten Phosphormolybdaten

P2

Spectroscopic, Crystallographic, and Electrochemical Study of Different Manganese(II)-Substituted Keggin-Type Phosphomolybdates

Jan-Christian Raabe, Jakob Albert, Maximilian J. Poller

Raabe, J. C.; Albert, J.; Poller, M. J. Spectroscopic, Crystallographic, and Electrochemical Study of Different Manganese(II)-Substituted Keggin-Type Phosphomolybdates. *Chem. – A Eur. J.* **2022**, 28 (49), e202201084. <https://doi.org/10.1002/chem.202201084>.

Das Synthesekonzept der Übergangsmetallsubstitution in Keggin-Typ Phosphormolybdaten konnte ebenfalls erfolgreich auf die Synthese Mn(II) und Mn(II)/V(V) gemischt substituierter POMs erweitert werden (P2, *Chem. Eur. J.* **2022**, 28, e202201084).^[247] Die POMs wurden dabei nach dem *self-assembly* Konzept synthetisiert. Es konnte gezeigt werden, dass der maximale Substitutionsgrad mit Mn(II) bei zwei liegt. Bei den elektrochemischen Messungen zeigte sich der Trend, dass sich die Peak-Potentiale in Abhängigkeit des Substitutionselementes im Vergleich zum unsubstituierten Phosphormolybdat verschieben, wie in Abbildung 21 gezeigt. Insbesondere für die Mn(II)/V(V) gemischt substituierten POMs wurde im Vergleich zum zweifach V(V) substituierten Keggin-Typ-Phosphormolybdat der Trend gefunden, dass der zusätzliche Einbau von Mn(II) bewirkt, dass sich das RedOx-Potential von V(V)/V(IV) im VO_2^+ -Kation zu geringeren Potentialwerten verschiebt (Abbildung 21). Diese Beobachtungen unterstützen die aufgestellte These, dass ein gezieltes Tuning der RedOx-Eigenschaften durch die Metallsubstitution in TMSPOMs möglich ist. Die hier dargestellten Ergebnisse bilden somit ein solides Fundament für zukünftige katalytische Studien an Mn(II) und Mn(II)/V(V) gemischt substituierten Phosphormolybdaten.^[247] Abbildung 21 repräsentiert dabei einen Ausschnitt aus den in P2 gesammelten Studienergebnissen, insbesondere aus den Ergebnissen der SWV-Daten, die den Potentialshift des V(V)/V(IV) RedOx-Paares zeigen.

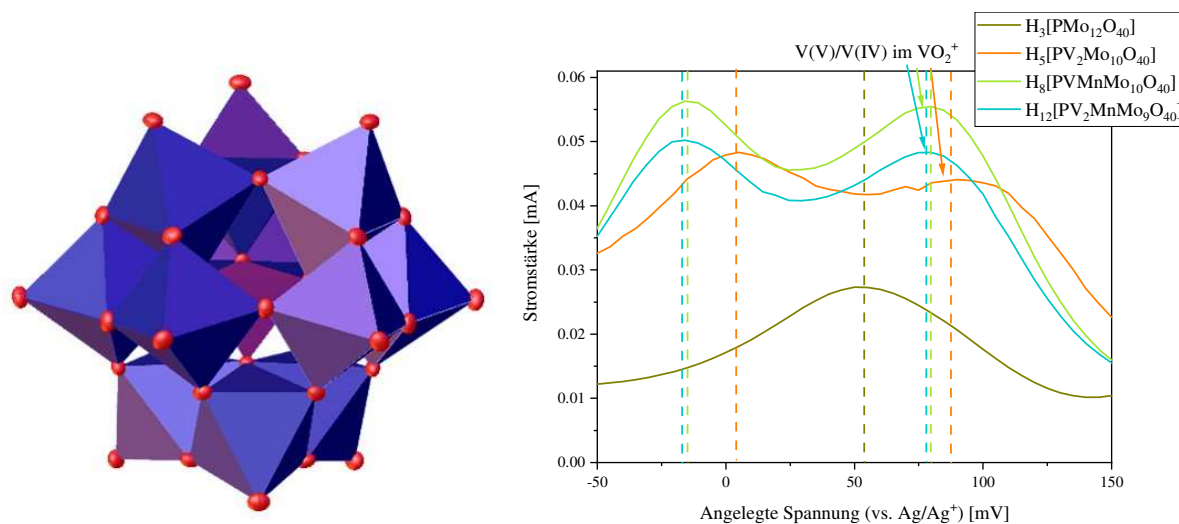


Abb. 21: Graphical abstract zu P2, *Chem. Eur. J.* **2022**, 28, e202201084 (links) und Einsicht in die elektrochemischen SWV-Daten der V(V) und Mn(II)/V(V) gemischt substituierten POMs im Vergleich mit dem unsubstituierten Phosphormolybdat (rechts).^[247]

Spectroscopic, Crystallographic, and Electrochemical Study of Different Manganese(II)-Substituted Keggin-Type Phosphomolybdates

Jan-Christian Raabe,^[a] Jakob Albert,^[a] and Maximilian J. Poller^{*[a]}

Abstract: Adjusting the RedOx activity of polyoxometalate catalysts is a key challenge for the catalysis of selective oxidation reactions. For this purpose, the possibility of influencing the RedOx potential by the introduction of an additional RedOx-active element was investigated. Thereby, Keggin-type polyoxometalates (POMs) with up to three different elements in the metal framework were created. An advanced and reproducible synthetic procedure to incorporate Mn^{II} and additionally V^V into Keggin-type heteropolyacids alongside comprehensive characterization of the new mole-

cules is presented. The success of our syntheses was confirmed by vibrational spectroscopy (IR and Raman) and elemental analysis. Furthermore, the new compounds were analyzed by NMR spectroscopy to investigate the characteristics of the POMs in solution. The structures of successfully crystallized compounds were determined by single-crystal X-ray diffraction. Moreover, all synthesized compounds were characterized using UV/Vis spectroscopy and electrochemical analysis to get further insights into the electronic transfer processes and redox potentials.

Introduction

Polyoxometalates (POMs) have been the focus of intensive research for more than a century. Nevertheless, new applications for functional polyoxometalates are still being investigated and the synthesis of new, fit-for purpose derivatives of POMs remains a very active field of research.^[1] Applications for POMs range from the medical field^[2] to electronic devices^[3,4] and to green catalysis.^[5–7] For catalytic applications, Keggin-type POMs have been proven particularly useful. Their high Brønsted acidity makes them suitable catalysts for acid catalyzed reactions such as ester hydrolysis.^[8] Additionally, by substituting the framework metal of Keggin-type POMs with a RedOx active transition metal,^[9] they become excellent bifunctional RedOx and acid catalysts.^[9,10] A prime example for this are vanadium substituted phosphomolybdates, specifically H₈PV₅Mo₇O₄₀ (HPA-5), which has been successfully applied as a catalyst for the conversion of biomass to formic acid^[6,10] and for the oxidative desulfurization of fuels.^[7]

To enable a broader range of RedOx catalytic applications, it is necessary to tune the RedOx potential of the POM to the desired application. Therefore, we have investigated the

possibility of introducing an additional RedOx-active element with the goal of adjusting the RedOx potential of the POM. Thereby, we created Keggin-type POMs with up to three different elements in the metal framework.

In general, the introduction of RedOx active metals into the POM framework can be achieved either by the reaction of a metal precursor with a lacunary-POM, or by adding a suitable metal precursor in the desired stoichiometry during the initial self-assembly based synthesis of the POM. A lacunary type POM is a defect POM structure in which one or more MO₆ octahedrons are removed from the parent POM structure.^[11,12] The defects can then be filled with suitable transition metal salts, resulting in substituted POMs. This method is limited to low substitution levels as the lacunary structure only allows filling up the number of vacancies (usually between 1 and 3).^[11,12] In contrast, the self-assembly process, entails combining the various metal precursors in the desired stoichiometry, so that under reaction conditions the precursor compounds arrange themselves to form the final POM structure.^[13] This method has been successfully employed for substitutions of up to half of the framework metals in the Keggin structure.^[9] Since the introduction of additional elements generally benefits from an overall higher substitution, we employed this synthetic strategy.

The transition metal of choice for our investigation was manganese, which is known for versatile redox chemistry. Although the use of Mn(II) substituted bimetallic POMs has been reported previously,^[14,15] no detailed synthetic procedure for higher Mn(II)-substituted POMs has been published and no detailed analytical characterization has been performed. The specific incorporation of Mn(II) into the H_(3+x)[PV_xMo_(12-x)O₄₀] Keggin framework has not yet been described in the literature at all. In this work we present a synthetic procedure leading to the introduction of Mn(II) to form bimetallic (Mn(II), Mo(VI)) and

[a] J.-C. Raabe, Prof. Dr. J. Albert, Dr. M. J. Poller
Institute of Technical and Macromolecular Chemistry
Hamburg University
Bundesstrasse 45, 20146 Hamburg (Germany)
E-mail: maximilian.poller@chemie.uni-hamburg.de

Supporting information for this article is available on the WWW under <https://doi.org/10.1002/chem.202201084>

© 2022 The Authors. Chemistry - A European Journal published by Wiley-VCH GmbH. This is an open access article under the terms of the Creative Commons Attribution Non-Commercial License, which permits use, distribution and reproduction in any medium, provided the original work is properly cited and is not used for commercial purposes.

Table 1. Results from ICP-OES and TGA analysis of the different HPA–X–Y compounds.

Compound	Molecular composition	P/V/Mn/Mo ratio ^[a]	Hydration water ^[b] [mol/mol-POM]
HPA-0-1	H ₇ [PMnMo ₁₁ O ₄₀]	1.14/0/1.07/11	8
HPA-0-2	H ₁₁ [PMn ₂ Mo ₁₀ O ₄₀]	1.05/0/2.03/10	10
HPA-1-1	H ₈ [PVMnMo ₁₀ O ₄₀]	1.26/1.03/1.05/10	8
HPA-1-2	H ₁₂ [PVMn ₂ Mo ₉ O ₄₀]	1.24/1.05/2.09/9	10
HPA-3-2	H ₁₄ [PV ₃ Mn ₂ Mo ₇ O ₄₀]	1.27/3.09/2.09/7	23
HPA-5-1	H ₁₂ [PV ₂ MnMo ₆ O ₄₀]	1.29/5.21/1.04/6	23

HPA-X-Y is H_(3+x+4y)[PV_xMn_yMo_(12-x-y)O₄₀]. [a] The ratios P/V/Mn/Mo were determined by ICP-OES analysis. The data were normalized to the targeted Mo content. H₃PO₄ was used in a slight excess during the synthesis, therefore the high P content may be attributed to residual H₃PO₄. [b] The content of hydration water was determined by TGA analysis.

trimetallic (Mn(II), V(V), Mo(VI)) Keggin-type POMs. To the best of our knowledge, this is the first time that Keggin-type POMs with three different elements in the position of the framework metal (i.e. without considering the heteroatom position) have been synthesized and fully characterized. Additionally, we have performed comprehensive analytical characterization of the new compounds, including electrochemical investigations to determine the influence of Mn(II) on the redox activity of the POM.

Results and Discussion

To achieve the incorporation of Mn(II) into the Keggin structure we have used manganese(II) acetate Mn(OAc)₂ as suggested by Patel and Pathan^[15] in an improved synthetic procedure based on the self-assembly synthesis of bimetallic V(V)-Mo(VI)-POMs described by Odyakov et al.^[16–18] In contrast to the synthesis via lacunary structures, this procedure allows higher degrees of substitution and is less pH sensitive.

In our procedure, we first prepared a solution of MoO₃ and phosphoric acid, to which the V(V) precursor solution and later the Mn(OAc)₂ were added. The ratio of the metal precursors corresponds to the stoichiometry of the final product. During the synthesis of the Mn(II) substituted POMs, a clear, homogeneous, characteristically coloured reaction solution was formed. No precipitate was observed, therefore it can be assumed that no insoluble Mn(II) species such as manganese(II) oxide or phosphate was formed. Subsequently the solvent was removed under reduced pressure and elevated temperature to yield the final product. On the basis of this procedure, we have successfully synthesized bimetallic Keggin-type POMs with a ratio of Mn(II)/Mo(VI) of 1/11 and 2/10 as well as trimetallic Keggin-type POMs with different Mn(II)/V(V)/Mo(VI) ratios ranging from 1/1/10 to 1/5/6. Experiments attempting the incorporation of more than two Mn(II) ions did not yield a defined product. Attempts to incorporate Mn(VII) into the Keggin structure, using potassium permanganate as a precursor, did not lead to the desired compounds. Detailed synthetic procedures for all described compounds with the corresponding analytical data in Figures S1–S36 can be found in the Supporting Information.

To verify the successful incorporation of Mn(II) in the Keggin cluster, the targeted stoichiometry was confirmed using ICP-OES (Table 1). In addition, we determined the amount of hydration water using thermogravimetric analysis (TGA). The low-substituted POMs (up to 3 atoms) have crystal water contents between 8 and 10 water molecules per Keggin unit, whereby the highly-substituted POMs (5 and 6 atoms out of 12) have contents of 23 water molecules per POM molecule.

The integrity of the Keggin structure was shown by ATR-FTIR (Figure 1 and 2) and Raman spectroscopy (Figure 3 and 4), respectively. IR spectroscopy of Keggin-type POMs in general has already been discussed in literature to a great extent.^[10,19,20] Therefore it is a well-established suitable method to confirm the structure type of the new compounds. The data of HPA-0-1 are consistent with those of Patel and Pathan.^[15] No literature data exist for HPA-0-2 and the V(V)/Mn(II) substituted POMs, here only the comparison to the V(V) substituted POMs published in the literature can be made.^[10] The FTIR spectra of the newly

IR spectroscopy

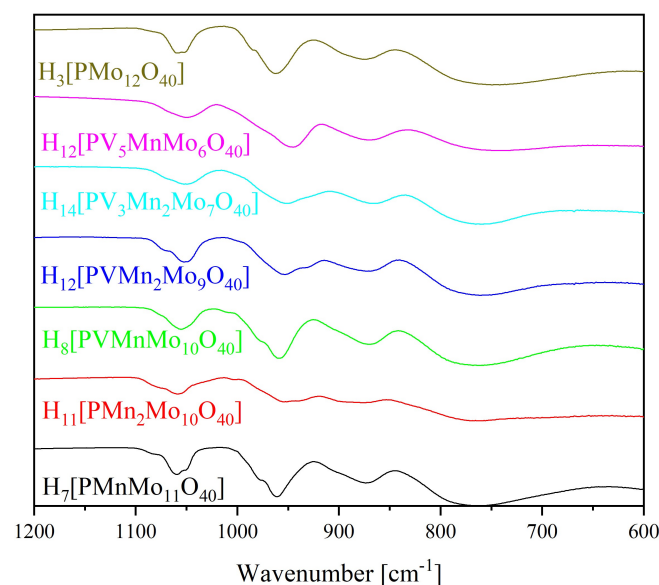


Figure 1. FTIR (ATR) spectra of the Mn^{II}-substituted HPA-X-Y POMs compared to H₃[PMo₁₂O₄₀].

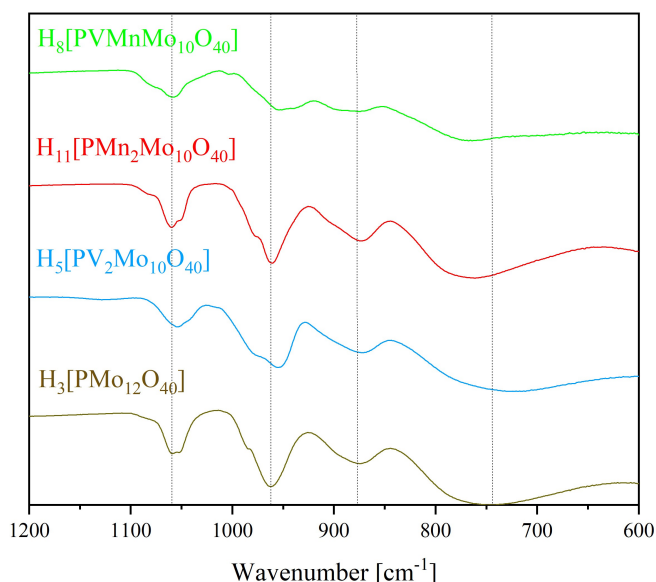


Figure 2. Superimposed IR spectra of the two-fold metal-substituted POMs HPA-1-1, HPA-0-2 and HPA-2-0, compared with the IR spectrum of HPA-0-0.

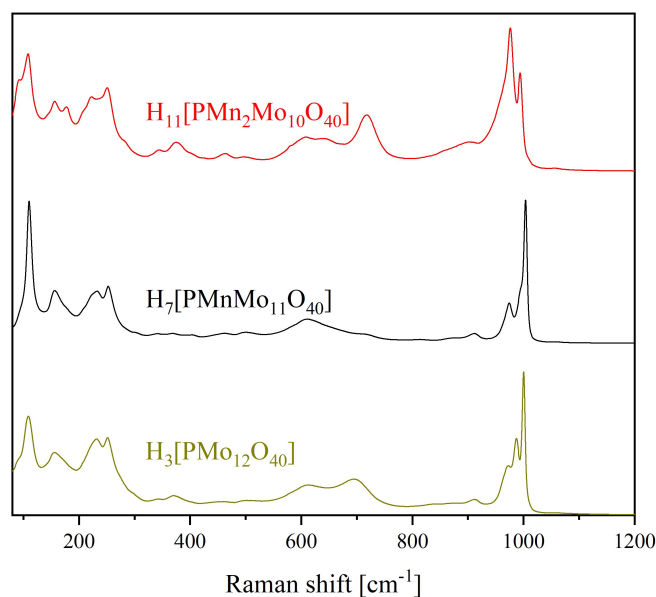


Figure 4. Superimposed Raman spectra of the only Mn^{II}-substituted POMs HPA-0-2, HPA-0-1 and in comparison with HPA-0-0.

Raman spectroscopy

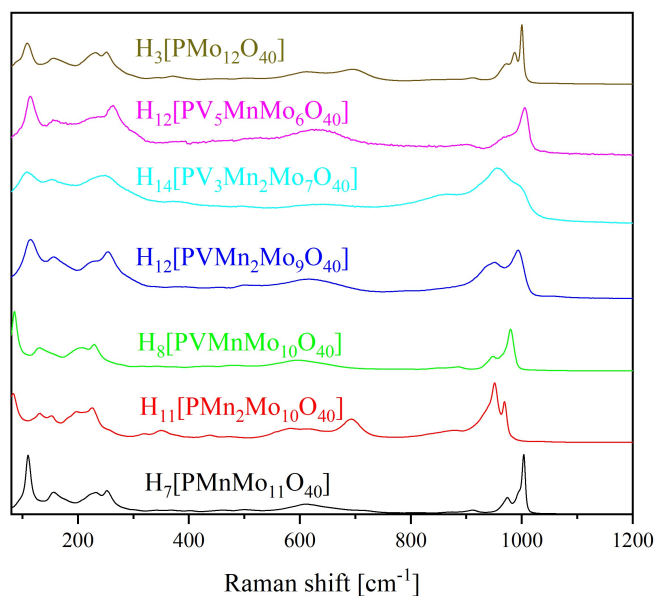


Figure 3. Raman spectra of the Mn^{II}-substituted HPA-X-Y POMs compared to H₃[PMo₁₂O₄₀].^[19]

synthesized POMs are shown in Figure 1 and 2, with spectra of H₃[PMo₁₂O₄₀] (HPA-0-0) for comparison.

The IR spectrum of HPA-0-0 shows bands for P–O vibration at 1059 cm⁻¹, for the terminal M=O_t vibration at 962 cm⁻¹, and for the M–O–M vibrations at 877 cm⁻¹ and 744 cm⁻¹, respectively. In comparison, the P–O, M=O_t and M–O–M bands of the substituted POMs are shifted to lower wavenumbers, indicating successful incorporation of the Mn(II) ions into the Keggin structure (Table 2). All spectra and more detailed tables can be found in the Supporting Information (Figure S43–S46 and Table 1–3 Supporting Information).

A closer look at the superimposed IR spectra of the two-fold substituted POMs (in Figure 2 with H₅[PV₂Mo₁₀O₄₀] (HPA-2-0) as HPA-X-0 equivalent) reveals that the peaks of the two-metal substituted POMs are shifted to lower wavenumbers compared to HPA-0-0. This can possibly be explained by the fact that the Mo(VI) positions are occupied by metals with significantly smaller ionic mass, so that the corresponding oscillation modes can be excited more easily. The appearance of a shoulder in the P–O-stretching has previously been reported as an indicator for substitution in Keggin structures.^[19] This is caused by substitution of the scaffolding metal (in our case Mo) with an element of significantly lower mass (Mn and V) and is therefore a strong indicator for the successful incorporation of a transition metal into the Keggin-type phosphomolybdate. Additionally, the main

Table 2. Position of the characteristic vibration bands for HPA-X-Y POMs in the IR spectrum.

Vibration type ν_{as}	HPA-0-0	HPA-0-1	HPA-0-2	HPA-1-1	HPA-1-2	HPA-3-2	HPA-5-1
(P=O)	1059	1060	1059	1055	1053	1052	1049
(M=O _t)	962	961	954	959	953	951	945
(M–O–M) _{vertex}	877	874	874	871	869	866	870
(M–O–M) _{edge}	744	762	767	762	757	759	743

	P ₁ –O ₁	O ₁ –M ₁	M ₁ –O _{2,3}	M ₁ –O ₄
Found bond length (mean value) [Å]	1.538	2.422	1.884	1.658
Sum of covalent radii ^[30] [Å]	1.74	2.01 (O–Mo) 1.97 (O–V) 1.82 (O–Mn)		

peaks in some spectra show a shift to lower wavenumbers with increasing substitution. This is in essence the same phenomenon, however, the small difference in excitation energy is not resolved for these broad peaks. As a result, the observed effect is a small shift of the peak maximum instead of the formation of a shoulder in the peak (which might also cause a shift of the peak maximum). Table 3 in the Supporting Information shows the IR data of the Mn(II) substituted POMs compared with the corresponding literature IR data of the analogous H_(3+x)[PV_xMo_(12-x)O₄₀] (HPA-X-0), in which the Mo(VI) position are only substituted by V(V).^[10]

In conclusion, the IR spectra confirm the Keggin structure type and the successful incorporation of the lighter transition metals (Mn(II), V(V)) into the Keggin structure. It can be observed that the trend of peak shift with increasing V(V) substitution can also be observed for the Mn(II) substituted POMs.

The same can be concluded from the Raman spectra (Figure 3 and 4).^[19,21] In particular, the Raman spectra of the substituted POMs (Figure 3 and 4) show very strong differences (especially in the range of the M=O_t vibration bands) compared to the unsubstituted HPA-0-0, suggesting successful incorporation of the transition metals into the Keggin structure (Figure 4).

Due to the incorporation of Mn(II) the M=O_t stretch band is shifted from 1001 cm⁻¹ (HPA-0-0) to 1004 cm⁻¹ (HPA-0-1). The M=O_t band at 987 cm⁻¹ (HPA-0-0) vanishes within the M=O_t band at 1004 cm⁻¹ in HPA-0-1 (resulting in a shoulder formation in HPA-0-1). The band at 1004 cm⁻¹ in HPA-0-1 shifts to 994 cm⁻¹ in HPA-0-2 and loses intensity, while the band at 975 cm⁻¹ in HPA-0-1 becomes an intense, broad band at 977 cm⁻¹ in HPA-0-2. The vibrational band in HPA-0-2 at 109 cm⁻¹, which can be assigned to an O–M–O vibration, becomes an additional shoulder at 93 cm⁻¹ due to the two-fold Mn(II) substitution, which is not visible in the Raman spectra of HPA-0-1 and HPA-0-0 (Figure 4). The change of shape of the peaks in the Raman spectra (see also Figure S45 and S46 in the Supporting Information) are a result of the different ionic masses of the different transition metals. This can be seen as an indicator for successful incorporation of Mn(II) into the [PMo₁₂O₄₀]³⁻ anion. Another advantage of Raman spectroscopy is that the range around 80 cm⁻¹ to 400 cm⁻¹ can be investigated, which was not possible with the available IR spectrometer. The Raman spectra (Figure 3, 4 and Figures S45 and S46 in the Supporting Information) show that the region below 400 cm⁻¹ is relevant for interpretation because there are some M–O–M vibrational bands in this region. The peaks in the range 80 cm⁻¹ to 300 cm⁻¹ show mainly the different types of

M–O–M vibrations. These peaks, as well as the M=O_t vibrations at 900 cm⁻¹ to 1000 cm⁻¹ are shifted and broadened with increasing V(V) and Mn(II) substitution. The cause for this is the same effect that has been discussed above for the formation of shoulders on the peaks. The P–O vibrational band is apparently not Raman active but can be seen in the IR spectra.

To elucidate correlations between structural features on the molecular level for performance in future catalytical applications, additional characterization by single-crystal X-ray diffraction (XRD) was carried out.^[22–29] Although several crystal structures of Keggin-type POMs are known, there is little literature for single crystals of Keggin-POMs in their protonated form, most likely due to the difficulty in crystallizing them.^[28,29] Nevertheless, we were able to successfully analyze single crystals of five out of the six new POMs presented in this paper. The crystals were obtained by slow evaporation of the solvent from an aqueous solution of the respective compound in a desiccator under reduced pressure.

Figure 5 shows the asymmetric unit of the POM HPA-1-1 with six atoms and the corresponding numbering of the atoms. Images of the other structures and tables of selected bond lengths can be found in the Supporting Information (Figures S47–S51), the full crystallographic information files (cif) are available through the CCDC database (deposition numbers: HPA-0-1: 2141261, HPA-0-2: 2141263, HPA-1-1: 2141259, HPA-1-2: 2141262, HPA-5-1: 2141260).

The asymmetric unit of the structures only contains one metal atom, indicating, that all twelve metal positions are

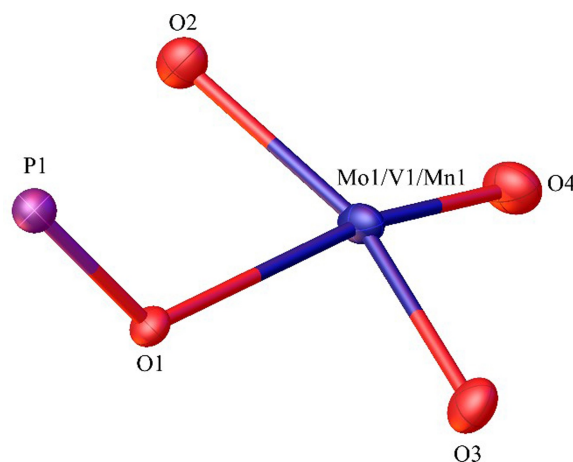


Figure 5. Asymmetric unit of a crystal of HPA-1-1 with the corresponding numbering of the atoms, hydrogen atoms have not been modeled. Purple: phosphorous, red: oxygen, and blue: metals (Mo, V, Mn).

equivalent. The incorporation of Mn(II) and V(V) becomes apparent, when comparing the refinement of the metal position with 12/12 occupancy Mo(VI) versus the metal ration determined by ICP-OES (e.g. 1/12 Mn(II), 1/12 V(V), 10/12 Mo(VI) for HPA-1-1), which results in a significantly better model (i.e. less residual negative electron density).

The crystal structures verify the Keggin structure type: the phosphorus atom as heteroatom in the center of the cluster is tetrahedrally coordinated by four oxygen atoms, while all metals are in distorted octahedral coordination surrounded by six oxygen atoms. All four oxygen atoms surrounding the central phosphorus atom are part of the four Mo_3O_{13} units. No other transition metal cations were identified outside the Keggin structure. Since H atoms do not have sufficient electron density to be located by XRD, they have been omitted in the refined model. Hydration water in the crystal lattice was strongly disordered and could not be modelled in most cases. Therefore, solvent mask (SQUEEZE) was applied to the residual voids and the electron density therein was assigned to hydration water, in order to obtain a better refinement.^[27]

Most of the POMs crystallize in highly symmetric cubic space groups. The POMs HPA-0-1 and HPA-0-2 crystallize in the cubic space group $Fd\bar{3}$ (203), while the V(V) containing POMs HPA-1-1 and HPA-1-2 exist in the cubic space group $Fd\bar{3}m$ (227). This coincides with the presence of only one metal atom in the asymmetric unit. As a result, a discrete substitution pattern cannot be recognized. The lattice parameters a , b and c are on average 23 Å and the lattice angles α , β and γ are 90°. Furthermore, it is noticeable that the POM with increased V(V) content HP-5-1 crystallizes in the trigonal space group $R\bar{3}$ (148), respectively. However, all metal elements are statistically distributed over all metal positions and therefore no discrete substitution pattern was recognized. For HPA-5-1, the lattice parameters a and b are 15.2 Å and c is 38.9 Å. The lattice angles α and β are 90° and γ 120° (Table 4 Supporting Information). It follows that the unit cells of the low-substituted POMs (up to 3 metals out of 12) are almost the same, while the unit cell of the high-substituted POMs (6 metals out of 12) is very different

from those of the low-substituted POMs and, all in all, have a much smaller volume. Table 3 shows an overview of selected bond lengths (mean value of all found bond lengths of all HPA-X-Y POMs) versus the sum of covalent radii^[30] of the elements involved:

The average bond length of the P-O bond is about 1.538 Å ($\text{P}_1\text{-O}_1$), while the average bond lengths of the oxygen-metal bonds connecting the metals to the central phosphorus atom is 2.422 Å ($\text{O}_1\text{-M}_1$). Assuming that the ideal bond lengths result from the sum of the covalent radii of the atoms involved, the length of the P-O bond (P: 111 pm; O: 63 pm) is 174 pm (1.74 Å).^[30] Thus, the P-O bond of 1.538 Å is significantly shorter than the sum of the covalent radii, indicating double bond character. Furthermore, the average metal-oxygen-metal bond is 1.884 Å long (Bond $\text{M}_1\text{-O}_{2,3}$), while the average bond lengths of the terminal oxygen-metal bonds are 1.658 Å ($\text{M}_1\text{=O}_4$) (see Supporting Information Table 5). Accordingly, the bond lengths for the O-Mo bond (Mo: 138 pm) would be 201 pm (2.01 Å), for the O-V bond (V: 134 pm) 197 pm (1.97 Å) and for the O-Mn bond (Mn: 119 pm) 182 pm (1.82 Å).^[30] Thus, the O-M bond of 1.884 Å is in the range between the O-V and O-Mn bond. When discussing the bond lengths, it is important to note that several metals and oxygen atoms are present in the asymmetric unit of the POM HPA-5-1 (Table 5 Supporting Information). Here, the metal-oxygen bonds are in the range between 1.798 Å and 2.044 Å, so that metal-oxygen bonds can be found that are in the range of O-Mn, O-V and O-Mo bond lengths. It is striking that the $\text{O}_1\text{-M}_1$ bond of 2.422 Å is significantly longer than all other bonds. The terminal $\text{M}_1\text{=O}_4$ bonds are significantly shorter with an average of 1.658 Å, which can be explained by the double bond character of the $\text{M}_1\text{=O}_4$ bond. Compared to the crystal structure of HPA-0-0, the following trend is noticeable: In HPA-0-0 the P-O bond is 1.534 Å, the $\text{O}_1\text{-M}_1$ bond is 2.439 Å, the $\text{M}_1\text{-O}_{2,3}$ bond is 1.916 Å and the $\text{M}_1\text{=O}_4$ bond is 1.674 Å.^[31] It follows that the P-O bond length gets about 0.004 Å longer due to the substitution with the foreign metals V(V) and Mn(II), while the $\text{O}_1\text{-M}_1$ bond shortens by about 0.017 Å. The $\text{M}_1\text{-O}_{2,3}$ bond shortens about 0.032 Å. Likewise, the $\text{M}_1\text{=O}_4$ bond short-

Table 4. Weighted average of calculated bond lengths (sum of covalent radii) and observed bond lengths of each bond in each POM.

	Sum of covalent radii*/observed bond length [Å]			
	$\text{P}_1\text{-O}_1$	$\text{O}_1\text{-M}_1$	$\text{M}_1\text{-O}_{2,3}$	$\text{M}_1\text{=O}_4$
HPA-0-0	1.74/1.534	2.01/2.439	2.01/1.916	2.01/1.674
HPA-0-1	1.74/1.536	1.99/2.433	1.99/1.839	1.99/1.681
HPA-0-2	1.74/1.539	1.98/2.430	1.98/1.836	1.98/1.678
HPA-1-1	1.74/1.537	1.99/2.422	1.99/1.913	1.99/1.663
HPA-1-2	1.74/1.532	1.98/2.425	1.98/1.913	1.98/1.666
HPA-5-1	1.74/1.543	1.98/2.404	1.98/1.923	1.98/1.637

*BL = $\frac{a(r_{\text{O}} + r_{\text{Mo}}) + b(r_{\text{O}} + r_{\text{V}}) + c(r_{\text{O}} + r_{\text{Mn}})}{a+b+c}$ with BL the weighted average bond length, r_x the covalent radii of the corresponding elements x and a , b and c the weighting factors (e.g. for HPA-1-1: $a = 10$, $b = 1$ and $c = 1$).

Table 5. Chemical shifts obtained from ^{31}P and ^{51}V NMR spectra of the HPA-X-Y compounds in comparison with the ^{31}P NMR shifts of HPA-0-0.^[10]

Compound	HPA-0-0	HPA-0-1	HPA-0-2	HPA-1-1	HPA-1-2	HPA-3-2	HPA-5-1
^{31}P NMR	-3.75	-2.96, -3.77	-2.88, -3.78	-4.04	-3.57, -3.99	Multiple signals -1.13 to -4.66	Multiple signals 0.09 to -4.95
^{51}V NMR	-	-	-	-532.1	-531.7, -538.8	Multiple signals -495.2 to -617.6	Multiple signals -508.7 to -608.1

ens by 0.016 Å.^[31] The result is an overall contraction of the averaged MO₆ octahedra with metal substitution (Table 4). This also indicates the successful incorporation of metals with a smaller covalent/ionic radius (Mo = 138 pm, V = 134 pm, Mn = 119 pm).^[30] Table 4 shows a comparison between the weighted sum of covalent radii (formula shown in Table 4) and the bond lengths found for each POM. So, a direct comparison between the expected and the found bond lengths is possible, indicating that the bond lengths vary depending on the substitution pattern.

As can be seen from the crystal structure data, the MO₆ octahedra are slightly distorted. In the following, the four bond angles of the O₄=M₁-O_{2,3} bonds were measured, and the mean value formed in each case. For HPA-0-1 this angle is 101.86 °, for HPA-0-2 101.83 °, for HPA-1-1 101.734 °, for HPA-1-2 101.768 ° and for HPA-5-1 100.612 °. This shows that the octahedra are distorted compared to the ideal octahedron, in which the optimal O–M–O angle is 90 °.^[32,33]

The distortion of the PO₄ tetrahedra in comparison with the ideal tetrahedron geometry was analyzed as follows: All three angles of the O₁-P₁-O₁ bonds were measured and the mean value was calculated. For HPA-0-1, HPA-0-2, HPA-1-1 and HPA-1-2, the angle is about 109.471 °. This means that the tetrahedral angles found are very close to the ideal value of 109.5 °.^[34,35] This shows that the metal substitution in the Keggin framework has no significant influence on the P–O bonds, especially the O–P–O bond angle. For the high metal-substituted Keggin-type POM, the tetrahedral bond angle is 109.416 ° for HPA-5-1. This shows that the P–O bond and its bond angles are slightly affected by metal substitution when high degrees of substitution are obtained (six out of twelve metals in HPA-5-1).

Figure 6 shows the exemplary solid-state structure of HPA-1-1. According to the single crystal structure analysis, the compound crystallizes in the space group Fd-3 m (227). The cell parameters *a*, *b* and *c* are equal according to the cubic crystal system and are about 23 Å. The lattice angles are all 90 °. There are six atoms in the asymmetric unit: The central phosphorus atom, the internal oxygen atom, one of the twelve metal atoms, the metal-metal bridging oxygen and the terminal oxygen atom. In total, there are eight formula units per elementary cell. In this structure, neither the V(V) nor the Mn(II) atom can be precisely assigned to a defined position. The atoms are statistically distributed in the Keggin framework. Thus, one in twelve of the twelve metal atoms is a V(V) or a Mn(II). The residual electron density of hydration water molecules, which could not be modeled due to high degree of disorder, was treated with a solvent mask function.

The powder XRD diffractograms of the individual substances and HPA-0-0 are shown in the Supporting Information in Figures S52–S58. The diffractograms differ from HPA-0-0 (Figure S52) and from each other, indicating successful incorporation of the metals. In general, the diffractograms show many reflexes, especially many reflexes with low intensity. This is an indicator that the powder contains different crystallographic phases of the same compound, which differ for example in their crystal water amount. The single crystals that were analyzed in

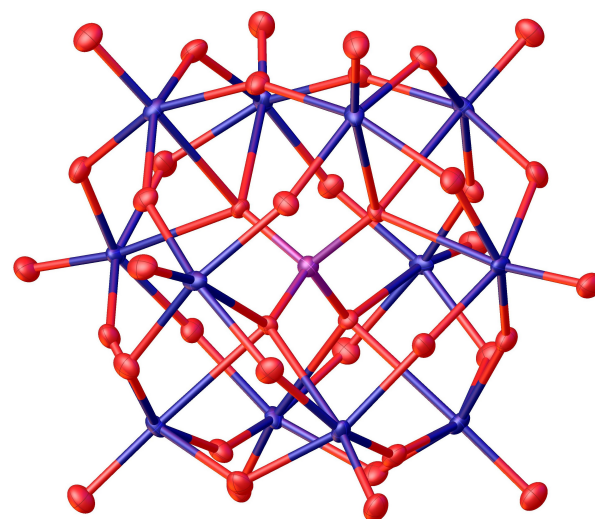


Figure 6. Structure of HPA-1-1 in the solid state as determined by x-ray diffraction, hydrogen atoms have not been modeled. The compound crystallized in space group Fd-3 m (227). There are six atoms in the asymmetric unit and eight formula units per elementary cell. Residual electron density attributed to hydration water has been refined with a solvent mask (aka SQUEEZE). R₁: 2.65, wR₂: 6.03 %, R_{int}: 2.78 %, GooF: 1.213. Purple: phosphorous, red: oxygen, and blue: metals (Mo, V, Mn).

this work on the other hand, consist of only one defined crystallographic phase. Different crystallographic phases can only be analyzed in the solid state via powder XRD, because the crystallographic phases are a phenomenon of the solid state and do not exist in solution.

The characteristics of the POMs in solution were investigated by ³¹P- and ⁵¹V NMR spectroscopy (Figure 7, Figure 8,

³¹P-NMR in H₂O/acetone-d₆ pH 1 (HCl)

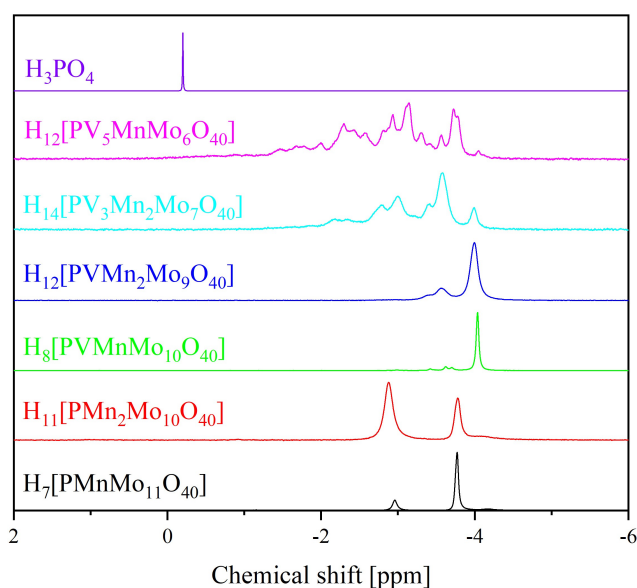


Figure 7. ³¹P NMR spectra of the HPA-X-Y POMs in a mixture of 90 % H₂O (pH 1) and 10 % acetone-d₆. The spectra were measured at 242.9 MHz. 85 % H₃PO₄ was used as external standard.

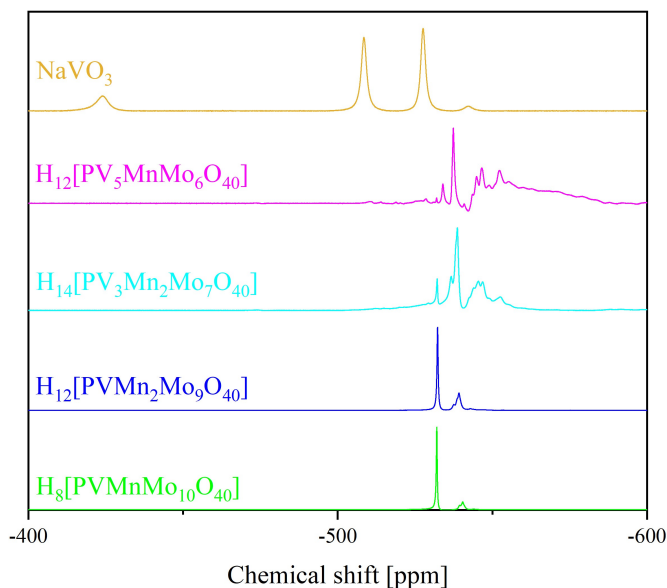
^{51}V -NMR in $\text{H}_2\text{O}/\text{acetone-d}_6$ pH 1 (HCl)

Figure 8. ^{51}V NMR spectra of the HPA-X-Y POMs in a mixture of 90% H_2O (pH 1) and 10% acetone-d_6 . The spectra were measured at 157.8 MHz. NaVO_3 was used as external standard.

and Figure 9) Although, in an unsubstituted structure like HPA-0-0, all metal centers are equivalent, the substitution of two or more metals leads to multiple possible isomers.^[10,36–40] This is also observed in the ^{31}P NMR spectra of the newly discovered POMs, which exhibit several signals in the range of -2 ppm to

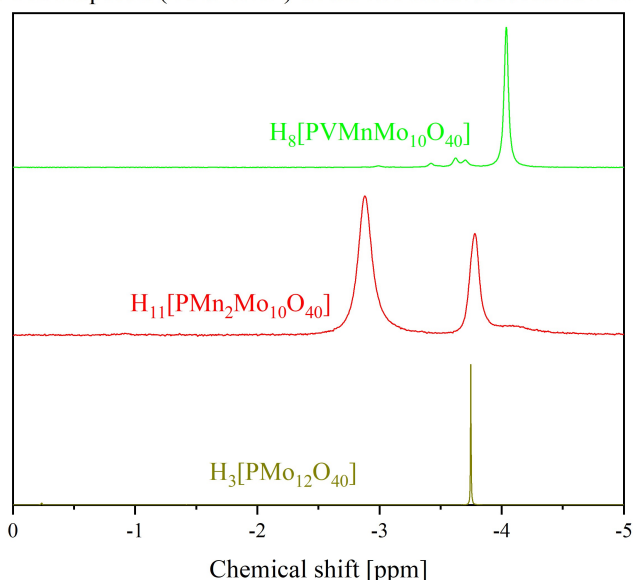
 ^{31}P NMR spectra (242.9 MHz) of the two metal substituted POMs

Figure 9. Comparison of the ^{31}P NMR spectra of the two metal substituted POMs HPA-0-2 and HPA-1-1 in comparison with HPA-0-0. The spectra indicate paramagnetism due to the broadening of the peaks in comparison to HPA-0-0.

-5 ppm. In particular, from the ^{31}P NMR spectra, the paramagnetism of Mn(II) is evident from broadening of the peaks. To visualize this, the ^{31}P NMR spectra of the two metal substituted POMs HPA-0-2 and HPA-1-1 were plotted in Figure 9 along with the ^{31}P NMR spectrum of HPA-0-0 which were all measured with the same parameters. The broadening of the peaks suggest the presence of the paramagnetic Mn(II) species.

^{51}V NMR spectroscopy can be used to verify the oxidation state of diamagnetic V(V) . V(V) in the d^0 -configuration is a diamagnetic species, while the reduced species, V(IV) , with a d^1 -configuration is a paramagnetic species that eludes observation by ^{51}V NMR spectroscopy.^[43] The ^{51}V NMR spectra of the POMs (Figure 8) show several peaks in the range of -530 ppm to -560 ppm. The different ^{31}P - and ^{51}V -signals indicate a coexistence of the various isomers.^[41,42] So the different peaks are attributed to the different positional isomers. It is also possible that two or more positional isomers have the same chemical shift and overlap in the spectra. Furthermore, it is also known that higher substituted POMs, especially those containing much V(V) , dissociate in aqueous solution to lower or higher substituted POMs according to $2 [\text{PM}_x\text{V}_y] \rightarrow [\text{PM}_{x+1}\text{V}_{y-1}] + [\text{PM}_{x-1}\text{V}_{y+1}]$.^[39] This was studied for HPA-5 by Evtuguin et al.^[39] It is also known that V(V) containing POMs set in aqueous solution one or more VO_2^+ cation free according to $[\text{PM}_x\text{V}_y] \rightarrow [\text{PM}_x\text{V}_{y-n}] + n \text{VO}_2^+$. The free VO_2^+ cations can be observed at -545 ppm in the ^{51}V spectra when they are present.^[39]

For the only V(V) substituted Keggin-type POMs HPA-X-0 the following trend is observed: For HPA-1-0 ($X=1$) all positions in the Keggin framework are equivalent, thus only one signal is observed in the ^{31}P - and ^{51}V NMR spectra, respectively. For HPA-2-0 there are 5, for HPA-3-0 13 and for HPA-6-0 there are even 48 positional isomers, so that 5, 13 and 48 signals can be detected in the respective spectra.^[36] Since the chemical shifts of the various position isomers differ only slightly, especially in the case of the more highly V(V) substituted POMs, the signals in the NMR spectra often overlap.^[10,36,39] Table 5 shows an overview of the chemical shifts obtained from ^{31}P - and ^{51}V NMR data (Figures 7 to 9) of the HPA-X-Y compounds in comparison with the ^{31}P NMR shifts of HPA-0-0.^[10]

For future catalytic applications, the HOMO-LUMO (HOMO = highest occupied molecular orbital, LUMO = lowest unoccupied molecular orbital) gap and the redox potentials of the new POMs are of great interest. In order to further investigate the former measurements, UV/Vis spectra were measured (Figure 10). Since the scaffolding metal of a POM is generally present in its highest oxidation state, the HOMO-LUMO excitation is usually a Ligand-to-Metal-Charge-Transfer (LMCT) transition.^[43–49] HPA-0-0 does not contain another foreign metal atom, therefore only the $\text{O} \rightarrow \text{Mo(VI)}\text{O}_6$ LMCT at 218 nm is visible in the UV/Vis spectrum (Table 6, Supporting Information).^[44–46] The HOMO of the POMs is mainly localized on the terminal oxygen atoms ($\text{M}=\text{O}$), so that its energetic position is not particularly affected by changes in the HPA framework. In contrast, the LUMO is more strongly influenced because the LUMO is localized on the d-orbitals of the framework metals and the bridging oxygen atoms ($\text{M}-\text{O}-\text{M}$). Changes in absorp-

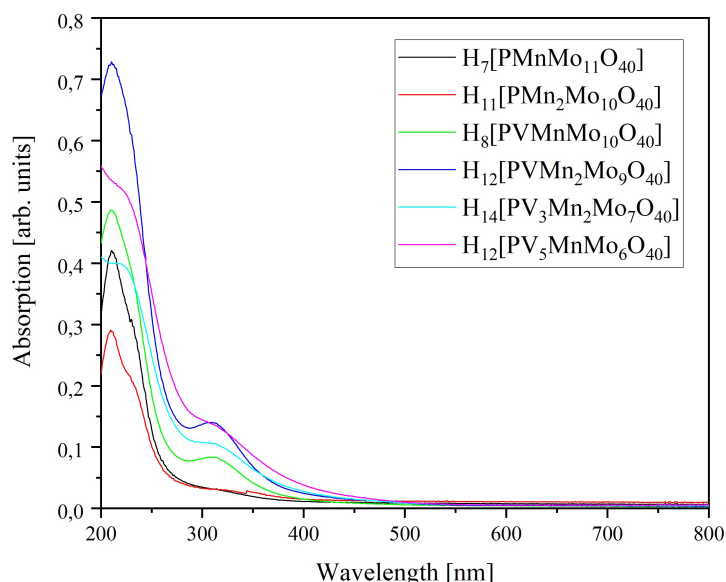


Figure 10. UV/Vis spectra of all HPA-X-Y compounds in water.

Table 6. LMCT peaks from all HPA-X-Y compounds in water.

LMCT	HPA-0-0	HPA-0-1	HPA-0-2	HPA-1-1	HPA-1-2	HPA-3-2	HPA-5-1
O→Mo(VI)O ₆	218	211	210	210	211	215	214
O→V(V)O ₆	–	–	–	311	309	305	310

tion therefore mainly reflect changes in the energetic position of the LUMO.^[44]

For V(V)-substituted POMs, two LMCT transitions are possible: ligand to Mo(VI) and ligand to V(V) (Table 6, Supporting Information). The incorporation of Mn(II) is not expected to add an additional transition, as Mn(II) is known for its d⁵-high spin configuration in which the transition between the metal d-orbitals are forbidden and there is no room for an LMCT excitation (see Figure S60 Supporting Information).^[43]

The spectra shown in Figure 10 exhibit maxima between 210 nm and 218 nm, which correspond to the LMCT excitation from oxygen to Mo(VI). The broad and less intense bands between 305 nm and 311 nm correspond to the LMCT transitions of oxygen to V(V) (Table 6). The LMCT bands of the V(V) are very broad and extend into the visible range. This is what gives rise to the different colors of the HPA-X-Y compounds. Since the HPA-0-1 does not contain V(V) and Mn(II) does not have a LMCT, this POM appears yellow, just like the parent POM HPA-0-0. As the amount of V(V) increases, the O→V(V) LMCT appears in the visible region, so the HPA-1-1 has a red color. With increasing amounts of V(V), the intensity of the V(V) LMCT increases accordingly, while the intensity of the Mo(VI) LMCT decreases proportionally. This results in a brown color dominating the POMs when more V(V) is incorporated into the Keggin structure.^[47] Figure 11 shows all HPA-X-Y POMs with their different colors sorted by degree of substitution.

In comparison with the LMCT bands of the HPA-X-0 POMs (Table 6 in the Supporting Information), it is noticeable that the

LMCT bands for Mo(VI) are in the range between 213 nm and 219 nm, while the LMCT bands for V(V) are in the range between 302 nm and 320 nm. This does not represent a significant difference to the HPA-X-Y POMs, so that it can be assumed that Mn(II) does not influence the position of the LMCT bands for Mo(VI) and V(V) strongly enough. However, it is already known for the HPA-X-0 compounds that the LMCT band for V(V) has a shoulder in the direction of longer wavelength. The band for the V(V) LMCT at smaller wavelength can be assigned to the V=O_t band (transition of an electron from the orbitals of the terminal oxygen atoms into the acceptor orbitals of the V(V) atoms) and the band causing the shoulder at larger wavelength can be assigned to the V-O_b/V-O_c bonds (transition of an electron from the orbitals of the metal-bridging oxygen atoms into the acceptor orbitals of the V(V) atoms).^[47,50] Similar trends have already been observed in the LMCT for Mo(VI).^[51] It is also known for the HPA-X-0 POMs that a red shift of the LMCT bands occurs with decreasing pH value.^[47,51]

Furthermore, the UV/Vis spectroscopy results compiled here can be used to indirectly infer the oxidation states of the elements involved: no LMCT can be expected for Mn(II) in the d⁵-high spin configuration because the transitions are forbidden. Mo(VI) and V(V) are in their respective highest oxidation states (d⁰-configuration). Reduced species of the elements Mo and V would not correspond to the d⁰-configuration, so that the transitions are forbidden and no LMCT can be observed.^[43]

Since the goal of our synthesis was to tune the POMs redox activity, electrochemical measurements were performed.^[52–58]

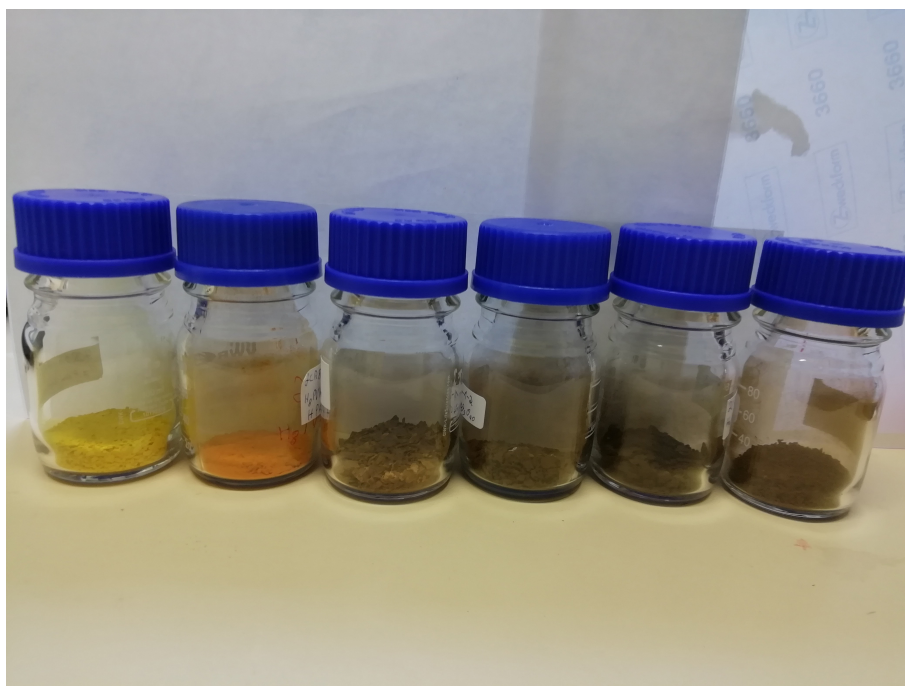


Figure 11. HPA-X-Y POMs synthesized in this work with their different colors. From left to the right: HPA-0-1, HPA-1-1, HPA-0-2, HPA-1-2, HPA-3-2, HPA-5-1.

The redox potentials of the new synthesized POMs were measured with cyclic voltammetry (CV) and square wave voltammetry (SWV). A comparison of the data from the two-fold substituted POMs is shown in Figure 12 (CV) and 13 (SWV), the remaining CV and SWV data of the individual POMs can be found in the Supporting Information (Figure S61 und S62),

respectively. The data of the two-fold substituted POMs in Figure 12 and 13 are compared with the two-fold only V(V) substituted POM HPA-2-0 and with the unsubstituted POM HPA-0-0 to get a better overview.

The CV/SWV curves of the two metal V(V) containing POMs, HPA-1-1 and HPA-2-0 are very similar, whereas the CV/SWV

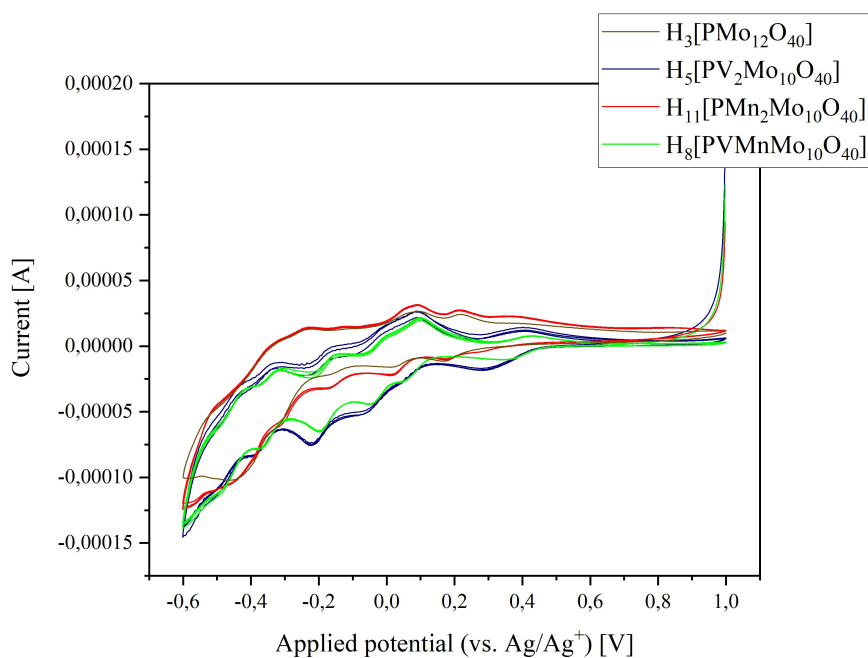


Figure 12. Comparison between the CV measurements of the two-fold metal substituted POMs HPA-2-0, HPA-0-2, HPA-1-1 and HPA-0-0 (concentration 1 mmol/L, scan rate 100 mV/s (CV)/5 mV/s (SWV) and pH 1).

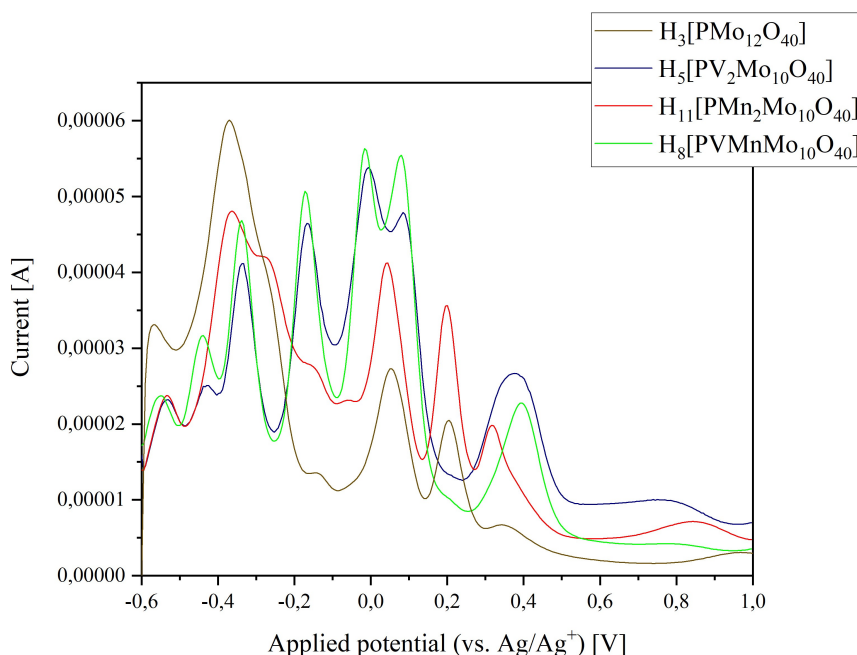


Figure 13. Comparison between the SWV measurements of the two-fold metal substituted POMs HPA-2-0, HPA-0-2, HPA-1-1 and HPA-0-0 (concentration 1 mmol/L, scan rate 100 mV/s (CV)/5 mV/s (SWV) and pH 1).

curve of the purely Mn(II) substituted HPA-0-2 deviates significantly. This leads to the conclusion that Mn(II) is present and takes part in the redox processes. In the SWV measurements, the V(V) containing two-fold substituted POMs both exhibit a pattern of two overlapping peaks in the range between -100 mV and 200 mV. In contrast, HPA-0-0 and HPA-0-2 do not show this pattern, indicating that these peaks are caused by the redox activity of V(V). HPA-0-0 and HPA-0-2 show only peaks at 50 mV (HPA-0-0) and 44.6 mV (HPA-0-2), respectively. These peaks can therefore only originate from redox processes of Mo(VI). Apparently, the Mn(II) incorporation leads to a shift of the redox processes from Mo(VI) to lower potentials.

The solely Mn(II) containing Keggin-type POMs HPA-0-2 shows three nearly overlapping peaks in the range between -400 and -100 mV, a feature not seen in the other V(V) containing POMs. The peak of HPA-0-2 at 201 mV is also not seen in the other V(V) substituted POMs, but for HPA-0-0 at 205 mV. Apparently, the peak of HPA-0-2 at 316 mV shifts through 377 mV for HPA-2-0 to 392 mV for HPA-1-1. For HPA-0-0, however, this peak is very weak at 340 mV.

The more V(V) the POMs contain, the more the signals merge in the range between -200 mV and 200 mV. This trend is particularly evident for the POMs HPA-3-2 and HPA-5-1 with three and five V(V) atoms in the structure (see CV and SWV data in the Supporting Information in Figures S30, S36 and S62). A table showing the peak maxima in all the SWV data and the maxima and minima in all the CV data is included in the Supporting Information (Table 7). The plot of the CV/SWV data of the POMs with three and five V(V) atoms in Figure S62 also contain the CV/SWV data of HPA-0-0, HPA-2-0 and HPA-0-2 to emphasize the differences to these compounds.

The electrochemical measurements of the triple and quintuple V(V) substituted POMs (Figure S62 Supporting Information) show significant differences from the low V(V) substituted POMs, while the Mn(II) substituted POMs show less significant differences. This can be explained by the fact that a maximum of six out of twelve Mo(VI) positions in the Keggin framework can be substituted by V(V), while only a maximum of two of the twelve positions can be occupied by Mn(II). The more metal atoms of the same species are integrated into the Keggin structure, the more significant its effects become, which

Table 7. Selected two-electron processes observed for the different HPA-0-Y species in comparison with HPA-0-0.

POM	Process	Peak maxima SWV [mV]
HPA-0-0	$[\text{PMo}^{\text{VI}}_{11}\text{Mo}^{\text{IV}}\text{O}_{40}]^{5-}/[\text{PMo}^{\text{VI}}_{12}\text{O}_{40}]^{3-}$	50
	$[\text{PMo}^{\text{VI}}_{10}\text{Mo}^{\text{IV}}_2\text{O}_{40}]^{7-}/[\text{PMo}^{\text{VI}}_{11}\text{Mo}^{\text{IV}}\text{O}_{40}]^{5-}$	205
HPA-0-1	$[\text{PMnMo}^{\text{VI}}_{10}\text{Mo}^{\text{IV}}\text{O}_{40}]^{9-}/[\text{PMnMo}^{\text{VI}}_{11}\text{O}_{40}]^{7-}$	39.5
	$[\text{PMnMo}^{\text{VI}}_9\text{Mo}^{\text{IV}}_2\text{O}_{40}]^{11-}/[\text{PMnMo}^{\text{VI}}_{10}\text{Mo}^{\text{IV}}\text{O}_{40}]^{9-}$	201
HPA-0-2	$[\text{PMn}_2\text{Mo}^{\text{VI}}_9\text{Mo}^{\text{IV}}\text{O}_{40}]^{13-}/[\text{PMn}_2\text{Mo}^{\text{VI}}_{10}\text{O}_{40}]^{11-}$	46.6
	$[\text{PMn}_2\text{Mo}^{\text{VI}}_8\text{Mo}^{\text{IV}}_2\text{O}_{40}]^{15-}/[\text{PMn}_2\text{Mo}^{\text{VI}}_9\text{Mo}^{\text{IV}}\text{O}_{40}]^{13-}$	201

Table 8. Shift of the RedOx potential V(V)→V(IV) depending on the substitution with V(V) and Mn(II).

POM	HPA-2-0	HPA-1-1	HPA-1-2
Redox potential V(V)→V(IV) [mV]	84.8	79.8	74.8

is also reflected in the SWV plot of $H_{11}PMn_2Mo_{10}O_{40}$ for two Mn(II) atoms in the structure.

From the literature it is known that HPA-0 (Figure S61 in the Supporting Information) has two significant two-electron processes (1: CV: 8.33 mV/87.7 mV; SWV: 50 mV and 2: CV: 167 mV/218 mV; SWV: 205 mV) resulting from $[PMo^{VI}_{11}Mo^{IV}O_{40}]^{5-}/[PMo^{VI}_{12}O_{40}]^{3-}$ and $[PMo^{VI}_{10}Mo^{IV}_2O_{40}]^{7-}/[PMo^{VI}_{11}Mo^{IV}O_{40}]^{5-}$.^[59,60] These processes are also found for the other POMs and are listed in Table 7:

The listed potentials become lower than in HPA-0-0 when Mn(II) is present for HPA-0-1 and HPA-0-2. This shows the trend that Mn(II) lowers the potentials for the different redox processes of a POM. For the higher substituted POMs these processes are not observed anymore, because of the overlapping redox processes of V(V). It is also possible, that anions with metals in different oxidation states and an overall charge greater than -12 , are not stable enough to form.

The peak at 84.8 mV (HPA-2-0), 79.8 mV (HPA-1-1) and 74.8 mV (HPA-1-2) belongs to the redox process of V(V)→V(IV) in the VO_2^+ ion (Table 8), which is formed via dissociation of the HPA-X-Y POMs in solution ($HPA-X-Y \rightarrow VO_2^+ + HPA-(X-1)-Y$).^[58] Vanadium is responsible for the catalytic redox activity: in the first step the reduction (V(V)→V(IV)) occurs, so that the substrate is oxidized. After this step the catalyst can be oxidized again (V(IV)→V(V)), e.g. with molecular oxygen.^[58] Our measurements show that the corresponding potentials are lowered by the introduction of Mn(II), thereby indicating that we have successfully tuned the redox potential.

Conclusion

A synthetic procedure that allows the substitution of the scaffolding metal of Keggin-type POMs with Mn(II) and V(V) was developed. Using this procedure, it was possible to synthesize and isolate several bi- and trimetallic Keggin-type-POMs. The composition and structure were confirmed by ICP-OES and vibrational spectroscopy. Furthermore, the new compounds were comprehensively characterized with NMR spectroscopy, UV/Vis spectroscopy, electrochemical methods and single crystal X-ray diffraction. We were able to show that the introduction of Mn(II) lowered the electrochemical potential of the V(V)/V(IV) RedOx process, which is a promising step towards tunable RedOx properties. Overall, our analytical results provide a solid basis for future investigations on the catalytic activity of Mn(II), and Mn(II)/V(V)-substituted phosphomolybdates.

Experimental Section

The following synthetic procedure was adapted from Odyakov and Zhizhina.^[9,16] Detailed synthetic procedures for each compound can be found in the Supporting Information.

For the synthesis of HPA-X-Y two separate solutions were prepared:

Solution 1: Divanadium pentoxide was added to deionized water and cooled to 5 °C. Then a 30% hydrogen peroxide solution in water was added dropwise to the orange-coloured suspension and stirred for some time, whereupon a brown solution was formed from which oxygen gas evolution was observed. The solution was then warmed to room temperature and a 25% phosphoric acid solution in water was added and the solution was cooled to 5 °C again.

Solution 2: Molybdenum trioxide was suspended in deionized water and a 25% phosphoric acid solution in water was added. Then the suspension was heated to reflux, whereupon a yellow, clear solution formed after about one hour.

The cool solution 1 was added dropwise to the boiling solution 2 and further heated to reflux. After 30 min, a manganese(II) acetate solution in water was added to the dark-coloured solution and heated to reflux for a further 90 min. The solution was then cooled to room temperature, filtered and concentrated under reduced pressure and elevated temperature (rotary evaporator with oil bath at 85 °C and 400 to 0 mbar).

The vanadium-free, manganese(II)-substituted POMs were synthesized according to the following modified prescription:

Deionized water was introduced, molybdenum trioxide and a 25% phosphoric acid solution in water were added and heated to reflux. After one hour, a yellow, clear solution was formed. Subsequently, a solution of manganese(II) acetate in water was added to the boiling solution and heated to reflux for another 60 minutes after the addition was completed. The solution was cooled to room temperature, filtered and concentrated under reduced pressure (rotary evaporator with oil bath at 85 °C and 400 to 0 mbar).

Further experimental details are provided in the Supporting Information.

Deposition Number(s) 2141261 (for HPA-0-1), 2141263 (for HPA-0-2), 2141259 (for HPA-1-1), 2141262 (for HPA-1-2), 2141260 (for HPA-5-1) contain(s) the supplementary crystallographic data for this paper. These data are provided free of charge by the joint Cambridge Crystallographic Data Centre and Fachinformationszentrum Karlsruhe Access Structures service.

Acknowledgements

The authors thank the central x-ray facility of Hamburg University, especially Dr. Frank Hoffmann for his help in solving and refining the structures and Isabelle Nevoigt for data collection. Furthermore, the authors gratefully acknowledge Prof. Irina Smirnova for allowing the use of her TGA machine at the Hamburg University of Technology. We further thank in particular Thomas Marx from the research group of Prof. Dr. Peter Burger for providing electrochemical equipment and helping with the electrochemical measurements. Open Access funding enabled and organized by Projekt DEAL.

Conflict of Interest

The authors declare no conflict of interest.

Keywords: crystallography · electrochemistry · polyoxometalates · redox active elements · NMR spectroscopy

- [1] N. I. Gumerova, A. Rompel, *Nat. Chem. Rev.* **2018**, *2*, 1–20.
- [2] F. Lu, M. Wang, N. Li, B. Tang, *Chem. Eur. J.* **2021**, *27*, 6422–6434.
- [3] L. Yang, J. Lei, J. M. Fan, R. M. Yuan, M. Sen Zheng, J. J. Chen, Q. F. Dong, *Adv. Mater.* **2021**, *33*, 1–25.
- [4] Y. F. Song, R. Tsunashima, *Chem. Soc. Rev.* **2012**, *41*, 7384–7402.
- [5] R. Neumann, *Inorg. Chem.* **2010**, *49*, 3594–3601.
- [6] J. Reichert, B. Brunner, A. Jess, P. Wasserscheid, J. Albert, *Energy Environ. Sci.* **2015**, *8*, 2985–2990.
- [7] B. Bertleff, J. Claußnitzer, W. Korth, P. Wasserscheid, A. Jess, J. Albert, *ACS Sustainable Chem. Eng.* **2017**, *5*, 4110–4118.
- [8] K. Inumaru, T. Ishihara, Y. Kamiya, T. Okuhara, S. Yamanaka, *Angew. Chem. Int. Ed.* **2007**, *46*, 7625–7628; *Angew. Chem.* **2007**, *119*, 7769–7772.
- [9] V. F. Odyakov, E. G. Zhizhina, *React. Kinet. Catal. Lett.* **2008**, *95*, 21–28.
- [10] J. Albert, D. Lüders, A. Bösmann, D. M. Guldi, P. Wasserscheid, *Green Chem.* **2014**, *16*, 226–237.
- [11] M. Abbessi, R. Contant, R. Thouvenot, G. Hervé, *Inorg. Chem.* **1991**, *30*, 1695–1702.
- [12] A. Patel, N. Narkhede, S. Singh, S. Pathan, *Catal. Rev. Sci. Eng.* **2016**, *58*, 337–370.
- [13] M. T. Pope, A. Müller, *Polyoxometalate Chemistry From Topology via Self-Assembly to Applications*, New York, Boston, Dordrecht, London, Moscow, **2002**.
- [14] A. Gaspar, D. V. Evtuguin, C. P. Neto, *Holzforchung* **2004**, *58*, 640–649.
- [15] A. Patel, S. Pathan, *J. Coord. Chem.* **2012**, *65*, 3122–3132.
- [16] V. F. Odyakov, E. G. Zhizhina, *Russ. J. Inorg. Chem.* **2009**, *54*, 361–367.
- [17] F. Zhang, M. Guo, H. Ge, J. Wang, *Front. Chem. Eng. China* **2007**, *1*, 296–299.
- [18] V. F. Odyakov, E. G. Zhizhina, R. I. Maksimovskaya, *Appl. Catal. A* **2008**, *342*, 126–130.
- [19] A. J. Bridgeman, *Chem. Eur. J.* **2004**, *10*, 2935–2941.
- [20] J. K. Lee, J. Melsheimer, S. Berndt, G. Mestl, R. Schlögl, K. Köhler, *Appl. Catal. A* **2001**, *214*, 125–148.
- [21] G. Mestl, T. Ilkenhans, D. Spielbauer, M. Dieterle, O. Timpe, J. Kröhnert, F. Jentoft, H. Knözinger, R. Schlögl, *Appl. Catal. A* **2001**, *210*, 13–34.
- [22] O. V. Dolomanov, L. J. Bourhis, R. J. Gildea, J. A. K. Howard, H. Puschmann, *J. Appl. Crystallogr.* **2009**, *42*, 339–341.
- [23] C. B. Hübschle, G. M. Sheldrick, B. Dittrich, *J. Appl. Crystallogr.* **2011**, *44*, 1281–1284.
- [24] A. L. Spek, *J. Appl. Crystallogr.* **2003**, *36*, 7–13.
- [25] G. M. Sheldrick, *Acta Crystallogr. Sect. A* **2008**, *64*, 112–122.
- [26] A. L. Spek, *Acta Crystallogr. Sect. D* **2009**, *65*, 148–155.
- [27] A. L. Spek, *Acta Crystallogr. Sect. C* **2015**, *71*, 9–18.
- [28] H. H. Wu, Z. M. Zhang, E. B. Wang, *Chin. Chem. Lett.* **2012**, *23*, 355–358.
- [29] H.-X. Liu, Q. Liu, L.-T. Wang, Q.-H. Fan, K.-Q. Ye, G. Zeng, X.-S. Tai, *Asian J. Chem.* **2014**, *26*, 4741–4743.
- [30] P. Pyykkö, M. Atsumi, *Chem. Eur. J.* **2009**, *15*, 186–197.
- [31] M. X. Xu, S. Lin, L. M. Xu, S. L. Zhen, *Transition Met. Chem.* **2004**, *29*, 332–335.
- [32] P. Kubáček, R. Hoffmann, *J. Am. Chem. Soc.* **1981**, *103*, 4320–4332.
- [33] M. Darari, A. Francés-Monerris, B. Marekha, A. Doudouh, E. Wenger, A. Monari, S. Haacke, P. C. Gros, *Molecules* **2020**, *25*, 5991–6011.
- [34] C. K. H. Borg, X. Zhou, C. Eckberg, D. J. Campbell, S. R. Saha, J. Paglione, E. E. Rodriguez, *Phys. Rev. B* **2016**, *93*, 1–10.
- [35] J. Li, A. W. Sleight, *J. Solid State Chem.* **2004**, *177*, 889–894.
- [36] M. T. Pope, T. F. Scully, *Inorg. Chem.* **1975**, *14*, 953–954.
- [37] L. Pettersson, I. Andersson, A. Selling, J. H. Grate, *Inorg. Chem.* **1994**, *33*, 982–993.
- [38] A. Selling, I. Andersson, J. H. Grate, L. Pettersson, *Eur. J. Inorg. Chem.* **2000**, 1509–1521.
- [39] D. V. Evtuguin, C. Pascoal Neto, J. Rocha, J. D. Pedrosa De Jesus, *Appl. Catal. A* **1998**, *167*, 123–139.
- [40] K. Lee, G. Pozarnsky, O. Zarembowitch, A. McCormick, *Chem. Eng. J. Biochem. Eng. J.* **1996**, *64*, 215–223.
- [41] J. Albert, M. Mendt, M. Mozer, D. Voß, *Appl. Catal. A* **2019**, *570*, 262–270.
- [42] S. Wesinger, M. Mendt, J. Albert, *ChemCatChem* **2021**, *13*, 3662–3670.
- [43] A. F. Holleman, E. Wiberg, Nils Wiberg, G. Fischer, *Lehrbuch Der Anorganischen Chemie*, Berlin, New York, **2009**.
- [44] K. P. Barteau, J. E. Lyons, I. K. Song, M. A. Barteau, *Top. Catal.* **2006**, *41*, 55–62.
- [45] I. K. Song, H. S. Kim, M. S. Chun, *Korean J. Chem. Eng.* **2003**, *20*, 844–849.
- [46] T. Yamase, *Chem. Rev.* **1998**, *98*, 307–325.
- [47] J. Claußnitzer, *Oxidative Entschwefelung von Mineralölkfraktionen Mit Vanadiumhaltigen Polyoxometallat-Katalysatoren*, Bayreuth, **2021**.
- [48] H. Salavati, N. Rasouli, *Mater. Res. Bull.* **2011**, *46*, 1853–1859.
- [49] H. Li, L. Swenson, R. J. Doedens, M. I. Khan, *Dalton Trans.* **2016**, *45*, 16511–16518.
- [50] N. K. K. Raj, A. V. Ramaswamy, P. Manikandan, *J. Mol. Catal. A* **2005**, *227*, 37–45.
- [51] Q. Gao, F. Li, M. Sun, L. Xu, Y. Wang, J. Bai, *CrystEngComm* **2014**, *16*, 7681–7688.
- [52] N. Elgrishi, K. J. Rountree, B. D. McCarthy, E. S. Rountree, T. T. Eisenhart, J. L. Dempsey, *J. Chem. Educ.* **2018**, *95*, 197–206.
- [53] M. Privman, T. Hepel, *J. Electroanal. Chem.* **1995**, *382*, 137–144.
- [54] C. Li, Y. Zhang, K. P. O'Halloran, J. Zhang, H. Ma, *J. Appl. Electrochem.* **2009**, *39*, 421–427.
- [55] M. Barth, M. Lapkowski, S. Lefrant, *Electrochim. Acta* **1999**, *44*, 2117–2123.
- [56] T. Ueda, *ChemElectroChem* **2018**, *5*, 823–838.
- [57] Z. Han, Y. Zhao, J. Peng, Y. Feng, J. Yin, Q. Liu, *Electroanalysis* **2005**, *17*, 1097–1102.
- [58] B. Bujanovic, S. Ralph, R. Reiner, K. Hirth, R. Atalla, *Materials* **2010**, *3*, 1888–1903.
- [59] D. Youn Hwang, S. Yong Ha, S. Kim, *Bull. Korean Chem. Soc.* **2001**, *22*, 441–442.
- [60] M. Sadakane, E. Steckhan, *Chem. Rev.* **1998**, *98*, 219–237.

Manuscript received: April 11, 2022
Accepted manuscript online: June 22, 2022
Version of record online: July 13, 2022

5.3 Vergleichende spektroskopische und elektrochemische Studie über V(V)
substituierte Keggin-Typ Phosphormolybdate und -wolframate

P3

Comparative Spectroscopic and Electrochemical Study of V(V)-Substituted Keggin-Type
Phosphomolybdates and -Tungstates

Jan-Christian Raabe, José Aceituno Cruz, Jakob Albert, Maximilian J. Poller

Raabe, J.-C.; Aceituno Cruz, J.; Albert, J.; Poller, M. J. Comparative Spectroscopic and
Electrochemical Study of V(V)-Substituted Keggin-Type Phosphomolybdates and -Tungstates.
Inorganics **2023**, *11* (4), 138. <https://doi.org/10.3390/inorganics11040138>.

Die vorliegende Studie (P3, *Inorganics*. **2023**, *11* (4), 138) beschäftigt sich mit dem spektroskopischen und elektrochemischen Vergleich der V(V) substituierten Phosphormolybdate und der -wolframate.^[248] Eine Isolierung der Wolframate als Säuren war nicht möglich, da die Etherat-Methode für die höhergeladenen TMSPOM-Anionen scheiterte. Aus spektroskopischer Sicht wurden insbesondere in der schwingungsspektroskopischen IR-Analyse signifikante Unterschiede gefunden, da die Massendifferenz zwischen W und V größer ist als die von Mo und V.^[248] In Abhängigkeit des Substitutionsgrades x ergaben sich daher für die Phosphorwolframate nicht nur Bandenshifts, sondern auch Aufspaltungen einiger Schwingungsbanden, was insbesondere an der P-O Schwingungsbande verdeutlicht wurde (Abbildung 22). In den NMR-Analysen (^{31}P und ^{51}V) zeigten beide Keggin-Typ Klassen komplexe Spektren, deren Komplexität mit steigenden x zunahm. Diese Beobachtung ist ein Resultat zahlreicher Positionisomere und komplexen, pH abhängigen Dissoziationsgleichgewichten, die mit zunehmendem x stärker ausgeprägt werden, was als ein Resultat der abnehmenden Stabilität der TMSPOMs in wässriger Lösung gedeutet wird. Aus elektrochemischer Sicht wurde deutlich, dass die Phosphorwolframate im Vergleich zu den Molybdaten deutlich weniger RedOx-Potentiale aufweisen, was sich insbesondere limitierend auf die RedOx-katalytischen Anwendungsmöglichkeiten der potenziellen Katalysatoren auswirken sollte. Daher ist es für die RedOx-Katalyse vorteilhafter auf die Phosphormolybdate zurückzugreifen, da deren RedOx-Chemie vielfältiger ausgeprägt ist als die der Wolframate (Abbildung 22) und diese direkt als POM-Säuren isoliert werden konnten. Eine Auswahl der spektroskopischen und elektrochemischen Resultate aus der Studie P3 sind in Abbildung 22 zusammengefasst.^[248]

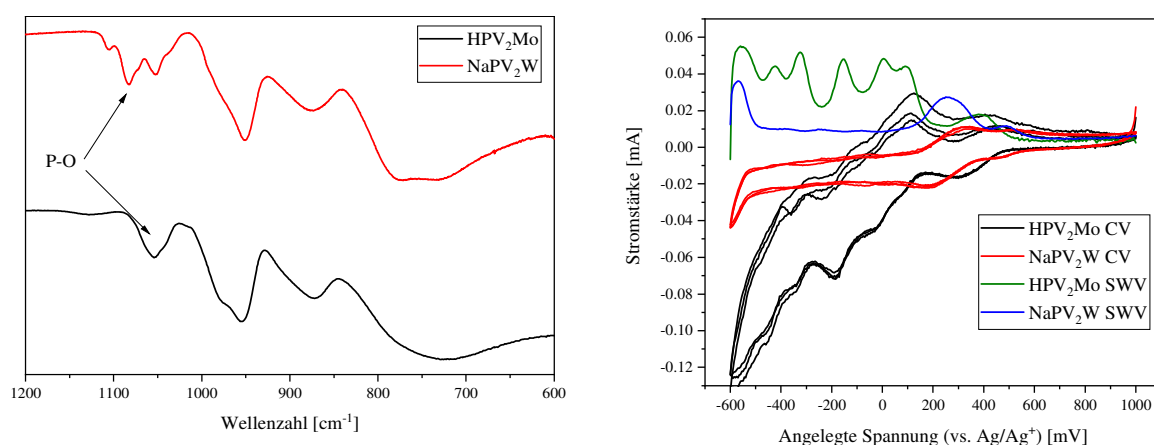


Abb. 22: Spektroskopischer und elektrochemischer Vergleich der V(V) substituierten Keggin-Typ Phosphormolybdate und -wolframate in P3, *Inorganics*. **2023**, *11* (4), 138. Repräsentative Ergebnisse hier am Beispiel der Anionen $[\text{PV}_2\text{Mo}_{10}\text{O}_{40}]^{5-}$ und $[\text{PV}_2\text{W}_{10}\text{O}_{40}]^{5-}$ dargestellt.^[248]

Article

Comparative Spectroscopic and Electrochemical Study of V(V)-Substituted Keggin-Type Phosphomolybdates and -Tungstates

Jan-Christian Raabe , José Aceituno Cruz , Jakob Albert and Maximilian J. Poller * 

Institute for Technical and Macromolecular Chemistry, Universität Hamburg, Bundesstraße 45, 20146 Hamburg, Germany

* Correspondence: maximilian.poller@uni-hamburg.de

Abstract: Vanadium-substituted Keggin-type heteropolyanions have been studied for a wide variety of applications, ranging from catalysis to antiviral/antimicrobial agents. While the V-substituted phosphomolybdates $[\text{PV}_x\text{Mo}_{12-x}\text{O}_{40}]^{(3+x)-}$ have been well investigated in this context, comparatively little is known about the corresponding phosphotungstates $[\text{PV}_x\text{W}_{12-x}\text{O}_{40}]^{(3+x)-}$. We have succeeded in synthesizing the sodium salts of the whole series $[\text{PV}_x\text{W}_{12-x}\text{O}_{40}]^{(3+x)-}$, for $x = 1$ to 6, and characterised them spectroscopically (FT-IR, UV-Vis, ^{31}P -, and ^{51}V -NMR) and electrochemically (CV and SWV). Thereby, direct comparisons between the vanadium-substituted phosphomolybdates and -tungstates, with substitution degrees from 1 to 6, can be established, which provides a solid basis for further investigations of potential applications.

Keywords: polyoxometalates; heteropolyanions; spectroscopy; electrochemistry; phosphotungstates; phosphomolybdates; vanadium



Citation: Raabe, J.-C.; Aceituno Cruz, J.; Albert, J.; Poller, M.J. Comparative Spectroscopic and Electrochemical Study of V(V)-Substituted Keggin-Type Phosphomolybdates and -Tungstates. *Inorganics* **2023**, *11*, 138. <https://doi.org/10.3390/inorganics11040138>

Academic Editor: Greta Ricarda Patzke

Received: 24 February 2023

Revised: 9 March 2023

Accepted: 17 March 2023

Published: 23 March 2023



Copyright: © 2023 by the authors. Licensee MDPI, Basel, Switzerland. This article is an open access article distributed under the terms and conditions of the Creative Commons Attribution (CC BY) license (<https://creativecommons.org/licenses/by/4.0/>).

1. Introduction

Polyoxometalates (POMs), especially those substituted with redox-active transition metals such as Vanadium (V), are used for a wide variety of applications, ranging from catalysis to the biomedical field. Examples of catalytic applications are, the conversion of biomass to formic acid and the oxidative catalytic desulfurization of fuels [1–9]. In the field of biomedicine, vanadium-containing POMs have shown antibacterial and antiviral effects, as well as anti-tumour properties [10–14].

The antibacterial activity of POMs was discovered in 1993, by Tajima et al. [15], and can be attributed to synergistic and direct antibacterial activity. Numerous POMs show no antibacterial activity on their own but become active in synergy with conventional antibiotics. The discovery of this property, first led to the discovery of the antibacterial phosphotungstate species known as “Factor T”, which was later identified as the lacunary anion $[\text{PW}_{11}\text{O}_{39}]^{7-}$ [11,15]. However, this effect was only shown in synergy with β -lactam antibiotics, against the bacterial strains *Staphylococcus epidermis* and *Staphylococcus auricularis* [13]. Based on these discoveries, various POM structures, especially tungstate structures, were identified as active [11]. A few POMs exhibit antibacterial properties, even without the addition of another antibiotic, including some tungsten and vanadium clusters. In addition, antibacterial properties of Keggin-type POMs H_3 $[\text{PMo}_{12}\text{O}_{40}]$ HPMo, H_3 $[\text{PW}_{12}\text{O}_{40}]$ HPW, and H_4 $[\text{SiW}_{12}\text{O}_{40}]$ HSiW, against the bacteria *Escherichia coli* (Gram-negative) and *Bacillus subtilis* (Gram-positive), are also known. The effect is triggered photocatalytically, by irradiation with UV light [11]. Antiviral activity of some V(V)-substituted tungstate structures was also confirmed in various in vitro and in vivo assays, against RNA viruses [12]. Thus, in vitro antiviral activities against HI virus were found, with the POM presumably binding to the gp-120 protein and thus interfering with the interaction of the anti-gp-120 antibody with the gp-120 protein [16]. In further studies, it was shown

that, especially tungstate-based POMs, also have the ability to inhibit DNA polymerase in retroviruses and thus show antiviral activity against the HI virus [14]. Another biomedical application of POMs is the anti-tumour effect of molybdenum-based POMs, induced by cell apoptosis. Presumably, the POM is preferentially taken up by tumour cells, where it is metabolised to a more toxic compound, that inhibits ATP generation. However, the mechanisms of the anti-tumour action of POMs are still the subject of current research [14].

Furthermore, the current interest in POMs is illustrated by a number of novel applications to current research topics. For example, the research group of Schimpf, demonstrated that POM anions can be used to create tuneable functional materials, by connecting POM anions with suitable transition metal cations [17,18].

This shows that, especially the tungsten-based POMs are of great interest for biomedical research. However, in contrast to the vanadium-substituted phosphomolybdates ($[\text{PV}_x\text{Mo}_{12-x}\text{O}_{40}]^{(3+x)-}$, $x = 1$ to 6), which have been comprehensively investigated in the context of catalysis, the corresponding tungstates ($[\text{PV}_x\text{W}_{12-x}\text{O}_{40}]^{(3+x)-}$) have not been studied as thoroughly.

The synthesis of tailor-made, transition metal-substituted POMs, can be generally achieved by two different strategies. In a self-assembly synthesis, the precursor compounds are combined in a defined stoichiometry, and under suitable reaction conditions, the monomeric precursor species then link, to form oligomeric cluster structures. Such synthesis strategies have been shown to be robust against pH fluctuations. Furthermore, high degrees of substitution with foreign metals, i.e., V(V), can be achieved. The synthesis of V-substituted phosphomolybdates, reported by Odyakov et al., is based on this strategy [19–22]. The second possibility is the lacunary approach. Here, the synthesis route starts from an intact (usually commercially available) POM structure. Under basic conditions, individual metal–oxygen polyhedra are dissolved out of the POM network, forming a defect POM structure containing vacancies (usually one to three vacancies), known as a lacunary POM structure [23]. The vacancies can now be filled with other metals, resulting in transition metal-substituted POM structures. This method is commonly utilised for the synthesis of substituted Keggin-tungstates. However, POM lacunary structures can be susceptible to pH fluctuations, as they are often stable only within a small pH window. Low degrees of substitution also result, since the theoretically maximum possible number of vacancies is severely limited [23–25].

We have adapted the self-assembly strategy, to successfully synthesise the $[\text{PV}_x\text{W}_{12-x}\text{O}_{40}]^{(3+x)-}$ for x up to 6. In this work, we present the resulting new heteropoly-anions, with their spectroscopic and electrochemical characteristics, in comparison with the corresponding molybdates.

2. Results and Discussion

The POMs $\text{H}_{3+x}[\text{PV}_x\text{Mo}_{12-x}\text{O}_{40}]$ (HPV_xMo), with $x = 1$ to 6, were synthesised according to the adapted literature procedure of Odyakov et al. [20–22], using molybdenum trioxide MoO_3 , phosphoric acid H_3PO_4 , and divanadium pentoxide V_2O_5 . $\text{Na}_{3+x}[\text{PV}_x\text{W}_{12-x}\text{O}_{40}]$ (NaPV_xW), with $x = 2$ to 3, were synthesised from the previously synthesised lacunary POM $[\text{PW}_9\text{O}_{34}]^{9-}$ species, whereas the POMs NaPV_xW , with $x = 4$ to 6, were synthesised starting from Na_2WO_4 , NaVO_3 , and H_3PO_4 , using a self-assembly approach. Compound NaPVW was synthesised via in situ lacunary $[\text{PW}_{11}\text{O}_{39}]^{7-}$ formation, starting from commercially available phosphotungstic acid hydrate (HPW) [26–30]. Since sodium-containing precursors were used for the synthesis of NaPV_xW , the POMs could only be isolated as sodium salts. The fact that the HPV_xMo analogues can be obtained as free acids in solution is due to the different synthetic strategy used, since for the molybdates, an alkali ion free synthesis from the respective metal oxides is possible. However, this approach is not suitable for the tungstate analogues, since the WO_3 does not present solubility properties compatible with the Keggin-type POM synthesis. Nevertheless, it is desirable to isolate the corresponding heteropolyacids. For example, in a study by Albert et al., (2014) [5], it was shown that catalytic applications of POMs in biomass conversion require bifunctional compounds, that

ensure the conversion of the substrate by acid/base catalysis (hydrolysis of the substrate), followed by redox catalysis (substrate oxidation). Thus, it could be advantageous to combine the acid/base effect, with the anion-mediated redox properties, in one molecule. In order to obtain bifunctional POMs, combining the acid/base and redox components, a suitable strategy was sought, to ensure the conversion of the obtained POM salts to their free acids. It was described by Tsigdinos et al. [31], that the free POM acids can be generated from the corresponding alkali salts by extraction of the POM with diethyl ether. However, this method failed in the attempt to obtain higher degrees of substitution than $x = 3$ [31]. In our experimental results (for details see Supporting Information), it was found that the yields of the extracted free acid decreases with increasing degree of substitution (61% for the formation of HPVW from NaPVW, 23% for HPV₂W from NaPV₂W, and only 3% for HPV₃W from NaPV₃W). In the case of NaPV₄W, the method failed completely. This result is consistent with the data found for the molybdates described by Tsigdinos et al. [31]. In addition, significant losses of the metals W(VI) and V(V) from the Keggin-structure, are observed already from a substitution level of 2, which leads to an additional limitation of this method for practical use (see Table 1).

Table 1 summarises the results obtained from the elemental analysis (AAS/ICP-OES), and from the TGA analysis. For interpretation, all results were normalised to the framework metal molybdenum or tungsten, respectively. The phosphorous content in the V(V)-substituted phosphomolybdates is increased, due to the excess of phosphoric acid used during the synthesis, as suggested by Odyakov et al. [20–22]. The elemental analysis method used to determine the tungsten content, has a systematic error, which causes the tungsten content to be determined too low, with the result that the contents of the other elements appear to be too high in relation to it, since the corresponding framework metals (tungsten in this case) were normalised for interpretation. When considering the POMs NaPVW to NaPV₃W, it can be assumed that the charge balance of the anions is completely ensured by the sodium cations, while for the POMs NaPV₄W to NaPV₆W, a lower cation content was found than would be necessary for a complete charge balance. The remaining charge balance can therefore only be ensured by protons originating from the acidic medium during synthesis. Thus, compounds NaPV₄W to NaPV₆W were obtained as mixed salts/acids. One possible reason for this, is that the tungstates with $x = 1$ to 3 and $x = 4$ to 6, were prepared by two different synthetic approaches (lacunary vs. self-assembly approach). However, it is also conceivable that the increased charge of the POM anions increases their basicity, which increases with increasing degree of substitution. This can lead to the heteropolyacid not dissociating completely in aqueous media, which means that not all protons can be exchanged by sodium ions.

Table 1. Results from AAS/ICP-OES and TGA analyses of the different POMs analysed in this work.

Compound	Molecular Composition	Element Ratio	Hydration Water [mol/mol-POM]
HPVMo	H ₄ [PVMo ₁₁ O ₄₀]	P/V/Mo 1.23 ^a /0.97/11	7
HPVW	H ₄ [PVW ₁₁ O ₄₀]	Na/P/V/W 0/1.08/1.07/11 ^b	18
NaPVW	Na ₄ [PVW ₁₁ O ₄₀]	Na/P/V/W 4.05/1.15 ^b /1.18 ^b /11 ^b	9
HPV ₂ Mo	H ₅ [PV ₂ Mo ₁₀ O ₄₀]	P/V/Mo 1.28 ^a /2.01/10	9
HPV ₂ W	H ₅ [PV ₂ W ₁₀ O ₄₀]	Na/P/V/W 0/1.02/1.78/10 ^b	15

Table 1. Cont.

Compound	Molecular Composition	Element Ratio	Hydration Water [mol/mol-POM]
NaPV ₂ W	Na ₅ [PV ₂ W ₁₀ O ₄₀]	Na/P/V/W 6.52 ^b /1.21 ^b /2.31 ^b /10 ^b	14
HPV ₃ Mo	H ₆ [PV ₃ Mo ₉ O ₄₀]	P/V/Mo 1.10 ^a /3.03/9	15
NaPV ₃ W	Na ₆ [PV ₃ W ₉ O ₄₀]	Na/P/V/W 7.12 ^b /1.17 ^b /3.32 ^b /9 ^b	13
HPV ₄ Mo	H ₇ [PV ₄ Mo ₈ O ₄₀]	P/V/Mo 1.41 ^a /4.03/8	23
NaPV ₄ W	Na ₇ [PVW ₈ O ₄₀]	Na/P/V/W 6.62/1.17 ^b /4.11 ^b /8 ^b	11
HPV ₅ Mo	H ₈ [PV ₅ Mo ₇ O ₄₀]	P/V/Mo 1.21 ^a /5.02/7	9
NaPV ₅ W	Na ₈ [PV ₅ W ₇ O ₄₀]	Na/P/V/W 6.79/1.10 ^b /5.13 ^b /7 ^b	11
HPV ₆ Mo	H ₉ [PV ₆ Mo ₆ O ₄₀]	P/V/Mo 1.28 ^a /6.11/6	11
NaPV ₆ W	Na ₉ [PV ₆ W ₆ O ₄₀]	Na/P/V/W 6.71/1.05/6.15 ^b /6 ^b	13

The element ratios were determined using AAS or ICP-OES, the water content was determined by TGA. All results were normalised to the framework metal (molybdenum or tungsten). ^a H₃PO₄ was used in a slight excess during synthesis, so a slightly higher P content is expected, due to phosphate impurities. ^b Tungsten values are determined systematically too low with the applied measurement method, so that the values for the other elements appear to be too high.

There is a tendency for the tungstates to have higher crystal water contents than the molybdates, which can be correlated with the size of W(VI) compared to Mo(VI), since W(VI) is thus able to coordinate more hydrate water molecules.

The integrity and the characterization in the solid-state of all investigated Keggin-type structures was performed by ATR-FT-IR and Raman spectroscopy. Figure 1 shows the IR spectra of the POMs NaPV_xW with $x = 1$ to 6, and a comparison between $x = 2$ for NaPV₂W, HPV₂W, and HPV₂Mo is shown in Figure 2. IR spectra of the POMs HPV_xMo with $x = 1$ to 6, and a comparison between the POMs with $x = 1$ for NaPVW, HPVW, and HPVMo, can be found in Figures S1 and S2 in the Supplementary Materials.

IR spectroscopy of Keggin-type POMs, represents a common method for verifying the structure type and has been discussed extensively in the literature [23,32,33]. In general, the trend is evident that the IR bands are broadened with increasing degree of substitution. This observation correlates with the fact that more positional isomers are generated with increasing degree of substitution. The more isomers there are, the broader the bands become overall. The importance of the positional isomers for the evaluation of the further analysis is discussed in detail in the section on NMR spectroscopy. In particular, the assignment of the individual signals to the vibration modes is known from the literature, and has already been substantiated by numerous theoretical simulations. The work of Bridgeman (2004) [32], presents a computational study in which IR and Raman bands were predicted for the different Keggin isomers and compared to the real measured data [32]. In agreement with the literature, the present IR spectra show characteristic bands of a Keggin structure type. All observed vibrational bands were assigned to the corresponding vibration modes, according to Lee et al. [33]. The bands in the region of $>1000\text{ cm}^{-1}$, correspond to the phosphorus–oxygen vibration mode P–O, while the vibrational bands in the region between 950 and 1000 cm^{-1} belong to the vibration modes of the terminal metal–oxygen bonds $M = O_t$. In the region between 850 and 900 cm^{-1} and in the region below 800 cm^{-1} , the

vibrational bands of the metal–metal bridging oxygen–metal bonds can be located for the corner- $(M-O-M)_{\text{vertex}}$ and the edge- $(M-O-M)_{\text{edge}}$ linked octahedrons [23,32,33].

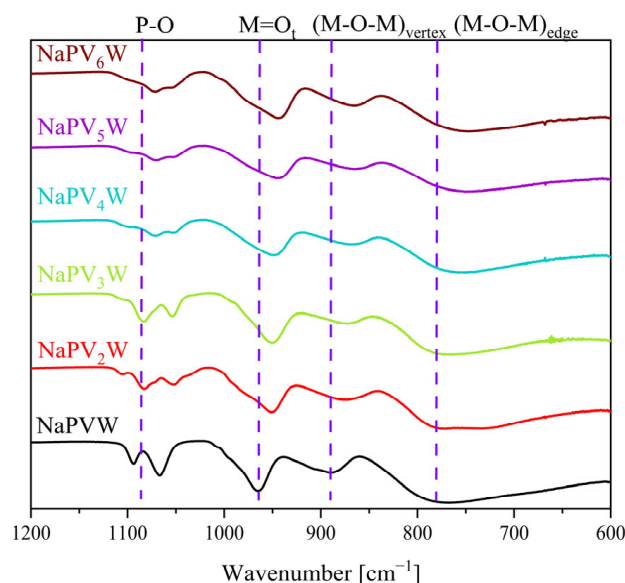


Figure 1. ATR-FT-IR spectra of the POMs NaPV_xW , with $x = 1$ to 6.

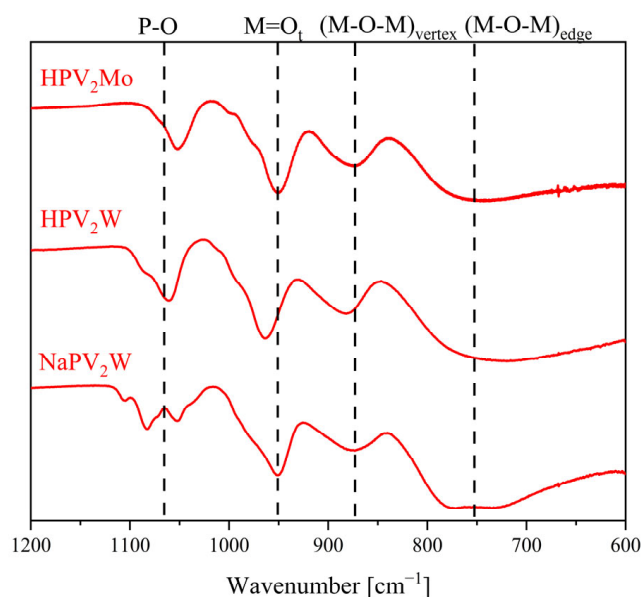


Figure 2. ATR-FT-IR spectra of the POMs NaPV_2W , HPV_2W , and HPV_2Mo .

As the W(VI) positions are increasingly substituted with V(V) atoms of significantly lower mass, the vibrational bands shift to lower wavenumbers, since the corresponding vibration is more easily excited. This effect is already well reported in the literature for various substituted Keggin POMs [23,32,33]. The same trend is also observed for the Keggin-type molybdate series, but the effect is much more significant for the tungstates, due to the larger mass difference between W(VI) and V(V) . In contrast to the molybdates, it is noticeable for the tungstates that the P–O vibrational band appears in two bands: the reason for this is the very same effect, although in this case the shift is sufficiently large to form a separate vibrational band. A closer look at the Keggin structure, reveals that the four oxygen atoms coordinating the central phosphorus atom tetrahedrally, are each part of an M_3O_{13} unit [34]. Thus, at higher wavenumbers, the vibrational band of the P–O mode

tends to originate from the P–O bond to whose oxygen atom a W(VI) rich W_3O_{13} unit is attached, while at lower wavenumbers the bands can be assigned to corresponding P–O vibrational bands of V(V) rich M_3O_{13} units.

The integrity of the Keggin structure has also been confirmed for the extracted heteropolyacids HPVW and HPV₂W (Figure 2 and Figure S2 Supplementary Materials). Here, the P–O band for the hetero-polyacid HPV₂W in Figure 2 is not split like that of NaPV₂W, which can be attributed to the V(V) loss during extraction (vide supra).

Table 2 illustrates the discussed trend, that the vibration bands for both the Keggin-type tungstates and respective molybdates shift to smaller wavenumbers with increasing degree of substitution. For the comparison between the V(V)-substituted tungstates and molybdates, the trend, especially for the degrees of substitution $x = 1$ to 3, is that for the same degree of substitution, the vibrational bands of the tungstates are shifted to higher wavenumbers. This trend is due to the higher mass of the element tungsten, so that the corresponding vibrational modes require more energy to be excited. The same trends can also be seen when comparing the IR data of the unsubstituted parent POMs, HPMo and HPW (Figure S3, Supplementary Materials).

Table 2. Positions of the characteristic vibration bands of all POMs investigated in this work.

POM/Vibration Mode	P–O	M = O _t	(M–O–M) _{vertex}	(M–O–M) _{edge}
HPMo	1059	962	877	744
HPW	1073	973	904	756
NaPVW	1094, 1066	965	890	764
HPVW	1070	959	876	735
HPVMo	1055	955	872	729
NaPV ₂ W	1083, 1054	952	875	773
HPV ₂ W	1061	964	884	724
HPV ₂ Mo	1054	955	872	729
NaPV ₃ W	1084, 1054	950	876	765
HPV ₃ Mo	1053	954	877	730
NaPV ₄ W	1072, 1053	948	868	756
HPV ₄ Mo	1048	951	871	720
NaPV ₅ W	1070, 1052	945	865	751
HPV ₅ Mo	1047	949	868	719
NaPV ₆ W	1071, 1059	944	868	748
HPV ₆ Mo	1051	949	874	710

The success of V(V) substitution into the Keggin-type phosphotungstate structure can also be verified by Raman spectroscopy. Figure 3 shows the Raman spectra of the POMs NaPV_xW ($x = 1$ to 6), and Figure 4 a comparison between the POMs NaPV₂W, HPV₂W, and HPV₂Mo. Raman spectra of the POMs HPV_xMo, with $x = 1$ to 6, and a comparison between the POMs with $x = 1$, for NaPVW, HPVW, and HPVMo, can be found in Figures S4 and S5 in the Supplementary Materials. Essentially, a Raman spectrum of a Keggin structure shows the various vibrational modes of the M = O_t bond in the region around 1000 cm⁻¹, and the various M–O–M vibrational modes, particularly pronounced in the region below 400 cm⁻¹ [32]. The vibrational modes of the P–O bonds are not Raman active. The success of the substitution is evident in the M = O_t bands, which strongly change their shape due to the substitution, and, especially in the case of the tungstates, shift to smaller wavenumbers with increasing degree of substitution. Due to the smaller mass of V(V) in comparison to W(VI), an additional shoulder forms with increasing degree of V(V) substitution. This is

the same phenomenon discussed above, for the IR spectra. A direct comparison between HPMo and HPW can be found in Figure S6, Supplementary Materials. Here the intensities of the vibration bands of HPW are not as intense, in comparison to HPMo.

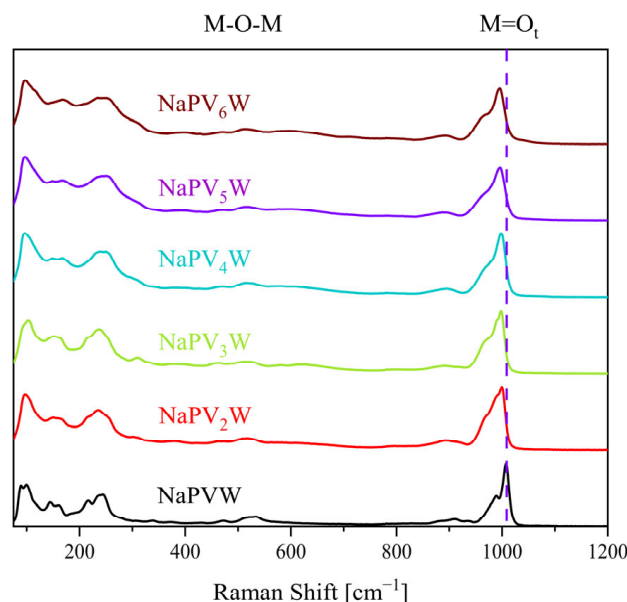


Figure 3. Raman spectra of the POMs NaPV_xW , with $x = 1$ to 6. The purple line runs through the peak maximum of an $\text{M} = \text{O}_t$ vibration band from NaPVW , to illustrate the trend of the peak shift dependence on the substitution degree.

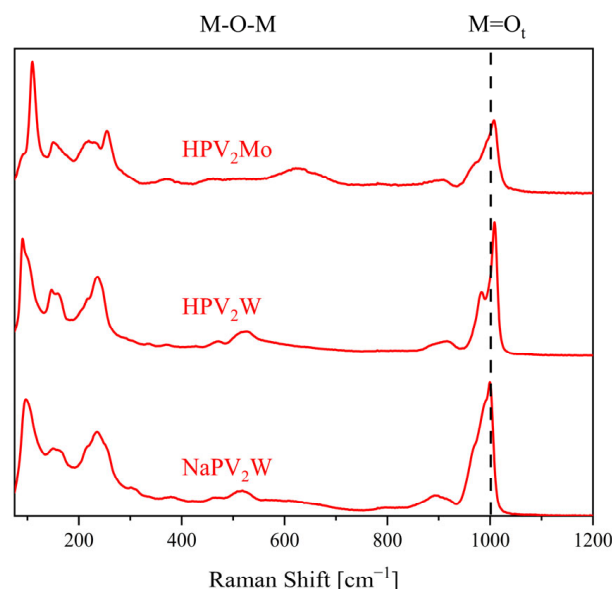


Figure 4. Raman spectra of the POMs NaPV_2W , HPV_2W , and HPV_2Mo . The black line runs through the peak maximum of an $\text{M} = \text{O}_t$ vibration band from NaPV_2W , to illustrate the trend of the peak shift dependence on the substitution degree.

To support our results from the solid-state characterization, we present two new single-crystal structures, of NaPV_5W in Figure 5 and Table 3, and NaPV_2W in Figure S7 (Supplementary Materials). The crystallographic information files (.cif) can be found in the CCDC database, with the deposition numbers: 2240685 (NaPV_2W) and 2240686 (NaPV_5W). Detailed refinement data are found in the Supplementary Materials, Section 2.9. All compounds were crystallised in the tetragonal space group $P4/mnc$ (128) and grown by

slow evaporation of water from an aqueous POM solution, in a desiccator, under reduced pressure. Further information about the unit cell and the space groups can be found in Table S4, Supplementary Materials. The crystal structures show a distinct disorder of the central phosphorous atom. This is a known disorder type, which is found in many Keggin-type crystal structures (e.g., CCDC database deposition number: 1628559). As suggested by the disorder of the central PO₄ tetrahedron, the phosphorus coordination appears cubic. However, it is a tetrahedral coordination, as can easily be seen if the four oxygen atoms are partially occupied (occupation 0.5). All metal atoms are in an octahedral coordination by six oxygen atoms, and have a terminal oxo ligand with double bond character, as can be seen from the shortened bond length (Table 3). All the crystallographic information of both structures is summarised in Table 3. To gain better insights into the obtained structures, the bond lengths are compared to the sum of covalent radii.

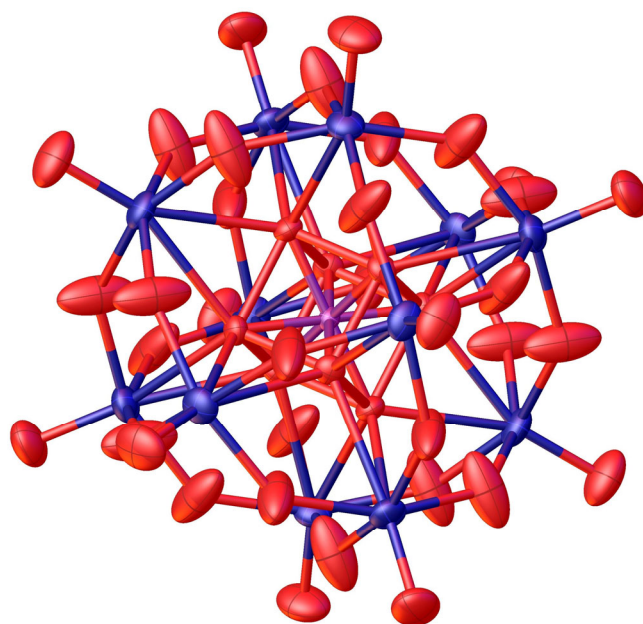


Figure 5. Solid-state structure of compound NaPV₅W, determined by X-ray diffraction. The compound was crystallised in the space group P4/mnc (128). Residual electron density attributed to hydration water has been refined with a solvent mask (SQUEEZE). R_1 : 2.64%, wR_2 : 6.46%, R_{int} : 5.86%, GooF: 1.032. Colour code: purple: phosphorous, red: oxygen, and blue: metals (W, V).

Table 3. Found bond lengths vs. weighted sum of covalent radii of the obtained single-crystal structures. Values for compound HPV₅Mo were taken from Poller et al. [35].

Bond Type	Found Bond Length [Å]			Weighted Sum of Covalent Radii [Å]	
	NaPV ₂ W	NaPV ₅ W	HPV ₅ Mo	NaPV ₂ W	NaPV ₅ W
P1–O1	1.532	1.540	1.540	1.740	1.740
O1–M1,2	2.445	2.416	2.400	1.995	1.988
M1,2–O2,3,4	1.887	1.870	1.919	1.995	1.988
M1,2=O5,6	1.653	1.649	1.635	1.995	1.988

$BL = \frac{a(ro+rw)+b(ro+rv)}{a+b}$, with BL the weighted bond length, a and b the weighing factors, and r the covalent radii of the elements O, W, and V.

From Table S4 (Supplementary Materials) it is visible that the lattice parameters decrease with increasing substitution degree, due to the smaller size of V(V) in comparison to W(VI).

Table 3 verifies the trend that the bond lengths of NaPV₅W are shorter than those of NaPV₂W. By comparing the found bond lengths with those of the weighted sums of covalent radii, it is obvious that the found P–O bond length is shorter than the calculated value for the sum of the covalent radii, indicating a stronger nature of this bond. The four oxygen atoms coordinating the central phosphorus, link the phosphorus to the twelve metal atoms of the Keggin structure. This bond type is denoted O1–M1.2 in this work. As expected for a Keggin-type structure, the O1–M1.2 bond length is longer than the calculated values in Table S4, indicating a more coordinative bond nature [23]. The bond length of the M1,2–O2,3,4 bond, linking the metals together, is found to be minimally longer than the sum of the covalent radii. In contrast, the bond length M1,2=O5,6, proves to be significantly shortened, since this bond type is characterised by partial double bond character. A specific substitution pattern could not be identified in both structures, because the V(V) atoms are statistically distributed over the W(VI) positions. Therefore, the W(VI) positions were refined with a corresponding partial occupation by V(V), assuming a statistical distribution.

The solid-state structure of NaPV₅W was compared to our previous published structure of HPV₅Mo, in the work of Poller et al. [35]. This structure is also available in the CCDC database, with the deposition number: 2177881. By comparing the found bond lengths of this compound in Table S4, with those of NaPV₅W, it is obvious that the bond lengths of NaPV₅W tend to higher values, due to the larger ionic size of W(VI) in comparison to Mo(VI). Only, the M1,2–O2,3,4 bond length deviates from this trend.

Characterization of the POMs in aqueous solution was performed using NMR and UV-Vis spectroscopy. The behaviour of the phosphotungstates in aqueous solution was analysed by ³¹P- and ⁵¹V-NMR spectroscopy. For comparable pH conditions, the pH was adjusted to 1 using hydrochloric acid, additionally, approx. 10% of deuterated acetone was added, to enable the solvent lock. In our experience, the NMR spectra of the free acids HPV_xMo ($x = 1–6$) cannot be measured with deuterated water as the solvent. Due to the acidic free protons of the POM, the protons rapidly exchange against deuterium from D₂O, which causes the NMR lock to fail during the measurement.

Figures 6 and 7 show the ³¹P and ⁵¹V NMR spectra of the NaPV_xW POMs, with $x = 1$ to 6, and Figures 8 and 9 the ³¹P- and ⁵¹V-NMR spectra of a comparison between NaPV₂W, HPV₂W, and HPV₂Mo. Spectra of the POMs HPV_xMo, with $x = 1$ to 6, are shown in Figures S8 and S9, together with a ³¹P- and ⁵¹V-NMR comparison for the POMs NaPVW, HPVW, and HPVMo, in Figures S10 and S11 in the Supplementary Materials.

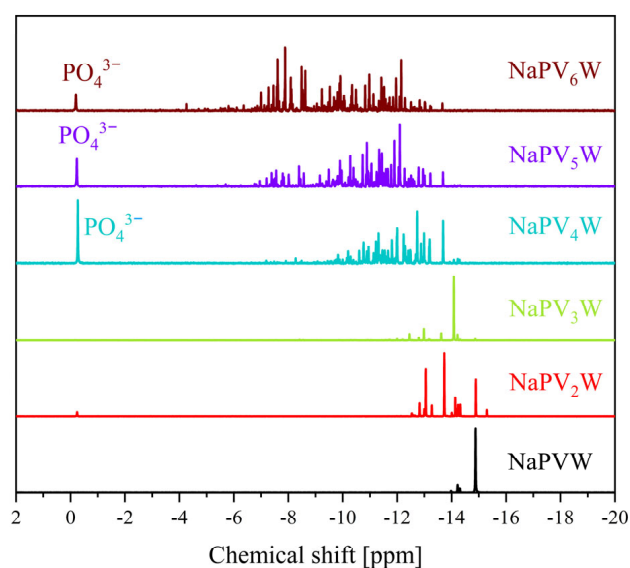


Figure 6. ³¹P-NMR spectra of the POMs NaPV_xW, with $x = 1$ to 6. All spectra were measured in a mixture of 70% water (pH 1) and 30% D₂O. Measurement frequency: 242.9 MHz; 85% H₃PO₄ was used as an external standard.

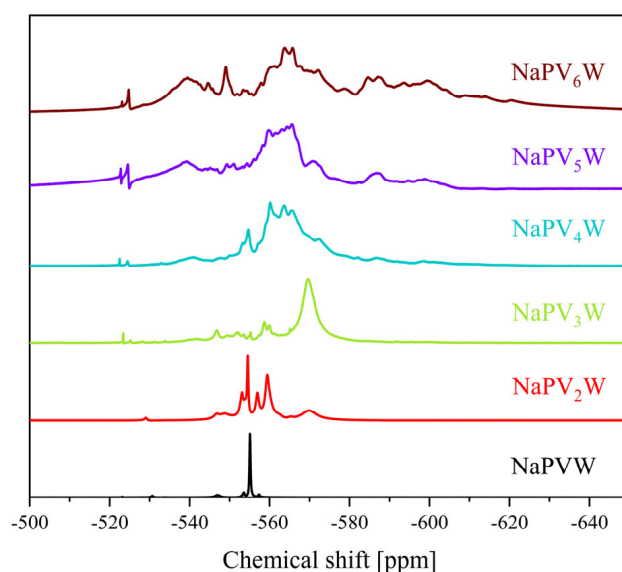


Figure 7. ^{51}V -NMR spectra of the POMs NaPV_xW , with $x = 1$ to 6. All spectra were measured in a mixture of 70% water (pH 1) and 30% D_2O . Measurement frequency: 157.8 MHz; NaVO_3 was used as an external standard.

All peaks for the V(V)-substituted POMs, appear in the ^{31}P -NMR spectra in the range between -5 and -2 ppm for HPV_xMo , and in the range between -15 and -6 ppm for NaPV_xW . This means that the phosphorus atom is significantly more shielded by the increased electron density of the tungstate atoms, compared to the molybdenum atoms. The intense peak around 0 ppm can be attributed to free phosphate, PO_4^{3-} , resulting from different, pH-dependent dissociation equilibria. In the ^{51}V -NMR spectra, the peaks appear in the range between -520 and -610 ppm. The difference in chemical shifts for HPV_xMo and NaPV_xW is not as significant as in the ^{31}P -NMR spectra. However, the ^{51}V chemical shifts for NaPV_xW also tend to lower values. The more V(V) substituted the tungstate, the more positive the ^{31}P chemical shifts tend to be, since the V(V) has significantly fewer electrons than the W(VI), resulting in a deshielding effect.

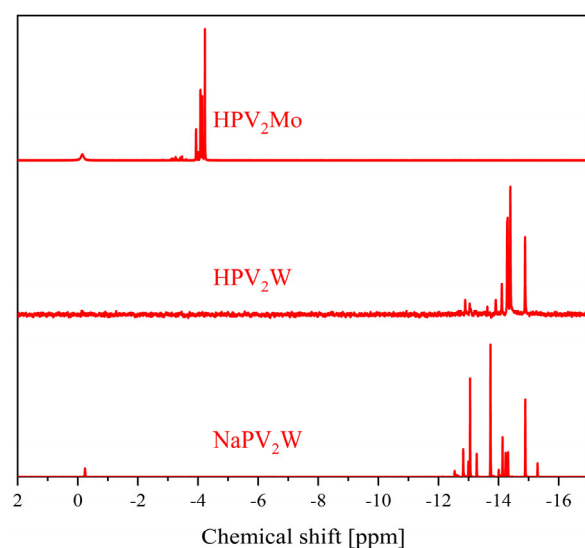


Figure 8. ^{31}P -NMR spectra of the POMs NaPV_2W , HPV_2W , and HPV_2Mo . Spectra for NaPV_2W and HPV_2W were measured in a mixture of 70% water (pH 1) and 30% D_2O , and spectra for HPV_2Mo were measured in a mixture of 90% water (pH 1) and 10% acetone- d_6 . Measurement frequency: 242.9 MHz; 85% H_3PO_4 was used as an external standard.

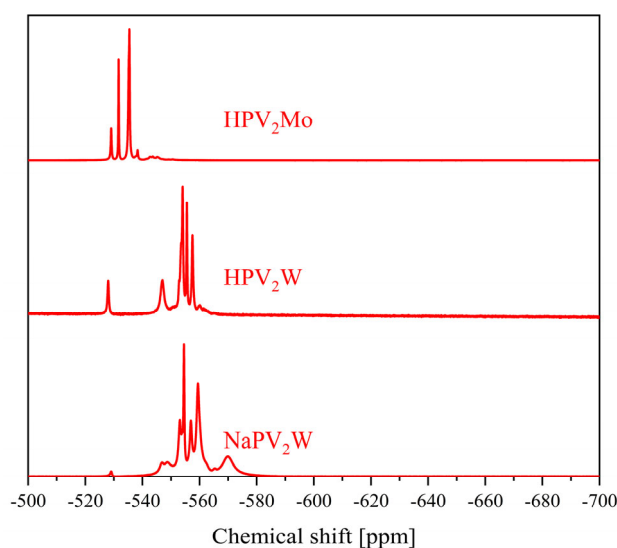


Figure 9. ^{51}V -NMR spectra of the POMs NaPV_2W , HPV_2W , and HPV_2Mo . Spectra for NaPV_2W and HPV_2W were measured in a mixture of 70% water (pH 1) and 30% D_2O , and spectra for HPV_2Mo were measured in a mixture of 90% water (pH 1) and 10% acetone- d_6 . Measurement frequency: 157.8 MHz; NaVO_3 was used as an external standard.

For the respective mono-substituted molybdates and tungstates, only one peak appears in both spectra: For the two-fold and higher substituted POMs, several signals appear in the ^{31}P - and ^{51}V -NMR spectra. This effect has already been discussed to a great extent in the literature for V(V), as well as Mn(II)/V(V)-substituted phosphomolybdates [23,36–38]. Once two framework metals are replaced by V(V), a total of five positional isomers are possible, so that a corresponding number of peaks can be identified in the NMR spectra. The more framework metals are replaced with V(V), the more positional isomers are possible, resulting in more NMR signals being observed. This trend is a result of there already being 27 position isomers for a substitution degree of $x = 4$, 38 for $x = 5$, and 48 for $x = 6$ [36]. This leads to an increase in the complexity of the NMR spectra. Therefore, it is easy to see that, especially for the more highly substituted molybdates and tungstates, with degrees of substitution of $x > 3$, multiple signals are found in the ^{31}P and ^{51}V data [37,38]. In particular, the ^{51}V -NMR shifts of the individual positional isomers are very similar, so that they merge into broad peaks, especially for the highly substituted analogues [23,36–38]. The positional isomers addressed, can be primarily assigned to α Keggin isomers: In addition to the positional isomerism, it must be considered that there are different structural isomer types of a Keggin structure, namely the α and the β type [39–41]. Two MO_6 octahedra can be connected by common edges and corners. The edge connection is the energetically less favourable variant, due to the increased Coulomb repulsion compared to the corner connection. Depending on which edges the octahedra share, the M–M–M angle can be 60, 90, 120, or 180°, with the 60° arrangement being energetically favoured. Thus, the arrangement of the four M_3O_{13} triads with the 60° M–M–M angle, with the octahedra linked by common corners, represents the geometry with the minimum Coulomb repulsion. This geometry is therefore also called the corresponding α isomer of the Keggin structure. The β isomer is obtained by rotating an M_3O_{13} triad by 60° of a three-fold axis of the α isomer, and represents the energetically less favourable isomer [39]. Even though the α isomer is energetically preferred, formation of the β isomer, along with corresponding β positional isomers, still occurs, increasing the complexity of the NMR spectra. However, the β Keggin isomers play a minor role compared to the α isomers, due to their higher instability, so that β isomer peaks are mainly expressed by low intensity signals in the NMR spectra. This can explain the peaks with low intensities, especially in the ^{31}P -NMR spectra. Thus, the lower intensity peak at ~ -14 ppm in the ^{31}P -NMR for NaPVW , can be assigned

to a β isomer of the Keggin structure, while the high intensity peak at -15.3 ppm, belongs to the corresponding α isomer [37,38,42].

For all POM species, different dissociation equilibria are found in aqueous acidic media [23]. This means that the complexity of the spectra is further increased, in addition to the positional and structural isomer (α/β) peaks.

It is known from the previous state of the literature, that the stability of the Keggin-type structures decreases with an increasing degree of substitution, which means that the maximum of substitution is the half of all framework metals ($x = 6$) [20–22]. Although the representatives with the degree of substitution $x = 6$ are sufficiently stable for many applications, the observed trend means only that Keggin structures with a degree of substitution of $x > 6$ are not synthetically accessible using our presented methods. Possible reasons for this observation are, the increasing anionic charge and basicity, since hexavalent metals are replaced by pentavalent ones. The anionic charge of the scaffold, on the other hand, always remains constant, due to the 40 oxygen atoms in oxidation state -II, which means that the total charge of the final Keggin anions must increase with increasing x . At some point, an anionic charge is exceeded (for $x = 6$, the anionic charge is 9), from which a POM anion can no longer be stabilised, since too much anionic charge meets too little surface or volume in a defined size of a Keggin-type cluster. In the ^{31}P - and ^{51}V -NMR spectra, this is reflected in the trend that, in addition to the isomer peaks, more dissociation peaks occur for higher x . Thus, the species with $x = 1$ also have only one peak each in the respective NMR spectra, since the dissociation in solution takes place only to a minor extent, due to the comparatively high POM stability. More than five peaks are already found for $x = 2$, suggesting an increased dissociation tendency. Thus, the more highly substituted POMs, especially those with $x > 3$, no longer have only 27, 38, or 48 signals, so the spectra show an increasing number of dissociation signals. Thus, the trend is also reflected in the increasingly complex NMR spectra in aqueous solution [36].

The extent of dissociation is strongly dependent on the pH value of the solution. A dissociation of the POM can take place, with the release of pervanadyl cations VO_2^+ and the corresponding lacunary species, according to $[\text{PV}_x\text{M}_{12-x}\text{O}_{40}]^{(3+x)-} \rightarrow n \text{VO}_2^+ + [\text{PV}_{x-n}\text{M}_{12-x}\text{O}_{40}]^{(3+x+n5)-}$ [43]. The formation of lower or higher substituted analogues has also been discussed in the literature, according to $2 [\text{PV}_x\text{M}_{12-x}\text{O}_{40}]^{(3+x)-} \rightarrow [\text{PV}_{x+1}\text{M}_{11-x-1}\text{O}_{40}]^{(3+x+1)-} + [\text{PV}_{x-1}\text{M}_{12-x+1}\text{O}_{40}]^{(3+x-1)-}$ [23,43]. Thus, the dissociation equilibria also contribute to the fact that different NMR signals can be observed. For example, a VO_2^+ cation is visible in the ^{51}V -NMR spectra, with a broad peak around -545 ppm [23,43]. Overall, this means that the POM solution contains a statistical mixture of differently substituted species. E.g., a sample of HPVMo would show a statistical distribution between HPMo/HPVMo/HPV₂Mo.

A comparison of the ^{31}P data between HPMo and HPW, is shown in Figure S12, Supplementary Materials. Here, the trend becomes visible that the ^{31}P peak of HPW appears at lower chemical shifts. As expected, only one signal is observed for both POMs. Table 4 shows an overview of the different chemical shifts of all of the POMs investigated in this work.

Table 4. ^{31}P and ^{51}V chemical shifts of the POMs investigated in this work.

Substitution Degree	Molybdates		Tungstates	
	^{31}P Shift [ppm]	^{51}V Shift [ppm]	^{31}P Shift [ppm]	^{51}V Shift [ppm]
0	-3.75	-	-15.3	-
1	-4.22	-531.6	-14.9	-555.1
2	-3.94, -4.00, -4.08, -4.14, -4.23	-529.0, -531.7, -535.4, -538.3	-12.8 to -14.9	-538.5 to -578.8

Table 4. Cont.

Substitution Degree	Molybdates		Tungstates	
	³¹ P Shift [ppm]	⁵¹ V Shift [ppm]	³¹ P Shift [ppm]	⁵¹ V Shift [ppm]
3	−3.15 to −3.64 and −3.98 to −4.23	−526.4, −531.6, −534.0, −534.7, −537.2, −540.2 to −549.7	−11.6 to −15.0	−519.5 to −589.7
4	−2.47 to −4.24	−531.2 to −554.4	−9.1 to −14.5	−519.0 to −623.6
5	−1.00 to −4.25	−490.0 to −610.0	−6.4 to −14.2	−519.0 to −617.9
6	−1.50 to −4.50	−500.0 to −590.0	−6.6 to −14.2	−520.2 to −640.8

In order to obtain deeper insights into the properties of the POMs in solution, UV-Vis measurements were carried out. Table 5 shows a list of the observed peaks, which have been attributed to the ligand-to-metal charge transfer (LMCT) bands of the POMs [23,44–48]. The corresponding spectra are shown in Figures S13–S17 in the Supplementary Materials. For the V(V)-substituted POMs, two LMCT bands appear in the UV-Vis spectrum: an LMCT band for the Mo(VI)/W(VI) at shorter wavelengths, and a band for V(V) at longer wavelengths. For the V(V) phosphomolybdates, it is known that the LMCT bands of Mo(VI) and V(V) have a shoulder towards higher wavelengths. The band at shorter wavelengths is assigned to the LMCT of $M = O_t$ (transition from the terminal oxygen atom to the metal), and the band causing the shoulder can be assigned to the LMCT of $M-O_b/M-O_c$ (transition from the bridging oxygen atoms to the metal) [23,47,48]. Figures S13 and S14 in the Supplementary Materials show a plot of the corresponding LMCT wavelength positions against the POMs, for the $NaPV_xW$ and HPV_xMo , with $x = 1$ to 6. For the $NaPV_xW$ POMs, only the LMCT of W(VI) can be clearly identified at wavelengths above the LMCT bands of Mo(VI). The LMCT band of V(V) on the other side cannot be identified in the spectra, for the degrees of substitution $x = 1$ to 3, even at elevated concentrations. Only at substitution degrees $x > 3$, can the LMCT for V(V) be observed, as an extremely broad band to which no clear peak maximum can be assigned. Thus, the spectra of the tungstates clearly differ from those of the molybdates. The peak positions of the LMCTs in Table 5 and Figures S13 and S14, clearly show the LMCTs for Mo(VI) in the range of 211 to 218 nm, while the LMCTs for W(VI) are in the range of 234 to 260 nm [26]. In general, the LMCT bands for W(VI) are shifted to higher wavelengths in comparison to Mo(VI), which indicates a smaller HOMO–LUMO gap in the tungstates. The LMCT bands for V(V) in the molybdates are found above 300 nm, in the range of 304 to 309 nm, in the case of the tungstates, the $O \rightarrow V(V)$ LMCT bands are very broad, in the range of 330 to 400 nm, which makes it impossible to determine the exact maximum. For the three LMCT λ bands, the following trend can be concluded: $\lambda_{Mo(VI)} < \lambda_{W(VI)} < \lambda_{V(V)}$.

Table 5. Peak positions of the LMCT determined for the molybdates and tungstates.

POM/LMCT	$O \rightarrow M(VI)$ ($M = Mo, W$)	$O \rightarrow V(V)$
HPMo	214.0	-
HPW	255.5	-
HPVMo	211.5	308.5
HPV ₂ Mo	214.5	308.0
HPV ₃ Mo	215.0	305.0
HPV ₄ Mo	218.0	304.0
HPV ₅ Mo	217.0	308.0

Table 5. Cont.

POM/LMCT	O → M(VI) (M = Mo, W)	O → V(V)
HPV ₆ Mo	217.0	308.0
NaPVW	260.0	*
NaPV ₂ W	242.0	*
NaPV ₃ W	250.0	*
NaPV ₄ W	240.0	*
NaPV ₅ W	235.0	*
NaPV ₆ W	234.0	*

* For the tungstates, the LMCT for V(V) cannot be reliably determined because of the peak width.

By looking at the UV-Vis spectra of the molybdates and tungstates in Figures S15 and S16 (Supplementary Materials), it is noticeable that, at the same concentration measured, the intensities of the LMCT bands for Mo(VI)/W(VI) decrease with increasing degree of substitution, while the intensities of the bands for the LMCT V(V) increase with increasing degree of substitution. This observation correlates with the Mo(VI)/W(VI)/V(V) content in the POMs, and can therefore be interpreted as an indicator of successful substitution [23,47,48].

For both POMs HPMo and HPW, only one LMCT band is visible in the UV-Vis spectra (Figure S19, Supplementary Materials), assigned to the LMCT bands of Mo(VI) and W(VI).

The LMCT peak maxima were analysed according to the Beer-Lambert law, and the extinction coefficients, ϵ_λ , were determined for each LMCT wavelength (Equation (1), Supplementary Materials). For this purpose, stock solutions of the POMs were first prepared, at a concentration of 1 g/L, which were then diluted in a dilution series to five different concentrations, used to construct the calibration curve (Equation (2), Supplementary Materials). The slope of the linear function can then be used to calculate the extinction coefficient for a defined wavelength (Equations (3) and (4)), Supplementary Materials). In this way, knowing the previously determined calibration lines, the extinction coefficients were calculated, and are summarised in Table 6. Figure 10 shows a plot of the extinction coefficients against the degree of substitution, for the molybdates and tungstates. All calibration lines can be found in the Supplementary Materials in Figures S20–S37.

Table 6. Extinction coefficients, ϵ_λ , calculated for the different LMCT wavelengths.

Substitution Degree, x	HPV _{x} Mo		NaPV _{x} W
	Mo(V) [L mol ⁻¹ cm ⁻¹]	V(V) [L mol ⁻¹ cm ⁻¹]	W(VI) [L mol ⁻¹ cm ⁻¹]
1	88,247	18,705	36,532
2	88,289	21,140	33,402
3	74,813	17,004	37,975
4	66,427	16,526	41,484
5	81,571	20,115	46,798
6	76,012	18,094	39,371

For consideration of Figure 10, it is important to note that the extinction coefficients determined for the V(V) LMCT are from the molybdates data. For the tungstates, the extinction coefficient for the V(V) LMCT could not be calculated, because the wavelength of the LMCT maxima could not be accurately determined in this case. Discussing the results in Table 6 and Figure 10, it is striking that the extinction coefficients for the V(V) LMCT are in the range of $1.6\text{--}2.1 \times 10^4$ L mol⁻¹ cm⁻¹, while the extinction coefficients for the W(VI) LMCT are in the range of $3.3\text{--}4.6 \times 10^4$ L mol⁻¹ cm⁻¹. The extinction coefficients for the

Mo(VI) LMCT bands show the highest values, in the range of $6.6\text{--}8.8 \times 10^4 \text{ L mol}^{-1} \text{ cm}^{-1}$. So, the following trend can be concluded: $\epsilon_{\lambda}^{\text{V(V)}} < \epsilon_{\lambda}^{\text{W(VI)}} < \epsilon_{\lambda}^{\text{Mo(VI)}}$.

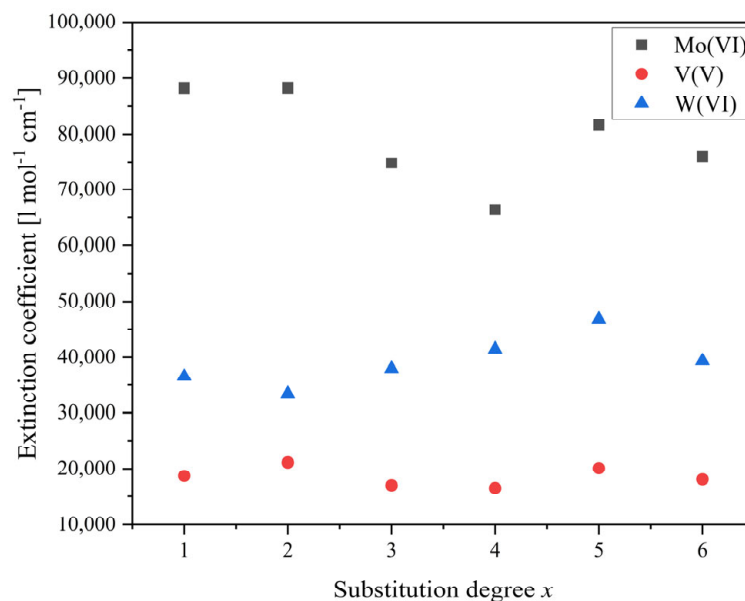


Figure 10. Plot of the extinction coefficients versus substitution degree.

The knowledge of the respective extinction coefficients proves to be particularly useful for different applications, e.g., in homogeneous catalysis. A problem with homogeneously based catalysts, is the difficult separation of the products from the product phase and the complete removal of the catalyst. Thus, by knowing the extinction coefficient, conclusions can be drawn about the remaining residual concentration of the POM in the purified product phases, using photometry. This conclusion can also be applied with regard to bio-based applications. Here, too, a photometric determination of the concentration of the POM can help to make a study successful.

Figures 11 and 12 show pictures of the different molybdate and tungstate solutions (concentration 1 g/L), with increasing degree of substitution from left to right. The higher the substitution degree, the more intense is the red colour of the POM solution, starting from yellow ($x = 1$) up to red ($x = 6$).

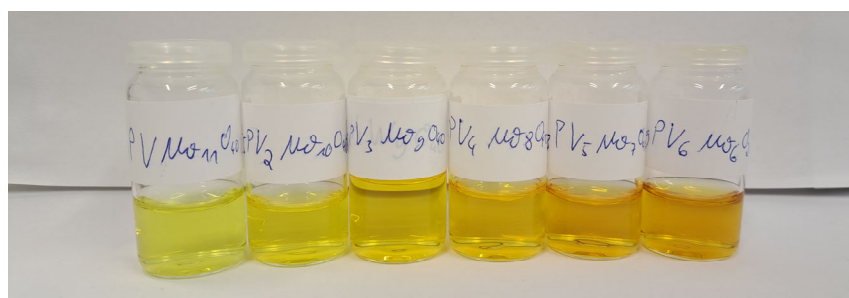


Figure 11. Solutions (1 g/L) of the different V(V)-substituted molybdates, with increasing degree of substitution from left to right, $x = 1\text{--}6$.

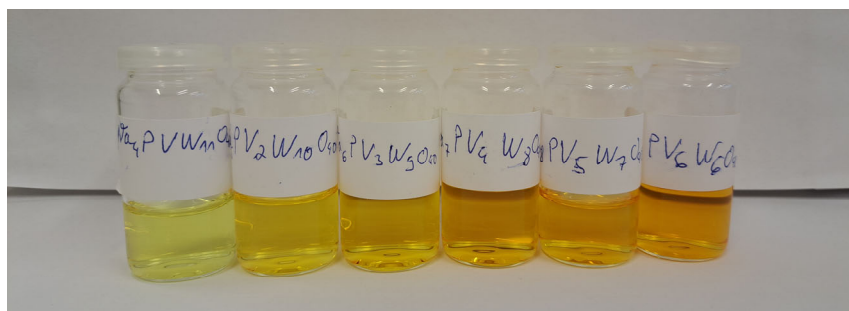


Figure 12. Solutions (1 g/L) of the different V(V)-substituted tungstates, with increasing degree of substitution from left to right, $x = 1-6$.

The redox potentials of the molybdates and tungstates were measured using CV and SWV. Our method worked at a pH of 1, which was previously adjusted with hydrochloric acid. This corresponds to a hydrogen ion concentration of 0.1 mol/L. The analyte concentration was 1 mmol/L. Thus, a ratio of electrolyte to analyte of 100:1 was used. All CV data can be found in the Supplementary Materials in Figures S38–S46, together with a tabular overview of the peak potential maxima, minima, and mean values from the CV data, and the maxima from the SWV data (Table S1, Supplementary Materials). The resolution of the CV data remains poor, since the various peak potentials partially overlap, especially for the molybdates. Figures 13 and 14 show the SWV data of the POMs NaPV_xW , with $x = 1$ to 6, and a comparison between the POMs NaPV_2W , HPV_2W , and HPV_2Mo . SWV data of the POMs HPV_xMo , with $x = 1$ to 6, and a comparison between the POMs NaPVW , HPVW , and HPVMo , are available in the Supplementary Materials, in Figures S42–S44.

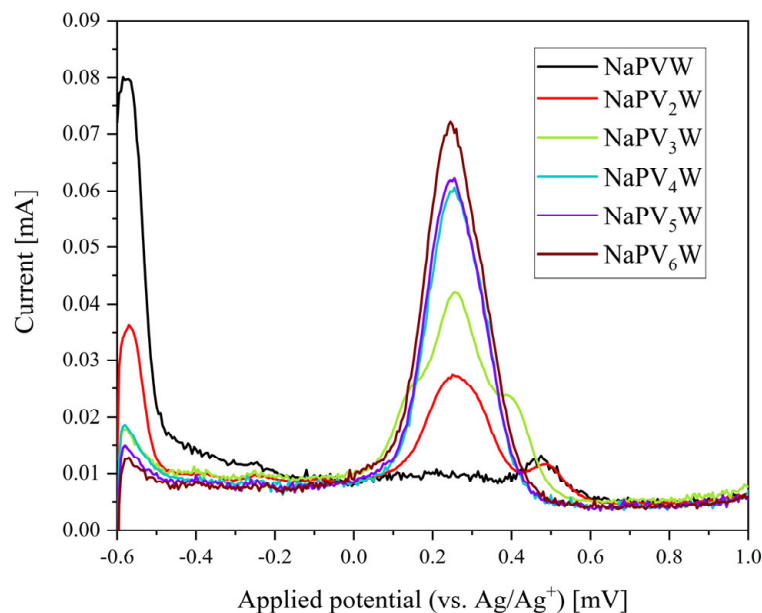


Figure 13. SWV data of the POMs NaPV_xW , with $x = 1$ to 6 (concentration 1 mmol/L, scan rate 5 mV and pH 1 (HCl as supporting electrolyte)).

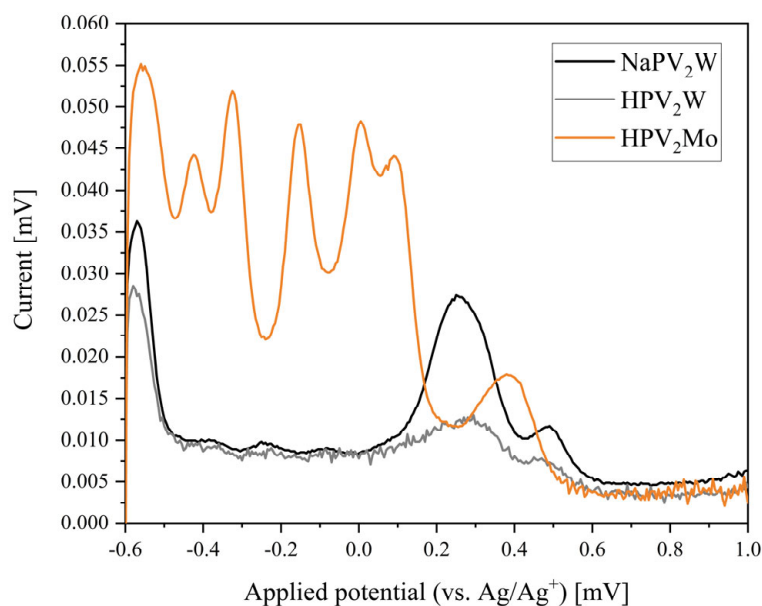


Figure 14. SWV data of the POMs NaPV₂W, HPV₂W, and HPV₂Mo (concentration 1 mmol/L, scan rate 5 mV and pH 1 (HCl as supporting electrolyte)).

The different redox behaviour of the tungstates in comparison to the molybdates, is already visible by comparing the CV and SWV data of the unsubstituted HPMo and HPW, in Figures S45 and S46. In the SWV data (Figure S46), six redox processes are observed for HPMo, whereas only two redox processes were detected for HPW.

Similarly, when comparing the CV and SWV data of the molybdates and tungstates (Figure 13 and Figure S38–S43), the molybdates generally show seven to eight redox processes, while only two to three redox processes are observed for the tungstates. This means that the redox chemistry of the tungstates is limited compared to the molybdates. In the SWV data of the substituted tungstates (Figure 13), mainly a broad peak potential in the range between 100 and 400 mV is recognizable, whose intensity increases with increasing degree of substitution. It is known from the literature, that the peak potentials of the molybdates are the result of numerous two-electron redox reactions, while for the tungstates mainly one-electron redox reactions are observed [23,26,49–51]. The substitution of the molybdate or tungstate framework with V(V), changes the entire electronic structure of the POM, which also changes the electrochemical potentials [23]. This observation is particularly evident for the substituted molybdates. The electrochemical process observed for the POMs HPV_xMo ($x = 1$ to 3) at ~70 mV, likely originates from the VO₂⁺ cation dissociating from the POM structure in the aqueous acidic media [23,43]. Especially noteworthy, is the shift of this potential to higher voltages, depending on the degree of substitution, starting from 70 mV for HPVMo, over 90 mV for HPV₂Mo, to 95 mV for HPV₃Mo (Figure S42, Supplementary Materials). Starting from a degree of substitution of $x = 4$, this peak eventually merges with the peak in the range between –200 and –100 mV and 0 to 200 mV. This results in a broad signal in the range between –200 and 200 mV, in which the individual electrochemical potential for the VO₂⁺ cation can no longer be identified (Figure S43, Supplementary Materials). In general, the other potentials of the substituted molybdates are also subject to a shift, with a trend toward shifting maxima (see Figure S42, Supplementary Materials) to larger potential values, particularly for the potentials below –400 mV. Thus, the V(V) substitution can be seen here as a tool for selective tailoring of the redox activity of a POM to a desired application [23]. This is particularly evident from the fact that, very low redox activity of the POM is observed in the case of the V(V)-substituted tungstates.

The electrochemical results suggest a significantly lower redox activity of the tungstates. It can therefore be concluded that for further redox applications (in catalysis or in biomedicine),

V(V)-substituted molybdates should be preferred instead of tungstates, since their redox activity is much more pronounced.

3. Materials and Methods

3.1. Chemicals

All chemicals used were purchased from common suppliers of research chemicals. A detailed list is provided in the Supplementary Materials.

3.2. Experimental

Detailed descriptions and additional data can be found in the Supplementary Materials.

3.3. Synthesis of $H_{3+x}[PV_xMo_{12-x}O_{40}]$, according to Odyakov et al. [20–22]

Step 1:

Molybdenum trioxide was suspended in deionised water and a 25% phosphoric acid solution in water was added. It was heated to reflux, wherein a clear yellow solution was formed.

Step 2:

Parallel to step 1, divanadium pentoxide was suspended in water and cooled to 0 °C. While stirring, a 30% hydrogen peroxide solution in water was added dropwise. Thereby, the divanadium pentoxide began to dissolve in the form of a red/brown solution and the release of oxygen gas was observed. After the divanadium pentoxide was completely dissolved, a 25% phosphoric acid solution in water was added to the batch, and stirred at room temperature.

The vanadium solution from step 2 was added dropwise to the refluxing molybdenum solution from step 1. It was further refluxed for 60 min and then cooled to room temperature. The solution was filtered and concentrated under reduced pressure. A red or dark brown solid was obtained.

3.4. Synthesis of $Na_{9-x}H_x[PW_9O_{34}]$, according to Domaille et al. [29]

The lacunary species $Na_{9-x}H_x[PW_9O_{34}]$, was synthesised according to Domaille et al. [29], starting from sodium tungstate dihydrate and phosphoric acid.

Sodium tungstate dihydrate was dissolved in deionised water and a 85% phosphoric acid solution in water was added. The final pH value was adjusted to 8.9. While stirring, glacial acetic acid was added dropwise, and during addition a colourless precipitate was formed. The pH changed to 7.4 after complete addition. After two hours of stirring, the colourless precipitate was removed by vacuum filtration and was dried in a desiccator for 24 h. The product was used without further purification. A colourless solid was obtained.

3.5. Synthesis of $Na_{3+x}[PV_xW_{12-x}O_{40}]$, with $x = 1$ to 3, according to Domaille et al. [29]

Compounds $Na_{3+x}[PV_xW_{12-x}O_{40}]$, with $x = 1$ to 3, were synthesised according to modified procedures of Domaille et al. [29], starting from commercially available HPW or the lacunary compound $Na_{9-x}H_x[PW_9O_{34}] \cdot x H_2O$.

$$x = 1$$

Phosphotungstic acid was dissolved in deionised water. The pH value of this solution was 0.5 and was adjusted to 4.8 by addition of small portions of sodium carbonate. In parallel, sodium metavanadate was dissolved in deionised water at 80 °C and added to the previous $[PW_{11}O_{39}]^{7-}$ solution. The pH value of the combined reaction mixture was adjusted to 2.0, by adding a 2 M hydrochloric acid solution in water, and then heated up to 60 °C. After cooling to room temperature, the pH value was 3.5, and was readjusted to 2.0 using a 2 M hydrochloric acid solution in water. The solution was then reheated to 60 °C. This procedure was repeated once, until upon cooling down to room temperature

the pH value remained stable around 2.0. Finally, the solution was filtered and desalinated by nanofiltration. A yellow solid was obtained.

$$x = 2 \text{ and } 3$$

Sodium acetate was dissolved in deionised water (30 mL), and after dissolution, acetic acid was added, until the pH value of the solution reached 4.8. In the next step, sodium metavanadate and sodium tungstate dihydrate were added, and after dissolution, $\text{Na}_{9-x}\text{H}_x[\text{PW}_9\text{O}_{34}] \cdot x \text{H}_2\text{O}$ was added and stirred for 48 h. The colour changed to dark red. It was filtered and the solution was desalinated by nanofiltration. An orange/red solid was obtained.

3.6. Synthesis of $\text{Na}_y\text{H}_z[\text{PV}_x\text{W}_{12-x}\text{O}_{40}]$, with $x = 4$ to 6 , via Self-Assembly, Based on the Procedure of Odyakov et al. [20–22]

Sodium metavanadate was dissolved in deionised water, at a temperature of 60 °C. Parallel to this step, sodium tungstate dihydrate was dissolved in deionised water, and an 85% solution of phosphoric acid in water was added. The solution was boiled and the aqueous sodium metavanadate solution was added dropwise. After the addition, the solution turned light brown and the final pH value was 7.5, which was adjusted to 1.5 using a 2 M hydrochloric acid solution in water. The dark brown solution was refluxed for 60 min. After cooling to room temperature, the solution was filtered and desalinated by nanofiltration. An intense red coloured solid was obtained.

3.7. Nanofiltration

Nanofiltration for removing the salts was performed using the setup developed by Esser et al. [52].

3.8. Etherate Method

The sodium salt NaPV_xW , was dissolved in deionised water, and a hydrochloric acid solution in water was added. In a separation funnel, the acidified solution was mixed with diethyl ether. Upon separation of the phases, a third new, oily, and heavy phase, with an intense colour, was formed at the bottom. The POM ether phase was separated. New acid fractions were added to the aqueous phase and the process was repeated until formation of the third, heavy phase was no longer observed. The combined POM ether phases were dried under reduced pressure, to yield a solid product (Figure S49, Supplementary Materials).

4. Conclusions

In summary, we have successfully synthesised a series of vanadium(V)-substituted phosphomolybdates (HPV_xMo) and phosphotungstates (NaPV_xW), with substitution degrees (x) of up to 6. All the molybdates are known in the literature, but especially the higher substituted tungstates ($x > 3$) have not been discussed and analysed in the literature yet in such detail. The molybdates were prepared using a self-assembly approach. Tungstates with $x = 1$ to 3 were synthesised using a lacunary approach, and tungstates with $x = 4$ to 6 were prepared using a self-assembly route. In order to obtain the respective free acids, acidic, aqueous solutions of the sodium salts of the tungstates were treated with diethyl ether, with the goal of extracting the protonated tungstates. However, this route is progressively limited by low yields and significant losses of the substitution metals, and is therefore not applicable to tungstates with higher V content.

We have comprehensively characterised the V-substituted Keggin POMs and compared the spectroscopic and electrochemical properties of the molybdates and tungstates NaPV_xW , with $x = 1$ to 6. Comparing the IR and Raman spectra, we found that the vibrational bands of the tungstates are shifted to higher wavenumbers in comparison to the molybdates, due to the higher mass of tungsten. The higher mass difference between W(VI) and V(V), in comparison to Mo(VI) and V(V), leads to the property that different P–O vibrational bands are observed in the IR spectra for the tungstates.

From the NMR spectroscopic investigations, we concluded that both the ^{31}P and ^{51}V signals of the tungstates are observed at significantly lower chemical shifts than the signals of the molybdates. We attribute this effect to the increased shielding effect of tungsten, caused by its higher electron density. With increasing degree of substitution with V(V), the ^{31}P signals of the tungstates appear at more positive values. This effect is attributed to the deshielding effect of the V(V). For both the molybdates and the tungstates, significantly more signals are observed with increasing degree of substitution, as more positional isomers are possible.

By applying UV-Vis spectroscopy, we found the following trend for the LMCT energies: $\lambda_{\text{Mo(VI)}} < \lambda_{\text{W(VI)}} < \lambda_{\text{V(V)}}$. For the extinction coefficients, the trend seems to be $\epsilon_{\lambda}^{\text{V(V)}} < \epsilon_{\lambda}^{\text{W(VI)}} < \epsilon_{\lambda}^{\text{Mo(VI)}}$. The higher the degree of substitution, the more significant is the intensity decrease in the Mo(VI)/W(VI) LMCT bands and the more intense becomes the V(V) LMCT band. This trend can also be seen as an indicator for successful substitution.

Finally, the electrochemical properties of the POMs were determined, using CV and SWV measurements. Significantly more redox processes were detected for the molybdates than for the corresponding tungstates. Therefore, the tungstates appear to be much less redox active than the molybdates. For the molybdates, there is a shift in the redox peak potentials depending on the degree of substitution. The results show that, the redox potentials of the POMs can be tuned by changing the framework metal and degree of substitution with an additional foreign element, such as V(V).

Together, the trends from the analytical data show that for subsequent applications of the POMs (e.g., in homogeneous catalysis) substituted molybdates should be used rather than tungstates, since molybdates, in contrast to tungstates, have a richer redox chemistry. In addition, the synthetic route for the molybdates allows the POMs to be isolated as heteropolyacids, providing bifunctionality (both redox and Brønsted acid sites) for catalytic applications. Generating tungstates as free acids is only possible to a very limited extent using our presented extraction method.

We were able to show, using our NMR spectra, that the POM stability decreases with an increasing degree of substitution, which is expressed by the observation of various dissociation peaks. This circumstance can be attributed to the increased anionic charge density of the POMs. However, all our POMs proved to be sufficiently stable during our investigations. Therefore, in the search for specific applications, both in catalysis and in biomedicine, higher substituted POM representatives can be used without limitations.

Overall, this report on the synthesis and spectroscopic, as well as electrochemical, properties, provides a solid foundation for further research on the application of V-substituted phosphomolybdates and -tungstates in catalysis or the biomedical field.

Supplementary Materials: The following supporting information can be downloaded at: <https://www.mdpi.com/article/10.3390/inorganics11040138/s1>, UV-Vis, NMR, Infrared and Raman Spectra of all compounds, as well as experimental and crystallographic details. References [53–60] are cited in the supplementary materials.

Author Contributions: J.-C.R.: investigation, writing (initial draft), visualisation; J.A.C.: investigation; J.A.: funding acquisition, resources, writing (review and editing); M.J.P.: conceptualisation, project administration, supervision, writing (review and editing). All authors have read and agreed to the published version of the manuscript.

Funding: We thank the Hansestadt Hamburg for financially supporting José Aceituno Cruz with the Degree Completion Grant for International Students provided through the University of Hamburg. This research received no further external funding; the APC has been waived by MDPI.

Data Availability Statement: Data is provided in the Supplementary Materials, Crystallographic information files (.cif) are available through the joint Cambridge Crystallographic Data Centre and Fachinformationszentrum Karlsruhe Access Structures service under the deposition numbers 2240685 (NaPV₂W) and 2240686 (NaPV₅W).

Acknowledgments: The authors gratefully thank the Fraunhofer-Zentrum für Angewandte Nanotechnologie CAN for performing thermogravimetric analysis, and the research group of Peter Burger, especially Thomas Marx, for the opportunity to measure CV and SWV. We also thank the elemental analysis service department led by Dirk Eifler for analysing our numerous POM samples.

Conflicts of Interest: The authors declare no conflict of interest.

References

1. Reichert, J.; Brunner, B.; Jess, A.; Wasserscheid, P.; Albert, J. Biomass oxidation to formic acid in aqueous media using polyoxometalate catalysts—Boosting FA selectivity by in-situ extraction. *Energy Environ. Sci.* **2015**, *8*, 2985–2990. [[CrossRef](#)]
2. Maerten, S.; Kumpidit, C.; Voß, D.; Bukowski, A.; Wasserscheid, P.; Albert, J. Glucose oxidation to formic acid and methyl formate in perfect selectivity. *Green Chem.* **2020**, *22*, 4311–4320. [[CrossRef](#)]
3. Albert, J.; Wasserscheid, P. Expanding the scope of biogenic substrates for the selective production of formic acid from water-insoluble and wet waste biomass. *Green Chem.* **2015**, *17*, 5164–5171. [[CrossRef](#)]
4. Veith, H.; Voges, M.; Held, C.; Albert, J. Measuring and Predicting the Extraction Behavior of Biogenic Formic Acid in Biphasic Aqueous/Organic Reaction Mixtures. *ACS Omega* **2017**, *2*, 8982–8989. [[CrossRef](#)]
5. Albert, J.; Lüders, D.; Bösmann, A.; Guldi, D.M.; Wasserscheid, P. Spectroscopic and electrochemical characterization of heteropoly acids for their optimized application in selective biomass oxidation to formic acid. *Green Chem.* **2014**, *16*, 226–237. [[CrossRef](#)]
6. Claußnitzer, J.; Bertleff, B.; Korth, W.; Albert, J.; Wasserscheid, P.; Jess, A. Kinetics of Triphase Extractive Oxidative Desulfurization of Benzothiophene with Molecular Oxygen Catalyzed by HPA-5. *Chem. Eng. Technol.* **2020**, *43*, 465–475. [[CrossRef](#)]
7. Bertleff, B.; Claußnitzer, J.; Korth, W.; Wasserscheid, P.; Jess, A.; Albert, J. Catalyst Activation and Influence of the Oil Matrix on Extractive Oxidative Desulfurization Using Aqueous Polyoxometalate Solutions and Molecular Oxygen. *Energy Fuels* **2018**, *32*, 8683–8688. [[CrossRef](#)]
8. Bertleff, B.; Goebel, R.; Claußnitzer, J.; Korth, W.; Skiborowski, M.; Wasserscheid, P.; Jess, A.; Albert, J. Investigations on Catalyst Stability and Product Isolation in the Extractive Oxidative Desulfurization of Fuels Using Polyoxometalates and Molecular Oxygen. *ChemCatChem* **2018**, *10*, 4602–4609. [[CrossRef](#)]
9. Bertleff, B.; Claußnitzer, J.; Korth, W.; Wasserscheid, P.; Jess, A.; Albert, J. Extraction Coupled Oxidative Desulfurization of Fuels to Sulfate and Water-Soluble Sulfur Compounds Using Polyoxometalate Catalysts and Molecular Oxygen. *ACS Sustain. Chem. Eng.* **2017**, *5*, 4110–4118. [[CrossRef](#)]
10. Gumerova, N.I.; Al-Sayed, E.; Krivosudský, L.; Ćipčić-Paljetak, H.; Verbanac, D.; Rompel, A. Antibacterial activity of polyoxometalates against *Moraxella catarrhalis*. *Front. Chem.* **2018**, *6*, 336. [[CrossRef](#)]
11. Bijelic, A.; Aureliano, M.; Rompel, A. The antibacterial activity of polyoxometalates: Structures, antibiotic effects and future perspectives. *Chem. Commun.* **2018**, *54*, 1153–1169. [[CrossRef](#)]
12. Colović, M.B.; Lacković, M.; Lalatović, J.; Mougharbel, A.S.; Kortz, U.; Krstić, D.Z. Polyoxometalates in Biomedicine: Update and Overview. *Curr. Med. Chem.* **2019**, *27*, 362–379. [[CrossRef](#)]
13. Shigeta, S.; Mori, S.; Kodama, E.; Kodama, J.; Takahashi, K.; Yamase, T. Broad spectrum anti-RNA virus activities of titanium and vanadium substituted polyoxotungstates. *Antiviral Res.* **2003**, *58*, 265–271. [[CrossRef](#)]
14. Yamase, T. Anti-tumor, -viral, and -bacterial activities of polyoxometalates for realizing an inorganic drug. *J. Mater. Chem.* **2005**, *15*, 4773. [[CrossRef](#)]
15. Tajima, Y.; Nagasawa, Z.; Tadano, J. A Factor Found in Aged Tungstate Solution Enhanced the Antibacterial Effect of β -Lactams on Methicillin-Resistant *Staphylococcus aureus*. *Microbiol. Immunol.* **1993**, *37*, 695–703. [[CrossRef](#)] [[PubMed](#)]
16. Shigeta, S.; Mori, S.; Yamase, T.; Yamamoto, N.; Yamamoto, N. Anti-RNA virus activity of polyoxometalates. *Biomed. Pharmacother.* **2006**, *60*, 211–219. [[CrossRef](#)] [[PubMed](#)]
17. Chen, L.; San, K.A.; Turo, M.J.; Gembicky, M.; Fereidouni, S.; Kalaj, M.; Schimpf, A.M. Tunable Metal Oxide Frameworks via Coordination Assembly of Preyssler-Type Molecular Clusters. *J. Am. Chem. Soc.* **2019**, *141*, 20261–20268. [[CrossRef](#)] [[PubMed](#)]
18. Chen, L.; Turo, M.J.; Gembicky, M.; Reinicke, R.A.; Schimpf, A.M. Cation-Controlled Assembly of Polyoxotungstate-Based Coordination Networks. *Angew. Chem. Int. Ed.* **2020**, *59*, 16609–16615. [[CrossRef](#)]
19. Long, D.-L.; Burkholder, E.; Cronin, L. Polyoxometalate clusters, nanostructures and materials: From self assembly to designer materials and devices. *Chem. Soc. Rev.* **2007**, *36*, 105–121. [[CrossRef](#)]
20. Odyakov, V.F.; Zhizhina, E.G.; Maksimovskaya, R.I. Synthesis of molybdovanadophosphoric heteropoly acid solutions having modified composition. *Appl. Catal. A Gen.* **2008**, *342*, 126–130. [[CrossRef](#)]
21. Odyakov, V.F.; Zhizhina, E.G. New process for preparing aqueous solutions of Mo-V-phosphoric heteropoly acids. *Russ. J. Inorg. Chem.* **2009**, *54*, 361–367. [[CrossRef](#)]
22. Odyakov, V.F.; Zhizhina, E.G. A novel method of the synthesis of molybdovanadophosphoric heteropoly acid solutions. *React. Kinet. Catal. Lett.* **2008**, *95*, 21–28. [[CrossRef](#)]
23. Raabe, J.-C.; Albert, J.; Poller, M.J. Spectroscopic, Crystallographic, and Electrochemical Study of Different Manganese(II)-Substituted Keggin-Type Phosphomolybdates. *Chem.-A Eur. J.* **2022**, *28*, e202201084. [[CrossRef](#)]

24. Abbessi, M.; Contant, R.; Thouvenot, R.; Hervé, G. Dawson Type Heteropolyanions. 1. Multinuclear (^{31}P , ^{51}V , ^{183}W) NMR Structural Investigations of Octadeca(molybdotungstovanado)diphosphates α -1,2,3-[$\text{P}_2\text{MM}'_2\text{W}_{15}\text{O}_{62}$] $^{n-}$ (M, M' = Mo, V, W): Syntheses of New Related Compounds. *Inorg. Chem.* **1991**, *30*, 1695–1702. [[CrossRef](#)]
25. Patel, A.; Narkhede, N.; Singh, S.; Pathan, S. Keggin-type lacunary and transition metal substituted polyoxometalates as heterogeneous catalysts: A recent progress. *Catal. Rev.* **2016**, *58*, 337–370. [[CrossRef](#)]
26. Himeno, S.; Takamoto, M.; Ueda, T. Synthesis, characterisation and voltammetric study of a β -Keggin-type [$\text{PW}_{12}\text{O}_{40}$] $^{3-}$ complex. *J. Electroanal. Chem.* **1999**, *465*, 129–135. [[CrossRef](#)]
27. Knoth, W.H.; Domaille, P.J.; Farlee, R.D. Anions of the type $(\text{RMOH}_2)_3\text{W}_{18}\text{P}_2\text{O}_{68}^{9-}$ and $[\text{H}_2\text{OC}_3\text{O}]_3\text{W}_{18}\text{P}_2\text{O}_{68}^{12-}$. A reinvestigation of “B β ”- $\text{W}_9\text{PO}_{34}^{9-}$. *Organometallics* **1985**, *4*, 62–68. [[CrossRef](#)]
28. Massart, R.; Contant, R.; Fruchart, J.M.; Ciabrini, J.P.; Fournier, M. Phosphorus-31 NMR studies on molybdc and tungstic heteropolyanions. Correlation between structure and chemical shift. *Inorg. Chem.* **1977**, *16*, 2916–2921. [[CrossRef](#)]
29. Domaille, P.J.; Watunya, G. Synthesis and tungsten-183 NMR characterization of vanadium-substituted polyoxometalates based on B-type tungstophosphate $\text{PW}_9\text{O}_{34}^{9-}$ -precursors. *Inorg. Chem.* **1986**, *25*, 1239–1242. [[CrossRef](#)]
30. Ginsberg, A.P. (Ed.) Vanadium (V) substituted dodecatungstophosphates. In *Inorganic Synthesis*; John Wiley & Sons, Ltd.: Hoboken, NJ, USA, 1990; Volume 27.
31. Tsigdinos, G.A.; Hallada, C.J. Molybdovanadophosphoric Acids and Their Salts. I. Investigation of Methods of Preparation and Characterization. *Inorg. Chem.* **1968**, *7*, 437–441. [[CrossRef](#)]
32. Bridgeman, A.J. Computational Study of the Vibrational Spectra of α - and β -Keggin Polyoxometalates. *Chem.-A Eur. J.* **2004**, *10*, 2935–2941. [[CrossRef](#)] [[PubMed](#)]
33. Lee, J.K.; Melsheimer, J.; Berndt, S.; Mestl, G.; Schlögl, R.; Köhler, K. Transient responses of the local electronic and geometric structures of vanado-molybdo-phosphate catalysts $\text{H}_{3+n}\text{PV}_n\text{Mo}_{12-n}\text{O}_{40}$ in selective oxidation. *Appl. Catal. A Gen.* **2001**, *214*, 125–148. [[CrossRef](#)]
34. Xu, M.X.; Lin, S.; Xu, L.-M.; Zhen, S.-L. Crystal structure and properties of $\text{H}_3[\text{PMo}_{12}\text{O}_{40}] \cdot 3 \text{C}_2\text{H}_6\text{O}$. *Transit. Met. Chem.* **2004**, *29*, 332–335. [[CrossRef](#)]
35. Poller, M.J.; Bönisch, S.; Bertleff, B.; Raabe, J.; Göring, A.; Albert, J. Elucidating activating and deactivating effects of carboxylic acids on polyoxometalate-catalysed three-phase liquid-liquid-gas reactions. *Chem. Eng. Sci.* **2022**, *264*, 118143. [[CrossRef](#)]
36. Pope, M.T.; Scully, T.F. Geometrical Isomerism Arising from Partial Substitution of Metal Atoms in Isopoly and Heteropoly Complexes. Possibilities for the Keggin Structure. *Inorg. Chem.* **1975**, *14*, 953–954. [[CrossRef](#)]
37. Pettersson, L.; Andersson, I.; Grate, J.H.; Selling, A. Multicomponent Poly-anions. 46. Characterization of the Isomeric Keggin Decamolybdodivanadophosphate Ions In Aqueous Solution by ^{31}P and ^{51}V NMR. *Inorg. Chem.* **1994**, *33*, 982–993. [[CrossRef](#)]
38. Selling, A.; Andersson, I.; Grate, J.H.; Pettersson, L. A Potentiometric and (^{31}P , ^{51}V) NMR Study of the Aqueous Molybdovanadophosphate System. *Eur. J. Inorg. Chem.* **2000**, *2000*, 1509–1521. [[CrossRef](#)]
39. Weinstock, I.A.; Cowan, J.J.; Barbuzzi, E.M.G.; Zeng, H.; Hill, C.L. Equilibria between α and β Isomers of Keggin Heteropolytungstates. *J. Am. Chem. Soc.* **1999**, *121*, 4608–4617. [[CrossRef](#)]
40. Sundaram, K.M.; Neiwert, W.A.; Hill, C.L.; Weinstock, I.A. Relative Energies of α and β Isomers of Keggin Dodecatungstogallate. *Inorg. Chem.* **2006**, *45*, 958–960. [[CrossRef](#)]
41. Neiwert, W.A.; Cowan, J.J.; Hardcastle, K.I.; Hill, C.L.; Weinstock, I.A. Stability and Structure in α - and β -Keggin Heteropolytungstates, $[\text{X}^{n+}\text{W}_{12}\text{O}_{40}]^{(8-n)-}$, X = p-Block Cation. *Inorg. Chem.* **2002**, *41*, 6950–6952. [[CrossRef](#)]
42. Himeno, S.; Takamoto, M.; Ueda, T. Formation of α - and β -Keggin-Type [$\text{PW}_{12}\text{O}_{40}$] $^{3-}$ Complexes in Aqueous Media. *Bull. Chem. Soc. Jpn.* **2005**, *78*, 1463–1468. [[CrossRef](#)]
43. Evtuguin, D.V.; Neto, C.P.; Rocha, J.; de Jesus, J.D.P. Oxidative delignification in the presence of molybdovanadophosphate heteropolyanions: Mechanism and kinetic studies. *Appl. Catal. A Gen.* **1998**, *167*, 123–139. [[CrossRef](#)]
44. Barteau, K.P.; Lyons, J.E.; Song, I.K.; Barteau, M.A. UV-visible spectroscopy as a probe of heteropolyacid redox properties: Application to liquid phase oxidations. *Top. Catal.* **2006**, *41*, 55–62. [[CrossRef](#)]
45. Song, I.K.; Kim, H.S.; Chun, M.S. On the reduction potential of cation-exchanged heteropolyacids (HPAs). *Korean J. Chem. Eng.* **2003**, *20*, 844–849. [[CrossRef](#)]
46. Yamase, T. Photo- and electrochromism of polyoxometalates and related materials. *Chem. Rev.* **1998**, *98*, 307–325. [[CrossRef](#)]
47. Salavati, H.; Rasouli, N. Synthesis and characterization of supported heteropolymolybdate nanoparticles between silicate layers of Bentonite with enhanced catalytic activity for epoxidation of alkenes. *Mater. Res. Bull.* **2011**, *46*, 1853–1859. [[CrossRef](#)]
48. Raj, N.K.K.; Ramaswamy, A.V.; Manikandan, P. Oxidation of norbornene over vanadium-substituted phosphomolybdic acid catalysts and spectroscopic investigations. *J. Mol. Catal. A Chem.* **2005**, *227*, 37–45. [[CrossRef](#)]
49. Sadakane, M.; Steckhan, E. Electrochemical Properties of Polyoxometalates as Electrocatalysts. *Chem. Rev.* **1998**, *98*, 219–238. [[CrossRef](#)]
50. Hwang, D.Y.; Ha, Y.S.; Kim, S. Electrode-Assisted Wacker Process: Phosphomolybdate-Mediated Oxidation of 1-Butene to Methyl Ethyl Ketone. *Bull. Korean Chem. Soc.* **2001**, *22*, 441–442.
51. Ueda, T. Electrochemistry of Polyoxometalates: From Fundamental Aspects to Applications. *ChemElectroChem* **2018**, *5*, 823–838. [[CrossRef](#)]

52. Esser, T.; Huber, M.; Voß, D.; Albert, J. Development of an efficient downstream process for product separation and catalyst recycling of a homogeneous polyoxometalate catalyst by means of nanofiltration membranes and design of experiments. *Chem. Eng. Res. Des.* **2022**, *185*, 37–50. [CrossRef]
53. Dolomanov, O.V.; Bourhis, L.J.; Gildea, R.J.; Howard, J.A.; Puschmann, H. OLEX2: A complete structure solution, refinement and analysis program. *J. Appl. Crystallogr.* **2009**, *42*, 339–341. [CrossRef]
54. SHELX. Available online: <https://www.noah-itn.eu/wp-content/uploads/2019/03/shelx-manual.pdf> (accessed on 22 February 2023).
55. Sheldrick, G.M. A short history of SHELX. *Acta Crystallogr. Sec. A: Found. Crystallogr.* **2008**, *64*, 112–122. [CrossRef]
56. User Guide to Crystal Structure Refinement with SHELXL. 2008.
57. Hübschle, C.B.; Sheldrick, G.M.; Dittrich, B. ShelXle: A Qt graphical user interface for SHELXL. *J. Appl. Crystallogr.* **2011**, *44*, 1281–1284. [CrossRef] [PubMed]
58. Available online: <https://digital-library.theiet.org/content/journals/10.1049/esn.1987.0025?fmt=text> (accessed on 22 February 2023).
59. Spek, A.L.J. Single-crystal structure validation with the program PLATON. *J. Appl. Crystallogr.* **2003**, *36*, 7–13. [CrossRef]
60. Spek, A.L. PLATON SQUEEZE: A tool for the calculation of the disordered solvent contribution to the calculated structure factors. *Acta Crystallogr. Sec. C: Struct. Chem.* **2015**, *71*, 9–18. [CrossRef] [PubMed]

Disclaimer/Publisher’s Note: The statements, opinions and data contained in all publications are solely those of the individual author(s) and contributor(s) and not of MDPI and/or the editor(s). MDPI and/or the editor(s) disclaim responsibility for any injury to people or property resulting from any ideas, methods, instructions or products referred to in the content.

5.4 Synthese und Anwendung Co(II) substituierter Keggin-Phosphormolybdatstrukturen in der homogenkatalysierten Hydroformylierung

P4

Synthesis and Characterization of Co(II) Substituted Keggin-Type Polyoxometalates as Novel Catalysts for the Hydroformylation of 1-Hexene in a Thermomorphic Solvent System

Jan-Christian Raabe, Lea Hombach, Maximilian J. Poller, Alberto Collauto, Maxie M. Roessler, Andreas Vorholt, Anna Katharina Beine, Jakob Albert

Raabe, J.-C.; Hombach, L.; Poller, M. J.; Collauto, A.; Roessler, M. M.; Vorholt, A.; Beine, A. K.; Albert, J. Synthesis and Characterization of Co(II) Substituted Keggin-Type Polyoxometalates as Novel Catalysts for the Hydroformylation of 1-Hexene in a Thermomorphic Solvent System. *ChemCatChem* **2024**, e202400395. <https://doi.org/10.1002/cctc.202400395>.

Eine Reihe Co(II) substituierter POMs auf Basis des Phosphormolybdates mit Substitutionsgraden $x = 1$ bis 3 wurde synthetisiert, mit dem Zweck diese in der homogenkatalysierten HyFo einzusetzen (P4, *ChemCatChem* **2024**, e202400395).^[249] Die POMs wurden dabei nach einem *self-assembly* Ansatz synthetisiert. Es zeigte sich, dass ein maximaler Substitutionsgrad von drei erreicht werden konnte. Höhere Stöchiometrien an Co(II) führten zur Präzipitation eines violettfarbenden Feststoffes, der als Cobalt-(II)-molybdat CoMoO_4 identifiziert werden konnte.^[249]

Die HyFo-Experimente wurden an 1-Hexen zu *n-iso*-Heptanal in einem thermomorphen TMS-System aus Wasser und 1-Butanol durchgeführt und sind nach bestem Wissen und Gewissen das erste Beispiel für TMSPOMs, die als HyFo Katalysatoren eingesetzt wurden. Es konnte eine Ausbeute an Heptanal von 46 % erreicht werden. HyFo-Experimente mit HPCo_3Mo führten zur Zersetzung des TMSPOMs, wodurch während der Reaktion CoMoO_4 präzipitierte. Für den POM HPCo_2Mo wurden Umsätze von bis zu 64 % und Ausbeuten der Aldehyde bis zu 19 % beobachtet, wobei das *n* zu *iso*-Verhältnis auf 3:1 bestimmt wurde. Die Katalysatorstabilität für HPCoMo und HPCo_2Mo ist durch *in-situ* Ramanspektroskopie verifiziert worden. Der Katalysator HPCo_2Mo wurde nach einem der katalytischen Experimente durch Abdampfen des Lösungsmittels zurückgewonnen. Mit der IR-Spektroskopie konnte im Vergleich des Materials vor und nach der Katalyse bestätigt werden, dass alle charakteristischen Schwingungsbanden der Keggin-Struktur weiterhin vorhanden waren. Durch ICP-OES-Messungen wurde die angestrebte Stöchiometrie P:Co:Mo von 1:2:10 verifiziert, woraus geschlossen werden konnte, dass während der Katalyse kein signifikantes Katalysator-*leaching* stattfand. Daher eignete sich der Katalysator HPCo_2Mo für weitere Optimierungsschritte. Bei 140 °C konnte der Alkenumsatz auf bis zu 95 % und die Aldehydausbeute auf bis zu 28 % gesteigert werden, wobei das *n* zu *iso*-Verhältnis von 3:1 weiterhin aufrechterhalten wurde. Temperaturen bzw. Drücke unter 130 °C bzw. 100 bar erwiesen sich als zu niedrig, um überhaupt Aldehyde in signifikanten Mengen zu bilden. In einem weiteren Optimierungsversuch bei dem das Synthesegasverhältnis CO zu H_2 auf 1:2 eingestellt wurde, konnte die *n*-Heptanal Ausbeute auf bis zu 46 % erhöht werden.^[249]

Die in P4 dargestellten Ergebnisse heben das Potential von Co(II) substituierten TMSPOMs hervor, insbesondere das von HPCo_2Mo , als vielversprechende HyFo-Katalysatoren für mittlere und länger-kettige Alkene zu fungieren. Die ersten Parameteroptimierungsversuche zeigten, dass durchaus noch Potential für weitere Optimierungsschritte vorhanden ist. Die im Rahmen

dieser Studie durchgeführten HyFo-Experimente mit Co(II) substituierten TMSPOMs, eröffnen einen neuen Zweig in der HyFo- und POM-Forschung, was das Interesse am Studium der Co(II) substituierten TMSPOMs steigert (Abbildung 23).^[249]

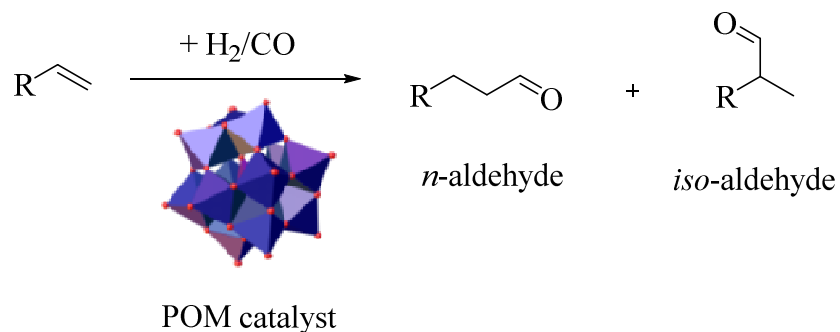


Abb. 23: Graphical abstract zu P4, *ChemCatChem* **2024**, e202400395: HyFo mit Co(II) substituierten Keggin-Phosphormolybdat-POMs.^[249]

Synthesis and Characterization of Co(II) Substituted Keggin-Type Polyoxometalates as Novel Catalysts for the Hydroformylation of 1-Hexene in a Thermomorphic Solvent System

Jan-Christian Raabe,^[a] Lea Hombach,^[b] Maximilian J. Poller,^[a] Alberto Collauto,^[c] Maxie M. Roessler,^[c] Andreas Vorholt,^[b] Anna Katharina Beine,^[b, d] and Jakob Albert^{*[a]}

Polyoxometalates (POMs) are a unique class of metal oxides, being of huge interest for the catalysis society. Co^{II}-substituted phosphomolybdate POMs (namely H₇[PCoMo₁₁O₄₀], H₁₁[PCo₂Mo₁₀O₄₀] and H₁₅[PCo₃Mo₉O₄₀]) have been successfully synthesized for the first time. The structure of the new Co^{II} substituted POMs was solved by single-crystal X-ray diffraction as well as vibrational (FT-IR and Raman) and nuclear magnetic/electron paramagnetic resonance (NMR and EPR) spectroscopy and found to be of the Keggin-type. The Co-POMs were then

applied as molecular catalysts for the hydroformylation of 1-hexene in a thermomorphic solvent mixture of water and 1-butanol. This is the very first example of a 1st row transition metal POM acting as a hydroformylation catalyst achieving 46% heptanal yield. The best results were obtained using H₁₁[PCo₂Mo₁₀O₄₀] as a catalyst at 140 °C, 150 bar CO/H₂ 1:2, and a reaction time of 4 h, paving the way for new POM-based catalysts in hydroformylation reactions.

Introduction

Polyoxometalates (POMs) are suitable catalysts for homogeneous RedOx or acid/base catalyzed reactions.^[1–3] POMs are prepared by selective substitution of one or more framework metals (e.g. Mo^{VI}) in the POM structure with RedOx active transition metals (e.g. V^V).^[4] In general, there are two possible synthesis strategies for transition-metal substituted POMs: the self-assembly process,^[5,6] in which the precursors are combined and reacted in the desired stoichiometry, and the lacunary approach.^[7–9] A lacunary structure is a POM defect structure with a defined number of vacancies (usually 1–3). The vacancies can be filled with foreign metals, regenerating the complete POM structure.^[7,10] The application of POMs in catalysis is

stimulated by their fascinating properties, including tunable acidity and RedOx properties, inherent resistance to oxidative composition, high thermal stability, as well as impressive sensitivity to light and electricity.^[11] The well-defined atomic connectivity of POMs provides the compositional diversity required by a rigorous assessment of the consequences of composition on catalytic reactivity.^[12] POMs have been used as homogeneous catalysts for a wide range of applications such as esterification, oxidation of biomass, desulfurization of fuels, delignification of wood or oxidative desulfurization processes.^[13–21]

One of the largest homogeneously catalyzed processes in the chemical industry today is hydroformylation. Here, olefins are converted to aldehydes using carbon monoxide and hydrogen. The first hydroformylation catalyst was the cobalt complex [HCo(CO)₄], which requires a high pressure system and a high partial pressure of CO to prevent reduction of the catalytically active Co^I-species.^[22,23] When a CO ligand is replaced by a phosphine ligand ([HCo(CO)₃(PR₃)]), the catalyst complex is stabilized by an electron donating effect of the alkylated phosphine, making reactions at lower pressure possible. The ligand unfortunately also decreases the complex activity so that higher temperatures are needed for a sufficient conversion.^[24] After these findings in the 1960s, research on Co-based hydroformylation catalysts dried up as Rh-based catalysts were found to be far more reactive. Nevertheless, the use of Co-catalysts is attractive, especially in terms of price, availability and sustainability, and so there has been some new research in this area in recent years.^[25–27] Cationic Co^{II} bisphosphine precursors were found to be highly stable in the hydroformylation of 1-hexene under comparably mild conditions (50 bar, 140 °C).^[25] Phosphine oxides were also found to be suitable ligands that enable Co-catalyzed hydroformylation under mild conditions.^[26] Even

[a] J.-C. Raabe, M. J. Poller, J. Albert
Institute of Technical and Macromolecular Chemistry, Hamburg University,
Bundesstr. 45, 20146 Hamburg, Germany
E-mail: Jakob.albert@uni-hamburg.de

[b] L. Hombach, A. Vorholt, A. K. Beine
Max Planck Institute for Chemical Energy Conversion, Stiftstraße 34–36,
45470 Mülheim an der Ruhr, Germany

[c] A. Collauto, M. M. Roessler
Department of Chemistry and Centre for Pulse EPR Spectroscopy, Imperial
College London, Molecular Sciences Research Hub, White City Campus,
London W12 0BZ, UK

[d] A. K. Beine
Department of Mechanical Engineering, University of Siegen, Paul-Bonatz-
Str. 9–11, Siegen 57076, Germany

Supporting information for this article is available on the WWW under
<https://doi.org/10.1002/cctc.202400395>

© 2024 The Authors. ChemCatChem published by Wiley-VCH GmbH. This is an open access article under the terms of the Creative Commons Attribution Non-Commercial NoDerivs License, which permits use and distribution in any medium, provided the original work is properly cited, the use is non-commercial and no modifications or adaptations are made.

unmodified $[\text{HCo}(\text{CO})_4]$ catalysts were further developed and numerous cobalt sources of various oxidation states were successfully applied as precursors for the active Co-carbonyl complex.^[27] To the best of our knowledge, Co-containing POMs have not yet been investigated as molecular catalysts in hydroformylation reactions.

In this study, we present three new Co^{II}-substituted phosphomolybdate POMs and show their potential as molecular catalysts for the hydroformylation of 1-hexene in a thermomorphic water/1-butanol reaction system.^[28]

Results and Discussion

Synthesis and Characterization of the Co-Substituted POM Catalysts

In this work, three different Co^{II}-substituted phosphomolybdate POM catalysts were synthesized according to our previously published self-assembly method.^[6] We could successfully expand this approach for the incorporation of Co^{II} into phosphomolybdic acid using Co^{II} acetate as a precursor.^[29] The synthesis of Co^{II}-substituted phosphomolybdates was chosen because the chemistry of transition-metal substituted phosphomolybdate structures is still widely unknown. Therefore, new compounds were synthesized in this work, which extend the spectrum of different transition-metal substituted POMs (TMSPOMs). On the other hand, Co^{II}-substituted phosphotungstate structures are only known in their fundamental features. For example, sandwich-like structures already exist that can be understood as dimers of the lacunary POM anions $[\text{PW}_9\text{O}_{34}]^{9-}$, in which four Co^{II} ions are linked coordinatively via the lacunary oxygen atoms. Such structures have already been successfully used as water oxidation catalysts.^[30] In detail, $\text{H}_7[\text{PCoMo}_{11}\text{O}_{40}]$ (HPCoMo), $\text{H}_{11}[\text{PCo}_2\text{Mo}_{10}\text{O}_{40}]$ (HPCo₂Mo) and $\text{H}_{15}[\text{PCo}_3\text{Mo}_9\text{O}_{40}]$ (HPCo₃Mo), could be successfully synthesized (for details see catalyst preparation section, ESI). The stoichiometry of the catalysts was verified using inductively-coupled plasma optical emission spectrometry (ICP-OES) and the crystal water amount was determined using thermogravimetric analysis (TGA) (Table 1).

Vibrational spectroscopy (ATR-FT-IR, Figure 1 and Raman spectroscopy, Figure 2) was used to verify the integrity of the Keggin-type structure. From the collected vibrational spectra, the Keggin-type structure could be verified for all three synthesized compounds (see Tables S1 and S2). As expected,

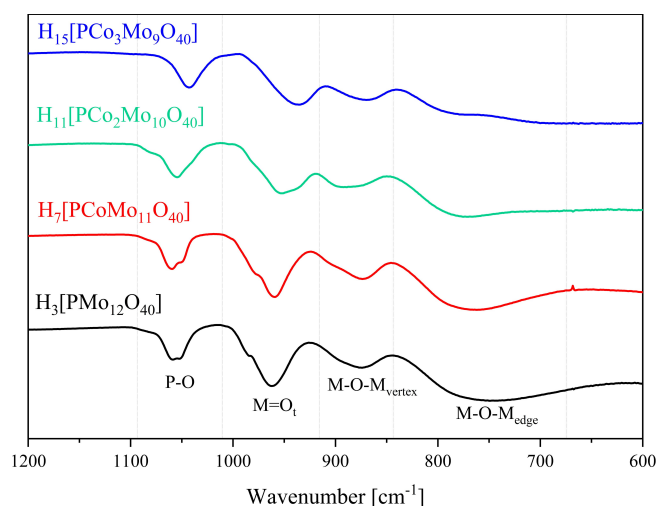


Figure 1. ATR-FT-IR spectra of the three synthesized POM compounds in comparison to HPMo.

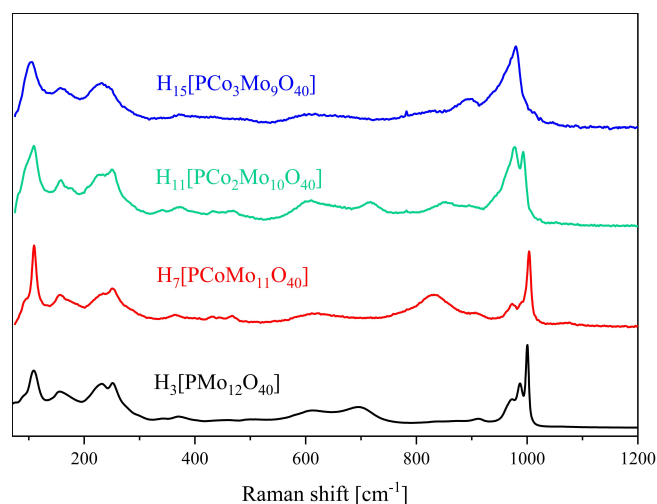


Figure 2. Raman spectra of the three different POM compounds in comparison with HPMo.

the ATR-FT-IR bands are shifted to lower wavenumbers with increasing substitution degree of Co^{II}. This is due to the fact that the corresponding vibration modes get excited more easily when the Mo^{VI} positions are substituted with a metal of significantly lower mass.^[31,32] The FT-IR data of HPCoMo can be

Table 1. Results of ICP-OES and TGA for the three synthesized Keggin-type POMs.

Compound	Targeted molecular composition	P/Co/Mo ratio ^a	Hydration water ^b [mol/mol-POM]
HPCoMo	$\text{H}_7[\text{PCoMo}_{11}\text{O}_{40}]$	0.972/1.03/11.0	8
HPCo ₂ Mo	$\text{H}_{11}[\text{PCo}_2\text{Mo}_{10}\text{O}_{40}]$	1.02/2.12/10.0	12
HPCo ₃ Mo	$\text{H}_{15}[\text{PCo}_3\text{Mo}_9\text{O}_{40}]$	0.955/2.81/9.00	16

HPCo_xMo is $\text{H}_{3+4x}[\text{PCo}_x\text{Mo}_{12-x}\text{O}_{40}]$
^aThe P/Co/Mo ratio was determined using ICP-OES. The data were normalized to the target Mo content. ^bThe content of hydration water was determined by TGA.

compared to those of the corresponding Co^{II} substituted phosphotungstate $\text{K}_3\text{H}_2[\text{PCoW}_{11}\text{O}_{40}]$.^[33] For the tungstate, the P-O band appears in two separate bands at 1076 and 1058 cm^{-1} . The $\text{M}=\text{O}_t$ band appears at 955 cm^{-1} , and the different M-O-M bands at 883 cm^{-1} , 802 cm^{-1} and one split band at 750 cm^{-1} resp. 711 cm^{-1} . The P-O and one of the M-O-M vibrational bands are partially shifted to higher wavenumbers due to the higher mass of W^{VI} compared to Mo^{VI} . This is also the reason why some of the bands are splitted, since the mass difference of W^{VI} to Co^{II} is larger than that of Mo^{VI} to Co^{II} . The significantly lower mass of Co^{II} also influences the energetic position for the excitation of the P-O vibration, so that one band appears at higher and the other at lower wavenumbers. The M-O-M bands at lower wavenumbers belong to those of the W-O-Co oscillations.^[33]

The integrity of the Keggin-type structure was also verified by single-crystal X-ray diffraction (s-XRD) for HPCoMo and HPCo_2Mo , respectively. Full crystallographic information files (.cif) can be found in the CCDC database with their corresponding deposition numbers 2195090 and 2195091. The solid-state structure of HPCo_2Mo is shown in Figure 3 (for the asymmetric unit, see Figure S1) whereas the structure of HPCoMo can be found in Figure S2 together with a short crystallographic discussion (Table S3).

The obtained crystallographic data for both POMs confirm the Keggin-type structure, with the phosphorous atom in a tetrahedral coordination of four oxygen atoms. All metal atoms are in an octahedral coordination of six oxygen atoms with a terminal oxo ligand terminating the structure. The MO_6 octahedrons are slightly distorted with an average bond angle of $\sim 102^\circ$. Therefore, the value determined for the bond angles deviates by 12° from the ideal octahedron angle of 90° . The

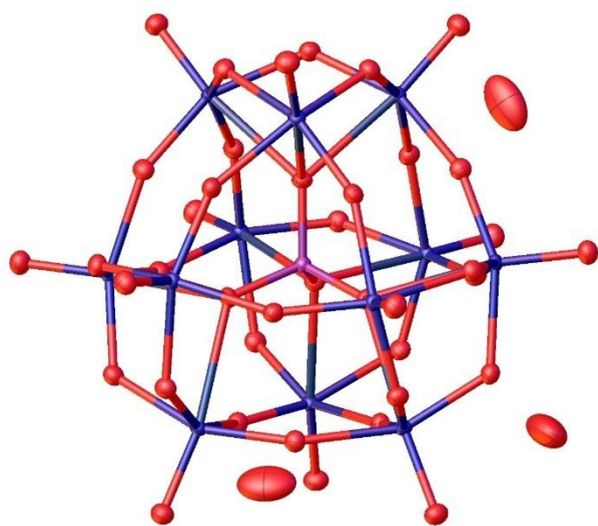


Figure 3. Solid-state structure of HPCo_2Mo as determined by s-XRD. Space group: $Fd\bar{3}m$ (70) (orthorhombic). R_1 : 1.32%, wR_2 : 3.80%, GooF : 1.176 and R_{int} : 3.39%. Thermal ellipsoids are drawn at 50% probability level. Color code: purple: phosphorous, red: oxygen, and blue: metals (Mo, Co). Full .cif file is available through the joint Cambridge Crystallographic Data Centre and Fachinformationszentrum Karlsruhe Access Structures service (deposition number: 2195091).

distortion of the PO_4 tetrahedrons was determined to be $\sim 109.4^\circ$ and thus agrees well with the ideal tetrahedron angle of 109.5° .^[6]

Furthermore, the behavior of the synthesized catalysts in solution was studied using ^{31}P -Nuclear Magnetic Resonance (NMR) spectroscopy (Figure 4 and Table S4).

Considering ^{31}P -NMR data of Co^{II} containing samples, it is necessary to note that Co^{II} is a paramagnetic species. Therefore, the peaks in the spectra become broader, indicating also a successful incorporation of the Co^{II} ion into the Keggin anion.^[32] The chemical shift of the compounds HPCoMo and HPCo_2Mo differ slightly of that from HPMo , but for both there is an additional peak with low intensity at around -3 ppm. This peak results from a dissociative, pH-dependent, and reversible process of those compounds in aqueous solution according to $[\text{PCo}_x\text{Mo}_{12-x}] \rightarrow [\text{PCo}_{x-m}\text{Mo}_{12-x}] + m \text{Co}^{2+}$.^[4,6,34,35] Those dissociation processes have been reported by Evtuguin *et al.*^[36] for V^{V} substituted phosphomolybdates where the POM dissociates according to $[\text{PV}_x\text{Mo}_{12-x}] \rightarrow [\text{PV}_{x-m}\text{Mo}_{12-x}] + m \text{VO}_2^+$. HPCo_3Mo shows a very different chemical shift compared to HPCoMo and HPCo_2Mo at -0.78 ppm. The NMR spectrum of HPCo_3Mo also shows evidence of dissociation to the lower substituted representatives HPCoMo and HPCo_2Mo . Similar dissociation equilibria were also described by Zhizhina *et al.*^[35] for Mo-V containing Keggin-type POMs.

The continuous wave electron paramagnetic resonance (CW-EPR) spectra of frozen solutions of both successfully synthesized POMs, HPCo_2Mo (Figure 5) and HPCoMo (Figure S3), are characteristic of high-spin Co^{II} ($S=3/2$) with a $M_S = \pm 1/2$ ground state. EPR signals could only be detected for temperatures below 40 K; at higher temperatures relaxation broadening sets in and leads to complete loss of the signal. The small rhombicity value ($E/D=0.07$) obtained from the simulation of

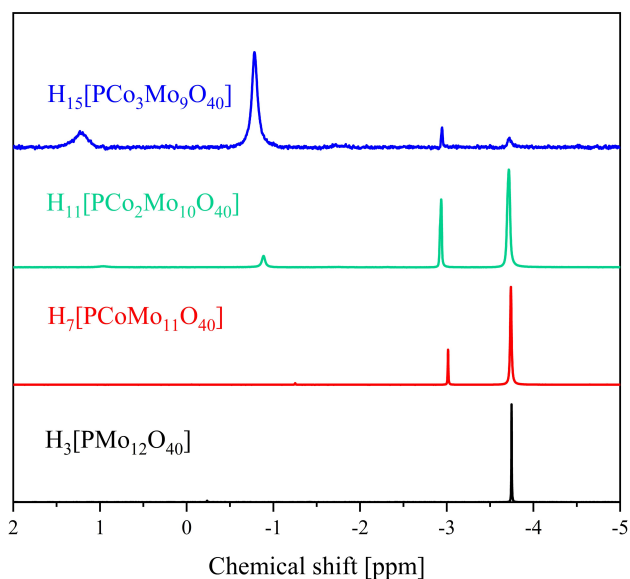


Figure 4. ^{31}P -NMR spectra of the three different compounds in comparison with HPMo . All spectra were measured in a mixture of 90% water (pH 1) and 10% acetone- d_6 . The spectra were measured at 242.9 MHz. 85% H_3PO_4 was used as external standard.

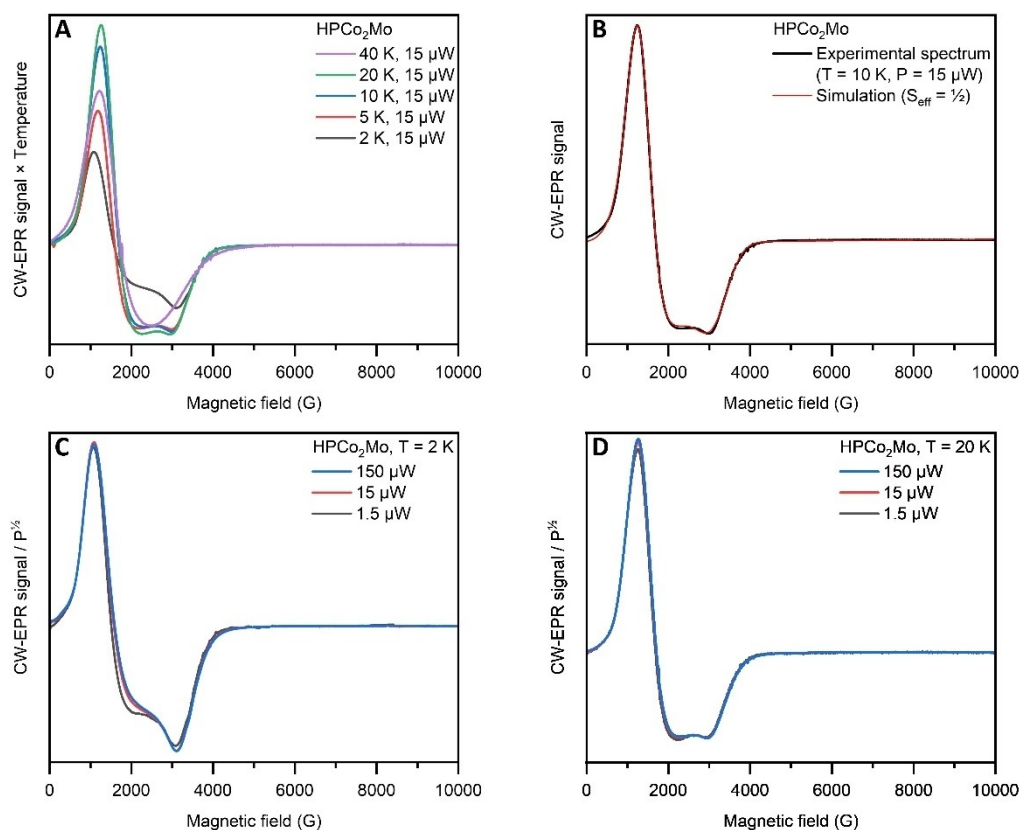


Figure 5. CW-EPR spectra of the HPCo₂Mo POM. **A:** temperature dependence of the spectra recorded under non-saturating conditions in the 2 K – 20 K range. **B:** simulation of the 10 K spectrum as a $S = 1/2$ effective spin system with g_{eff} values of 5.06 (g strain = 2.08), 4.17 (g strain = 3.46) and 2.26 (g strain = 0.64), corresponding to an $M_S = \pm 1/2$ ground state with $g_{\text{real}} = 2.31$ and $E/D = 0.07$ (see ESI 1.2 for further details). **C:** power saturation behavior at 2 K. **D:** power saturation behavior at 20 K.

the experimental spectra is consistent with a symmetric environment of the metal centers, characteristic of Keggin-type structures.^[37,38] Notably, no hyperfine splitting originating from the coupling of the unpaired electron spin with the ⁵⁹Co nuclear spin ($I = 7/2$, 100% natural abundance) could be resolved. This is attributed to the presence of a wide distribution of micro-heterogeneous structures, resulting in a sizeable g strain.^[38] Although the EPR spectra of the two POMs are similar, potential magnetic interactions occurring between the two Co^{II} centers in HPCo₂Mo may be invisible if the exchange coupling is large or masked by the broad lines.

Considering UV-Vis spectra of POMs it is already known that the HOMO-LUMO excitation is usually a Ligand-to-Metal-Charge-Transfer (LMCT) transition.^[39–44] For the Co^{II} substituted POMs there is only the O→Mo^{VI}O₆ LMCT visible. Co^{II} does not have a LMCT band, because Co^{II} is in d⁷-high spin configuration in which a transition between the d-orbitals is forbidden and there is no room for an LMCT.^[45]

All Mo^{VI} LMCT peaks in the UV-Vis spectra (Figure 6, Table S5) were analyzed according to Beer-Lambert's law and the extinction coefficients ϵ_λ were calculated (Figures S5 to S7 and Table S6). For catalytic applications, it is particularly useful to know the extinction coefficients for further process steps, for example when the catalyst has to be removed from the reaction

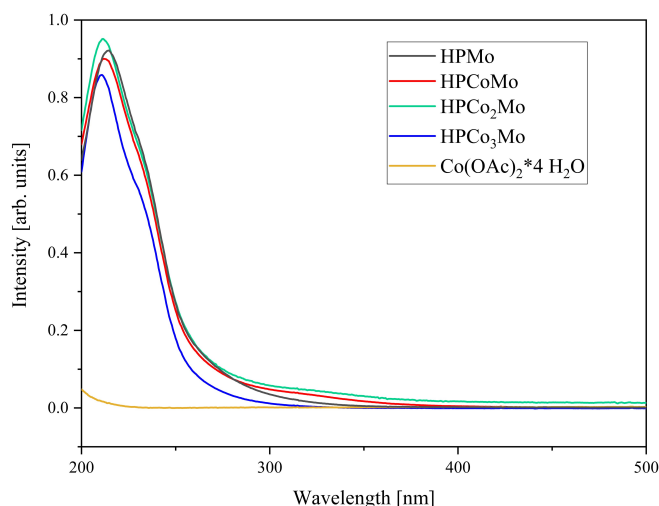


Figure 6. UV-Vis spectra of the three catalyst compounds in water in comparison with Co^{II} acetate tetrahydrate. There is only one LMCT band for Mo^{VI} with a shoulder to higher wavelengths.

mixture. Thus, a photometric determination of the residual catalyst concentration in the reaction mixture is possible.^[4]

To get further insights into the RedOx chemistry of those compounds, additional electrochemical measurements were performed.^[4,6,7,46–48] The three compounds were analyzed using

cyclic voltammetry (CV) and square wave voltammetry (SWV). Figure 7 shows a compilation of the SWV data of the three different Co-substituted phosphomolybdate POMs in comparison to the parent HPMo. Further CV data of the synthesized compounds in comparison with HPMo can be found in Figure S8. Additional data for the electrochemical measurements are summarized in Figures S9, S10 and Table S7. Moreover, reference data for Co^{II} acetate and HPMo are given in Figures S11 to S18. The SWV data in Figure 7 show that the RedOx potentials of the Co^{II} substituted POMs are shifted to higher potentials in comparison to HPMo. This observation is consistent with the previously reported trend that transition-metal substitution can selectively influence the RedOx potentials of the resulting POMs.^[6]

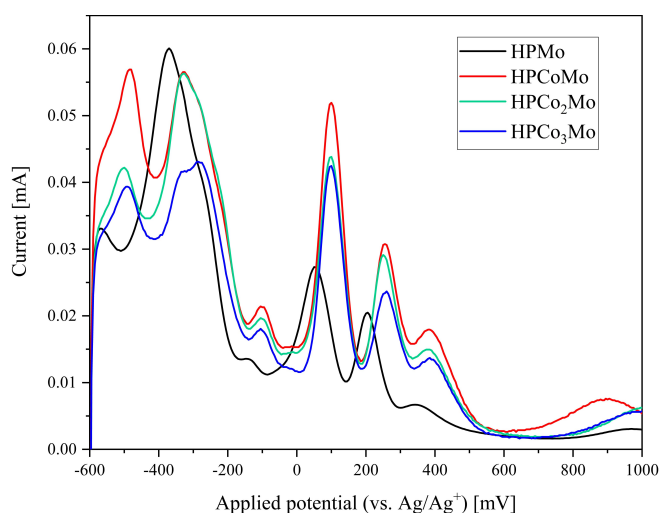


Figure 7. SWV measurements of all catalysts in comparison with HPMo using hydrochloric acid (pH 1) as supporting electrolyte (concentration 1 mmol/L, scan rate 100 mV/s).

Hydroformylation of 1-Hexene using the Synthesized Co-Substituted POM-Catalysts

The hydroformylation of 1-hexene to *n*-heptanal is an industrially important application for homogeneous Co-based catalysts and served as a model reaction to investigate the catalytic performance of Co-substituted phosphomolybdate POMs. Reactions were carried out in stainless steel autoclaves using 0.67 g of substrate and 1 mol% Co in a volumetric 1:1 mixture of 1-butanol and water. Typical conditions were $T=130^{\circ}\text{C}$, $p=150$ bar CO/H₂ (1/1) and a reaction time of 4 h (for details see Tables S9 and S10). The solvent system used belongs to the group of temperature dependent multi-component solvent (TMS) systems. At room temperature, the catalyst in the aqueous and the organic substrates in the organic 1-butanol phase form two separate phases. Under reaction conditions above 100 °C, the two phases combine to one homogeneous phase. After cooling down to room temperature, two separate phases are formed again, thus allowing facile catalyst recycling in future research.^[28] Comparing the three synthesized Co-containing POMs with the commercially available HPMo in the hydroformylation shows 1-hexene conversions between 19 and 63% (Table 2, entries 1–4). For HPCo₃Mo (entry 4) the isomerization of 1-hexene to 2- and 3-hexene is the only observed reaction taking place. During the reaction a purple precipitate was formed, which could be identified as Co^{II} molybdate by elemental analysis (see Table S8 and Figures S19 and S20). This indicates that HPCo₃Mo decomposed during the harsh reaction conditions which can be explained by its high substitution degree with Co^{II}, resulting in a high anionic charge of -15 and is also reflected by its low catalytic activity. For the unmodified HPMo (entry 1) and HPCoMo (entry 2) additionally small amounts of the desired *n*- and *iso*-heptanal were formed with an overall yield of 5%. The unsubstituted HPMo was commercially purchased and used as received (for details see ESI). X-ray fluorescence (XRF) measurements revealed impurities with 115 ppm of Co, explaining the observed blind activity. For the higher substituted HPCo₂Mo (entry 3) a significant increase both in conversion (up to 64%) as well as in the yield of aldehydes (up to 19%) was observed. An *n*:*iso* ratio of

Table 2. Catalyst screening of HPMo and the synthesized Co^{II} POMs in the hydroformylation of 1-hexene. Conditions: $m(1\text{-hexene})=0.673$ g, 1 mol% Co, $V(\text{H}_2\text{O}/\text{BuOH})=4$ mL, 130°C , 150 bar CO/H₂ (1:1), $t=4$ h.

#	catalyst	1 mol% [Co] 150 bar CO/H ₂ H ₂ O/BuOH, 130 °C, 4 h				S(heptanal) [%]
		X(1-hexene) [%]	Y(<i>n</i> -heptanal) [%]	Y(<i>iso</i> -heptanal) [%]	Y(isomers) [%]	
1 ^[a]	HPMo	36	3	2	16	14
2	HPMoCo	36	3	2	8	14
3	HPMoCo ₂	64	14	5	22	30
4	HPMoCo ₃	19	0	0	3	0
5	blank	2	0	0	0	–

[a] 1 mol% Mo.

approximately 3:1 was obtained as it is typically observed for Co due to its high isomerization activity.^[25] The higher catalytic activity of HPCo_2Mo can be explained by the two active Co centers, providing more coordination sites for the reactants. Theoretically, only terminal oxygen can be split-off from the neighbored Co-centers creating an active vacancy.^[14] Moreover, the electronic structure of the POM is influenced by the incorporation of one, two or three Co atoms which could alter the catalytic activity. Further mechanistic studies to elucidate the individual reaction steps should be carried out in the future. A blank experiment without catalyst (entry 5) did not yield any detectable products. The observed gap between yield and conversion in all reactions can be explained by the evaporation of the volatile substrate due to the reaction procedure. In the liquid phase, no peaks of unknown by-products appear in the GC chromatogram (see Figure S21).

The stability and integrity of the Keggin-structure of the low substituted POMs HPCoMo (Figure S22) and HPCo_2Mo before

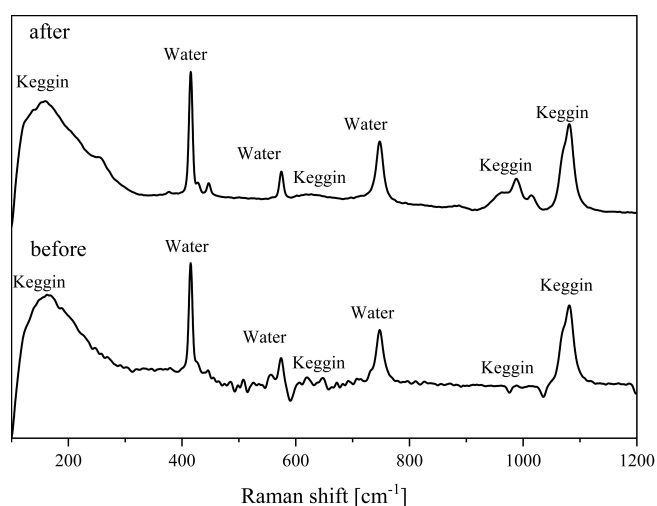


Figure 8. Raman spectroscopic data of HPCo_2Mo in aqueous solution before and after catalytic experiments.

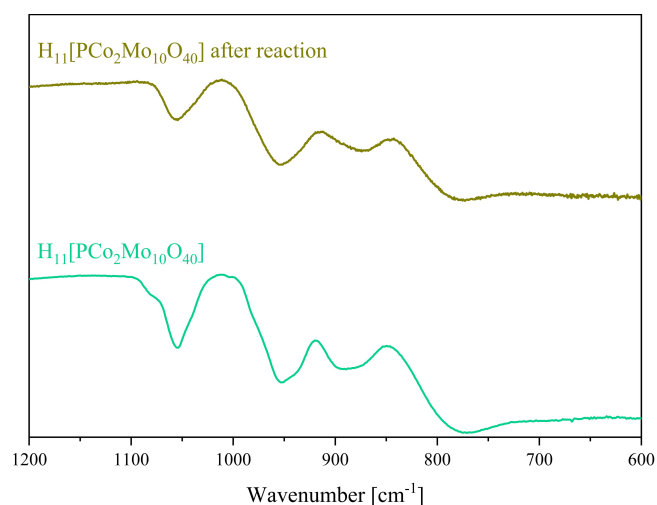


Figure 9. ATR-FT-IR spectra of HPCo_2Mo before (bottom) and after catalysis (top).

and after reaction (Figure 8) was demonstrated by Raman spectroscopy of the reaction solutions. It can be seen that the catalysts are intact after the reaction. The water peaks in the Raman spectra were assigned based on separately measured spectra of water (see Figure S23). Furthermore, Figure S23 shows the Raman data of 1-butanol, which cannot be identified in the measured Raman spectra.

Additionally, HPCo_2Mo was recovered after the reaction by evaporation of solvent and further analyzed by IR spectroscopy (see Figure 9) and ICP-OES (see ESI). By comparing the IR and Raman data of the catalysts before and after the reaction we could show that all characteristic vibration bands for the Keggin-type structure are still present. ICP-OES revealed a Co-content of 6.40% for the spent catalyst which is comparable to 6.32% Co found for the fresh catalyst. These results clearly show that the POM structure is maintained, and no Co-leaching appears, so it can be concluded that the catalyst does not undergo any structural changes during catalysis.

Further increase of the reaction temperature to 140 °C using the most promising HPCo_2Mo catalyst lead to an increase of both 1-hexene conversion (up to 95 %) as well as aldehyde yield (up to 28 %) while maintaining an *n*:*iso*-ratio of 3:1 (Figure 10a). On the other hand, reaction temperatures below 130 °C were found to be too low to produce a detectable yield for aldehydes, reaching a low 1-hexene conversion of only 15%. In addition, the variation of the total syngas pressure at 130 °C showed that no aldehydes were formed at lower pressure of 100 bar. The requirement of harsh reaction conditions, meaning high pressure and temperature, is commonly known for Co-catalysts in hydroformylation.^[49] By increasing the pressure to 120 bar and further up to 150 bar, a linear increase in conversion of 1-hexene and aldehyde yield was observed (see Figure S24). Moreover, a significant influence was observed for a variation of the gas phase composition at 150 bar (Figure 10b and Table S11). By increasing the $\text{CO}:\text{H}_2$ -ratio to 2:1, a significant decrease both in conversion as well as aldehyde yield could be observed. With a decreased $\text{CO}:\text{H}_2$ -ratio of 1:2, almost full conversion (>99%) of 1-hexene and a total aldehyde yield up to 46% was achieved. This can be explained by a stabilization of the Co-hydride species at higher H_2 -partial pressures as the rate-determining step in the catalytic cycle.^[50,51] Additionally, an increase of the partial CO-pressure leads to the formation of a possible resting state that inhibits the H_2 -coordination that is already well-known from the unmodified cobalt cycle.^[50,51] Finally, the reproducibility of the results could be proven by repeating the standard experiment at 130 °C and a pressure of 150 bar using $\text{CO}:\text{H}_2$ (ratio of 1:1) for three times (see Figure S25).

Materials and Methods

Three Co^{II} substituted phosphomolybdates were synthesized in this work. All compounds were characterized using elemental analysis (AAS/ICP-OES) and solid-state characterization by vibrational spectroscopy (FT-IR, Raman) as well as crystallography (single X-ray crystal structure analysis) and TGA. Moreover, liquid-phase characterization using ^{31}P -NMR spectroscopy, UV-Vis spectroscopy and

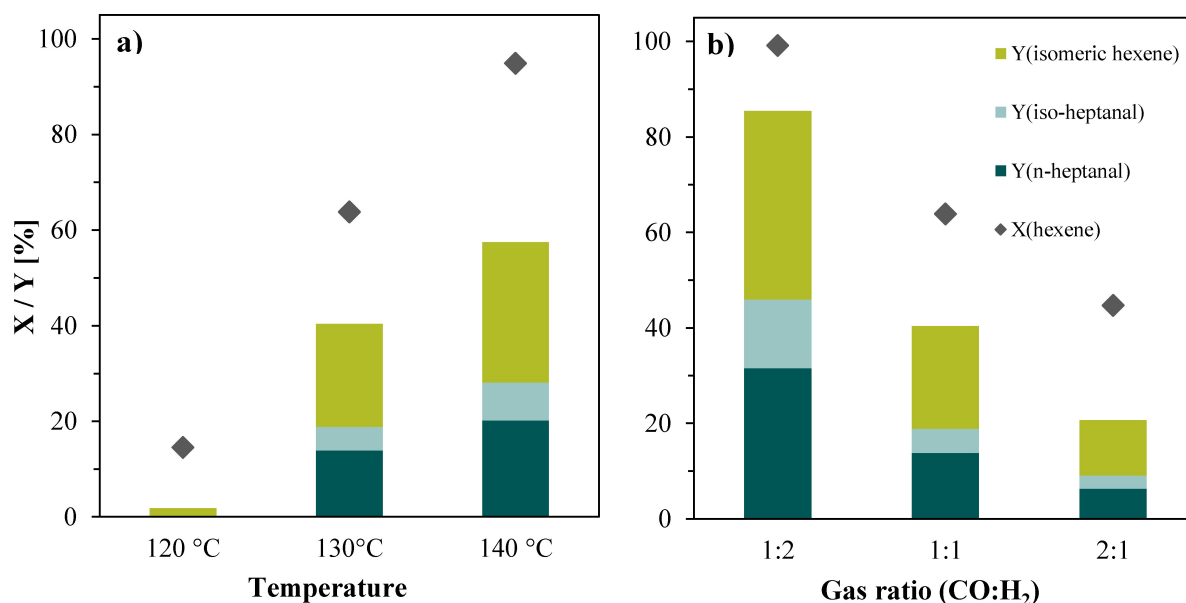


Figure 10. Variation of a) temperature and b) gas composition using HPCo₂Mo as a catalyst. Conditions: *m*(1-hexene) = 0.673 mg, 79 mg HPCo₂Mo (0.04 mmol, 1 mol% Co), *V* (H₂O/BuOH) = 4 mL, 100 - 140 °C, 150 bar CO/H₂, *t* = 4 h.

CW EPR spectroscopy was carried out. The RedOx behavior in solution was elucidated using electrochemistry (CV and SWV). Catalytic experiments were carried out for the hydroformylation of 1-hexene.

Detailed information on catalyst preparation, characterization as well as catalytic data on hydroformylation can be found in the ESI.

Conclusions

In this study, we reported the synthesis and characterization of three new Co^{II}-substituted Keggin-type POMs and showed their potential as hydroformylation catalysts for 1-hexene in a thermomorphic 1-butanol/water solvent system for the first time. The synthesis success was verified using elemental analysis as well as crystallography (*s*-XRD), vibrational spectroscopy, and other spectroscopic methods. With our results we were able to show that the RedOx potentials of our newly synthesized POMs were shifted to higher values in comparison to the unsubstituted HPMo species, indicating a certain RedOx activity. The data presented here highlight the potential of the two-times substituted HPCo₂Mo POM as a promising catalyst for the hydroformylation of medium- and long-chain olefins. A first parameter optimization study shows that there is room for further improvement. By adjusting the ratio of CO and H₂ to 1:2, the yield of *n*-heptanal could be increased to 46%. The stability of the HPCo₂Mo was shown by vibrational (Raman and IR) spectroscopy as well as ICP-OES of the recovered catalyst, highlighting its potential for industrial application.

Acknowledgements

JCR and JA thank the central analytics department at UHH for measuring elemental analysis, crystallography, NMR spectroscopy as well as Prof. Burger and Thomas Marx for supporting our project with electrochemical measurements. The EPR measurements were performed at the Centre for Pulse EPR at Imperial College London (PEPR), supported by the EPSRC grant EP/T031425/1. Open Access funding enabled and organized by Projekt DEAL.

Conflict of Interests

There are no conflicts to declare.

Data Availability Statement

The data that support the findings of this study are available from the corresponding author upon reasonable request.

- [1] J.-C. Raabe, M. J. Poller, D. Voß, J. Albert, *ChemSusChem* **2023**, *16*, 2013–2015.
- [2] J. Reichert, B. Brunner, A. Jess, P. Wasserscheid, J. Albert, *Energy Environ. Sci.* **2015**, *8*, 2985–2990.
- [3] S. Maerten, C. Kumpidit, D. Voß, A. Bukowski, P. Wasserscheid, J. Albert, *Green Chem.* **2020**, *22*, 4311–4320.
- [4] J.-C. Raabe, J. Aceituno Cruz, J. Albert, M. J. Poller, *Inorganics* **2023**, *11*, 138.
- [5] M. T. Pope, A. Müller, *Polyoxometalate Chemistry From Topology via Self-Assembly to Applications*, Kluwer Academic Publishers, New York, Boston, Dordrecht, London, Moscow, **2002**.
- [6] J.-C. Raabe, J. Albert, M. J. Poller, *Chem. – A Eur. J.* **2022**, *28*, 1–12.
- [7] J.-C. Raabe, T. Esser, F. Jameel, M. Stein, J. Albert, M. J. Poller, *Inorg. Chem. Front.* **2023**, *10*, 4854–4868.

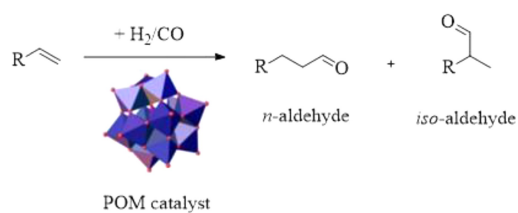
- [8] R. G. Finke, M. W. Droegge, P. J. Domaille, *Inorg. Chem.* **1987**, *26*, 3886–3896.
- [9] R. G. Finke, B. Rapko, R. J. Saxton, P. J. Domaille, *J. Am. Chem. Soc.* **1986**, *108*, 2947–2960.
- [10] M. Abbessi, R. Contant, R. Thouvenot, G. Hervé, *Inorg. Chem.* **1991**, *30*, 1695–1702.
- [11] S.-S. Wang, G.-Y. Yang, *Chem. Rev.* **2015**, *115*, 4893–4962.
- [12] J. Macht, M. J. Janik, M. Neurock, E. Iglesia, *Angew. Chemie Int. Ed.* **2007**, *46*, 7864–7868.
- [13] S. Ponce, M. Trabold, A. Drochner, J. Albert, B. J. M. Etzold, *Chem. Eng. J.* **2019**, *369*, 443–450.
- [14] M. J. Poller, S. Bönisch, B. Bertleff, J.-C. Raabe, A. Görling, J. Albert, *Chem. Eng. Sci.* **2022**, *264*, 118143.
- [15] M. S. Huber, M. Poller, J. Tochtermann, W. Korth, J. Andreas, J. Albert, *Chem. Commun.* **2023**, 4079–4082.
- [16] A. Bukowski, D. Esau, A. A. Rafat Said, A. Brandt-Talbot, J. Albert, *Chempluschem* **2020**, *85*, 373–386.
- [17] B. Bertleff, J. Claußnitzer, W. Korth, P. Wasserscheid, A. Jess, J. Albert, *ACS Sustain. Chem. Eng.* **2017**, *5*, 4110–4118.
- [18] Z. Li, X. Yi, Q. Wang, Y. Li, D. Li, R. Palkovits, A. K. Beine, C. Liu, X. Wang, *ACS Catal.* **2023**, *13*, 4575–4586.
- [19] A. R. Gaspar, J. A. F. Gamelas, D. V. Evtuguin, C. Pascoal Neto, *Green Chem.* **2007**, *9*, 717–73.
- [20] I. V. Kozhevnikov, *Chem. Rev.* **1998**, *98*, 171–198.
- [21] R. Neumann, M. de la Vega, *J. Mol. Catal.* **1993**, *84*, 93–108.
- [22] R. F. Heck, D. S. Breslow, *J. Am. Chem. Soc.* **1960**, *82*, 4438–4439.
- [23] R. F. Heck, D. S. Breslow, *J. Am. Chem. Soc.* **1961**, *83*, 4023–4027.
- [24] L. H. Slaugh, R. D. Mullineaux, *J. Organomet. Chem.* **1968**, *13*, 469–477.
- [25] D. M. Hood, R. A. Johnson, A. E. Carpenter, J. M. Younker, D. J. Vinyard, G. G. Stanley, *Science (80-)*. **2020**, *367*, 542–548.
- [26] F. G. Delolo, J. Yang, H. Neumann, E. N. dos Santos, E. V. Gusevskaya, M. Beller, *ACS Sustain. Chem. Eng.* **2021**, *9*, 5148–5154.
- [27] B. Zhang, C. Kubis, R. Franke, *Science (80-)*. **2022**, *377*, 1223–1227.
- [28] A. Behr, G. Henze, L. Johnen, C. Awungacha, *J. Mol. Catal. A Chem.* **2008**, *285*, 20–28.
- [29] A. Patel, S. Pathan, *J. Coord. Chem.* **2012**, *65*, 3122–3132.
- [30] K. Azmani, M. Besora, J. Soriano-López, M. Landolsi, A.-L. Teillout, P. de Oliveira, I.-M. Mbomekallé, J. M. Poblet, J.-R. Galán-Mascarós, *Chem. Sci.* **2021**, *12*, 8755–8766.
- [31] J. Albert, D. Lüders, A. Bösmann, D. M. Guldi, P. Wasserscheid, *Green Chem.* **2014**, *16*, 226–237.
- [32] J. K. Lee, J. Melsheimer, S. Berndt, G. Mestl, R. Schlögl, K. Köhler, *Appl. Catal. A Gen.* **2001**, *214*, 125–148.
- [33] J. H. Choi, J. K. Kim, D. R. Park, T. H. Kang, J. H. Song, I. K. Song, *J. Mol. Catal. A Chem.* **2013**, *371*, 111–117.
- [34] M. Hunger, J. Weitkamp, *Angew. Chemie - Int. Ed.* **2001**, *40*, 2954–2971.
- [35] E. G. Zhizhina, V. F. Odyakov, M. V. Simonova, *Kinet. Catal.* **2008**, *49*, 773–781.
- [36] D. V. Evtuguin, C. Pascoal Neto, J. Rocha, J. D. Pedrosa de Jesus, *167*, 123–139.
- [37] B. Bennett, R. C. Holz, *J. Am. Chem. Soc.* **1997**, *119*, 1923–1933.
- [38] B. Bennett, R. C. Holz, *Biochemistry* **1997**, *36*, 9837–9846.
- [39] K. P. Barteau, J. E. Lyons, I. K. Song, M. A. Barteau, *Top. Catal.* **2006**, *41*, 55–62.
- [40] I. K. Song, H. S. Kim, M. S. Chun, *Korean J. Chem. Eng.* **2003**, *20*, 844–849.
- [41] T. Yamase, *Chem. Rev.* **1998**, *98*, 307–325.
- [42] H. Salavati, N. Rasouli, *Mater. Res. Bull.* **2011**, *46*, 1853–1859.
- [43] H. Li, L. Swenson, R. J. Doedens, M. I. Khan, *Dalt. Trans.* **2016**, *45*, 16511–16518.
- [44] N. K. K. Raj, A. V. Ramaswamy, P. Manikandan, *J. Mol. Catal. A Chem.* **2005**, *227*, 37–45.
- [45] A. F. Holleman, E. N. Wiberg, G. Fischer, *Lehrbuch der Anorganischen Chemie*, Berlin, New York, 2009.
- [46] N. Elgrishi, K. J. Rountree, B. D. McCarthy, E. S. Rountree, T. T. Eisenhart, J. L. Dempsey, *J. Chem. Educ.* **2018**, *95*, 197–206.
- [47] M. Privman, T. Hepel, *J. Electroanal. Chem.* **1995**, *382*, 137–144.
- [48] T. Ueda, *ChemElectroChem* **2018**, *5*, 823–838.
- [49] F. Hebrard, P. Kalck, *Chem. Rev.* **2009**, *109*, 4272–4282.
- [50] C. De, R. Saha, S. K. Ghosh, A. Ghosh, K. Mukherjee, S. S. Bhattacharyya, B. Saha, *Res. Chem. Intermed.* **2013**, *39*, 3463–3474.
- [51] C. Crause, L. Bennie, L. Damoense, C. L. Dwyer, C. Grove, N. Grimmer, W. J. van Rensburg, M. M. Kirk, K. M. Mokheseng, S. Otto, P. J. Steynberg, *Dalt. Trans.* **2003**, 2036–2042.

Manuscript received: February 27, 2024

Revised manuscript received: March 21, 2024

Accepted manuscript online: March 21, 2024

Version of record online: ■■, ■■



Especially from the IR data it is visible that the vibrational bands are shifted to lower wavenumbers with increas-

ing Co^{II} substitution degree, indicating that Co^{II} is successfully incorporated into the Keggin structure.

*J.-C. Raabe, L. Hombach, M. J. Poller, A. Collauto, M. M. Roessler, A. Vorholt, A. K. Beine, J. Albert**

1 – 9

Synthesis and Characterization of Co(II) Substituted Keggin-Type Polyoxometalates as Novel Catalysts for the Hydroformylation of 1-Hexene in a Thermomorphic Solvent System



5.5 Einfluss des Heteroelementes auf die Polyoxometallat-Strukturtypbildung

P5

Heteroelements in polyoxometalates: a study on the influence of different group 15 elements on polyoxometalate formation

Jan-Christian Raabe, Froze Jameel, Matthias Stein, Jakob Albert, Maximilian J. Poller

Raabe, J.-C.; Jameel, F.; Stein, M.; Albert, J.; Poller, M. J. Heteroelements in Polyoxometalates: A Study on the Influence of Different Group 15 Elements on Polyoxometalate Formation. *Dalt. Trans.* **2024**, 53, 454-466. <https://doi.org/10.1039/D3DT03883A>.

In einer DFT und experimentell gestützten Studie (P5, *Dalton Trans.* **2024**, 53, 454-466)^[250] wurde der Einfluss verschiedener Gruppe 15 Heteroelemente auf die POM-Strukturtypbildung von Wolframaten analysiert.^[250] Die Wahl fiel auf die Gruppe 15 Elemente, da mit diesen Elementen die stabilsten POM-Vertreter gebildet werden können.^[1] Als Modelle für die zu analysierenden Strukturtypbildungen dienten hier der Keggin- und der Anderson-Evans-Strukturtyp. Als Maß zur Abschätzung der relativen Stabilitäten der verschiedenen, heteroatomsubstituierten POMs diente die thermodynamische Gibb'sche Bildungsenergie. Für den Keggin-Strukturtyp mit dem Heteroelement P wurde die niedrigste Gibb'sche Bildungsenergie bestimmt, während die Gibb'schen Bildungsenergien für P über As bis hin zum Sb stetig steigen. Somit ist die Keggin-Typ-Bildung mit dem Element P deutlich favorisiert, während eine Bildung mit den Elementen As und Sb weniger favorisiert ist. Mit dem Element Stickstoff N resultierte eine weit- aus höhere Gibb'sche Bildungsenergie, wodurch die Keggin-Typ Bildung mit N als Heteroelement nicht zugänglich ist. Trends in umgekehrter Reihenfolge ergaben sich für die betreffenden Elemente im Anderson-Evans-Strukturtyp: Die relative Gibb'sche Bildungsenergie liegt am niedrigsten für Sb und steigt für As bis hin zum P stetig an, während eine Vorhersage für N als Heteroelement mit dem verwendeten Modell nicht möglich war.^[250]

Die Ergebnisse der experimentell gestützten Studie sind in Abbildung 24 zusammengefasst, wobei die Experimente bei zwei verschiedenen pH-Werten (5 und 1) durchgeführt wurden. Alle experimentellen Ergebnisse konnten in Einklang mit den computergestützten DFT-Vorhersagen gebracht werden. Eine Einbindung von N als Heteroelement war bei beiden pH-Werten nicht möglich. Bei einem pH-Wert von 5 wurde stattdessen die Bildung des Anions $[W_{12}O_{40}]^{8-}$ beobachtet, das sich bei pH 1 zu den Oxiden umsetzte. Die Bildung des Keggin-Typ-Anions $[PW_{12}O_{40}]^{3-}$ erfolgte erwartungsgemäß bei pH 1 und verläuft zuvor (bei pH 5) über die Bildung eines weniger bekannten Anions, dem $[P_4W_{14}O_{58}]^{12-}$. Mit dem Element As war bei beiden pH-Werten die Bildung einer Keggin- oder Anderson-Evans-Typ-Struktur nicht möglich. Stattdessen wurde die Bildung einer dimeren, lacunären Struktur $[AsW_9O_{34}]^{9-}$ beobachtet, deren Entstehung bei beiden pH-Werten erfolgte. Für Sb wurde im Einklang mit der DFT-Vorhersage die Bildung der Anderson-Evans-Struktur $[SbW_6O_{24}]^{7-}$ nur bei pH 5 beobachtet, die sich im stärker sauren Medium (pH 1) ebenfalls zu den Oxiden umsetzte. Sowohl aus den DFT- als auch aus den experimentellen Ergebnissen ließ sich schlussfolgern, dass die Keggin-Struktur bevorzugt mit Elementen kleinerer Atomradien (Periode 3) gebildet wird, während zur Anderson-Evans-Bildung Elemente mit größeren Radien (Periode 5) benötigt werden. Die so gewonnenen Ergeb-

nisse erweitern das Verständnis der POM-Bildung in Abhängigkeit des Heteroelementes und ebnen das Fundament zum Verständnis der Bildung komplexerer POM-Strukturtypen.^[250]

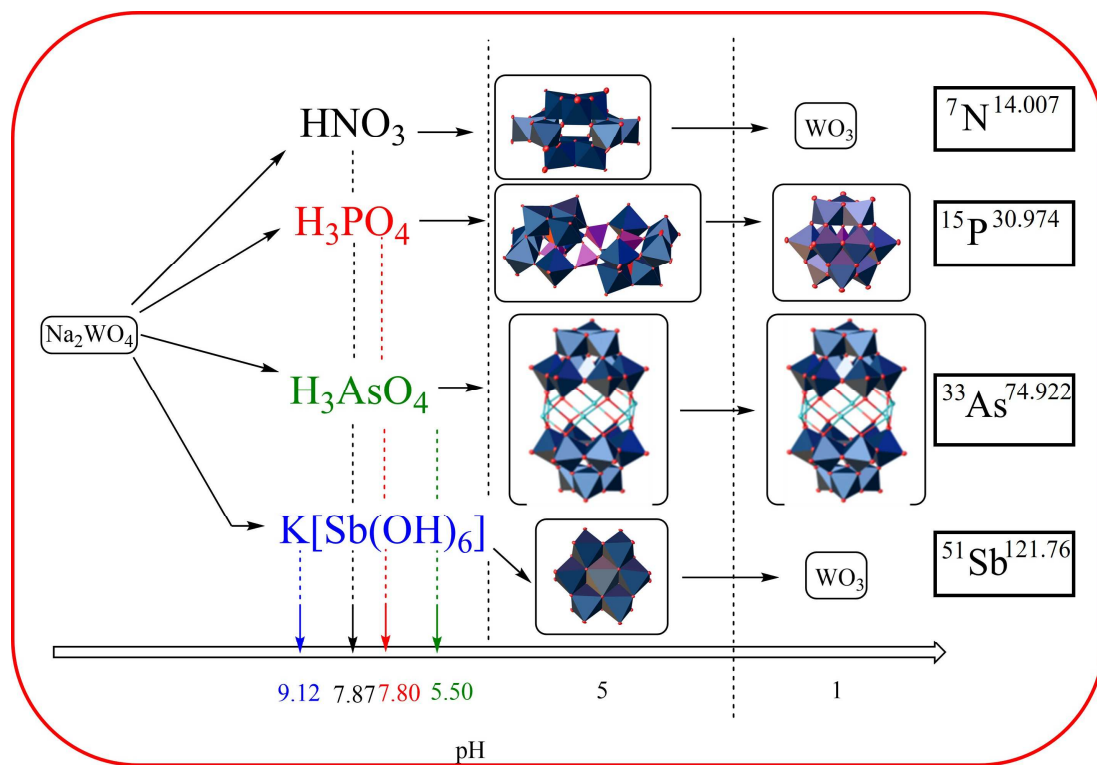


Abb. 24: Graphical abstract von P5, *Dalton Transactions* **2024**, 53, 454-466: POM-Strukturtypbildung in Abhängigkeit des Heteroelementes und pH-Wertes.^[250]

Cite this: *Dalton Trans.*, 2024, **53**, 454

Heteroelements in polyoxometalates: a study on the influence of different group 15 elements on polyoxometalate formation†

Jan-Christian Raabe,^a Froze Jameel,^b Matthias Stein,^b Jakob Albert^a and Maximilian J. Poller^{*a}

In the field of polyoxometalate (POM) chemistry, different heteroelements are integrated into the cage-like structures, to obtain different structural types of so-called heteropolyanions (HPAs). While it is generally accepted, that some elements favor certain types of structure, a systematic study is still missing. In this article, we present a systematic investigation of the influence of the group 15 elements nitrogen, phosphorous, arsenic, and antimony on the formation of different POM structure types. Our study is comprised of DFT calculations and corresponding experimental structural analysis. In this context, the DFT study establishes the thermodynamics of formation of different coordination geometries with various heteroelements on two POM structure types, the Keggin and the Anderson–Evans structures. Our POM synthesis experiments were performed at two different pH values (1 and 5) and resulted in a variety of heteropolytungstates, which were identified and characterized by elemental analysis as well as single crystal X-ray diffraction and vibrational spectroscopy. With these methods, we were able to establish a clear trend, showing that heavier elements lead to formation of different structure types than lighter elements. These results signify a large step towards a better understanding of POM formation specifically with respect to the choice of heteroelement.

Received 20th November 2023,
Accepted 30th November 2023

DOI: 10.1039/d3dt03883a

rsc.li/dalton

1. Introduction

Polyoxometalates (POMs) are a class of inorganic polyanionic clusters, consisting of different transition metals (often Mo or W in their highest oxidation states), which are connected *via* oxo ligands.¹ A subclass of POMs are the so-called heteropolyanions (HPAs), which contain an additional heteroelement in the center of their structure.^{2–6} Most of the HPA structures are formed with group 15 elements, but structures with group 14 and 16 elements are also known.^{7–10} However, some of those HPAs tend to be less stable than others, making a detailed study of those POMs difficult.¹¹ The most common structures are formed with a tetrahedrally coordinated phosphorus(v) atom such as the Keggin type $[\text{PM}_{12}\text{O}_{40}]^{n-}$ or the Wells–Dawson type $[\text{P}_2\text{M}_{18}\text{O}_{62}]^{n-}$ anions.^{3,6,12–18}

In a typical Keggin-type structure the heteroelement X is tetrahedrally coordinated by four oxygen atoms. Each of these oxygen atoms is part of a M_3O_{13} unit. All twelve octahedrally coordinated metal atoms are bridged *via* oxo ligands resulting in M–O–M motifs. On each metal atom is one terminally coordinated oxo ligand with partial double bond character as indicated by a shortened bond length.^{5,12,19–21} The stabilizing effect caused by P(v) in the Keggin-type POMs goes so far that a substitution of the addenda framework metal with other elements such as vanadium(v), niobium(v), iron(III), manganese(II), cobalt(II) *etc.* is possible without compromising the structural integrity of the cluster.^{12–15,21,22}

On the other hand, in the Anderson–Evans HPA structures, the heteroelement is in an octahedral coordination geometry of six oxo ligands. It is surrounded by six octahedrally coordinated framework metal atoms with two terminally coordinated oxo ligands on each metal atom. The oxo ligands of the central XO_6 octahedron are connected to all six metal atoms.²³ The resulting Anderson–Evans structure is planar (α isomer), with a disk-like appearance.²³ A schematic representation of the both structure types is given in Fig. 1.

The difference in the preferred coordination number of the heteroelements correlates with their atomic radii.^{24–30} There are two main coordination motifs found in POM chemistry:

^aInstitute for Technical and Macromolecular Chemistry, Universität Hamburg, Bundesstraße 45, 20146 Hamburg, Germany.

E-mail: maximilian.poller@uni-hamburg.de

^bMax Planck Institute for Dynamics of Complex Technical Systems, Molecular Simulations and Design Group, Sandtorstrasse 1, 39106 Magdeburg, Germany

† Electronic supplementary information (ESI) available. CCDC 2293848–2293851.

For ESI and crystallographic data in CIF or other electronic format see DOI:

<https://doi.org/10.1039/d3dt03883a>



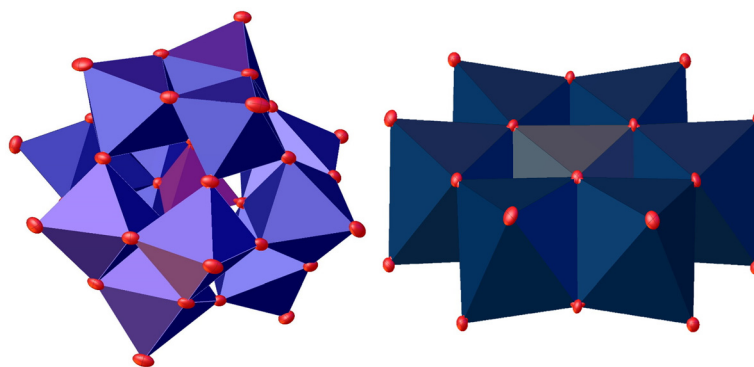


Fig. 1 Schematic representation of a Keggin (left) and a planar Anderson–Evans-type structure (right).

the tetrahedral (CN 4) and the octahedral geometry (CN 6), whereby heavier elements (larger radii) prefer the octahedral configuration and lighter elements (smaller radii) prefer the tetrahedral configuration.¹ This can be exemplarily seen when comparing the oxides of phosphorus (P_4O_{10}) and antimony (Sb_2O_5). The pnictogen is coordinated tetrahedrally in the former but octahedrally in the latter.^{31,32} In our here presented study, we systematically investigated the influence of the group 15 elements nitrogen, phosphorus, arsenic, and antimony on the formation of POM structures. To this end, we combined suitable precursors of the group 15 elements with sodium tungstate under conditions that lead to the formation of POMs *via* polycondensation of the tungstate. Afterwards, we structurally characterized the resulting products using single crystal X-ray diffraction and vibrational spectroscopy. The results of these heteroatom substitutions are complemented by Density

Functional Theory (DFT) calculations of the structural changes and relative free energies of the Keggin and the Anderson–Evans structures containing different elements of group 15.

2. Results and discussion

2.1. Thermodynamics of formation and structural parameters upon inclusion of heteroatoms

DFT calculations were performed to probe the structural and thermodynamic differences by exchanging the central group 15 atom of Keggin and Anderson–Evans type complexes (see Fig. 2 and 3). The structural changes in POM (Keggin and Anderson–Evans) structure upon exchanging the central heteroatoms were characterized based on: (i) non-metal heteroatom–oxygen distance ($X-O_a$), (ii) distance of oxygen co-

Keggin Heteroelement Substitution				
	$[NW_{12}O_{40}]^{3-}$	$[PW_{12}O_{40}]^{3-}$	$[AsW_{12}O_{40}]^{3-}$	$[SbW_{12}O_{40}]^{3-}$
$\Delta G_{\text{solu.}}$ [kJ/mol]	332.6	0.0	62.2	179.7
Molecular Volume [\AA^3]	733	711	713	715
$X-O_a$ [\AA]	1.39	1.53	1.66	1.82
O_a-W [\AA]	2.62	2.45	2.38	2.29

Fig. 2 Effect of different heteroatoms on thermodynamics and structures of Keggin complex formation. Characteristic structural parameters and molecular volume are given. The thermodynamic stability (Gibbs energy of formation) are reported relative to the Keggin complex with phosphorous as central heteroatom.



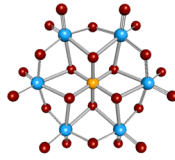
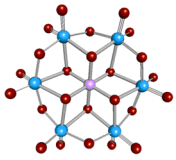
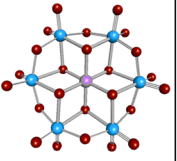
Anderson-Evans Heteroelement Substitution			
			
	[PW ₆ O ₂₄] ⁷⁻	[AsW ₆ O ₂₄] ⁷⁻	[SbW ₆ O ₂₄] ⁷⁻
$\Delta G_{\text{solu.}}$ [kJ/mol]	0.0	-163.4	-292.5
Molecular Volume [Å ³]	416	423	432
X-O _a [Å]	1.76	1.88	2.01
O _a -W [Å]	2.25	2.24	2.24

Fig. 3 Effect of different heteroatom substitutions on thermodynamics and structures of Anderson–Evans complex structures. Gibbs energies of formation are given relative to the Anderson–Evans complex with phosphorous as heteroatom.

ordinated to the central non-metal atom and the neighboring tungsten atoms (O_a–W) and the molecular volume of the complexes with optimized Keggin and Anderson–Evans type complexes containing different non-metal heteroelements.

In the DFT optimized Keggin complex with nitrogen as heteroatom, the X–O_a bond distance is reduced by 0.14 Å when compared to the Keggin complex with phosphorous as central non-metal heteroatom due to the smaller atomic radius of nitrogen compared to phosphorous. This reduction in the atomic radii also weakens the tungsten–oxygen coordination as the O_a–W distance increases by 0.17 Å in [NW₁₂O₄₀]³⁻ compared to an O_a–W distance in [PW₁₂O₄₀]³⁻ Keggin complex. The molecular volume expansion by 22 Å³ for the Keggin complex, when phosphorous is substituted by nitrogen, shows that non-metallic heteroatom exchange with an atom having small atomic radius such as nitrogen, significantly affects the shape of the Keggin complex (see Fig. 2). The expansion of molecular volume by introducing smaller atoms seems to be counterintuitive. The Gibbs energies of formation were calculated from isodesmic reactions of the Keggin and Anderson–Evans complexes with their respective acids (hybrid DFT functional, thermodynamic corrections plus solvation are included; see ESI†). From DFT calculations, however, it can be shown that the relative thermodynamics, here the Gibbs energy for the formation, of a Keggin-type complex with nitrogen as heteroatom is significantly higher ($\Delta G = 332 \text{ kJ mol}^{-1}$) compared to the Keggin complex with phosphorous as central non-metal atom. This shows that the formation of a Keggin complex with nitrogen as central heteroatom is structurally and thermodynamically inaccessible.

However, when phosphorous is exchanged with the heavier elements within group 15 such as arsenic (As) and antimony (Sb), there is a very small change of a mere 2 and 4 Å³ in molecular volume compared to the [PW₁₂O₄₀]³⁻ complex. For both As and Sb exchange, the elongation in X–O_a bond distances due to larger atomic radii is partially compensated by the reduction in the O_a–W distances, thus conserving the mole-

cular volume of the resulting [AsW₁₂O₄₀]³⁻ and [SbW₁₂O₄₀]³⁻ complexes. Since the Gibbs energy of formation for the Keggin complexes containing arsenic and antimony as non-metal central heteroatoms is higher compared to the [PW₁₂O₄₀]³⁻, the formation of Keggin complexes with As and Sb as heteroatoms is thermodynamically less favorable (see Fig. 2).

Despite several efforts, the optimization of an Anderson–Evans type complex with nitrogen as the central non-metal heteroatom, was not successful due to the small atomic radius of the nitrogen atom. However, for atoms of group 15 with larger atomic radii such as phosphorous, arsenic and antimony, DFT calculations show that the formation of Anderson–Evans complex with antimony as heteroatom is energetically favored compared to the complexes with arsenic and phosphorous as heteroatoms. With the increase in the atomic radius going down the group, the molecular volume increases by only 7 and 9 Å³ for the substitution of phosphorous with arsenic and antimony, respectively. Similarly, the X–O_a distance increases however, the O_a–W remains almost the same (see Fig. 3).

Our DFT calculations show that the formation of a Keggin-type POM structure appears to be only favorable for elements with small atomic radii and unfavorable for elements with larger radii. In contrast, heteroatom substitutions for Anderson–Evans type structures are favored for elements with larger atomic radii and less so for those with small radii. This observation is in full agreement with inorganic structure concepts and thus explained by the different coordination geometries of the heteroelement in both structural motifs.^{33,34} In the Keggin structure, the coordination geometry for the heteroelement is a tetrahedron (CN 4) and for the Anderson–Evans structure an octahedron (CN 6).^{19,23} The coordination geometry correlates with the atomic radius of the element of interest. Ligands coordinating a central element tend to maximize the distance between them due to the repulsion of their electron shells. Therefore, for CN 4 the tetrahedral and for CN 6 the octahedral coordination geometry is the most thermodynamically favorable arrangement. The higher the atomic



radius of the element, the more ligands can be coordinated by an element and the more the octahedral geometry is preferred. Elements with a small atomic radius can coordinate fewer ligands, resulting in a preference for the tetrahedral geometry.^{33,34} Likewise, the Anderson–Evans structure with large elements as heteroelements could be stabilized by adopting planarity. The planarity results in an opening for the introduction of a heteroelement perpendicular to the plane upwards and downwards, giving the heteroelement more space.

These trends are also confirmed by our experimental observations: using different group 15 elements together with sodium tungstate, we performed typical POM synthesis procedures at pH values 1 and 5, which are typical for the synthesis of Keggin- and Anderson-type POMs respectively.^{35,36} Nitric acid was used as precursor for N(v), phosphoric acid for P(v), arsenic(III) oxide for As(v) and potassium hexahydroxoantimonate for Sb(v). Arsenic(III) oxide was oxidized *in situ* with hydrogen peroxide to the required As(v) species. The obtained products were desalinated using our previously reported nanofiltration technique^{21,37} and the powder samples were then recrystallized to identify the resulting structure by single-crystal X-ray diffraction (scXRD). Detailed experimental procedures are provided in our ESI.†

2.2. Experimental synthesis and characterization of heteroelement incorporation

2.2.1. Incorporation of nitrogen as a heteroelement.

The product resulting from the combination of nitric acid and sodium tungstate at pH 5 was identified as paradodecatungstate B $[\text{W}_{12}\text{O}_{40}]^{8-}$ anion (Fig. 4).^{38–41}

It is composed of four corner-linked WO_6 triads, with the linking of the triads resulting in a large cavity inside the structure. Important bond lengths of our investigated structural

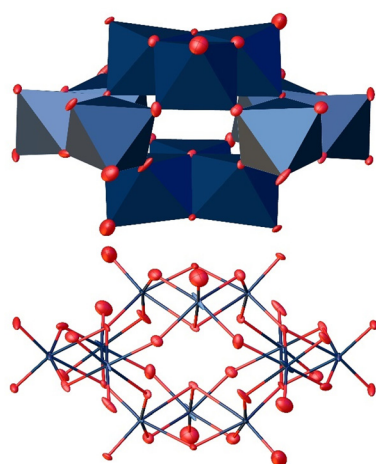


Fig. 4 Solid-state structure of the anion $[\text{W}_{12}\text{O}_{40}]^{8-}$ determined by scXRD. Polyhedra representation above and atom model bottom. The compound was crystallized in the triclinic space group $P\bar{1}$ (2). R_1 : 4.74%, wR_2 : 9.47%, R_{int} : 4.76%, Goof : 1.078. Color code: blue: metal atoms (W), red: oxygen atoms. The .cif file is available in the CCDC database. Deposition number: 2293850.†

motifs are summarized in Table 1. In order to confirm the structure of the bulk product, the material was characterized by vibrational spectroscopy (Fig. 5 and 6). Typical vibrational bands of POM structures include the terminal oxygen–metal vibrational bands $\text{W}=\text{O}$ in the range of $800\text{--}1000\text{ cm}^{-1}$, and different types of $\text{W}-\text{O}-\text{W}$ vibrational modes below 900 cm^{-1} .^{42–45} From comparison of the experimental and calculated spectra for the above described structure, the following vibrational assignments can be made: in the IR spectrum of $\text{Na}_8[\text{W}_{12}\text{O}_{40}]$ the peaks appearing at 944 and 930 cm^{-1} agree well with the small peaks at 912 and 903 cm^{-1} in the DFT calculated IR spectrum that corresponds to the asymmetric $\text{W}=\text{O}_t$ stretches. The peak at 955 , 882 and 878 cm^{-1} in the experimental spectrum differs by only 13 , 9 and 7 cm^{-1} (968 ,

Table 1 Assignment of peak positions in IR and Raman spectra of $[\text{W}_{12}\text{O}_{40}]^{8-}$

Peak position/ cm^{-1}	Assignment ^c
96^b	$\text{O}_t\text{-W-O}$ (out-of-plane)
109^b	$\text{W}=\text{O}$ wagging (out-of-plane)
133^b	$\text{O}-\text{W}-\text{O}$ twist (out of plane)
161^b	$\text{O}_t\text{-W-O}$ (in-plane)
217^b	$\text{W}-\text{O}-\text{W}$ bend along vertex (out-of-plane)
238^b	$\text{W}-\text{O}-\text{W}$ bend along vertex (in-plane)
311^b	$\text{W}=\text{O}$ scissoring (in-plane)
360^b	$\text{W}=\text{O}$ bend (out-of-plane)
638^a	$\text{W}-\text{O}-\text{W}$ stretch (asymmetric)
656^b	
740^a	$\text{W}-\text{O}-\text{W}$ stretch along vertex (symmetric)
847^a	
878^a	$\text{W}=\text{O}_t$ stretch (symmetric)
$892^{a,b}$	
912^b	$\text{W}=\text{O}_t$ stretch (asymmetric)
930^a	
944^a	
955^a	$\text{W}=\text{O}$ stretch (symmetric)
965^b	

^a FTIR. ^b Raman. ^c Based on computations.

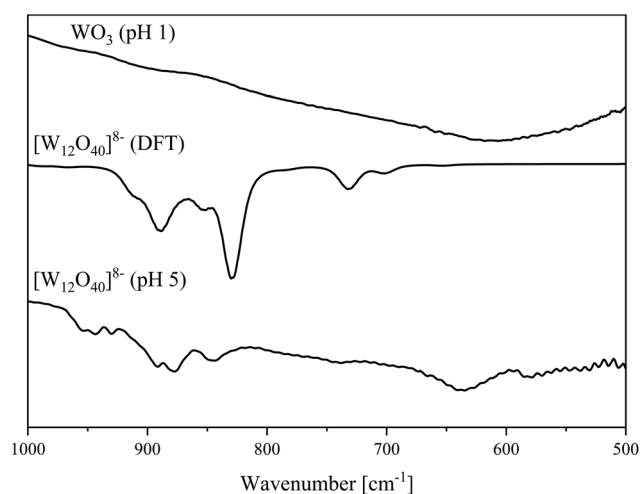


Fig. 5 IR spectra of the $[\text{W}_{12}\text{O}_{40}]^{8-}$ anion determined in the solid-state (bottom) and DFT calculated (middle). Spectrum of WO_3 (top).



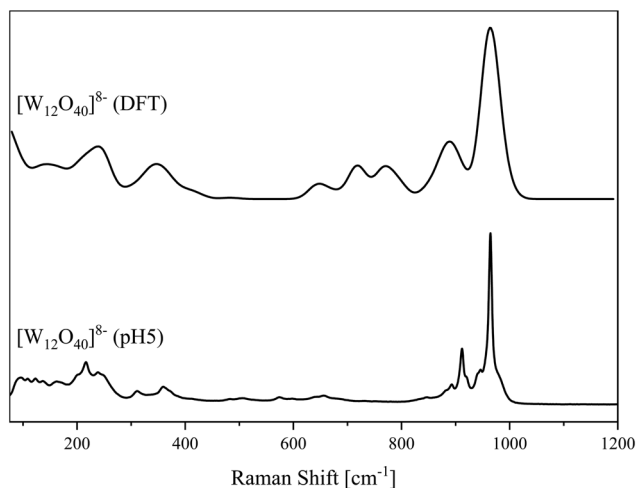


Fig. 6 Raman spectra of the $[W_{12}O_{40}]^{8-}$ anion determined in the solid-state (bottom) and DFT calculated (top).

891 and 871 cm^{-1}) from the calculated spectrum and belongs to symmetric $W=O_t$ bond stretches. Similarly, the broad peak at 847 cm^{-1} in the experimental spectrum can be assigned to the peaks appearing at 853 and 829 cm^{-1} in the calculated spectrum of $Na_8[W_{12}O_{40}]$, where both peaks corresponds to a symmetric $W-O-W$ distortion along the vertex. A peak 740 cm^{-1} in the experimental spectrum appears at 732 cm^{-1} in the calculated spectrum and corresponds to the asymmetric $W-O-W$ bond stretch. Finally, peaks at 638 cm^{-1} in the experimental spectrum and 652 cm^{-1} (calculated) refer to asymmetric $W-O-W$ stretches. Overall, the comparison of the calculated and experimental vibrational spectra leads to the conclusion that the isolated paradodecatungstate is the main product of this reaction. Critical spectral peak positions from IR and Raman are summarized in Table 1.

Performing the same reaction at a pH of 1, which should usually lead to the formation of a Keggin-type structure, resulted in the formation of tungsten oxide, which was identified by powder X-ray diffraction (Fig. 7). The oxides formed were identified as a mixture of different phases of the tungsten oxides WO_3 and $W_{18}O_{49}$ using comparative data from measurements of commercial WO_3 and from the ICSD database, with only two WO_3 and one $W_{18}O_{49}$ phase being used for visualization.

The fact that the $N(v)$ atom is not part of the POM structure shows that nitrogen is not a suitable heteroelement for the formation of heteropolyanions. This result is consistent with the particularly high relative energy of the hypothetical $[NW_{12}O_{40}]^{3-}$ anion in our DFT calculations and the absence of a convergence in DFT calculations for the hypothetical $[NW_6O_{24}]^{7-}$. NO_3^- is known for its trigonal-planar geometry³⁴ and a NO_4^{3-} analogous to the phosphate anion PO_4^{3-} does not exist. To the best of our knowledge there is no structural motif known in which $N(v)$ is coordinated octahedrally.³³ Therefore, the formation of a Keggin- or Anderson-Evans-structure is excluded for geometrical reasons. From our previous work on

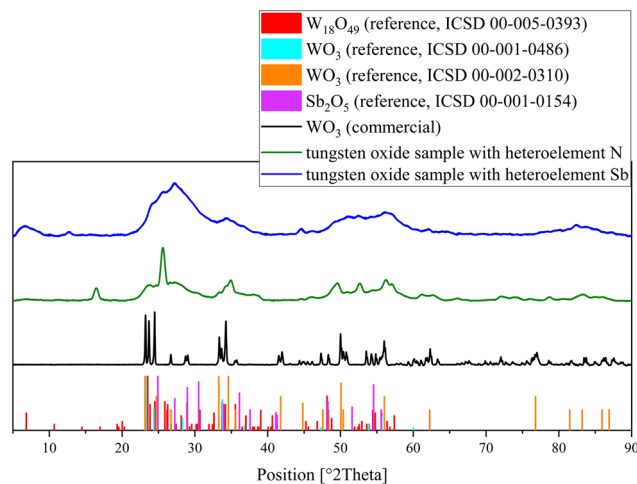


Fig. 7 Powder XRD of the different tungsten oxide samples obtained from the reaction mixtures in comparison with different solid-state phases of WO_3 , $W_{18}O_{49}$, Sb_2O_5 and commercially available WO_3 .

Keggin structures, we know that the diameter of the PO_4^{3-} tetrahedron in the center of the Keggin structure is approximately 3.074 \AA .¹² To estimate the size of a hypothesized NO_4^{3-} anion, we measured the dimensions of a tetramethylammonium cation (CCDC database deposition number: 1916596), since the carbon atom is similar in size to the oxygen atom. This would give an approximate size of 2.984 \AA for a hypothetical NO_4^{3-} tetrahedron, which is smaller than the PO_4^{3-} tetrahedron and presumably too small to act as the center of a Keggin-type structure.

2.2.2. Incorporation of phosphorus as a heteroelement. Analogous experiments were performed using H_3PO_4 . As expected, at pH 1, H_3PO_4 and Na_2WO_4 form the well-known Keggin-type phosphotungstate $Na_3[PW_{12}O_{40}]$, which was identified by FT-IR (Fig. 8) and ^{31}P -NMR spectroscopy as shown in Fig. S2 (ESI[†]).^{22,46–48}

In agreement with our previous published study, the ^{31}P NMR peak for $Na_3[PW_{12}O_{40}]$ was found at -15.3 ppm .²² The big peak at $\sim 0\text{ ppm}$ is a result of the excess H_3PO_4 used during the experimental procedure.

At a pH value of 5, we unexpectedly obtained a polyoxoanion with the composition $[P_4W_{14}O_{58}]^{12-}$ (Fig. 9).⁴⁹ For this structure type, we were not able to find a .cif file in the CCDC/ICSD database.

The structure is composed of two oppositely oriented hemispheres connected by two central tetrahedrally coordinated $P(v)$ atoms. Both are composed of seven WO_6 octahedra, which are held together by a central PO_4^{3-} tetrahedron. In total, this structure motif consists of 14 WO_6 octahedra and four PO_4^{3-} tetrahedra, resulting in the final 4 : 14 P : W ratio.⁵⁰

The IR and Raman spectra of the bulk material (Fig. 8 and 10) show the typical vibrational bands of the $[P_4W_{14}O_{58}]^{12-}$ anion. In addition to the different types of $W=O$ and $W-O-W$ vibrational bands, the P-O band is found as a split band in the IR spectrum at 1080 and 1037 cm^{-1} . This can be explained by considering the solid-state structure in Fig. 9 which has two



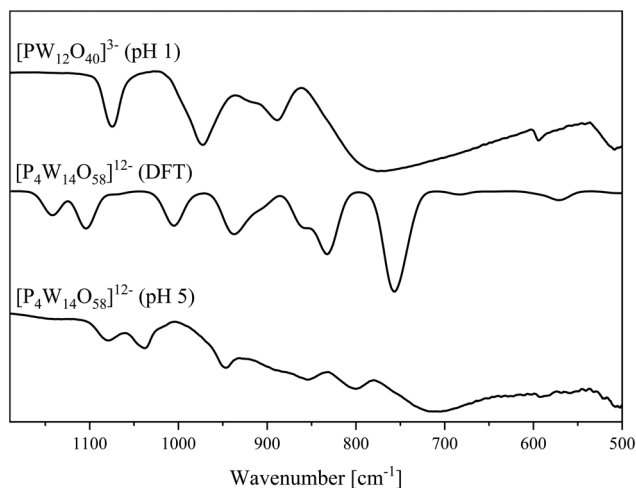


Fig. 8 IR spectra of the $[P_4W_{14}O_{58}]^{12-}$ anion determined in the solid-state (bottom) and DFT calculated (middle). Spectrum of $[PW_{12}O_{40}]^{3-}$ (top).

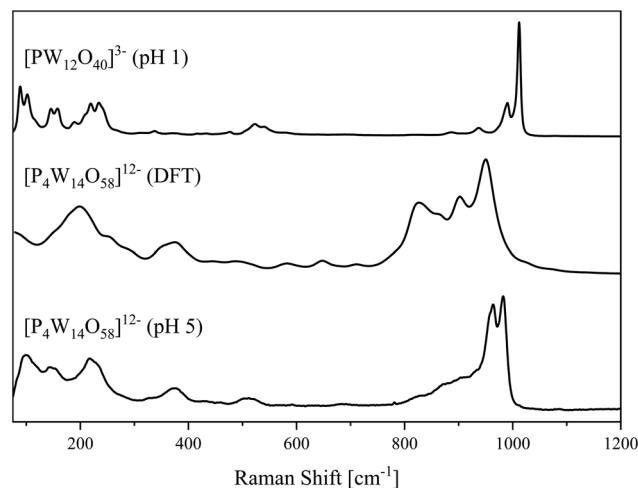


Fig. 10 Raman spectra of the $[W_{12}O_{40}]^{8-}$ anion determined in the solid-state (bottom) and DFT calculated (middle). Spectrum of $[PW_{12}O_{40}]^{3-}$ (top).

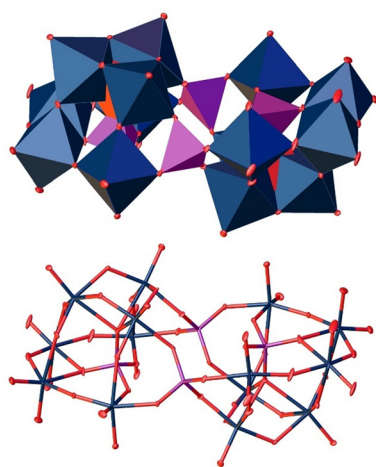


Fig. 9 Solid-state structure of the anion $[P_4W_{14}O_{58}]^{12-}$ determined by scXRD. Polyhedra representation above and atom model bottom. The compound was crystallized in the triclinic space group $P\bar{1}$ (2). R_1 : 2.83%, wR_2 : 7.19%, R_{int} : 7.53%, GooF: 1.076. Color code: blue: metal atoms (W), red: oxygen atoms, purple: phosphorous. The .cif file is available in the CCDC database. Deposition number: 2293849.†

different types of P–O tetrahedra: two PO_4 tetrahedra in the center of each hemisphere and two PO_4 tetrahedra connecting the hemispheres. The agreement between calculated and experimental IR spectra is excellent and allows a spectral assignment of peaks which correspond to symmetric and anti-symmetric P–O bond stretches for all four phosphates groups, respectively (1005 and 1071 cm^{-1}). The peaks at 1104 and 1142 cm^{-1} belong to the P–O bond stretches in the phosphates connecting two hemispheres and the central PO_4^{3-} tetrahedra, respectively. The peak corresponding to vibration of the terminal $W=O_t$ bonds appears at 941 and 862 cm^{-1} in the calculated spectrum and can be found at 950 and 856 cm^{-1} respectively, in the experimental spectrum. The peak at 800 cm^{-1} in

the experimental spectrum match well with calculated peaks at 851, 835 and 827 cm^{-1} and refer to the W–O–W bond stretches along the vertex. The broad peak at 713 in the calculated spectrum appears at 760 cm^{-1} in the calculated IR spectrum and corresponds the W–O–W bond vibrations along the edge.

In summary, the calculated and experimental spectra match the structure of the isolated single crystal, confirming the structure of the bulk material. Important IR and Raman peak positions are summarized in Table 2.

2.2.3. Incorporation of arsenic as a heteroelement. In order to perform the same experiments with As, we oxidized arsenic(III) oxide to arsenic(V) acid (H_3AsO_4) *in situ*, using hydrogen peroxide. At both pH values (1 and 5) the resulting product was identified as the tri-lacunary Keggin anion $[AsW_9O_{34}]^{9-}$, in which As(V) is in a tetrahedral coordination as shown in Fig. 11.^{21,51–53} The single crystal was obtained from the experiment at pH 5, but the bulk products were shown to be identical by vibrational spectroscopy (Fig. 12). Additionally,

Table 2 Assignment of peak positions in IR and Raman spectra of $[P_4W_{14}O_{58}]^{12-}$

Peak position/ cm^{-1}	Assignment ^c
100 ^b	$O_t=O_t=O_t$ rock (symmetric)
145 ^b	$O_t=O_t=O_t$ rock (asymmetric)
216 ^b	P=O=W twist (out-of-plane)
373 ^b	O=W=O scissoring (in-plane)
507 ^b	W=O=W bend (in-plane)
713 ^a	W–O–W (edge)
800 ^a	W–O–W (vertex)
856 ^a	W=O _t stretch (symmetric)
950 ^a	
964 ^b	P–O stretch (symmetric)
983 ^b	
1037 ^a	
1080 ^a	

^a FTIR. ^b Raman. ^c From calculations.



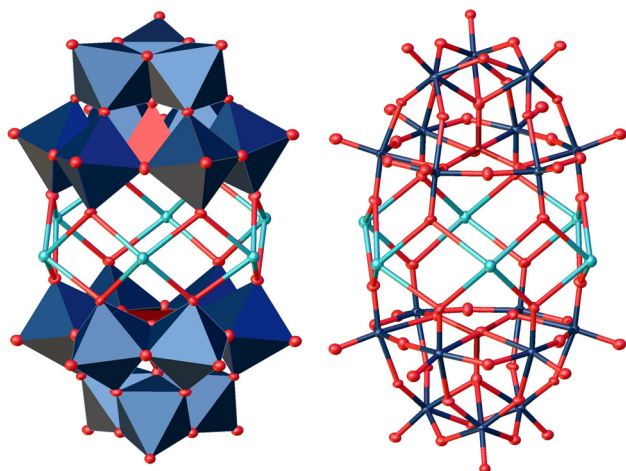


Fig. 11 Solid-state structure of the anion $[\text{AsW}_9\text{O}_{34}]^{9-}$ determined by scXRD resulting from the experiment with As(v). Two $[\text{AsW}_9\text{O}_{34}]^{9-}$ anions are bridged by coordinating *via* six sodium cations. Polyhedral representation left and atom model right. The compound was crystallized in the triclinic space group $P\bar{1}(2)$. R_1 : 4.23%, wR_2 : 10.71%, R_{int} : 6.65%, Goof : 1.115. Color code: brown: arsenic (As), blue: metal atoms (W), red: oxygen atoms and turquoise: sodium cations. The .cif file is available in the CCDC database. Deposition number: 2293851.†

the composition was confirmed by elemental analysis (ICP-OES, Table S3, ESI†).

In the solid-state structure, two $[\text{AsW}_9\text{O}_{34}]^{9-}$ units are joined by six sodium cations. Here, the terminal oxo ligands of the vacancy positions are coordinating to the sodium cations.

The crystallographic dataset shows that the diameter of a tetrahedrally coordinated AsO_4^{3-} is 3.377 Å (literature: 3.295 Å⁵⁴), which is significantly larger than the PO_4^{3-} tetrahedron (3.085 Å, CCDC deposition number 2177881).¹² These observations are in agreement with our DFT calculations in which the Keggin-type structure $[\text{AsW}_{12}\text{O}_{40}]^{3-}$ also has a

significantly higher relative energy of formation than the classical Keggin-type structure $[\text{PW}_{12}\text{O}_{40}]^{3-}$. A Keggin anion $[\text{AsW}_{12}\text{O}_{40}]^{3-}$ has been reported previously but has been characterized as unstable.^{55–57} Presumably, the larger AsO_4^{3-} tetrahedron is too bulky to comfortably fit in the Keggin structure, leading to the formation of the tri-lacunary Keggin units which provide more space. This can specifically be observed when comparing the O–O distances of the O atoms coordinating to Na^+ in the $[\text{AsW}_9\text{O}_{34}]^{9-}$ dimer (4.121 Å) with the corresponding distances of bridging O atoms in the $[\text{PW}_{12}\text{O}_{40}]^{3-}$ Keggin ion (2.753 Å).⁴⁸ The Na^+ ions saturate the open coordination sites on the lacunary O atoms, leading to the observed coordination dimer. The bond length between the lacunary O and Na^+ ions is 2.830 Å which exceeds the sum of the respective covalent radii (Na: 1.55 Å and O: 0.63 Å = 2.18 Å). This suggests a weak bonding interaction. The distance is comparable to the O–Na distance between a Keggin-type anion and its Na^+ counterions (2.986 Å), which we observed in a recently published crystal structure of $\text{Na}_6[\text{PV}_3\text{Mo}_9\text{O}_{40}]$ (deposition number 2205007).²¹

Vibrational spectroscopy of the products obtained at pH 1 and pH 5 confirm that they are identical. Additionally, the vibrational spectra were simulated based on the above-described structure (Fig. 12 and 13). The spectra exhibit peaks at 928 cm^{-1} (929 cm^{-1} in the calculated spectrum) that correspond to symmetric $\text{W}=\text{O}_t$ bond stretch. The experimental IR peaks at 855 and 866 cm^{-1} appears at 859 and 869 cm^{-1} in the calculated spectrum belonging to the asymmetric $\text{W}=\text{O}_t$ bond stretch and asymmetric $\text{As}=\text{O}$ bond vibration, respectively. The peak at 803 cm^{-1} (797 cm^{-1} in the calculated spectrum) can be assigned to the $\text{As}-\text{O}-\text{W}$ and $(\text{W}-\text{O}-\text{W})_{\text{vertex}}$ bond vibrations, and the peak at 729 cm^{-1} (calculated 723 cm^{-1}) corresponding to $\text{W}-\text{O}-\text{W}$ bond vibrations along the edge of the octahedra. The peak at 763 cm^{-1} in the calculated spectrum corresponds to the $(\text{W}-\text{O}-\text{W})_{\text{bridging}}$ bond vibrations. Additionally, a small shoulder peak appears at 837 cm^{-1} in the

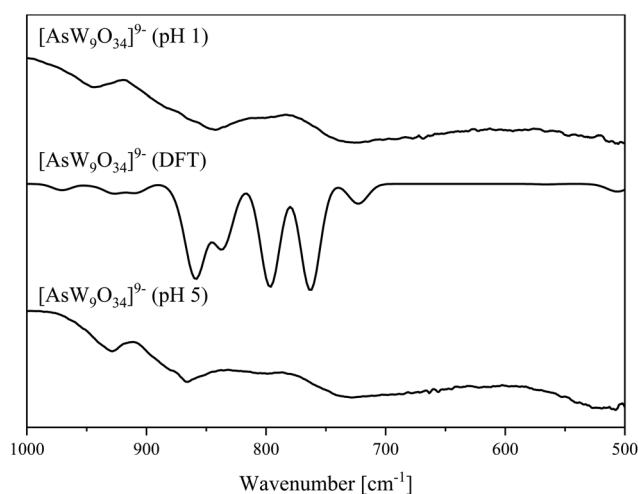


Fig. 12 IR spectra of the $[\text{AsW}_9\text{O}_{34}]^{9-}$ anion (pH 5 and 1) determined in the solid-state (bottom/top) and DFT calculated (middle).

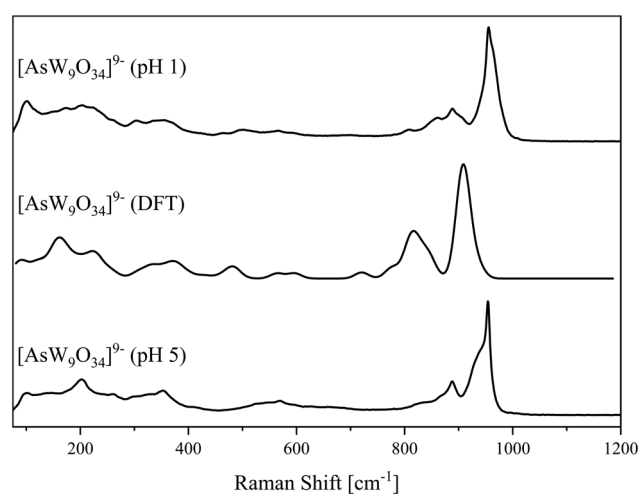


Fig. 13 Raman spectra of the $[\text{AsW}_9\text{O}_{34}]^{9-}$ anion (pH 5 and 1) determined in the solid-state (bottom and top) and DFT calculated (middle).



calculated spectrum, which belongs to an asymmetric W–O–As bond stretching vibration. Critical IR and Raman spectral peak positions and their assignments are summarized in Table 3.

2.2.4. Incorporation of antimony as a heteroelement.

Finally, we performed the same experiments using potassium hexahydroxoantimonate(v) as an antimony precursor, which has been reported previously as a precursor for incorporating Sb(v) into a POM structure.⁴⁵

At the pH value of 5, we observed the formation of the Anderson–Evans-type anion $[\text{SbW}_6\text{O}_{24}]^{7-}$, which was first identified by singly crystal XRD (Fig. 14).

This structure type consists of six WO_6 octahedra surrounding one central SbO_6 octahedron. The bond length between Sb and O ($\text{Sb}-\text{O}_a$), was measured as 1.984 Å, slightly longer than the distance between the W and the bridging O atoms ($\text{W}-\text{O}_b$) of 1.941 Å. This is the longest heteroatom–oxygen distance

Table 3 Assignment of IR and Raman spectral peak positions of $[\text{AsW}_9\text{O}_{34}]^{9-}$

Peak position/ cm^{-1}	Assignment ^c
262 ^b	$\text{O}=\text{W}=\text{O}_t$ rock (in-plane)
352 ^b	$\text{O}_t=\text{W}=\text{O}_t$ scissoring (in-plane)
566 ^b	W–O–W along edge (symmetric)
729 ^a	As–O–W stretch W–O–W (vertex)
803 ^a	
865 ^a	W= O_t stretch (symmetric)
866 ^a	As=O stretch (asymmetric)
888 ^b	W= O_t stretch (symmetric)
929 ^a	
954 ^b	

^a FTIR. ^b Raman. ^c From calculations.

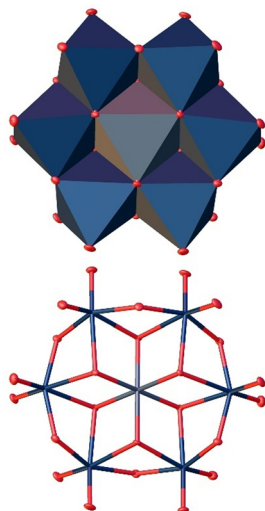


Fig. 14 Solid-state structure of the anion $[\text{SbW}_6\text{O}_{24}]^{7-}$ determined by scXRD. Polyhedra representation above and atom model bottom. The compound was crystallized in the triclinic space group $P\bar{1}$ (2). R_1 : 2.54%, wR_2 : 6.89%, R_{int} : 5.45%, GoF : 1.136. Color code: blue: metal atoms (W), red: oxygen atoms. The .cif file is available in the CCDC database. Deposition number: 2293848.†

reported in this work, which is consistent with the increasing radii of the heteroatoms⁵⁸ that consequently leads to a larger coordination number. These observations are also in agreement with our above presented quantum chemical calculations, indicating that the formation of the Anderson–Evans structure is energetically favored for Sb(v).

Again, the bulk material was characterized by vibrational spectroscopy (Fig. 15 and 16). Few peaks can be assigned to the Anderson–Evans structure based on previous literature.⁴⁵ To fully assign the vibrational bands, the IR and Raman spectra of $[\text{SbW}_6\text{O}_{24}]^{7-}$ were calculated on the basis of the above described structure using computational methods.

Going from lower to higher wavenumbers, the peaks appearing at 435 and 470 cm^{-1} in the calculated spectrum (experimental 419 cm^{-1}) correspond to anti-symmetric degenerate bending and anti-symmetric degenerate stretching Sb–O

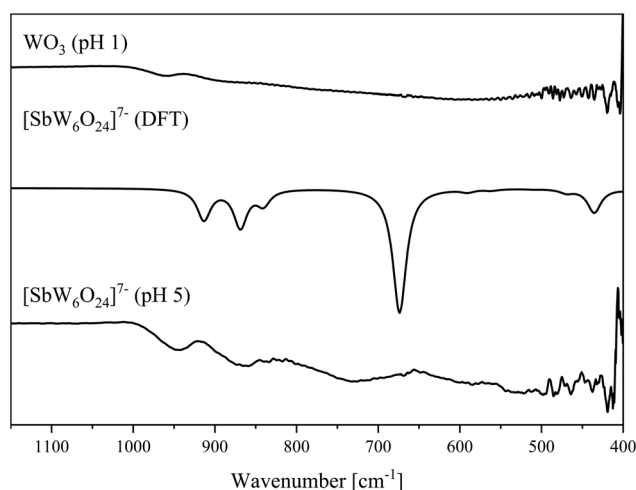


Fig. 15 IR spectra of the $[\text{SbW}_6\text{O}_{24}]^{7-}$ anion determined in the solid-state (bottom) and DFT calculated (middle). Spectrum of WO_3 (top).

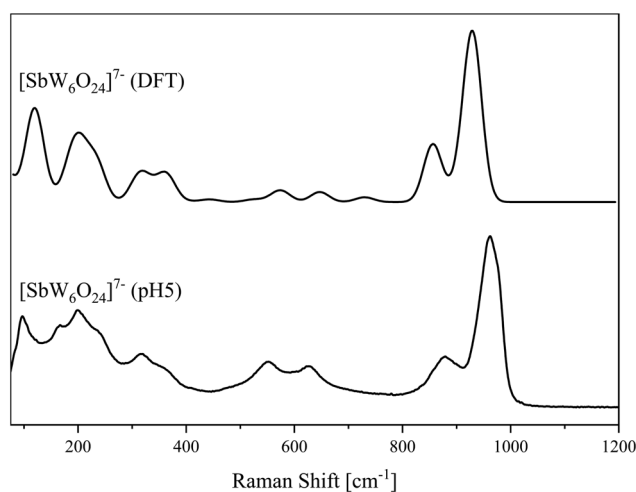


Fig. 16 Raman spectra of the $[\text{SbW}_6\text{O}_{24}]^{7-}$ anion determined in the solid-state (bottom) and DFT calculated (top).



bonds. The peak at 523 cm^{-1} in the experimental spectrum shifts by 13 cm^{-1} and thus appears at 510 cm^{-1} in the calculated spectrum and shows symmetric degenerate stretching of Sb–O bonds. The small peak at 590 cm^{-1} in the calculated spectrum correlates with the experimental peak at 585 cm^{-1} and refers to asymmetric of Sb–O bonds stretch. The large peak at 674 cm^{-1} in the calculated spectrum (experimental 727 cm^{-1}) shows the O–W–O bond stretch along the vertex. The peaks at 865 and 945 cm^{-1} in the experimental spectrum appear at 869 and 914 cm^{-1} in the calculated spectrum and belong to the anti-symmetric and symmetric $\text{W}=\text{O}_t$ bond stretches, respectively. In summary, the vibrational spectra confirm the Anderson–Evans structure for the bulk material. The assignment of IR and Raman spectral peaks is summarized in Table 4.

The same experiment was also performed at a pH value of 1, which however yielded a mixture of tungsten oxide (WO_3) and antimony(v) oxide Sb_2O_5 , which were identified by powder X-ray diffraction (Fig. 7).

Table 4 Assignment of IR and Raman spectral peak positions of $[\text{SbW}_6\text{O}_{24}]^{7-}$

Peak position/ cm^{-1}	Assignment ^c
352^b	$\text{O}_t=\text{Sb}=\text{O}_t$ scissoring
419^a	Sb–O (bending) Sb–O (stretching)
523^a	Sb–O scissoring (in-plane)
553^b	$\text{W}=\text{O}=\text{W}$ bending
585^a	Sb–O stretch (asymmetric)
727^a	O–W–O (vertex)
865^a	$\text{W}=\text{O}_t$ (anti-symmetric)
945^a	$\text{W}=\text{O}_t$ (symmetric)

^a FTIR. ^b Raman. ^c From calculations.

2.2.5. Comparative summary. In summary, we observed several different structure types being formed by the combination of group 15 precursors with sodium tungstate (Fig. 17). Selected structural features are summarized in Table 5.

The experimental results are summarized in Fig. 17. From these results in combination with our computational studies, we conclude that the formation of the different structure types depends not only on the pH value, but is also highly dependent of the atomic radius of the heteroelement involved.

In agreement with our computational and experimental results, $\text{N}(\text{v})$ is too small (0.16 \AA)³³ for both coordination motifs, furthermore it forms the planar NO_3^- ion instead of a tetrahedral NO_4^{3-} ion. Therefore, the thermodynamically preferred structure type of tungstate at pH 5 is formed without a heteroatom. In the strongly acidic medium (pH 1), decomposition of the paradodecatungstate B anion to the tungsten oxide was observed, which can be explained by an instability caused by the absence of a heteroatom. $\text{P}(\text{v})$ (0.38 \AA)³³ forms a tetrahedral PO_4^{3-} structural motif, which in agreement with the DFT calculations leads to the formation of a Keggin anion in highly acidic media (pH 1). At higher pH values (5) the Keggin structure of $[\text{PW}_{12}\text{O}_{40}]^{3-}$ becomes unstable and the $[\text{P}_4\text{W}_{14}\text{O}_{58}]^{12-}$ anion is formed instead, which still contains tetrahedrally coordinated P atoms. Mechanistically, the latter structure is probably formed *via* the former structure *via* a Keggin-lacunary intermediate, which is known to form in more basic media, as the lower proton concentration leads to dissociation of individual metal–oxygen polyhedra from the POM cluster.⁵⁹ $\text{As}(\text{v})$ (atomic radius of 0.46 \AA)³³ is known to prefer the tetrahedral coordination geometry (*e.g.* in H_3AsO_4),³⁴ but the Keggin formation seems to be more difficult due to the, compared to $\text{P}(\text{v})$, high atomic radius and subsequent larger heteroatom polyhedron. Thus, the formation of the open lacunary Keggin structure seems to be thermodynamically preferred. This structure is further stabil-

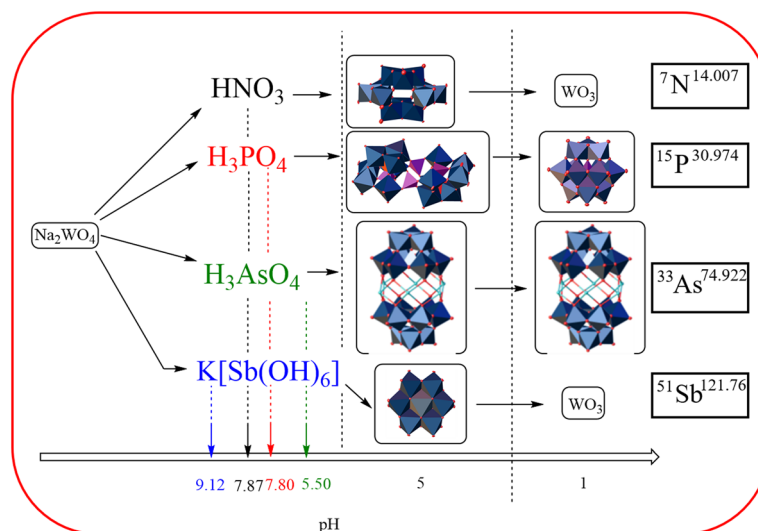


Fig. 17 Formation of different POM structure types in dependence of the heteroelement and pH value.



Table 5 Selected bond lengths in single-crystal structures (comparison to the calculated values)

	Bond length [Å]				
	[W ₁₂ O ₄₀] ⁸⁻	[P ₄ W ₁₄ O ₅₈] ¹²⁻	[AsW ₉ O ₃₄] ⁹⁻	[SbW ₆ O ₂₄] ⁷⁻	Sum of covalent radii ⁵⁸
P–O _a	n.a.	1.537 (1.524)	n.a.	n.a.	1.74
As–O _a	n.a.	n.a.	1.683 (1.678)	n.a.	1.84
Sb–O _a	n.a.	n.a.	n.a.	1.984 (2.01)	2.03
O _a –W	n.a.	2.262 (2.33)	2.370 (2.373)	2.224 (2.243)	2.00
W–O _b	1.935 (1.971)	1.879 (1.869)	1.943 (1.939)	1.941 (1.951)	2.00
W–O _c	2.236 (2.172)	2.131 (2.195)			2.00
W=O _t	1.742 (1.743)	1.738 (1.737)	1.742 (1.754)	1.748 (1.765)	2.00
O _t –Na	2.410	2.370	2.878 (2.491)	n.a.	2.18
Na–O _w	2.419	2.395	2.583	2.406	2.18

n.a.: not applicable.

ized by the formation of a coordination dimer, in which two [AsW₉O₃₄]⁹⁻ units are held together by six alkali ions. The stability of this structure is sufficiently high, that its formation is unaffected by the different pH values. In contrast, Sb(v) (0.60 Å) preferentially forms octahedral motifs (coordination number 6).³³ As predicted by DFT calculations, the addition of Sb(v) leads to the formation of an Anderson–Evans type POM at pH 5 in which all metal atoms, including the central heteroatom, are coordinated octahedrally. Outside of the pH range in which Anderson–Evans structures are stable, the respective oxides (WO₃, Sb₂O₅) are formed.

3. Experimental procedures

Detailed synthetic procedures can be found in the ESI.†

The arsenic(v) solution was prepared by dissolving arsenic (iii) oxide in a mixture of a 30% solution of hydrogen peroxide (30 mL) and water (30 mL) under reflux for two hours.

The antimony(v) solution was prepared by refluxing potassium hexahydroxoantimonate(v) in water (100 mL) for one hour.

In a general procedure sodium tungstate dihydrate was dissolved in water or added to the respective As(v)/Sb(v) solution. The start volume of the reaction mixture was always 100 mL of an aqueous solution. For the experiments with the heteroelements N(v) and P(v) a 4 M solution of nitric acid or 25 wt% phosphoric acid solution in water was added to the aqueous sodium tungstate solution. The pH value was adjusted to 5 or 1 using a 37% solution of hydrochloric acid in water and the solution was concentrated under reduced pressure (85 °C, 200 to 0 mbar). All compounds were purified according to our previous published dialysis approach.^{21,37}

Further characterization of all POMs by compositional analysis (ICP-OES) and thermogravimetric analysis, (TGA) is shown in the ESI, Table S3.† ³¹P-NMR spectroscopy was done for Na₁₂[P₄W₁₄O₅₈] and Na₃[PW₁₂O₄₀] and is presented in Fig. S1 and S2.† UV-Vis measurements were performed for all POMs and the data were analyzed according to the Lambert–Beer's law as shown in Tables S5, S6 and Fig. S3–S8 (ESI†). Precise analytical characterization of the anion [PW₁₂O₄₀]³⁻

was done in our previously published study,²² therefore we do not present further characterization of this compound here.

Computational details can be found in the ESI.†

4. Conclusion

In this work, we present a combined computational and experimental study on the influence of different group 15 elements on the formation of various POM structures. Our DFT calculations suggest that the formation of a Keggin-type structure is preferred for elements with small atomic radii (such as P) and unlikely for elements with large radii (such as Sb). The trend is reversed for the formation of the Anderson–Evans structure. Our crystallographic and spectroscopic data are in agreement with the computational results. For P(v), the Keggin anion [PW₁₂O₄₀]³⁻ was formed in strongly acidic (pH 1) media vs. the formation of [P₄W₁₄O₅₈]¹²⁻ at pH 5. Here, P(v) was found to be tetrahedrally coordinated in both structural motifs. As(v) also prefers tetrahedral coordination motifs, but the larger As(v) atom radius causes stress on the confined Keggin structure, resulting in the formation of lacunary structures such as the [AsW₉O₃₄]⁹⁻ anion. In agreement with the calculations, the formation of the Anderson–Evans anion [SbW₆O₂₄]⁷⁻ was observed at pH 5 using Sb(v). In contrast, decomposition of the anion to oxidic materials was observed at pH 1. In agreement with the computational data, the small N(v) atom is an outlier due to its small atomic radius, and the anomaly of forming a tri-coordinate oxoanion (NO₃⁻). As a result, it is not involved in the formation of POM structures. This can be seen in the relative thermodynamics of formation, which gave the highest relative energy (compared to [PW₁₂O₄₀]³⁻) for the hypothetical [NW₁₂O₄₀]³⁻ anion, while structural optimization for the [NW₆O₂₄]⁷⁻ anion was not successful.

All compounds were characterized by additional spectroscopic methods in the solid-state and in aqueous solution. An assignment of the different vibrational bands to the vibrational modes was possible using DFT calculated peak positions. The data obtained are of particular interest for the less common structure types such as the lacunar-based motifs [AsW₉O₃₄]⁹⁻,



$[P_4W_{14}O_{58}]^{12-}$, and even the Anderson–Evans structure $[SbW_6O_{24}]^{7-}$. In contrast to the Keggin structure, where the P–O vibrational band is observed in the range 1000 to 1100 cm^{-1} , the various As–O–W vibrational bands in the lacunar-based structural motifs are found at 837 and 797 cm^{-1} . For the Anderson–Evans structure, the different types of Sb–O vibrational bands were found at 435, 470, 510 and 590 cm^{-1} .

The results presented here contribute to the understanding and control of POM formation, in particular, the formation of different structure types as a function of heteroelement and pH. From the results presented here, a clear trend can be observed for the group 15 elements P(v), As(v) and Sb(v), whereas N(v) is incompatible for POM chemistry.

Author contributions

Jan-Christian Raabe: conceptualization, investigation, visualization, writing the original draft. Froze Jameel: investigation, visualization, writing – review and editing. Matthias Stein: funding acquisition, resources, supervision, investigation, writing – review and editing. Jakob Albert: funding acquisition, resources, writing – review and editing. Maximilian J. Poller: project administration, supervision, conceptualization, writing – review and editing.

Conflicts of interest

The authors declare no conflict of interest.

Acknowledgements

The authors thank the central elemental analysis team of Dr Dirk Eifler for measuring numerous ICP-OES samples for different elements. We thank Ute Gralla for measuring the Raman spectra, and the X-ray service team of Dr Frank Hoffmann and especially Isabelle Nevoigt for measuring numerous single-crystal XRD samples. Prof. Dr Matthias Stein and Froze Jameel are grateful to the Max Planck Society of the Advancement of Science for financial support and the Research Initiative “SmartProSys: Intelligent Process Systems for the Sustainable Production of Chemicals” funded by the Ministry for Science, Energy, Climate Protection and the Environment of the State of Saxony-Anhalt.

References

- 1 R. Dehghani, S. Aber and F. Mahdizadeh, Polyoxometalates and Their Composites as Photocatalysts for Organic Pollutants Degradation in Aqueous Media—A Review, *Clean: Soil, Air, Water*, 2018, **46**, DOI: [10.1002/clean.201800413](https://doi.org/10.1002/clean.201800413).
- 2 M. T. Pope and A. Müller, Chemie der Polyoxometallate: Aktuelle Variationen über ein altes Thema mit interdisziplinären Bezügen, *Angew. Chem.*, 1991, **103**, 56–70.
- 3 J. Albert, D. Lüders, A. Bösmann, D. M. Guldi and P. Wasserscheid, Spectroscopic and electrochemical characterization of heteropoly acids for their optimized application in selective biomass oxidation to formic acid, *Green Chem.*, 2014, **16**, 226–237.
- 4 M. T. Pope and A. Müller, Polyoxometalate Chemistry: An Old Field with New Dimensions in Several Disciplines, *Angew. Chem., Int. Ed. Engl.*, 1991, **30**, 34–48.
- 5 J.-C. Raabe, M. J. Poller, D. Voß and J. Albert, $H_8[PV_5Mo_7O_{40}]$ – A Unique Polyoxometalate for Acid and RedOx Catalysis: Synthesis, Characterization, and Modern Applications in Green Chemical Processes, *ChemSusChem*, 2023, **16**, 2013–2015.
- 6 A. Modvig, C. Kumpidet, A. Riisager and J. Albert, Ru-Doped Wells–Dawson Polyoxometalate as Efficient Catalyst for Glycerol Hydrogenolysis to Propanediols, *Materials*, 2019, **12**, 2175.
- 7 I. A. Weinstock, J. J. Cowan, E. M. G. Barbuzzi, H. Zeng and C. L. Hill, Equilibria between α and β Isomers of Keggin Heteropolytungstates, *J. Am. Chem. Soc.*, 1999, **121**, 4608–4617.
- 8 D. Lockey, C. Mathis, H. N. Miras and L. Cronin, Investigating the autocatalytically driven formation of Keggin-based polyoxometalate clusters, *Matter*, 2022, **5**, 302–313.
- 9 L. E. Briand, H. J. Thomas and G. T. Baronetti, Thermal stability and catalytic activity of Wells-Dawson tungsten heteropoly salts, *Appl. Catal., A*, 2000, **201**, 191–202.
- 10 J. D. H. Strickland, The Preparation and Properties of Silicomolybdic Acid. I. The Properties of Alpha Silicomolybdic Acid, *J. Am. Chem. Soc.*, 1952, **74**, 862–867.
- 11 J. Canny, R. Thouvenot, A. Teze, G. Herve, M. Leparulo-Loftus and M. T. Pope, Disubstituted tungstosilicates. 2. .gamma.- and .beta.-isomers of tungstovanadosilicate, $[SiV_2W_{10}O_{40}]^{6-}$: syntheses and structure determinations by tungsten-183, vanadium-51 and silicon-29 NMR spectroscopy, *Inorg. Chem.*, 1991, **30**, 976–981.
- 12 J.-C. Raabe, J. Albert and M. J. Poller, Spectroscopic, Crystallographic, and Electrochemical Study of Different Manganese(II)-Substituted Keggin-Type Phosphomolybdates, *Chem. – Eur. J.*, 2022, **28**, 1–12.
- 13 V. F. Odyakov and E. G. Zhizhina, A novel method of the synthesis of molybdovanadophosphoric heteropoly acid solutions, *React. Kinet. Catal. Lett.*, 2008, **95**, 21–28.
- 14 V. F. Odyakov, E. G. Zhizhina and R. I. Maksimovskaya, Synthesis of molybdovanadophosphoric heteropoly acid solutions having modified composition, *Appl. Catal., A*, 2008, **342**, 126–130.
- 15 V. F. Odyakov and E. G. Zhizhina, New process for preparing aqueous solutions of Mo-V-phosphoric heteropoly acids, *Russ. J. Inorg. Chem.*, 2009, **54**, 361–367.
- 16 E. G. Zhizhina and V. F. Odyakov, Alteration of the physico-chemical properties of catalysts based on aqueous solu-



- tions of Mo-V-P heteropoly acids in redox processes, *React. Kinet. Catal. Lett.*, 2008, **95**, 301–312.
- 17 I.-M. Mbomekalle, Y. W. Lu, B. Keita and L. Nadjo, Simple, high yield and reagent-saving synthesis of pure α - $K_6P_2W_{18}O_{62} \cdot 14H_2O$, *Inorg. Chem. Commun.*, 2004, **7**, 86–90.
 - 18 D. R. Park, H. Kim, J. C. Jung, S. H. Lee and I. K. Song, Reduction potentials of $H_{3+x}PMo_{12-x}V_xO_{40}$ and $H_{6+x}P_2Mo_{18-x}V_xO_{62}$ heteropolyacid (HPA) catalysts and their catalytic activity for the vapor-phase oxidative dehydrogenation of isobutyric acid, *Catal. Commun.*, 2008, **9**, 293–298.
 - 19 M.-X. Xu, S. Lin, L.-M. Xu and S.-L. Zhen, Crystal structure and properties of $H_3[PMo_{12}O_{40}] \cdot 3C_2H_6O$, *Transition Met. Chem.*, 2004, **29**, 332–335.
 - 20 M. J. Poller, S. Bönisch, B. Bertleff, J.-C. Raabe, A. Görling and J. Albert, Elucidating activating and deactivating effects of carboxylic acids on polyoxometalate-catalysed three-phase liquid–liquid–gas reactions, *Chem. Eng. Sci.*, 2022, **264**, 118143.
 - 21 J.-C. Raabe, T. Esser, F. Jameel, M. Stein, J. Albert and M. J. Poller, Study on the incorporation of various elements into the Keggin lacunary-type phosphomolybdate $[PMo_9O_{34}]^{9-}$ and subsequent purification of the polyoxometalates by nanofiltration, *Inorg. Chem. Front.*, 2023, **10**, 4854–4868.
 - 22 J.-C. Raabe, J. Aceituno Cruz, J. Albert and M. J. Poller, Comparative Spectroscopic and Electrochemical Study of V(V)-Substituted Keggin-Type Phosphomolybdates and -Tungstates, *Inorganics*, 2023, **11**, 138.
 - 23 K. J. Schmidt, G. J. Schrobilgen and J. F. Sawyer, Hexasodium Hexatungstotellurate(VI) 22-Hydrate, *Acta Crystallogr., Sect. C: Cryst. Struct. Commun.*, 1986, **42**, 1115–1118.
 - 24 D. Ghosh and R. Biswas, Theoretical Calculation of Absolute Radii of Atoms and Ions. Part 1. The Atomic Radii, *Int. J. Mol. Sci.*, 2002, **3**, 87–113.
 - 25 J. C. Slater, Atomic Radii in Crystals, *J. Chem. Phys.*, 1964, **41**, 3199–3204.
 - 26 R. D. Shannon and C. T. Prewitt, Effective ionic radii and crystal chemistry, *J. Inorg. Nucl. Chem.*, 1970, **32**, 1427–1441.
 - 27 Y. Q. Jia, Crystal radii and effective ionic radii of the rare earth ions, *J. Solid State Chem.*, 1991, **95**, 184–187.
 - 28 R. D. Shannon, Revised effective ionic radii and systematic studies of interatomic distances in halides and chalcogenides, *Acta Crystallogr., Sect. A: Cryst. Phys., Diffraction, Theor. Gen. Crystallogr.*, 1976, **32**, 751–767.
 - 29 R. D. Shannon and C. T. Prewitt, Revised values of effective ionic radii, *Acta Crystallogr., Sect. B: Struct. Crystallogr. Cryst. Chem.*, 1970, **26**, 1046–1048.
 - 30 M. Rahm, R. Hoffmann and N. W. Ashcroft, Atomic and Ionic Radii of Elements 1–96, *Chem. – Eur. J.*, 2016, **22**, 14625–14632.
 - 31 D. W. J. Cruickshank, Refinements of structures containing bonds between Si, P, S or Cl and O or N. V. P_4O_{10} , *Acta Crystallogr.*, 1964, **17**, 677–679.
 - 32 M. Jansen, Die Kristallstruktur von Antimon(V)-oxid, *Acta Crystallogr., Sect. B: Struct. Crystallogr. Cryst. Chem.*, 1979, **35**, 539–542.
 - 33 U. Müller, *Anorganische Strukturchemie*, Vieweg+Teubner, Wiesbaden, 6th edn, 2008.
 - 34 A. F. Holleman, E. Wiberg, N. Wiberg and G. Fischer, *Lehrbuch der Anorganischen Chemie*, Berlin, New York, 2009.
 - 35 D. Drewes, E. M. Limanski and B. Krebs, The Anderson-Type Anion $(TeMo_6O_{24})^{6-}$ – A Multidentate Ligand for Trivalent Rare Earth Cations, *Eur. J. Inorg. Chem.*, 2004, 4849–4853.
 - 36 S. Himeno, M. Hashimoto and T. Ueda, Formation and conversion of molybdophosphate and -arsenate complexes in aqueous solution, *Inorg. Chim. Acta*, 1999, **284**, 237–245.
 - 37 T. Esser, M. Huber, D. Voß and J. Albert, Development of an efficient downstream process for product separation and catalyst recycling of a homogeneous polyoxometalate catalyst by means of nanofiltration membranes and design of experiments, *Chem. Eng. Res. Des.*, 2022, **185**, 37–50.
 - 38 K. Sifaki, N. I. Gumerova, G. Giester and A. Rompel, Crystal structure of hexasodium tetraserinolium paratungstate B decahydrate, $[Na_6\{(CH_2OH)_2CHNH_3\}_4][W_{12}O_{40}(OH)_2] \cdot 10H_2O$, *Acta Crystallogr., Sect. E: Crystallogr. Commun.*, 2022, **78**, 207–210.
 - 39 X. Qu, Y. Yang, F. Zhang and X. Yu, Synthesis and characterization of a three-dimensional framework built up of paradodecatungstate-B clusters and transition metals as linkers, *Struct. Chem.*, 2012, **23**, 1867–1872.
 - 40 C.-J. Zhang, H.-J. Pang and Y.-G. Chen, Highest Connectivity in a Purely Inorganic 3D Compound Based on Paradodecatungstate-B Clusters: Synthesis and Magnetic Properties, *Z. Naturforsch. B*, 2009, **64**, 809–814.
 - 41 X. Qu, Y. Yang, X. Yu, Z. Lv, M. Ji and S. Y. Feng, A novel paradodecatungstate-B compound decorated by transition metal copper, $Na_2Cu_5(H_2O)_{24}(OH)_2[H_2W_{12}O_{42}] \cdot 10H_2O$: Synthesis, structure and antitumor activities, *Inorg. Chem. Commun.*, 2015, **60**, 126–130.
 - 42 B. Courcot and A. J. Bridgeman, Structural and Vibrational Study of $[Mo_7O_{24}]^{6-}$ and $[W_7O_{24}]^{6-}$, *J. Phys. Chem. A*, 2009, **113**, 10540–10548.
 - 43 A. J. Bridgeman, Computational Study of Solvent Effects and the Vibrational Spectra of Anderson Polyoxometalates, *Chem. – Eur. J.*, 2006, **12**, 2094–2102.
 - 44 A. J. Bridgeman and G. Cavigliasso, A Comparative Investigation of Structure and Bonding in Mo and W $[TeM_6O_{24}]^{6-}$ and $[PM_{12}O_{40}]^{3-}$ Heteropolyanions, *J. Phys. Chem. A*, 2003, **107**, 6613–6621.
 - 45 K. Sifaki, N. I. Gumerova, G. Giester and A. Rompel, Synthesis and characterization of the Anderson–Evans tungstoantimonate $[Na_5(H_2O)_{18}\{(HOCH_2)_2CHNH_3\}_2][SbW_6O_{24}]$, *Acta Crystallogr., Sect. C: Struct. Chem.*, 2021, **77**, 420–425.
 - 46 J. K. Lee, J. Melsheimer, S. Berndt, G. Mestl, R. Schlögl and K. Köhler, Transient responses of the local electronic and geometric structures of vanado-molybdo-phosphate catalysts



- $H_{3+n}PV_nMo_{12-n}O_{40}$ in selective oxidation, *Appl. Catal., A*, 2001, **214**, 125–148.
- 47 S. Himeno, M. Takamoto and T. Ueda, Formation of α - and β -Keggin-Type $[PW_{12}O_{40}]^{3-}$ Complexes in Aqueous Media, *Bull. Chem. Soc. Jpn.*, 2005, **78**, 1463–1468.
- 48 J. F. Keggin, The structure and formula of 12-phosphotungstic acid, *Proc. R. Soc. London, Ser. A*, 1934, **144**, 75–100.
- 49 P. Pérez-Romo, C. Potvin, J.-M. Manoli and G. Djéga-Mariadassou, Phosphorus-Doped Tungsten Oxynitrides: Synthesis, Characterization, and Catalytic Behavior in Propene Hydrogenation and n-Heptane Isomerization, *J. Catal.*, 2002, **205**, 191–198.
- 50 R. Thouvenot, A. Teze, R. Contant and G. Herve, Synthesis, structure, and phosphorus-31 and tungsten-183 NMR spectra of tungstophosphate, $P_4W_{14}O_{58}^{12-}$, *Inorg. Chem.*, 1988, **27**, 524–529.
- 51 L. H. Bi, E. B. Wang, J. Peng, R. D. Huang, L. Xu and C. W. Hu, Crystal structure and replacement reaction of coordinated water molecules of the heteropoly compounds of sandwich-type tungstoarsenates, *Inorg. Chem.*, 2000, **39**, 671–679.
- 52 N. I. Gumerova, E. Al-Sayed, L. Krivosudský, H. Čipčić-Paljetak, D. Verbanac and A. Rempel, Antibacterial activity of polyoxometalates against *Moraxella catarrhalis*, *Front. Chem.*, 2018, **6**, 1–9.
- 53 L. Berța Grama, F. Boda, G. Borodi, A. Rusu, H. Kelemen, A. Man, A. Mare and Ș. A. Gâz-Florea, Two new sandwich-type compounds based on $\{AsW_9\}$ with Pd^{2+} and Pt^{4+} cations – synthesis, characterization and antibacterial activity, *Farmacia*, 2017, **65**, 63–68.
- 54 J. R. Rea, J. B. Anderson and E. Kostiner, The crystal structures of copper chloroarsenate and cobalt chloroarsenate, $Cu_2(AsO_4)Cl$ and $Co_2(AsO_4)Cl$, *Acta Crystallogr., Sect. B: Struct. Crystallogr. Cryst. Chem.*, 1977, **33**, 975–979.
- 55 S. Himeno, M. Takamoto, R. Santo and A. Ichimura, Redox Properties and Basicity of Keggin-Type Polyoxometalate Complexes, *Bull. Chem. Soc. Jpn.*, 2005, **78**, 95–100.
- 56 C. Rocchiccioli-Deltcheff, M. Fournier, R. Franck and R. Thouvenot, Vibrational investigations of polyoxometalates. 2. Evidence for anion-anion interactions in molybdenum(VI) and tungsten(VI) compounds related to the Keggin structure, *Inorg. Chem.*, 1983, **22**, 207–216.
- 57 J. Piquemal, L. Salles, G. Chottard, P. Herson, C. Ahcine and J. Brégeault, Another Example of the Instability of a Keggin-Type Heteropolyanion in the Presence of Aqueous Hydrogen Peroxide: From $[AsW_{12}O_{40}]_3^-$ to Low-Nuclearity Oxoperoxotungstates – Crystal Structure of $[(nHex)_4N]_3[AsO_4\{W_2O_2(\mu-O_2)_2(O_2)_2\}_2]$, *Eur. J. Inorg. Chem.*, 2006, 939–947.
- 58 P. Pyykkö and M. Atsumi, Molecular Single-Bond Covalent Radii for Elements 1–118, *Chem. – Eur. J.*, 2009, **15**, 186–197.
- 59 D. Gabb, C. P. Pradeep, H. N. Miras, S. G. Mitchell, D.-L. Long and L. Cronin, Organic-soluble lacunary $\{M_2(P_2W_{15})_2\}$ polyoxometalate sandwiches showing a previously unseen $\alpha\beta\beta\alpha$ isomerism, *Dalton Trans.*, 2012, **41**, 10000–10005.



5.6 Synthese, Charakterisierung und katalytische Anwendungen V(V) substituierter Anderson-Evans Polyoxometallate für die oxidative Umsetzung von Monofuranderivaten

P6

Synthesis and characterization of V substituted Anderson-type telluro-molybdates and tungstates for catalytic oxidation of furan derivatives to formic and maleic acid

Jan-Christian Raabe, Tobias Esser, Maximilian J. Poller, Jakob Albert

Raabe, J.-C.; Esser, T.; Poller, M. J.; Albert, J. Synthesis and characterization of V substituted Anderson-type telluro-molybdates and tungstates for catalytic oxidation of furan derivatives to formic and maleic acid. *Catal. Today* **2024**, *441*, 114899. <https://doi.org/10.1016/j.cattod.2024.114899>.

In der Studie P6 konnte das Konzept der Übergangsmetallsubstitution erfolgreich auf den Anderson-Evans-Strukturtyp erweitert werden (P6, *Catal. Today* **2024**, *441*, 114899).^[251] Als Substitutionselement diente V(V) und als Modellstrukturen wurden die schon bekannten Molybdo- und Wolframatotellurate verwendet. Die Synthese der substituierten TMSPOMs gelang nach einer *self-assembly* Prozedur bei pH 5 in wässriger Lösung. Dabei erwiesen sich die V(V) substituierten Molybdotellurate als instabil in wässriger Lösung, da die Lösungen das unsubstituierte Molybdotellurat abschieden. Eine Isolierung der TMSPOMs als Reinstoff war daher nicht möglich, da die zur Präzipitation neigenden TMSPOMs nicht über die Nanofiltration entsalzt werden konnten. Wässrige Lösungen der V(V) substituierten Wolframatotellurate erwiesen sich auch über einen längeren Zeitraum hinweg als lagerstabil und konnten mittels Nanofiltration erfolgreich entsalzt werden. Die TMSPOMs wurden allesamt mit verschiedenen spektroskopischen, kristallographischen und elektrochemischen Methoden charakterisiert, siehe hierzu Abbildung 25. Zwar zeigten die V(V) substituierten Molybdotellurate in den elektrochemischen Daten eine ausgeprägtere RedOx-Chemie als die Wolframatotellurate, jedoch war eine Verwendung der V(V) substituierten Molybdotellurate als homogene RedOx-Katalysatoren nicht möglich. Daher wurden die katalytischen Experimente nur mit den V(V) substituierten Wolframatotelluraten durchgeführt. Untersucht wurde die oxidative Umsetzung von verschiedenen Monofuranderivaten. In einem ersten Katalysatorscreening konnte der TMSPOM NaTeV₃W als aktivster Katalysator in Bezug auf die Umsetzung von Furfural zu Maleinsäure (MS) und FA identifiziert werden, sodass die zweite Substratscreeningexperimentreihe mit NaTeV₃W als Katalysator geplant wurden. Als Produkte wurden im Wesentlichen die Plattformchemikalien FA (C₁) und MS (C₄) gefunden, wobei FA durch oxidative Spaltung des sauerstofffunktionalisierten C₁-Fragmentes der Monofuranderivate gebildet wurde. MS bildete sich anschließend durch Umlagerung bzw. Oxidation am verbleibenden C₄-Fragment. Auf Basis der mittels *high performance liquid chromatography* (HPLC) gefundenen Reaktionsprodukte wurde ein potenzieller Katalysemechanismus postuliert. In den katalytischen Umsetzungen zeigte der TMSPOM-Katalysator NaTeV₃W eine besonders hohe Reaktivität gegenüber bereits sauerstofffunktionalisierten Monofuranderivaten. Limitierungen ergaben sich für die nicht- (Furanon) bzw. geringfügig funktionalisierten Derivate (2-Methylfuran), da an den Substraten keine funktionellen Gruppen für den Angriff des Katalysators vorhanden sind. Die so gewonnenen Struktur-Eigenschaftsbeziehungen erweitern das Verständnis in Bezug auf die oxidative Umsetzung komplexerer Biomassepolymere, deren Zusammensetzung auf Monofuranmonomeren ba-

siert. Als Beispiel lässt sich die katalytische Umsetzung von Huminen zu Wertprodukten anführen, die sonst als Abfallprodukte gelten und daher meistens entsorgt werden.^[251]

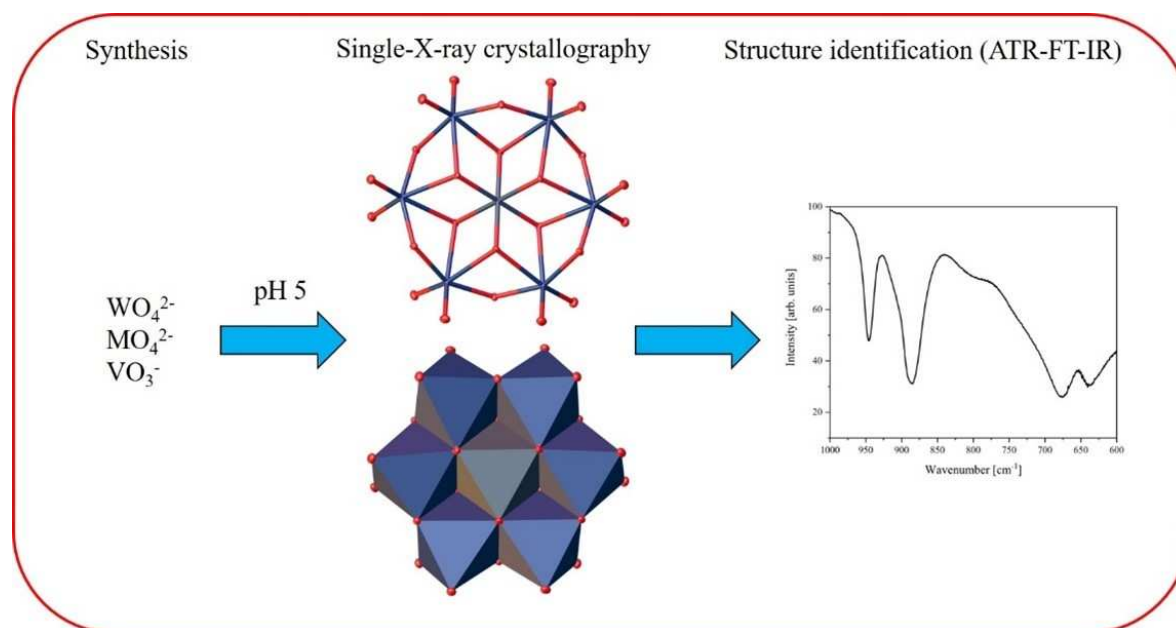


Abb. 25: Strukturidentifikation der Anderson-Evans-Typ POMs aus P6, *Catal. Today* **2024**, *441*, 114899. Synthese eines POMs in wässriger Lösung, Analyse der zugehörigen sc-XRD Daten und Interpretation des IR-Schwingungsspektrums vom Bulk-Material.^[251]



Synthesis and characterization of V substituted Anderson-type telluro-molybdates and tungstates for catalytic oxidation of furan derivatives to formic and maleic acid

Jan-Christian Raabe¹, Tobias Esser², Maximilian J. Poller³, Jakob Albert^{*,4}

Institute for Technical and Macromolecular Chemistry, Universität Hamburg, Bundesstraße 45, Hamburg 20146, Germany

ARTICLE INFO

Keywords:

Polyoxometalate
Transition-element substitution
Anderson-Evans structure
Catalysis
Oxidation
Biomass

ABSTRACT

Transition-metal substitution in polyoxometalates (POMs) is a well-established concept in POM chemistry. However, so far there are no well-founded studies in literature that deal with the selective substitution of one or more framework/addenda elements in the Anderson-Evans structure. Therefore, a concept of synthesizing Anderson-Evans-type POMs where the addenda elements are replaced by various RedOx active transition-metals would be useful from a catalytic point of view to produce new structures for RedOx catalytic applications. An interesting RedOx-active element is vanadium in the oxidation state +V. In this study, we report an experimental procedure to synthesize different V(+V) substituted Anderson-Evans-type molybdo- and tungstotellurates. The new compounds were characterized in detail both in solid-state as well as in aqueous solution by using different spectroscopic and electrochemical methods like vibrational (FTIR-, Raman) as well as magnetic (⁵¹V NMR) and UV-Vis spectroscopy. Finally, the successfully synthesized Anderson-Evans structures were applied as homogeneous catalysts in aqueous solution for the selective catalytic oxidation of monofuran derivatives to short-chain carboxylic acids to investigate their potential as RedOx catalysts.

1. Introduction

The Anderson-Evans structure represents a polyoxometalate (POM) structure-type composed of seven metal-oxygen octahedra in a planar arrangement. [1–3] The planar geometry was already postulated by Anderson [5] in 1937 and confirmed by Evans [6] in 1948 using single crystal structure analysis of the molybdotellurate anion [TeMo₆O₂₄]⁶⁻. The metal (usually Mo or W) can be the same for all octahedra forming a so-called isopolyanion, or alternatively the central octahedron contains a different “hetero-“ element (e.g. Te), thereby forming a heteropolyanion. [1,4] [7]

Prominent examples of Anderson-Evans isopolyanions are [Mo₇O₂₄]⁶⁻ and [W₇O₂₄]⁶⁻, which are known as paramolybdate/isopolymolybdate and paratungstate/isopolytungstate. [7] The latter polyanion presumably exists only in aqueous solution and it is impossible to

isolate it without the use of complex organometallic cations. [8,9] This can be explained by the fact that the paratungstate A [W₇O₂₄]⁶⁻ ion is in equilibrium with the paratungstate B anion [H₂W₁₂O₄₂]¹⁰⁻, and the position of the equilibrium shifts to the side of the paratungstate B anion during crystallization. [10] Therefore, the shift of the equilibrium in favor of the paratungstate A anion requires special crystallization conditions, such as the addition of special inorganic/organic cations. [11] The anion [Mo₇O₂₄]⁶⁻ on the other hand is stable and commercially available e.g. as ammonium salt (NH₄)₆[Mo₇O₂₄]. [12]

Most Anderson-Evans type compounds belong to the heteropolyanion category, in which X is clearly defined, e.g., as tellurium Te, whereby different cations are used. [2,13,14] There are also studies known where the central heteroelement position is replaced by an additional transition-element e.g. vanadium, nickel, chromium, or manganese, resulting in structures like [VMo₆O₂₄]⁷⁻, [NiMo₆O₂₄]¹⁰⁻,

* Corresponding author.

E-mail addresses: JanChristian.Raabe@uni-hamburg.de (J.-C. Raabe), Tobias.Esser@uni-hamburg.de (T. Esser), Maximilian.Poller@uni-hamburg.de (M.J. Poller), jakob.albert@uni-hamburg.de (J. Albert).

¹ ORCID: 0000-0002-8240-1355

² ORCID: 0000-0002-7939-3593

³ ORCID: 0000-0002-7146-131X

⁴ ORCID: 0000-0002-3923-2269

[CrMo₆O₂₄]⁶⁻, [MnW₆O₂₄]⁸⁻. [9,15,16] The addenda elements of choice are Mo and W, resulting in the parent compounds [TeMo₆O₂₄]⁶⁻ (molybdotellurate) and [TeW₆O₂₄]⁶⁻ (tungstotellurate). [17–19] In contrast, the selective substitution of one or more addenda elements by additional transition-elements in the Anderson-Evans structure is not yet established. For other structure-types, such as the Keggin-, the Wells-Dawson- and the Lindqvist-structure, the substitution of addenda elements already represents a well-established research area. [4,20–28] An interesting transition-element for substitution is vanadium in the oxidation state +V as it introduces additional RedOx activity as V(+V). [20,28] The resulting transition-metal substituted POMs (TMSPOMs) are interesting candidates for RedOx catalytic applications, since the V (+V) improves the RedOx activity of the corresponding molybdate or tungstate accordingly. [29–31] The numerous applications of TMSPOMs highlight the relevance of applying the concept of transition-metal substitution to other types of POM-compounds such as the Anderson-Evans structure. Herein, we want to apply the V-substituted molybdo- and tungstotellurates as RedOx catalysts for the homogeneously catalyzed oxidation of furan(derivatives) to short-chain carboxylic acids.

2. Results and discussion

2.1. Synthetic strategy

The synthesis of the different V(+V) substituted Anderson-Evans POMs is based on a *self-assembly* approach analogue to Wood *et al.* [18] as shown in Figs. 1 and 2.

Sodium tungstate or molybdate, sodium vanadate, and telluric acid where dissolved in deionized water in the desired target stoichiometry and heated to 60 °C. The formation of the Anderson-Evans structure is then induced by adjusting the pH value to 5 by addition of concentrated hydrochloric acid. Subsequently, the unavoidable sodium chloride, formed during the synthetic procedure, was removed using a previously reported nanofiltration process. [24,32] Finally, the solvent was removed at 85 °C under reduced pressure, to obtain the pure compound as a solid powder.

During the synthetic procedures (see ESI and Table S1 and S2), aqueous solutions of the V(+V) substituted tungstates remain stable over time, whereby aqueous solutions of the V(+V) substituted molybdates NaTeMo showed partial precipitation. Therefore, the synthesis

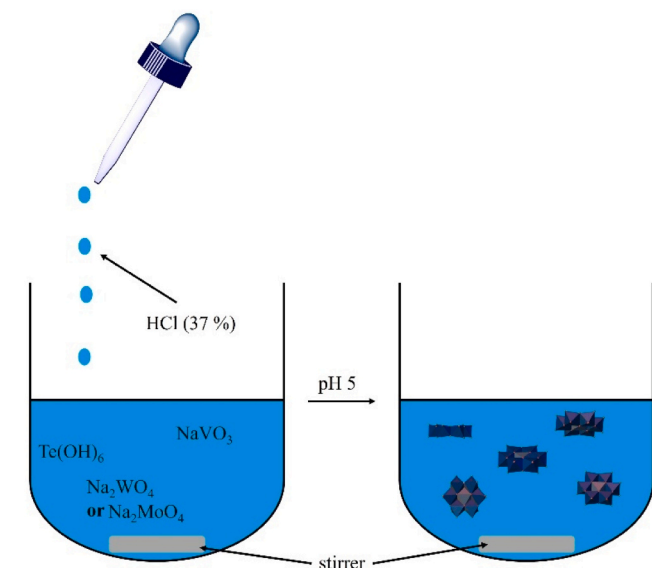


Fig. 1. : Schematic representation of the synthetic procedure for the Anderson-Evans type POMs using a *self-assembly* approach.

mixtures of the molybdates have been completely dried directly after synthesis without further purification steps to isolate the substituted Anderson-Evans structures.

A detailed description of the experimental procedure is provided in the ESI.

2.2. Solid-state analysis

Different V(+V) substituted Anderson-Evans type tungstates and molybdates Na_{6+x}[TeV_xM_{6-x}O₂₄] were synthesized and analyzed in the present study. The tungstates and molybdates were compared regarding their individual spectroscopic and electrochemical properties.

All compounds were analyzed using elemental analysis (AAS/ICP-OES) to determine the target stoichiometry. In addition, the hydration water content was determined by thermogravimetric analysis (TGA). Details are summarized in Table 1.

The precipitate observed during the synthesis of the molybdenum derivatives was identified as Na₆[TeMo₆O₂₄] by elemental analysis (Table S3, ESI). Since the nanofiltration step was skipped in these instances, excess sodium was found in the elemental analysis of the molybdates as shown in Table 1, indicating the presence of NaCl impurities. For the tungstate derivatives, it appears that during the desalting process tellurium migrated from the reaction mixture (retentate/feed fraction) into the permeate (salt) fraction (see Table S4, ESI). Nevertheless, it could be shown by sc-XRD that the resulting structure-type is still an Anderson-Evans structure (Figure S2, ESI). For the higher substituted tungstates, it can be shown that the anionic charges (for $x = 1^{7-}$, $x = 2^{8-}$ and for $x = 3^{9-}$) are not completely compensated by sodium cations. This means that the excess charge has to be compensated by protons resulting from the acidic pH value during the synthetic procedure. One reason for this is that the basicity of the POM anion increases with increasing charge, so that the protons are not completely released into solution.

The structural characterization of the newly synthesized Anderson-Evans-type POMs was done by ATR-FT-IR, Raman-spectroscopy, and sc-XRD. All compounds were compared to their corresponding unsubstituted representatives NaTeW and NaTeMo. Vibrational spectroscopy (FT-IR and Raman) of POMs is a common method to determine the structure-type of a POM. [33] In general by vibrational spectroscopy on POMs the vibrations between the heteroelement X and the O atoms and the different types of M-O vibrations are observed. The ATR-FT-IR and Raman spectra are shown in Figs. 3 and 4 for compounds NaTeV_xW and NaTeV_xMo, respectively.

It is obvious in the IR spectra of the molybdates that the signal intensities decrease with increasing degree of substitution, which is due to the dilution effect resulting from the fact that the POMs are contaminated with alkali salts.

All vibrational bands were assigned to the corresponding vibrational modes for a typical Anderson-Evans cluster according to Bridgeman. [34] The bands in the range of 950–850 cm⁻¹ (IR)/1000–900 cm⁻¹ (Raman) can be attributed to the two types of terminal oxygen-metal M=O_t vibrations. Different types of M-O-M and Te-O vibrational bands are found in the range of 700–600 cm⁻¹ (IR)/700–550 cm⁻¹ (Raman). Vibrational bands under 600 cm⁻¹ (IR) are attributed to different types of Te-O and M-O-M vibrational modes. All bands below 400 cm⁻¹ (Raman) are assigned to different types of O-Te-O and M-O-M vibrations as shown in Table S5, ESI. [34]

Especially from the Raman data in Figs. 3 and 4 the successful V(+V) substitution can be deduced, as the M=O_t vibrational bands at ~960 cm⁻¹ are split into additional bands as a result of the mass differences between V(+V) and Mo(+VI)/W(+VI). [23,35] Based on the results of vibrational spectroscopy, the synthesis strategy was successful, both for the V(+V) substituted tungstates as well as for their corresponding molybdates.

The presence of an Anderson-Evans structure could furthermore be verified by the sc-XRD data (see also ESI Figures S2 to S4). Fig. 5 illustrates the different types of bonds present in the Anderson-Evans POM

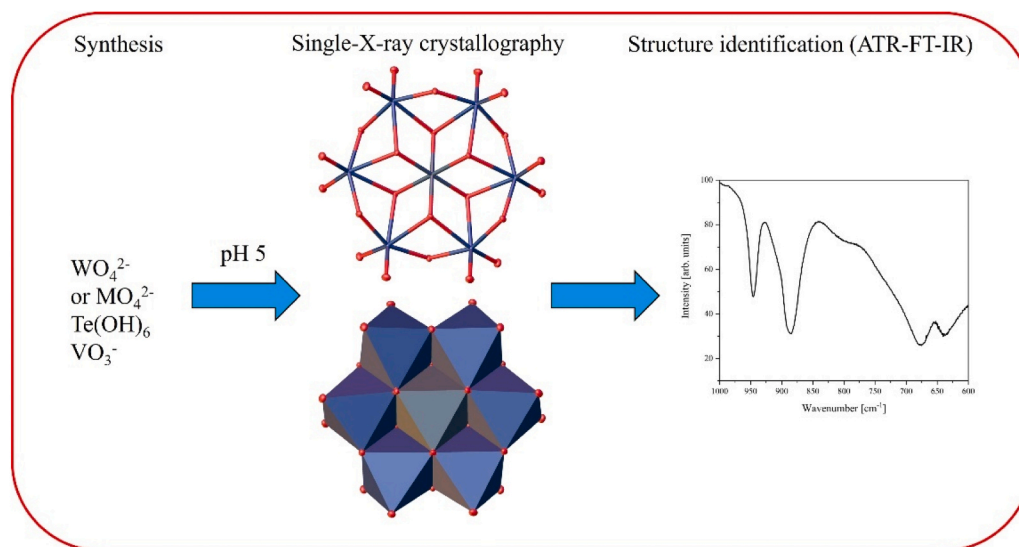


Fig. 2. : Structure elucidation of the newly synthesized Anderson-Evans-type POMs.

Table 1

Results from elemental analysis (AAS/ICP-OES) and TGA.

Compound	Molecular composition	Element ratio ^a	Hydration water content [mol/mol-POM] ^b
NaTeW	Na ₆ [TeW ₆ O ₂₄]	Na/K/Te/W ^c 6.41/0.00/ 1.11/6	4
NaTeVW	Na ₇ [TeVW ₅ O ₂₄]	Na/K/Te/V/W ^c 8.26/0.00/ 0.722/0.982/5	3
NaTeV ₂ W	Na ₈ [TeV ₂ W ₄ O ₂₄]	Na/K/Te/V/W ^c 7.04/0.00/ 0.488/1.95/4	3
NaTeV ₃ W	Na ₉ [TeV ₃ W ₃ O ₂₄]	Na/K/Te/V/W ^c 6.04/0.00/ 0.680/3.26/3	5
NaTeMo	Na ₆ [TeMo ₆ O ₂₄]	Na/K/Te/Mo ^c 6.21/0.00/ 1.09/6	4
NaTeVMo	Na ₇ [TeVMo ₅ O ₂₄]	Na/K/Te/V/ Mo ^c 9.97/0.0181/ 1.01/0.948/5	3
NaTeV ₂ Mo	Na ₈ [TeV ₂ Mo ₄ O ₂₄]	Na/K/Te/V/ Mo ^c 8.70/0.00/ 1.06/1.95/4	3
NaTeV ₃ Mo	Na ₉ [TeV ₃ Mo ₃ O ₂₄]	Na/K/Te/V/ Mo ^c 7.94/0.00/ 1.05/2.91/3	4

^a Element ratios were determined using AAS/ICP-OES analysis.

^b The hydration water content was determined using TGA.

^c All data were normalized to the framework metal Mo/W.

anion. The bond lengths found were compared with the sums of the covalent radii [36] in Table 2.

In general, it makes sense to investigate the different bond lengths for POMs, as different types of chemical bonds (covalent, coordinative, and ionic) exist in POMs. The sums of the covalent radii according to Pyykkö [36] represent a measure for classification. It is assumed that a covalent bond is present if the value of the bond length is in the range of the sum of the covalent radii. Significantly shorter bond lengths indicate a particularly strong covalent bond, possibly with multiple bond character. On the other hand, extended bond lengths can indicate a more coordinative or ionic character. In addition to the sum of the covalent

radii, the type of atoms involved is also relevant for the classification of the bond type, which must also be considered in the interpretation.

Here, the bond length of the Te-O_a bond (1.928 Å) is in the range of the sum of covalent radii of Te and O (1.99 Å) and in the same dimension of the Te-O bond length found in telluric acid (1.906 Å), indicating that the bond is a covalent bond. The Te-O_a bond in the investigated crystal structure is expanded by 0.022 Å compared to telluric acid, which means that the Te-O bond is weakened by incorporation of the TeO₆ octahedron into the Anderson-Evans structure. In general, this observation is expected since the bonding nature between Te and O should not change due to the incorporation of the TeO₆ octahedron into the Anderson-Evans structure. The W-O_a bond (2.271 Å) is significantly elongated (compared to 2.00 Å), indicating the dative bond character. This means that the TeO₆ octahedron is coordinating to the W₆O₁₈ framework. The bond between O_a and W is a new bond formed by POM formation and is therefore of particular interest. All metal-oxygen-metal bond lengths W-O_b (1.943 Å) are also in the range of the weighted sum of covalent radii (2.00 Å). So, this bond type is of covalent nature. The shortening by 0.57 Å shows that the bond between the O and W atoms is of a strong nature, which is due to the increased stability of an W-O bond or the oxophilicity of the metals. [37] Characteristic for an Anderson-Evans structure are the two terminal oxygen-metal bonds W=O_b, which are significantly shortened (1.733 Å in comparison to 2.00 Å), indicating the well-known double bond character. This means that the bonds between W and O_t are strong, covalent in nature. These results are similar to the observations found in a previous studies. [4,23] The details mentioned make it clear that there are different types of bonds in POMs to discuss and one W-O is not necessarily the same as another. Furthermore, the bond lengths between the O_t and the cations (Na⁺) also exceed the sums of the covalent radii, but this interaction is electrostatic and therefore ionic in nature.

2.3. Characterization in solution

The behavior of the newly synthesized Anderson-Evans structures in aqueous solution was investigated using ⁵¹V NMR and UV-Vis spectroscopy. Fig. 6 shows the NMR spectra of the V(+V) substituted tungstates and molybdates. The peak positions of the NMR data are listed in Table S6, ESI.

All ⁵¹V NMR spectra were measured in diluted, aqueous hydrochloric acid solution at pH 5. For all three tungstates, only one sharp NMR signal was observed. In contrast for the molybdates significantly more and broader NMR signals were observed. It can be assumed that the

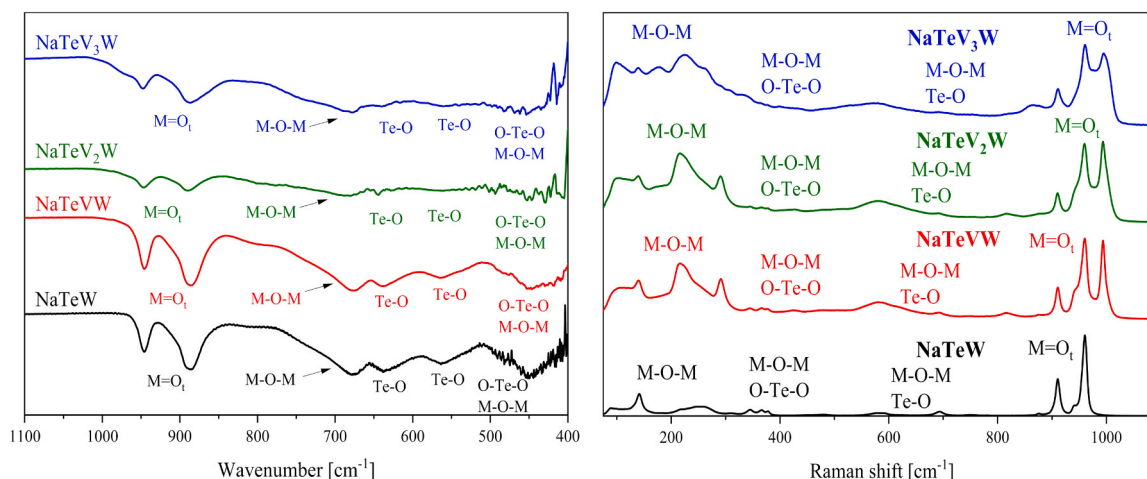


Fig. 3. : ATR-FT-IR (left) and Raman spectra (right) of the V(+V) substituted Anderson-Evans tungstates NaTeV_xW with $x = 0-3$.

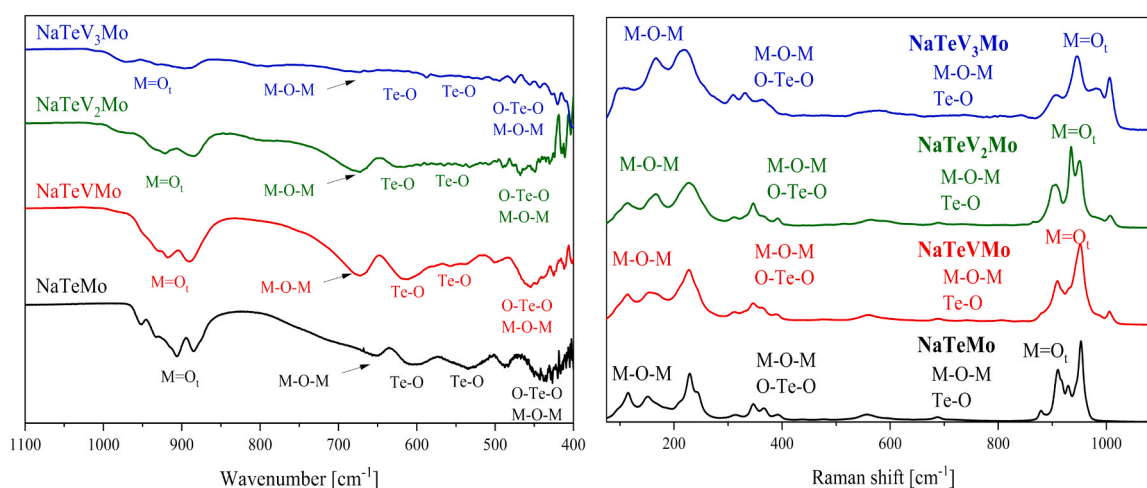


Fig. 4. : ATR-FT-IR (left) and Raman spectra (right) of the V(+V) substituted Anderson-Evans molybdates NaTeV_xMo with $x = 0-3$.

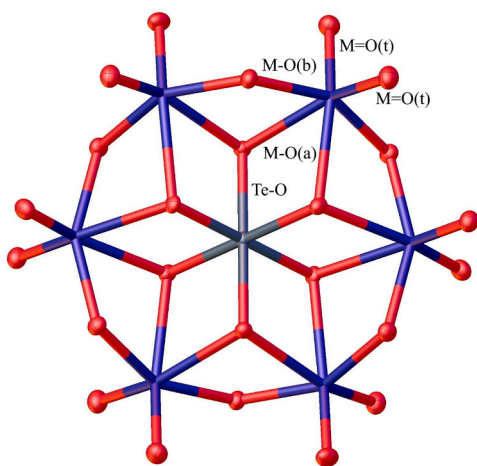


Fig. 5. : Different bond types in the Anderson-Evans-type anion verified by sc-XRD. The full crystallographic information file (.cif) is available through the joint Cambridge Crystallographic Data Centre and Fachinformationszentrum Karlsruhe Access Structures service (deposition number: 2321175).

Table 2

Measured bond lengths vs. weighted sum of covalent radii[36] for the single-crystal structure of NaTeVW .

Bond type	NaTeVW	Weighted sum of covalent radii [Å] [36]
Te-O _a	1.928	1.99
W-O _a	2.271	2.00
W-O _b	1.943	2.00
W=O _t	1.733	2.00

$$BL = \frac{a(r_o + r_w) + b(r_o + r_v)}{a + b}, \text{ with } BL \text{ the weighted bond length, } a \text{ and } b \text{ the weighing factors and } r \text{ the covalent radii of the elements O, W and V.}$$

decomposition of the substituted molybdates to NaTeMo already takes place in aqueous solution, so that different V(+V) species remain in solution. For the various V(+V) substituted Anderson-Evans POMs, positional isomers would be possible, as described for the Keggin-type POMs. [23] However, since only one signal was observed for the substituted tungstates, it could be assumed that either all positional isomers have the same chemical shift or only one isomer was preferentially formed. Computer supported simulations would be helpful here to calculate the relative stabilities of the respective positional isomers. To verify that V(+V) was incorporated into the POM structure an aqueous

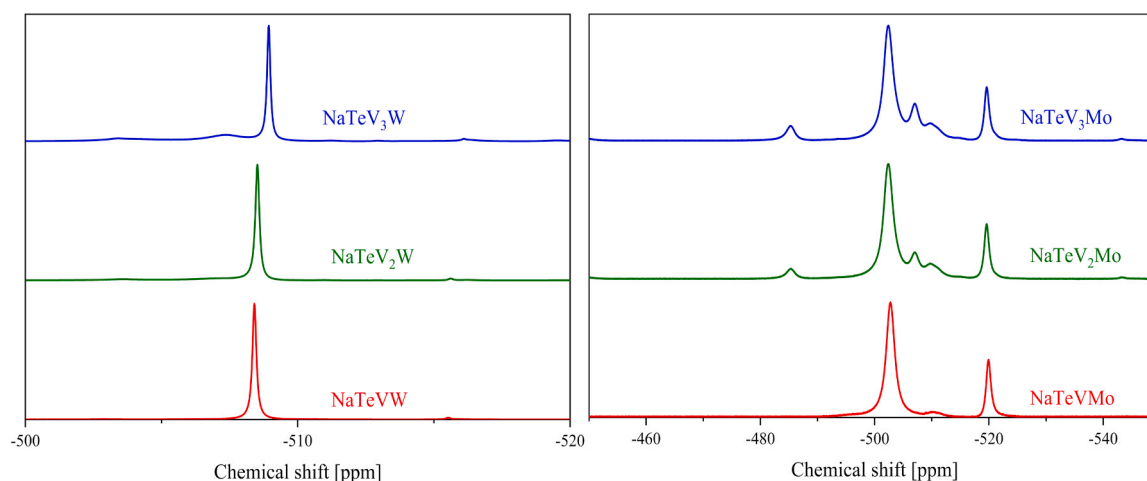


Fig. 6. ^{51}V NMR data of the V(+V) substituted tungstates (left) and molybdates (right) with substitution degrees of $x = 1-3$, measured in a mixture of 90 % diluted, aqueous hydrochloric acid solution in water (pH 5) and 10 % acetone- d_6 as deuterated solvent. The measurement frequency was 157.8 MHz using NaVO_3 as external standard.

solution of pure NaVO_3 was analyzed at pH 5. It is known in literature that vanadate rearranges in aqueous, slightly acidic solution (pH 4–6) to the decavanadate anion $[\text{V}_{10}\text{O}_{28}]^{6-}$, which shows three significant ^{51}V NMR signals at ~ -422 , ~ -498 , and ~ -520 ppm, as illustrated in Figure S5, ESI. [38] In contrast, the NaTeV_xW POMs show only one sharp signal ~ -508 ppm in the ^{51}V NMR data. The characteristic ^{51}V signals for decavanadate at -520 , -498 and -422 ppm are absent, indicating that there is no decavanadate present.

Different ligand-to-metal-charge-transfer (LMCT) bands were observed in the UV-Vis spectra for W(+VI)/Mo(+VI) and V(+V) as shown in Fig. 7 and Table S7, ESI. [4,23,39] A LMCT band for POMs essentially consists of two separate maxima. For both V(+V) and Mo(+VI)/W(+VI) there are two electronic transitions, the transition of the bridging oxygen atoms $\text{O}_b \rightarrow \text{M}$ and the transition of the terminal oxygen atoms to the respective metal $\text{O}_t \rightarrow \text{M}$. The latter tends to higher wavelengths, which is manifested in the peaks by a broadening or by a shoulder formation to longer wavelengths.[4]

It is well known that the LMCT bands for W(+VI) are out of the measurement range (< 200 nm), while the Mo(+VI) and V(+V) LMCT bands can be clearly identified below 250 nm and in the range of 300–500 nm (Fig. 7). [4,23] However, the LMCT bands for V(+V) are extremely broad. There is a clear trend that the V(+V) LMCT bands become more intense with increasing degree of substitution at the same concentration. This is a further indication of the successful incorporation of V(+V) into the Anderson-Evans structure. [23] The LMCT peak

maxima are listed in Table S7, ESI. There is no LMCT band for Te(+VI) observed, as can be seen from the UV-Vis data of pure telluric acid, Figure S6, ESI. This observation can be explained by the fact that the d orbitals in Te(+VI) are fully occupied, so d-d transitions are not possible and therefore electrons cannot get transferred from the oxo ligand p orbitals to the Te(+VI) d orbitals. Furthermore, the chemistry of Te(+VI) is dominated by the p orbitals, so that an LMCT transition of Te(+VI) would mean that an electron would have to be transferred from the oxo p orbitals to the p orbitals of Te(+VI). Such transitions are forbidden by Laporte/parity, as the parity would not change (an electron would be excited from an odd-parity p orbital into another odd-parity p orbital). [40]. As expected, the extinction coefficients of the V(+V) LMCT bands are smaller in magnitude than those of the Mo(+VI) LMCT bands. This observation also correlates with the lower intensity of the V(+V) LMCT band and is a result of the stability of the respective oxidation states +V and +VI for Mo. An LMCT formally corresponds to a one-electron reduction. Since the oxidation state +V in V is significantly more stable than +VI in Mo, it can be assumed that the intensity of the respective V(+V) LMCT band and the value of the associated extinction coefficient is significantly lower than that of Mo(VI). [40] Furthermore, the values of the extinction coefficients of V(+V) increase with increasing degree of substitution, while the values for Mo(+VI) decrease. Consequently, a similar trend is expected for the values of W(+VI) (see Figure S7-S17 and Table S8, ESI).

The RedOx potentials of all compounds studied in this work were

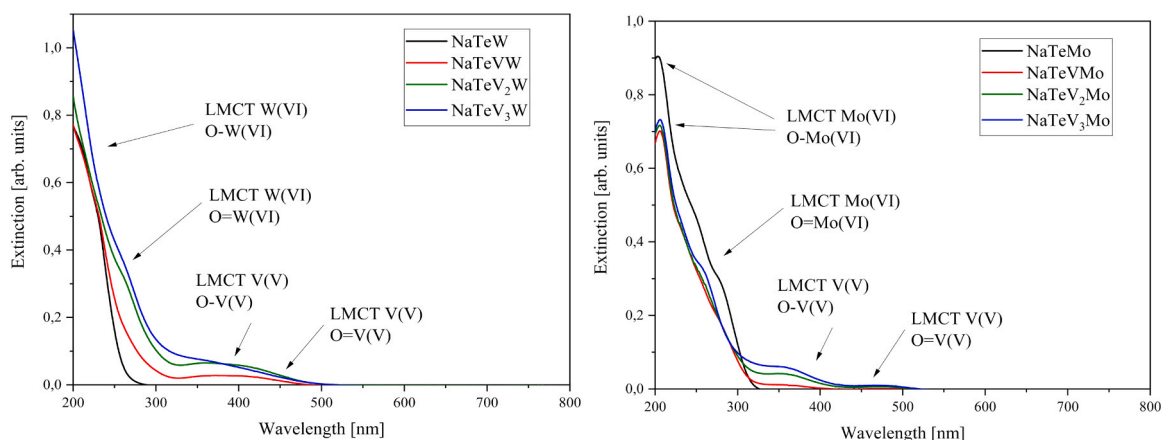


Fig. 7. : UV-Vis spectra of the V(+V) substituted tungstates (left) and molybdates (right) in aqueous solution.

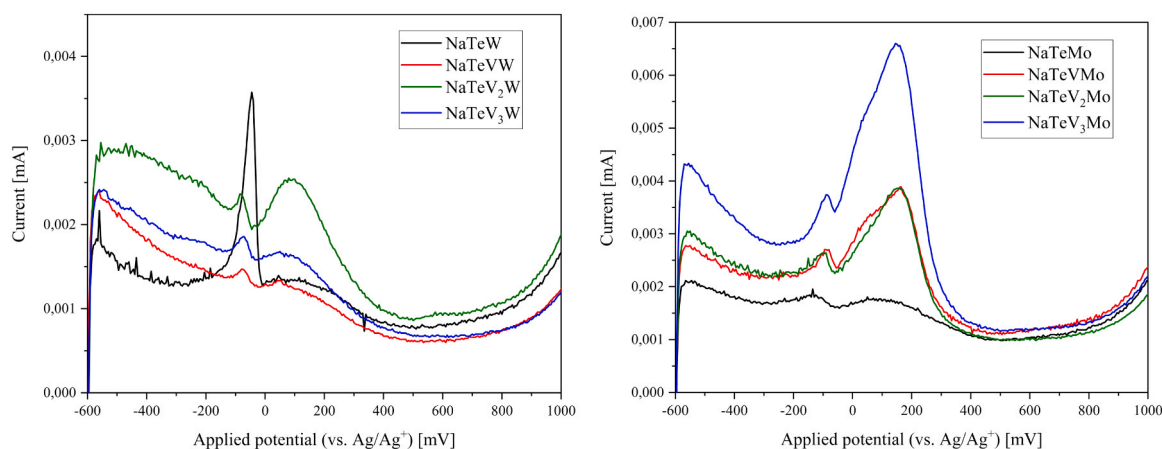


Fig. 8. : SWV data of the V(+V) substituted tungstates (left) and molybdates (right), measured in diluted hydrochloric acid solution at pH 5 (1 mmol/L, 1 equivalent) with sodium chloride as supporting electrolyte (1 mol/L, 1000 equivalents).

analyzed by electrochemical measurements, in particular cyclic voltammetry (CV) and square-wave voltammetry (SWV) as shown in Fig. 8 (SWV) and Figure S18, ESI (CV). Due to the pH sensitivity of the Anderson-Evans structure, the electrochemical measurements were performed in demineralized water in the presence of sodium chloride as the supporting electrolyte at pH 5 (hydrochloric acid). The optimum analyte to supporting electrolyte ratio was found to be 1–1000. All peak potentials found for these POMs are summarized in Table S9, ESI. In general V(+V) substituted Anderson-Evans POMs show less peak potentials than the corresponding Keggin-type POMs. [4,23,24] The unsubstituted POM NaTeW shows an intense peak potential at -45 mV, whereas a broad peak potential is formed in the range of 40 – 80 mV for the V(+V) substituted POMs. This peak potential lies in the range for the RedOx potential of V(+V)/V(+IV) of the pervanadyl cation VO_2^+ , which has already been studied for the V(+V) substituted Keggin-type POMs. [4,23,41] The unsubstituted POM NaTeMo shows two peak potentials in the range -135 mV and 80 mV, both of which can be assigned to RedOx processes of the Mo(+VI) species. With increasing V(+V) substitution, an extremely broad peak potential in the range 145 mV to 160 mV gains intensity, which can be assigned to a RedOx process that is mediated by V(+V). In general, the trend is that the peak potential mediated by V(+V) shifts to higher potential values in the Mo(+VI) based structures, while the peak potential caused by the framework metal Mo(+VI)/W(+VI) is found at more negative potential values, especially in the Mo(+VI) based structures. The V(+V) substitution in the Anderson-Evans structure has a significant influence on the position of the RedOx potentials, which underlines the hypothesis that transition-metal substitution enables fine-tuning of the RedOx potentials of a POM structure. [4,23,24]

The research on TMSPOs based on the Anderson-Evans structure represents an essential step towards developing tailor-made POM catalysts for homogeneous RedOx catalysis in aqueous solution.

2.4. Catalytic oxidation of monofuran derivatives to formic and maleic acid

In this study various monofuran derivatives were selectively oxidized to short-chain carboxylic acids like formic (FA) and maleic (MA) acid using our newly designed Anderson-Evans-type POMs. Monofuran derivatives represent structural building blocks for biomass based substrates (e.g. humins). [42,43] Studying the oxidative conversion of monofuran derivatives paves the way for understanding the conversion of more complex, hemicellulose-based biomass. Esser *et al.* [44] already showed that Keggin-type POMs could be used for the selective catalytic oxidation of furan derivatives to short-chain carboxylic acids using various transition-metal substituted POMs. The catalytic study done in

this work extends the study by Esser *et al.* [44] using the new V(+V) substituted Anderson-Evans tungstates as versatile homogeneous POM catalysts. Note that the use of the molybdenum-based Anderson-Evans derivatives as homogeneous catalysts in aqueous media is not possible due to the instability of these structures.

The monofuran derivatives shown in Fig. 9 have been selected to cover various chemical functionalities accessing the substrate scope for this catalytic application. These include the furan derivatives furfuryl alcohol, furfural, furoic acid, furanone, 2-methylfuran and 5-hydroxymethylfurfural (5-HMF) with a great variety of functional groups.

In the first step, the three successfully synthesized NaTeV_xW (x = 1–3) were tested for their ability as RedOx catalysts in the oxidative conversion of furfural, as shown in Table 3. The catalysts were compared according to their activity and selectivity at 90 °C and 30 bar oxygen pressure for 15 hours reaction time in aqueous media. High performance liquid chromatography (HPLC) was used for analyzing the composition of the aqueous reaction mixture. Detailed information for the experimental procedures can be found in the experimental part.

The mono-vanadium-substituted NaTeVW (Table 3, Entry 2) showed the lowest conversion (9.3 %) and only small amounts of MA (3.2 %) and FA (0.9 %) were formed. With increasing degree of V-substitution, the catalytic activity significantly increased up to 82.2 % for NaTeV₂W (Table 3, Entry 3) and further up to 98.4 % for NaTeV₃W (Table 3, Entry 4). Hereby, the yields of the industrial relevant products FA and MA drastically increased up to 33.2 % FA using NaTeV₃W whereby the maximum amount of MA with 8.1 % was achieved using NaTeV₂W. Moreover, over-oxidation leading to CO₂ also increases with higher V-substitution which is in line with the determined RedOx potentials (see Fig. 8 & Table S9, ESI). Since NaTeVW showed the lowest performance for the catalytic oxidation of furfural, it was excluded for the catalytic conversion of more complex substrates. This can be explained by the fact that the catalyst weights were all normalized to the V content. In addition, as more framework elements in the Anderson-Evans structure are substituted by V(+V), the comparatively small structure results in significantly more V(+V) atoms being neighboring each other. This results in the formation of peroxocomplexes, which can explain the increased activity compared to the less substituted POMs. A density functional theory (DFT) based study for the analogous Keggin-type structures has revealed this effect. [22] In general, furfural proves to be a very reactive substrate, which is also reflected in the difficult control of selectivity.

In the second step, the most promising Anderson-Evans type POM NaTeV₃W was further tested for the oxidation of the other monofuran derivatives. This was done for investigating different structural motifs and functionalities to determine structure-activity-selectivity correlations of the NaTeV₃W with these functional groups. The results of the

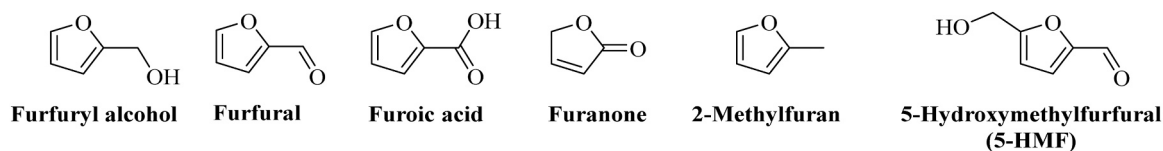


Fig. 9. : Monofuran derivatives investigated in this work.

Table 3

Furfural conversion X and product yields Y using $V(+V)$ substituted Anderson-Evans-type POMs. Data from entry 1 was taken from Esser et al. [44].

Entry ^a	Catalyst ^b	X [%] ^c	Yield Y [%]			
			MA ^c	FA ^c	hydroxy-furanone ^c	CO ₂ ^d
1	-	56.4	5.6	7.8	-	6.5
2 ^e	NaTeVW	9.3	3.2	0.9	0.3	1.1
3 ^e	NaTeV ₂ W	82.2	8.1	23.2	29.5	8.9
4 ^e	NaTeV ₃ W	98.4	6.8	33.2	25.6	17.5

Experimental Conditions:

^a) 10-fold reaction system, 90 °C, 30 bar O₂, 15 has, 1000 rpm, 10 mL stock solution of furfural (12.5 mmol carbon), 0.14 mmol of metal (M) for substitution (90 mol_{Carbon} mol⁻¹ M),

^b) analyzed as described in corresponding section of the experimental part,

^c) determined with HPLC-RID,

^d) determined with GC-TCD,

^e) liquid-phase products determined by ¹H NMR.

substrate screening experiment are summarized in Table 4 and Figure S19, ESI).

The conversion of the substrates using NaTeV₃W were > 97 % except for those of 2-methylfuran and furanone. Essentially the oxidation products FA (C₁) and MA (C₄) are found in all experiments as main products. This can be attributed to the oxygen functionalities of these substrates, which make it relatively easy to split off a C₁ unit so that the remaining molecular C₄ fragments can easily be converted to MA. In addition to the main product FA (33.2 %), the conversion of furfural results in 5-hydroxyfuran-(2H)-one with a yield of 25.6 %, which can be explained by the fact that 5-hydroxyfuran-(2H)-one is an intermediate that is formed by the cleavage of a C₁ unit (the aldehyde group) from the furfural molecule. A possible mechanism for this conversion is shown in Fig. 10. It should be noted that the mechanism was formulated based on the reaction products found. MA, for example, was found to be one of the main products for the conversion of furfural and furoic acid, with significant amounts of 5-hydroxyfuran-(2H)-one. The suggested mechanism therefore contains a plausible explanation of how 5-hydroxyfuran-(2H)-one is formed from the substrates mentioned above and how it can be further converted to MA. It is clear from the reaction mechanism that the formation of MA is possible because the Z geometry is already given in the respective monofuran five-membered ring. 5-hydroxyfuran-(2H)-

Table 4

Conversion X and product yields Y for the substrate screening experiments using NaTeV₃W as a catalyst.

Entry ^a	Catalyst	Substrate	X [%] ^c	Yield Y [%]				
				MA ^b	FA ^b	Levulinic acid ^b	Hydroxy-furanone ^d	CO ₂ ^c
1 ^e	NaTeV ₃ W	Furfural	98.4	6.8	33.2	1.6	25.6	17.5
2 ^e		Furoic acid	97.6	31.2	13.0	0.4	4.6	28.2
3 ^e		Furanone	18.5	7.9	5.9	0.0	0.3	4.8
4 ^e		Furfuryl alcohol	100	2.2	17.2	1.2	0.3	19.8
5 ^e		2-methylfuran	50.0	1.3	10.1	1.2	0.0	21.6
6 ^e		5-HMF	98.3	7.4	40.6	0.0	0.4	34.2

Experimental Conditions:

^a) 10-fold reaction system, 90 °C, 30 bar O₂, 15 has, 1000 rpm, 10 mL stock solution of furfural (12.5 mmol carbon), 0.14 mmol of metal (M) for substitution (90 mol_{Carbon} mol⁻¹ M),

^b) determined with HPLC-RID,

^c) determined with GC-TCD,

^d) liquid-phase products determined by ¹H NMR.

one has a semi-acetal functionality and can therefore be in a chemical equilibrium with the open-chain form shown in Fig. 10, (Z)-4-oxobut-2-enoic acid. The equilibrium is on the side of the 5-hydroxyfuran-(2H)-one and can be shifted to the open-chain side when the aldehyde functionality is directly oxidized by the POM catalyst, resulting in the formation of MA.

The 5-HMF molecule has two different oxygen functionalities on both sides that can be attacked by the POM, which explains the high conversion of 98.3 %. The main oxidation product using NaTeV₃W was FA (40.6 %), which is formed from the oxidative cleavage of C₁ oxygen functionalities at both side chains of the molecule. MA is only formed with a low yield of 7.4 %. This can be explained because both C₁ units first had to be cleaved from the 5-HMF before a C₄ product such as MS could be formed from the C₆ substrate.

During the catalytic oxidation of furfuryl alcohol, the formation of a solid was observed, which initially reduced the mass balance. The mass balance can be closed by taking the precipitated solid into account. Presumably, the oxygen functionality of the furfuryl alcohol tends to dimerize under acid catalysis to form a humin like structure. [45] The resulting solid is then no longer water-soluble and can agglomerate and settle on the reactor walls, so that the catalyst can no longer convert the separated solid. However, not enough substance could be isolated from the solid to analyze it further.

The conversions of furanone and 2-methylfuran were particularly low (18.5 and 50.0 %). The reason for this is that furanone has not a C₁ unit on the five-membered ring, which could be cleaved and oxidized to FA. Therefore, the POM catalyst lacks sufficient attack surface for these substrates. However, 2-methylfuranone has a methyl group, an unfunctionalized C₁ fragment, which could be oxidized by the POM. This explains the higher conversion compared to furanone. Unfunctionalized C-fragments are much more difficult to oxidize than already functionalized fragments, which explains the lower conversion compared to substrates already containing functionalized C₁ fragments.

To verify the catalyst stability of NaTeV₃W in aqueous media, an ⁵¹V NMR spectra was measured after the catalytic experiment using furfural as a substrate (see Figure S20, ESI). Moreover, the reaction mixture of the experiment was concentrated and an IR spectrum was recorded from the remaining residue that verified the integrity of the Anderson-Evans-type structure (see Figure S21, ESI). In combination with the ⁵¹V NMR spectra it can be assumed that the catalyst stability is given under the

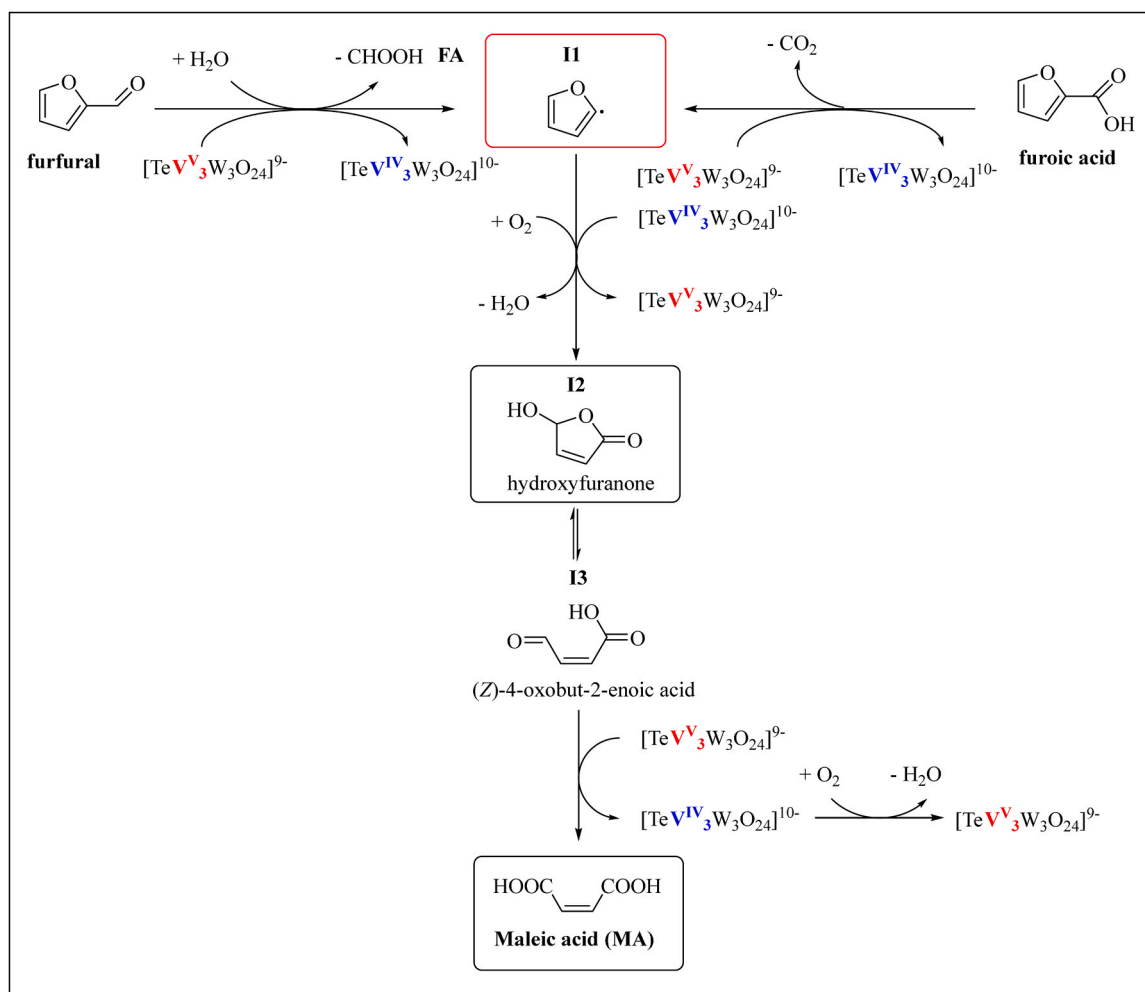


Fig. 10. : Postulated mechanism for the catalytic conversion of furfural and furoic acid to MA via hydroxyfuranone as an intermediate.[44].

process conditions.

In summary, it could be shown that the Anderson-Evans POM NaTeV_3W effectively converts the aldehyde, carboxylic acid, and alcohol functionalities of monofuran derivatives. However, difficulties were found in the conversion of the lactone functionality of furanone and for 2-methylfuran. Presumably, the methyl group of methylfuran prevents the catalyst from attacking the oxygen functionality of the furan ring. 5-HMF, furanic acid and furfural were converted in high yields to the industrially relevant value products MA and FA.

3. Conclusions

In the present study, the concept of transition-metal substitution, already established for structural motifs such as the Keggin, the Wells-Dawson, and the Lindqvist structure, was successfully extended to the Anderson-Evans structure-type. Three $\text{V}(+\text{V})$ substituted Anderson-Evans telluromolybdates and tellurotungstates were synthesized. It was shown that the $\text{V}(+\text{V})$ substituted tungstotellurates are more stable in aqueous media than the corresponding molybdotellurates, which precipitate NaTeMo from aqueous solution after some time. Both POM classes show interesting electrochemical properties, which make them potentially interesting for oxidative catalysis. Due to the instability of the $\text{V}(+\text{V})$ substituted molybdotellurates, the catalytic experiments were performed only with the tungstotellurates. Various monofuran derivatives were successfully oxidized using the novel Anderson-Evans structures, and the NaTeV_3W was found to be the most active catalyst for monofuran conversion. Moreover, NaTeV_3W showed high reactivity

towards alcohol, aldehyde, and carboxylic acid functionality, which was reflected in the high conversion of the corresponding monofuran derivatives. The main products found were the industrially relevant products FA and MA with yields up to 41 % (FA) and 31 % (MA). These results are of fundamental importance for the understanding of the catalytic conversion of more complex biomass-based substrates.

4. Experimental

4.1. Catalyst synthesis

In a typical synthesis, sodium vanadate was dissolved in deionized water by heating an aqueous suspension to $60\text{ }^\circ\text{C}$. After 30 min a colorless solution was formed. Sodium molybdate or tungstate dihydrate was added to the aqueous vanadate solution followed by the addition of telluric acid. The amounts of the precursors were chosen based on the desired target stoichiometry, exact values can be found in the detailed description provided in the ESI. The pH value (~ 8) was adjusted to 5, using concentrated hydrochloric acid. The solution was then heated to $80\text{ }^\circ\text{C}$ for 30 min before it was allowed to cool down to room temperature. The reaction solution was filtered and purified according to a previously published nanofiltration method.[24] Finally, the solvent was removed under reduced pressure ($85\text{ }^\circ\text{C}$ oil bath temperature, 200–30–40 mbar pressure).

Compound NaTeMo was synthesized according to Wood et al.[18]. Telluric acid, molybdenum trioxide were mixed in water and sodium hydroxide was added. A colorless solution was formed and concentrated

under reduced pressure to yield a colorless powder (oil bath 85 °C and 200–0 mbar pressure). Details of the synthetic procedure can be found in the POM synthesis and characterization part of the [Supporting Information](#).

As shown in a previous study, desalination of POMs using a specially developed nanofiltration process, results in purities of > 99 %, as the residual chloride content is less than 1 per mille. [24]

4.2. Catalytic experiments

For catalytic oxidation experiments using the novel V(+V)-substituted Anderson-Evans POMs, a 10-fold reaction system existing of 10 identical 20 mL Hastelloy (C-276) autoclaves in batch mode was used. Each autoclave was connected to an oxygen supply line enabling oxygen pressures up to 100 bar. The experimental setup was equipped with a heating plate allowing reaction temperatures up to 200 °C and a magnetic stirring plate. Due to safety reasons, each autoclave was connected to a ventilation line sealed by a burst disk, which limits the maximum pressure to 90 bar.

In a typical experiment of the first screening phase (catalyst screening), 10 mL of an aqueous substrate solution containing 250 mmol L⁻¹ furfural, corresponding to 12.5 mmol of carbon per reactor was added to the adequate amount of the respective catalyst (0.14 mmol of vanadium). Thus, a carbon to vanadium ration of about 90 mol_C mol_V⁻¹ was set and maintained for all further experiments. The closed and by Teflon gaskets sealed autoclaves were purged 3 times using 30 bar of oxygen to ensure pure oxygen atmosphere inside the autoclaves. After pressurizing the autoclaves to a pre-heating pressure of about 26 bar, the heating plate was set to a temperature of 90 °C and the stirring speed was increased to 300 rpm optimizing the heat transfer during the heating phase. When the desired reaction temperature and pressure was reached, the stirring speed was set to 1000 rpm marking the beginning of the experiment. After a reaction time of 15 h, the temperature of the heating plate was decreased to ambient temperature and the autoclaves were removed from the setup. At a temperature below 30 °C, samples of the gas phase were taken and analyzed by gas chromatography using a thermal conductivity detector (GC-TCD). After venting the autoclaves, the liquid phase was filtered and samples for quantitative measurements using high performance liquid chromatography (HPLC) were taken. Furthermore, samples for qualitative nuclear magnetic resonance (NMR) measurements were also taken.

The aforementioned experimental procedure was also applied for the second screening phase (substrate screening). Since not all substrates were soluble in water, the appropriate amount of the respective substrate (12.5 mmol carbon) was added to an aqueous solution of NaTeV₃W (0.14 mmol of vanadium).

Further descriptions of a HPLC and GC methods are provided in the ESI.

CRedit authorship contribution statement

Jakob Albert: Writing – review & editing, Resources, Funding acquisition. **Maximilian J Poller:** Writing – review & editing. **Tobias Esser:** Writing – original draft, Investigation. **Jan-Christian Raabe:** Writing – original draft, Visualization, Investigation, Conceptualization.

Declaration of Competing Interest

The authors declare that they have no known competing financial interests or personal relationships that could have appeared to influence the work reported in this paper.

Data availability

Data will be made available on request.

Acknowledgement

We would like to thank the central element analysis department led by Dr. Dirk Eifler for measuring numerous AAS/ICP-OES samples. Thanks also go to the X-ray service of Dr. Frank Hoffmann and Isabelle Nevoigt for measuring a single crystals and powder XRDs. Furthermore, we would like to thank the NMR service of Dr. Thomas Hackl and the Raman service of Ute Gralla for the measurements on our samples. Special thanks also go to the research group of Prof. Dr. Peter Burger and especially to Thomas Marx for providing the Ivium. We would like to express a sincere thanks to all the persons and groups mentioned.

Appendix A. Supporting information

Supplementary data associated with this article can be found in the online version at [doi:10.1016/j.cattod.2024.114899](https://doi.org/10.1016/j.cattod.2024.114899).

References

- [1] R. Dehghani, S. Aber, F. Mahdizadeh, Polyoxometalates and their composites as photocatalysts for organic pollutants degradation in aqueous media—a review, *CLEAN – Soil, Air, Water* 46 (2018) 1800413, <https://doi.org/10.1002/clean.201800413>.
- [2] P. Wu, Y. Wang, B. Huang, Z. Xiao, Anderson-type polyoxometalates: From structures to functions, *Nanoscale* 13 (2021) 7119–7133, <https://doi.org/10.1039/d1nr00397f>.
- [3] K. Nomiyama, T. Takahashi, T. Shirai, M. Miwa, Anderson-type heteropolyanions of molybdenum(VI) and tungsten(VI), *Polyhedron* 6 (1987) 213–218, [https://doi.org/10.1016/S0277-5387\(00\)80791-3](https://doi.org/10.1016/S0277-5387(00)80791-3).
- [4] J.-C. Raabe, J. Albert, M.J. Poller, Spectroscopic, crystallographic, and electrochemical study of different manganese(II)-substituted Keggin-type phosphomolybdates, *Chem. – A Eur. J.* 28 (2022) 1–12, <https://doi.org/10.1002/chem.202201084>.
- [5] J.S. Anderson, Constitution of the poly-acids, *Nature* 140 (1937) 1937.
- [6] H.T. Evans, The crystal structures of ammonium and potassium molybdo-tellurates, *J. Am. Chem. Soc.* 70 (1948) 1291–1292, <https://doi.org/10.1021/ja01183a521>.
- [7] B. Caco, A.J. Bridgeman, Structural and vibrational study of [Mo7O24]6- and [W7O24]6-, *J. Phys. Chem. A* 113 (2009) 10540–10548, <https://doi.org/10.1021/jp9063438>.
- [8] R.I. Maksimovskaya, K.G. Burtseva, 17O and ¹⁸³W NMR studies of the paratungstate anions in aqueous solutions, *Polyhedron* 4 (1985) 1559–1562, [https://doi.org/10.1016/S0277-5387\(00\)87227-7](https://doi.org/10.1016/S0277-5387(00)87227-7).
- [9] Q. Gao, D.-H. Hu, M.-H. Duan, D.-H. Li, A novel organic-inorganic hybrid built upon both [VMo6O24]6- and [Mo7O24]6- units: synthesis, crystal structure, surface photovoltage and electrocatalytic activities, *J. Mol. Struct.* 1184 (2019) 400–404, <https://doi.org/10.1016/j.molstruc.2018.12.110>.
- [10] J. Martín-Caballero, B. Artetxe, S. Reinoso, L. San Felices, O. Castillo, G. Beobide, J. L. Vilas, J.M. Gutiérrez-Zorrilla, Thermally-triggered crystal dynamics and permanent porosity in the first heptatungstate-metalorganic three-dimensional hybrid framework, *Chem. – A Eur. J.* 23 (2017) 14962–14974, <https://doi.org/10.1002/chem.201703585>.
- [11] Y. Guo, D. Li, C. Hu, Y. Wang, E. Wang, Y. Zhou, S. Feng, Photocatalytic degradation of aqueous organochlorine pesticide on the layered double hydroxide pillared by Paratungstate A ion, Mg12Al6(OH)36 (W7O24)·4H2O, *Appl. Catal. B Environ.* 30 (2001) 337–349, [https://doi.org/10.1016/S0926-3373\(00\)00246-0](https://doi.org/10.1016/S0926-3373(00)00246-0).
- [12] A. Bi, J. Zhu, Hydrothermal synthesis of W and Mo co-doped VO2(B) nanobelts, *J. Exp. Nanosci.* 8 (2013) 46–53, <https://doi.org/10.1080/17458080.2011.559588>.
- [13] Y. Sun, J. Liu, E. Wang, Preparation and properties of some new 6-heteropoly-tellurate compounds of tungsten and molybdenum containing vanadium, *Inorg. Chim. Acta* 117 (1986) 23–26, [https://doi.org/10.1016/S0020-1693\(00\)88061-5](https://doi.org/10.1016/S0020-1693(00)88061-5).
- [14] J. Kang, J. Ahn, H. Shin, S. Pyo, H. Yun, J. Do, Crystal structure of tris (piperazinium) hexakis[(μ3-oxo)(μ2-oxo)- dioxotungsten]tellurate(VI) hexahydrate, [C4H12N2]3[TeW6O24]·6H2O, *Z. F. üR. Krist. - N. Cryst. Struct.* 226 (2011) 129–130, <https://doi.org/10.1524/ncrs.2011.0059>.
- [15] E. Matijevic, M. Kerker, H. Beyer, F. Theubert, Heteropoly Compounds. VII. Triheteropoly Nickelates, *Inorg. Chem.* 2 (1963) 581–585, <https://doi.org/10.1021/ic50007a038>.
- [16] A.L. Nolan, R.C. Burns, G.A. Lawrance, D.C. Craig, Octasodium hexatungstomanganate(IV) octadecahydrate, *Acta Crystallogr. Sect. C. Cryst. Struct. Commun.* 56 (2000) 729–730, <https://doi.org/10.1107/S010827010000408X>.
- [17] A. Bijelic, A. Rempel, Ten good reasons for the use of the tellurium-centered anderson-evans polyoxotungstate in protein crystallography, *Acc. Chem. Res.* 50 (2017) 1441–1448, <https://doi.org/10.1021/acs.accounts.7b00109>.
- [18] S.R. Wood, A. Carlson, The preparation and identification of three alkali molybdo-tellurates, *J. Am. Chem. Soc.* 61 (1939) 1810–1812, <https://doi.org/10.1021/ja01876a048>.
- [19] H.T. Evans, The molecular structure of the hexamolybdo-tellurate ion in the crystal complex with telluric acid (NH4)6[TeMo6O24]·Te(OH)6·7H2O, *Acta Crystallogr.*

- Sect. B Struct. Crystallogr. Cryst. Chem. 30 (1974) 2095–2100, <https://doi.org/10.1107/s0567740874006546>.
- [20] V.F. Odyakov, E.G. Zhizhina, R.I. Maksimovskaya, Synthesis of molybdovanadophosphoric heteropoly acid solutions having modified composition, *Appl. Catal. A Gen.* 342 (2008) 126–130, <https://doi.org/10.1016/j.apcata.2008.03.008>.
- [21] E.G. Zhizhina, V.F. Odyakov, Alteration of the physicochemical properties of catalysts based on aqueous solutions of Mo-V-P heteropoly acids in redox processes, *React. Kinet. Catal. Lett.* 95 (2008) 301–312, <https://doi.org/10.1007/s11144-008-5423-2>.
- [22] M.J. Poller, S. Bönisch, B. Bertleff, J.-C. Raabe, A. Görling, J. Albert, Elucidating activating and deactivating effects of carboxylic acids on polyoxometalate-catalysed three-phase liquid–liquid–gas reactions, *Chem. Eng. Sci.* 264 (2022) 118143, <https://doi.org/10.1016/j.ces.2022.118143>.
- [23] J.-C. Raabe, J. Aceituno Cruz, J. Albert, M.J. Poller, Comparative spectroscopic and electrochemical study of V(V)-substituted Keggin-type phosphomolybdates and -tungstates, *Inorganics* 11 (2023) 138, <https://doi.org/10.3390/inorganics11040138>.
- [24] J.-C. Raabe, T. Esser, F. Jameel, M. Stein, J. Albert, M.J. Poller, Study on the incorporation of various elements into the Keggin lacunary-type phosphomolybdate [PMo₉O₃₄]⁹⁻ and subsequent purification of the polyoxometalates by nanofiltration, *Inorg. Chem. Front.* 10 (2023) 4854–4868, <https://doi.org/10.1039/D3QI00937H>.
- [25] R.G. Finke, B. Rapko, R.J. Saxton, P.J. Domaille, Trisubstituted heteropolytungstates as soluble metal oxide analogs. III. Synthesis, characterization, phosphorus-31, silicon-29, vanadium-51, and 1- and 2-D tungsten-183 NMR, deprotonation, and proton mobility studies of organic solvent solute forms of Hx, *J. Am. Chem. Soc.* 108 (1986) 2947–2960, <https://doi.org/10.1021/ja00271a025>.
- [26] J. Albert, J. Mehler, J. Tucher, K. Kastner, C. Streb, One-step synthesizable lindqvist–isopolyoxometalates as promising new catalysts for selective conversion of glucose as a model substrate for lignocellulosic biomass to formic acid, *ChemistrySelect* 1 (2016) 2889–2894, <https://doi.org/10.1002/slct.201600797>.
- [27] C. Wang, L. Weng, Y. Ren, C. Du, B. Yue, M. Gu, H. He, Mixed-addenda lindqvist-type polyoxoanion [V₂W₄O₁₉]⁴⁻-supported copper complexes, *Z. F. üR. Anorg. Und Allg. Chem.* 637 (2011) 472–477, <https://doi.org/10.1002/zaac.201000332>.
- [28] V.F. Odyakov, E.G. Zhizhina, A novel method of the synthesis of molybdovanadophosphoric heteropoly acid solutions, *React. Kinet. Catal. Lett.* 95 (2008) 21–28, <https://doi.org/10.1007/s11144-008-5374-7>.
- [29] D. Voß, H. Pickel, J. Albert, Improving the fractionated catalytic oxidation of lignocellulosic biomass to formic acid and cellulose by using design of experiments, *ACS Sustain. Chem. Eng.* 7 (2019) 9754–9762, <https://doi.org/10.1021/acssuschemeng.8b05095>.
- [30] S. Wesinger, M. Mendt, J. Albert, Alcohol-activated vanadium-containing polyoxometalate complexes in homogeneous glucose oxidation identified with ⁵¹V NMR and EPR spectroscopy, *ChemCatChem* 13 (2021) 3662–3670, <https://doi.org/10.1002/cctc.202100632>.
- [31] J. Albert, D. Lüders, A. Bösmann, D.M. Guldi, P. Wasserscheid, Spectroscopic and electrochemical characterization of heteropoly acids for their optimized application in selective biomass oxidation to formic acid, *Green. Chem.* 16 (2014) 226–237, <https://doi.org/10.1039/c3gc41320a>.
- [32] T. Esser, M. Huber, D. Voß, J. Albert, Development of an efficient downstream process for product separation and catalyst recycling of a homogeneous polyoxometalate catalyst by means of nanofiltration membranes and design of experiments, *Chem. Eng. Res. Des.* 185 (2022) 37–50, <https://doi.org/10.1016/j.cherd.2022.06.045>.
- [33] J.-C. Raabe, F. Jameel, M. Stein, J. Albert, M.J. Poller, Heteroelements in polyoxometalates: a study on the influence of different group 15 elements on polyoxometalate formation, *Dalt. Trans.* 53 (2024) 454–466, <https://doi.org/10.1039/D3DT03883A>.
- [34] A.J. Bridgeman, Computational study of solvent effects and the vibrational spectra of anderson polyoxometalates, *Chem. - A Eur. J.* 12 (2006) 2094–2102, <https://doi.org/10.1002/chem.200500802>.
- [35] J.K. Lee, J. Melsheimer, S. Berndt, G. Mestl, R. Schlögl, K. Köhler, Transient responses of the local electronic and geometric structures of vanado-molybdophosphate catalysts H₃+nPVnMo₁₂–nO₄₀ in selective oxidation, *Appl. Catal. A Gen.* 214 (2001) 125–148, [https://doi.org/10.1016/S0926-860X\(01\)00485-9](https://doi.org/10.1016/S0926-860X(01)00485-9).
- [36] P. Pyykkö, M. Atsumi, Molecular single-bond covalent radii for elements 1–118, *Chem. - A Eur. J.* 15 (2009) 186–197, <https://doi.org/10.1002/chem.200800987>.
- [37] I.A. Weinstock, Homogeneous-phase electron-transfer reactions of polyoxometalates, *Chem. Rev.* 98 (1998) 113–170, <https://doi.org/10.1021/cr9703414>.
- [38] N. Samart, Z. Arhouma, S. Kumar, H.A. Murakami, D.C. Crick, D.C. Crans, Decavanadate inhibits mycobacterial growth more potently than other oxovanadates, *Front. Chem.* 6 (2018) 1–16, <https://doi.org/10.3389/fchem.2018.00519>.
- [39] N.K.K. Raj, A.V. Ramaswamy, P. Manikandan, Oxidation of norbornene over vanadium-substituted phosphomolybdic acid catalysts and spectroscopic investigations, *J. Mol. Catal. A Chem.* 227 (2005) 37–45, <https://doi.org/10.1016/j.jmolcata.2004.10.005>.
- [40] B. Weber, *Koordinationschemie*, Springer Berlin Heidelberg, Berlin, Heidelberg, 2014, <https://doi.org/10.1007/978-3-642-41685-9>.
- [41] D.V. Evtuguin, C.P. Neto, J. Rocha, J.D. Pedrosa de Jesus, Oxidative delignification in the presence of molybdovanadophosphate heteropolyanions: mechanism and kinetic studies, *Appl. Catal. A Gen.* 167 (1998) 123–139, [https://doi.org/10.1016/S0926-860X\(97\)00306-2](https://doi.org/10.1016/S0926-860X(97)00306-2).
- [42] I. Van Zandvoort, E.J. Koers, M. Weingarth, P.C.A. Bruijninx, M. Baldus, B. M. Weckhuysen, Structural characterization of 13C-enriched humins and alkali-treated 13C humins by 2D solid-state NMR, *Green. Chem.* 17 (2015) 4383–4392, <https://doi.org/10.1039/c5gc00327j>.
- [43] L. Filiciotto, A.M. Balu, A.A. Romero, C. Angelici, J.C. van der Waal, R. Luque, Reconstruction of humins formation mechanism from decomposition products: a GC-MS study based on catalytic continuous flow depolymerizations, *Mol. Catal.* 479 (2019) 110564, <https://doi.org/10.1016/j.mcat.2019.110564>.
- [44] T. Esser, A. Wassenberg, J. Raabe, D. Voß, J. Albert, Catalytic valorization of humins by selective oxidation using transition-metal-substituted Keggin-type polyoxometalate catalysts, *ACS Sustain. Chem. Eng.* 12 (2024) 543–560, <https://doi.org/10.1021/acssuschemeng.3c06539>.
- [45] A. Wassenberg, T. Esser, M.J. Poller, J. Albert, Investigation of the formation, characterization, and oxidative catalytic valorization of humins, *Materials* 16 (2023) 2864, <https://doi.org/10.3390/ma16072864>.

6 Diskussion

Im folgenden Kapitel werden die im Rahmen dieser Arbeit erzielten Ergebnisse abschließend diskutiert und die Fragestellungen dieser Arbeit beantwortet.

1. Erweiterung des Synthesekonzeptes der V(V) substituierten Phosphormolybdate auf andere Übergangsmetalle

Das Konzept der Übergangmetallsubstitution in POMs konnte erfolgreich auf verschiedene Übergangsmetalle erweitert werden. So wurden Mn(II), Mn(II)/V(V) gemischt und Co(II) substituierte Keggin-Typ Phosphormolybdate nach dem *self-assembly* Ansatz synthetisiert und mit verschiedenen spektroskopischen, elektrochemischen und kristallographischen Methoden charakterisiert.^[247] Die hier dargestellten Ergebnisse zeigen, dass die Übergangmetallsubstitution mit dem *self-assembly* Ansatz problemlos möglich ist, wenn ein geeigneter, wasserlöslicher Übergangmetallprecursor vorliegt. Für die Elemente Mn(II) und Co(II) wurden die jeweiligen Acetate als Precursoren verwendet.^[110] Jedoch hängt der maximale Substitutionsgrad, der mit dem betreffenden Übergangsmetall erreicht werden kann, stark von der Oxidationsstufe des Substitutionselementes ab. Hierbei konnte eine Korrelation mit der Ladung des finalen POM-Anions aufgestellt werden. Je höher die anionische Ladung des POM-Anions ist, desto mehr negative Ladung muss bei annähernd gleichbleibender Größe über das Keggin-Gerüst verteilt werden. So zeigte sich, dass anionische Ladungen über 15 nicht mehr stabilisiert werden können und ein Keggin-Typ-POM nicht mehr gebildet werden kann. Im Umkehrschluss bedeutet diese Beobachtung, dass der maximale Substitutionsgrad kleiner wird, je geringer die Oxidationsstufe des betreffenden Übergangsmetalls ist. Dies steht im Einklang mit der Beobachtung der maximalen Substitutionsgrade von zwei für Mn(II) (anionische Ladung 11), drei für Co(II) (anionische Ladung 15) und sechs für V(V) (anionische Ladung 9).^[247,249]

Das im Rahmen dieser Arbeit weiterentwickelte Lacunary-Konzept auf Basis des Anions $[\text{PMo}_9\text{O}_{34}]^{9-}$ stellt ebenfalls eine mächtige Methode dar, um TMSPOMs auf Basis des Phosphormolybdates herzustellen. Jedoch ist der maximale Substitutionsgrad auf drei limitiert. Insgesamt konnten die d^0 Übergangsmetalle V(V), Nb(V), W(VI), Fe(III) d^5 , Co(II) d^7 und Ni(II) d^8 erfolgreich in die Lacunary-Struktur eingebaut werden. Limitierungen wurden für die späten Übergangsmetalle Cu(II) d^9 und Zn(II) d^{10} , sowie für die Hauptgruppenelemente In $d^{10}s^2p^1$ und Sn $d^{10}s^2p^2$ gefunden, was darauf zurückzuführen ist, dass die d-Orbitale der betreffenden Metalle weitestgehend voll (Cu(II)) bzw. vollständig (Zn(II)) besetzt sind. Insbesondere für späte d^{10}

Übergangsmetalle sind koordinative Bindungen mit einer Beteiligung von s- und p-Orbitalen bekannt. So wurden Übergänge beschrieben, in denen die Metalle von der reinen d^{10} Konfiguration zu einer $d^9s^x p^{1-x}$ Konfiguration wechseln.^[252–255] Daher ist davon auszugehen, dass in den vorliegenden TMSPOM Anionen $[\text{PCu}_2\text{Mo}_{10}\text{O}_{40}]^{11-}$ und $[\text{PZnMo}_{11}\text{O}_{40}]^{7-}$ für das Fremdelement eine ähnliche Bindungssituation vorliegt. Solche Bindungen lassen sich hauptsächlich durch gute π -Akzeptorliganden stabilisieren.^[255] Da im Oxoliganden die p-Orbitale vollständig besetzt sind, stehen diese Orbitale für eine π -Rückbindung nicht zur Verfügung, wodurch die Bindung insgesamt schwächer ist. Der Oxoligand ist somit ein π -Donorligand.^[243] Daher ist davon auszugehen, dass solche Bindungstypen mit Oxoliganden nicht favorisiert sind. Die dargestellte Situation lässt sich auch durch Anwendung der Molekülorbitaltheorie (MO-Theorie) erklären. Abbildung 26 zeigt ein genähertes MO-Schema eines allgemeinen, oktaedrischen Übergangsmetallkomplexes. Generell sind für die Metalle der n -Periode aus dem PSE die Atomorbitale nd , $(n+1)s$ und $(n+1)p$ für die Betrachtung relevant. Unter Beachtung der Oktaedersymmetrie hat das s-Orbital a_{1g} - und die dreifach entarteten p-Orbitale haben t_{1u} -Symmetrie. Die d-Orbitale spalten auf in zwei Sets mit e_g - (d_{z^2} und $d_{x^2-y^2}$) und t_{2g} -Symmetrie (d_{xy} , d_{yz} , d_{xz}). Die Oxoliganden liefern je ein Orbital, die a_{1g} -, t_{1u} - und e_g -Symmetrien aufweisen.^[256]

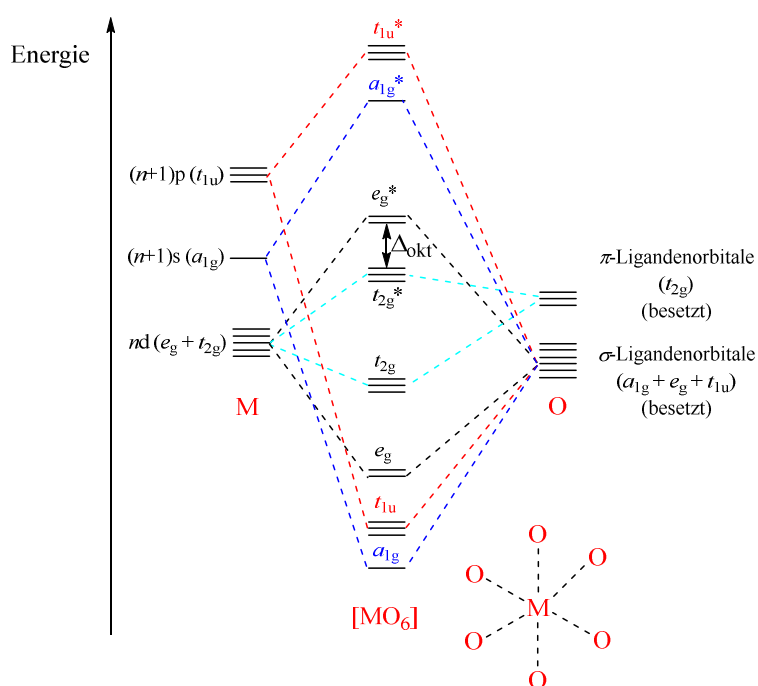


Abb. 26: Schematisches MO-Diagramm eines oktaedrischen Übergangsmetallkomplexes für π -Donorliganden. Dabei besitzen die e_g - und t_{2g} -MOs, deren Energieunterschied die Aufspaltung des oktaedrischen Ligandenfeldes ausmacht, antibindenden Charakter, deren Besetzung mit einer zunehmenden Anzahl an Metallvalenzelektronen die Metall-Oxoligand-Bindung zunehmend schwächt.^[256]

In einem σ -Komplex wären die d_{xy} -, d_{yz} - und d_{xz} -Orbitale nicht-bindende Orbitale. Da es sich bei den Oxoliganden jedoch um π -Donorliganden handelt, können die besetzten Ligand-p-Orbitale Elektronen zum Metall übertragen. Es bilden sich bindende t_{2g} - und antibindende t_{2g}^* -MOs. Dabei entspricht der Energieunterschied zwischen den t_{2g}^* - und den e_g^* -MOs der Aufspaltung des oktaedrischen Ligandenfeldes Δ_{okt} . Die sechs π -Donor-Oxoliganden liefern insgesamt 18 Elektronen (zwölf σ - und sechs π -Elektronen), die die bindenden a_{1g} -, t_{1u} -, e_g - und t_{2g} -MOs in Abbildung 26 besetzen. Sobald ein Metall nicht wie Mo(VI), W(VI) oder V(V) eine d^0 -Konfiguration besitzt, werden die Valenzelektronen des Metalls relevant, die die antibindenden t_{2g}^* - und e_g^* -MOs besetzen müssen. Durch die Besetzung der antibindenden MOs wird die Oxoligand-Metallbindung stetig geschwächt, wobei für die späten Übergangsmetalle die t_{2g}^* - und e_g^* -antibindenden MOs vollständig besetzt sind. Hieraus resultiert eine signifikante Schwächung der Metall-Oxoligand-Bindung, was die beobachtete Instabilität der betreffenden POMs mit den späten Übergangselementen erklärt.^[256] Für die Bindungssituationen von Hauptgruppenelementen in POMs müssten DFT-Simulationen erstellt werden, um die Stabilitäten von In(III) und Sn(IV) in POMs abschätzen und aussagekräftige Trends formulieren zu können.

2. Einfluss der verschiedenen Substitutionselemente auf die RedOx-Potentiale der POMs

In den Studien P1-4^[243,247-249] konnte durch den Einbau verschiedener RedOx aktiver Elemente gezeigt werden, dass ein gezieltes Tuning der RedOx Eigenschaften möglich ist. Dabei wurde gezeigt, dass sich im Vergleich zum unsubstituierten Phosphormolybdat die Peak-Potentiale durch den Einbau von Mn(II) tendenziell zu niedrigeren und im Fall von Co(II) zu höheren Potentialwerten verschieben, wie in Abbildung 27 anhand einiger TMSPOM Beispiele gezeigt.^[247,249] Generell erwies sich aus elektrochemischer Sicht der Einbau der Elemente Nb(V) und W(VI) als weniger zielführend, da hier im Vergleich zum Phosphormolybdat deutlich weniger RedOx-Potentiale in den Voltammogrammen zu beobachten waren. Somit sind diese Elemente für RedOx katalytische Anwendungen weniger geeignet.^[243] Ähnliche Ergebnisse konnten auch im direkten elektrochemischen Vergleich der beiden Anionenklassen $[\text{PV}_x\text{Mo}_{12-x}\text{O}_{40}]^{(3+x)-}$ und $[\text{PV}_x\text{W}_{12-x}\text{O}_{40}]^{(3+x)-}$ in Studie P3 gefunden werden, woraus geschlossen werden konnte, dass eine Verwendung der V(V) substituierten Keggin-Phosphorwolframate für RedOx-katalytische Anwendungen eher ungeeignet ist.^[248] Zudem konnten die V(V) substituierten Phosphorwolframate nicht als freie POM-Säuren erhalten werden. Daher ist eine Anwendung sowohl in RedOx- als auch in säurekatalysierten Prozessen nicht möglich. Dieser Nachteil konnte jedoch für die V(V) substituierten Phosphormolybdate umgangen werden, da

diese aus den Oxiden hergestellt werden konnten und somit keine störenden Alkalikationen vorhanden sind. Eine bifunktionelle Katalyse ist somit möglich.^[248]

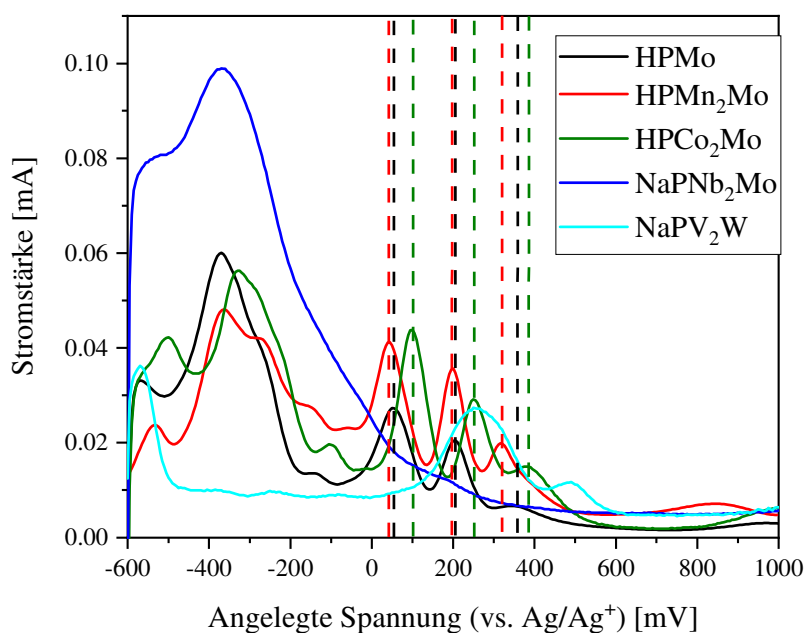


Abb. 27: Elektrochemischer Vergleich (SWV) zwischen den verschiedenen TMSPOM Spezies, der zweifach substituierten Keggin-Spezies, die die in P1-4 beobachteten Verschiebungen der Peak-Potentiale im Vergleich zum unsubstituierten Phosphormolybdat verdeutlichen.^[243,247–249]

3. Entwicklung eines effektiven Entsalzungsprozesses als Reinigungskonzept für TMSPOMs

Für die Entsalzung von TMSPOMs, die in wässrigen Medien synthetisiert wurden, konnte ein effizientes Nanofiltrationsverfahren durch eine nanoporöse Membran etabliert werden. Der Chloridgehalt galt dabei nach vier Zyklen der Diafiltration als vernachlässigbar, wodurch eine hohe POM-Ausbeute mit hoher Reinheit nach vier Zyklen gewährleistet werden konnte. Somit kann in Zukunft auf den Einsatz weniger effizienter Reinigungsverfahren wie der Umkristallisation und der Etherat-Methode verzichtet werden, wobei die Etherat-Methode insbesondere für höher geladene TMSPOM Anionen scheiterte.^[243,248]

Das Prinzip der Nanofiltration basiert darauf, dass die Alkalisalz-/TMSPOM-Lösung (Feed-Lösung) unter Hochdruck (33 bar) durch ein System gefördert wird. Aufgrund der geringen Ionen-größe der Alkalikationen und der Chloridanionen, sind nur diese dazu befähigt die nanoporöse Membran zu durchqueren und reichern sich in der sogenannten Permeatfraktion an. Die TMSPOM-Anionen sind durch ihre enorme Größe nicht dazu befähigt die Membran zu passie-

ren und reichern sich entsprechend in der Retentatfraktion an. Die hier genannten Effekte basieren auf dem Größenausschlussprinzip. Weiterhin ist zu beachten, dass die Alkalikationen schwächer gebundene Hydrathüllen tragen und sich beim Passieren der nanoporösen Membran von ihrer Hydrathülle lösen. Hingegen haben höher geladene Ionen, wie die TMSPOM-Anionen stärker gebundene Hydrathüllen, wodurch die effektive Größe der Anionen steigt und eine Durchquerung der Membran zusätzlich erschwert wird.^[257] Es ist dabei zu beachten, dass auf diese Weise die Alkalikationenkonzentration auf einen Wert absinkt, der der Konzentration an Kationen entspricht, die zur Aufrechterhaltung der Elektroneutralität mit dem TMSPOM-Anion benötigt wird. Mittels EDX wurde der Chloridgehalt in der Retentatfraktion nach vier Zyklen der Diafiltration auf unter 1 Promille bestimmt, was für eine effiziente Entsalzung spricht.^[243,248,258]

4. Kristallographisches Studium der TMSPOM-Strukturen

Ein kristallographisches Studium der POMs erwies sich als besonders zielführend, da neben einfachen Informationen, wie der Identifikation des Strukturtyps, auch tiefgehendere Informationen abgeleitet werden konnten, die in den nachfolgenden Absätzen diskutiert werden.

Beim kristallographischen Studium der verschiedenen POM-Strukturen konnten zunächst die Größen der einzelnen POM-Cluster bestimmt werden (Tabelle 1). Dabei ist zu beachten, dass die Keggin-Struktur, aus Symmetriegründen eine nahezu sphärische und die Lindqvist-Struktur eine nahezu oktaedrische Geometrie aufweist, sodass die Dimensionen Länge, Breite und Höhe identisch sind. Die Grundfläche der Anderson-Evans-Struktur ist aus Symmetriebetrachtungen nahezu sphärisch (gleiche Länge und Breite), während die Höhe der Struktur ungefähr 0.28 nm betrug, wodurch der planare Eindruck dieses Strukturmotivs entsteht.^[250,251]

Aus Tabelle 1 wird ersichtlich, dass sich die Größen der Standardstrukturen (Keggin-, Wells-Dawson-, Anderson-Evans- und Lindqvist-Struktur) im Bereich zwischen 0.83 und 1.34 nm befinden, wodurch die hier untersuchten Struktur motive als nanostrukturierte Verbindungen beschrieben werden können.^[243,247,250,259,260]

Weitere strukturelle Eigenschaften, die aus den kristallographischen Daten erhalten wurden, sind die Bindungslängen. Insbesondere für verschiedene HPA-Strukturen (Keggin-, Anderson-Evans und Wells-Dawson) konnten im Einklang mit der Literatur für die verschiedenen

Metall-Sauerstoff-Bindungen unterschiedliche Bindungslängen gefunden werden, sodass sich die entsprechenden Bindungstypen in unterschiedliche Gruppen aufteilen ließen.^[243,250,251]

Diese Beobachtung wurde insbesondere an der in P1 beschriebenen Keggin-Lacunary-Struktur $[\text{PMo}_9\text{O}_{34}]^{9-}$ in Abbildung 28 und Tabelle 2 deutlich, mit der die Literaturkenntnisse insbesondere am Studium lacunärer Struktur motive erweitert wurden.^[243] Als Grundlage zur Diskussion der verschiedenen Bindungslängen dienten die Summen der kovalenten Radien.^[40]

Tab. 1: Typische Größen [nm] verschiedener POM-Struktur motive, ermittelt aus den sc-XRD-Daten.^[243,250,259]

Strukturtyp	Länge [nm]	Breite [nm]	Höhe [nm]
Keggin* $[\text{XM}_{12}\text{O}_{40}]^{n-}$	1.03		
Wells-Dawson* $[\text{X}_2\text{M}_{18}\text{O}_{62}]^{n-}$	1.03		1.34
Anderson-Evans* $[\text{XM}_6\text{O}_{24}]^{n-}$	0.844		0.275
Lindqvist* $[\text{M}_6\text{O}_{19}]^{n-}$	0.832		
Keggin-Lacunary* $[\text{PMo}_9\text{O}_{34}]^{9-}$ <i>deposition number:</i> 2205006	0.6524(5)	0.9047(4)	
$[\text{W}_{12}\text{O}_{40}]^{8-}$ <i>deposition number:</i> 2293850	1.1724(12)	1.067(3)	0.664(11)
$[\text{P}_4\text{W}_{14}\text{O}_{58}]^{12-}$ <i>deposition number:</i> 2293849	1.5243(6)	1.0079(7)	0.6423(6)
Keggin-Lacunary-Monomer $[\text{AsW}_9\text{O}_{34}]^{9-}$ <i>deposition number:</i> 2293851	0.6318(9)	1.0403(12)	
Keggin-Lacunary-Dimer $[\text{AsW}_9\text{O}_{34}]^{9-}$ <i>deposition number:</i> 2293851	1.5761(14)	1.0403(12)	

*Die Werte ergeben sich als mittlere Werte aus verschiedenen sc-XRD-Daten.

Die .cif Dateien wurden in der Datenbank der *Cambridge Crystallographic Data Centre and Fachinformationszentrum Karlsruhe Access Structures service* unter ihren jeweiligen *deposition numbers* publiziert.

Die Bindungslänge des P-Atoms zum O_P änderte sich durch die POM-Bildung nur geringfügig und lag nah beim Literaturwert für eine P-O Bindung im freien PO_4^{3-} , bei 1.53 Å.^[261] Mit einer

Bindungslänge von 1.54(7) Å lag dieser Wert deutlich unter dem Wert der Summe der kovalenten Radien von 1.74 Å, was auf einen starken, kovalenten Bindungscharakter hindeutet. Auffällig war die deutlich verlängerte Bindungslänge zwischen dem O_P und den Mo-Atomen von 2.36(1) Å, die die Summe der kovalenten Radien von 2.01 Å überschritt. Diese Beobachtung deutete auf eine koordinative, dative Natur dieses Bindungstyps hin, mit der das PO₄³⁻ Anion an das Metallgerüst koordiniert. Die Bindungslängen der verbrückenden O_b-Liganden zu den Mo-Atomen von 1.91(4) Å, lagen im Bereich der Summe der kovalenten Radien, was auf einen kovalenten Bindungscharakter hindeutete. Besonders auffällig waren die verkürzten Längen der terminal koordinierenden O_t-Liganden von 1.69(8) Å, was im Einklang mit dem berichteten Doppelbindungscharakter des Mo=O_t Bindungstyps stand.^[243]

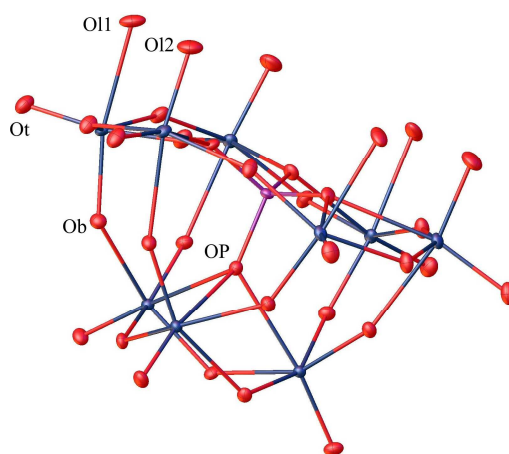


Abb. 28: Bindungstypen in der Keggin-Lacunary-Struktur [PMo₉O₃₄]⁹⁻. Die .cif Datei wurde in der Datenbank der *Cambridge Crystallographic Data Centre and Fachinformationszentrum Karlsruhe Access Structures service* mit der *deposition number* 2205006 publiziert. Farbcode: O-Atome (rot), Metalle (blau) und P-Atom (violett).^[243]

Tab. 2: Typische Bindungslängen [Å] der unterschiedlichen Bindungstypen am Beispiel des Lacunary-Anions [PMo₉O₃₄]⁹⁻ im Vergleich mit den jeweiligen Summen der kovalenten Radien.^[243]

Bindungstyp	Bindungslängen [Å]	Summe der kovalenten Radien ^[40] [Å]
P-O_P	1.54(7)	1.74
Mo-O_P	2.36(1)	2.01
Mo-O_b	1.91(4)	2.01
Mo-O_t	1.69(8)	2.01
Mo-O₁₁	2.20(8)	2.01
Mo-O₁₂	1.70(7)	2.01

Bindungsdistanzen: für O_P (Phosphat), O_b (verbrückend, *bridging*), O_t (terminal), O_l (Lacunary)

Für das Lacunary-Anion ließen sich weiterhin die Bindungslängen der Lacunary-O-Atome O_l analysieren. Es wurde ein auffälliger Trend gefunden, der eine Unterteilung dieser Bindungstypen in zwei Klassen zuließ. Dabei zeigte sich in alternierender Abfolge ein verlängertes Mo- O_l (O_{l1}) und ein verkürztes Mo- O_l (O_{l2}) Bindungsmotiv. Für das verlängerte Bindungsmotiv wurde eine Länge von 2.20(8) Å gefunden, die die Summe der kovalenten Radien überschreitet, was auf einen dativen Bindungscharakter schließen ließ. Für das verkürzte Bindungsmotiv wurde eine typische Bindungslänge von 1.70(7) Å gefunden, deren Bindungsabstand im Bereich der Mo= O_t Bindungslängen von 1.69(8) Å lagen. Den Bindungslängen nach zu urteilen könnte es sich bei diesem Bindungstyp auch um einen Doppelbindungscharakter Mo= O_{l2} handeln.^[243] Für eine genauere Untersuchung der Mo- O_l Bindungseigenschaften, wären computergestützte Simulationen (DFT) hilfreich, um die jeweiligen Bindungsordnungen berechnen zu können.

Im Allgemeinen kann die Beobachtung der verkürzten M= O_t und der verlängerten M- O_p Bindungslänge durch den *trans*-Einfluss im Grundzustand erklärt werden. Der O_t und der PO_4^{3-} Ligand befinden sich in der oktaedrischen Geometrie *trans*-ständig zueinander und teilen sich ein Orbital des Metalls. Beide Liganden konkurrieren um die Elektronendichte, jedoch übt der O_t Ligand einen stärkeren *trans*-Einfluss aus, wodurch die Bindung zu O_p geschwächt wird, wodurch sich eine verlängerte (O_p) und eine verkürzte Bindungslänge (O_t) ergibt.^[256,262,263]

Ein Studium der Bindungslängen in den sc-XRD-Daten erwies sich insbesondere für POMs als zweckmäßig, da hier Einblicke in die Bindungssituationen der zwischen den Liganden und Metallen bestehenden Bindungen getroffen werden konnten, die sich ansonsten aus komplexen, computergestützten Rechnungen ableiten lassen. Aus dem Studium der Bindungslängen in TMSPOMs konnten zudem wertvolle Informationen und Trends abgeleitet werden, die sich durch den Einbau eines oder verschiedener Elemente ergaben, wie im folgenden Abschnitt veranschaulicht.^[247]

Tab. 3: Bindungslängen [Å] der verschiedenen POMs in Mn(II) und Mn(II)/V(V) gemischt substituierten TMSPOMs.^[247]

POM	P- O_p	M- O_p	M- O_b	M= O_t
HPMo	1.534	2.439	1.916	1.674
HPMnMo	1.536	2.433	1.839	1.681
HPMn₂Mo	1.539	2.430	1.836	1.678
HPVMnMo	1.537	2.422	1.913	1.663
HPVMn₂Mo	1.532	2.425	1.913	1.666
HPV₅MnMo	1.543	2.404	1.923	1.637

Für die Mn(II) und Mn(II)/V(V) gemischt substituierten TMSPOMs in P2 ergaben sich auffällige Trends in den Bindungslängen, die mit dem Substitutionsgrad korreliert werden konnten (Tabelle 3).^[247] Die M-O_P Bindungslänge im unsubstituierten Phosphormolybdat betrug 2.439 Å und zeigte eine auffällige Kontraktion mit zunehmenden Mn(II) Substitutionsgrad y . Für HPMnMo betrug die Bindungslänge 2.433 Å und sank für HPMn₂Mo auf 2.430 Å. Diese Beobachtung ließ sich auf die geringere Ionengröße des Mn(II) im Vergleich zum Mo(VI) zurückführen. Durch den zusätzlichen Einbau von V(V) wurde eine weitere Reduktion dieser Bindungslänge auf 2.422 Å im HPVMnMo und 2.404 Å im HPV₅MnMo beobachtet. Die Bindungstypen M-O_b erfuhren durch den Mn(II) Einbau zunächst eine Kontraktion auf 1.839 Å für HPMnMo und 1.836 Å für HPMn₂Mo. Durch den zusätzlichen Einbau von V(V) wurde jedoch eine Aufweitung der Bindungslängen beobachtet, deren Werte wieder nah bei dem für das unsubstituierte Phosphormolybdat gefundenen Werten von 1.916 Å lagen. Die Bindungslängen der M=O_t Bindungsmotive sind durch den Einbau von Mn(II) nicht besonders stark beeinflusst worden, jedoch ergab sich eine auffällige Kontraktion der Bindungslängen durch den zusätzlichen Einbau von V(V) in den Mn(II)/V(V) gemischt substituierten TMSPOMs. Wie zu erwarten, werden die P-O_b Bindungslängen durch den Einbau der Fremdelemente nicht beeinflusst und entsprachen weiterhin den typischen Bindungslängen einer P-O Bindung im PO₄³⁻.^[247]

Weitere Auffälligkeiten, die durch das kristallographische Studium verschiedener POM-Strukturen getätigt wurden, betrafen die Bindungswinkel der MO₆ Oktaeder. Hier wurden Bindungswinkel im Bereich 100 bis 102 ° gefunden, was einer Verzerrung der Oktaeder im Vergleich zum idealen Oktaederwinkel von 90 ° entsprach.^[247,264,265] Eine Verzerrung der Oktaederwinkel ist aus geometrischen Gründen nötig, um den geschlossenen Strukturverband der POM-Strukturen zu gewährleisten.^[247]

Unter Verwendung der sc-XRD-Daten konnten auch die Interaktionen der POM-Anionen mit den Kationen untersucht werden. Die einzige Art Kationen, die im Rahmen dieser Arbeit untersucht wurden, waren Alkalikationen (meistens Natrium), wie am Beispiel einer Anderson-Evans-Struktur in Abbildung 29 veranschaulicht.^[250]

Die Beobachtungen, die am Beispiel der Anderson-Evans-Struktur getätigt wurden, konnten auch bei anderen Strukturmotiven gefunden werden. Es zeigte sich, dass die Alkalikationen über die terminalen Sauerstoffatome der POM-Anionen an das POM-Netzwerk binden (Na-O_t) und sich in einer oktaedrischen Umgebung (angedeutet durch die türkisen Oktaeder) befinden. Diese Umgebung rührt durch die O_t-Liganden der POM-Anionen und die vorhandenen Hydrat-

wassermoleküle (angedeutet durch die alleinstehenden roten O-Atome in Abbildung 29, genannt Na-O_{Hydrat}) her. Die Bindungswinkel lagen dabei in einem Bereich zwischen 96 und 106 °. Aus den Daten ergab sich, dass einzelne POM-Anionen teilweise über mehrere, kantenverknüpfte NaO₆ Oktaeder verbunden sind, die sich dabei in schichtartigen Strukturen zwischen den POM-Anionen aufreihen.^[250,251]

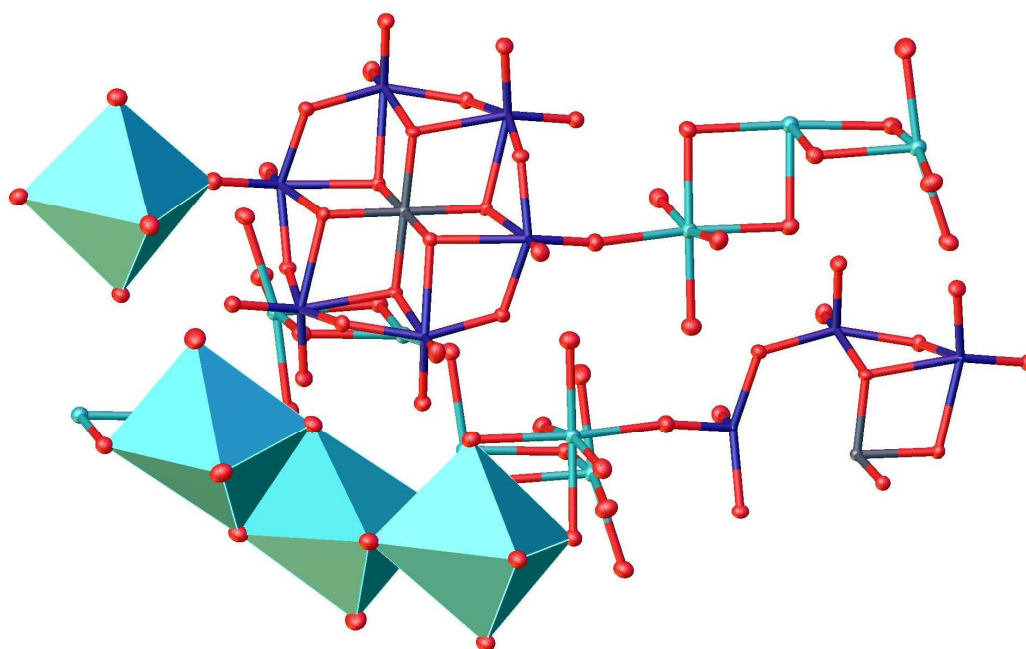


Abb. 29: Untersuchung der POM-Anion-Kationeninteraktion am Beispiel einer Anderson-Evans-Struktur. Farbcode: O-Atome (rot), Metalle (blau), Heteroelement (grau) und Na-Alkalikationen (türkis). Die .cif Datei wurde in der Datenbank der *Cambridge Crystallographic Data Centre and Fachinformationszentrum Karlsruhe Access Structures service* mit der *deposition number* 2321175 publiziert.^[251]

Ein Vergleich der gefundenen Na-O Bindungslängen mit der Summe der kovalenten Radien^[40] ergab, dass die Bindungseigenschaften der Na-O_t Bindungen eher elektrostatischer Natur (vergrößerte Bindungslänge) und die der Na-O_{Hydrat} Bindungen eher dativer Natur sind, wie aus Tabelle 4 hervorgeht.^[251]

Tab. 4: Vergleich der verschiedenen Na-O Bindungslängen mit der Summe der kovalenten Radien.^[40,251]

Bindungsmotiv	Na-O _t	Na-O _{Hydrat}	Summe der kovalenten Radien ^[40] [Å]
Bindungslänge [Å]	2.326	2.383	2.18

In dem Reviewartikel (*ChemSusChem* **2023**, *16*, e202300072)^[260] wurde zum ersten Mal die Einkristallstruktur des Katalysators HPA-5 vorgestellt, wobei die .cif-Datei mit der Originalpublikation von Poller *et al.* (*Chem. Eng. Sci.* **2022**, *264*, 118143)^[259] veröffentlicht wurde. Anhand von den sc-XRD-Daten des HPA-5 können einerseits die Problematiken, die bei der Verfeinerung von TMSPOM-Kristallstrukturen auftraten und andererseits das allgemeine Vorgehen zum Verfeinern von sc-XRD-Datensätzen für TMSPOMs, illustriert werden.^[259] Daher verdienen die gefundenen Resultate gesonderten Raum zur Diskussion.

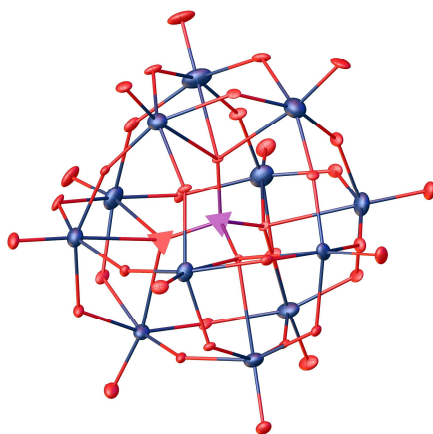


Abb. 30: Verfeinerungsergebnis unter der Annahme, dass alle Metallpositionen (blau) als Mo verfeinert wurden. Es wurden NPDs (Andeutung durch die Pyramiden) auf dem zentralen P- (violett) und einem O-Atom (rot) erhalten. R_1 : 5.44 % und wR_2 : 17.41 %.^[259]

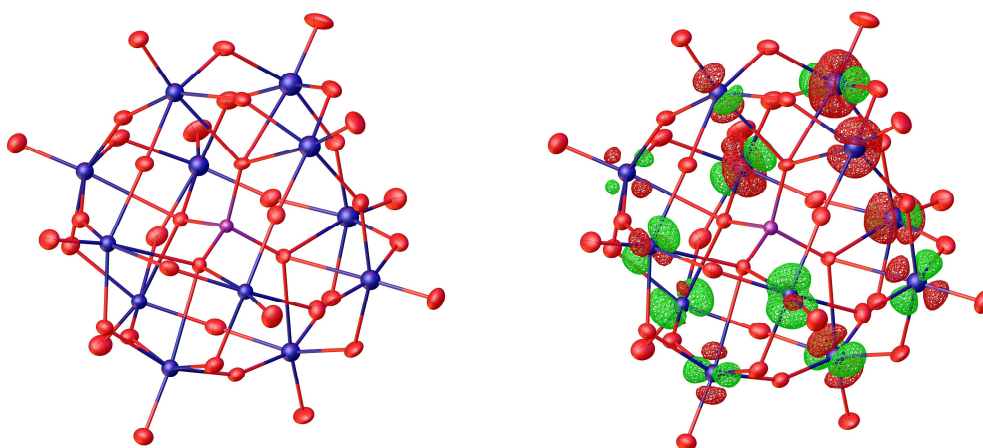


Abb. 31: Verfeinerungsergebnis unter der Annahme einer statistischen Verteilung von Mo (7/12) und V (5/12) über alle zwölf Metallpositionen (links) führt zu positiver und negativer Restelektronendichte (rechts), angedeutet durch die roten und grünen Markierungen auf den Metallatomen (blau). R_1 : 4.51 % und wR_2 : 12.11 %.^[259]

Die Lösung des Phasenproblems wurde mit dem Algorithmus ShelXT (Intrinsic Phasing) und die Verfeinerungen mit dem Algorithmus ShelXL (L.S.) in der Raumgruppe P-1 (2) durchgeführt. Ein konkretes V(V) Substitutionsmuster konnte bei der Strukturverfeinerung nicht identifiziert werden, was zur Annahme führte, dass die V- und Mo-Atome statistisch über die Metallpositionen verteilt sind. Daher wurde die Struktur zunächst verfeinert unter der Annahme, dass alle Metallpositionen mit Mo besetzt sind. Dies führte zu einem R_1 -Wert von 5.44 %, einem wR_2 -Wert von 17.41 % und hinterließ zwei *non-positive definite* (NPD) auf dem zentralen P- und einem der an das P-Atom bindenden O-Atome (Abbildung 30).^[259]

Verfeinerung der Struktur unter partieller Besetzung der Mo-Positionen mit V verbesserte das Modell auf einen R_1 -Wert von 4.51 % und einen wR_2 -Wert von 12.11 %, wodurch die NPDs verschwanden (Abbildung 31, links). Um die statistische Verteilung zu simulieren, wurden hierfür zunächst die partiellen Besetzungsfaktoren für Mo (Part 1) auf 7/12 und V (Part 2) auf 5/12 gesetzt. Jedoch zeigte sich in der Elektronendichteverteilung, dass noch eine hohe restliche positive und negative Elektronendichte vorhanden war (Abbildung 31, rechts), was darauf hindeutete, dass die Verteilung der Elemente über alle Metallpositionen nicht homogen ist.^[259] Zur Minimierung der positiven und negativen Elektronendichte wurden daher für die Verfeinerung freie Variablen definiert und die Besetzungsfaktoren der Metallpositionen individuell verfeinert. Hierfür musste die Bedingung gelten, dass die Summen der Mo- bzw. V-Besetzungsfaktoren auf allen zwölf Metallpositionen jeweils sieben bzw. fünf ergaben, damit die vorher durch die ICP-OES-Messungen verifizierte Stöchiometrie des HPA-5 Mo/V von 7/5 durch das Modell repräsentiert wurde. Nach der Verfeinerung mit den vorher definierten freien Variablen, wurden die Werte normiert. Hierfür wurde jeweils der Besetzungsfaktor von Mo bzw. V auf allen zwölf Metallpositionen durch die aufsummierten Besetzungsfaktoren einer Spezies (V und Mo) dividiert und mit fünf für V bzw. sieben für Mo multipliziert. Es resultierten die finalen Besetzungsfaktoren für V und Mo auf allen zwölf Metallpositionen (Tabelle 5), wodurch der R_1 -Wert auf 3 % sank, was für eine signifikante Verbesserung des Modells sprach. Das Ergebnis zeigte, dass die Verteilung der Elemente nicht gleich für alle Metallpositionen ist. Für HPA-5 existieren insgesamt 38 Positionsisomere, was bedeutet, dass es 38 kombinatorische Möglichkeiten gibt, fünf V-Atome auf den zwölf Metallpositionen einer Keggin-Struktur zu verteilen.^[223] Somit könnte das Ergebnis darauf hindeuten, dass einige Positionsisomere der HPA-5 Struktur durch die *self-assembly*-Synthese bevorzugt gebildet werden, was für unterschiedliche, thermodynamische Stabilitäten einzelner Positionsisomere spricht.^[259,260]

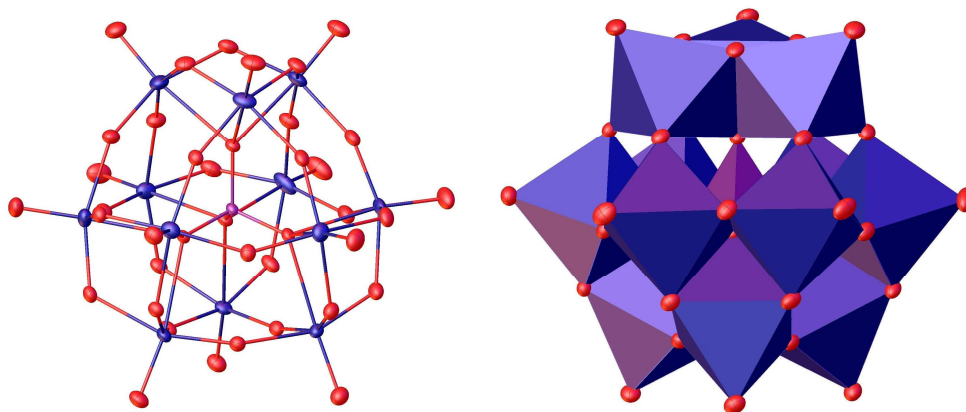


Abb. 32: Verfeinerungsergebnis unter Verwendung freier Variablen. R_1 : 2.78 % und wR_2 : 7.66 %.^[259,260]

An dieser Stelle wären computergestützte DFT-Simulationen sinnvoll, um die relativen, thermodynamischen Stabilitäten der 38 unterschiedlichen Positionsisomere zu berechnen.

Tab. 5: Besetzungsfaktoren der Metallpositionen in der Festkörperstruktur von HPA-5.^[259]

Metallposition	Besetzungsfaktor Mo	Besetzungsfaktor V
1	0.76824	0.26805
2	0.50571	0.47906
3	0.64267	0.36897
4	0.78408	0.25532
5	0.40300	0.56161
6	0.64267	0.36897
7	0.64267	0.36897
8	0.64267	0.36897
9	0.45654	0.51859
10	0.52235	0.46568
11	0.48455	0.49607
12	0.50485	0.47975
Σ Besetzung	7	5

Die isolierten Sauerstoffatome ließen sich dem Hydratwasser zuordnen und erwiesen sich zudem als stark fehlgeordnet. Hierfür wurde der Datensatz mit einer sogenannten *solvent mask*

(aka SQUEEZE)^[220] behandelt, wodurch die finalen R -Werte von R_1 2.78 % und wR_2 7.66 % erhalten wurden (Abbildung 32). Der mittels SQUEEZE gefundene *void* wurde insgesamt 128 Elektronen zugeordnet, was gerundet 13 Hydratwassermolekülen entsprach, da ein Molekül Wasser aus zehn Elektronen besteht. Mit den zwei nicht-fehlgeordneten Hydratwassersauerstoffatomen, die daher nicht in der *solvent mask* berücksichtigt wurden, ergab sich aus der Kristallstruktur ein 15 Hydrat für das HPA-5.^[259]

Generell zeigte sich aus der Kristallstruktur von HPA-5, dass das Keggin-Anion als ein Resultat der unterschiedlichen Ionengrößen von Mo(VI) und V(V) stark verzerrt ist, sodass die asymmetrische Einheit ein komplettes HPA-5 Anion mit zwölf Metallpositionen enthält.^[259]

Die .cif Datei zu diesem Datensatz wurde in der Datenbank der *Cambridge Crystallographic Data Centre and Fachinformationszentrum Karlsruhe Access Structures service* mit der *deposition number* 2177881 veröffentlicht.^[259,260]

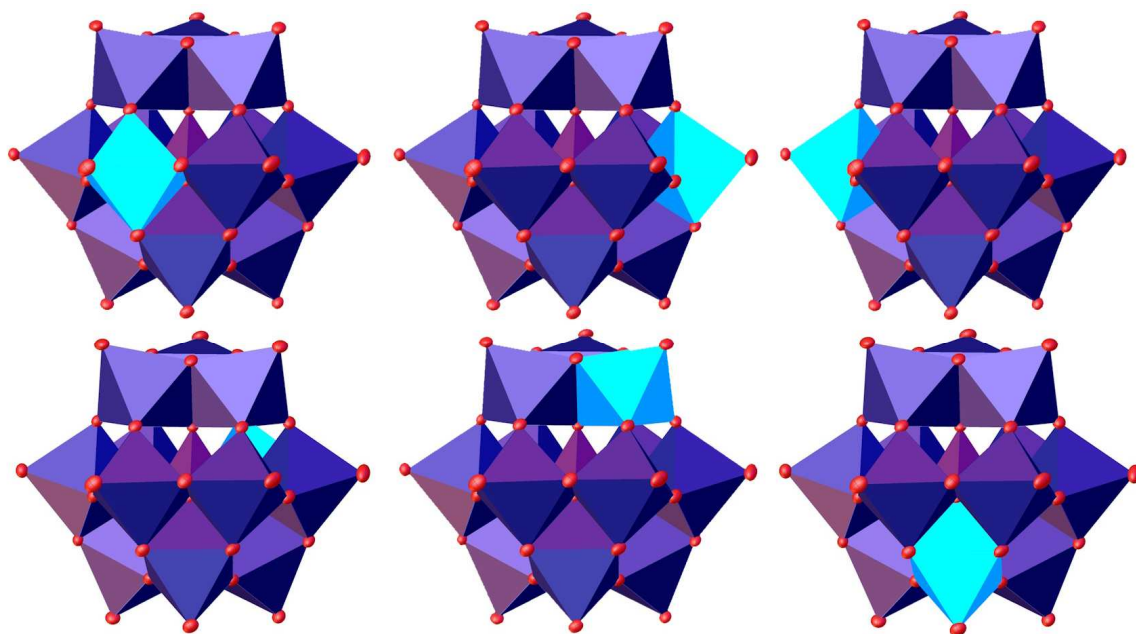


Abb. 33: Schematische Übersicht wie eine Packung der Keggin-Anionen eines einfach substituierten TMSPOM aussehen könnte. Dadurch, dass die Orientierung des Oktaeders, das das Fremdelement enthält, variieren kann, wirkt es im Mittel so, als sei das Fremdelement über alle zwölf Metallpositionen statistisch verteilt.

Die hier dargestellten Ergebnisse repräsentieren die Problematiken, die generell beim kristallographischen Studium von TMSPOMs beobachtet wurden. Es zeigte sich, dass eine durch den *self-assembly* Ansatz synthetisierte TMSPOM-Struktur kein konkretes Substitutionsmuster auf-

weist, was im Einklang mit der Beobachtung steht, dass insbesondere für höher substituierte TMSPOMs mehrere Positionsisomere gebildet werden können.^[223] Jedoch konnten auch für die niedriger substituierten TMSPOMs keine konkreten Substitutionsmuster in den sc-XRD-Daten identifiziert werden. Jedoch war hier, wie sich an den *R*-Werten bemerkbar machte, die Annahme einer homogenen, statistischen Verteilung der Fremdelemente über alle Metallpositionen zutreffender.^[247] Während der Einkristall einer TMSPOM-Struktur wächst, kann es zu verschiedenen Arten der Packungen der Keggin-Anionen, mit jeweils unterschiedlichen Orientierungen des Oktaeders, das das Fremdelement enthält, kommen, sodass das Fremdelement im Mittel über alle zwölf Metallpositionen statistisch verteilt erscheint, wie aus Abbildung 33 hervorgeht.

5. Katalytische Anwendungen für die TMSPOMs

Für die POMs HPCo_xMo und NaTeV_xW konnten im Rahmen dieser Arbeit bereits erste katalytische Anwendungen gefunden werden (P4 und P6).^[249,251] Die POMs HPCo_xMo zeigten eine katalytische Aktivität für die HyFo an 1-Hexen, wobei der POM HPCo_3Mo unter den praktizierten Reaktionsbedingungen nicht stabil blieb. Diese Beobachtung ließ sich auf die mangelnde Stabilität des 15fach anionisch-geladenen Keggin-POMs zurückführen. Mit dem Katalysator HPCo_2Mo (P4) konnte bei einem CO:H_2 Verhältnis von 1:2, einem Druck von 150 bar, einer Temperatur von 130 °C und einer Reaktionszeit von vier Stunden eine *n*-Heptanal Ausbeute von 46 % erreicht werden. Ähnlich zu den Beobachtungen aus dem OxFA-Prozess konnte die erhöhte katalytische Aktivität des POMs HPCo_2Mo im Gegensatz zum HPCoMo durch das Keggin-Positionsisomer erklärt werden, bei dem beide Co(II) Zentren direkt benachbart sind, wodurch für die Substrate mehr freie Koordinationsstellen zur Verfügung stehen.^[259] In den Ergebnissen der HyFo-Studie ergaben sich ähnliche Beobachtungen, die auch schon von anderen Co-Katalysatorsystemen bekannt sind, unter anderem die Reaktionsführung bei hohen Drücken und Reaktionstemperaturen. Jedoch wurde mit der Verwendung von Co(II) substituierten POM-Anionen eine neue, potentielle Substanzklasse als Katalysatoren für die HyFo aufgezeigt, die nach dem aktuellen Stand der Literatur noch nicht in der HyFo untersucht wurde. Hierdurch bekommt das Studium an weiteren Co(II) substituierten POMs in der HyFo eine neue Motivation, den Einfluss des POM-Gerüsts auf das Ergebnis der HyFo-Katalyse genauer zu analysieren. Möglicherweise wäre eine Reaktionsführung bei deutlich niedrigeren Reaktionstemperaturen und Drücken möglich, wenn anstatt des Co(II) das Rh(III) in die Keggin-Struktur eingebaut

werden würde. Generell wird jedoch die Motivation mit Rh zu arbeiten durch den hohen Rh-Preis abgeschwächt.^[249]

Mit den V(V) substituierten Wolframatotelluraten, insbesondere mit NaTeV₃W (P6), wurde die oxidative Umsetzung verschiedener Monofuranderivate studiert. Insbesondere die mit funktionalisierten C₁-Fragmenten substituierten Monofuranderivate zeigten eine Tendenz zur FA Bildung, die durch Abspaltung des C₁-Fragmentes hervorgerufen wurde. Die verbleibenden C₄-Fragmente lagerten sich, induziert durch die Z-Geometrie des Monofuranringes, zu MS um. Für das bifunktionalisierte Monofuranderivat HMF ergaben sich besonders hohe Umsätze und FA-Ausbeuten, da der POM-Katalysator beide Seiten des Moleküls oxidativ umsetzen konnte. Unter anderem wurde mit NaTeV₃W ein Umsatz an Furfural von 98.4 %, eine Ausbeute von FA von 33.2 % und eine Ausbeute an MS von 6.8 % erhalten (90 °C, 30 bar Sauerstoff und 15 Stunden Reaktionszeit). Die höchste MS Ausbeute (31.2 %) wurde mit Furosäure und die höchste FA Ausbeute (40.6 %) mit HMF als Substrat erhalten. Limitierungen in den katalytischen Umsetzungen ergaben sich für die nicht-funktionalisierten Monofuranderivate Furanon und 2-Methylfuranon, bei denen sich keine Angriffsfläche für den POM-Katalysator bot. Somit könnten sich auch in Studien an realen Biopolymeren auf Basis des Monofurans Limitierungen ergeben, wenn die Monofuranringmonomere nur geringfügig funktionalisiert sind.^[251,266]

6. Mechanistische Grundlagen für die Bildung verschiedener POM-Strukturtypen

Im Rahmen dieser Arbeit konnte in P5 gezeigt werden, dass die POM-Strukturtypbildung stark von der Wahl bzw. von dem Atomradius des betreffenden Heteroelementes abhängt.^[250] Computergestützt (durch Berechnung der thermodynamischen Gibb'schen Bildungsenergien) und experimentell konnte gezeigt werden, dass eine Keggin-Strukturtypbildung mit Elementen kleinerer Atomradien (Periode 3) wie dem P (Radius 0.38 Å) thermodynamisch begünstigt ist, während die Bildung der Keggin-Struktur mit Elementen größerer Radien (As 0.46 Å, Sb 0.60 Å) nicht beobachtet werden konnte. Die Beobachtung lässt sich dadurch erklären, dass in der Keggin-Struktur das Heteroelement tetraedrisch koordiniert ist und eine tetraedrische Koordination bevorzugt mit Elementen kleinerer Radien gebildet wird.^[267] Auf der anderen Seite ist die Anderson-Evans Strukturtypbildung mit Elementen größerer Atomradien thermodynamisch bevorzugt und weniger favorisiert für Elemente kleinerer Atomradien. Diese Beobachtung steht im Einklang mit der Beobachtung, dass die oktaedrische Koordinationsgeometrie bevorzugt mit Elementen größerer Radien ausgebildet wird.^[267] Für As wurde die Bildung einer offenen, lacunären Keggin-Struktur beobachtet. Diese Beobachtung wurde in Einklang mit dem größeren

Radius des As-Atoms im Vergleich zum P-Atom gebracht. Daraus resultiert ein AsO_4^{3-} Tetraeder mit einer Größe von 3.377 Å, der im Vergleich zum PO_4^{3-} Tetraeder mit 3.074 Å um 0.303 Å vergrößert ist. So kann die Keggin-Strukturtypbildung für As offenbar nicht stabilisiert werden. Durch die Bildung einer offenen, vakanten Keggin-Lacunary-Struktur, kann die Spannung ausgeglichen werden, die im Inneren der Struktur durch den AsO_4^{3-} Tetraeder verursacht wird.^[250] Auf der anderen Seite zeigte sich auch, dass das As-Atom noch zu klein ist, um sechs O-Atome zu koordinieren, wodurch sich die Anderson-Evans-Struktur mit As nicht ausbilden kann. Diese Beobachtung stand auch im Einklang mit der im Vergleich zum Sb höheren Gibb'schen Bildungsenergie für die Anderson-Evans-Bildung mit As.^[250] Das Element Stickstoff N (0.16 Å) ist im Einklang mit den experimentellen und computergestützten Resultaten nicht befähigt überhaupt an der POM-Bildung beteiligt zu sein. Diese Beobachtung wurde auf den besonders kleinen Atomradius des N-Atoms zurückgeführt, wodurch N weder zur Annahme einer tetraedrigen noch einer oktaedrischen Koordination fähig ist, was auch im Einklang mit dem Fehlen eines zum PO_4^{3-} analogen NO_4^{3-} Anions steht. Bedingt durch den kleinen Radius vom N-Atom würden sich die O-Atome in einer erzwungenen, tetraedrigen bzw. oktaedrischen Umgebung zu nah kommen, sodass die repulsiven Kräfte zwischen den Atomen dominieren. Dies erklärt

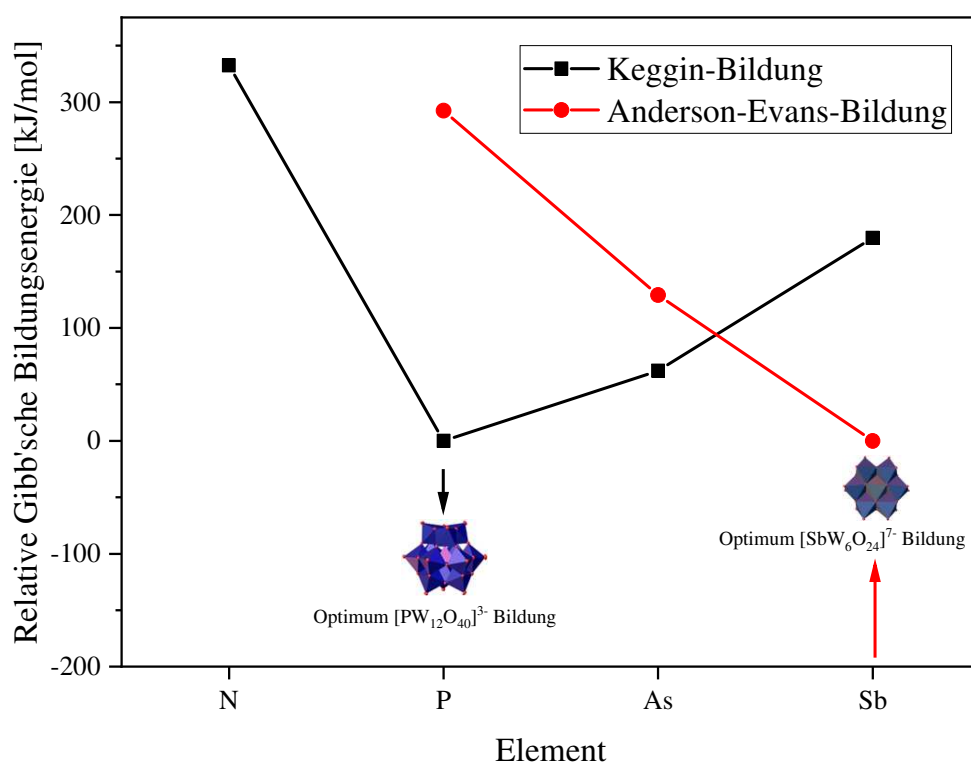


Abb. 34: Auftragung der relativen Gibb'schen Bildungsenergien für die Keggin- und Anderson-Evans-Strukturtypbildungen in Abhängigkeit des Heteroelementes aus Gruppe 15. Es wurde für P auf jeweils Null normiert.^[250]

Die neuen Anderson-Evans POMs zeigten dabei in den CV- und SWV-Daten deutlich weniger RedOx-Potentiale als es für die schon vorher untersuchten Keggin-Typ TMSPOM-Strukturen der Fall war.^[251] Dies legt die These nahe, dass neben dem Substitutionselement auch der jeweilige Strukturtyp einen Einfluss auf die RedOx-Aktivität eines POMs nehmen könnte. Um aussagekräftige Trends formulieren zu können, wären hierfür weitere elektrochemische Analysen an weiteren V(V) substituierten POM-Strukturtypen sinnvoll. Wie schon in P3 gezeigt, weisen die V(V) substituierten Molybdotellurate deutlich intensivere Peak-Potentiale als die Wolframotellurate auf.^[248] Jedoch ist ein RedOx-katalytisches Studium der Molybdotellurate nicht möglich, da wässrige Lösungen NaTeMo abscheiden und somit eine Zersetzung des Katalysators daher nicht zu verhindern ist.^[251]

7 Literaturliste

- [1] R. Dehghani, S. Aber, F. Mahdizadeh, *CLEAN – Soil, Air, Water* **2018**, *46*, 1800413.
- [2] M. Ammam, *J. Mater. Chem. A* **2013**, *1*, 6291.
- [3] C. L. Hill, C. M. Prosser-McCartha, *Coord. Chem. Rev.* **1995**, *143*, 407–455.
- [4] J. J. Borrás-Almenar, E. Coronado, A. Müller, M. Pope, *Polyoxometalate Molecular Science*, Springer Netherlands, Dordrecht, **2003**.
- [5] K. Nomiya, M. Miwa, *Polyhedron* **1985**, *4*, 1407–1412.
- [6] F. Steffler, G. F. De Lima, H. A. Duarte, *J. Mol. Struct.* **2020**, *1213*, 128159.
- [7] T. Ueda, Y. Nishimoto, R. Saito, M. Ohnishi, J. Nambu, *Inorganics* **2015**, *3*, 355–369.
- [8] H. S. Booth, Ed. , *Inorganic Syntheses*, John Wiley & Sons, Inc., Hoboken, NJ, USA, **1939**.
- [9] J. D. H. Strickland, *J. Am. Chem. Soc.* **1952**, *74*, 862–867.
- [10] J. Canny, A. Teze, R. Thouvenot, G. Herve, *Inorg. Chem.* **1986**, *25*, 2114–2119.
- [11] J. Canny, R. Thouvenot, A. Teze, G. Herve, M. Leparulo-Loftus, M. T. Pope, *Inorg. Chem.* **1991**, *30*, 976–981.
- [12] K. J. Schmidt, G. J. Schrobilgen, J. F. Sawyer, *Acta Crystallogr. Sect. C Cryst. Struct. Commun.* **1986**, *42*, 1115–1118.
- [13] S. Yerra, S. R. Amanchi, S. K. Das, *J. Mol. Struct.* **2014**, *1062*, 53–60.
- [14] A. Müller, E. Krickemeyer, J. Meyer, H. Bögge, F. Peters, W. Plass, E. Diemann, S. Dillinger, F. Nonnenbruch, M. Randerath, C. Menke, *Angew. Chemie Int. Ed. English* **1995**, *34*, 2122–2124.
- [15] A. Müller, E. Beckmann, H. Bögge, M. Schmidtman, A. Dress, *Angew. Chemie Int. Ed.* **2002**, *41*, 1162–1167.
- [16] U. Kortz, A. Müller, J. van Slageren, J. Schnack, N. S. Dalal, M. Dressel, *Coord. Chem.*
-

- Rev.* **2009**, 253, 2315–2327.
- [17] M. T. Pope, A. Müller, *Angew. Chemie* **1991**, 103, 56–70.
- [18] M. B. Čolović, M. Lacković, J. Lalatović, A. S. Mougharbel, U. Kortz, D. Z. Krstić, *Curr. Med. Chem.* **2019**, 27, 362–379.
- [19] S. Shigeta, S. Mori, T. Yamase, N. Yamamoto, N. Yamamoto, *Biomed. Pharmacother.* **2006**, 60, 211–219.
- [20] T. Yamase, *J. Mater. Chem.* **2005**, 15, 4773.
- [21] D. L. Long, E. Burkholder, L. Cronin, *Chem. Soc. Rev.* **2007**, 36, 105–121.
- [22] A. F. Holleman, E. und Nils Wiberg, G. Fischer, *Lehrbuch Der Anorganischen Chemie*, Berlin, New York, **2009**.
- [23] J. H. Kyle, *J. Chem. Soc., Dalt. Trans.* **1983**, 2609–2612.
- [24] S. Sheshmani, M. A. Fashapoyeh, M. Mirzaei, B. A. Rad, S. N. Ghortolmesh, M. Yousefi, *Indian J. Chem. - Sect. A Inorganic, Phys. Theor. Anal. Chem.* **2011**, 50, 1725–1729.
- [25] T. Moeller, *Inorganic Syntheses*, John Wiley & Sons, Inc., Hoboken, NJ, USA, **1990**.
- [26] S. Himeno, M. Takamoto, T. Ueda, *Bull. Chem. Soc. Jpn.* **2005**, 78, 1463–1468.
- [27] P. A. Abramov, A. A. Shmakova, M. Haouas, G. Fink, E. Cadot, M. N. Sokolov, *New J. Chem.* **2017**, 41, 256–262.
- [28] V. Štengl, V. Houšková, S. Bakardjieva, N. Murafa, P. Bezdička, *J. Mater. Res.* **2010**, 25, 2015–2024.
- [29] G. Brauer, *Handbuch Der Präparativen Anorganischen Chemie*, **1978**.
- [30] J. K. Lee, J. Melsheimer, S. Berndt, G. Mestl, R. Schlögl, K. Köhler, *Appl. Catal. A Gen.* **2001**, 214, 125–148.
- [31] J. J. Berzelius, *Ann. Phys.* **1826**, 82, 369–392.
-

- [32] J.-C. G. de Marignac, *Ann. Chim. Phys.* **1860**, 257–307.
- [33] A. Rosenheim, O. Liebknecht, *Justus Liebig's Ann. der Chemie* **1899**, 308, 40–67.
- [34] M. T. Pope, M. Sadakane, U. Kortz, *Eur. J. Inorg. Chem.* **2019**, 2019, 340–342.
- [35] A. Miolati, R. Pizzighelli, *J. für Prakt. Chemie* **1908**, 77, 417–456.
- [36] L. Pauling, *J. Am. Chem. Soc.* **1929**, 51, 2868–2880.
- [37] J. F. Keggin, *Proc. R. Soc. London. Ser. A, Contain. Pap. a Math. Phys. Character* **1934**, 144, 75–100.
- [38] M. X. Xu, S. Lin, L.-M. Xu, S.-L. Zhen, *Transit. Met. Chem.* **2004**, 29, 332–335.
- [39] X. U. Yan, X. U. Ji-Qing, G. Y. U. Yang, G. D. I. Yang, Y. Xing, Y. H. Lin, H. Q. Jia, *Acta Crystallogr. Sect. C Cryst. Struct. Commun.* **1998**, 54, 9–11.
- [40] P. Pyykkö, M. Atsumi, *Chem. - A Eur. J.* **2009**, 15, 186–197.
- [41] F. Kehrmann, *Zeitschrift für Anorg. Chemie* **1894**, 7, 406–426.
- [42] A. Rosenheim, J. Jaenicke, *Zeitschrift für Anorg. und Allg. Chemie* **1917**, 101, 235–275.
- [43] B. Dawson, *Acta Crystallogr.* **1953**, 6, 113–126.
- [44] A. F. Wells, *Structural Inorganic Chemistry*, Oxford, **1984**.
- [45] I.-M. Mbomekalle, Y. W. Lu, B. Keita, L. Nadjo, *Inorg. Chem. Commun.* **2004**, 7, 86–90.
- [46] C. R. Graham, R. G. Finke, *Inorg. Chem.* **2008**, 47, 3679–3686.
- [47] P. Wu, Y. Wang, B. Huang, Z. Xiao, *Nanoscale* **2021**, 13, 7119–7133.
- [48] A. A. Mukhacheva, V. V. Volchek, V. V. Yanshole, N. B. Kompankov, A. L. Gushchin, E. Benassi, P. A. Abramov, M. N. Sokolov, *Inorg. Chem.* **2020**, 59, 2116–2120.
- [49] A. Bijelic, A. Rompel, *Acc. Chem. Res.* **2017**, 50, 1441–1448.
- [50] H. J. Lunk, H. Hartl, *ChemTexts* **2021**, 7, 1–30.
-

- [51] J. S. Anderson, *Nature* **1937**, *140*, 1937.
- [52] H. T. Evans, *J. Am. Chem. Soc.* **1948**, *70*, 1291–1292.
- [53] L. Zhao, S. Shen, H. Yu, *Zeitschrift für Naturforsch. - Sect. B J. Chem. Sci.* **2008**, *63*, 799–803.
- [54] A. L. Nolan, R. C. Burns, G. A. Lawrance, D. C. Craig, *Acta Crystallogr. Sect. C Cryst. Struct. Commun.* **2000**, *56*, 729–730.
- [55] K. Y. Monakhov, C. Gourlaouen, R. Pattacini, P. Braunstein, *Inorg. Chem.* **2012**, *51*, 1562–1568.
- [56] M. Nyman, T. M. Alam, F. Bonhomme, M. A. Rodriguez, C. S. Frazer, M. E. Welk, *J. Clust. Sci.* **2006**, *17*, 197–219.
- [57] I. Lindqvist, O. Hassel, M. Webb, M. Rottenberg, *Acta Chem. Scand.* **1950**, *4*, 1066–1074.
- [58] O. Linnenberg, A. Kondinski, K. Y. Monakhov, in *Supramol. Syst.*, **2017**, pp. 39–66.
- [59] O. Nagano, Y. Sasaki, *Acta Crystallogr. Sect. B Struct. Crystallogr. Cryst. Chem.* **1979**, *35*, 2387–2389.
- [60] X. López, J. J. Carbó, C. Bo, J. M. Poblet, *Chem. Soc. Rev.* **2012**, *41*, 7537–7571.
- [61] A. J. Bridgeman, G. Cavigliasso, *Faraday Discuss.* **2003**, *124*, 239.
- [62] F.-Q. Zhang, H.-S. Wu, Y.-Y. Xu, Y.-W. Li, H. Jiao, *J. Mol. Model.* **2006**, *12*, 551–558.
- [63] D. J. Sures, P. I. Molina, P. Miró, L. N. Zakharov, M. Nyman, *New J. Chem.* **2016**, *40*, 928–936.
- [64] P. Müscher-Polzin, C. Näther, W. Bensch, *Zeitschrift für Naturforsch.* **2020**, *75*, 583–588.
- [65] M. Dabbabi, M. Boyer, *J. Inorg. Nucl. Chem.* **1976**, *38*, 1011–1014.
- [66] G. Mestl, T. Ilkenhans, D. Spielbauer, M. Dieterle, O. Timpe, J. Kröhnert, F. Jentoft, H. Knözinger, R. Schlögl, *Appl. Catal. A Gen.* **2001**, *210*, 13–34.
-

- [67] A. Patel, N. Narkhede, S. Singh, S. Pathan, *Catal. Rev. - Sci. Eng.* **2016**, *58*, 337–370.
- [68] Y. Sakai, A. Shinohara, K. Hayashi, K. Nomiya, *Eur. J. Inorg. Chem.* **2006**, *2006*, 163–171.
- [69] L. A. Combs-Walker, C. L. Hill, *Inorg. Chem.* **1991**, *30*, 4016–4026.
- [70] C. Marchal-Roch, E. Ayrault, L. Lisnard, J. Marrot, F.-X. Liu, F. Sécheresse, *J. Clust. Sci.* **2006**, *17*, 283–290.
- [71] P. J. Domaille, G. Watunya, *Inorg. Chem.* **1986**, *25*, 1239–1242.
- [72] W. H. Knoth, P. J. Domaille, R. D. Farlee, *Organometallics* **1985**, *4*, 62–68.
- [73] R. Massart, R. Contant, J. M. Fruchart, J. P. Ciabrini, M. Fournier, *Inorg. Chem.* **1977**, *16*, 2916–2921.
- [74] V. F. Odyakov, E. G. Zhizhina, *Russ. J. Inorg. Chem.* **2009**, *54*, 361–367.
- [75] V. F. Odyakov, E. G. Zhizhina, R. I. Maksimovskaya, *Appl. Catal. A Gen.* **2008**, *342*, 126–130.
- [76] V. F. Odyakov, E. G. Zhizhina, *Russ. J. Inorg. Chem.* **2009**, *54*, 361–367.
- [77] Y. Sun, J. Liu, E. Wang, *Inorganica Chim. Acta* **1986**, *117*, 23–26.
- [78] C. P. Pradeep, D.-L. Long, C. Streb, L. Cronin, *J. Am. Chem. Soc.* **2008**, *130*, 14946–14947.
- [79] R. S. Winter, J. M. Cameron, L. Cronin, *J. Am. Chem. Soc.* **2014**, *136*, 12753–12761.
- [80] S. Passadis, T. Kabanos, Y.-F. Song, H. Miras, *Inorganics* **2018**, *6*, 71.
- [81] D. E. Salazar Marcano, S. Lentink, M. A. Moussawi, T. N. Parac-Vogt, *Inorg. Chem.* **2021**, *60*, 10215–10226.
- [82] N. I. Gumerova, A. Rompel, *Chem. Soc. Rev.* **2020**, *49*, 7568–7601.
- [83] S. Pathan, A. Patel, *Ind. Eng. Chem. Res.* **2013**, *52*, 11913–11919.
-

- [84] S. Mir, B. Yadollahi, R. Omidyan, G. Azimi, *RSC Adv.* **2020**, *10*, 33718–33730.
- [85] C. Li, K. Yamaguchi, K. Suzuki, *Angew. Chemie* **2021**, *133*, 7036–7040.
- [86] S. Himeno, M. Hashimoto, T. Ueda, *Inorganica Chim. Acta* **1999**, *284*, 237–245.
- [87] R. Strandberg, *Acta Chem. Scand.* **1974**, *28a*, 217–225.
- [88] C. Li, K. Yamaguchi, K. Suzuki, *Chem. Commun.* **2021**, *57*, 7882–7885.
- [89] C. Li, A. Jimbo, K. Yamaguchi, K. Suzuki, *Chem. Sci.* **2021**, *12*, 1240–1244.
- [90] C. Li, N. Mizuno, K. Yamaguchi, K. Suzuki, *J. Am. Chem. Soc.* **2019**, *141*, 7687–7692.
- [91] S. M. Kulikov, O. M. Kulikova, R. I. Maksimovskaya, I. V. Kozhevnikov, *Bull. Acad. Sci. USSR Div. Chem. Sci.* **1990**, *39*, 1763–1766.
- [92] J. A. Dias, S. C. L. Dias, E. Caliman, J. Bartis, L. Francesconi, in *Inorg. Synth.*, **2014**, pp. 210–217.
- [93] G. S. Girolami, A. P. Sattelberger, Eds., *Inorganic Syntheses: Volume 36*, Wiley, **2014**.
- [94] V. F. Odyakov, E. G. Zhizhina, *React. Kinet. Catal. Lett.* **2008**, *95*, 21–28.
- [95] S. Himeno, M. Takamoto, T. Ueda, *J. Electroanal. Chem.* **1999**, *465*, 129–135.
- [96] J. M. Brégeault, M. Vennat, S. Laurent, J. Y. Piquemal, Y. Mahha, E. Briot, P. C. Bakala, A. Atlamsani, R. Thouvenot, *J. Mol. Catal. A Chem.* **2006**, *250*, 177–189.
- [97] T. Ueda, K. Yamashita, A. Onda, *Appl. Catal. A Gen.* **2014**, *485*, 181–187.
- [98] R. G. Finke, M. W. Droege, P. J. Domaille, *Inorg. Chem.* **1987**, *26*, 3886–3896.
- [99] D. R. Park, H. Kim, J. C. Jung, S. H. Lee, I. K. Song, *Catal. Commun.* **2008**, *9*, 293–298.
- [100] H. Xu, Z. Bai, G. Wang, K. P. O'Halloran, L. Tan, H. Pang, H. Ma, *Microchim. Acta* **2017**, *184*, 4295–4303.
- [101] L. E. Briand, G. M. Valle, H. J. Thomas, *J. Mater. Chem.* **2002**, *12*, 299–304.
- [102] D. Drewes, E. M. Limanski, B. Krebs, *Eur. J. Inorg. Chem.* **2004**, *2004*, 4849–4853.
-

- [103] J. Albert, J. Mehler, J. Tucher, K. Kastner, C. Streb, *ChemistrySelect* **2016**, *1*, 2889–2894.
- [104] K. F. Jahr, J. Fuchs, R. Oberhauser, *Chem. Ber.* **1968**, *101*, 477–481.
- [105] J. Fuchs, K. F. Jahr, *Zeitschrift für Naturforsch. B* **1968**, *23*, 1380–1380.
- [106] K.-H. Tytko, B. Schönfeld, *Zeitschrift für Naturforsch. B* **1975**, *30*, 471–484.
- [107] H. Avcı Özbek, *Chem. Pap.* **2023**, *77*, 5663–5669.
- [108] J. Fuchs, K. F. Jahr, G. Heller, *Chem. Ber.* **1963**, *96*, 2472–2484.
- [109] V. G. Maiorov, A. I. Nikolaev, V. K. Kopkov, V. Y. Kuznetsov, N. L. Mikhailova, *Russ. J. Appl. Chem.* **2011**, *84*, 1137–1140.
- [110] A. Patel, S. Pathan, *J. Coord. Chem.* **2012**, *65*, 3122–3132.
- [111] A. J. Gaunt, I. May, M. J. Sarsfield, D. Collison, M. Helliwell, I. S. Denniss, *Dalt. Trans.* **2003**, *3*, 2767–2771.
- [112] M. Y. Darensbourg, Ed. , *Inorganic Syntheses*, Wiley, Hoboken, NJ, USA, **1998**.
- [113] D. R. Park, J. H. Choi, S. Park, I. K. Song, *Appl. Catal. A Gen.* **2011**, *394*, 201–208.
- [114] D. K. Lyon, W. K. Miller, T. Novet, P. J. Domaille, E. Evitt, D. C. Johnson, R. G. Finke, *J. Am. Chem. Soc.* **1991**, *113*, 7209–7221.
- [115] R. Contant, J.-P. Ciabrini, *J. Inorg. Nucl. Chem.* **1981**, *43*, 1525–1528.
- [116] T. Boyd, S. G. Mitchell, D. Gabb, D.-L. Long, L. Cronin, *Chem. - A Eur. J.* **2011**, *17*, 12010–12014.
- [117] S. Sugiarto, M. Sadakane, *Chem. – A Eur. J.* **2023**, *13*, 287–288.
- [118] D. P. Smith, M. T. Pope, *Inorg. Chem.* **1973**, *12*, 331–336.
- [119] Z. Wang, X. Xin, M. Zhang, Z. Li, H. Lv, G. Yang, *Sci. China Chem.* **2022**, *65*, 1515–1525.
-

- [120] M. Abbessi, R. Contant, R. Thouvenot, G. Hervé, *Inorg. Chem.* **1991**, *30*, 1695–1702.
- [121] W. Huang, L. C. Francesconi, T. Polenova, *Inorg. Chem.* **2007**, *46*, 7861–7869.
- [122] L. E. Briand, H. J. Thomas, G. T. Baronetti, *Appl. Catal. A Gen.* **2000**, *201*, 191–202.
- [123] C. Wang, L. Weng, Y. Ren, C. Du, B. Yue, M. Gu, H. He, *Zeitschrift für Anorg. und Allg. Chemie* **2011**, *637*, 472–477.
- [124] E. G. Zhizhina, V. F. Odyakov, *React. Kinet. Catal. Lett.* **2008**, *95*, 301–312.
- [125] G. A. Tsigdinos, C. J. Hallada, *Inorg. Chem.* **1968**, *7*, 437–441.
- [126] J. H. Grate, *J. Mol. Catal. A Chem.* **1996**, *114*, 93–101.
- [127] D. R. Park, H. Kim, J. C. Jung, S. H. Lee, I. K. Song, *Res. Chem. Intermed.* **2008**, *34*, 845–851.
- [128] R. G. Finke, B. Rapko, R. J. Saxton, P. J. Domaille, *J. Am. Chem. Soc.* **1986**, *108*, 2947–2960.
- [129] L. H. Bi, E. B. Wang, J. Peng, R. D. Huang, L. Xu, C. W. Hu, *Inorg. Chem.* **2000**, *39*, 671–679.
- [130] J. H. Choi, D. R. Park, S. Park, I. K. Song, *Korean J. Chem. Eng.* **2011**, *28*, 2137–2141.
- [131] L. M. Sanchez, Á. G. Sathicq, G. T. Baronetti, H. J. Thomas, G. P. Romanelli, *Catal. Letters* **2014**, *144*, 172–180.
- [132] J. Fuchs, W. Freiwald, H. Hartl, *Acta Crystallogr. Sect. B Struct. Crystallogr. Cryst. Chem.* **1978**, *34*, 1764–1770.
- [133] K. Nishikawa, A. Kobayashi, Y. Sasaki, *Bull. Chem. Soc. Jpn.* **1975**, *48*, 889–892.
- [134] I. A. Weinstock, *Chem. Rev.* **1998**, *98*, 113–170.
- [135] J. Kaur, I. V. Kozhevnikov, *Chem. Commun.* **2002**, 2508–2509.
- [136] Y. Izumi, K. Matsuo, K. Urabe, *J. Mol. Catal.* **1983**, *18*, 299–314.
-

- [137] N. Mizuno, K. Katamura, Y. Yoneda, M. Misono, *J. Catal.* **1983**, 83, 384–392.
- [138] I. V. Kozhevnikov, *Russ. Chem. Rev.* **1987**, 56, 811–825.
- [139] I. V. Kozhevnikov, *Chem. Rev.* **1998**, 98, 171–198.
- [140] J. Reichert, J. Albert, *ACS Sustain. Chem. Eng.* **2017**, 5, 7383–7392.
- [141] J. Albert, R. Wölfel, A. Bösmann, P. Wasserscheid, *Energy Environ. Sci.* **2012**, 5, 7956–7962.
- [142] J. Albert, D. Lüders, A. Bösmann, D. M. Guldi, P. Wasserscheid, *Green Chem.* **2014**, 16, 226–237.
- [143] J. Albert, P. Wasserscheid, *Green Chem.* **2015**, 17, 5164–5171.
- [144] J. Reichert, B. Brunner, A. Jess, P. Wasserscheid, J. Albert, *Energy Environ. Sci.* **2015**, 8, 2985–2990.
- [145] S. G. Maerten, D. Voß, M. A. Liauw, J. Albert, *ChemistrySelect* **2017**, 1, 1–8.
- [146] H. Veith, M. Voges, C. Held, J. Albert, *ACS Omega* **2017**, 2, 8982–8989.
- [147] P. Preuster, J. Albert, *Energy Technol.* **2018**, 6, 501–509.
- [148] S. Ponce, M. Trabold, A. Drochner, J. Albert, B. J. M. Etzold, *Chem. Eng. J.* **2019**, 369, 443–450.
- [149] J. Albert, M. Mendt, M. Mozer, D. Voß, *Appl. Catal. A Gen.* **2019**, 570, 262–270.
- [150] D. Voß, S. Ponce, S. Wesinger, B. J. M. Etzold, J. Albert, *RSC Adv.* **2019**, 9, 29347–29356.
- [151] A. Bukowski, D. Esau, A. A. Rafat Said, A. Brandt-Talbot, J. Albert, *Chempluschem* **2020**, 85, 373–386.
- [152] S. Maerten, C. Kumpidet, D. Voß, A. Bukowski, P. Wasserscheid, J. Albert, *Green Chem.* **2020**, 22, 4311–4320.
- [153] D. Voß, M. Kahl, J. Albert, *ACS Sustain. Chem. Eng.* **2020**, 8, 10444–10453.
-

- [154] S. Wesinger, M. Mendt, J. Albert, *ChemCatChem* **2021**, *13*, 3662–3670.
- [155] S. Ponce, S. Wesinger, D. Ona, D. A. Streitwieser, J. Albert, *Biomass Convers. Biorefinery* **2023**, *13*, 7199–7206.
- [156] B. Bertleff, J. Claußnitzer, W. Korth, P. Wasserscheid, A. Jess, J. Albert, *ACS Sustain. Chem. Eng.* **2017**, *5*, 4110–4118.
- [157] B. Bertleff, R. Goebel, J. Claußnitzer, W. Korth, M. Skiborowski, P. Wasserscheid, A. Jess, J. Albert, *ChemCatChem* **2018**, *10*, 4602–4609.
- [158] B. Bertleff, J. Claußnitzer, W. Korth, P. Wasserscheid, A. Jess, J. Albert, *Energy and Fuels* **2018**, *32*, 8683–8688.
- [159] J. Claußnitzer, B. Bertleff, W. Korth, J. Albert, P. Wasserscheid, A. Jess, *Chem. Eng. Technol.* **2020**, *43*, 465–475.
- [160] M. Ahmadian, M. Anbia, *Energy and Fuels* **2021**, *35*, 10347–10373.
- [161] F. M. Li, M. Q. Hua, Y. C. Wei, J. X. Liu, J. H. Gong, C. Wang, P. W. Wu, Y. Huang, H. M. Li, W. S. Zhu, *Pet. Sci.* **2021**, *18*, 983–993.
- [162] I. A. Weinstock, R. H. Atalla, U. P. Agarwal, J. L. Minor, C. Petty, *Spectrochim. Acta Part A Mol. Spectrosc.* **1993**, *49*, 819–829.
- [163] D. V. Evtuguin, C. P. Neto, J. Rocha, J. D. Pedrosa de Jesus, *Appl. Catal. A Gen.* **1998**, *167*, 123–139.
- [164] D. V. Evtuguin, C. Pascoal Neto, J. Rocha, *Holzforschung* **2000**, *54*, 381–389.
- [165] D. V. Evtuguin, A. I. D. Daniel, A. J. D. Silvestre, F. M. L. Amado, C. Pascoal Neto, *J. Mol. Catal. A-Chem.* **2000**, *154*, 217–224.
- [166] A. Carneiro, A. Abreu, V. Evtuguin, C. P. Neto, G. Guebitz, A. C. Paulo, *J. Mol. Catal. B Enzym.* **2000**, *9*, 293–295.
- [167] A. A. Shatalov, D. V. Evtuguin, C. Pascoal Neto, *Carbohydr. Polym.* **2000**, *43*, 23–32.
- [168] M. Suchy, D. S. Argyropoulos, *Tappi J.* **2001**, *785*, 2–43.
-

- [169] A. Gaspar, D. V. Evtuguin, C. P. Neto, *Holzforschung* **2004**, 58, 640–649.
- [170] A. R. Gaspar, D. V. Evtuguin, C. P. Neto, *Ind. Eng. Chem. Res.* **2004**, 43, 7754–7761.
- [171] A. A. Ibrahim, M. El-Sakhawy, S. Kamel, *Palpu Chongi Gisul/Journal Korea Tech. Assoc. Pulp Pap. Ind.* **2005**, 37, 56–62.
- [172] A. R. Gaspar, J. A. F. Gamelas, D. V. Evtuguin, C. Pascoal Neto, *Green Chem.* **2007**, 9, 717–73.
- [173] A. R. Gaspar, J. A. F. Gamelas, D. V. Evtuguin, C. P. Neto, *Chem. Eng. Commun.* **2009**, 196, 801–811.
- [174] A. A. Shatalov, H. Pereira, *Chem. Eng. J.* **2009**, 155, 380–387.
- [175] A. A. Shatalov, H. Pereira, *Bioresour. Technol.* **2010**, 101, 4616–4621.
- [176] A. A. Shatalov, H. Pereira, *Bioresour. Technol.* **2010**, 101, 9330–9334.
- [177] S. Cao, X. Ma, X. Luo, F. Huang, L. Huang, L. Chen, *Oxygen Pulping Selectivity*, **2013**.
- [178] H. Lange, S. Decina, C. Crestini, in *Eur. Polym. J.*, **2013**, pp. 1151–1173.
- [179] A. A. Shatalov, *Green Chem.* **2017**, 19, 5092–5102.
- [180] R. Ma, M. Guo, X. Zhang, *Catal. Today* **2018**, 302, 50–60.
- [181] W. Guan, C.-W. Tsang, C. S. K. Lin, C. Len, H. Hu, C. Liang, *Bioresour. Technol.* **2020**, 298, 122432.
- [182] A. R. Mankar, A. Modak, K. K. Pant, *Adv. Sustain. Syst.* **2021**, 1–25.
- [183] T. M. C. Hoang, E. R. H. Van Eck, W. P. Bula, J. G. E. Gardeniers, L. Lefferts, K. Seshan, *Green Chem.* **2015**, 17, 959–972.
- [184] N. V. Gromov, T. B. Medvedeva, K. N. Sorokina, Y. V. Samoylova, Y. A. Rodikova, V. N. Parmon, *ACS Sustain. Chem. Eng.* **2020**, 8, 18947–18956.
- [185] S. Enthaler, J. von Langermann, T. Schmidt, *Energy Environ. Sci.* **2010**, 3, 1207–1217.
-

- [186] A. K. Singh, S. Singh, A. Kumar, *Catal. Sci. Technol.* **2016**, *6*, 12–40.
- [187] *Angew. Chemie* **1948**, *60*, 211–214.
- [188] F. Hebrard, P. Kalck, *Chem. Rev.* **2009**, *109*, 4272–4282.
- [189] A. Behr, D. W. Agar, J. Jörissen, A. J. Vorholt, *Einführung in Die Technische Chemie*, Springer Berlin Heidelberg, Berlin, Heidelberg, **2016**.
- [190] R. F. Heck, D. S. Breslow, *J. Am. Chem. Soc.* **1960**, *82*, 4438–4439.
- [191] R. F. Heck, D. S. Breslow, *J. Am. Chem. Soc.* **1961**, *83*, 4023–4027.
- [192] L. H. Slaugh, R. D. Mullineaux, *J. Organomet. Chem.* **1968**, *13*, 469–477.
- [193] E. R. Tucci, *I&EC Prod. Res. Dev.* **1968**, *7*, 125–128.
- [194] G. Süss-Fink, J. Reiner, *J. Mol. Catal.* **1982**, *16*, 231–242.
- [195] F. E. Paulik, *Catal. Rev.* **1972**, *6*, 49–84.
- [196] C. W. Kohlpaintner, R. W. Fischer, B. Cornils, *Appl. Catal. A Gen.* **2001**, *221*, 219–225.
- [197] A. Behr, G. Henze, L. Johnen, C. Awungacha, *J. Mol. Catal. A Chem.* **2008**, *285*, 20–28.
- [198] D. Steinborn, *Grundlagen Der Metallorganischen Komplexkatalyse*, Springer Berlin Heidelberg, Berlin, Heidelberg, **2019**.
- [199] P. M. Maitlis, D. Belli Dell'Amico, *Organometallics* **2014**, *33*, 6989–7006.
- [200] F. Calderazzo, *Angew. Chemie* **1977**, *89*, 305–317.
- [201] A. R. Siedle, W. B. Gleason, R. A. Newmark, R. P. Skarjune, P. A. Lyon, C. G. Markell, K. O. Hodgson, A. L. Roe, *Inorg. Chem.* **1990**, *29*, 1667–1673.
- [202] S. Sartipi, M. J. Valero Romero, E. Rozhko, Z. Que, H. A. Stil, J. de With, F. Kapteijn, J. Gascon, *ChemCatChem* **2015**, *7*, 3243–3247.
- [203] S. Feng, Q. Yu, X. Ma, X. Yu, N. Yan, *Natl. Sci. Open* **2023**, *2*, 20220064.
- [204] J. Sneddon, M. D. Vincent, *Anal. Lett.* **2008**, *41*, 1291–1303.
-

- [205] G. Tyler, J. Yvon, *ICP-OES, ICP-MS and AAS Techniques Compared*, **2003**.
- [206] A. W. Coats, J. P.- Redfern, *Analyst* **1963**, 88, 906.
- [207] W. Deboucha, N. Leklou, A. Khelidj, M. N. Oudjit, *Constr. Build. Mater.* **2017**, 146, 687–701.
- [208] A. J. Bridgeman, *Chem. - A Eur. J.* **2004**, 10, 2935–2941.
- [209] R. Mattes, H. Bierbüsse, J. Fuchs, *Zeitschrift für Anorg. und Allg. Chemie* **1971**, 385, 230–242.
- [210] A. L. Spek, *Acta Crystallogr. Sect. D Biol. Crystallogr.* **2009**, 65, 148–155.
- [211] C. B. Hübschle, G. M. Sheldrick, B. Dittrich, *J. Appl. Crystallogr.* **2011**, 44, 1281–1284.
- [212] L. J. Farrugia, *J. Appl. Crystallogr.* **2012**, 45, 849–854.
- [213] L. J. Farrugia, *J. Appl. Crystallogr.* **1999**, 32, 837–838.
- [214] S. R. Parkin, *Acta Crystallogr. Sect. E Crystallogr. Commun.* **2021**, 77, 452–465.
- [215] O. V. Dolomanov, L. J. Bourhis, R. J. Gildea, J. A. K. Howard, H. Puschmann, *J. Appl. Crystallogr.* **2009**, 42, 339–341.
- [216] C. F. Macrae, I. J. Bruno, J. A. Chisholm, P. R. Edgington, P. McCabe, E. Pidcock, L. Rodriguez-Monge, R. Taylor, J. Van De Streek, P. A. Wood, *J. Appl. Crystallogr.* **2008**, 41, 466–470.
- [217] G. M. Sheldrick, *Acta Crystallogr. Sect. A Found. Crystallogr.* **2008**, 64, 112–122.
- [218] A. L. Spek, *J. Appl. Crystallogr.* **2003**, 36, 7–13.
- [219] A. Linden, *Acta Crystallogr. Sect. E Crystallogr. Commun.* **2020**, 76, 765–775.
- [220] A. L. Spek, *Acta Crystallogr. Sect. C Struct. Chem.* **2015**, 71, 9–18.
- [221] D. Rehder, *Bull. Magn. Reson.* **1982**, 4, 33–83.
- [222] K. Lee, G. Pozarnsky, O. Zarembowitch, A. McCormick, *Chem. Eng. J. Biochem. Eng.*
-

- J.* **1996**, *64*, 215–223.
- [223] M. T. Pope, T. F. Scully, *Inorg. Chem.* **1975**, *14*, 953–954.
- [224] L. Pettersson, I. Andersson, J. H. Grate, A. Selling, *Inorg. Chem.* **1994**, *33*, 982–993.
- [225] A. Selling, I. Andersson, J. H. Grate, L. Pettersson, *Eur. J. Inorg. Chem.* **2000**, *2000*, 1509–1521.
- [226] H. Salavati, N. Rasouli, *Mater. Res. Bull.* **2011**, *46*, 1853–1859.
- [227] H. Li, L. Swenson, R. J. Doedens, M. I. Khan, *Dalt. Trans.* **2016**, *45*, 16511–16518.
- [228] T. Yamase, *Chem. Rev.* **1998**, *98*, 307–325.
- [229] K. P. Barteau, J. E. Lyons, I. K. Song, M. A. Barteau, *Top. Catal.* **2006**, *41*, 55–62.
- [230] N. K. K. Raj, A. V. Ramaswamy, P. Manikandan, *J. Mol. Catal. A Chem.* **2005**, *227*, 37–45.
- [231] I. K. Song, H. S. Kim, M. S. Chun, *Korean J. Chem. Eng.* **2003**, *20*, 844–849.
- [232] N. Elgrishi, K. J. Rountree, B. D. McCarthy, E. S. Rountree, T. T. Eisenhart, J. L. Dempsey, *J. Chem. Educ.* **2018**, *95*, 197–206.
- [233] M. Privman, T. Hepel, *J. Electroanal. Chem.* **1995**, *382*, 137–144.
- [234] J. J. J. Chen, M. A. Barteau, *Ind. Eng. Chem. Res.* **2016**, *55*, 9857–9864.
- [235] F. M. Zonoz, *Electrocatalysis* **2016**, *7*, 215–225.
- [236] Z. Han, Y. Zhao, J. Peng, Y. Feng, J. Yin, Q. Liu, *Electroanalysis* **2005**, *17*, 1097–1102.
- [237] P. Galloni, V. Conte, B. Floris, *Coord. Chem. Rev.* **2015**, *301–302*, 240–299.
- [238] M. Sadakane, E. Steckhan, *Chem. Rev.* **1998**, *98*, 219–237.
- [239] T. Ueda, *ChemElectroChem* **2018**, *5*, 823–838.
- [240] M. S. Freund, N. S. Lewis, *Inorg. Chem.* **1994**, *33*, 1638–1643.
-

- [241] J. A. Thompson, R. González-Cabaleiro, L. Vilà-Nadal, *Inorg. Chem.* **2023**, *62*, 12260–12271.
- [242] D. Y. Hwang, Y. S. Ha, S. Kim, *Bull. Korean Chem. Soc.* **2001**, *22*, 441–442.
- [243] J.-C. Raabe, T. Esser, F. Jameel, M. Stein, J. Albert, M. J. Poller, *Inorg. Chem. Front.* **2023**, *10*, 4854–4868.
- [244] F. Zonnevillje, C. M. Tourne, G. F. Tourne, *Inorg. Chem.* **1982**, *21*, 2742–2750.
- [245] X. Wu, T. Huang, Q. Wu, L. Xu, *Dalt. Trans.* **2015**, *45*, 271–275.
- [246] E. Rafiee, I. M. Baltork, S. Tangestaninejad, A. Azad, S. Moinee, *Zeitschrift für Naturforsch. - Sect. B J. Chem. Sci.* **2006**, *61*, 601–606.
- [247] J.-C. Raabe, J. Albert, M. J. Poller, *Chem. – A Eur. J.* **2022**, *28*, 1–12.
- [248] J.-C. Raabe, J. Aceituno Cruz, J. Albert, M. J. Poller, *Inorganics* **2023**, *11*, 138.
- [249] J.-C. Raabe, L. Hombach, M. J. Poller, A. Collauto, M. M. Roessler, A. Vorholt, A. K. Beine, J. Albert, *ChemCatChem* **2024**, DOI 10.1002/cctc.202400395.
- [250] J.-C. Raabe, F. Jameel, M. Stein, J. Albert, M. J. Poller, *Dalt. Trans.* **2024**, *53*, 454–466.
- [251] J.-C. Raabe, T. Esser, M. J. Poller, J. Albert, *Catal. Today* **2024**, 114899.
- [252] K. M. Merz, R. Hoffmann, *Inorg. Chem.* **1988**, *27*, 2120–2127.
- [253] P. K. Mehrotra, R. Hoffmann, *Inorg. Chem.* **1978**, *17*, 2187–2189.
- [254] S. Sakaki, M. Ogawa, Y. Musashi, *J. Phys. Chem.* **1995**, *99*, 17134–17138.
- [255] A. N. Desnoyer, W. He, S. Behyan, W. Chiu, J. A. Love, P. Kennepohl, *Chem. – A Eur. J.* **2019**, *25*, 5259–5268.
- [256] C. E. Housecroft, A. G. Sharpe, *Anorganische Chemie*, Pearson Studium, München, **2006**.
- [257] B. Tansel, J. Sager, T. Rector, J. Garland, R. F. Strayer, L. Levine, M. Roberts, M. Hummerick, J. Bauer, *Sep. Purif. Technol.* **2006**, *51*, 40–47.
-

- [258] T. Esser, M. Huber, D. Voß, J. Albert, *Chem. Eng. Res. Des.* **2022**, *185*, 37–50.
- [259] M. J. Poller, S. Bönisch, B. Bertleff, J.-C. Raabe, A. Görling, J. Albert, *Chem. Eng. Sci.* **2022**, *264*, 118143.
- [260] J.-C. Raabe, M. J. Poller, D. Voß, J. Albert, *ChemSusChem* **2023**, *16*, 2013–2015.
- [261] I. Persson, M. Trublet, W. Klysubun, *J. Phys. Chem. A* **2018**, *122*, 7413–7420.
- [262] J. Breibeck, N. I. Gumerova, A. Rompel, *ACS Org. Inorg. Au* **2022**, *2*, 477–495.
- [263] J.-P. Wang, W. Guan, L.-K. Yan, Z.-M. Su, *Comput. Theor. Chem.* **2011**, *976*, 1–7.
- [264] P. Kubáček, R. Hoffmann, *J. Am. Chem. Soc.* **1981**, *103*, 4320–4332.
- [265] M. Darari, A. Francés-Monerris, B. Marekha, A. Doudouh, E. Wenger, A. Monari, S. Haacke, P. C. Gros, *Molecules* **2020**, *25*, 5991–6011.
- [266] T. Esser, A. Wassenberg, J. Raabe, D. Voß, J. Albert, *ACS Sustain. Chem. Eng.* **2024**, *12*, 543–560.
- [267] U. Müller, *Anorganische Strukturchemie*, Vieweg+Teubner, Wiesbaden, **2008**.
- [268] A. L. Spek, *Acta Crystallogr. Sect. E Crystallogr. Commun.* **2020**, *76*, 1–11.

Anhang

Gefahrstoffliste

Die in dieser Arbeit verwendeten Chemikalien, Produkte und Lösungsmittel sind in Tabelle 6 und 7 mit den entsprechenden H- und P-Sätzen sowie Hinweisen zur Entsorgung aufgelistet.

Tab. 6: Im Rahmen dieser Arbeit verwendete Chemikalien und Lösungsmittel.

Substanz	Gefahrenpiktogramme	H-Sätze	P-Sätze	Entsorgung
Aceton- d_6	GHS02 GHS07 Gefahr	H225, H319, H336, EUH066	P210, P233, P240, P241, P242, P305+P351+P338	a
Acetonitril	GHS02 GHS07 Gefahr	H225, H302+H312+H332, H319	P210, P280, P301+P312, P303+P361+P353, P304+P340+P312, P305+P351+P338	a
Arsen-(III)-oxid	GHS06 GHS08 GHS05 GHS09 Gefahr	H300, H314, H350, H410	P201, P280, P301+P330+P331, P305+P353+P338, P308+P313, P273	b
Cobalt-(II)-acetat Tetrahydrat	GHS08 GHS09 Gefahr	H302, H319, H334, H317, H341, H350i, H360F, H410	P201, P273, P280, P301+P312+P330, P302+P352, P308+P313	c
Demineralisiertes Wasser	Kein Gefahrstoff nach GHS.			d
Deuteriumoxid	Kein Gefahrstoff nach GHS.			d
Diethylether	GHS02 GHS07 Gefahr	H224, H302, H336, EUH019, EUH066	P210, P233, P240, P241, P301+P312, P403+P233	a
Dinatriumhydrogen- phosphat	Kein Gefahrstoff nach GHS.			e
Diniob-(V)-oxid	Kein Gefahrstoff nach GHS.			f
Divanadium-(V)- pentoxid	GHS06 GHS08 GHS09 Gefahr	H301, H330, H335, H341, H350, H361fd, H362, H372, H411	-	g

Eisen-(III)-chlorid	GHS05 GHS07 Gefahr	H302, H315, H318	P280, P301+P312+P330, P302+P352, P305+P351+P338+ P310	c
Essigsäure	GHS02 GHS05 Gefahr	H226, H314	P210, P280, P301+P330+P331, P303+P361+P353, P305+P351+P338	a
2-Furaldehyd/Furfural	GHS02 GHS06 GHS08 Gefahr	H226, H301, H312, H330, H315, H319, H335, H351	P210, P280, P302+P352, P304+P340, P305+P351+P338, P310	h
Furanon	Kein Gefahrstoff nach GHS.			h
Furfurylalkohol	GHS06 GHS08 Gefahr	H301+H311, H315, H319, H330, H335, H351, H373	P280, P302+P352, P304+P340, P310, P362, P305+P351+P338, P403+P233	h
Furosäure	GHS05 Gefahr	H314	P260, P280, P303+P361+P353, P304+P340+P310, P305+P351+P338, P363	h
5-(Hydroxymethyl)- furfural/HMF	GHS07 Achtung	H315, H319	P264, P280, P302+P352, P305+P351+P338, P332+P313, P337+P313	h
Indium-(III)-hydroxid	GHS08 Gefahr	H372, H412	P260, P264, P270, P273, P314, P501	b
Kaliumchlorid	Kein Gefahrstoff nach GHS.			c
Kaliumhexahydroxo- antimonat(V)	GHS07 GHS09 Achtung	H302+H411	P271, P264, P270, P301+P312, P304+P340+P312	i
Kaliumhydroxid	GHS05 GHS07 Gefahr	H290, H302, H314	P234, P260, P280, P301+P312, P303+P361+P353, P305+P351+P338	e
Kupfer-(II)-chlorid Dihydrat	GHS05 GHS07 GHS09 Gefahr	H302+H312, H315, H318, H410	P273, P280, P301+P312+P330, P302+P352+P312, P305+P351+P338 +P310	c

Mangan-(II)-acetat	GHS07 Achtung	H315, H319	P280, P302+P352, P305+P351+P338, P362	c
2-Methylfuran	GHS06 GHS02 Gefahr	H225, H301, H330	P210, P233, P240, P241, P242, P304+P340+P310, P403+P235	h
Molybdän-(VI)-trioxid	GHS08 GHS07 Achtung	H319, H335, H351	P201, P202, P261, P264, P305+P351+P338, P308+P313	f
Natriumacetat	Kein Gefahrstoff nach GHS.			c
Natriumcarbonat	GHS07 Achtung	H319	P264, P280, P305+P351+P338, P337+P313	e
Natriumhydroxid	GHS05 Gefahr	H290, H314	P280, P301+P330+P331, P305+P351+P338, P308+P310	e
Natriumchlorid	Kein Gefahrstoff nach GHS.			c
Natriummolybdat-Dihydrat	Kein Gefahrstoff nach GHS.			c
Natriumvanadat	GHS06 GHS08 GHS09 Gefahr	H301, H332, H319, H361, H372, H411	P260, P280, P304+P340, P314, P305+P351+P338, P273	i
Natriumwolframat-Dihydrat	GHS07 Achtung	H302	P264, P270, P301+P312, P330, P501	c
Nickel-(II)-acetat Tetrahydrat	GHS07 GHS08 GHS09 Gefahr	H302+H332, H317, H334, H341, H350i, H360, H372, H410	P201, P273, P280, P301+P312+P330, P302+P352, P308+P313	c
Phosphorsäure	GHS05 GHS07 Gefahr	H290, H302, H314	P234, P270, P280, P301+P312, P303+P361+P353	c
Salpetersäure	GHS03 GHS06 GHS05 Gefahr	H272, H290, H330, H314, EUH071	P210, P220, P280, P303+P361+P353, P304+P340+P310, P305+P351+P338	j
Salzsäure	GHS05 GHS07 Gefahr	H290, H314, H335	P280, P303+P361+P353, P305+P351+P338 +P310	c

Tellursäure	GHS07 Achtung	H332	P261, P271, P304+P340+P312	c
Tetrabutylammonium- bromid	GHS08 GHS07 Achtung	H302, H315, H319, H361fd, H412	P202, P273, P301+P312, P302+P352, P305+P351+P338, P308+P313	h
Wasserstoffperoxid 30 %	GHS03 GHS05 GHS07 Gefahr	H272, H302, H332, H318	P220, P261, P280, P305+P351+P338	k
Wolfram-(VI)-trioxid	Kein Gefahrstoff nach GHS.			g
Zink	GHS02 GHS09 Gefahr	H250, H260, H410	P222, P210, P231+P232, P280, P370+P378, P273, P302+P335+P334	l
Zinn	Kein Gefahrstoff nach GHS.			l

Alle verwendeten POMs mit Hinweisen zur Entsorgung sind in Tabelle 7 aufgelistet.

Tab. 7: Im Rahmen dieser Arbeit verwendete POMs als Produkte oder Zwischenprodukte.

Substanz	Pikto- gramme	H-Sätze	P-Sätze	Entsorgung
$\text{Na}_9[\text{PMo}_9\text{O}_{34}]$	Keine Einstufung nach GHS. Daher besondere Vorsicht!			c
$\text{Na}_6[\text{P}_2\text{Mo}_{18}\text{O}_{62}]$				c
$\text{H}_{3+4x}[\text{PCo}_x\text{Mo}_{12-x}\text{O}_{40}]$				c
$\text{H}_{3+x}[\text{PV}_x\text{Mo}_{12-x}\text{O}_{40}]$				c
$\text{H}_{3+x+4y}[\text{PV}_x\text{Mn}_y\text{Mo}_{12-x-y}\text{O}_{40}]$				c
$\text{Na}_{3+4x}[\text{PCo}_x\text{Mo}_{12-x}\text{O}_{40}]$				c
$(\text{Na}_a(\text{nBu}_4\text{N})_b)_{3+4x}[\text{PCu}_x\text{Mo}_{12-x}\text{O}_{40}]$				h
$\text{Na}_{3+3x}[\text{PFe}_x\text{Mo}_{12-x}\text{O}_{40}]$				c
$\text{Na}_{3+3x}[\text{PIn}_x\text{Mo}_{12-x}\text{O}_{40}]$				c
$\text{Na}_{3+x}[\text{PNb}_x\text{Mo}_{12-x}\text{O}_{40}]$				c
$\text{Na}_{3+4x}[\text{PNi}_x\text{Mo}_{12-x}\text{O}_{40}]$				c
$\text{Na}_{3+2x}[\text{PSn}_x\text{Mo}_{12-x}\text{O}_{40}]$				c
$\text{Na}_3[\text{PW}_x\text{Mo}_{12-x}\text{O}_{40}]$				c
$\text{Na}_{3+4x}[\text{PZn}_x\text{Mo}_{12-x}\text{O}_{40}]$				c
Phosphormolybdänsäure	GHS03 GHS05 Gefahr	H272, H314	P210, P220, P260, P280, P303+P361+P353, P305+P351+P338	c

Phosphorwolframsäure	GHS05 GHS07 GHS09 Gefahr	H302, H314, H411	P260, P273, P280, P301+P312, P303+P361+P353, P305+P351+P338	c
$K_8[Nb_6O_{19}]$	Keine Einstufung nach GHS. Daher besondere Vorsicht!			m
$Na_8[W_{12}O_{40}]$				c
$Na_9[AsW_9O_{34}]$				c
$Na_9[PW_9O_{34}]$				c
$Na_{12}[P_4W_{14}O_{58}]$				c
$Na_7[SbW_6O_{24}]$				c
$Na_6[TeMo_6O_{24}]$				c
$Na_7[TeVMo_5O_{24}]$				c
$Na_8[TeV_2Mo_4O_{24}]$				c
$Na_9[TeV_3Mo_3O_{24}]$				c
$Na_6[TeW_6O_{24}]$				c
$Na_7[TeVW_5O_{24}]$				c
$Na_8[TeV_2W_4O_{24}]$				c
$Na_9[TeV_3W_3O_{24}]$				c
$Na_{3+x}[PV_xW_{12-x}O_{40}]$				c

Folgende Entsorgungsbehälter stehen am Fachbereich Chemie der Universität Hamburg zur Verfügung:

- (1) Kontaminierte Betriebsmittel
- (2) Andere Säuren (nitratfrei)
- (3) Andere Säuren (nitrathaltig)
- (4) Andere Basen
- (5) Halogenfreie, organische Lösungsmittel
- (6) Halogenhaltige, organische Lösungsmittel

Entsorgungsschlüssel

- (a) In Sammelbehälter (5) entsorgen.
- (b) In Salzsäure suspendieren und vorsichtig erwärmen, bis sich eine klare Lösung bildet. Die Lösung in Sammelbehälter (2) entsorgen.
- (c) In Wasser lösen oder verdünnen und die Lösung in Sammelbehälter (2) entsorgen.
- (d) In Sammelbehälter (2) entsorgen.
- (e) In Wasser lösen und die Lösung in Sammelbehälter (4) entsorgen.
- (f) In Sammelbehälter (1) entsorgen.

- (g) In Wasser suspendieren und mit Natriumhydroxid einen basischen pH-Wert einstellen, bis sich eine klare Lösung bildet. Die Lösung in Sammelbehälter (4) entsorgen.
- (h) In Aceton lösen und die Lösung in Sammelbehälter (5) entsorgen.
- (i) In Wasser suspendieren und refluxieren, bis sich eine klare Lösung bildet. Die Lösung in Sammelbehälter (4) entsorgen.
- (j) In Wasser lösen oder verdünnen und die Lösung in Sammelbehälter (3) entsorgen.
- (k) In Wasser verdünnen und vorsichtig mit einer wässrigen Natriumthiosulfat-Lösung versetzen. Die Lösung dann in Sammelbehälter (2) entsorgen.
- (l) Vorsichtig kleine Mengen in verdünnter Salzsäure-Lösung einrühren. Die Lösung dann in Sammelbehälter (2) entsorgen.
- (m) In wässriger Kaliumhydroxid-Lösung lösen und die Lösung in Sammelbehälter (4) entsorgen.


Folgende KMR-Stoffe der Kategorien 1A und 1B wurden im Rahmen dieser Arbeit verwendet (Tabelle 8).









Tab. 8: Im Rahmen dieser Arbeit verwendeten KMR-Stoffe der Kategorien 1A und 1B.

CAS-RN	Stoffname (IUPAC) und Kategorie	Verfahren
1327-53-3	Arsen-(III)-oxid	Synthese
6147-53-1	Cobalt-(II)-acetat Tetrahydrat	Synthese
6018-89-9	Nickel-(II)-acetat Tetrahydrat	Synthese
1314-62-1	Divanadium-(V)-pentoxid	Synthese

Die folgenden Seiten enthalten eine Auflistung aller *Globally Harmonized System of Classification and Labelling of Chemicals* (GHS) Symbole (Tabelle 9):

Tab. 9: GHS-Symbole mit entsprechender Bedeutung.

Kodierung	Piktogramm	Beschreibung	Signalwort	Gefahrenbezeichnung	Buchstabe	Gefahrenklasse
GHS01		Explodierende Bombe	Gefahr	Explosionsgefährlich	E	Instabile, explosive Substanzen oder Gemische

GHS02		Flamme	Gefahr/ Achtung	Entzündlich Leicht- entzündlich Hochentzündlich	F F+	Entzündbar
GHS03		Flamme über einem Kreis	Gefahr	Brandfördernd	O	Entzündend oder oxidierend wirkend
GHS04		Gasflasche	Achtung	-	-	Gase unter Druck (verdichtet)
GHS05		Ätzende Flüssigkeit tropfend aus Reagenzgläsern auf Hand und Oberfläche	Gefahr/ Achtung	Ätzend	C	Korrosiv wirkend auf Metalle und/oder hautätzend
GHS06		Totenkopf mit gekreuzten Knochen	Gefahr	Giftig Sehr giftig	T T+	Akute Toxizität
GHS07		Dickes Ausrufezei- chensymbol	-	Reizend	Xi	
GHS08		Menschlicher Oberkörper angriffen/verletz t durch eine Substanz	Gefahr/ Achtung	Gesundheits- schädlich	Xn	Diverse Gesund- heits- gefahren
GHS09		Umwelt, abgestorbener Baum, toter Fisch und totes Gewässer	Ach- tung/ Gefahr	Umweltge- fährlich	N	Gewässer- gefährdend

Online verfügbare „supporting information“

Im folgenden Kapitel befindet sich eine Auflistung aller online zur Verfügung stehenden „supporting information“ in der Reihenfolge wie auch die Publikationen im Rahmen dieser Arbeit aufgeführt wurden.

Electronic Supporting Information

1	Experimental Details	4
1.1	Chemicals	4
1.2	Analytical methods	5
1.3	Synthesis of Na ₉ [PMo ₉ O ₃₄]	9
1.4	Synthesis of K ₈ [Nb ₆ O ₁₉]	10
1.5	Nanofiltration.....	16
1.6	Synthesis of the transition metal substituted POMs using LHPA-3.....	18
1.6.1	In situ Lacunary synthesis	18
1.6.2	Synthesis of Co(II), Ni(II), Cu(II), Fe(III), V(V) and W(VI) substituted POMs.....	19
1.6.3	Synthesis of the In(III) substituted POM	20
1.6.4	Synthesis of Zn(II) and Sn(IV) substituted POMs	20
1.6.5	Synthesis of Nb(V) and Nb(V)/V(V) mixed substituted POMs.....	21
1.7	Characterization.....	22
1.8	Computational Methods	31
2	Additional data	43
2.1	Vibrational spectroscopy	44
2.1.1	Infrared- and Raman-spectra of transition metal substituted Keggin POMs	44
2.1.2	Assignment of peaks to structural features/vibration modes	46
2.2	NMR spectroscopy	47
2.3	UV-Vis spectroscopy.....	50
2.4	Electrochemistry	54
2.4.1	Electrochemical characterization of LHPA-3	54
2.4.2	Electrochemical characterization of the transition metal substituted POMs.....	56
2.5	X-ray diffraction	63

2.6	Microscopy	70
3	Literature.....	74

Different element substituted phosphomolybdates were synthesized in this work. Every compound was analyzed in detail using vibrational spectroscopy (infrared (IR) and Raman), ultraviolet visible (UV-Vis) spectroscopy and inductively coupled plasma optical emission spectrometry (ICP-OES). Hydration water contents (unit mol of water/mol of POM) were calculated from datasets that have been obtained using thermogravimetric analysis (TGA). Single crystals were prepared, and the structure was determined using single crystal X-ray diffraction (sc-XRD). Furthermore, powder X-ray diffractograms (p-XRD) were measured of each compound. Moreover, ^{31}P and if possible ^{51}V nuclear magnetic resonance (NMR) spectroscopy was used to characterize the compounds in solution. The Redox activity was investigated using electrochemical methods such as cyclic voltammetry (CV) and square wave voltammetry (SWV).

1 Experimental Details

1.1 Chemicals

The chemicals used in this work were obtained from the following suppliers:

- Sodium molybdate dihydrate: Carl Roth with a purity of 99.5 %
- Sodium tungstate dihydrate: VWR chemical with a purity of 99 %
- Disodium hydrogen phosphate: Merck (pro analysis)
- Sodium vanadium oxide: Alfa Aesar with a purity of 96 %
- Niobium(V) oxide: Alfa Aesar with a purity of 99.5 % (metals basis)
- Tin (grained pure): Merck (Art. 780a)
- Iron(III) chloride: Merck (anhydrous)
- Indium hydroxide: Thermo scientific with a purity of 99.8 % (metals basis)
- Cobalt(II) acetate tetrahydrate: ABCR chemical with a purity of 98 %
- Nickel(II) acetate tetrahydrate: Aldrich Chemistry with a purity of 99.0 %
- Copper(II) chloride dihydrate: Alfa Aesar with a purity of 99 %
- Zinc (grained pure): Merck
- Hydrochloric acid: VWR chemicals as 37 % solution in water
- Hydrogen peroxide: VWR chemicals as 30 % solution in water
- Potassium hydroxide: Chemsolute with a purity of 85 % (Art. 1681.1000)
- Potassium chloride: Thermoscientific with a purity of 99 %
- Sodium carbonate: Grüssing with a purity of 99.5 %
- Tetrabutylammonium bromide (TBAB): Carl Roth with a purity of 99 %
- Deuterium oxide: Deutero GmbH with a purity of 99.9 %
- Acetonitrile: VWR chemicals (HiPerSolv Chromanorm for HPLC-SUPER GRADIENT Reag. Ph. Eur., USP, ACS; water < 30 ppm – suitable for UPLC/UHPLC instruments)

Further used:

- Campingaz, mixture of butane and propane
- Deionized water was used as solvent

For some precursor compounds, stoichiometry was calculated based on mass fraction of the metal rather than nominal molar mass, to account for impurities or hydration water. The following values were used:

- Iron(III) chloride: 25.95 wt-% Fe.
- Cobalt(II) acetate dihydrate: 23.2 wt-% Co.
- Nickel(II) acetate dihydrate: 22.7 wt-% Ni.
- Copper(II) chloride: 35.65 wt-% Cu.

Potassium hexaniobate x hydrate: Before KNb was used for synthesis, elemental analysis was used to determine the Nb content, which is the basis for all stoichiometric calculations. The mass percentages for Nb fluctuate in the range between 37 % and 41 % depending on the crystal water content.

1.2 Analytical methods

ICP-OES:

All samples were analyzed using an ICP-OES-spectrometer for elemental analysis (Fa. Spectro, type ARCOS) for Mo, W, V, In and P (method ICP-OES). The elements Fe, Co, Ni, Cu, Zn and Sn were measured with an AAS-F (Fa. Thermo, type Solaar S Series) (method: F-AES without HKL).

- Sample preparation KNb: the initial weight was dissolved in water (1 mL), 30 % hydrogen peroxide in water (1 mL) and acidified with 37 % hydrochloric acid solution in water.
- Sample preparation NaPV₃Mo, NaPIn₃Mo, NaPCoMo, NaPNiMo and LHPA-3: the initial weight was dissolved in water (5 mL), acidified with a 65 % nitric acid solution in water (100 μ L), and the solution was filled up with water to 25 mL in a volumetric flask.
- Sample preparation NaKPV₂NbMo, NaKPVNb₂Mo, NaPFeMo and NaPZnMo: the initial weight was dissolved in water (5 mL) and the solution was filled up with water to 25 mL in a volumetric flask.
- Sample preparation NaKPNbMo and NaKPNb₃Mo: the initial weight was dissolved in water (5 mL) and the solution was filled up with water to 25 mL in a volumetric flask.
- Sample preparation NaKPNb₂Mo: the initial weight was dissolved in water (5 mL), warmed up to ensure complete dissolution and the solution was filled up with water to 25 mL in a volumetric flask.

- Sample preparation NaPSnMo: the initial weight was dissolved in 96 % sulfuric acid (2 mL), 65 % nitric acid (0.5 mL), 37 % hydrochloric acid (10 mL) and the solution was filled up with 3 M hydrochloric acid solution in water to 50 mL in a volumetric flask.
- Sample preparation nBu₄NPCu₂Mo: the initial weight was dissolved in inverse aqua regia (3 HNO₃/1 HCl) (6 mL), hydrofluoric acid (1 mL) and was filled up with water to 25 mL in a volumetric flask (Anton Paar/Organic high).

TGA analysis:

TGA measurements were performed with a TG 209 F1 Libra of NETZSCH. The data were processed with the software Proteus from NETZSCH. About 20 mg of the sample was weighed into a duran-glas crucible and the change in mass was measured at the following temperature program:

- Tare
- 1 minute waiting time
- Heating to 30 °C with maximum heating rate
- Stay at 30 °C for 15 minutes
- Heating to 350 °C with a heating rate of 10 K/min
- Stay at 350 °C for 30 minute
- The sample was then cooled to room temperature

Starting temperature was below 30 °C. During all measurements, a nitrogen flow of 60 sccm/min was passed through the instrument. A measurement with an empty crucible was used for background correction. The TGA data show three regions: hygroscopic water (water that comes from the air), lattice water (water from crystal association) and the mass consistency (pure POM without any moisture). The final data were exported as a *x/y* text document. With the use of Origin® 2019b the TGA data were plotted as follows: on the *y*-axis the mass difference measured in mg and on the *x*-axis the temperature measured in °C.

IR spectroscopy

IR spectra were measured in attenuated total reflection (ATR) measurement mode on a QATR™-S single-reflection ATR (with a diamond prism) from Shimadzu. From the raw data obtained, the baseline was corrected, and the peaks were determined manually. The IR data were then exported as an *x/y* text document.

Raman spectroscopy

Raman spectra were measured on a SENTERRA Raman microscope from Bruker Optik GmbH. The aperture was set to 50 x 1000 μm . A 20 objective was used on the microscope. The excitation laser has a wavelength of 785 nm and the measurement range used was between 75 cm^{-1} and 1525 cm^{-1} . The integration time was 16 seconds, the number of scans was 8 and the Raman laser power was 10 mW.

Single crystal structures:

A description on how the crystals were obtained can be found below.

All single crystals were measured on a 4-circle single crystal diffractometer SuperNova from Oxford Diffraction (Company: Agilent Technologies, Acquisition: Nov. 2011, using a molybdenum and copper source (dual instrument), Microfocus tubes, cryostream-700 Plus nitrogen steam cooling, 100-500 K (Oxford Cryosystems)). The crystal structure data were solved and refined using Olex2 v1.5 and the ShelX algorithm, as well as the PLATON software.¹⁻⁵ In some cases, Shelxtl XPREP tool was used for space group determination. Some details on the refinement of the individual crystal structure data sets in Olex2 v1.5 are explained below:

- The crystals were obtained by slow evaporation of water on air. Dataset for LHPA-3 was solved using ShelXS, direct methods and refined using ShelXL (L. S.). The space group is $P6_3$ (173). Hydrogen atoms of the hydration water molecules were not modeled due to the low scattering contribution. A solvent mask (SQUEEZE) was used (1.167 molecules water). R_1 : 1.85 %, wR_2 : 5.38 %, R_{int} : 3.28 % and Goof: 1.098. The .cif file is available in the CCDC data base with the deposition number 2205006.
- The crystals were obtained by crystallizing from an aqueous concentrated solution. Dataset for KNb was solved using ShelXS, direct methods and refined using ShelXL (L. S.). The space group is $P2_1/c$ (14) (space group determination Shelxtl XPREP). Hydrogen atoms of the hydration water molecules were not modeled due to the low scattering contribution. R_1 : 2.58 %, wR_2 : 6.73 %, R_{int} : 3.08 % and Goof: 1.252. The .cif file is available in the CCDC data base with the deposition number 2216947.
- The crystals were obtained by slow evaporation of water under reduced pressure in a desiccator. Dataset NaPV₃Mo was solved using ShelXS, direct methods and refined using ShelXL (L. S.). The space group is $P-42_1c$ (114) (space group determination Shelxtl XPREP). The crystal structure dataset is a twinned structure with an inversion twin (Flack

parameter ~ 0.5). So, the following twin law was used: -1 0 0 0 -1 0 0 0 -1 (BASF 0.5). Hydrogen atoms of the hydration water molecules were not modeled due to the low scattering contribution. R_1 : 3.03 %, wR_2 : 7.84 %, R_{int} : 4.49 % and Goof: 1.089. The .cif file is available in the CCDC data base with the deposition number 2205007.

- The crystals were obtained by slow evaporation of water on air. Dataset $[\text{P}_2\text{Mo}_{18}\text{O}_{62}]^{6-}$ was solved and refined using ShelXT, intrinsic phasing. The space group is $P-1$ (2). Hydrogen atoms of the hydration water molecules were not modeled due to the low scattering contribution. A solvent mask (SQUEEZE) did not improve the model. R_1 : 3.83 %, wR_2 : 10.07 %, R_{int} : 2.98 % and Goof: 1.030. The .cif file is available in the CCDC data base with the deposition number 2216946.

Powder XRD:

Powder XRD diffractograms were measured on an X'Pert Pro diffractometer (Panalytical MPD Corp.) using $\text{Cu-K}\alpha$ radiation ($\lambda = 1.5418 \text{ \AA}$) in the range of $5-90^\circ$ (step size 0.013° , counting time 73 seconds) using a PIXcel-Detektor (256 canals with the angle range $3.12^\circ 2\theta$). For this purpose, the background was determined, and the data smoothed. The reflexes were then determined.

NMR spectroscopy

All NMR spectra were measured with a Bruker AVANCEII 600 MHz. The samples were prepared as follows: The respective POM (70 mg) was dissolved in deionized water (0.63 mL), which had previously been adjusted to pH 1 with a 2 M hydrochloric acid solution in deionized water, and D_2O (0.07 mL) was added. Sample $\text{nBu}_4\text{NPCu}_2\text{Mo}$ was measured only in acetone- d_6 . All ^{31}P spectra were measured with a Time Domain Data Sizes (TD) of 32 K, the Number of Scans (NS) were set to 2k (= 2048), the Transmitter Frequency Offset for Channel F1 (O1) and the Spectral Width (SW) were -1 and 40 ppm. The Delay D1 was set to 1 s. For the ^{51}V experiments TD was 32 K, O1 and SW -520 and 400 ppm, D1 0.5 s and NS was set to 4 K. ^{119}Sn -NMR experiment was done using tetramethyl tin in benzene- d_6 as external standard. The NMR analyses were carried out with the software MestReNova®. In MestReNova®, the peaks were first determined, and the data subsequently exported in .csv format.

UV-Vis spectroscopy

The UV-Vis spectra were measured with a Cary 60 UV-Vis spectrometer (Agilent Technologies) in a 3 mL Quartz cuvette (QS). The measurements were carried out using the Cary WinUV software. Measurements were taken in the measuring range between 200 nm and

800 nm. The absorption was measured in the slow measurement mode. The data were then exported as a csv data set. All samples were prepared as follows: The POMs (10 mg) were dissolved in water (10 mL) and the resulting solution was diluted in a cuvette with a total volume of 3 mL to corresponding 3 mL solution volume (usually make up 0.01 mL of stock solution to 3 mL water in the cuvette). Sample nBu₄NPCu₂Mo was handled analogue but the solvent was acetonitrile.

Electrochemistry (CV and SWV):

The CV/SWV measurements were carried out in aqueous, hydrochloric acid medium at pH 1 and a concentration of 1 mmol/L on a Metrohm - Autolab PGSTAT101. For nBu₄NPCu₂Mo the solvent was acetonitrile and to the solution tetrabutylammonium hexafluorophosphate was added as a conducting salt. During the measurement, the solution was purged with nitrogen. The working electrode was a glassy carbon electrode (diameter: 3 mm), the reference electrode was the Ag/Ag⁺ electrode. The counter electrode was a platinum electrode. Measurements were taken in the measuring range between -0.6 and 1 V with a scan rate (for CV) of 100 mV/s for 3 scans. All SWV measurements were taken with a scan rate of 5 mV/s, a modulation amplitude of 20 mV and a frequency of 25 Hz. The measurements were carried out with the software Ivium and the data was subsequently exported as an *x/y* text document.

Other:

The exported *x/y* data were then imported into Origin® 2019b and plotted as corresponding graphs. All graphs in this paper were thus created in Origin®.

1.3 Synthesis of Na₉[PMo₉O₃₄]

Sodium molybdate dihydrate (9.7027 g, 40.10 mmol, 6.95 equivalents) and disodium hydrogen phosphate (0.8186 g, 5.766 mmol, 1 equivalent) were dissolved in water (50 mL). The pH of the colorless solution was 8.987 and was adjusted to 1.035 with a 37% hydrochloric acid solution in water, turning the solution yellow. The mixture was evaporated on air, yielding a yellow solid as well as single crystals for X-ray diffraction. A yellow solid (3 g) was obtained, which still contains a significant amount of NaCl.

Characterization:

³¹P-NMR (242.9 MHz, H₂O/acetone-*d*₆, 20 °C): δ [ppm] = -0.232 (broad, PO₄³⁻), -3.10 (s, LHPA-3), -3.73 (s, HPMo).

IR (ATR): $\tilde{\nu}$ [cm⁻¹] = 3379 (w, O-H, H₂O), 1613 (O-H, hydration H₂O), 1059, 1008 (me, P-O), 961, 937, 925, 904 (me, M=O_t), 849 (me, (M-O-M)_{vertex}), 767, 698 (st, (M-O-M)_{edge}).

UV-Vis [nm]: 215, 317.

ICP-OES: Calculated for Na₉[PMo₉O₃₄] · 6 H₂O: 49.245 % Mo, 1.766 % P, 11.8 % Na, 0 % K. Found for Na₉[PMo₉O₃₄] · 6 H₂O: 32.5 % Mo, 1.40 % P, 18.0 % Na, 0 % K. Data normalised to molybdenum. P/Mo/Na/K ratio: 1.2/9/20.8/0.

This compound is not pure. There is an excess of NaCl impurities.

TGA: 6.180 % weight loss upon drying, this corresponds to 6 mol lattice water per mol of the POM.

The crystals were obtained using the slow evaporation method on air.

1.4 Synthesis of K₈[Nb₆O₁₉]

Diniobiumpentoxide (22.6273 g, 85.13 mmol, 1 equivalent) and potassium hydroxide (71.0398 g, 1.27 mol, 14.87 equivalents) were mixed and the mixture was added in portions to a nickel crucible heated over a gas burner flame (Campingaz, mixture butane/propane). The reaction mixture began to bubble due to carbon dioxide formation and water evaporation. The diniobiumpentoxide began to dissolve in the potassium hydroxide melt. After the addition was completed, the reaction mixture was heated further until the bubbling stopped and the melt became viscous. It was cooled to room temperature and water was added to the solidified, hard, gray melt and heat evolution was observed. To dissolve the melt, it was first mechanically crushed in the crucible. The colorless solution was filtered and the crucible rinsed several times. Subsequently, the volume of the filtrate was reduced to one-eighth under reduced pressure, resulting in precipitation of a colorless solid. The supernatant turned brownish. It was cooled to 4 °C overnight. The precipitate was filtered and washed several times with ethanol cooled to 4 °C. This was followed by drying at 60 °C. A colorless solid (25.2479 g) was obtained.

Characterization:

IR (ATR): $\tilde{\nu}$ [cm^{-1}] = 2950 (w, O-H, H_2O), 1636 (O-H, hydration H_2O), 1551, 1453, 1374 (w, CO_3^{2-}), 849, 829 (me, M=O_t), 656 (st, (M-O-M)_{asym.}), 512 (st, (M-O-M)_{sym.}).

UV-Vis [nm]: 247.

ICP-OES: Calculated for $\text{K}_8[\text{Nb}_6\text{O}_{19}] \cdot 5 \text{H}_2\text{O}$: 44.091 % Nb, 24.74 % K, 0 % Na. Found for $\text{K}_8[\text{Nb}_6\text{O}_{19}] \cdot 5 \text{H}_2\text{O}$: 40.92 % Nb, 24.8 % K, 0.09 % Na. Data normalised to niobium. K/Na/Nb ratio: 8.64/0.053/6.

TGA: 7.369 % weight loss upon drying, this corresponds to 5 mol lattice water per mol of the POM.

The crystals were obtained by slow evaporation of an aqueous solution under ambient conditions.

Synthesis of $\text{K}_8[\text{Nb}_6\text{O}_{19}]$ (KNb) was adapted from the literature procedure.^{6,7} Elemental analysis and TGA results summarized in Table 1:

Table 1: Results from ICP-OES and TGA analysis of KNb.

Compound	Molecular composition	K/Na/Nb ratio ^a	Hydration water ^b [mol/mol-POM]
KNb	$\text{K}_8[\text{Nb}_6\text{O}_{19}]$	8.64/0.0533/6	5

KNb is $\text{K}_8[\text{Nb}_6\text{O}_{19}]$

^aThe ratio K/Na/Nb were determined by AAS/ICP-OES analysis. The data were normalized to the target Nb content. There is a little bit more K than expected, due to the carbonates that are forming while heating a melted KOH solution.

^bThe content of hydration water was determined by TGA analysis.

Data are normalized to the target Nb content. There is more K than expected for KNb. During heating a melted KOH solution, the KOH reacts with carbon dioxide from air to form potassium carbonate.⁸ Normally carbonate decomposes at these temperatures, but apparently carbonate is also formed during the cooling phase that remains stable after cooling. Hydration water content was determined to be five molecules water per POM molecule using TGA.

Figure S1 shows an ATR-FT-IR spectrum from KNb with the characteristic vibrational bands.

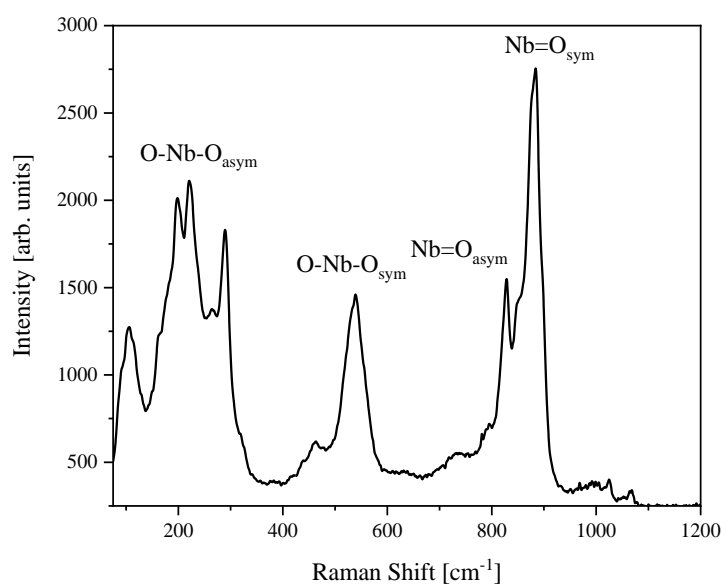


Figure S2: Raman data of KNb. Vibration of terminal oxygen-metal bonds $\text{Nb}=\text{O}_t$ (884 cm^{-1} and 828 cm^{-1}) and asymmetric and symmetric vibration of $\text{Nb}-\text{O}-\text{Nb}$ (656 cm^{-1} and 510 cm^{-1}).

An UV-Vis spectrum of KNb measured in an aqueous potassium hydroxide solution is shown in Figure S3:

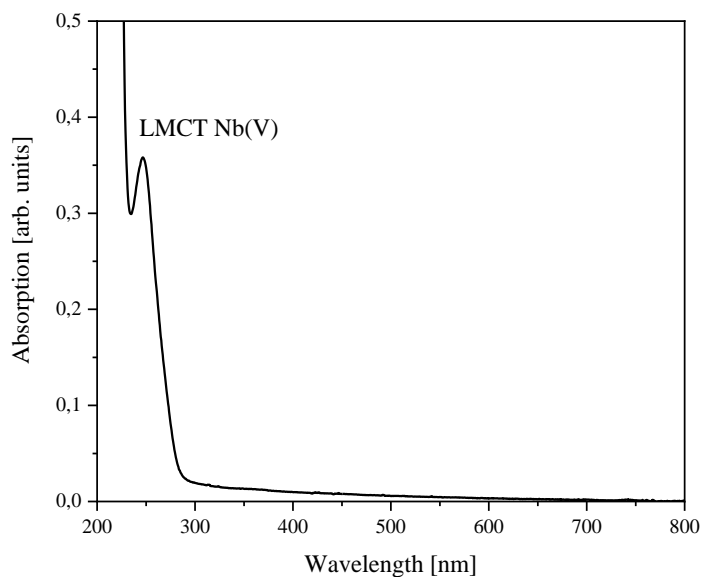


Figure S3: UV-Vis data of KNb in aqueous potassium hydroxide solution.

The LMCT $\text{O} \rightarrow \text{Nb}(\text{V})\text{O}_6$ was found at 247 nm .

The CV and SWV data in Figure S4 and S5 for KNb in aqueous potassium hydroxide solution.

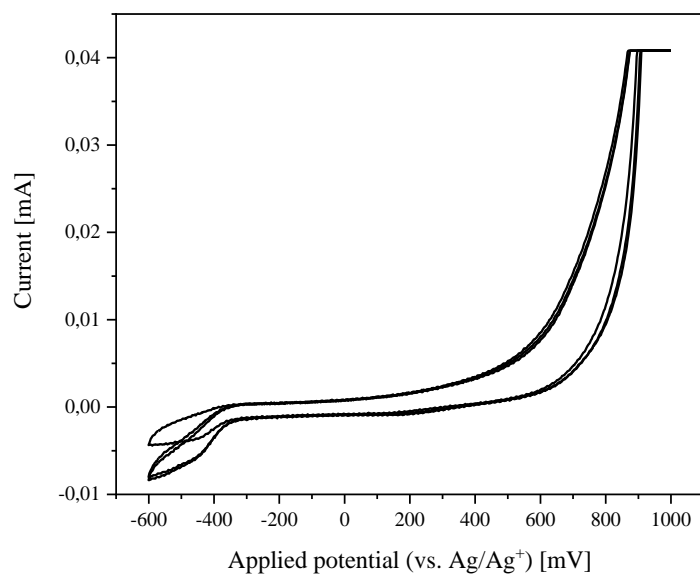


Figure S4: CV measurements of KNb in aqueous potassium hydroxide solution (concentration 1 mmol/L, scan rate 100 mV/s (CV)). Potassium hydroxide was used as conducting salt.

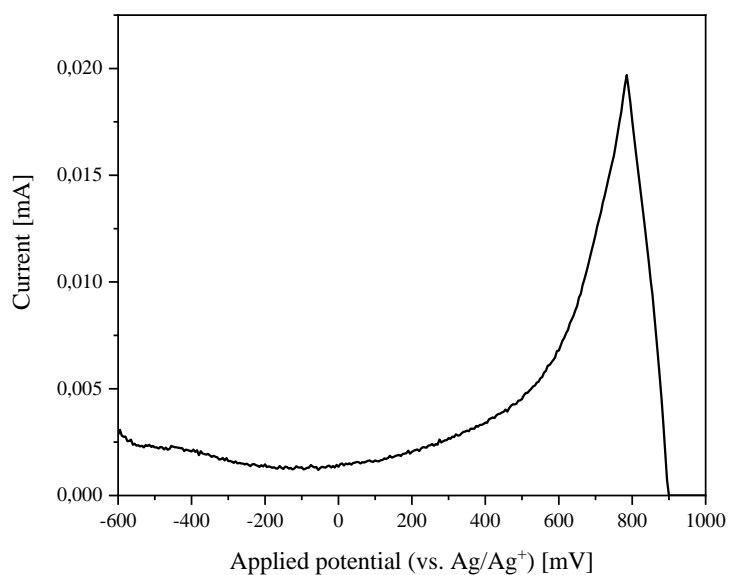


Figure S5: SWV measurements of KNb in aqueous potassium hydroxide solution (concentration 1 mmol/L, scan rate 5 mV/s (SWV)). Potassium hydroxide was used as conducting salt.

Synthesis of KNb (Figure S6):



Figure S6: Molten mixture over a gas flame of potassium hydroxide and niobium pentoxide for synthesizing KNb. A nickel crucible is used (left). Cooled melt of KNb and potassium hydroxide after KNb synthesis. A nickel crucible is used (right).

1.5 Nanofiltration

For purification, four cycles of nanofiltration were conducted. For this purpose, the start volume of the reaction solution (feed) was always 100 mL. The pressure in the system was set to 33 bar, a flow was set to 15 mL/min and the emergency shutdown pressure was set to 34 bar. In the first step, 5 mL of the feed solution was taken for analysis. The process was then started by flowing the feed solution through the system for 15 min under process conditions, where the permeate flow was recombined with the retentate flow. After this period, the permeate flow was separated from the retentate and collected. In the first cycle, 65 mL of permeate was collected and the concentrated retentate solution was diluted with 70 mL of water. In the second cycle, 70 mL of permeate was collected and the concentrated retentate solution was diluted again with 70 mL of water. A total of four cycles were performed in this manner.

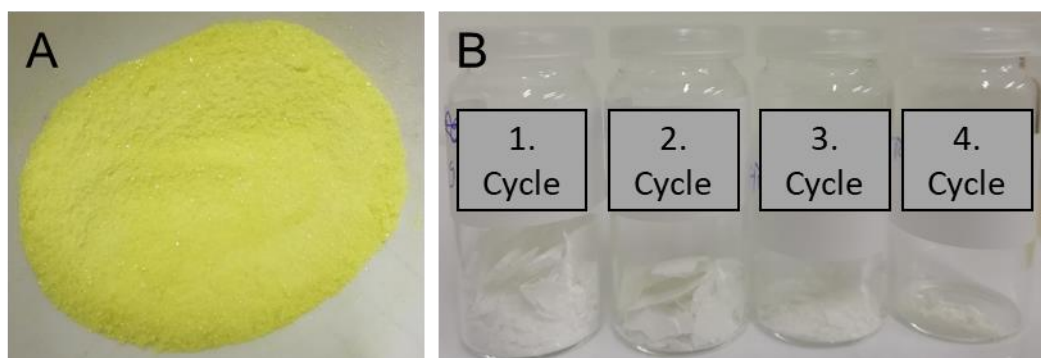


Figure S7: Visual comparison of a) intensely yellow product and b) salt fractions, both obtained by concentrating the retentate and permeate, respectively, over a rotary evaporator.

Subsequently, 5 mL of the retentate and permeate fractions were separated and used for further analysis by ICP-OES and AAS. Both the permeate and retentate fractions were dried under reduced pressure.

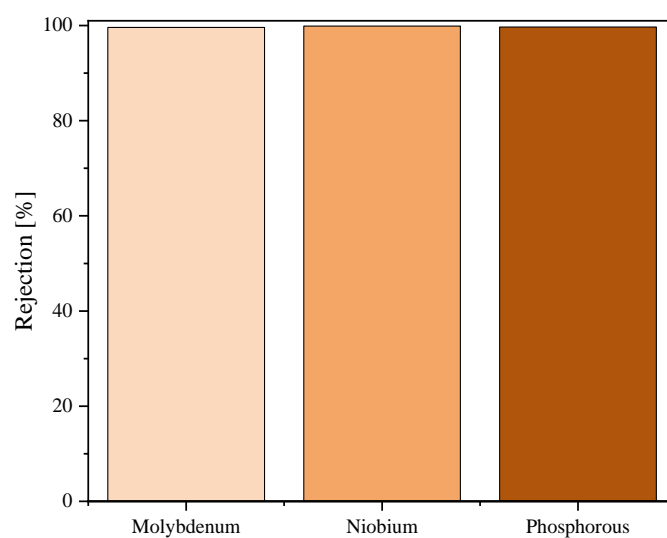


Figure S8: Rejection of the catalyst compounds Mo(VI), Nb(V) and P(V) for the $[\text{PNb}_3\text{Mo}_9\text{O}_{40}]^{6-}$ anion in our investigated nanofiltration membrane process.

The powder XRD data of the dried permeate fractions (Figure S9) all show reflexes belonging to NaCl.

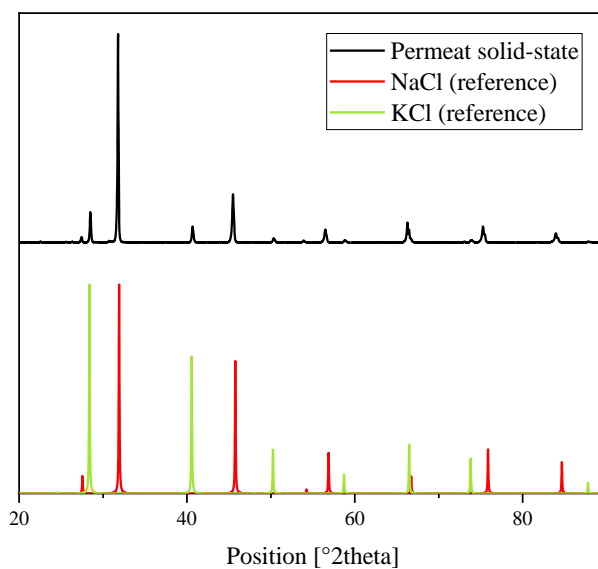


Figure S9: Comparison of the powder XRD diffractogram of the permeate fraction of the purification experiment of NaKPNb_3Mo with NaCl (ICSD: 142801) and KCl (ICSD: 165593). To get a better view all data were normalized.^{12,13}

Furthermore, there are low intensity reflexes that can be assigned to KCl.^{12,13} Thus, the permeate fraction can be identified without doubt as a mixture of NaCl and KCl, which was to be shown.

1.6 Synthesis of the transition metal substituted POMs using LHPA-3

In general the idea for the synthesis of the transition metal substituted POMs based on the following concept: the lacunary LHPA-3 was prepared *in situ* and the foreign metal precursor compound(s) were added in the right stoichiometry. If necessary, sodium molybdate dihydrate was added to fill the remaining vacancies of the lacunary compound. The reaction mixture was heated to reflux for 30-60 minutes and then cooled to room temperature. After cooling the pH value was measured and if necessary corrected to ~1 by adding a 37 % solution of hydrochloric acid in water. The reaction mixture was filtered and desalinated using our newly presented nanofiltration process.

1.6.1 In situ Lacunary synthesis

Sodium molybdate dihydrate and disodium hydrogen phosphate were dissolved in water. The pH of the colorless solution was ~8.7 and was adjusted to ~1 with a 37 % hydrochloric acid solution in water, turning the solution yellow.

Table 2 shows an overview of the precise weights of the precursor compounds for the respective POMs:

Table 2: Weights of all precursor compounds for *in situ* synthesis of LHPA-3 for each experiment.

POM	Sodium molybdate dihydrate [g]	Disodium hydrogen phosphate [g]	Volume of water [mL]
NaPCoMo	10.0058	0.6535	50
NaPNiMo	10.0000	0.6540	50
nBu ₄ NPCu ₂ Mo	10.0064	0.6545	50
NaPZnMo	8.1400	0.5333	50
NaPFeMo	10.0024	0.6544	50
NaPIn ₃ Mo	10.0056	0.6538	50
NaPSnMo	10.2486	0.6692	50
NaPNbMo	10.0069	0.6537	50
NaPNb ₂ Mo	10.0005	0.6532	50
NaPNb ₃ Mo	10.0063	0.6561	50
NaPV ₂ NbMo	15.0041	0.9801	50
NaPVNb ₂ Mo	10.0021	0.6528	50
NaPV ₃ Mo	10.0029	0.6570	50

1.6.2 Synthesis of Co(II), Ni(II), Cu(II), Fe(III), V(V) and W(VI) substituted POMs

For Co(II), Ni(II), Cu(II), Fe(III), V(V) and W(VI) substitution the corresponding precursor compound was added in the right stoichiometry to the *in situ* formed LHPA-3 lacunary species. Then sodium molybdate dihydrate was added to fill the remaining vacancies of LHPA-3 and the solution was heated to reflux for 30 min. After this procedure the solution was cooled to room temperature and the pH value was measured. If necessary, the pH value was adjusted to ~1 by adding a 37 % solution of hydrochloric acid in water. In the next step the mixture was filtered and purified using the dialysis nanofiltration process.

Table 3 summarizes all amounts for the corresponding precursor compounds and the pH values used for the synthesis. For some metal precursor compounds it was necessary to first determine the metal content by elemental analysis, since some preliminary experiments showed that the precursor compounds apparently contain more hydration water than indicated by the supplier. With the help of the determined metal content, it was then possible to calculate a more accurate weight for the respective precursor compound, based on the foreign metal.

Table 3: Weights of the precursor compounds/pH values used for the experiments to synthesize Co(II), Ni(II), Cu(II), Fe(III) and V(V) substituted POMs.

POM	Foreign metal precursor [g]	Equivalents	Sodium molybdate dihydrate [g]	Equivalents	pH value after addition	pH value corrected
NaPCoMo	1.3648 (cobalt(II) acetate tetrahydrate)	1 (according to Co(II))	2.2233	2	4.888	1.496
NaPNiMo	1.1875 (nickel(II) acetate tetrahydrate)	1	2.2222	2	4.498	1.646
nBu4NPCu ₂ Mo	1.8917 (copper(II) chloride)	2.3 (according to Cu(II))	1.1123	1	1.664	-
NaPFeMo	0.9872 (iron(III) chloride)	1 (according to Fe(III))	2.2228	2	1.910	-

NaPV₃Mo	1.6808 (sodium vanadate)	3	-	-	4.420	-
NaPW₃Mo	4.5450 (sodium tungstate dihydrate)	3	-	-	8.701	1.858

For product isolation of nBu₄NPCu₂Mo the compound was precipitated by adding a colorless solution of tetrabutylammonium bromide (17.7826 g, 55.16 mmol, 11.96 equivalents) in water (30 mL) to the green reaction solution. A green precipitate was formed which was collected by filtering and was washed several times using water. The green solid was dried using a desiccator over orange yellow. During this time the color changed from green to brown.

1.6.3 Synthesis of the In(III) substituted POM

For compound NaPIn₃Mo the In(III) precursor was treated as follows:

Indium(III) hydroxide (2.2859 g, 13.78 mmol, 3.00 equivalents) was dissolved in a 37 % hydrochloric acid solution in water (10 mL). A clear, colorless solution was formed.

The In(III) solution was added to the LHPA-3 solution, refluxed for 30 min and was then cooled to room temperature. The pH value was -0.566 and was adjusted to 1.947 using a 1 M sodium carbonate solution in water. In the next step the mixture was filtered and purified using the dialysis nanofiltration process.

1.6.4 Synthesis of Zn(II) and Sn(IV) substituted POMs

The precursor compounds for the experiments to synthesize Zn(II) and Sn(IV) substituted POMs were the corresponding elements Zn and Sn.

Grained zinc (0.2445 g, 3.738 mmol, 1.00 equivalent) was dissolved in a 37 % hydrochloric acid solution in water (10 mL). A gas formation and bubbling was visible and the mixture became hot. A clear, colorless solution was formed.

Tin granules (0.5587 g, 4.706 mmol, 1.00 equivalent) were dissolved in a 37 % hydrochloric acid solution in water (22 mL). A gas formation was visible and the mixture became warm. For complete dissolution of tin, the mixture was heated to 100 °C until everything was dissolved. A clear, colorless solution was formed.

After addition of the Sn(II) solution to the LHPA-3 solution, the solution turned into dark. A 30 % solution of hydrogen peroxide in water (12 mL) was added to oxidize Sn(II) to Sn(IV). The mixture was then heated to reflux for 60 min. During this time the color of the reaction mixture turned from dark to yellow and was then cooled to room temperature. In the next step the reaction mixture was extracted three times using diethyl ether (30 mL). During the extraction process a third phase formed and sat down. The collected and united POM ether phases were concentrated under reduced pressure to yield a yellow solid.

1.6.5 Synthesis of Nb(V) and Nb(V)/V(V) mixed substituted POMs

The V(V) free, only Nb(V) substituted POMs were prepared as follows:

Potassium hexaniobate was dissolved in a 1.5 % hydrogen peroxide solution in water (20 mL) and was directly added to the LHPA-3 reaction solution. The mixture gets then refluxed. In some cases, after potassium hexaniobate addition a clear, orange colored solution is forming or a solid is precipitating. This is not always a problem when the solution is heated up fast enough. Then a clear orange solution is formed and sodium molybdate dihydrate is added. After the addition of sodium molybdate dihydrate the color turned into yellow again. The solution was heated to reflux for 60 min and was then cooled to room temperature. The pH value was adjusted to ~1.6 using a 37 % hydrochloric acid solution in water. In the next step the mixture was filtered and purified using the dialysis nanofiltration process.

V(V) and Nb(V) mixed substituted POMs were prepared as follows:

Potassium hexaniobate was dissolved in a 1.5 % hydrogen peroxide solution in water (20 mL) and was directly added to the reaction solution. The mixture gets then refluxed. In some cases after potassium hexaniobate addition a clear, orange colored solution is forming or a solid is precipitating. This is not always a problem when the solution gets fast enough heated up. Then a clear orange colored solution gets formed. In the next step sodium vanadate was added and a clear, red colored solution was formed. The solution was heated to reflux for 30 min and was then cooled to room temperature. The pH value was adjusted to ~1.6 by adding a 37 % hydrochloric acid solution in water. In the next step the mixture was filtered and purified using the dialysis nanofiltration process.

Table 4 summarizes the amounts of the foreign metal precursors used for synthesizing the Nb(V) and Nb(V)/V(V) mixed substituted POMs. Since different batches of potassium hexaniobate contain different amounts of hydration water, from every batch the Nb(V)

content was determined using elemental analysis. From this value the exact weights were calculated:

Table 4: Weights of the precursor compounds/pH values used for the experiments to synthesize Nb(V) and Nb(V)/V(V) mixed substituted POMs.

POM	KNb [g]	Equivalents according to Nb(V)	Sodium vanadate/Sodium molybdate tetrahydrate [g]	Equivalents	pH value after addition	pH value corrected
NaKPNbMo	1.1216	1	2.2241 (molybdate)	2	5.142	1.604
NaKPNb ₂ Mo	2.1642	2	1.1118 (molybdate)	1	4.789	1.322
NaKPNb ₃ Mo	3.3621	3	-	-	5.450	1.690
NaKPV ₂ NbMo	1.8222	1	1.6815 (vanadate)	2	5.351	-
NaKPVNb ₂ Mo	2.1632	2	0.5598 (vanadate)		5.235	1.858

1.7 Characterization

NaPCoMo:

³¹P-NMR (242.9 MHz, H₂O/D₂O, 20 °C): δ [ppm] = -0.54, -1.77, -3.36.

IR (ATR): $\tilde{\nu}$ [cm⁻¹] = 3505 (w, O-H, H₂O), 1618 (O-H, hydration H₂O), 1049 (w, P-O), 946 (me, M=O_t), 869 (me, (M-O-M)_{vertex}), 772, 707 (st, (M-O-M)_{edge}).

UV-Vis [nm]: 210.

ICP-OES: Calculated for Na₇[PCoMo₁₁O₄₀] · 8 H₂O: 50.488 % Mo, 2.819 % Co, 1.482 % P, 0 % K, 7.699 % Na. Found for Na₇[PCoMo₁₁O₄₀] · 8 H₂O: 51.90 % Mo, 2.77 % Co, 1.54 % P, 0.01 % K, 3.97 % Na. Data normalized to molybdenum. Na/K/P/Co/Mo ratio: 3.51/0.005/1.01/0.956/11.

TGA: 6.882 % weight loss upon drying, this corresponds to 8 mol lattice water per mol of the POM.

Additional protocol for the nanofiltration process:

- Cycle 1: 65 mL permeate in 29 min

- Cycle 2: 70 mL permeate in 54 min
- Cycle 3: 70 mL permeate in 77 min
- Cycle 4: 70 mL permeate in 98 min

NaPNiMo:

³¹P-NMR (242.9 MHz, H₂O/D₂O, 20 °C): δ [ppm] = -0.42, -1.68, -3.22, -3.90.

IR (ATR): $\tilde{\nu}$ [cm⁻¹] = 3454 (w, O-H, H₂O), 1610 (O-H, hydration H₂O), 1047 (w, P-O), 942 (me, M=O_i), 869 (me, (M-O-M)_{vertex}), 783 (st, (M-O-M)_{edge}).

UV-Vis [nm]: 210.

ICP-OES: Calculated for Na₇[PNiMo₁₁O₄₀] · 8 H₂O: 50.494 % Mo, 2.808 % Ni, 1.482 % P, 0 % K, 7.7 % Na. Found for Na₇[PNiMo₁₁O₄₀] · 8 H₂O: 52.58 % Mo, 2.58 % Ni, 1.62 % P, 0.00 % K, 4.58 % Na. Data normalized to molybdenum. Na/K/P/Ni/Mo ratio: 3.99/0.00/1.05/0.881/11.

TGA: 10.27 % weight loss upon drying, this corresponds to 12 mol lattice water per mol of the POM.

- Cycle 1: 65 mL permeate in 36 min
- Cycle 2: 70 mL permeate in 62 min
- Cycle 3: 70 mL permeate in 87 min
- Cycle 4: 70 mL permeate in 110 min

nBu₄NPCu₂Mo:

³¹P-NMR (242.9 MHz, acetone-*d*₆, 20 °C): δ [ppm] = -3.02, -3.60.

IR (ATR): $\tilde{\nu}$ [cm⁻¹] = 3421 (w, O-H, H₂O), 2960, 2936, 2874 (w, CH₃-/-CH₂-valence vibration), 1636 (w, O-H, hydration H₂O), 1482, 1460 (w, CH₃-/-CH₂-deformation vibration), 1380 (w, CH₃-deformation vibration), 1053 (w, -C-N valence vibration), 1077, 1055 (w, P-O), 935 (me, M=O_i), 864 (me, (M-O-M)_{vertex}), 777 (st, (M-O-M)_{edge}).

UV-Vis [nm]: 214, 306.

ICP-OES: Calculated for $(n\text{Bu}_4\text{N})_{11}[\text{PCu}_2\text{Mo}_{10}\text{O}_{40}]$: 21.684 % Mo, 2.872 % Cu, 0.700 % P, 0 % K, 0 % Na. Found for $(n\text{Bu}_4\text{N})_{11}[\text{PCu}_2\text{Mo}_{10}\text{O}_{40}]$: 34.37 % Mo, 1.85 % Cu, 1.24 % P, 0 % K, 1.83 % Na. Data normalized to molybdenum. Na/K/P/Cu/Mo ratio: 2.22/0/1.11/0.813/10.

The incorporation of Cu(II) is not complete.

NaPZnMo:

^{31}P -NMR (242.9 MHz, $\text{H}_2\text{O}/\text{D}_2\text{O}$, 20 °C):
 δ [ppm] = -0.53, -0.79, -1.59, -1.66, -1.90, -2.45, -3.15, -3.27, -3.41, -3.90.

IR (ATR): $\tilde{\nu}$ [cm^{-1}] = 3515 (w, O-H, H_2O), 1620 (O-H, hydration H_2O), 1075, 1060 1045 (w, P-O), 939 (me, M=O_i), 900 (me, (M-O-M)_{vertex}), 775 (st, (M-O-M)_{edge}).

UV-Vis [nm]: 210, 311.

ICP-OES: Calculated for $\text{Na}_7[\text{PZnMo}_{11}\text{O}_{40}] \cdot 8 \text{H}_2\text{O}$: 50.332 % Mo, 3.12 % Zn, 1.477 % P, 0 % K, 7.675 % Na. Found for $\text{Na}_7[\text{PZnMo}_{11}\text{O}_{40}] \cdot 8 \text{H}_2\text{O}$: 51.88 % Mo, 1.21 % Zn, 1.6 % P, 0.00 % K, 4.12 % Na. Data normalized to molybdenum. Na/K/P/Zn/Mo ratio: 3.65/0/1.06/0.377/11.

The incorporation of Zn(II) is not complete.

TGA: 6.993 % weight loss upon drying, this corresponds to 8 mol lattice water per mol of the POM.

Additional protocol for the nanofiltration process:

- Cycle 1: 65 mL permeate in 26 min
- Cycle 2: 70 mL permeate in 47 min
- Cycle 3: 70 mL permeate in 65 min
- Cycle 4: 70 mL permeate in 82 min

NaPFeMo:

^{31}P -NMR (242.9 MHz, $\text{H}_2\text{O}/\text{D}_2\text{O}$, 20 °C): δ [ppm] = no signal observed.

IR (ATR): $\tilde{\nu}$ [cm^{-1}] = 3423 (w, O-H, H_2O), 1613 (O-H, hydration H_2O), 1051 (w, P-O), 945 (me, M=O_i), 864 (me, (M-O-M)_{vertex}), 767 (st, (M-O-M)_{edge}).

UV-Vis [nm]: 211, 305.

ICP-OES: Calculated for $\text{Na}_6[\text{PFeMo}_{11}\text{O}_{40}] \cdot 8 \text{H}_2\text{O}$: 51.126 % Mo, 2.705 % Fe, 1.501 % P, 0.00 % K, 6.682 % Na. Found for $\text{Na}_6[\text{PFeMo}_{11}\text{O}_{40}] \cdot 8 \text{H}_2\text{O}$: 51.3 % Mo, 3.10 % Fe, 1.60 % P, 0.01 % K, 3.96 % Na. Data normalized to molybdenum. Na/K/P/Fe/Mo ratio: 3.54/0.0053/1.06/1.14/9

TGA: 7.085 % weight loss upon drying, this corresponds to 8 mol lattice water per mol of the POM.

Additional protocol for the nanofiltration process:

- Cycle 1: 65 mL permeate in 23 min
- Cycle 2: 70 mL permeate in 45 min
- Cycle 3: 70 mL permeate in 66 min
- Cycle 4: 70 mL permeate in 90 min

NaPIn₃Mo:

³¹P-NMR (242.9 MHz, H₂O/D₂O, 20 °C): δ [ppm] = -0.56, -1.72, -2.31, -3.19, -3.93.

IR (ATR): $\tilde{\nu}$ [cm⁻¹] = 3344 (w, O-H, H₂O), 1611 (O-H, hydration H₂O), 1058 (w, P-O), 956 (me, M=O_t), 867 (me, (M-O-M)_{vertex}), 770 (st, (M-O-M)_{edge}).

UV-Vis [nm]: 211.

ICP-OES: Calculated for $\text{Na}_{12}[\text{PIn}_3\text{Mo}_9\text{O}_{40}] \cdot 20 \text{H}_2\text{O}$: 34.332 % Mo, 13.696 % In, 1.232 % P, 0.00 % K, 10.969 % Na. Found for $\text{Na}_{12}[\text{PIn}_3\text{Mo}_9\text{O}_{40}] \cdot 20 \text{H}_2\text{O}$: 41.35 % Mo, 13.91 % In, 1.48 % P, 0.00 % K, 1.78 % Na. Data normalized to molybdenum. Na/K/P/In/Mo ratio: 1.62/0/1/2.53/9.

The incorporation of In(III) is not complete.

TGA: 14.37 % weight loss upon drying, this corresponds to 20 mol lattice water per mol of the POM.

Additional protocol for the nanofiltration process:

- Cycle 1: 65 mL permeate in 46 min

- Cycle 2: 70 mL permeate in 81 min
- Cycle 3: 70 mL permeate in 110 min
- Cycle 4: 70 mL permeate in 138 min

NaPSnMo:

This compound was identified to be HPMo using only NMR- FT-IR and the calculated ICP-OES data.

$^{31}\text{P-NMR}$ (242.9 MHz, $\text{H}_2\text{O}/\text{D}_2\text{O}$, 20 °C): δ [ppm] = -3.90.

IR (ATR): $\tilde{\nu}$ [cm^{-1}] = 3507 (w, O-H, H_2O), 1604 (O-H, hydration H_2O), 1058 (w, P-O), 957 (me, $\text{M}=\text{O}_\text{t}$), 879 (me, $(\text{M-O-M})_{\text{vertex}}$), 744 (st, $(\text{M-O-M})_{\text{edge}}$).

ICP-OES: Calculated for $\text{Na}_5[\text{PSnMo}_{11}\text{O}_{40}] \cdot 9 \text{H}_2\text{O}$: 49.731 % Mo, 5.594 % Sn, 1.460 % P, 0.00 % K, 5.417 % Na. Found for $\text{Na}_5[\text{PSnMo}_{11}\text{O}_{40}] \cdot 9 \text{H}_2\text{O}$: 56.97 % Mo, 0.00 % Sn, 1.69 % P 0.00 % K, 0.07 % Na. Data normalized to molybdenum. Na/K/P/Sn/Mo ratio: 0.0571/0/1.01/0/11. Calculated for $\text{H}_3[\text{PMo}_{12}\text{O}_{40}] \cdot 9 \text{H}_2\text{O}$: 57.929 % Mo, 1.559 % P, 0.00 % K, 0.00 % Na.

TGA: 7.817 % weight loss upon drying, this corresponds to 9 mol lattice water per mol of the POM.

NaPNbMo:

$^{31}\text{P-NMR}$ (242.9 MHz, $\text{H}_2\text{O}/\text{D}_2\text{O}$, 20 °C):
 δ [ppm] = -1.28, -1.37, -1.43, -2.99, -3.29, -3.30, -3.36, -3.38, -3.66

IR (ATR): $\tilde{\nu}$ [cm^{-1}] = 3396 (w, O-H, H_2O), 1615 (O-H, hydration H_2O), 1058, 1034 (w, P-O), 944 (me, $\text{M}=\text{O}_\text{t}$), 859 (me, $(\text{M-O-M})_{\text{vertex}}$), 741 (st, $(\text{M-O-M})_{\text{edge}}$).

UV-Vis [nm]: 209, 301.

ICP-OES: Calculated for $\text{Na}_4[\text{PNbMo}_{11}\text{O}_{40}] \cdot 6 \text{H}_2\text{O}$: 52.264 % Mo, 4.601 % Nb, 1.534 % P, 0.00 % K, 4.554 % Na. Found for $\text{Na}_4[\text{PNbMo}_{11}\text{O}_{40}] \cdot 6 \text{H}_2\text{O}$: 44.77 % Mo, 4.33 % Nb, 1.17 % P 0.75 % K, 4.84 % Na. Data normalized to molybdenum. Na/K/P/Nb/Mo ratio: 4.96/0.45/0.893/1.10/11.

TGA: 4.933 % weight loss upon drying, this corresponds to 6 mol lattice water per mol of the POM.

Additional protocol for the nanofiltration process:

- Cycle 1: 65 mL permeate in 25 min
- Cycle 2: 70 mL permeate in 46 min
- Cycle 3: 70 mL permeate in 68 min
- Cycle 4: 70 mL permeate in 88 min

NaPNb₂Mo:

³¹P-NMR (242.9 MHz, H₂O/D₂O, 20 °C):
 δ [ppm] = -0.28, -0.36, -1.26, -1.33, -1.40, -2.45, -2.51, -2.63, -2.92, -2.96, -3.04, -3.09, -3.19, -3.27, -3.28, -3.33, -3.37, -3.46, -2.64.

IR (ATR): $\tilde{\nu}$ [cm⁻¹] = 3412 (w, O-H, H₂O), 1613 (O-H, hydration H₂O), 1049 (w, P-O), 947 (me, M=O_t), 856 (me, (M-O-M)_{vertex}), 757 (st, (M-O-M)_{edge}).

UV-Vis [nm]: 209, 292.

ICP-OES: Calculated for Na₅[PNb₂Mo₁₀O₄₀] · 5 H₂O: 47.467 % Mo, 9.193 % Nb, 1.532 % P, 0.00 % K, 5.687 % Na. Found for Na₅[PNb₂Mo₁₀O₄₀] · 5 H₂O: 47.74 % Mo, 8.456 % Nb, 1.50 % P 1.36 % K, 4.565 % Na. Data normalized to molybdenum. Na/K/P/Nb/Mo ratio: 3.99/0.70/0.98/1.83/10.

TGA: 4.652 % weight loss upon drying, this corresponds to 5 mol lattice water per mol of the POM.

Additional protocol for the nanofiltration process:

- Cycle 1: 65 mL permeate in 22 min
- Cycle 2: 70 mL permeate in 43 min
- Cycle 3: 70 mL permeate in 63 min
- Cycle 4: 70 mL permeate in 83 min

NaKPNb₃Mo:

³¹P-NMR (242.9 MHz, H₂O/D₂O, 20 °C):
 δ [ppm] = -2.36, -2.48, -2.52, -2.61, -2.73, -2.78, -2.91, -2.96, -3.04, -3.09, -3.18, -3.26, -3.28, -3.33, -3.37, -3.63.

IR (ATR): $\tilde{\nu}$ [cm⁻¹] = 3388 (w, O-H, H₂O), 1613 (O-H, hydration H₂O), 1047 (w, P-O), 944 (me, M=O_t), 857 (me, (M-O-M)_{vertex}), 760 (st, (M-O-M)_{edge}).

UV-Vis [nm]: 210, 292.

ICP-OES: Calculated for Na₆[PNb₃Mo₉O₄₀] · 7 H₂O: 41.569 % Mo, 13.418 % Nb, 1.491 % P, 0.00 % K, 6.641 % Na. Found for Na₆[PNb₃Mo₉O₄₀] · 7 H₂O: 38.54 % Mo, 12.03 % Nb, 1.26 % P 2.37 % K, 4.30 % Na. Data normalized to molybdenum. Na/K/P/Nb/Mo ratio: 4.19/1.36/0.91/2.90/9.

TGA: 6.297 % weight loss upon drying, this corresponds to 7 mol lattice water per mol of the POM.

Additional protocol for the nanofiltration process:

- Cycle 1: 65 mL permeate in 18 min
- Cycle 2: 70 mL permeate in 36 min
- Cycle 3: 70 mL permeate in 54 min
- Cycle 4: 70 mL permeate in 75 min

NaKPV₂NbMo:

³¹P-NMR (242.9 MHz, H₂O/D₂O, 20 °C): δ [ppm] = -2.50 to -4.30.

⁵¹V-NMR (157.8 MHz, H₂O/D₂O, 20 °C):
 δ [ppm] = -517.7, -525.9, -531.3, -532.8, -533.2, -533.8, -534.3, -535.7, -538.5, -540 to -546.

IR (ATR): $\tilde{\nu}$ [cm⁻¹] = 3374 (w, O-H, H₂O), 1610 (O-H, hydration H₂O), 1046 (w, P-O), 941 (me, M=O_t), 847 (me, (M-O-M)_{vertex}), 750 (st, (M-O-M)_{edge}).

UV-Vis [nm]: 208, 300.

ICP-OES: Calculated for Na₆[PV₂NbMo₉O₄₀] · 7 H₂O: 43.319 % Mo, 4.661 % Nb, 5.111 % V, 1.554 % P, 0.00 % K, 6.92 % Na. Found for Na₆[PV₂NbMo₉O₄₀] · 7 H₂O: 38.50 % Mo,

4.38 % Nb, 5.225 % V 1.52 % P 1.38 % K, 6.49 % Na. Data normalized to molybdenum.
Na/K/P/V/Nb/Mo ratio: 6.33/0.792/1.10/2.3/1.06/9.

TGA: 5.901 % weight loss upon drying, this corresponds to 7 mol lattice water per mol of the POM.

Additional protocol for the nanofiltration process:

- Cycle 1: 65 mL permeate in 29 min
- Cycle 2: 70 mL permeate in 63 min
- Cycle 3: 70 mL permeate in 92 min
- Cycle 4: 70 mL permeate in 122 min

NaKPVNb₂Mo:

³¹P-NMR (242.9 MHz, H₂O/D₂O, 20 °C): δ [ppm] = -4.92, -5.08, -5.27 to -5.36, -5.49, -5.62, -5.69, -5.93, -5.96, -5.99, -6.04, -6.20, -6.30, -6.42, -6.43, -6.49, -6.54, -6.73, -6.77, -6.86, -6.88, -6.89, -6.90.

⁵¹V-NMR (157.8 MHz, H₂O/D₂O, 20 °C): δ [ppm] = -519.8, -527.9, -532.7, -533.7, -534.4, -535.4, -537.1, -545.1.

IR (ATR): $\tilde{\nu}$ [cm⁻¹] = 3391 (w, O-H, H₂O), 1615 (O-H, hydration H₂O), 1048 (w, P-O), 944 (me, M=O_t), 859 (me, (M-O-M)_{vertex}), 762 (st, (M-O-M)_{edge}).

UV-Vis [nm]: 209, 297.

ICP-OES: Calculated for Na₆[PVNb₂Mo₉O₄₀] · 5 H₂O: 43.191 % Mo, 9.294 % Nb, 2.548 % V, 1.549 % P, 0.00 % K, 6.90 % Na. Found for Na₆[PVNb₂Mo₉O₄₀] · 5 H₂O: 42.28 % Mo, 8.915 % Nb, 2.19 % V 1.46 % P 1.545 % K, 4.645 % Na. Data normalized to molybdenum.
Na/K/P/V/Nb/Mo ratio: 4.13/0.81/0.964/0.880/1.96/9.

TGA: 4.077 % weight loss upon drying, this corresponds to 5 mol lattice water per mol of the POM.

Additional protocol for the nanofiltration process:

- Cycle 1: 65 mL permeate in 20 min
- Cycle 2: 70 mL permeate in 41 min

- Cycle 3: 70 mL permeate in 63 min
- Cycle 4: 70 mL permeate in 81 min

NaPV₃Mo:

³¹P-NMR (242.9 MHz, H₂O/D₂O, 20 °C): δ [ppm] = -0.15, -2.70, -2.96, -3.02, -3.06, 3.26, -3.34, -3.42, -3.49, -3.52, -3.56, -3.62, -3.72, -4.05, -4.06, -4.13, -4.20, -4.21.

⁵¹V-NMR (157.8 MHz, H₂O/D₂O, 20 °C): δ [ppm] = -521.1, -532.0, -533.3, -533.6, -535.2, -536.8, -535.9, -540.8, -541.3, -542.9, -544, -547.8, -549.4.

IR (ATR): $\tilde{\nu}$ [cm⁻¹] = 3561, 3307 (w, O-H, H₂O), 1618 (O-H, hydration H₂O), 1064, 1048 (w, P-O), 937 (me, M=O_i), 846 (me, (M-O-M)_{vertex}), 758 (st, (M-O-M)_{edge}).

UV-Vis [nm]: 214, 308.

ICP-OES: Calculated for Na₆[PV₃Mo₉O₄₀] · 8 H₂O: 43.846 % Mo, 7.76 % V, 1.573 % P, 0.00 % K, 7.004 % Na. Found for Na₆[PV₃Mo₉O₄₀] · 8 H₂O: 46.88 % Mo, 8.205 % V 1.61 % P 0.00 % K, 6.75 % Na. Data normalized to molybdenum. Na/K/P/V/Mo 5.41/0/0.957/2.97/9

TGA: 7.128 % weight loss upon drying, this corresponds to 8 mol lattice water per mol of the POM.

NaPW₃Mo:

³¹P-NMR (242.9 MHz, H₂O/D₂O, 20 °C): δ [ppm] = 0.61 (PO₄³⁻), -1.63 to -12.45.

IR (ATR): $\tilde{\nu}$ [cm⁻¹] = 3464, 3307 (w, O-H, H₂O), 1620 (O-H, hydration H₂O), 1058 (w, P-O), 964 (me, M=O_i), 909, 865 (me, (M-O-M)_{vertex}), 799 (st, (M-O-M)_{edge}).

UV-Vis [nm]: < 200.

ICP-OES: Calculated for Na₃[PW₃Mo₉O₄₀] · 28 H₂O: 32.469 % Mo, 20.739 % W, 1.165 % P, 0.00 % K, 2.593 % Na. Found for Na₃[PW₃Mo₉O₄₀] · 28 H₂O: 32.0 % Mo, 20.62 % W 1.20 % P 0.01 % K, 4.61 % Na. Data normalised to molybdenum. Na/K/P/W/Mo ratio: 4.88/0.00690/1.05/3.03/9.

TGA: 19.15 % weight loss upon drying, this corresponds to 28 mol lattice water per mol of the POM.

Additional protocol for the nanofiltration process:

- Cycle 1: 65 mL permeate in 25 min
- Cycle 2: 70 mL permeate in 47 min
- Cycle 3: 70 mL permeate in 68 min
- Cycle 4: 70 mL permeate in 90 min

1.8 Computational Methods

All DFT calculations were performed using TURBOMOLE v. 7.5.1 2021.¹⁴ Structures were optimized using the PBE0 hybrid functional¹⁵ using an Ahlrichs' triple- ζ valence polarization (def2-TZVP) basis set for all atoms.¹⁶ The resolution of identity approximation was applied using the corresponding auxiliary def2-TZVP basis set to approximate the Coulomb potentials. Geometry optimizations were carried out in gas phase with strict scf convergence criteria (10^{-8}) and a fine m4 grid. Each optimized structure was characterized to be a minimum by absence of any imaginary frequency. IR and Raman spectra are displayed 'as calculated' without any scaling factor. Thermodynamic corrections for all species were evaluated at 298 K and 1 bar within the rigid-rotor harmonic-oscillator approximation. The implicit COSMO¹⁷ (Conductor like Solvation MOdel) for water was used to consider solvation effects.

Cartesian coordinates of the optimized structures in Å

LHPA-3

Mo	4.9128525	1.3010269	2.2832149
Mo	8.2145369	0.6924210	2.0301763
Mo	7.6612561	5.9560831	5.0679291
P	7.0444109	4.0460266	2.1996211
O	6.7671426	2.6024777	1.7513330
O	7.0372216	4.0541309	3.7633554
O	7.8942395	7.1241158	6.2478147
O	5.9601333	5.1216517	5.8488260
O	6.2991625	0.1601465	2.4653000
O	9.5672377	1.8332170	1.7726079
O	3.5862828	0.2699677	2.3720676
O	7.6460321	0.4935344	0.2525159
O	8.1142001	1.3311517	3.8754795

O	5.0722152	1.2303405	0.2711932
O	8.9884334	-0.7751590	2.2698572
O	4.9698971	2.0967253	3.9120548
O	8.4198767	4.5185533	1.7381396
O	5.9354884	4.9836174	1.7138934
Mo	10.5837680	3.5396628	2.2914661
Mo	9.3983699	6.7012827	1.9417749
Mo	5.1583447	3.6511849	5.1783555
O	4.0103171	3.2608089	6.3357536
O	6.6692254	2.5711666	5.8386373
O	10.8361426	5.3172228	2.3894427
O	7.7415543	7.3230953	1.7467773
O	12.1308752	2.9298087	2.5159044
O	9.8446058	6.2665978	0.1829759
O	8.9407866	6.3290270	3.8343238
O	10.5627292	3.6786321	0.3017256
O	10.2970372	8.0996917	2.1540683
O	9.8033025	3.2476758	3.9124682
Mo	5.7550416	7.3987487	2.2197673
Mo	3.6262835	4.7634116	2.0516991
Mo	8.3776465	2.6292086	5.1483618

Mo	2.6540861	-0.9939516	7.0270233
Mo	4.7341535	-1.9126923	4.4850736
P	5.5286806	5.4646117	4.7635737
P	4.0404707	1.5332942	4.9621201
O	4.0241483	5.5497683	5.0408101
O	6.2612192	4.7446824	5.9003553
O	5.8059175	4.7937519	3.4144154
O	6.0837082	6.9303076	4.6903322
O	1.9529450	6.8993674	5.4533395
O	4.4066327	5.5428321	7.8518583
O	7.9562999	4.7397314	7.7471995
O	8.3430856	3.8697222	4.1847434
O	6.7225390	4.8750598	1.0838001
O	3.3411169	5.6719774	2.3206936
O	3.6433989	7.9799696	3.5296217
O	4.1917554	7.8455097	6.6638146
O	6.4966906	7.0981227	7.5538033
O	8.7111967	6.0762331	5.5090971
O	8.2920907	6.1903417	2.9636977
O	5.4454603	7.1328882	1.8863594
O	5.4016643	9.4412097	4.7840066
O	7.7145888	8.6172585	5.8182492
O	7.3623037	8.6181010	3.1765900
O	1.5098756	4.7419652	3.9246661
O	2.0414716	4.5939644	6.9632968
O	5.7389406	3.3612855	8.3568784
O	7.8762579	2.3524416	6.3687108
O	7.1533704	2.5229933	2.2989031
O	4.3880009	3.4188087	1.2609511

O	2.8676532	2.4893602	5.2028695
O	5.1083212	1.6824012	6.0507841
O	4.6404380	1.7328626	3.5666009
O	3.4849340	0.0679721	5.0367880
O	0.4359795	2.8877528	5.6607511
O	3.2059921	2.5023337	7.9928330
O	6.4408073	0.7268451	7.9463657
O	7.1925506	0.8081154	4.3850610
O	5.1995205	0.8630646	1.2842697
O	2.2171113	2.5979303	2.4434822
O	0.9548890	0.8718812	3.9226016
O	1.5122573	0.7356009	7.0525466
O	3.8339835	-0.0187207	7.8963106
O	6.0370734	-1.0428566	5.8395245
O	5.5711661	-0.9133460	3.3032793
O	2.7236758	0.0323775	2.2391085
O	1.3486329	-1.3471915	5.4926656
O	3.7484565	-2.2187109	6.2535382
O	3.1269686	-2.1154132	3.6633708
O	1.1214668	7.2932501	2.8672278
O	2.0510340	6.9783831	8.1900987
O	6.3983941	5.6409784	9.8199222
O	10.1147334	3.8309346	6.3241204
O	9.3178309	4.1217438	1.5708364
O	4.4437609	5.6484783	-0.2290551
O	5.8023644	9.9038097	7.4725182
O	9.9460259	8.1756444	4.2618530
O	5.2082552	9.8568892	1.9828845
O	-0.4396402	3.1062131	3.0738820
O	0.4516298	2.8129929	8.4045562
O	4.8076954	1.4717990	10.0173482
O	8.5430437	-0.3499328	6.5490717
O	7.7324959	-0.0480477	1.7981023
O	2.8708760	1.4698392	-0.0366160
O	0.4385313	-1.6139488	2.9055335
O	1.8573268	-1.8797521	8.2315817
O	5.4467354	-3.4429811	4.3382750

[PMo₁₂O₄₀]⁻³

O	-0.8301282	4.2498370	20.9158558
O	0.7790832	3.3097849	23.1694028
Mo	0.9893851	-0.0971768	19.7037802
O	5.9726430	1.9058505	22.3734621
O	-4.4152602	2.1460484	22.7164288
O	-0.5656007	5.0552603	24.5322718
O	-2.6554930	-0.0442710	22.4390694
O	0.8428032	5.7955742	22.4399589
O	2.0872030	-0.7473277	20.9910982
Mo	-0.9613395	0.6183535	25.4964723

O	0.7325321	-1.4737585	23.0499818
O	-2.0621961	3.2662412	18.5331207
Mo	-1.0278911	2.6671498	19.7037253
O	3.1310979	-2.7720573	22.7167164
O	-0.4709450	1.1438619	23.1692797
O	-2.1388561	2.0405477	20.9920870
O	-1.8492934	6.3452180	22.3743713
O	2.0608168	5.0194443	24.6359011
O	0.5699747	4.7065678	27.0119595
Mo	2.7308976	0.9824469	25.4973009
O	-0.4806507	-0.7200386	20.9142240
O	3.6975507	3.4972554	23.0505756
O	-1.7810631	-2.6512493	22.3744348
Mo	2.5853110	4.9195274	22.8889406
O	4.1510233	-0.1531361	22.4399234
O	3.3439870	0.6281393	27.0131595
Mo	0.5703074	3.9978189	25.4965413
Mo	-1.1711637	-1.1029418	22.5460836
O	-1.5748963	0.2664512	27.0126831
O	2.0299268	1.1449323	23.1694320
O	-0.5030953	1.0539129	19.0268380
Mo	4.3264688	1.6621814	22.5459691
O	-2.0935619	3.5784598	23.0500074
Mo	-0.8168610	5.0403995	22.5472835
O	2.3884545	4.3048486	20.9918305
O	3.6489951	2.0681840	20.9148487
O	-1.3101387	-0.8936931	24.5331252
Mo	2.5206927	-1.2240884	22.8896329
O	4.2138194	1.4368633	24.5328056
O	2.1246389	1.1640751	19.0264595
O	3.6172689	6.2247003	22.7156834
Mo	2.3748441	3.0309234	19.7022241
O	3.4097660	3.6292911	18.5317752
O	2.0409430	2.6486794	25.6811580
O	0.8270058	0.3836576	25.6801092
O	2.8691190	-0.8205090	24.6364692
P	0.7792496	1.8660841	22.6586287
O	-0.5265881	2.5667145	25.6791002
O	0.7785628	1.8659200	21.1270724
O	0.9885488	-1.2901990	18.5312837
O	-2.5916263	1.3991011	24.6357598
O	0.7153212	3.3834151	19.0259439
Mo	-2.7688575	1.9041557	22.8892264

[PMo₁₁CoO₄₀]⁻⁷

O	0.0052418	1.2863145	-3.6800646
O	1.9699480	3.2199196	-0.6143543
O	-0.0926238	5.1493326	-0.0494637
O	0.9636086	-3.6063564	1.9393325

O 2.0619690 -0.0472550 2.6601165
O 3.2922733 -0.0795938 -0.3602121
Mo -1.5410381 1.6254840 -2.7743475
O -0.1263215 -1.4125457 3.1289249
Mo 1.4531961 -0.1017454 -3.2135793
O 2.2477216 1.1931210 -2.2790192
O -2.4820938 -2.7412471 -3.8329207
O -1.3207958 -0.1654457 0.8019751
Mo 1.5548012 1.6804038 2.6684781
O -2.7682692 1.2988227 2.4359681
Mo -1.6070258 -0.0882797 3.1928864
O 0.8295928 -1.4068477 0.4117978
O 2.2303811 -1.4198358 -2.2667857
O -0.2490312 -0.1506832 -1.4766970
O -0.1381482 1.2505313 3.2015663
O -2.7019249 -1.6187728 -1.1955615
O 2.2556896 -2.5415527 4.0719706
O 2.2702188 2.3442735 4.0810023
Mo 3.0737699 1.7742138 -0.4133429
O -0.6665192 -3.1495423 -1.8362370
O 3.1744786 1.9668598 1.3826101
Co 0.1312437 -3.8501766 -0.0239718
O -4.4825043 -2.8446887 0.6579856
O 2.2860408 -0.1074351 -4.7146537
Mo 0.0315707 3.4399123 0.0695634
O 4.6123197 -2.5134471 -0.9279724
O 4.5929849 2.3586859 -0.9609614
Mo -3.1932576 1.5788307 0.6297871
O -2.3449652 2.7560867 -3.7849251
O -0.0461777 -5.7602078 -0.1306177
O 3.1227120 -2.1282886 1.3998795
O -1.5236557 2.9233998 0.7721537
O -2.2823952 0.0588725 -3.2059422
Mo -1.5079052 -1.8968174 -2.6952713
O 2.1010822 -3.5108221 -0.6626251
Mo 3.0348659 -2.0432380 -0.4404190
O -0.0767631 -1.3177089 -3.7313976
O -2.0877458 -0.1186787 4.8227033
O -2.6486502 1.6792065 -1.1465222
O -4.0176742 0.0271463 0.4656812
O -4.4706132 2.7232873 0.7285442
O 0.9455471 3.2696716 1.7785490
O -2.8476541 -1.4113425 2.4153254
Mo 1.5022311 -2.0808712 2.5993880
O 0.7951277 1.1252356 0.4170324
O -0.4492200 2.8433581 -1.5954463
O -1.7833815 -3.2250821 0.6911808
P 0.0237558 -0.1552110 0.0399461
Mo -2.9933424 -1.9845943 0.6357047

[PMo₁₁FeO₄₀]⁻⁶

O	0.1018818	1.2690916	-3.7680417
O	1.9145590	3.2041140	-0.6340538
O	-0.1114766	5.0992492	-0.1510562
O	0.8222310	-3.4342720	1.8726973
O	1.9369294	-0.1769270	2.7239347
O	3.3448291	-0.1406303	-0.2689018
Mo	-1.6602250	1.6446340	-2.6581117
O	-0.2346278	-1.4519292	3.2682450
Mo	1.3776452	0.0820565	-3.3449334
O	2.2915587	1.1574110	-2.1962770
O	-2.2653227	-2.8208782	-3.7944734
O	-1.3167503	-0.1070203	0.7976839
Mo	1.5249115	1.7040054	2.6573702
O	-2.8055117	1.3313780	2.5297112
Mo	-1.5015777	-0.2231298	3.2810234
O	0.7866958	-1.4002064	0.3356665
O	2.2689250	-1.4055971	-2.2398745
O	-0.2863337	-0.0695966	-1.4975966
O	-0.2830660	1.1773898	3.1495532
O	-2.7113353	-1.5714533	-1.2575350
O	2.3905946	-2.6441964	3.9968816
O	2.1692791	2.3599420	4.0779666
Mo	3.0594189	1.6774142	-0.3996243
O	-0.5558217	-2.9634466	-1.6509262
O	3.0826953	1.9611123	1.4022315
Fe	0.1131184	-3.4356788	0.1007559
O	-4.4025103	-2.7528321	0.6556713
O	2.3536929	0.0328080	-4.7416394
Mo	0.1133296	3.4229021	0.0272897
O	4.4695658	-2.6620297	-1.1184116
O	4.5672097	2.2970610	-0.8892074
Mo	-3.1166903	1.6669083	0.8096551
O	-2.3789767	2.7078129	-3.7825947
O	-0.1755041	-5.0142403	0.0021706
O	3.1365005	-2.1770920	1.3593899
O	-1.5739606	2.8124298	0.6258855
O	-2.1155031	-0.0276742	-3.2976362
Mo	-1.4082193	-1.8309397	-2.7012914
O	1.9132772	-3.5082390	-0.5618735
Mo	2.9386302	-2.0468214	-0.6867387
O	0.1092066	-1.3575868	-3.7153444
O	-2.0296466	-0.1641012	4.9037628
O	-2.7796331	1.6522957	-1.2773332
O	-3.8996606	0.0575419	0.4771990
O	-4.4189565	2.7696996	0.8416315
O	0.7796698	3.3079884	1.7489482
O	-2.8372070	-1.2813430	2.4630884
Mo	1.7520096	-2.0387822	2.5344719
O	0.8320506	1.1065712	0.4114325

O	-0.4610984	2.7490482	-1.6773624
O	-1.6567443	-2.9383680	0.7114608
P	-0.0005880	-0.1168965	0.0093291
Mo	-2.9906227	-1.7966742	0.5773113

[PMo₁₁InO₄₀]⁻⁶

O	0.1587737	1.3271914	-3.7249133
O	1.8256643	3.3452149	-0.5349308
O	-0.2119001	5.1431227	0.0654313
O	0.8614428	-3.6012943	1.9000104
O	2.0619839	-0.0443686	2.7173756
O	3.3475238	0.0324889	-0.2410113
Mo	-1.3907765	1.7302372	-2.8012600
O	-0.1682972	-1.3538029	3.0880570
Mo	1.3834386	-0.1757672	-3.3049663
O	2.2520574	1.2989259	-2.2275694
O	-2.5143986	-2.6240635	-3.7905224
O	-1.2946360	-0.0927399	0.7809789
Mo	1.7676026	1.7002410	2.5987405
O	-2.7485334	1.2775913	2.5032257
Mo	-1.5508071	0.1129050	3.1887715
O	0.8685840	-1.3294016	0.4121380
O	2.2767537	-1.2754096	-2.1687094
O	-0.2385920	-0.1038894	-1.4865346
O	-0.1266810	1.2278659	3.1513779
O	-2.7756507	-1.5912826	-1.2097646
O	2.1489228	-2.5579353	4.0406015
O	2.3681894	2.3495762	4.0554881
Mo	2.9749639	1.7470816	-0.6266458
O	-0.6268976	-3.0046864	-1.8545265
O	3.0666585	2.1120599	1.3973274
In	0.0196970	-4.2337993	-0.1010386
O	-4.4487308	-2.7562768	0.8337972
O	2.3556080	-0.1510519	-4.6993263
Mo	0.0917069	3.4735516	0.1878055
O	4.5587232	-2.4447133	-0.8890132
O	4.4722047	2.4494591	-1.0369131
Mo	-3.1135852	1.6383959	0.4893679
O	-2.1723970	2.8222337	-3.8466649
O	-0.1701107	-6.1513512	-0.2531572
O	3.0597777	-2.1255663	1.4088603
O	-1.5772770	2.7862305	0.7326354
O	-2.1136415	0.0990057	-3.2430732
Mo	-1.6249395	-1.7804953	-2.6093609
O	2.0694014	-3.4963474	-0.7032988
Mo	2.9756476	-2.0263647	-0.4237015
O	0.0436057	-1.2966158	-3.7610021
O	-1.9682900	0.0533790	4.8360519
O	-2.7639756	1.6648305	-1.2729797

O	-3.8860281	-0.0019109	0.5498912
O	-4.4289145	2.7052657	0.6673265
O	0.7798015	3.3116227	1.8848617
O	-2.7389249	-1.3556895	2.5206987
Mo	1.4216452	-2.0860150	2.5741231
O	0.8346090	1.1763320	0.3874375
O	-0.5169327	2.8212415	-1.5835120
O	-1.7500250	-3.0843680	0.6699645
P	0.0484381	-0.1012764	0.0266486
Mo	-2.9996602	-1.8672845	0.7669889

[PMo₁₁NiO₄₀]⁻⁵

O	0.1587737	1.3271914	-3.7249133
O	1.8256643	3.3452149	-0.5349308
O	-0.2119001	5.1431227	0.0654313
O	0.8614428	-3.6012943	1.9000104
O	2.0619839	-0.0443686	2.7173756
O	3.3475238	0.0324889	-0.2410113
Mo	-1.3907765	1.7302372	-2.8012600
O	-0.1682972	-1.3538029	3.0880570
Mo	1.3834386	-0.1757672	-3.3049663
O	2.2520574	1.2989259	-2.2275694
O	-2.5143986	-2.6240635	-3.7905224
O	-1.2946360	-0.0927399	0.7809789
Mo	1.7676026	1.7002410	2.5987405
O	-2.7485334	1.2775913	2.5032257
Mo	-1.5508071	0.1129050	3.1887715
O	0.8685840	-1.3294016	0.4121380
O	2.2767537	-1.2754096	-2.1687094
O	-0.2385920	-0.1038894	-1.4865346
O	-0.1266810	1.2278659	3.1513779
O	-2.7756507	-1.5912826	-1.2097646
O	2.1489228	-2.5579353	4.0406015
O	2.3681894	2.3495762	4.0554881
Mo	2.9749639	1.7470816	-0.6266458
O	-0.6268976	-3.0046864	-1.8545265
O	3.0666585	2.1120599	1.3973274
In	0.0196970	-4.2337993	-0.1010386
O	-4.4487308	-2.7562768	0.8337972
O	2.3556080	-0.1510519	-4.6993263
Mo	0.0917069	3.4735516	0.1878055
O	4.5587232	-2.4447133	-0.8890132
O	4.4722047	2.4494591	-1.0369131
Mo	-3.1135852	1.6383959	0.4893679
O	-2.1723970	2.8222337	-3.8466649
O	-0.1701107	-6.1513512	-0.2531572
O	3.0597777	-2.1255663	1.4088603
O	-1.5772770	2.7862305	0.7326354
O	-2.1136415	0.0990057	-3.2430732

Mo	-1.6249395	-1.7804953	-2.6093609
O	2.0694014	-3.4963474	-0.7032988
Mo	2.9756476	-2.0263647	-0.4237015
O	0.0436057	-1.2966158	-3.7610021
O	-1.9682900	0.0533790	4.8360519
O	-2.7639756	1.6648305	-1.2729797
O	-3.8860281	-0.0019109	0.5498912
O	-4.4289145	2.7052657	0.6673265
O	0.7798015	3.3116227	1.8848617
O	-2.7389249	-1.3556895	2.5206987
Mo	1.4216452	-2.0860150	2.5741231
O	0.8346090	1.1763320	0.3874375
O	-0.5169327	2.8212415	-1.5835120
O	-1.7500250	-3.0843680	0.6699645
P	0.0484381	-0.1012764	0.0266486
Mo	-2.9996602	-1.8672845	0.7669889

[PMo₁₁VO₄₀]⁻⁴

O	0.1485867	1.2537809	-3.7194954
O	1.8814303	3.3232053	-0.5527801
O	-0.2098787	5.1034221	0.1056142
O	0.7441777	-3.5273878	1.7127265
O	2.0250131	-0.1579835	2.7016786
O	3.3204569	-0.0728897	-0.2482496
Mo	-1.3362925	1.7025930	-2.7557004
O	-0.2100881	-1.3657847	3.1112615
Mo	1.3917719	-0.2675552	-3.3082136
O	2.2505837	1.1921229	-2.2120812
O	-2.4692737	-2.7122628	-3.7150730
O	-1.3280416	-0.0665251	0.7671857
Mo	1.7701738	1.6228788	2.5661492
O	-2.7659801	1.2740887	2.4719440
Mo	-1.5634137	0.1086067	3.1943123
O	0.8105999	-1.3132093	0.3909389
O	2.2585282	-1.3781749	-2.1823269
O	-0.2625842	-0.0715083	-1.4986058
O	-0.1162567	1.2032413	3.1083599
O	-2.7660499	-1.6413364	-1.1899164
O	2.0125044	-2.7222182	4.0063044
O	2.3983668	2.2391512	4.0004929
Mo	2.9230887	1.8253236	-0.6579338
O	-0.5516239	-2.8879866	-1.6839336
O	3.0844817	1.9668357	1.3495653
V	0.1756770	-3.5932610	-0.1546980
O	-4.2831015	-2.9145375	0.8668039
O	2.3486192	-0.2465600	-4.6931465
Mo	0.0266000	3.4426406	0.2394898
O	4.5197938	-2.4919117	-0.8501079
O	4.4348827	2.4266435	-1.0870654

Mo	-3.1424656	1.5378592	0.5084529
O	-2.1455272	2.7663037	-3.7774954
O	-0.0963049	-5.1309955	-0.3051965
O	3.0029392	-2.2109041	1.4239418
O	-1.5919792	2.8100429	0.7441944
O	-2.1283789	0.0149104	-3.2386691
Mo	-1.6526563	-1.7217198	-2.6266097
O	1.8811788	-3.4231146	-0.6310194
Mo	3.0244012	-1.8838869	-0.3756824
O	0.0238404	-1.3689953	-3.7474751
O	-1.9667129	0.0983908	4.8274342
O	-2.6820949	1.5717014	-1.2326279
O	-3.9171129	-0.1000990	0.5533112
O	-4.4488254	2.5944805	0.6122969
O	0.8555805	3.2705946	1.8664795
O	-2.7249968	-1.3573091	2.5318814
Mo	1.3741389	-2.0848367	2.5843675
O	0.8088674	1.1801571	0.3822432
O	-0.4675952	2.8114472	-1.5713727
O	-1.5534412	-2.9711425	0.6413596
P	0.0069439	-0.0747463	0.0098334
Mo	-2.9497061	-1.8892964	0.7784329

[PMo₁₁NbO₄₀]⁻⁴

O	-1.9256808	0.5715342	-3.3850107
O	-0.4637654	3.7535783	-1.1254789
O	-2.8614035	4.3304410	0.1095220
O	3.0617950	-2.1261851	1.3147609
O	2.4289677	1.4434542	1.7203819
O	2.5615600	1.6326147	-1.5033301
Mo	-3.0887798	0.1413657	-1.7819091
O	1.6392049	-0.6488396	2.9293664
Mo	-0.1998645	0.0510302	-3.6014272
O	0.3359536	1.8443415	-2.8346271
O	-1.7408670	-4.1741573	-2.6317345
O	-0.7201698	-0.4891971	1.2586132
Mo	1.1717472	2.8771264	1.7685834
O	-1.9710972	0.1814730	3.4531851
Mo	0.0368406	-0.1347157	3.5592755
O	1.4143752	-0.6137628	-0.0456846
O	1.6540313	-0.3119996	-2.9269102
O	-0.7729625	-0.4419951	-1.2500996
O	0.2631312	1.5718633	3.0321422
O	-1.7557335	-2.9462584	-0.1646883
O	4.4723257	-0.1823152	2.6898303
O	1.8317547	3.9413871	2.8906443
Mo	1.2412056	2.8750266	-1.6578924
O	0.5104825	-3.0564475	-1.4851328
O	1.7678283	3.5345210	0.1776358

Nb	1.9416508	-3.0316316	-0.0527204
O	-1.8344865	-4.3167887	2.3712631
O	0.0964159	0.3203554	-5.2352731
Mo	-1.7463384	3.0753444	0.0144153
O	4.4059520	-0.0764406	-2.8049868
O	1.9199226	4.0928407	-2.6012329
Mo	-2.9867808	0.1432129	1.9497142
O	-4.5993887	0.4953512	-2.4330599
O	2.5951421	-4.6219151	-0.0972967
O	3.9471168	0.0058319	-0.0068908
O	-2.4719169	1.7990974	1.3338786
O	-2.8327190	-1.6141118	-2.2568135
Mo	-1.2386054	-2.7607932	-1.8665497
O	3.1079782	-2.0535446	-1.4192825
Mo	3.0773185	-0.2755831	-1.7942914
O	-0.5543360	-1.7124625	-3.5134154
O	0.2343210	-0.0901594	5.2309922
O	-3.4009738	-0.1423348	-0.0398555
O	-2.8673104	-1.7736986	1.9231530
O	-4.5474903	0.3875101	2.5280063
O	-0.5356588	3.5546213	1.4890985
O	-0.6475430	-2.0386437	3.3611732
Mo	3.1786159	-0.2988459	1.6226779
O	0.1122900	1.5230542	0.0217321
O	-2.4627197	1.9390519	-1.2283733
O	0.4010479	-3.1729189	1.1643328
P	0.0085962	-0.0075548	-0.0018730
Mo	-1.2863861	-2.8151277	1.8493656

[PMo₁₁WO₄₀]⁻³

O	0.1331552	1.2380096	-3.7166771
O	1.8629096	3.3283368	-0.5396216
O	-0.2185810	5.1038006	0.1379699
O	0.7659580	-3.5307791	1.7406721
O	2.0302717	-0.1621313	2.6971252
O	3.3416297	-0.0607145	-0.2450426
Mo	-1.3249773	1.7414438	-2.7504987
O	-0.1996374	-1.3727535	3.1070266
Mo	1.3824669	-0.2777365	-3.2897177
O	2.2307817	1.1865364	-2.2030659
O	-2.5161598	-2.6679128	-3.7430516
O	-1.3263801	-0.0746067	0.7700773
Mo	1.7759476	1.6410954	2.5653466
O	-2.7703232	1.2544965	2.4594825
Mo	-1.5552714	0.1121938	3.1929376
O	0.7801733	-1.3520741	0.3564129
O	2.2585843	-1.3796823	-2.1546798
O	-0.2823746	-0.0671366	-1.5052557
O	-0.1076937	1.1932085	3.1126698

O -2.7291507 -1.6611807 -1.1917627
O 2.0390624 -2.6705474 4.0366537
O 2.4066339 2.2397934 3.9942222
Mo 2.9169502 1.8319168 -0.6607547
O -0.5446229 -2.9198382 -1.7122145
O 3.0816578 1.9732808 1.3466956
W 0.1415632 -3.6102880 -0.1352408
O -4.3099802 -2.8791906 0.8553150
O 2.3331140 -0.2682546 -4.6666944
Mo 0.0385977 3.4550245 0.2493757
O 4.5634655 -2.4588512 -0.8337082
O 4.4110498 2.4407241 -1.1035208
Mo -3.1188848 1.5475101 0.4995045
O -2.1255869 2.7965687 -3.7726003
O -0.1289035 -5.2845960 -0.2935866
O 3.0020165 -2.1954993 1.4210285
O -1.5847069 2.7912157 0.7378339
O -2.1611487 0.0239052 -3.2690849
Mo -1.6986877 -1.6617209 -2.6863794
O 1.9336373 -3.4449574 -0.6330549
Mo 3.0698328 -1.8622696 -0.3760061
O 0.0038280 -1.3831803 -3.7262496
O -1.9627851 0.0938784 4.8154571
O -2.6663630 1.5632346 -1.2457061
O -3.9049658 -0.1169804 0.5299381
O -4.4242926 2.5891990 0.5951599
O 0.8515032 3.2622753 1.8822575
O -2.7290008 -1.3731775 2.5212696
Mo 1.4108910 -2.0394376 2.6217325
O 0.8192052 1.1492290 0.3810931
O -0.4669938 2.8374429 -1.5739005
O -1.5581902 -2.9918183 0.6605131
P -0.0035150 -0.0827851 -0.0012698
Mo -2.9928646 -1.8519361 0.7831539

2 Additional data

In Figure S10 the principle of the TBA POM precipitation is shown:

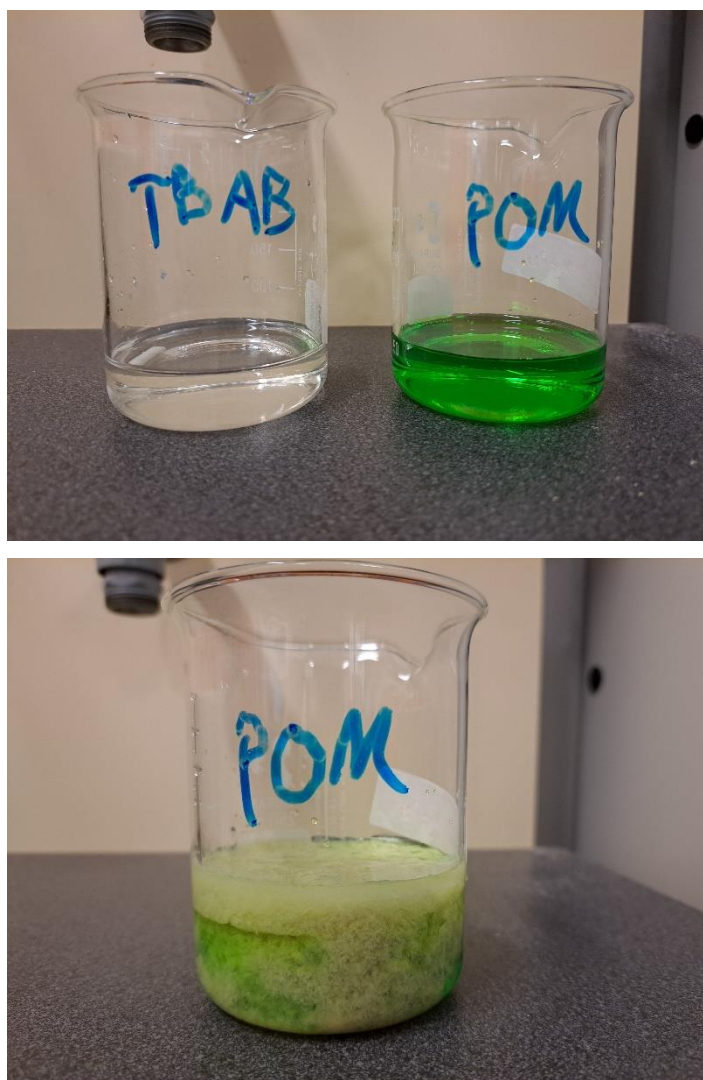


Figure S10: Aqueous TBAB solution (left) and aqueous PCu_2Mo solution (right).

2.1 Vibrational spectroscopy

2.1.1 Infrared- and Raman-spectra of transition metal substituted Keggin POMs

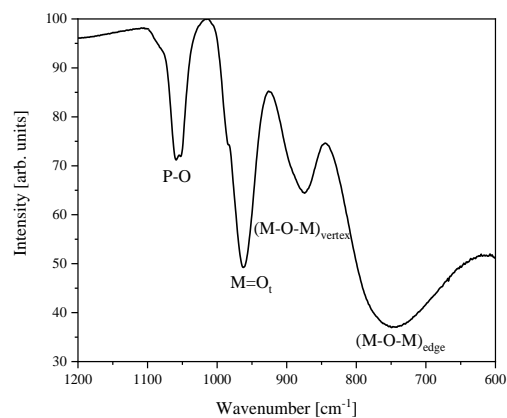


Figure S11: ATR-FT-IR spectrum of HPMo with the characteristic vibration bands.

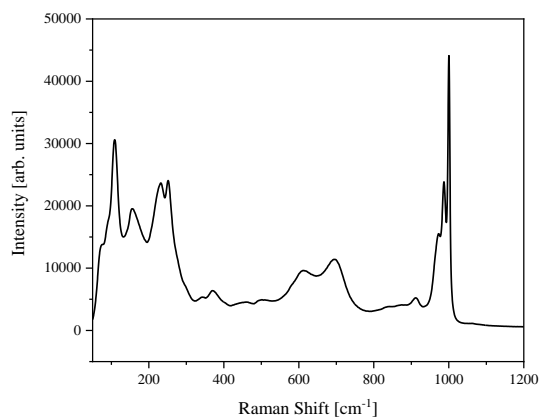


Figure S12: Raman spectrum of HPMo.

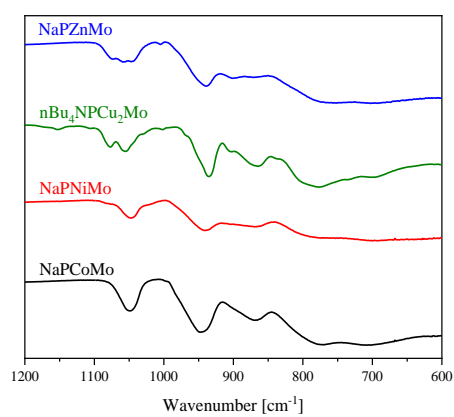


Figure S13: ATR-FT-IR spectra of the with divalent elements substituted POMs.

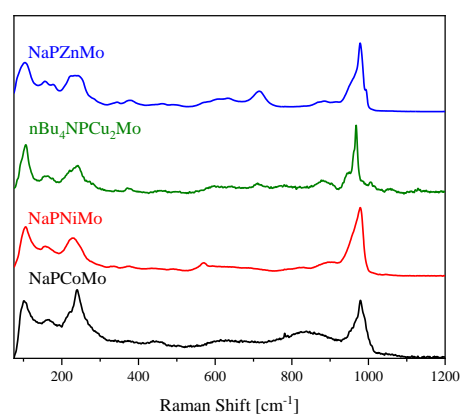


Figure S14: Raman spectra of the with divalent elements substituted POMs.

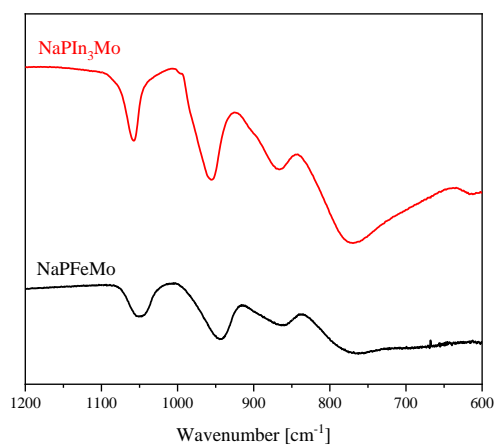


Figure S15 ATR-FT-IR spectra of the with trivalent elements substituted POMs.

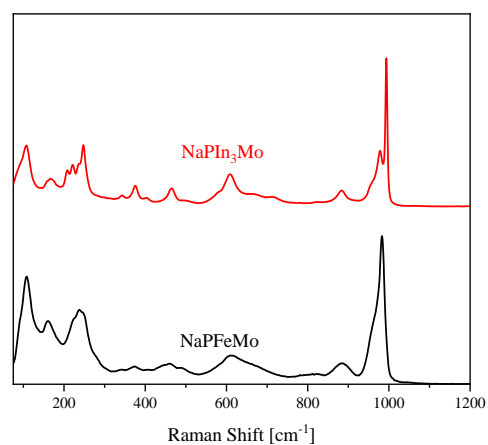


Figure S16: Raman spectra of the with trivalent elements substituted POMs.

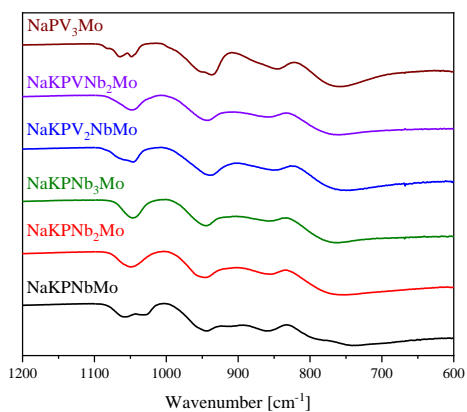


Figure S17: ATR-FT-IR spectra of the with pentavalent elements substituted POMs.

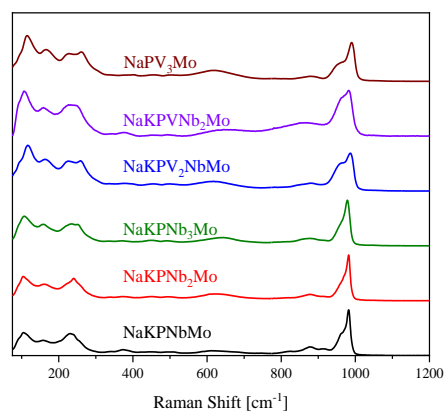


Figure S18: Raman spectra of the with pentavalent elements substituted POMs.

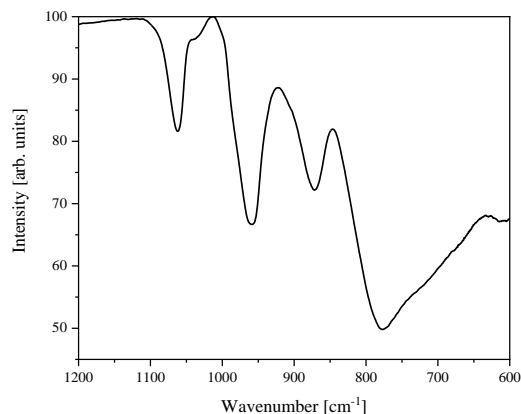


Figure S19: ATR-FT-IR spectra of the with hexavalent elements substituted POM.

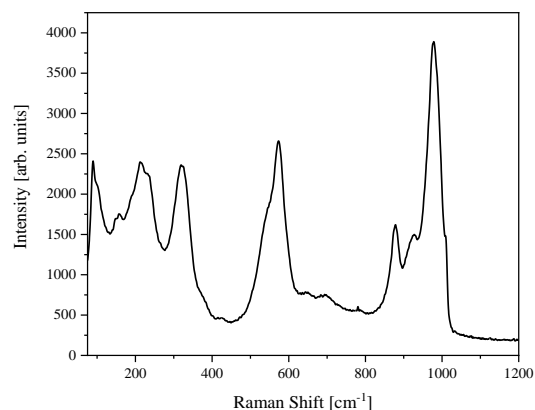


Figure S20: Raman spectra of the with hexavalent elements substituted POMs.

2.1.2 Assignment of peaks to structural features/vibration modes

Table 5: Assignment of the FT-IR peaks of each POM to the corresponding vibration modes.

POM	P-O	M=O _t	(M-O-M) _{vertex}	(M-O-M) _{edge}
HPMo ¹⁸	1059	962	877	744
NaPCoMo	1049	946	869	772, 707
NaPNiMo	1047	942	869	783
nBu ₄ NPCu ₂ Mo	1077, 1055	935	864	777
NaPZnMo	1075, 1060 1045	939	900	775
NaPFeMo	1051	945	864	766
NaPIn ₃ Mo	1058	956	867	770
NaKPNbMo	1058, 1034	944	859	741
NaKPNb ₂ Mo	1049	947	856	757
NaKPNb ₃ Mo	1047	944	857	760
NaKPV ₂ NbMo	1045	942	847	750
NaKPVNb ₂ Mo	1048	944	859	762
NaPV ₃ Mo	1064, 1048	937	846	758
NaPW ₃ Mo	1058	964	909, 865	799

2.2 NMR spectroscopy

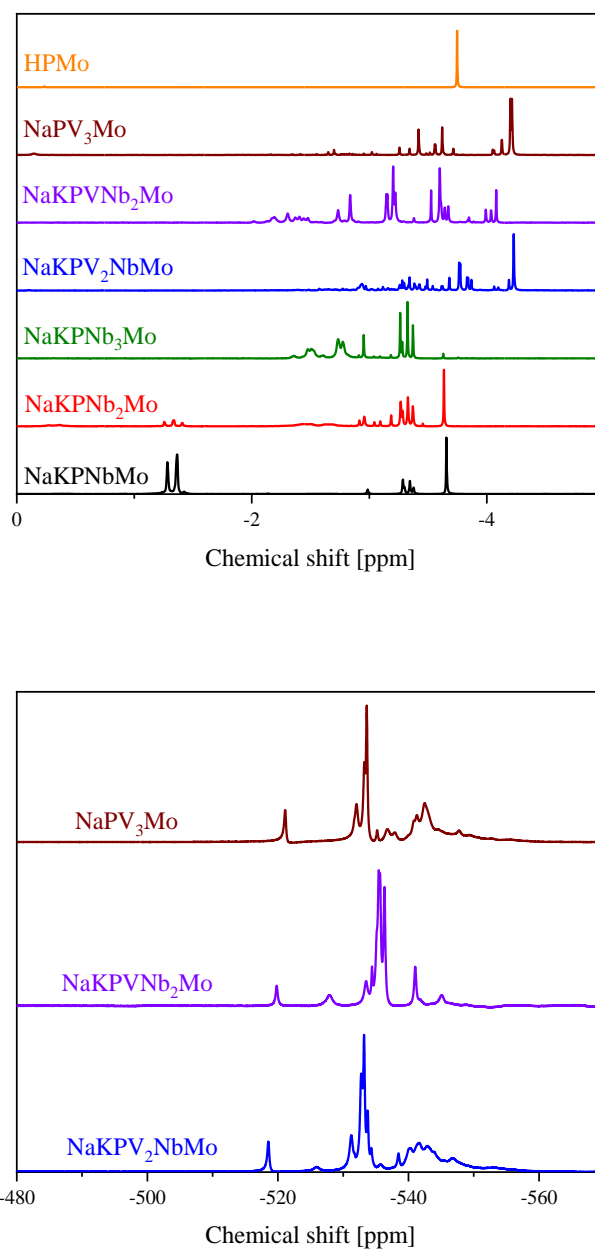


Figure S21: ^{31}P -NMR (top) and ^{51}V -NMR spectra (bottom) of the with pentavalent elements substituted POMs in a mixture of 90 % H₂O (pH 1) and 10 % D₂O. The spectra were measured at 242.9 MHz (^{31}P) 157.8 MHz (^{51}V). A 85 % H₃PO₄ and NaVO₃ were used as external standards.

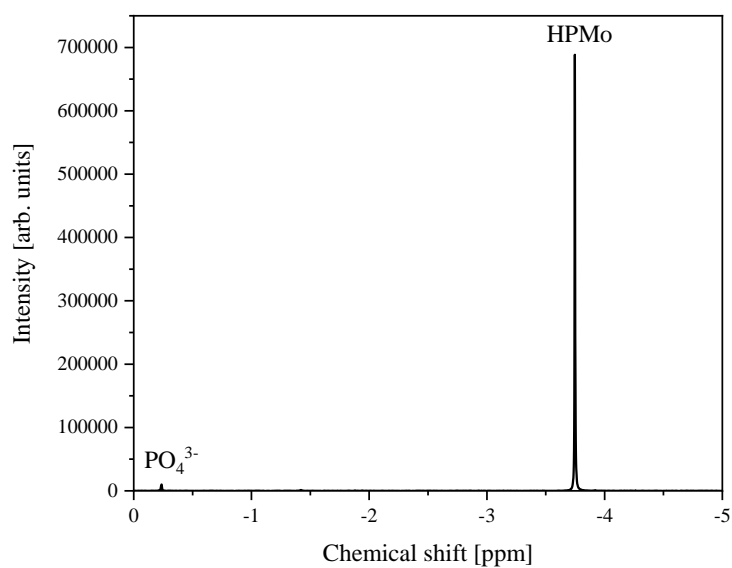


Figure S22: ^{31}P -NMR spectrum of HPMo in a mixture of 90 % H_2O (pH 1) and 10 % acetone- d_6 . The spectrum was measured at 242.9 MHz. 85 % H_3PO_4 was used as external standard.

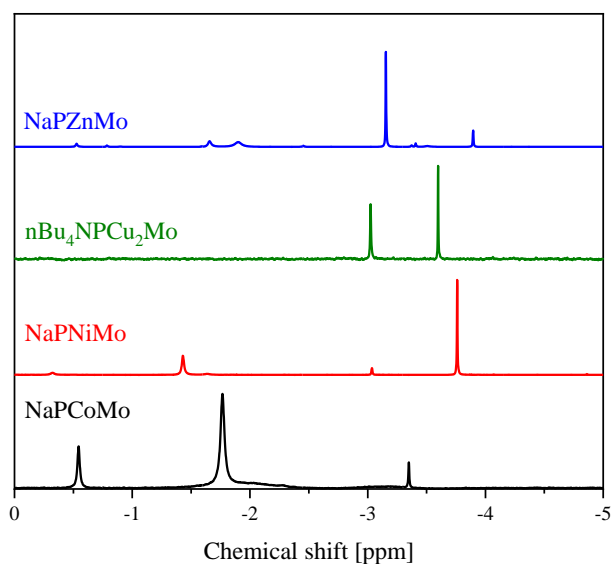


Figure S23: ^{31}P -NMR spectra of the with divalent elements substituted POMs in a mixture of 90 % H_2O (pH 1) 10 % D_2O . The spectra were measured at 242.9 MHz. 85 % H_3PO_4 was used as external standard.

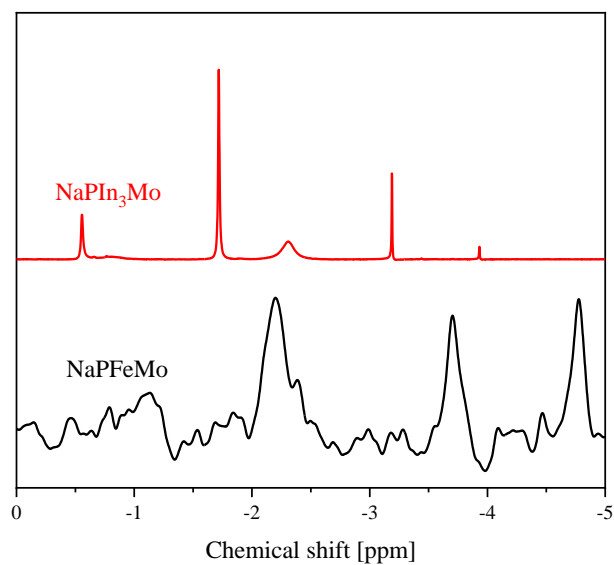


Figure S24: ^{31}P -NMR spectra of the with trivalent elements substituted POMs in a mixture of 90 % H_2O (pH 1) 10 % D_2O . The spectra were measured at 242.9 MHz. 85 % H_3PO_4 was used as external standard.

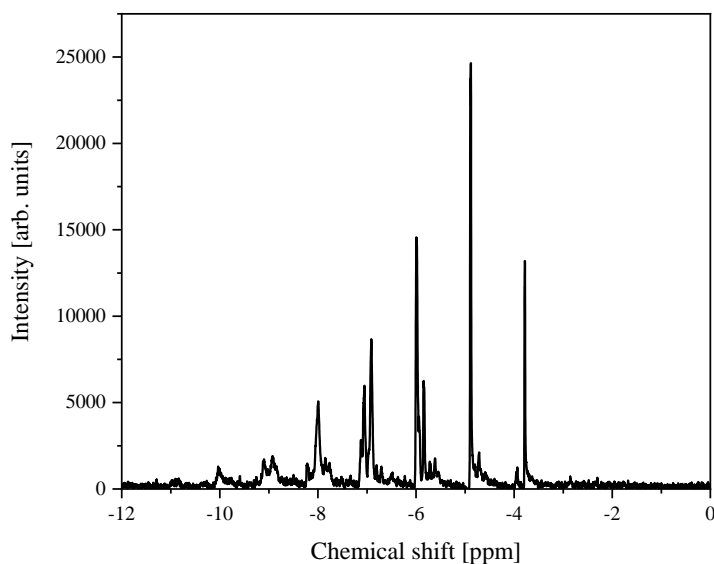


Figure S25: ^{31}P -NMR spectra of the with hexavalent elements substituted POMs in a mixture of 90 % H_2O (pH 1) and 10 % D_2O . The spectra were measured at 242.9 MHz. 85 % H_3PO_4 was used as external standard.

The ^{51}V NMR spectra of NaPV_3Mo , $\text{NaKPVNb}_2\text{Mo}$, and $\text{NaKPV}_2\text{NbMo}$ (Figure S21) show a fairly similar pattern of signals in the range of -510 ppm to -560 ppm, with each peak

representing an isomer or dissociation derivative of the respective compound. A broad peak at about -540 ppm indicates the presence of the VO_2^+ cation,¹⁹ which may be formed through the above described dissociation. Additional NMR spectra of the POMs substituted with different elements are found in Figures S22-S25.

Table 6: Chemical shifts obtained from the ^{31}P and ^{51}V NMR spectra of the different compounds.

POM	^{31}P shift [ppm]	^{51}V shift [ppm]
HPMo	-3.75	-
NaPCoMo	-0.54, -1.77, -3.36	-
NaPNiMo	-3.76	-
nBu₄NPCu₂Mo	-3.02, -3.60	-
NaPZnMo	-0.53, -0.79, -1.59, -1.66, -1.90, -2.45, -3.15, -3.27, -3.41, -3.90	-
NaPFeMo	-	-
NaPIn₃Mo	-0.56, -1.72, -2.31, -3.19, -3.93	-
NaKPNbMo	-1.28, -1.37, -1.43, -2.99, -3.29, -3.30, -3.36, -3.38, -3.66	-
NaKPNb₂Mo	-0.28, -0.36, -1.26, -1.33, -1.40, -2.45, -2.51, -2.63, -2.92, -2.96, -3.04, -3.09, -3.19, -3.27, -3.28, -3.33, -3.37, -3.46, -2.64	-
NaKPNb₃Mo	-2.36, -2.48, -2.52, -2.61, -2.73, -2.78, -2.91, -2.96, -3.04, -3.09, -3.18, -3.26, -3.28, -3.33, -3.37, -3.63	-
NaKPV₂NbMo	-2.50 to -4.30	-517.7, -525.9, -531.3, -532.8, -533.2, -533.8, -534.3, -535.7, -538.5, -540 to -546
NaKPVNb₂Mo	-4.92, -5.08, -5.27 to -5.36, -5.49, -5.62, -5.69, -5.93, -5.96, -5.99, -6.04, -6.20, -6.30, -6.42, -6.43, -6.49, -6.54, -6.73, -6.77, -6.86, -6.88, -6.89, -6.90	-519.8, -527.9, -532.7, -533.7, -534.4, -535.4, -537.1, -545.1
NaPV₃Mo	-0.15, -2.70, -2.96, -3.02, -3.06, 3.26, -3.34, -3.42, -3.49, -3.52, -3.56, -3.62, -3.72, -4.05, -4.06, -4.13, -4.20, -4.21	-521.1, -532.0, -533.3, -533.6, -535.2, -536.8, -535.9, -540.8, -541.3, -542.9, -544.5, -547.8, -549.4
NaPW₃Mo	-1.63 to -12.45	-

2.3 UV-Vis spectroscopy

Additional UV-Vis spectra of the POMs substituted with different elements are found in Figures S26-S29:

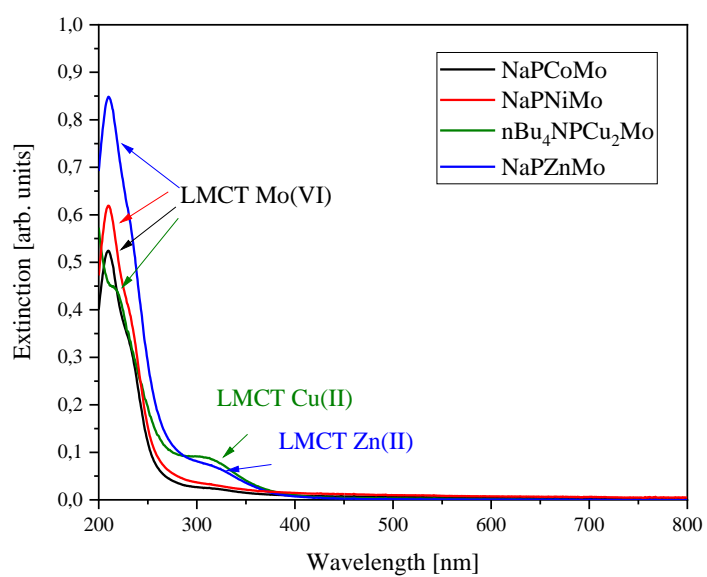


Figure S26: UV-Vis spectra of the with divalent elements substituted POMs in water.

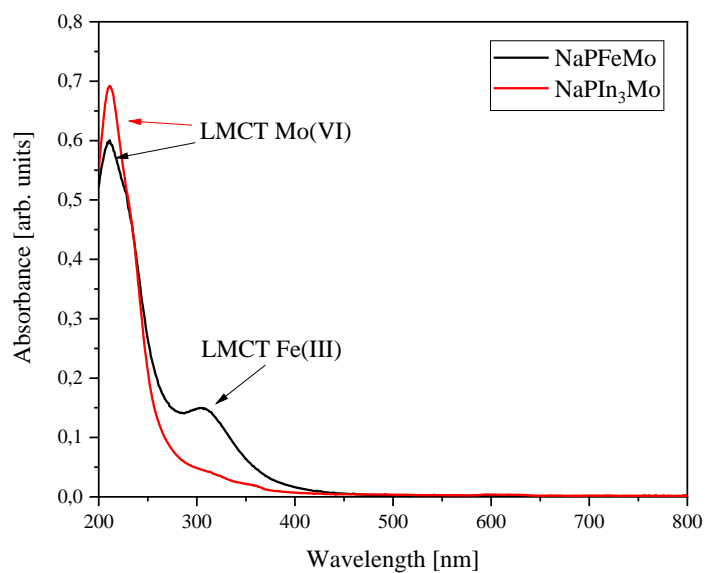


Figure S27: UV-Vis spectra of the with trivalent elements substituted POMs in water.

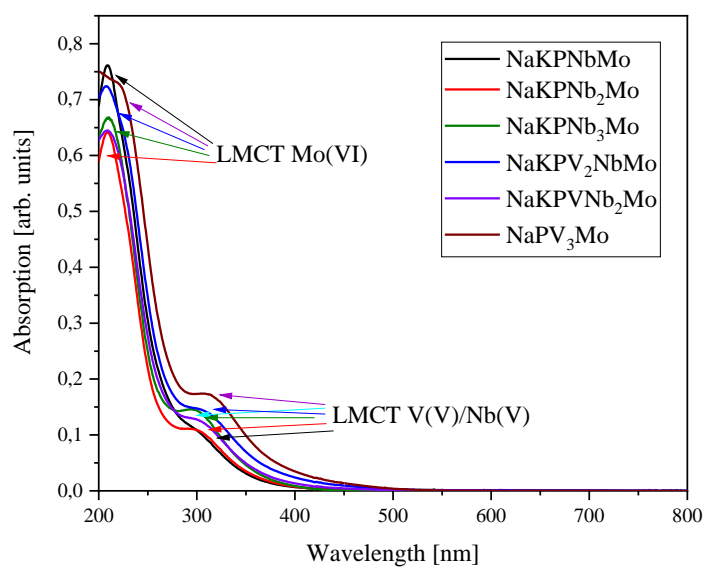


Figure S28: UV-Vis spectra of the with pentavalent elements substituted POMs in water.

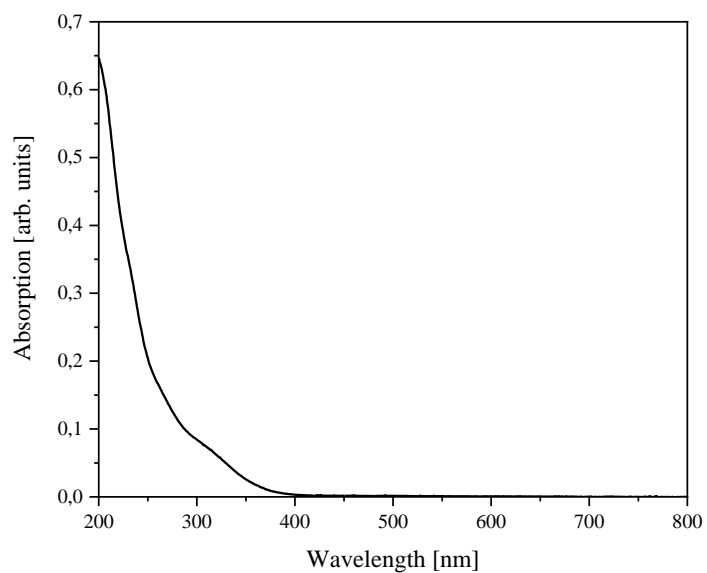


Figure S29: UV-Vis spectra of the with hexavalent elements substituted POMs in water.

Table 7: LMCT positions of the different POMs measured using UV-Vis spectroscopy.

POM/LMCT [nm]	Mo(VI)	W(VI)	Cu(II)	Zn(II)	Fe(III)	V(V)	Nb(V)
HPMo	218	-	-	-	-	-	-
NaPCoMo	210	-	-	-	-	-	-
NaPNiMo	210	-	-	-	-	-	-
nBu₄NPCu₂Mo	214	-	306	-	-	-	-
NaPZnMo	210	-	-	311	-	-	-
NaPFeMo	211	-	-	-	305	-	-
NaPIn₃Mo	211	-	-	-	-	-	-
NaKPNbMo	209	-	-	-	-	-	301
NaKPNb₂Mo	209	-	-	-	-	-	292
NaKPNb₃Mo	210	-	-	-	-	-	292
NaKPV₂NbMo	208	-	-	-	-	-	300
NaKPVNb₂Mo	209	-	-	-	-	-	297
NaKPV₃Mo	214	-	-	-	-	308	-
NaKPW₃Mo	299	-	-	-	-	-	-

2.4 Electrochemistry

2.4.1 Electrochemical characterization of LHPA-3

In order to complete the characterisation of LHPA-3 and provide a solid analytical basis for the characterisation of transition metal substituted POMs, LHPA-3 was also studied with electrochemical methods, specifically CV and SWV (Figure S30 and S31).

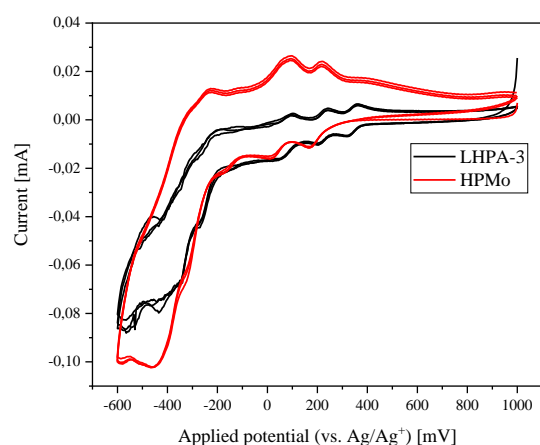


Figure S30: CV measurements of LHPA-3 and HPMo (concentration 1 mmol/L, scan rate 100 mV/s and pH 1). Hydrochloric acid was used as supporting electrolyte.

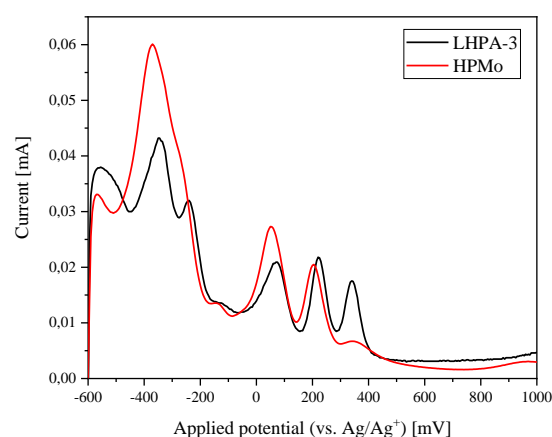


Figure S31: SWV measurements of LHPA-3 and HPMo (concentration 1 mmol/L, scan rate 5 mV/s and pH 1). Hydrochloric acid was used as supporting electrolyte.

Table 8 lists the electrochemical potentials identified in these electrochemical investigations. In comparison to HPMo, the Redox potentials of LHPA-3 are shifted to higher voltages. The SWV voltammogram shows an additional peak for LHPA-3 in the range of -600 to -200 mV, which is not resolved for HPMo, although the peak at -370 mV appears asymmetric with a shoulder on its right side. This indicates that the peak is caused by two overlapping signals.

Table 8: Electrochemical potentials of LHPA-3 and HPMo as determined by CV and SWV.

Redox process ^{a)}	CV potential ^{b)} [mV]	SWV potential ^{c)} [mV]
LHPA-3		
	-	-555
	-	-350
	-	-240
$[\text{PMo}^{\text{VI}}_9\text{O}_{34}]^{9-} / [\text{PMo}^{\text{VI}}_8\text{Mo}^{\text{IV}}\text{O}_{34}]^{11-}$	80	70

$[\text{PMo}^{\text{VI}}_8\text{Mo}^{\text{IV}}_1\text{O}_{40}]^{11-} /$ $[\text{PMo}^{\text{VI}}_7\text{Mo}^{\text{IV}}_2\text{O}_{40}]^{13-}$	223	220
	340	340
HPMo		
	-	-570
	-	-370
	-198	-150
$[\text{PMo}^{\text{VI}}_{12}\text{O}_{40}]^{3-} / [\text{PMo}^{\text{VI}}_{11}\text{Mo}^{\text{IV}}\text{O}_{40}]^{5-}$	-39.7	50
$[\text{PMo}^{\text{VI}}_{11}\text{Mo}^{\text{IV}}\text{O}_{40}]^{5-} /$ $[\text{PMo}^{\text{VI}}_{10}\text{Mo}^{\text{IV}}_2\text{O}_{40}]^{7-}$	193	205
	-	340

^{a)} assignment based on literature values ^{20,21}, ^{b)} mean value between oxidation and reduction pathway, ^{c)} peak maximum

This leads to the fundamental conclusion, that LHPA-3 and HPMo undergo similar Redox processes. However, the structural changes cause a shift in the respective potentials. The cyclic voltammograms indicate that the observed Redox processes are reversible, which makes LHPA-3 a suitable basis for the development of Redox catalysts.

Table 9: Peak maxima from SWV data, peak maxima (oxidation pathway) and peak minima (reduction pathway) from the CV data of LHPA-3 in comparison with HPMo in solution (solvent water) at pH 1 (HCl): concentration 1 mmol/L: scan rate 100 mV/s (CV) and 5 mV/s (SWV).

Maximum oxidation pathway (CV) [mV]	Minimum reduction pathway (CV) [mV]	Mean value (CV) [mV]	Maximum SWV [mV]	Redox process ^{20,21}
LHPA-3				
-	-	-	-555	-
-	-	-	-350	-
-	-	-	-240	-
100	60	80	70	$[\text{PMo}^{\text{VI}}_8\text{Mo}^{\text{IV}}\text{O}_{34}]^{11-}$
240	205	223	220	$[\text{PMo}^{\text{VI}}_7\text{Mo}^{\text{IV}}_2\text{O}_{40}]^{13-}$
360	320	340	340	-
HPMo				
-	-	-	-570	-
-	-	-	-370	-
-227	-169	-198	-150	.
-87.7	8.33	-39.7	50	$[\text{PMo}^{\text{VI}}_{11}\text{Mo}^{\text{IV}}\text{O}_{40}]^{5-}$
218	167	193	205	$[\text{PMo}^{\text{VI}}_{10}\text{Mo}^{\text{IV}}_2\text{O}_{40}]^{7-}$
-	-	-	340	-

2.4.2 Electrochemical characterization of the transition metal substituted POMs

Additional CV and SWV data of the POMs substituted with different elements are found in Figures S32-S39:

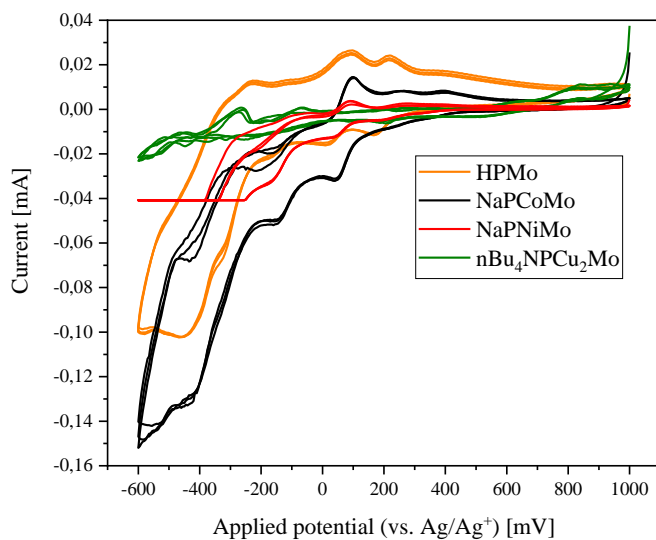


Figure S32: Comparison between the CV measurements of the with divalent elements substituted POMs in comparison with HPMo (concentration 1 mmol/L, scan rate 100 mV/s (CV) and pH 1). Hydrochloric acid was used as supporting electrolyte. nBu₄NPCu₂Mo was measured in acetonitrile. Tetrabutylammonium hexafluorophosphate was used as supporting electrolyte.

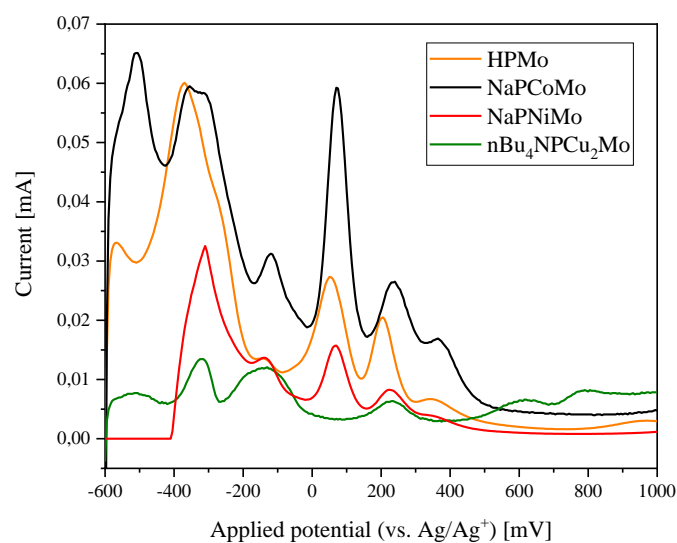


Figure S33: Comparison between the SWV measurements of the with divalent elements substituted POMs in comparison with HPMo (concentration 1 mmol/L, scan rate 5 mV/s (SWV) and pH 1). Hydrochloric acid was used as supporting electrolyte. nBu₄NPCu₂Mo was measured in acetonitrile. Tetrabutylammonium hexafluorophosphate was used as supporting electrolyte.

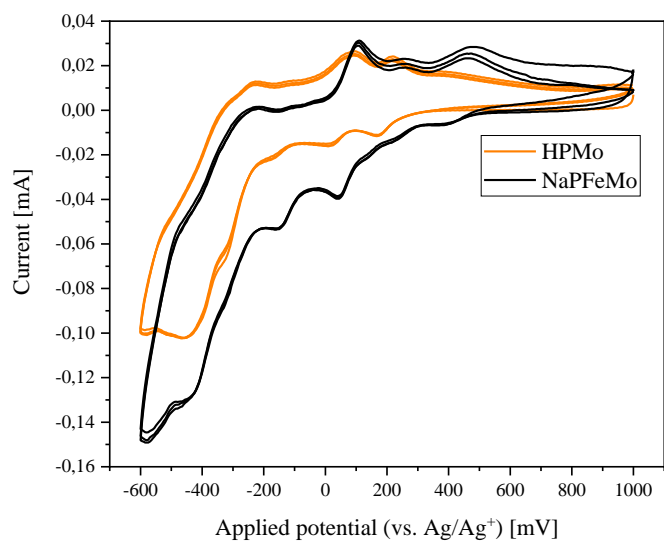


Figure S34: Comparison between the CV measurements of the with trivalent elements substituted POMs in comparison with HPMo (concentration 1 mmol/L, scan rate 100 mV/s (CV) and pH 1). Hydrochloric acid was used as supporting electrolyte.

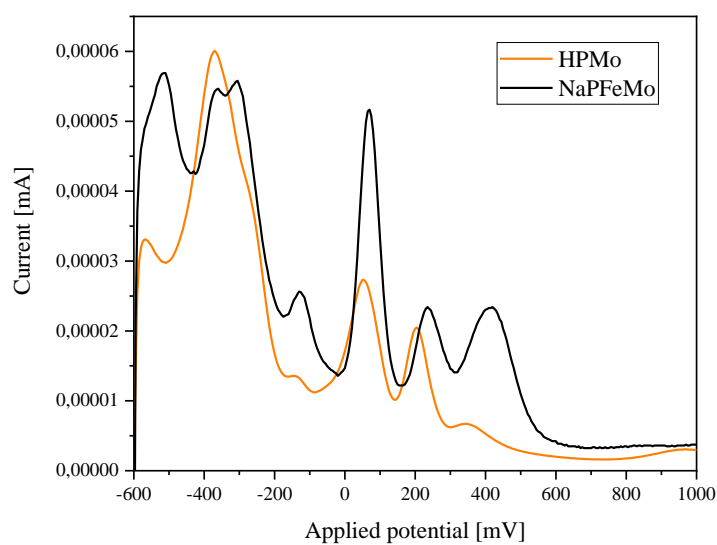


Figure S35: Comparison between the SWV measurements of the with trivalent elements substituted POMs in comparison with HPMo (concentration 1 mmol/L, scan rate 5 mV/s (SWV) and pH 1). Hydrochloric acid was used as supporting electrolyte.

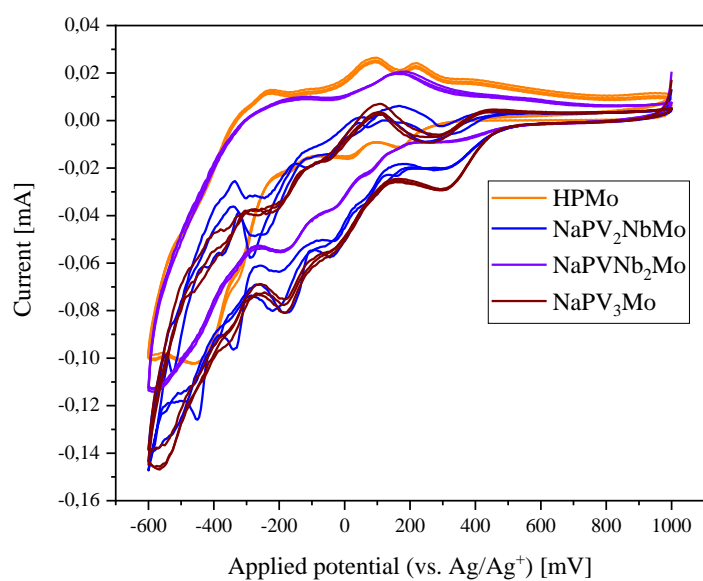
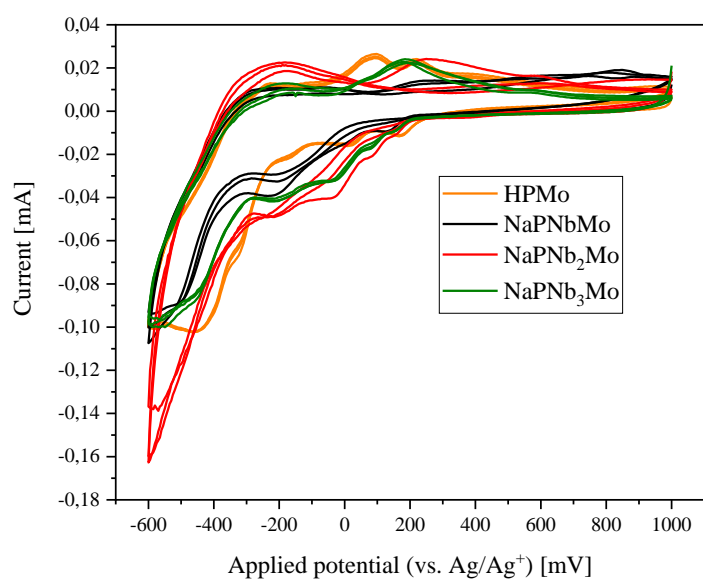


Figure S36: Comparison between the CV measurements of the with pentavalent elements substituted POMs in comparison with HPMo (concentration 1 mmol/L, scan rate 100 mV/s (CV) and pH 1). Hydrochloric acid was used as supporting electrolyte.

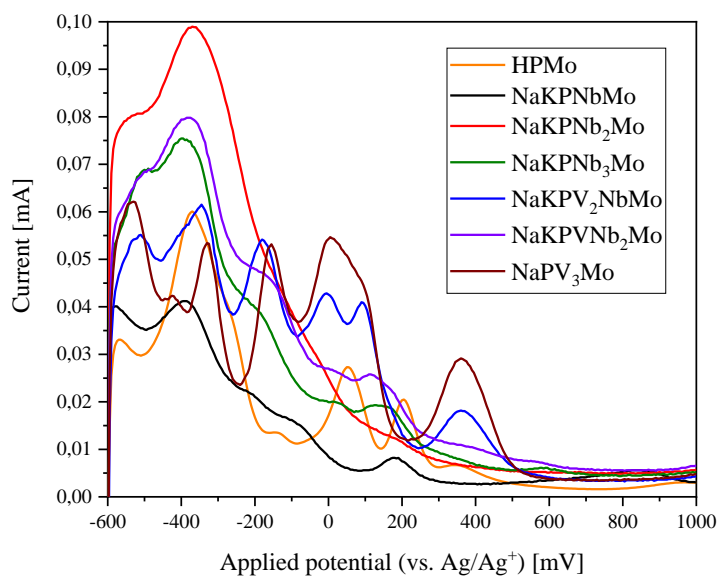


Figure S37: Comparison between the SWV measurements of the with pentavalent elements substituted POMs in comparison with HPMo (concentration 1 mmol/L, scan rate 5 mV/s (SWV) and pH 1). Hydrochloric acid was used as supporting electrolyte.

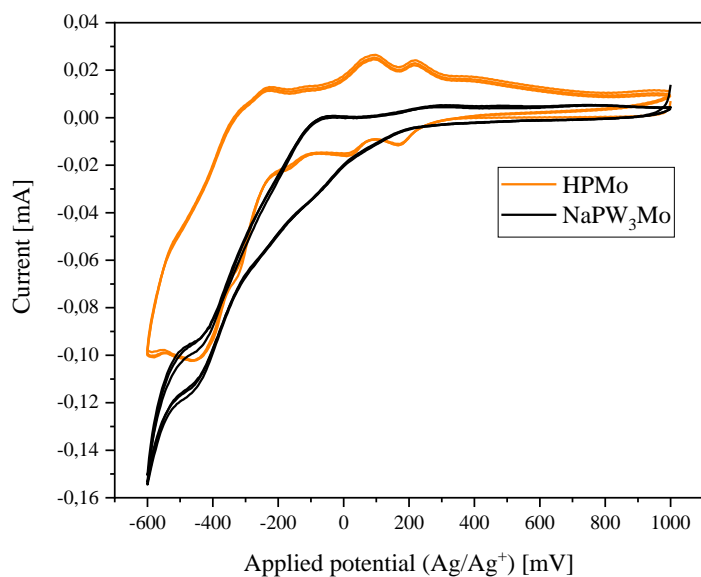


Figure S38: Comparison between the CV measurements of the with hexavalent elements substituted POMs in comparison with HPMo (concentration 1 mmol/L, scan rate 100 mV/s (CV) and pH 1). Hydrochloric acid was used as supporting electrolyte.

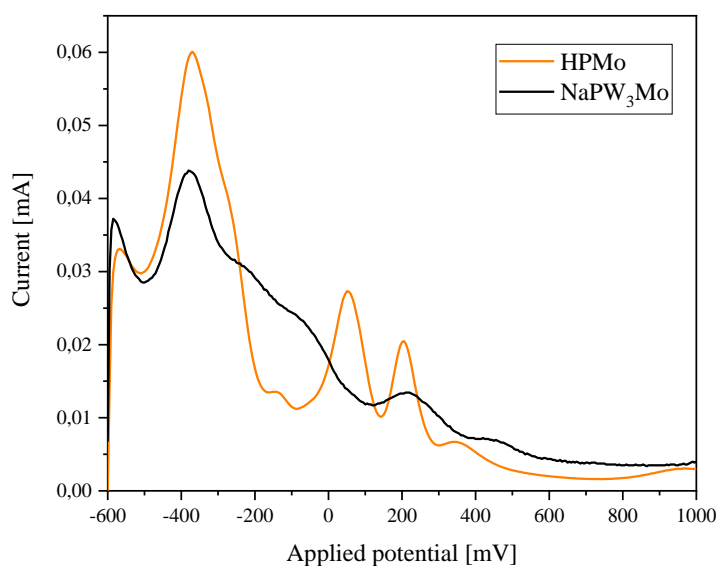


Figure S39: Comparison between the SWV measurements of the with hexavalent elements substituted POMs in comparison with HPMo (concentration 1 mmol/L, scan rate 5 mV/s (SWV) and pH 1). Hydrochloric acid was used as supporting electrolyte.

Table 10: Peak maxima from SWV data, peak maxima (oxidation pathway) and peak minima (reduction pathway) from the CV data of the POMs in solution (solvent water; acetonitrile for nBu₄NPCu₂Mo) at pH 1 (HCl): concentration 1 mmol/L: scan rate 100 mV/s (CV) and 5 mV/s (SWV).

Maximum oxidation pathway (CV) [mV]	Minimum reduction pathway (CV) [mV]	Mean value (CV) [mV]	Maximum SWV [mV]	Redox process ^{20,21}
HPMo				
-	-	-	-570	-
-	-	-	-370	-
-227	-169	-198	-150	.-
-87.7	8.33	-39.7	50	[PMo ^{VI} ₁₁ Mo ^{IV} O ₄₀] ⁵⁻
218	167	193	205	[PMo ^{VI} ₁₀ Mo ^{IV} ₂ O ₄₀] ⁷⁻
-	-	-	340	-
NaPCoMo				
-465	-440	-453	-510	-
-	-	-	-355	-
-300	-	-	-315	-
-225	-155	-190	-120	-
-60	-	-	-	-
100	35	78	70	[PCoMo ^{VI} ₁₀ Mo ^{IV} O ₄₀] ⁹⁻
265	-	-	240	[PCoMo ^{VI} ₉ Mo ^{IV} ₂ O ₄₀] ¹¹⁻
390	-	-	360	-
NaPNiMo				

	-	-	-310	
-50	-	-	-135	
90	35	63	65	[PNiMo ^{VI} ₁₀ Mo ^{IV} O ₄₀] ⁹⁻
270	185	228	225	[PNiMo ^{VI} ₉ Mo ^{IV} ₂ O ₄₀] ¹¹⁻
385	-	-	334	
nBu₄NPCu₂Mo				
			-525	-
-460	-450	-455		-
			-325	-
-265	-255	-260		-
-70	-	-	-135	-
200	-	-	230	[PCu ₂ Mo ^{VI} ₈ Mo ^{IV} ₂ O ₄₀] ¹⁵⁻
640	-	-	615	-
840	-	-	790	-
NaPFeMo				
-475	-440	-458	-515	-
			-365	-
			-305	-
-230	-155	-193	-	-
110	40	75	70	[PFeMo ^{VI} ₁₀ Mo ^{IV} O ₄₀] ⁸⁻
260	225	243	235	[PFeMo ^{VI} ₉ Mo ^{IV} ₂ O ₄₀] ¹⁰⁻
475	380	428	420	-
NaKPNbMo				
-515	-520	-518	-580	-
			-395	-
-245	-230	-238	-225	-
-	-	-	-105	-
-60	-	-	-	-
230	120	178	175	[PNbMo ^{VI} ₉ Mo ^{IV} ₂ O ₄₀] ⁸⁻
620	-	-	-	-
845	-	-	840	-
NaKPNb₂Mo				
-	-	-	-545	-
-	-	-	-370	-
-185	-215	-200	-	-
-	-35	-	-	-
-	70	-	-	[PNb ₂ Mo ^{VI} ₉ Mo ^{IV} O ₄₀] ⁷⁻
-	140	-	150	[PNb ₂ Mo ^{VI} ₈ Mo ^{IV} ₂ O ₄₀] ⁹⁻
250	-	-	-	-
NaKPNb₃Mo				
-	-	-	-580	-
-455	-460	-458	-500	-
-	-	-	-400	-
-190	-215	-203	-220	-
-	-40	-	-	-
-	80	-	10	[PNb ₃ Mo ^{VI} ₈ Mo ^{IV} O ₄₀] ⁸⁻
180	140	160	125	[PNb ₃ Mo ^{VI} ₇ Mo ^{IV} ₂ O ₄₀] ¹⁰⁻
-	-	-	155	-
555	-	-	575	-

NaKPV₂NbMo				
-545	-	-	-515	-
-	-450	-	-	-
-335	-340	-338	-345	-
-145	-175	-160	-180	-
-	-45	-	-10	-
40	-	-	90	[PV ₂ NbMo ^{VI} ₈ Mo ^{IV} O ₄₀] ⁸⁻
105	-	-	-	[PV ₂ NbMo ^{VI} ₇ Mo ^{IV} ₂ O ₄₀] ¹⁰⁻
170	145	158	-	-
-	230	-	-	-
-	-	-	360	-
430	-	-	-	-
NaKPVNb₂Mo				
-	-	-	-570	-
-	-	-	-505	-
-	-	-	-385	-
-165	-210	-188	-195	-
-	-55	-	-	-
-	65	-	10	[PVNb ₂ Mo ^{VI} ₈ Mo ^{IV} O ₄₀] ⁸⁻
160	-	-	115	[PVNb ₂ Mo ^{VI} ₇ Mo ^{IV} ₂ O ₄₀] ¹⁰⁻
-	305	-	-	-
NaPV₃Mo				
-485	-	-	-530	-
-380	-	-	-425	-
-305	-	-	-	-
-300	-355	-328	-330	-
-115	-185	-150	-155	-
-	-35	-	5	[PV ₃ Mo ^{VI} ₈ Mo ^{IV} O ₄₀] ⁸⁻
90	-	-	-	[PV ₃ Mo ^{VI} ₇ Mo ^{IV} ₂ O ₄₀] ¹⁰⁻
430	305	368	360	-
NaPW₃Mo				
-	-	-	-585	-
-490	-460	-475	-	-
-	-	-	-380	-
-	-	-	-245	-
-70	-	-	-10	-
250	-	-	210	-
-	-	-	450	-

2.5 X-ray diffraction

Figure S40 and S41 show the asymmetric unit and the solid-state structure of LHPA-3:

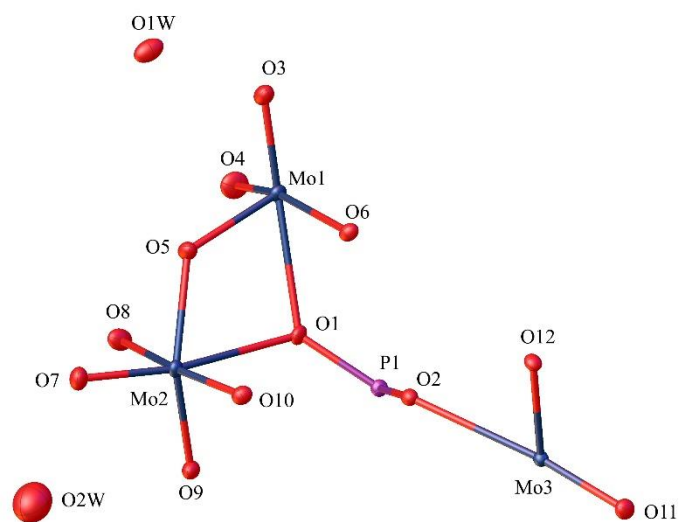


Figure S40: Asymmetric unit of the solid-state structure of LHPA-3 containing 18 atoms (one P, three Mo, twelve O of the POM structure and two additional O from crystal water molecules named OW).

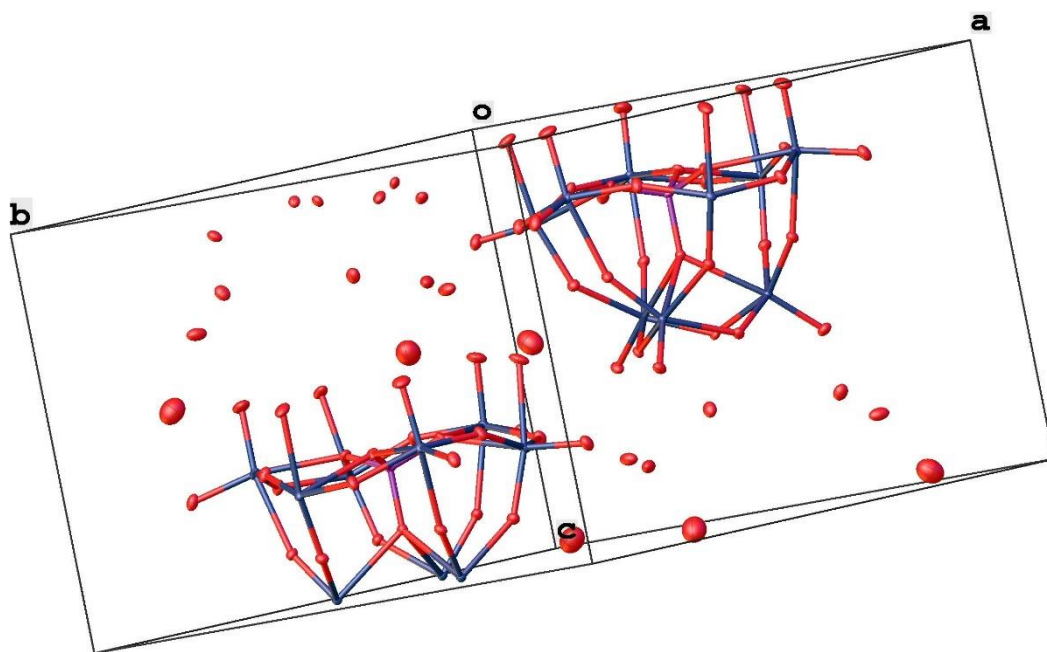


Figure S41: Unit cell of the solid-state structure of LHPA-3.

Table 11: Found bond lengths in LHPA-3 in comparison with sum of covalent radii.²²

Bond	Average length [Å]	Sum of covalent radii [Å]
P - O _P	1.545	1.74
O _P - Mo	2.361	2.01
O _b - Mo	1.882	2.01
Mo - O _t	1.700	2.01
Mo - O _i	1.956	2.01

Furthermore, analogous to the species [PW₉O₃₄]⁹⁻ already known²³ in the literature, a dimerization of LHPA-3 to a corresponding Wells-Dawson structure [P₂Mo₁₈O₆₂]⁶⁻ was observed, which is thermally induced.²⁴ The presence of the dimerized species was confirmed by X-ray single crystal structure analysis, see Figure S42 and S43:

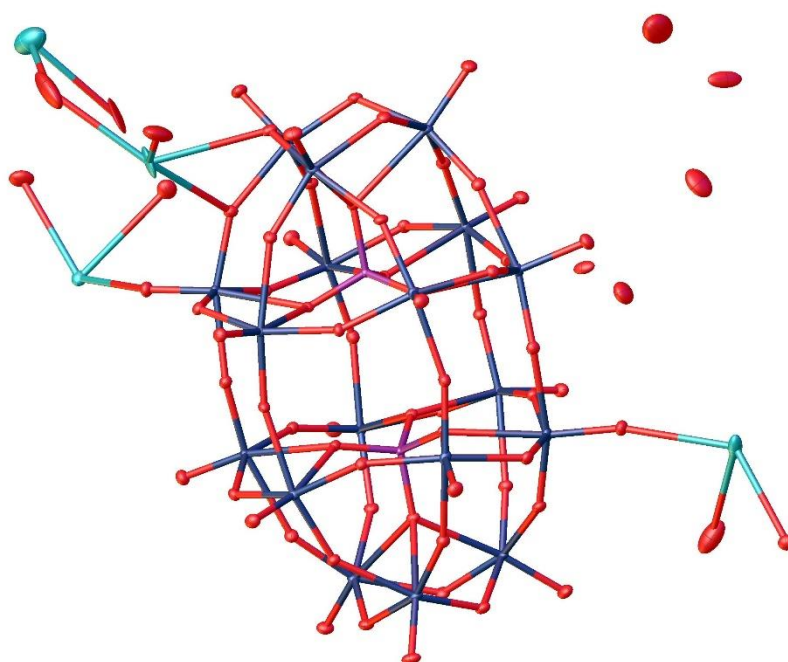


Figure S42: Solid-state structure and asymmetric unit of the dimerized LHPA-3 species as determined by single crystal X-ray diffraction. The compound crystallizes in the triclinic space group *P*-1 (2). Hydrogen atoms have not been modeled. R_1 : 3.11 %, wR_2 : 7.93 %, R_{int} : 2.98 %, GooF: 1.029. Color code: purple: phosphorous, blue: molybdenum, red: oxygen and turquoise: alkali cations (sodium and potassium).

The LHPA-3 dimer shown in Figure S42 is a Wells-Dawson type structure in which the total 18 Mo atoms are in an octahedral coordination by six oxygen atoms. Each 9 Mo atoms originate from one LHPA-3 monomer. The structure is terminated by the presence of terminal oxygen atoms. Characteristic of a Wells-Dawson type structure are the two phosphorus heteroatoms, all in a tetrahedral coordination of four oxygen atoms, in the centre of the

structure, with one P atom each contributed by an LHPA-3 monomer. There are a total of four alkali cations in the asymmetric unit, with two cations refined as sodium (between O1W to O3W) and two others as potassium (O4W to O7W). The alkali metal counterions coordinate to the terminal oxygen atoms and are all in a distorted octahedral environment of six oxygen atoms, with two alkali metal ions bridged by two hydrate water molecules each. Hydrate water molecules are visualized by individual oxygen atoms in Figure 42, where the H atoms were not modeled due to the low scattering contribution in X-ray crystallography.

The compound was crystallized in the triclinic space group *P*-1 (2) with lattice parameters of $a = 12.7114(1) \text{ \AA}$, $b = 14.7642(2) \text{ \AA}$, $c = 19.7054(2) \text{ \AA}$, $\alpha = 102.465(1)^\circ$, $\beta = 99.119(1)^\circ$, and $\gamma = 114.620(1)^\circ$. The crystallographic data are available as a .cif file in the CCDC database (deposition number: 2216946).

The average bond length of the P1,2-O1-4,26-29 bonds are 1.543 \AA , while the average bond lengths of the O1-4,26-29-Mo1-18 bonds are 2.346 \AA . Compared with the sum of the covalent radii²⁵ of a P-O (1.74 \AA) and an O-Mo (2.01 \AA) bond, it is noticeable that the P1,2-O1-4,26-29 bonds are shorter than the sum of the covalent radii and thus stronger in nature, while the O1-4,26-29-Mo1-18 bonds are significantly longer and thus have more coordinative character. The bond lengths of the oxygen-metal bridging bonds are approximately 1.943 \AA , which is shorter than the bond distance calculated by the sum of the covalent radii (2.01 \AA). Here, too, the terminal oxygen atoms with an average bond length of 1.689 \AA show a significantly shortened distance due to the double bond character. The average distance of the alkali metal counterions was determined to be 2.698 \AA , while the average distance of the alkali ions to the coordinated hydrate water molecules is 2.729 \AA . Compared to the sum of the covalent radii, the calculated bond distance (K: 196 pm ; O: 63 pm^{25}) is 2.59 \AA (259 pm) for a O-K bond and 2.18 \AA (218 pm) for a O-Na bond (Na: 155 pm ; O: 63 pm^{25}). Since the values found are above the extrapolated value, the coordinative bonding nature of the POM/hydrated water alkali ion interaction is also evident here.

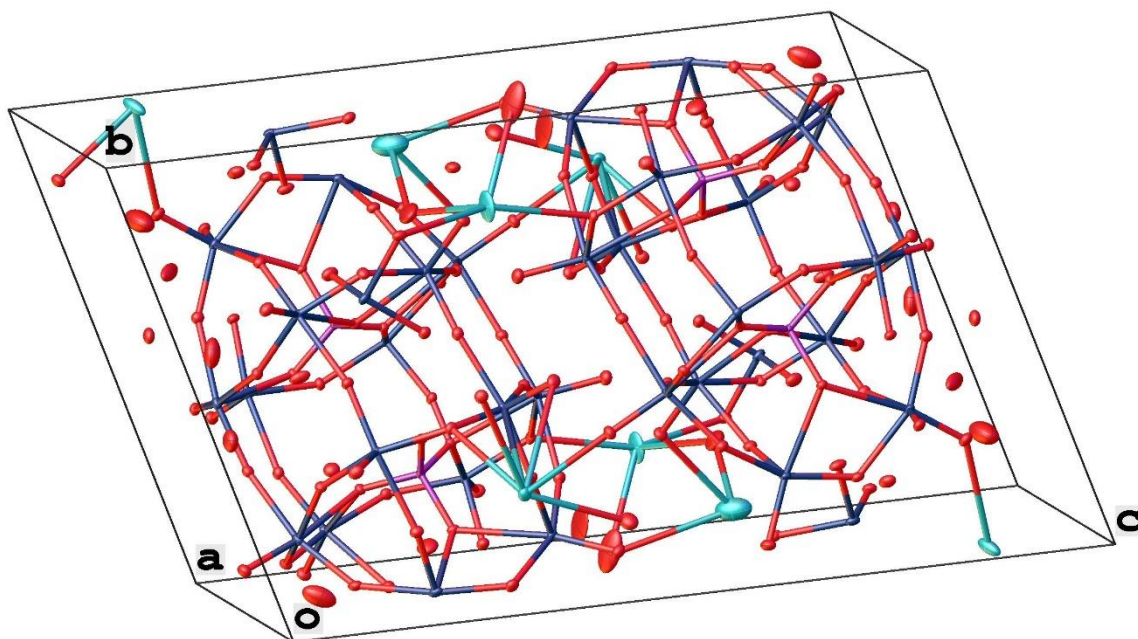


Figure S43: Unit cell of the solid-state structure of dimerized LHPA-3.

The solid-state structure of KNb is shown in Figure S44:

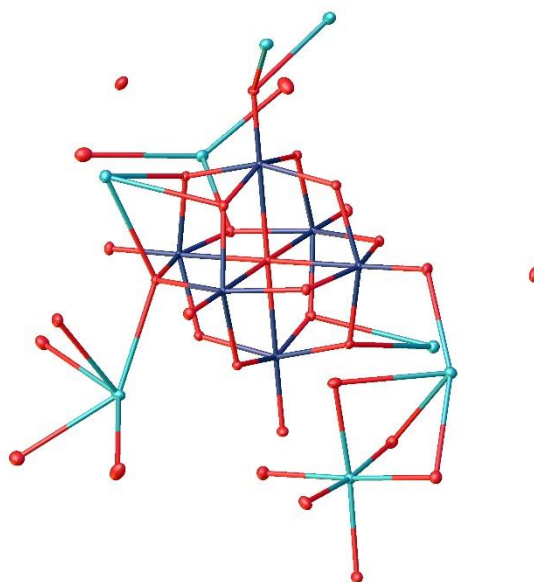


Figure S44: Solid-state structure and asymmetric unit of KNb determined by single crystal X-ray diffraction. The compound crystallizes in the monoclinic space group $P2_1/c$ (14). Hydrogen atoms have not been modeled. R_1 : 2.58 %, wR_2 : 6.73 %, R_{int} : 3.08 %, GooF: 1.252. Color code: turquoise: potassium/sodium, blue: niobium, and red: oxygen.

The compound was crystallized in the hexagonal space group $P2_1/c$ (14) with the lattice parameters $a = 12.63957(11)$ Å, $b = 10.69819(9)$ Å and $c = 24.23416(18)$ Å and the lattice angles $\alpha = 90^\circ$, $\beta = 92.1646(7)^\circ$ and $\gamma = 90^\circ$. For the isopolyanion (IPA) there are six Nb(V) atoms in a distorted octahedral coordination geometry by six oxygen atoms. The central oxygen atom is in an octahedral coordination of the six Nb(V) atoms. Potassium atoms are in an octahedral environment of six oxygen atoms: the cations are coordinated by four oxygen atoms of hydration water molecules and by two terminal oxygen atoms. So, one potassium is connecting two IPAs. During the refinement process it was observed that the electron density for K1 is too high. One reason is that this position is in some unit cells occupied with an alkali ion of lower electron density such as sodium. This is likely due to the low purity of the potassium hydroxide used of 85 %. So, this position was refined using free variables with sodium and potassium. As a result, the occupancy for potassium was refined to be 0.87894 and for sodium to 0.12106. The sum of both is an occupancy of 1. A similar problem arose for K2: here, as the best result, its position was completely occupied and refined with sodium (occupancy of 1).

The average bond length of O1-Nb1-6 is 2.529 Å, the average bond length of the metal bridging bonds O2-13-Nb1-6 are 1.992 Å and the average length of the terminal oxygen metal bonds Nb1-6=O14-19 are 1.798 Å. Here, as expected, the bond length of Nb1-6=O14-19 is significant shorter than the sum of covalent radii²² of 2.10 Å, due to the mentioned double bond character. It is also striking that the bond length of the central oxygen atom to the Nb(V) atoms O1-Nb1-6 is significant longer. This indicates the coordinative bond character as mentioned for the other crystal structures. The average distance between a terminal oxygen and an alkali cation was determined to be 2.760 Å. Furthermore, the average distance between hydration water molecules and alkali cations is 2.637 Å. So, those bond lengths are significant longer than the sum of covalent radii (see Table 12), indicating the coordinative bond character.

In comparison to Nb₂O₅ the bond lengths are about 1.65 Å to 1.68 Å.²⁶ Comparing to the sum of covalent radii of a Nb-O bond of 210 pm/2.10 Å (Nb: 147 pm, O: 63 pm²²), the Nb-O bond in the oxide seems to be shorter, indicating covalent bond character. In the POM the Nb-O bond is than a little bit longer, but still shorter than the sum of covalent radii.^{22,26}

Table 12 shows an comparison of the found bond lengths vs. the sum of covalent radii (Nb: 147 pm (1.47 Å) and O: 63 pm (0.63 Å)):²²

Table 12: Found bond lengths in KNb in comparison with sum of covalent radii.²²

Bond	Average length [Å]	Sum of covalent radii [Å]
O1-Nb1-6	2.529	2.10
O2-13-Nb1-6	1.992	2.10
Nb1-6=O14-19	1.798	2.10
O14-19-Na1,2/O14-19-K1,3-7	2.760	2.18/2.59
O1W-12W-Na1,2/O1W-12W-K1,3-7	2.637	2.18/2.59

Asymmetric unit of the solid-state structure of NaPV₃Mo in Figure S45:

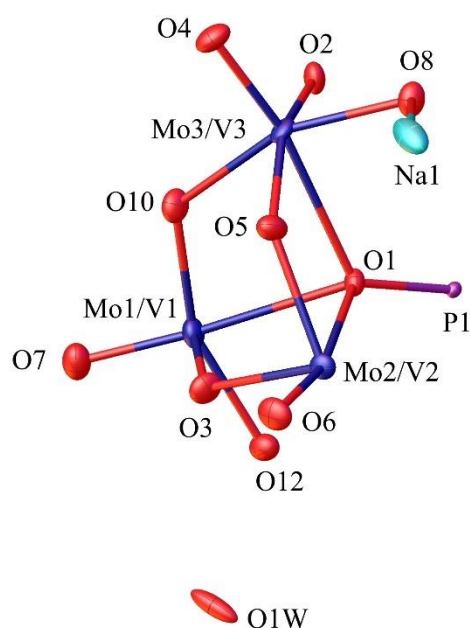


Figure S45: Asymmetric unit of the solid-state structure of NaPV₃Mo containing 18 atoms (one P, three Mo/V, twelve O of the POM structure, an additional O from crystal water molecules named OW and a Na cation).

Table 13: Weighted average of calculated bond lengths (sum of covalent radii) and observed bond lengths of each bond in each POM.

Bond types	P1-O1	O1-M1-3	O2-7-M1-3	M1-3=O8-10
Sum of covalent radii* [Å]	1.74	2.00	2.00	2.00
Observed bond length [Å]	1.537	2.410	1.921	1.665

* $BL = \frac{a(r_O + r_{Mo}) + b(r_O + r_V)}{a + b}$ with BL the weighted average bond length, r_x the covalent radii of the corresponding elements x and a and b the weighting factors (e. g. for NaPV₃Mo: $a = 9$ and $b = 3$).

Table 14: Crystal structure data and structure refinement for compounds LHPA-3, LHPA-3 dimer, NaPV₃Mo and KNb.

Compound	LHPA-3	LHPA-3 dimer	NaPV ₃ Mo	KNb
Empirical formula	Mo ₁₈ O ₈₀ P ₂	K ₂ Mo ₁₈ Na ₂ O _{74.96} P ₂	Mo ₉ Na ₄ O ₄₂ PV ₃	K _{6.91} Na _{1.09} Nb ₆ O ₃₃
Formula weight	3068.86	3112.40	1811.21	1380.74
Temperature/K	99.95(13)	99.95(16)	100.01	99.96(13)
Crystal system	hexagonal	triclinic	tetragonal	Monoclinic
Space group	<i>P</i> 6 ₃	<i>P</i> -1	<i>P</i> -42 ₁ <i>c</i>	<i>P</i> 2 ₁ / <i>c</i>
<i>a</i> [Å]	14.11802(9)	12.71140(10)	12.486(3)	2.63957(11)
<i>b</i> [Å]	14.11802(9)	14.7642(2)	12.486(3)	10.69819(9)
<i>c</i> [Å]	10.65823(8)	19.7054(2)	17.510(7)	24.26416(18)
α [°]	90	102.4650(10)	90	90
β [°]	90	99.1190(10)	90	92.1646(7)
γ [°]	120	114.6200(10)	90	90
Volume [Å ³]	1839.77(3)	3151.58(6)	2729.9(15)	3278.67(5)
<i>Z</i>	1	2	2	4
ρ_{calc} [g/cm ³]	2.770	3.280	2.203	2.797
μ [mm ⁻¹]	3.121	3.781	2.626	3.030
F(000)	1426.0	2891.0	1684.0	2613.0
Crystal size [mm ³]	0.28 × 0.2 × 0.14	0.18 × 0.15 × 0.12	0.089 × 0.062 × 0.054	0.3 × 0.25 × 0.15
Radiation	Mo K α ($\lambda = 0.71073$)	Mo K α ($\lambda = 0.71073$)	MoK α ($\lambda = 0.71073$)	Mo K α ($\lambda = 0.71073$)
2 θ range for data collection [°]	6.924 to 65.774	5.654 to 59.132	4.006 to 61.148	5.948 to 65.832
Index ranges	-20 ≤ <i>h</i> ≤ 21, - 20 ≤ <i>k</i> ≤ 21, - 15 ≤ <i>l</i> ≤ 16	-17 ≤ <i>h</i> ≤ 17, -20 ≤ <i>k</i> ≤ 20, -27 ≤ <i>l</i> ≤ 27	-17 ≤ <i>h</i> ≤ 17, -17 ≤ <i>k</i> ≤ 17, -25 ≤ <i>l</i> ≤ 25	-19 ≤ <i>h</i> ≤ 18, -15 ≤ <i>k</i> ≤ 16, -36 ≤ <i>l</i> ≤ 36
Reflections collected	118316	139713	140274	204566
Independent reflections	4488 [<i>R</i> _{int} = 0.0328, <i>R</i> _{sigma} = 0.0094]	16650 [<i>R</i> _{int} = 0.0298, <i>R</i> _{sigma} = 0.0162]	4184 [<i>R</i> _{int} = 0.0449, <i>R</i> _{sigm} = 0.0103]	11834 [<i>R</i> _{int} = 0.0308, <i>R</i> _{sigma} = 0.0112]
Data/restraints/parameters	4488/1/152	16650/0/886	4184/0/135	11834/0/425
Goodness-of-fit on F ²	1.111	0.829	1.089	1.252
Final <i>R</i> indexes [<i>I</i> >= 2 σ (<i>I</i>)]	<i>R</i> ₁ = 0.0181, <i>wR</i> ₂ = 0.0497	<i>R</i> ₁ = 0.0311, <i>wR</i> ₂ = 0.0800	<i>R</i> ₁ = 0.0303, <i>wR</i> ₂ = 0.0779	<i>R</i> ₁ = 0.0258, <i>wR</i> ₂ = 0.0670
Final <i>R</i> indexes [all data]	<i>R</i> ₁ = 0.0182, <i>wR</i> ₂ = 0.0498	<i>R</i> ₁ = 0.0328, <i>wR</i> ₂ = 0.0813	<i>R</i> ₁ = 0.0308, <i>wR</i> ₂ = 0.0784	<i>R</i> ₁ = 0.0264, <i>wR</i> ₂ = 0.0673
Largest diff. peak/hole [e Å ⁻³]	2.22/-0.68	6.56/-1.95	2.89/-0.65	2.49/-1.27
Deposition number	2205006	2216946	2205007	2216947

2.6 Microscopy

SEM images of the powder samples NaKPNb₃Mo are shown in Figure S46-S48.

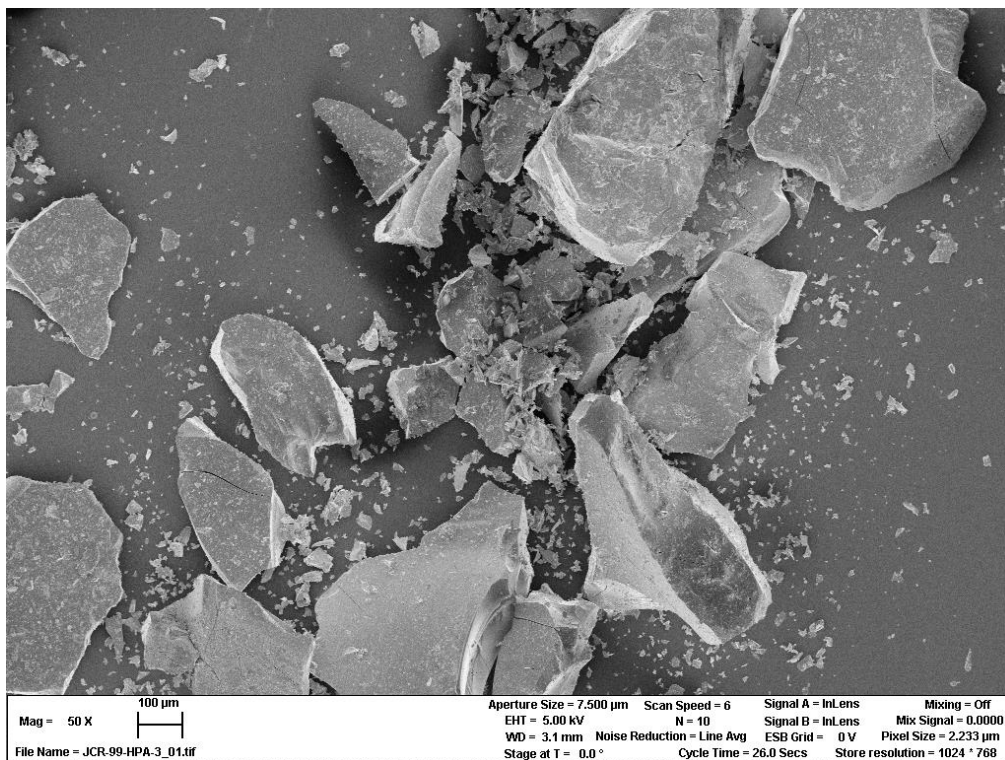


Figure S46: First SEM image of a selected area of a POM particle sample of NaKPNb₃Mo.

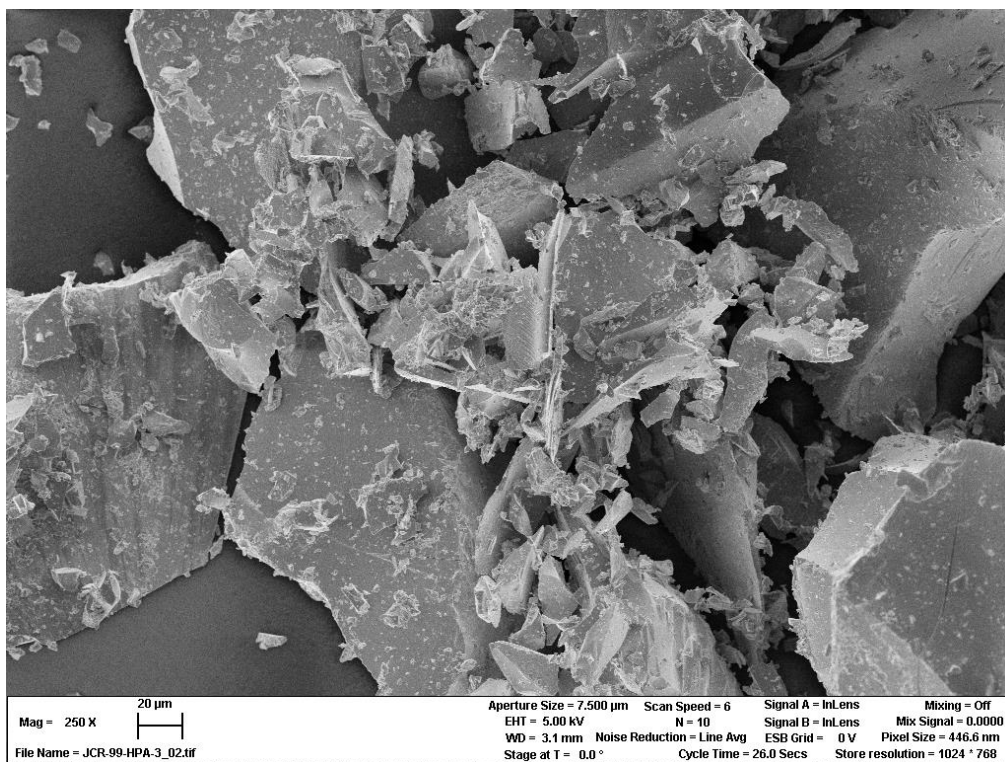


Figure S47: Second SEM image of a selected area of a POM particle sample of NaKPNb₃Mo.



Figure S48: Third SEM image of a selected area of a POM particle sample of NaKPNb₃Mo.



Figure S49: Membrane plant used for nanofiltration to remove salts from the POM solution. Here: purification of NaKPNb_3Mo (yellow solution).

3 Literature

- 1 A. L. Spek, Structure validation in chemical crystallography, *Acta Crystallogr. Sect. D Biol. Crystallogr.*, 2009, **65**, 148–155.
- 2 O. V. Dolomanov, L. J. Bourhis, R. J. Gildea, J. A. K. Howard and H. Puschmann, OLEX2: a complete structure solution, refinement and analysis program, *J. Appl. Crystallogr.*, 2009, **42**, 339–341.
- 3 G. M. Sheldrick, A short history of SHELX, *Acta Crystallogr. Sect. A Found. Crystallogr.*, 2008, **64**, 112–122.
- 4 C. B. Hübschle, G. M. Sheldrick and B. Dittrich, ShelXle: a Qt graphical user interface for SHELXL, *J. Appl. Crystallogr.*, 2011, **44**, 1281–1284.
- 5 A. L. Spek, Single-crystal structure validation with the program PLATON, *J. Appl. Crystallogr.*, 2003, **36**, 7–13.
- 6 T. Ressler, O. Timpe and F. Girgsdies, In situ bulk structural study on solid-state dynamics and catalytic activity correlations of a H₄[PNbMo₁₁O₄₀] partial oxidation catalyst, *Zeitschrift für Krist.*, 2005, **220**, 295–305.
- 7 M. Nyman, T. M. Alam, F. Bonhomme, M. A. Rodriguez, C. S. Frazer and M. E. Welk, Solid-state structures and solution behavior of alkali salts of the [Nb₆O₁₉]⁸⁻ Lindqvist ion, *J. Clust. Sci.*, 2006, **17**, 197–219.
- 8 Y. C. Li, G. Lee, T. Yuan, Y. Wang, D.-H. Nam, Z. Wang, F. P. Garcíá De Arquer, Y. Lum, C.-T. Dinh, O. Voznyy and E. H. Sargent, CO₂ Electroreduction from Carbonate Electrolyte, *ACS Energy Lett.*, 2019, **4**, 1427–1431.
- 9 M. Tatzber, M. Stemmer, H. Spiegel, C. Katzlberger, G. Haberhauer and M. H. Gerzabek, An alternative method to measure carbonate in soils by FT-IR spectroscopy, *Environ. Chem. Lett.*, 2007, **5**, 9–12.
- 10 R. Mattes, H. Bierbüsse and J. Fuchs, Schwingungsspektren und Kraftkonstanten von Polyanionen mit M₆O₁₉-Gruppen, *Zeitschrift für Anorg. und Allg. Chemie*, 1971, **385**, 230–242.

- 11 P. Müscher-Polzin, C. Näther and W. Bensch, Hexaniobate anions connected by [Ni(cyclam)]²⁺ complexes yield two interpenetrating three-dimensional networks, *Zeitschrift für Naturforsch.*, 2020, **75**, 583–588.
- 12 V. Tsirelson and A. Stash, Orbital-free quantum crystallography: view on forces in crystals, *Acta Crystallogr. Sect. B Struct. Sci. Cryst. Eng. Mater.*, 2020, **76**, 769–778.
- 13 V. L. Cherginets, V. N. Baumer, S. S. Galkin, L. V. Glushkova, T. P. Rebrova and Z. V. Shtitelman, Solubility of Al₂O₃ in Some Chloride–Fluoride Melts, *Inorg. Chem.*, 2006, **45**, 7367–7371.
- 14 TURBOMOLE, V7.5.1 2021, a development of University of Karlsruhe and Forschungszentrum Karlsruhe GmbH, 1989–2007, TURBOMOLE GmbH, since 2007; available from <http://www.turbomole.com>.
- 15 M. Ernzerhof and G. E. Scuseria, Assessment of the Perdew–Burke–Ernzerhof exchange–correlation functional, *J. Chem. Phys.*, 1999, **110**, 5029–5036.
- 16 A. Schäfer, H. Horn and R. Ahlrichs, Fully optimized contracted Gaussian basis sets for atoms Li to Kr, *J. Chem. Phys.*, 1992, **97**, 2571–2577.
- 17 A. Klamt and G. Schüürmann, COSMO: a new approach to dielectric screening in solvents with explicit expressions for the screening energy and its gradient, *J. Chem. Soc., Perkin Trans. 2*, 1993, 799–805.
- 18 J.-C. Raabe, J. Albert and M. J. Poller, Spectroscopic, Crystallographic, and Electrochemical Study of Different Manganese(II)-Substituted Keggin-Type Phosphomolybdates, *Chem. – A Eur. J.*, 2022, **28**, 1–12.
- 19 C. Slobodnick and V. L. Pecoraro, Solvent effects on 51V NMR chemical shifts: characterization of vanadate and peroxovanadate complexes in mixed water/acetonitrile solvent, *Inorganica Chim. Acta*, 1998, **283**, 37–43.
- 20 D. Y. Hwang, Y. S. Ha and S. Kim, Electrode-Assisted Wacker Process: Phosphomolybdate-Mediated Oxidation of 1-Butene to Methyl Ethyl Ketone, *Bull. Korean Chem. Soc.*, 2001, **22**, 441–442.
- 21 M. Sadakane and E. Steckhan, Electrochemical Properties of Polyoxometalates as

- Electrocatalysts, *Chem. Rev.*, 1998, **98**, 219–237.
- 22 P. Pyykkö and M. Atsumi, Molecular single-bond covalent radii for elements 1-118, *Chem. - A Eur. J.*, 2009, **15**, 186–197.
- 23 P. J. Domaille and G. Watunya, Synthesis and tungsten-183 NMR characterization of vanadium-substituted polyoxometalates based on B-type tungstophosphate PW9O349-precursors, *Inorg. Chem.*, 1986, **25**, 1239–1242.
- 24 C. Marchal-Roch, E. Ayrault, L. Lisnard, J. Marrot, F.-X. Liu and F. Sécheresse, Dimerization in Acetonitrile of [H6PMo9O34]3– into [P2Mo18O62]6–: Structural Characterization of the Tetrabutyl Ammonium Salt, *J. Clust. Sci.*, 2006, **17**, 283–290.
- 25 P. Pyykkö and M. Atsumi, Molecular Single-Bond Covalent Radii for Elements 1-118, *Chem. - A Eur. J.*, 2009, **15**, 186–197.
- 26 F. D. Hardcastle and I. E. Wachs, Determination of niobium-oxygen bond distances and bond orders by Raman spectroscopy, *Solid State Ionics*, 1991, **45**, 201–213.

Chemistry–A European Journal

Supporting Information

**Spectroscopic, Crystallographic, and Electrochemical Study
of Different Manganese(II)-Substituted Keggin-Type
Phosphomolybdates**

Jan-Christian Raabe, Jakob Albert, and Maximilian J. Poller*

Content

1	Experimental details	7
1.1	Synthesis of $H_7[PMnMo_{11}O_{40}]$	7
1.2	Synthesis of $H_{11}[PMn_2Mo_{10}O_{40}]$	12
1.3	Synthesis of $H_8[PVMnMo_{10}O_{40}]$	17
1.4	Synthesis of $H_{12}[PVMn_2Mo_9O_{40}]$	23
1.5	Synthesis of $H_{14}[V_3Mn_2Mo_7O_{40}]$	29
1.6	Synthesis of $H_{12}[PV_5MnMo_6O_{40}]$	35
2	Vibrational spectroscopy	44
3	Crystallography	48
4	Nuclear magnetic resonance spectroscopy	57
5	UV-Vis spectroscopy	58
6	Electrochemistry	60
7	References	64

Six POMs were synthesized in this work. All POMs were characterized with vibrational spectroscopy (infrared (IR) and Raman) to identify characteristic vibration modes for Keggin-type POMs, ultraviolet visible (UV-Vis) spectroscopy (to see the characteristic ligand-to-metal charge transfer (LMCT) bands) and with inductively coupled plasma optical emission spectrometry (ICP-OES) to verify the right composition of the elements. Furthermore, nuclear magnetic resonance (NMR) spectroscopy for the nuclei ^{31}P and ^{51}V was used to study the behaviour in solution. The crystal water molecules per mol of the respective POMs (unit mol of water/mol of POM) were determined with thermogravimetric analysis (TGA). The respective redox potentials were determined with cyclic voltammetry (CV) and square wave voltammetry (SWV). To determine the crystal structures of the respective POMs single crystals were obtained; with this data the space group and parameters of the unit cell could be determined (the cell constants a , b and c and the cell angles α , β and γ). The resulting data were compared with the respective powder x-ray diffraction (XRD) data.

Chemicals

The chemicals were obtained from the following traders: Divanadium pentoxide (V_2O_5), manganese(II) acetate ($\text{C}_4\text{H}_6\text{O}_4\text{Mn}$) and molybdenum trioxide (MoO_3) from Alfa Aesar, and hydrogen peroxide (H_2O_2) from VWR Chemicals. Phosphoric acid was obtained as 85 % solution in water from Grüssing and diluted with deionised water to a concentration of 25 %. Deionised water was used as the solvent for all synthesis. $\text{H}_5[\text{PV}_2\text{Mo}_{10}\text{O}_{40}]$ (HPA-2-0) was synthesized according to Odyakov *et al.*^[1,2] $\text{H}_3[\text{PMo}_{12}\text{O}_{40}]$ (HPA-0-0) was obtained from Sigma Aldrich. The last two mentioned substances were used as references for comparing the analytical data.

NMR spectroscopy

All NMR spectra were measured with a Bruker AVANCEII 600 MHz. The samples were prepared as follows: The respective POM (70 mg) was dissolved in deionised water (0.63 mL), which had previously been adjusted to pH 1 with a 2 M hydrochloric acid solution in deionised water, and acetone- d_6 (0.07 mL) was added. All ^{31}P spectra were measured with a Time Domain Data Sizes (TD) of 32 K, the Number of Scans (NS) were set to 2k (= 2048), the Transmitter Frequency Offset for Channel F1 (O1) and the Spectral Width (SW) were -1 and 40 ppm. The Delay D1 was set to 1 s. For the ^{51}V experiments TD was 32 K, O1 and SW -520 and 400 ppm, D1 0.5 s and NS was set to 4 K. The interpretation of the NMR data was carried out with the

software MestReNova®. Subsequently the spectra were exported in csv format and plotted with Origin®.

Deuterium oxide (D₂O) should not be used for the NMR measurements because the high Bronsted acidity of the POMS makes a successful solvent lock with D₂O impossible.

IR spectroscopy

IR spectra were measured in attenuated total reflection (ATR) measurement mode on a QATR™-S single-reflection ATR (with a diamond prism).

From the raw data obtained, the baseline was corrected, and the peaks were determined manually. The IR data were then exported as an *x/y* text document.

Raman spectroscopy

Raman spectra were measured on a SENTERRA Raman microscope from Bruker Optik GmbH. The aperture was set to 50 x 1000 μm. A 20 objective was used on the microscope. The laser has a wavelength of 785 nm and the measurement range used was between 75 cm⁻¹ and 1525 cm⁻¹. The integration time was 16 seconds, the number of scans was 8 and the Raman laser power was 10 mW.

UV-Vis spectroscopy

The UV-Vis spectra were measured with a Cary 60 UV-Vis spectrometer (Agilent Technologies) in a 3 mL Quartz cuvette (QS). The measurements were carried out using the Cary WinUV software. Measurements were taken in the measuring range between 200 nm and 800 nm. The absorption was measured in the slow measurement mode. The data were then exported as a csv data set.

TGA analysis:

Approximately 20 mg of the sample was weighed into a quart crucible and the change in mass was measured at the following temperature program:

- Tare
- 1 minute waiting time
- Heating to 30 °C with maximum heating rate

- Stay at 30 °C for 15 minutes
- Heating to 350 °C with a heating rate of 10 K/min
- Stay at 350 °C for 30 minutes
- The sample was then cooled to room temperature

The starting temperature was below 30 °C. During the measurement, a nitrogen flow of 60 sccm/min was passed through the instrument. A measurement with an empty crucible was used for background correction. The TGA data show three regions: hygroscopic water (water that comes from the air), lattice water (water from crystal association) and the mass consistency (pure POM without any moisture). The final data were exported as a *x/y* text document. With the use of Origin® 2019b the TGA data were plotted as follows: on the *y*-axis the mass difference measured in mg and on the *x*-axis the temperature measured in °C.

Electrochemistry CV and SWV:

The CV/SWV measurements were carried out in aqueous, hydrochloric acid medium at pH 1 and a concentration of 1 mmol/L on a Metrohm - Autolab PGSTAT101. During the measurement, the solution was purged with nitrogen. The working electrode was a glassy carbon electrode (diameter: 3 mm), the reference electrode was the Ag/Ag⁺ electrode. The counter electrode was a platinum electrode. Measurements were taken in the measuring range between -0.6 and 1 V with a scan rate (for CV) of 100 mV/s for 3 scans. All SWV measurements were taken with a scan rate of 5 mV/s, a modulation amplitude of 20 mV and a frequency of 25 Hz. The measurements were carried out with the software Nova 2.1.1 and the data was subsequently exported as an *x/y* text document.

Single crystal structures:

The crystal structure data were solved and refined using Olex2 v1.3 and the ShelX algorithm, as well as the PLATON software.^[3-8] Some details on the solution of the individual crystal structure data sets in Olex2 v1.3 are explained below:

- The data set for H₇[PMnMo₁₁O₄₀] was solved and refined with ShelXS and the method "Direct Methods" in the space group Fd-3 (203). For each refinement step 20 cycles were used. A twin law was integrated into the solution. Further refinement was done with ACTA and the LIST command from ShelXI 2013.^[8] The SQUEEZE function was run in PLATON and then refined in Olex2 and the "Solvent Mask" was activated. The twin law simulates a

higher Laue class of the cubic crystal system, which still results in B-level alerts. We note that the space group Fd-3m proposed in the B-Level Alerts was also tested for the solution, however this can be excluded as the r_{int} value is 26 %. R_1 : 1.39 %; wR_2 : 4.21 %. The CIF file is available in the CCDC database with the deposition number: 2141261.

- The data set of $\text{H}_{11}[\text{PMn}_2\text{Mo}_{10}\text{O}_{40}]$ was solved and refined using ShelXS and the method "Direct Methods" in the space group Fd-3 (203). For each refinement step, 27 cycles were passed through. A twin law was integrated into the solution. The SQUEEZE function was performed analogously to the dataset $\text{H}_7[\text{PMnMo}_{11}\text{O}_{40}]$ in PLATON.^[8] For the same reason as the previous dataset, the same B-level alerts suggesting the space group Fd-3m instead of Fd-3 also result here. Here, too, the space group Fd-3 can be excluded due to the reasons mentioned above. R_1 : 1.52 %; wR_2 : 4.25 %. The CIF file is available in the CCDC database with the deposition number: 2141263.
- The data set for $\text{H}_8[\text{PVMnMo}_{10}\text{O}_{40}]$ was solved and refined using ShelXS and the "Direct Methods" method in the space group Fd-3m (227). For each refinement step 20 cycles were used. The SQUEEZE function was applied. R_1 : 2.65 %; wR_2 : 6.03 %. The CIF file is available in the CCDC database with the deposition number: 2141259.
- The data set of $\text{H}_{12}[\text{PVMn}_2\text{Mo}_9\text{O}_{40}]$ was solved and refined using ShelXT and the method "Intrinsic Phasing" in the space group Fd-3m (227). For each refinement step, 25 cycles were passed through. The SQUEEZE function was applied. R_1 : 2.75 %; wR_2 : 6.83 %. The CIF file is available in the CCDC database with the deposition number: 2141262.
- The data set of $\text{H}_{12}[\text{PV}_5\text{MnMo}_6\text{O}_{40}]$ was solved and refined with ShelXL and the method "Direct Methods" in the space group R-3 (148). For each refinement step, 25 cycles were passed through. The SQUEEZE function was applied. R_1 : 3.77 %; wR_2 : 12.03 %. The CIF file is available in the CCDC database with the deposition number: 2141260.

Powder XRD:

Powder XRD diffractograms were measured on an X'Pert Pro diffractometer (PANalytical Corp.) using Cu-K α radiation ($\lambda = 1.5418 \text{ \AA}$) in the range of 5-90 °. For this purpose, the background was determined, and the data smoothed.

ICP-OES:

Sample preparation: the initial weight was dissolved in water (5 mL), acidified with a 37 % hydrochloric acid solution in water (4 mL), and the solution was filled up to 50 mL in a volumetric flask.

Other:

The exported x/y data were then imported into Origin® 2019b and plotted as corresponding graphs. All graphs in this paper were thus created in Origin®.

1 Experimental details

1.1 Synthesis of $\text{H}_7[\text{PMnMo}_{11}\text{O}_{40}]$

Deionised water (200 mL) was introduced, molybdenum trioxide (17.7081 g, 123.0 mmol, 11 equivalents) and a 25 % phosphoric acid solution in water (4.3880 g, 11.19 mmol, 1 equivalent) were added and heated to reflux. After one hour, a yellow, clear solution was formed. Subsequently, a solution of manganese(II) acetate (1.9357 g, 11.19 mmol, 1 equivalent) in water (100 mL) was added to the boiling solution and heated to reflux for another 60 minutes after the addition was completed. The solution was cooled to room temperature, filtered and dried under reduced pressure (rotary evaporator with oil bath at 85 °C). A yellow powder was obtained (20.1573 g).

Characterisation:

^{31}P -NMR (242.9 MHz, $\text{H}_2\text{O}/\text{acetone-}d_6$, 20 °C): δ [ppm] = -2.96, -3.77.

IR (ATR): $\tilde{\nu}$ [cm^{-1}] = 3459 (w, O-H, H_2O), 1604 (O-H, lattice H_2O), 1060 (w, P-O), 961 (me, M=O_t), 874 ((M-O-M)_{vertex}), 762 ((M-O-M)_{edge}).

UV-Vis: 211 nm.

ICP-OES: Calculated for $\text{H}_7[\text{PMnMo}_{11}\text{O}_{40}] \cdot 8 \text{H}_2\text{O}$: 54.61 % Mo, 2.843 % Mn, 1.603 % P. Found for $\text{H}_7[\text{PMnMo}_{11}\text{O}_{40}] \cdot 8 \text{H}_2\text{O}$: 50.995 % Mo, 2.83 % Mn, 1.7 % P. Data normalised to molybdenum. P/Mn/Mo ratio: 1.14/1.07/11.

TGA: 7.503 % weight loss upon drying, this corresponds to 8 mol water per mol of the POM.

The crystals were obtained using the slow evaporation method: For this purpose, the substances were dissolved in water and the solvent was removed under reduced pressure in the desiccator until crystals were formed.

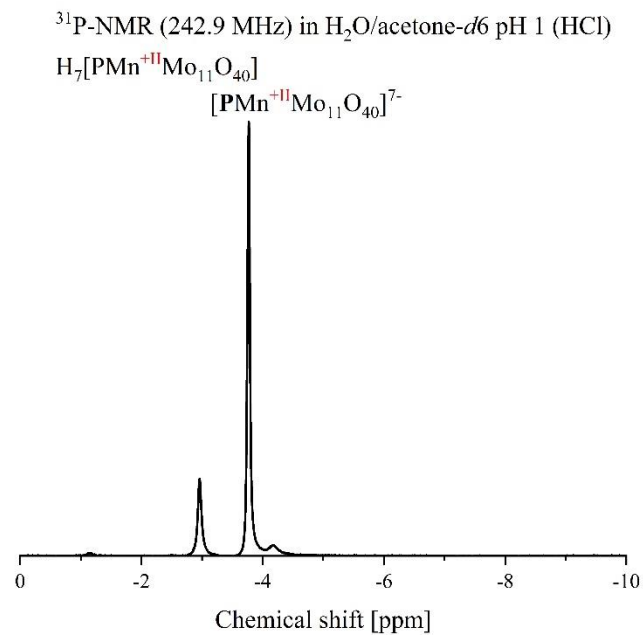


Figure S1. ^{31}P NMR spectrum of $\text{H}_7[\text{PMnMo}_{11}\text{O}_{40}]$ in a mixture of 90 % water (pH 1) and 10 % acetone- d_6 .

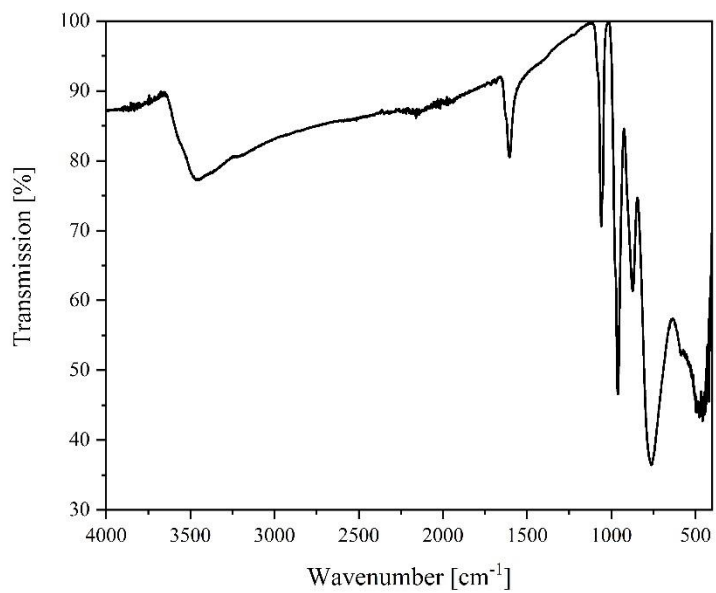


Figure S2. FT-IR (ATR) spectrum of $\text{H}_7[\text{PMnMo}_{11}\text{O}_{40}]$.

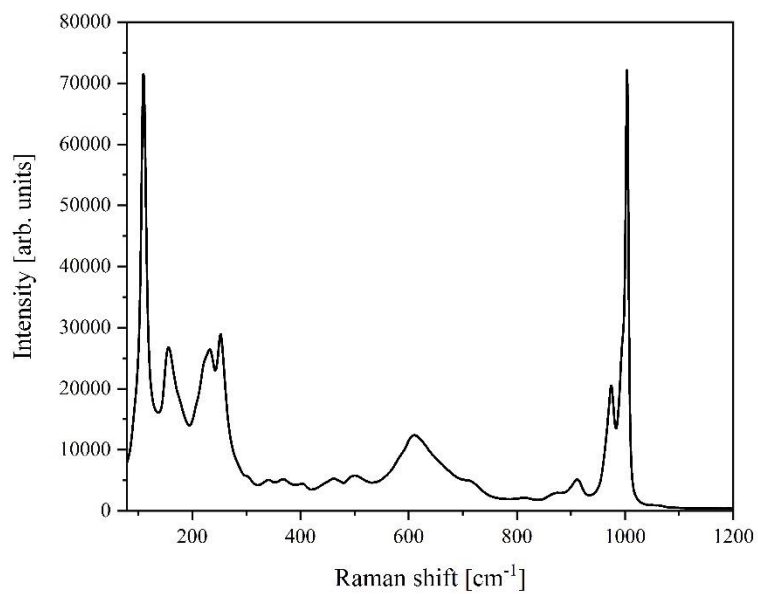


Figure S3. Raman spectrum of H₇[PMnMo₁₁O₄₀].

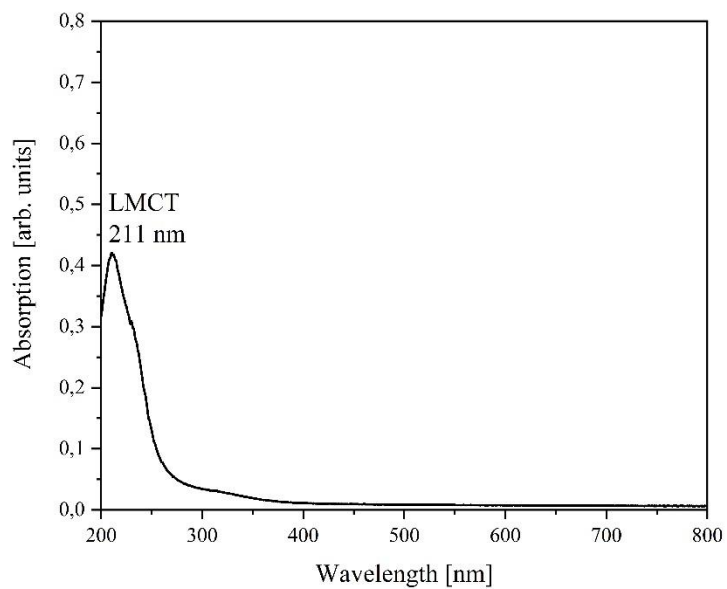


Figure S4. UV-Vis spectrum of H₇[PMnMo₁₁O₄₀] in deionised water.

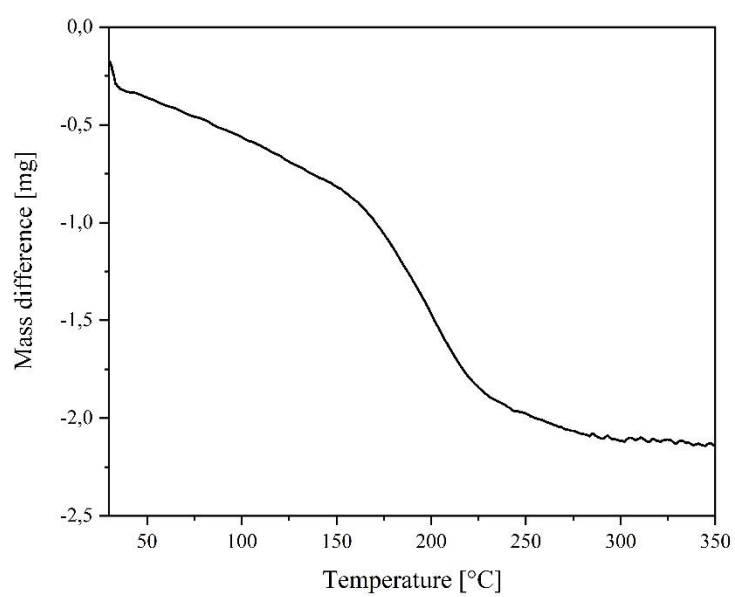


Figure S5. TGA data of H₇[PMnMo₁₁O₄₀].

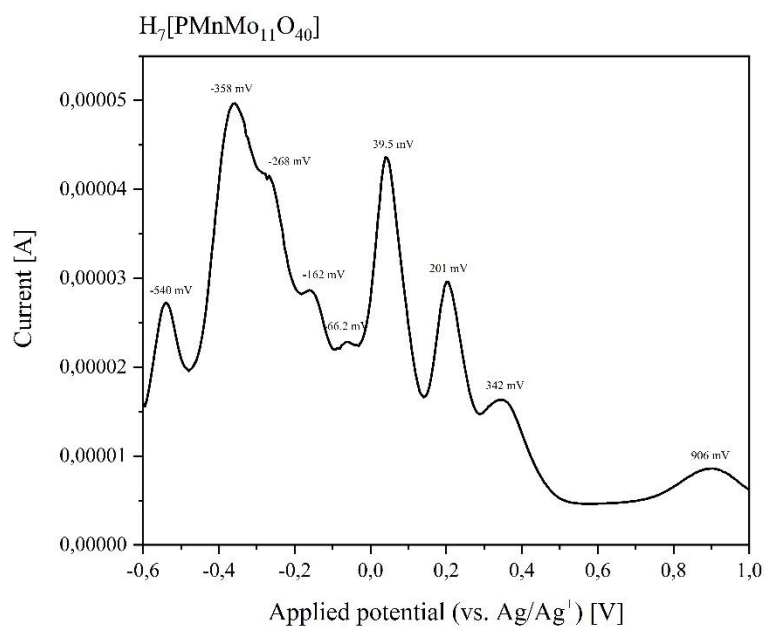
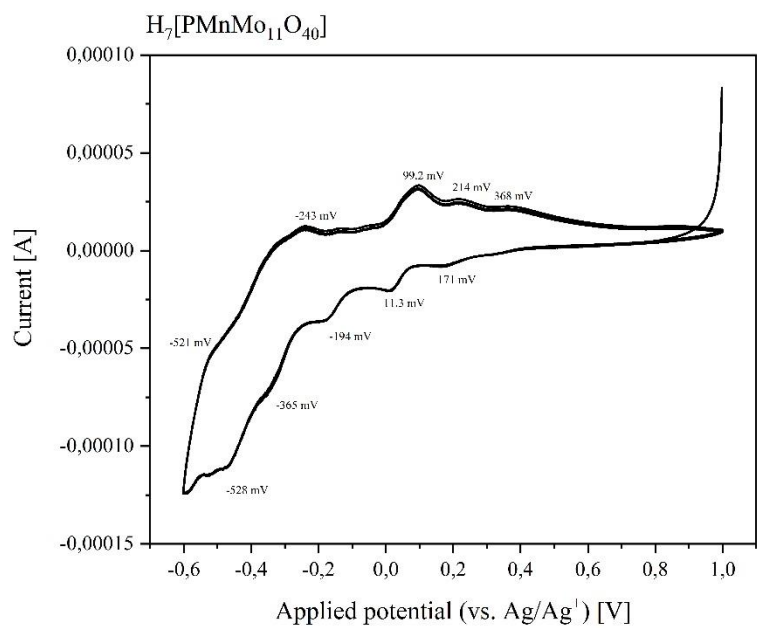


Figure S6. CV (top) and SWV (bottom) data of $H_7[PMnMo_{11}O_{40}]$ in deionised water at pH 1 with a scan rate of 100 mV/s (CV) and 5 mV/s (SWV).

1.2 Synthesis of $H_{11}[PMn_2Mo_{10}O_{40}]$

Deionised water (185 mL) was introduced, molybdenum trioxide (16.4380 g, 114.2 mmol, 10 equivalents) and a 25 % phosphoric acid solution in water (4.4816 g, 11.43 mmol, 1 equivalent) were added and heated to reflux. After one hour, a yellow, clear solution was formed. Subsequently, a solution of manganese(II) acetate (3.9523 g, 22.84 mmol, 2 equivalents) in water (50 mL) was added to the boiling solution and heated to reflux for another 60 minutes after the addition was completed. The solution was cooled to room temperature, filtered and concentrated under reduced pressure (rotary evaporator with oil bath at 85 °C). A brown powder was obtained (19.9653 g).

Characterisation:

^{31}P -NMR (242.9 MHz, H_2O /acetone- d_6 , 20 °C): δ [ppm] = -2.88, -3.78.

IR (ATR): $\tilde{\nu}$ [cm^{-1}] = 3364 (w, O-H, H_2O), 1608 (O-H, lattice H_2O), 1059 (w, P-O), 954 (me, M=O_t), 874 ((M-O-M)_{vertex}), 767 ((M-O-M)_{edge}).

UV-Vis: 210 nm.

ICP-OES: Calculated for $H_{11}[PMn_2Mo_{10}O_{40}] \cdot 10 H_2O$: 49.67 % Mo, 5.689 % Mn, 1.618 % P. Found for $H_{11}[PMn_2Mo_{10}O_{40}] \cdot 10 H_2O$: 48.285 % Mo, 5.625 % Mn, 1.64 % P. Data normalised to molybdenum. P/Mn/Mo ratio: 1.05/2.03/10.

TGA: 9.469 % weight loss upon drying, this corresponds to 10 mol lattice water per mol of the POM.

The crystals were obtained using the slow evaporation method: For this purpose, the substances were dissolved in water and the solvent was removed under reduced pressure in the desiccator until crystals were formed.

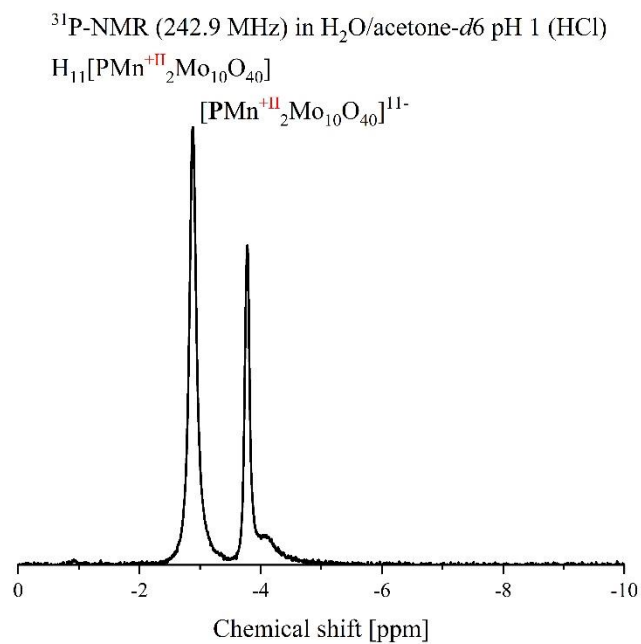


Figure S7. ^{31}P -NMR spectrum of $\text{H}_{11}[\text{PMn}_2\text{Mo}_{10}\text{O}_{40}]$ in mixture of 90 % water (pH 1) and 10 % acetone- d_6 .

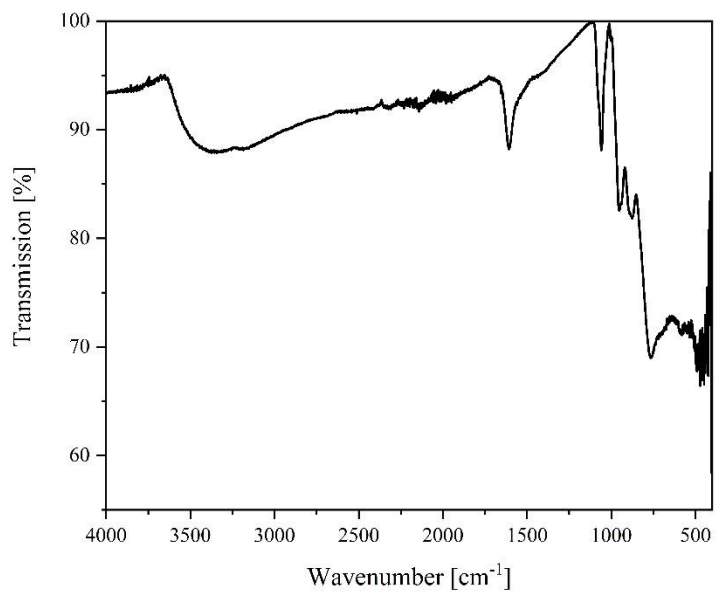


Figure S8. FT-IR (ATR) spectrum of $\text{H}_{11}[\text{PMn}_2\text{Mo}_{10}\text{O}_{40}]$.

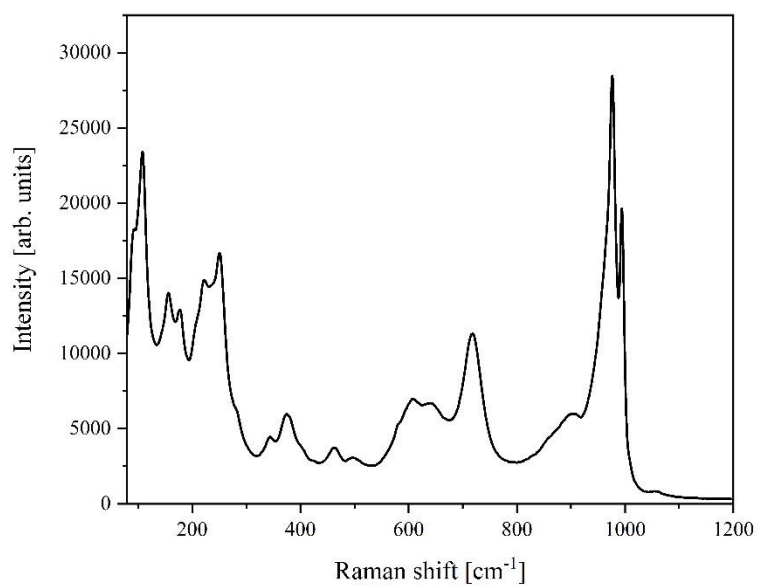


Figure S9. Raman spectrum of H₁₁[PMn₂Mo₁₀O₄₀].

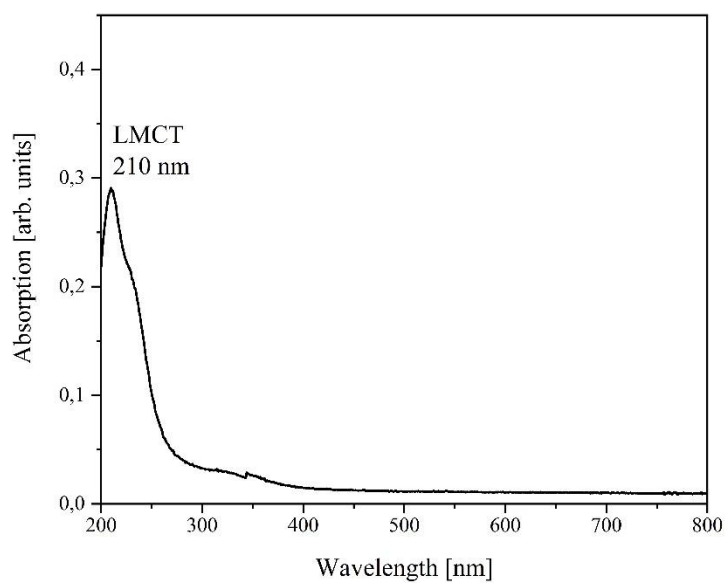


Figure S10. UV-Vis spectrum of H₁₁[PMn₂Mo₁₀O₄₀] in deionised water.

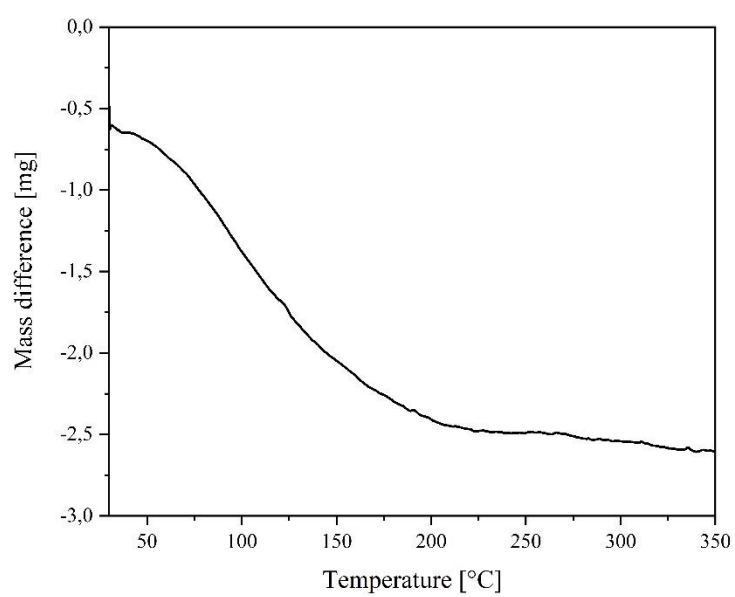


Figure S11. TGA data of $H_{11}[PMn_2Mo_{10}O_{40}]$.

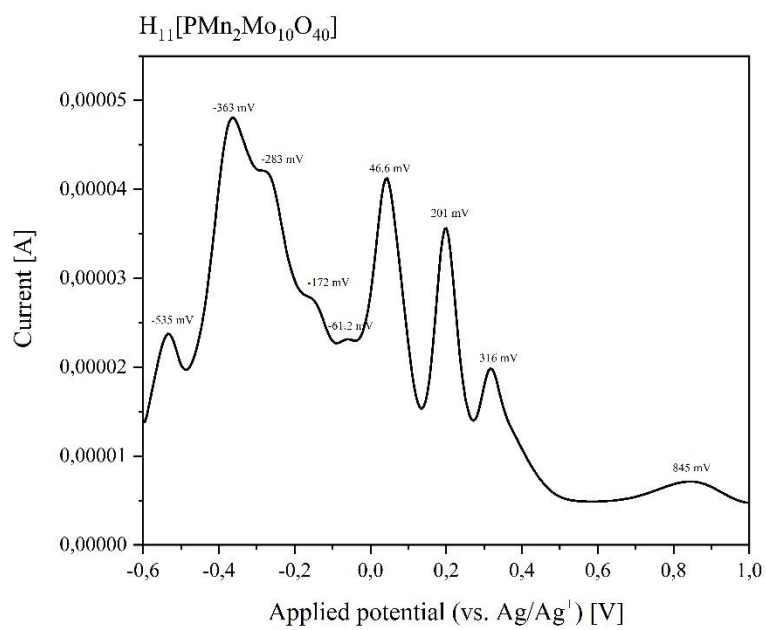
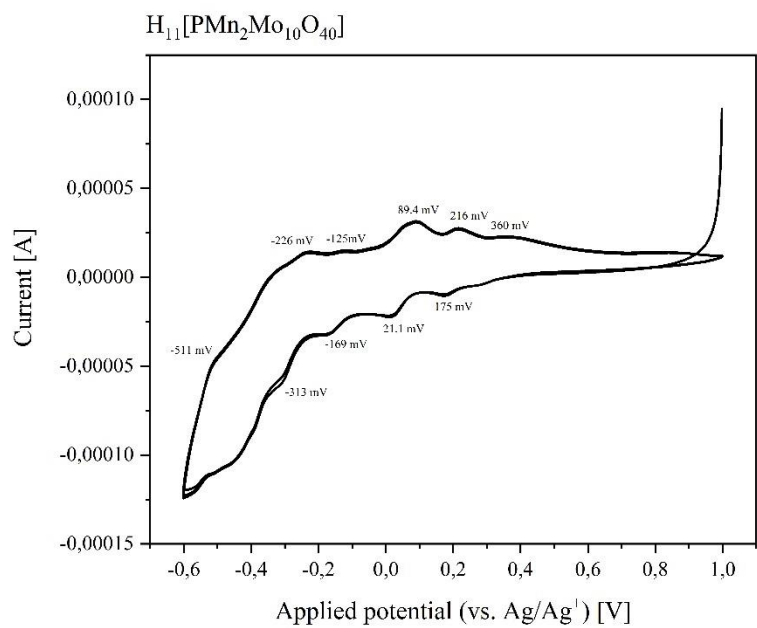


Figure S12. CV (top) and SWV (bottom) data of $H_{11}[PMn_2Mo_{10}O_{40}]$ in deionised water at pH 1 with a scan rate of 100 mV/s (CV) and 5 mV/s (SWV).

1.3 Synthesis of $\text{H}_8[\text{PVMnMo}_{10}\text{O}_{40}]$

Solution 1:

Water (29.0 mL) was introduced, divandium pentoxide (0.7657 g, 4.210 mmol, 0.5 equivalent) added and cooled to 5 °C. A 30 % hydrogen peroxide solution in water (5.0 mL, 49 mmol, 5.8 equivalents) was added dropwise to the orange coloured suspension, whereupon, after stirring for some time, a brown solution was formed from which oxygen gas evolution was observed. The solution was then warmed to room temperature and a 25 % phosphoric acid solution in water (0.5748 g, 1.466 mmol, 0.17 equivalents) was added and the solution was cooled to 5 °C again.

Solution 2:

Water (100 mL) and molybdenum trioxide (12.1153 g, 84.17 mmol, 10 equivalents) were introduced and a 25 % phosphoric acid solution in water (3.2940 g, 8.403 mmol, 1 equivalent) was added. The suspension was heated to reflux, whereupon a yellow, clear solution formed after about one hour.

Cooled solution 1 was added dropwise to the boiling solution 2 and further heated to reflux. After 30 min, manganese(II) acetate (1.4583 g, 8.428 mmol, 1 equivalent) in water (100 mL) was added to the red-coloured solution and heated to reflux for a further 90 min. The solution was then cooled to room temperature, filtered and dried under reduced pressure (rotary evaporator with oil bath at 85 °C). An orange powder was obtained (10.6091 g).

Characterisation:

$^{31}\text{P-NMR}$ (242.9 MHz, $\text{H}_2\text{O}/\text{acetone-}d_6$, 20 °C): δ [ppm] = -4.04.

$^{51}\text{V-NMR}$ (157.8 MHz, $\text{H}_2\text{O}/\text{acetone-}d_6$, 20 °C): δ [ppm] = -532.

IR (ATR): $\tilde{\nu}$ [cm^{-1}] = 3481 (w, O-H, H_2O), 1603 (O-H, lattice H_2O), 1055 (w, P-O), 959 (me, M=O_t), 871 ((M-O-M)_{vertex}), 762 ((M-O-M)_{edge}).

UV-Vis: 210 nm, 311 nm.

ICP-OES: Calculated for $\text{H}_8[\text{PVMnMo}_{10}\text{O}_{40}] \cdot 8 \text{H}_2\text{O}$: 50.81 % Mo, 2.698 % V, 2.909 % Mn, 1.64 % P. Found for $\text{H}_8[\text{PVMnMo}_{10}\text{O}_{40}] \cdot 8 \text{H}_2\text{O}$: 50.1 % Mo, 2.75 % V, 3.01 % Mn, 2.03 % P. Data normalised to molybdenum. P/V/Mn/Mo ratio: 1.26/1.03/1.05/10.

TGA: 7.424 % weight loss upon drying, this corresponds to 8 mol lattice water per mol of the POM.

The crystals were obtained using the slow evaporation method: For this purpose, the substances were dissolved in water and the solvent was removed under reduced pressure in the desiccator until crystals were formed.

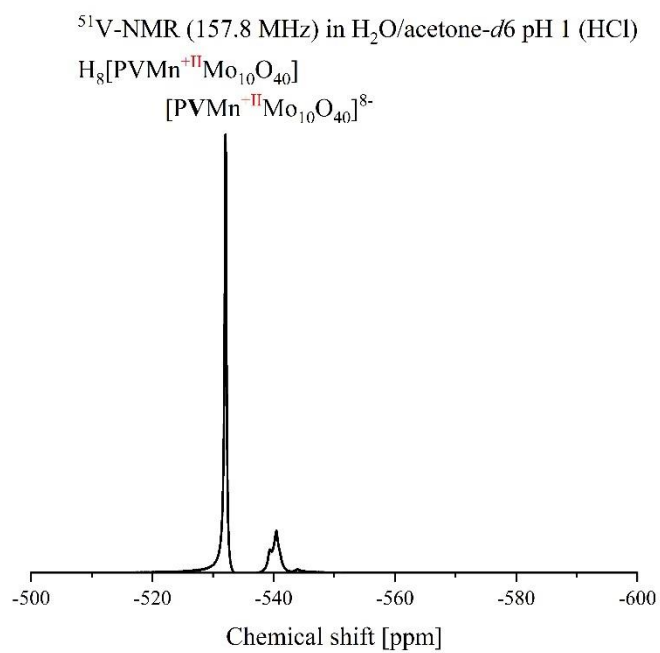
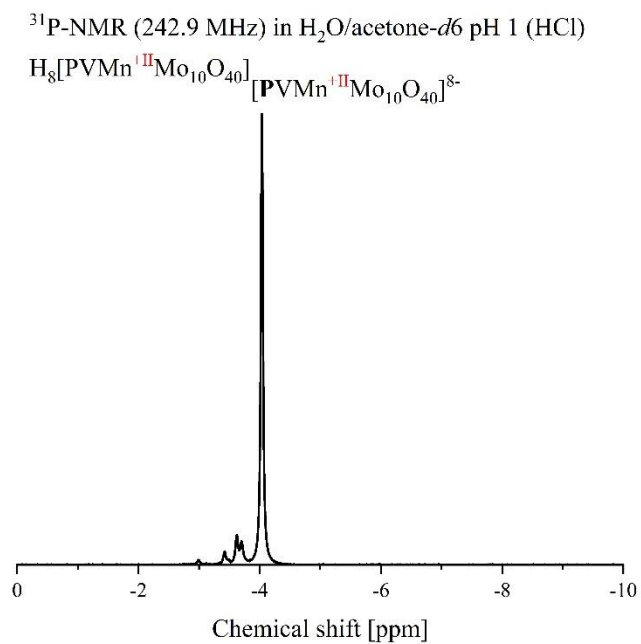


Figure S13. ^{31}P - and ^{51}V -NMR spectrum of $\text{H}_8[\text{PVMnMo}_{10}\text{O}_{40}]$ in mixture of 90 % water (pH 1) and 10 % acetone- d_6 .

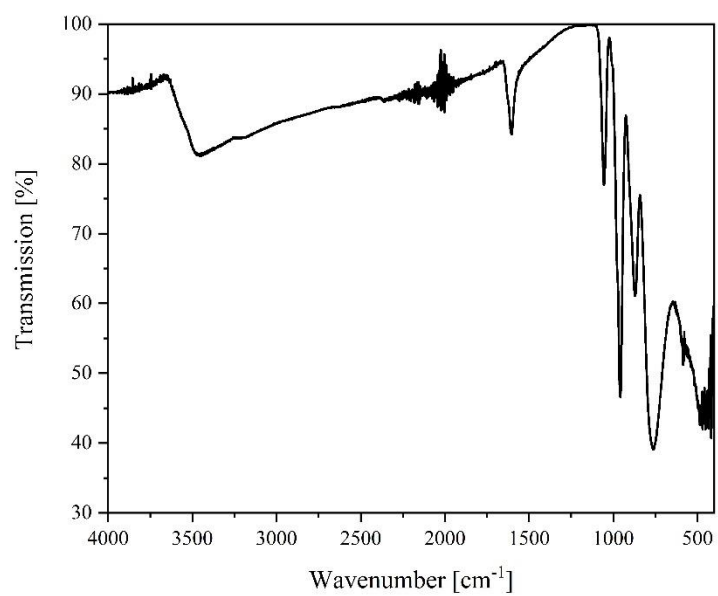


Figure S14. FT-IR (ATR) spectrum of $H_8[PVMnMo_{10}O_{40}]$.

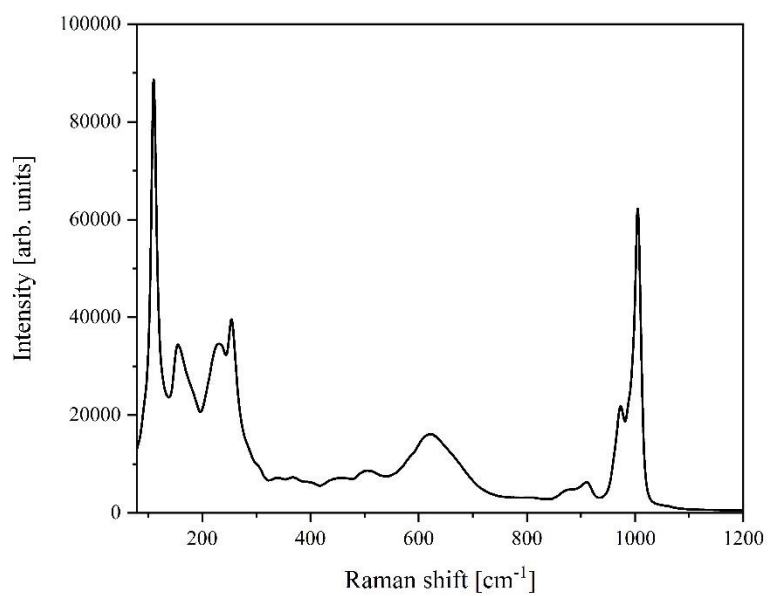


Figure S15. Raman spectrum of $H_8[PVMnMo_{10}O_{40}]$.

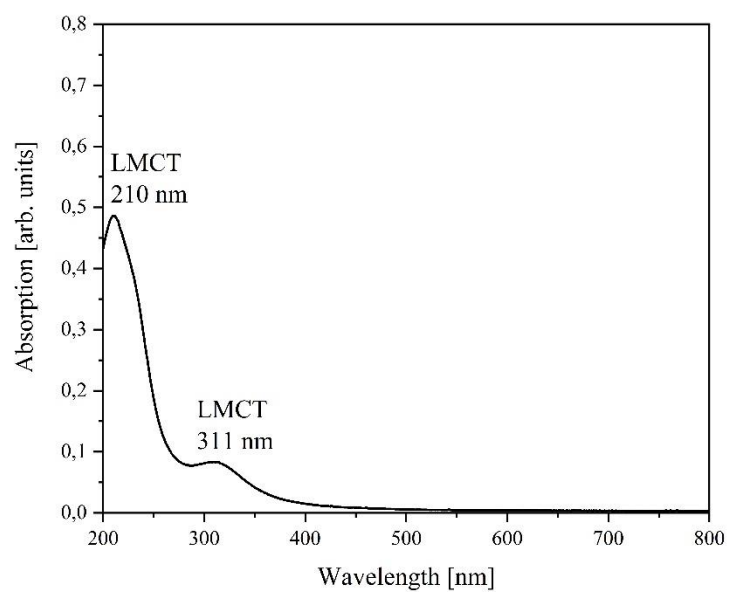


Figure S16. UV-Vis spectrum of $H_8[PVMnMo_{10}O_{40}]$ in deionised water.

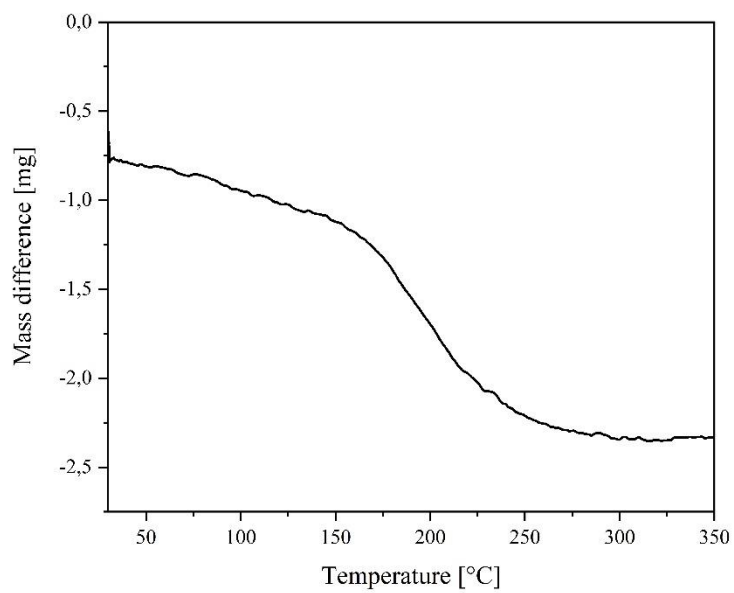


Figure S17. TGA data of $H_8[PVMnMo_{10}O_{40}]$.

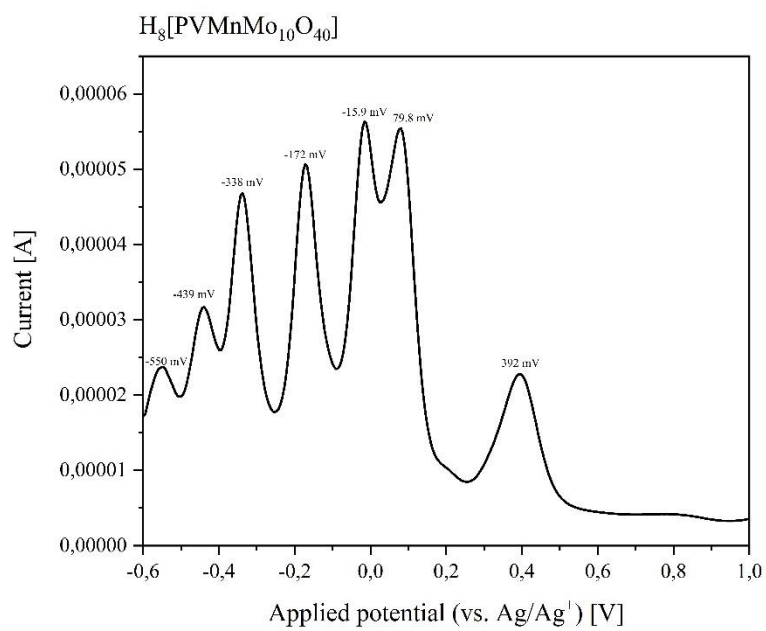
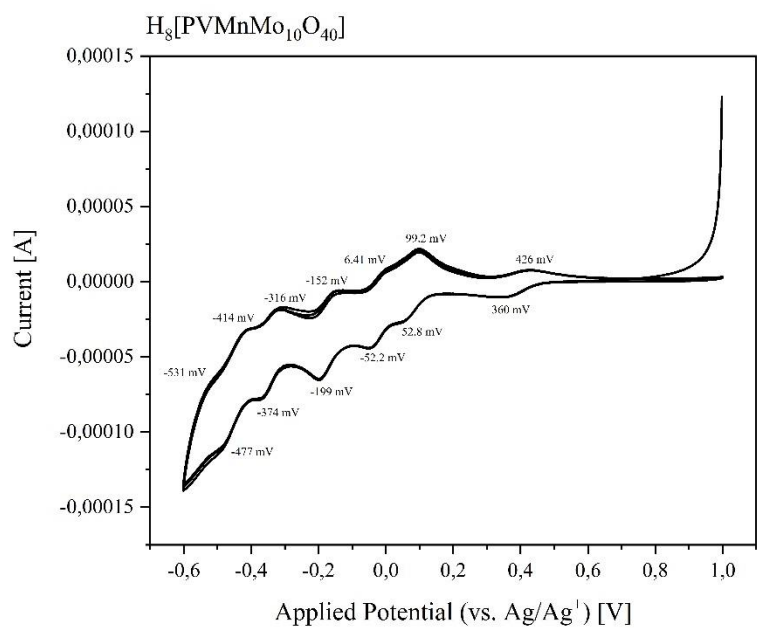


Figure S18. CV (top) and SWV (bottom) data of $H_8[PVMnMo_{10}O_{40}]$ in deionised water at pH 1 with a scan rate of 100 mV/s (CV) and 5 mV/s (SWV).

1.4 Synthesis of $\text{H}_{12}[\text{PVMn}_2\text{Mo}_9\text{O}_{40}]$

Solution 1:

Water (40 mL) was introduced, divandium pentoxide (1.0663 g, 5.86 mmol, 0.5 equivalent) added and cooled to 5 °C. A 30 % hydrogen peroxide solution in water (7.0 mL, 61.74 mmol, 5.27 equivalents) was added dropwise to the orange coloured suspension, whereupon, after stirring for some time, a brown solution was formed from which oxygen gas evolution was observed. The solution was then warmed to room temperature and a 25 % phosphoric acid solution in water (0.7929 g, 2.02 mmol, 0.172 equivalents) was added and the solution was cooled to 5 °C again.

Solution 2:

Water (171 mL) and molybdenum trioxide (15.1753 g, 105.4 mmol, 9 equivalents) were introduced and a 25 % phosphoric acid solution in water (4.5940 g, 11.72 mmol, 1 equivalent) was added. The suspension was heated to reflux, whereupon a yellow, clear solution formed after about one hour.

Cooled solution 1 was added dropwise to the boiling solution 2 and further heated to reflux. After 30 min, manganese(II) acetate (4.0538 g, 23.43 mmol, 2 equivalents) in water (100 mL) was added to the dark-coloured solution and heated to reflux for a further 90 min. The solution was then cooled to room temperature, filtered and dried under reduced pressure (rotary evaporator with oil bath at 85 °C). A brown powder was obtained (20.2069 g).

Characterisation:

^{31}P -NMR (242.9 MHz, $\text{H}_2\text{O}/\text{acetone-}d_6$, 20 °C): δ [ppm] = -3.57, -3.99.

^{51}V -NMR (157.8 MHz, $\text{H}_2\text{O}/\text{acetone-}d_6$, 20 °C): δ [ppm] = -532, -539.

IR (ATR): $\tilde{\nu}$ [cm^{-1}] = 3413 (w, O-H, H_2O), 1606 (O-H, lattice H_2O), 1053 (w, P-O), 953 (me, M=O_t), 869 ((M-O-M)_{vertex}), 757 ((M-O-M)_{edge}).

UV-Vis: 211 nm, 309 nm.

ICP-OES: Calculated for $\text{H}_{12}[\text{PVMn}_2\text{Mo}_9\text{O}_{40}] \cdot 10 \text{H}_2\text{O}$: 45.75 % Mo, 2.699 % V, 5.821 % Mn, 1.641 % P. Found for $\text{H}_{12}[\text{PVMn}_2\text{Mo}_9\text{O}_{40}] \cdot 10 \text{H}_2\text{O}$: 44.99 % Mo, 2.795 % V, 5.985 % Mn, 2.005 % P. Data normalised to molybdenum. P/V/Mn/Mo ratio: 1.24/1.05/2.09/9.

TGA: 9.318 % weight loss upon drying, this corresponds to 10 mol lattice water per mol of the POM.

The crystals were obtained using the slow evaporation method: For this purpose, the substances were dissolved in water and the solvent was removed under reduced pressure in the desiccator until crystals were formed.

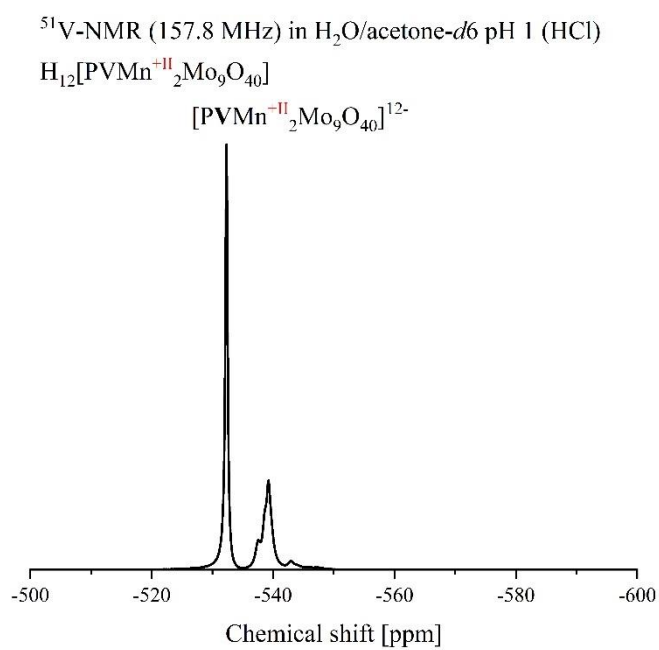
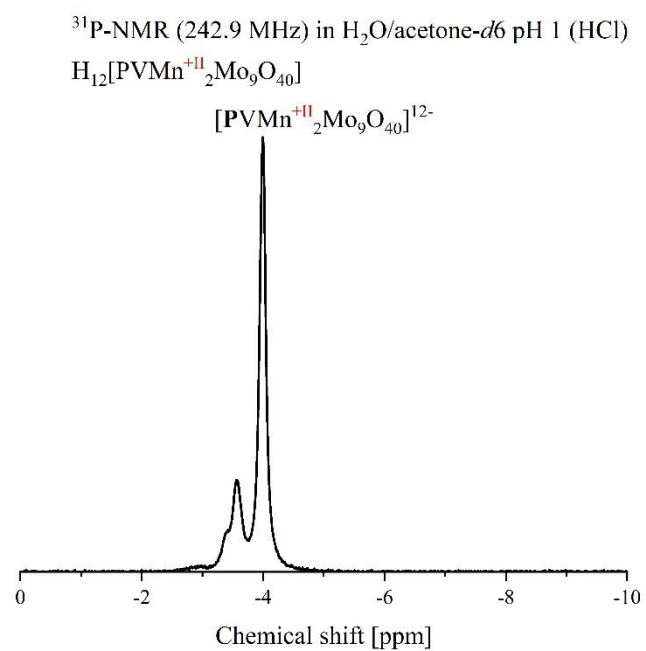


Figure S19. ^{31}P - and ^{51}V -NMR spectrum of $\text{H}_{12}[\text{PVMn}_2\text{Mo}_9\text{O}_{40}]$ in mixture of 90 % water (pH 1) and 10 % acetone- d_6 .

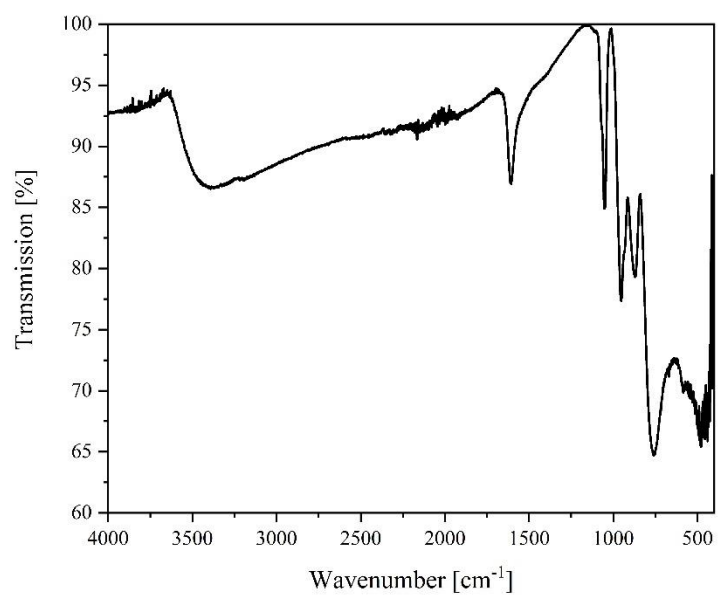


Figure S20. FT-IR (ATR) spectrum of $H_{12}[PVMn_2Mo_9O_{40}]$.

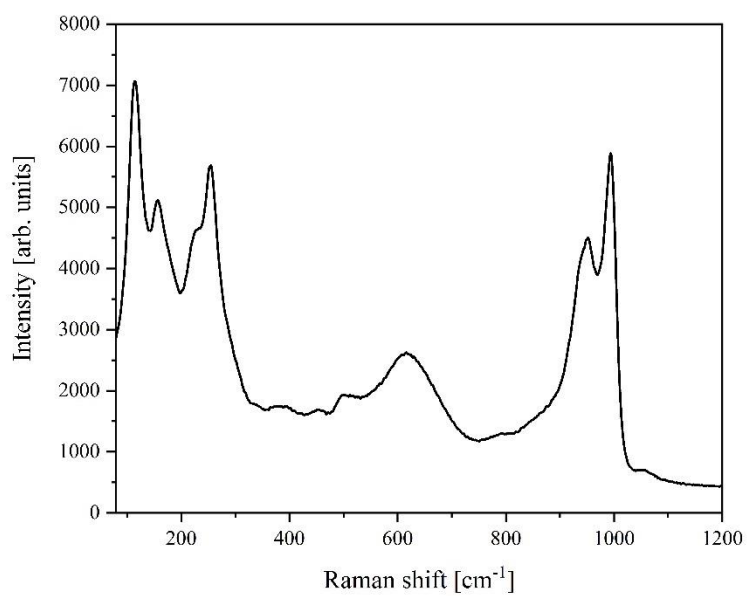


Figure S21. Raman spectrum of $H_{12}[PVMn_2Mo_9O_{40}]$.

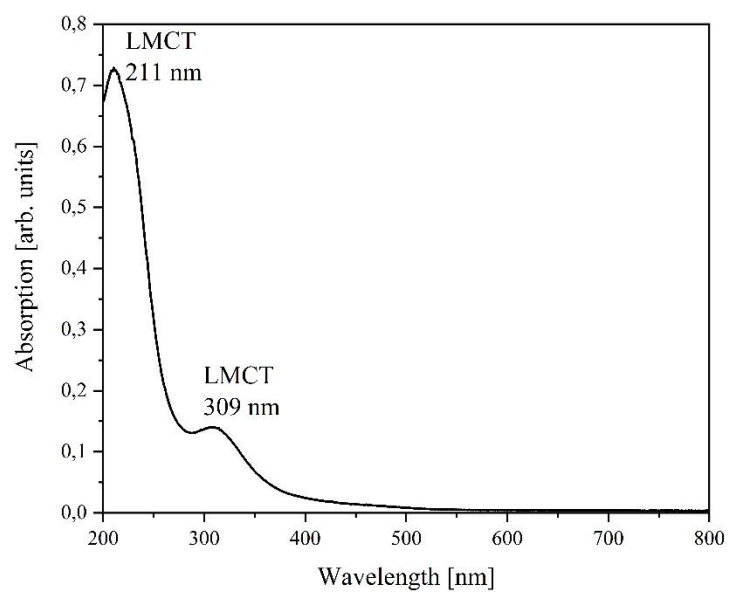


Figure S22. UV-Vis spectrum of $\text{H}_{12}[\text{PVMn}_2\text{Mo}_9\text{O}_{40}]$ in deionised water.

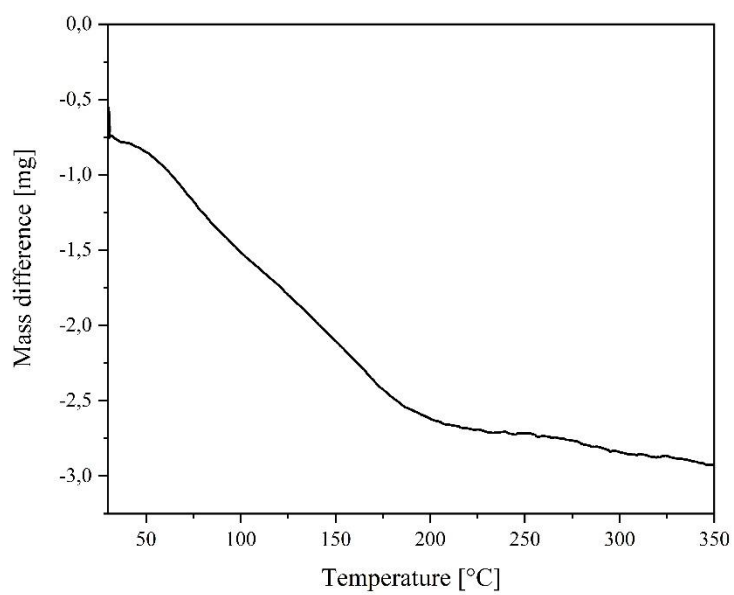


Figure S23. TGA data of $\text{H}_{12}[\text{PVMn}_2\text{Mo}_9\text{O}_{40}]$.

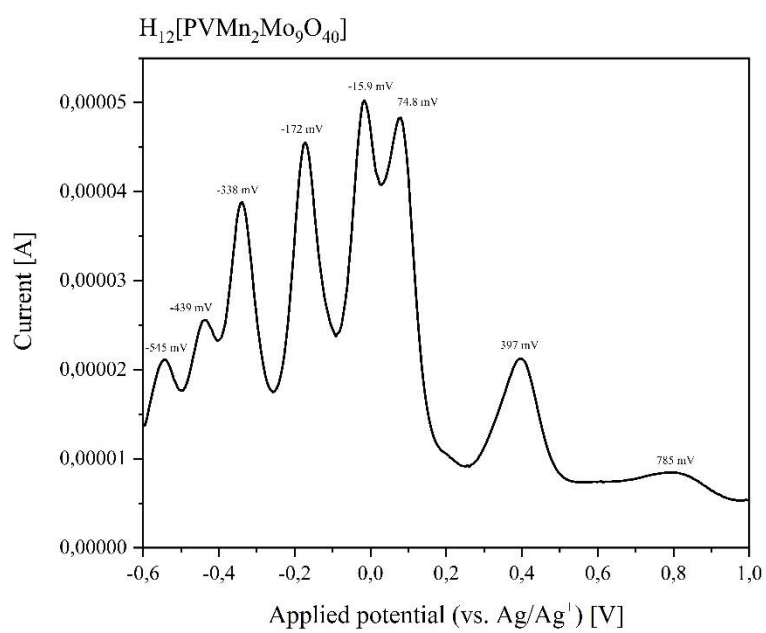
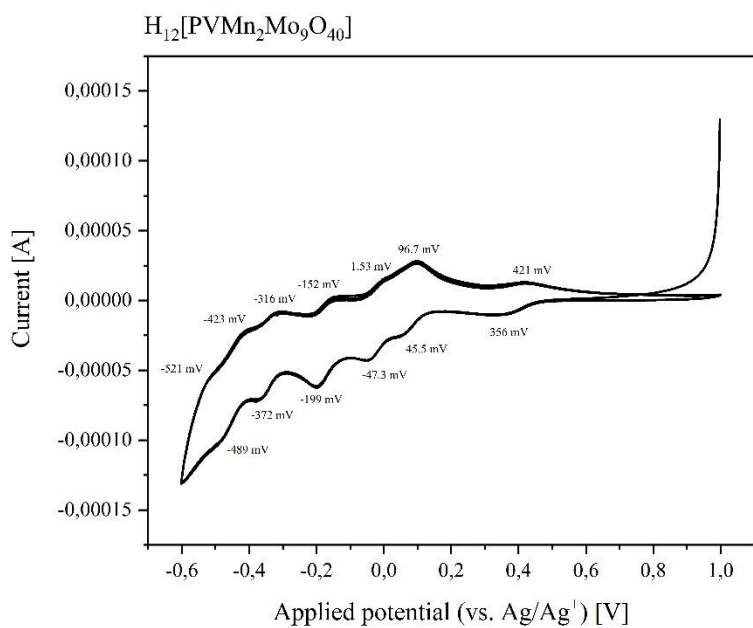


Figure S24. CV (top) and SWV (bottom) data of $H_{12}[PVMn_2Mo_9O_{40}]$ in deionised water at pH 1 with a scan rate of 100 mV/s (CV) and 5 mV/s (SWV).

1.5 Synthesis of $\text{H}_{14}[\text{V}_3\text{Mn}_2\text{Mo}_7\text{O}_{40}]$

Solution 1:

Water (127 mL) was introduced, divandium pentoxide (3.3692 g, 18.52 mmol, 1.5 equivalents) added and cooled to 5 °C. A 30 % hydrogen peroxide solution in water (22.0 mL, 194 mmol, 15.63 equivalents) was added dropwise to the orange coloured suspension, whereupon, after stirring for some time, a brown solution was formed from which oxygen gas evolution was observed. The solution was then warmed to room temperature and a 25 % phosphoric acid solution in water (0.8495 g, 2.17 mmol, 0.175 equivalents) was added and the solution was cooled to 5 °C again.

Solution 2:

Water (140 mL) and molybdenum trioxide (12.4446 g, 86.46 mmol, 7 equivalents) were introduced and a 25 % phosphoric acid solution in water (4.8626 g, 12.41 mmol, 1 equivalent) was added. The suspension was heated to reflux, whereupon a yellow, clear solution formed after about one hour.

Cooled solution 1 was added dropwise to the boiling solution 2 and further heated to reflux. After 30 min, manganese(II) acetate (4.2743 g, 24.70 mmol, 2 equivalents) in water (100 mL) was added to the dark-coloured solution and heated to reflux for a further 90 min. The solution was then cooled to room temperature, filtered and dried under reduced pressure (rotary evaporator with oil bath at 85 °C). A brown powder was obtained (20.0349 g).

Characterisation:

^{31}P -NMR (242.9 MHz, $\text{H}_2\text{O}/\text{acetone-}d_6$, 20 °C): δ [ppm] = -1.13 to -4.66.

^{51}V -NMR (157.8 MHz, $\text{H}_2\text{O}/\text{acetone-}d_6$, 20 °C): δ [ppm] = -495 to -618.

IR (ATR): $\tilde{\nu}$ [cm^{-1}] = 3408 (w, O-H, H_2O), 1608 (O-H, lattice H_2O), 1052 (w, P-O), 951 (me, M=O_t), 866 ((M-O-M)_{vertex}), 759 ((M-O-M)_{edge}).

UV-Vis: 315 nm, 305 nm.

ICP-OES: Calculated for $\text{H}_{14}[\text{PV}_3\text{Mn}_2\text{Mo}_7\text{O}_{40}] \cdot 23 \text{H}_2\text{O}$: 33.02 % Mo, 7.515 % V, 5.403 % Mn, 1.523 % P. Found for $\text{H}_{14}[\text{PV}_3\text{Mn}_2\text{Mo}_7\text{O}_{40}] \cdot 23 \text{H}_2\text{O}$: 35.195 % Mo, 8.245 % V, 5.995 % Mn, 2.065 % P. Data normalised to molybdenum. P/V/Mn/Mo ratio: 1.27/3.09/2.09/7.

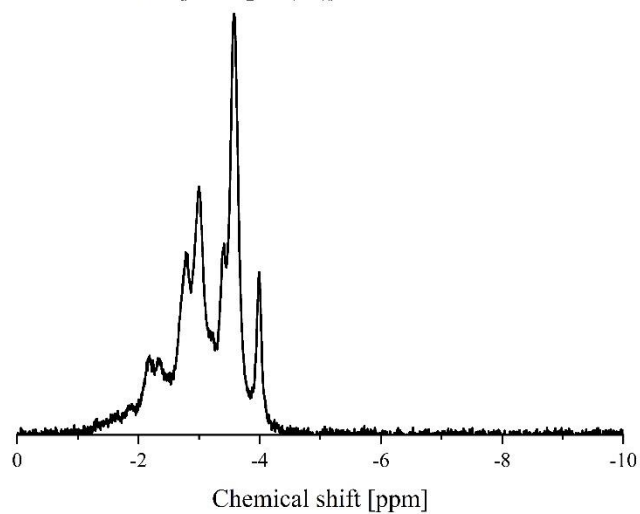
TGA: 20.46 % weight loss upon drying, this corresponds to 23 mol lattice water per mol of the POM.

The crystals were obtained using the slow evaporation method: For this purpose, the substances were dissolved in water and the solvent was removed under reduced pressure in the desiccator until crystals were formed.

^{31}P -NMR (242.9 MHz) in $\text{H}_2\text{O}/\text{acetone-}d_6$ pH 1 (HCl)

$\text{H}_{14}[\text{PV}_3\text{Mn}^{+II}_2\text{Mo}_7\text{O}_{40}]$

$[\text{PV}_3\text{Mn}^{+II}_2\text{Mo}_7\text{O}_{40}]^{14-}$



^{51}V -NMR (157.8 MHz) in $\text{H}_2\text{O}/\text{acetone-}d_6$ pH 1 (HCl)

$\text{H}_{14}[\text{PV}_3\text{Mn}_2\text{Mo}_7\text{O}_{40}]$

$[\text{PV}_3\text{Mn}^{-II}_2\text{Mo}_7\text{O}_{40}]^{14-}$

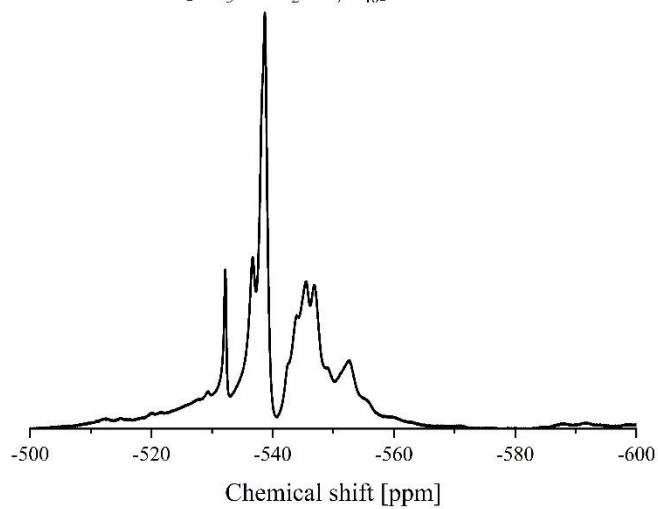


Figure S25. ^{31}P - and ^{51}V -NMR spectrum of $\text{H}_{14}[\text{PV}_3\text{Mn}_2\text{Mo}_7\text{O}_{40}]$ in a mixture of 90 % water (pH 1) and 10 % acetone- d_6 .

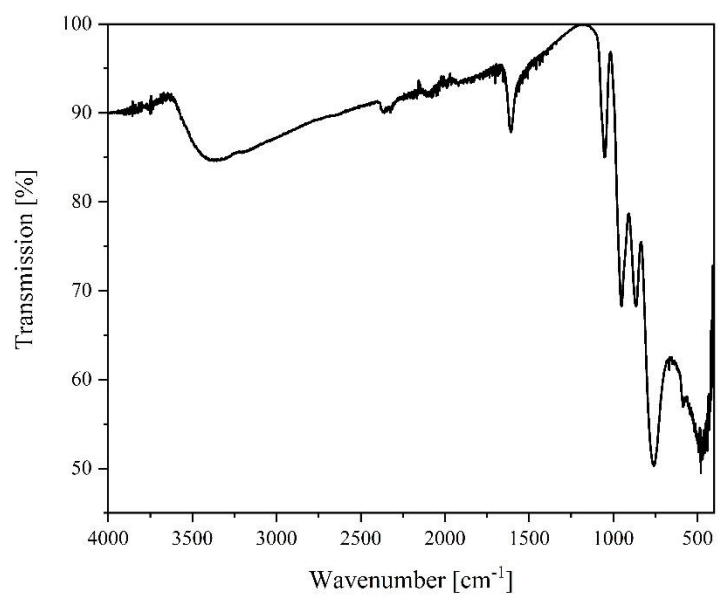


Figure S26. FT-IR (ATR) spectrum of $H_{14}[PV_3Mn_2Mo_7O_{40}]$.

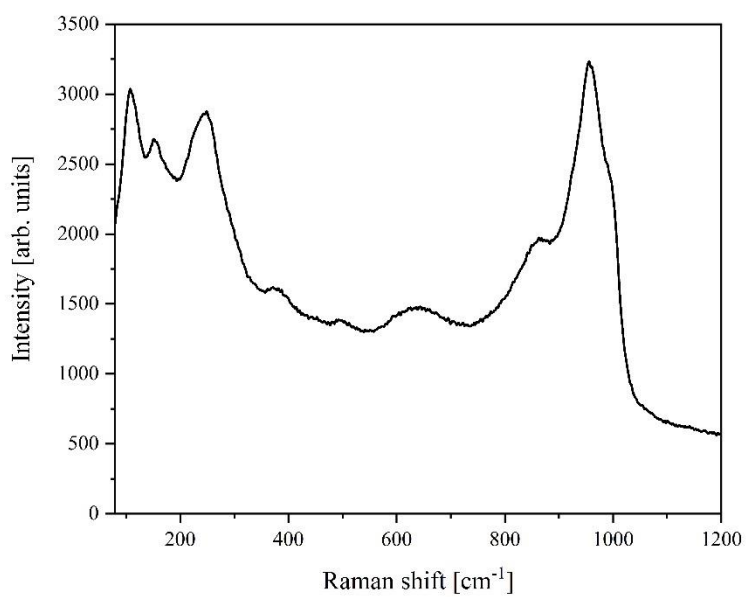


Figure S27. Raman spectrum of $H_{14}[PV_3Mn_2Mo_7O_{40}]$.

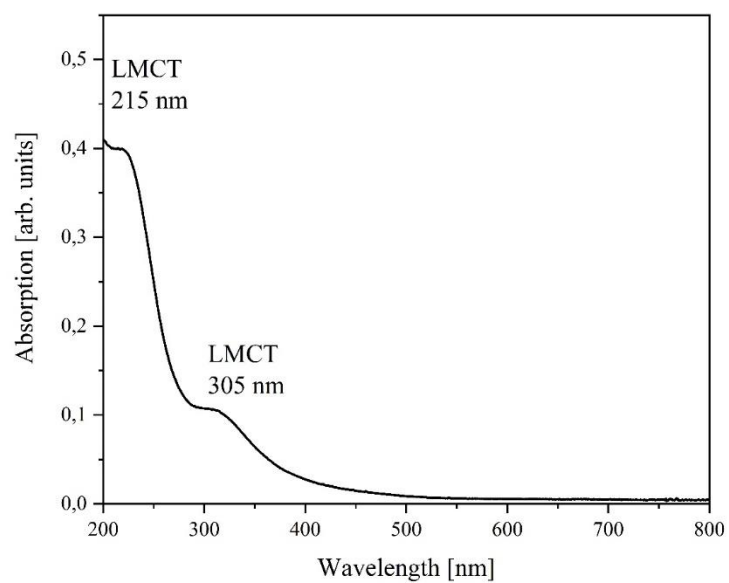


Figure S28. UV-Vis spectrum of $H_{14}[PV_3Mn_2Mo_7O_{40}]$ in deionised water.

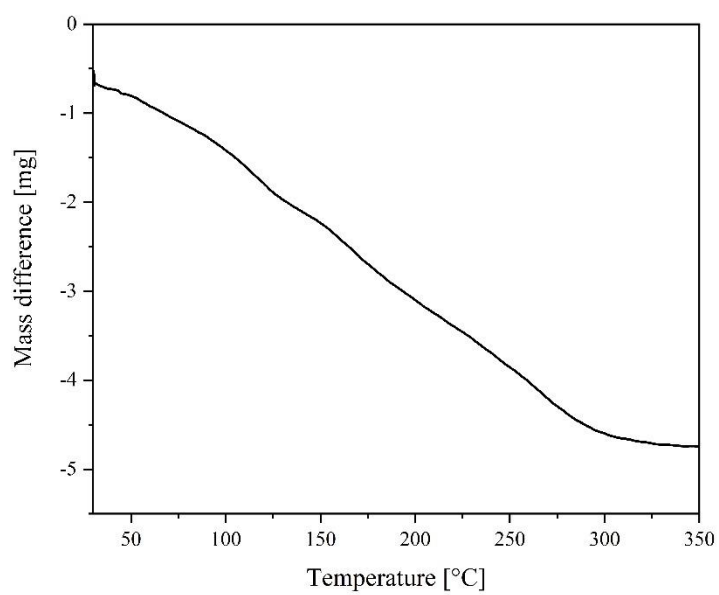


Figure S29. TGA data of $H_{14}[PV_3Mn_2Mo_7O_{40}]$.

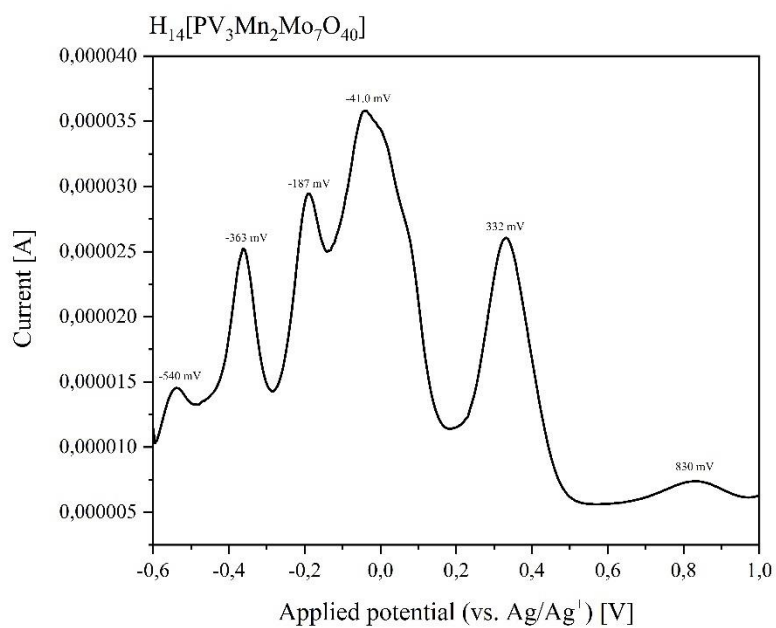
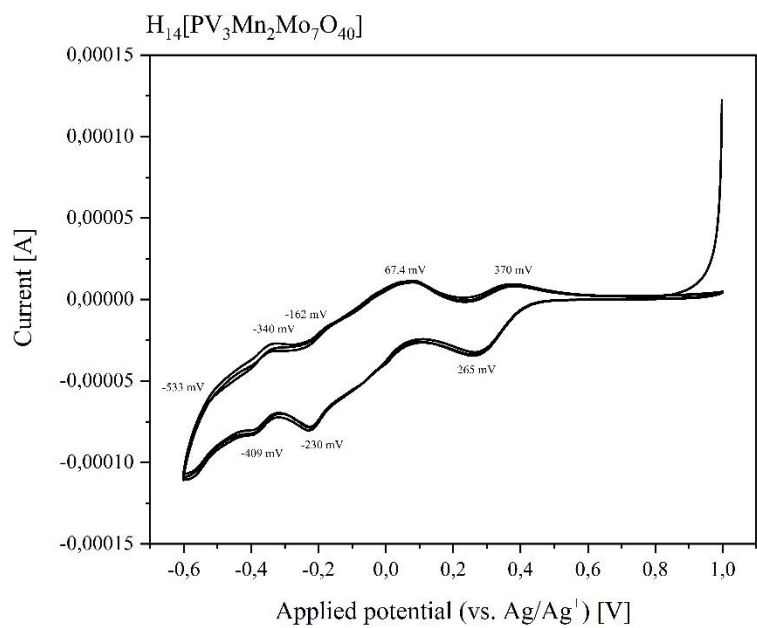


Figure S30. CV (top) and SWV (bottom) data of $H_{14}[PV_3Mn_2Mo_7O_{40}]$ in deionised water at pH 1 with a scan rate of 100 mV/s (CV) and 5 mV/s (SWV).

1.6 Synthesis of $\text{H}_{12}[\text{PV}_5\text{MnMo}_6\text{O}_{40}]$

Solution 1:

Water (164 mL) was introduced, divandium pentoxide (4.3485 g, 23.91 mmol, 2.5 equivalent) added and cooled to 5 °C. A 30 % hydrogen peroxide solution in water (29 mL, 28 mmol, 2.93 equivalents) was added dropwise to the orange coloured suspension, whereupon, after stirring for some time, a brown solution was formed from which oxygen gas evolution was observed. The solution was then warmed to room temperature and a 25 % phosphoric acid solution in water (0.6684 g, 1.705 mmol, 0.18 equivalents) was added and the solution was cooled to 5 °C again.

Solution 2:

Water (93 mL) and molybdenum trioxide (8.2610 g, 57.39 mmol, 6 equivalents) were introduced and a 25 % phosphoric acid solution in water (3.7506 g, 9.568 mmol, 1 equivalent) was added. The suspension was heated to reflux, whereupon a yellow, clear solution formed after about one hour.

Cooled solution 1 was added dropwise to the boiling solution 2 and further heated to reflux. After 30 min, manganese(II) acetate (1.6519 g, 9.547 mmol, 1 equivalent) in water (100 mL) was added to the dark-coloured solution and heated to reflux for a further 90 min. The solution was then cooled to room temperature, filtered and evaporated under reduced pressure (rotary evaporator with oil bath at 85 °C). A brown powder was obtained (15.3776 g).

Characterisation:

^{31}P -NMR (242.9 MHz, $\text{H}_2\text{O}/\text{acetone-}d_6$, 20 °C): δ [ppm] = 0.90 to -4.95.

^{51}V -NMR (157.8 MHz, $\text{H}_2\text{O}/\text{acetone-}d_6$, 20 °C): δ [ppm] = -509 to -608.

IR (ATR): $\tilde{\nu}$ [cm^{-1}] = 3173 (w, O-H, H_2O), 1608 (O-H, lattice H_2O), 1049 (w, P-O), 945 (me, M=O_t), 870 ((M-O-M)_{vertex}), 743 ((M-O-M)_{edge}).

UV-Vis: 214 nm, 310 nm.

ICP-OES: Calculated for $\text{H}_{12}[\text{PV}_5\text{MnMo}_6\text{O}_{40}] \cdot 23 \text{H}_2\text{O}$: 29.03 % Mo, 12.85 % V, 2.771 % Mn, 1.562 % P. Found for $\text{H}_{12}[\text{PV}_5\text{MnMo}_6\text{O}_{40}] \cdot 23 \text{H}_2\text{O}$: 32.765 % Mo, 15.115 % V, 3.255 % Mn, 2.28 % P. Data normalised to molybdenum. P/V/Mn/Mo ratio: 1.29/5.21/1.04/6.

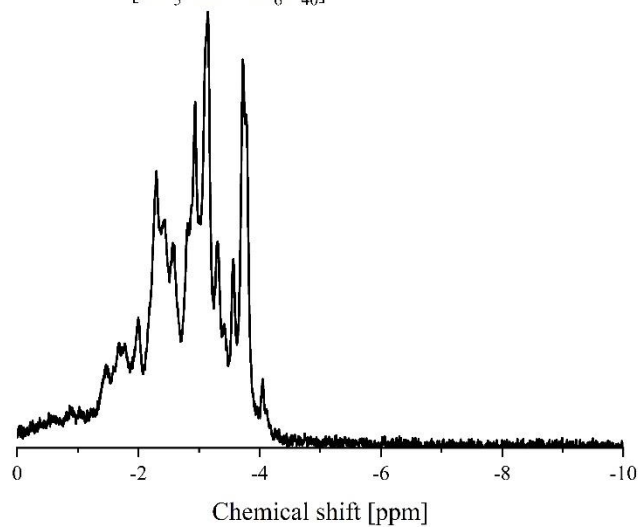
TGA: 20.61 % weight loss upon drying, this corresponds to 23 mol lattice water per mol of the POM.

The crystals were obtained using the slow evaporation method: For this purpose, the substances were dissolved in water and the solvent was removed under reduced pressure in the desiccator until crystals were formed.

^{31}P -NMR (242.9 MHz) in $\text{H}_2\text{O}/\text{acetone-}d_6$ pH 1 (HCl)

$\text{H}_{12}[\text{PV}_5\text{Mn}^{\text{II}}\text{Mo}_6\text{O}_{40}]$

$[\text{PV}_5\text{Mn}^{\text{II}}\text{Mo}_6\text{O}_{40}]^{12-}$



^{51}V -NMR (157.8 MHz) in $\text{H}_2\text{O}/\text{acetone-}d_6$ pH 1 (HCl)

$\text{H}_{12}[\text{PV}_5\text{Mn}^{\text{II}}\text{Mo}_6\text{O}_{40}]$

$[\text{PV}_5\text{Mn}^{\text{II}}\text{Mo}_6\text{O}_{40}]^{12-}$

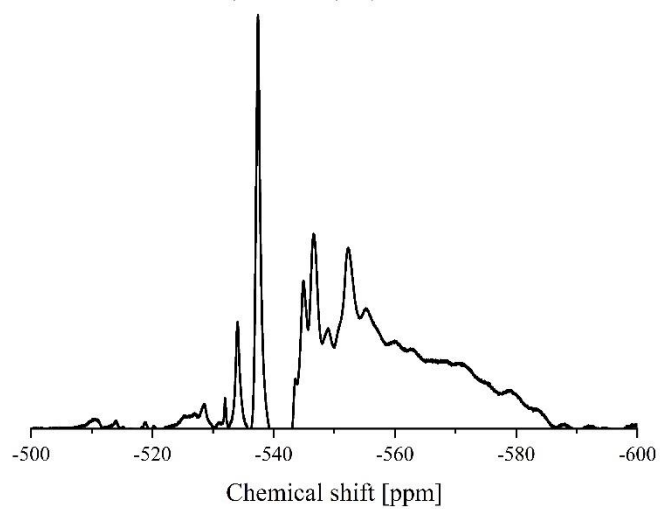


Figure S31. ^{31}P - and ^{51}V -NMR spectrum of $\text{H}_{12}[\text{PV}_5\text{MnMo}_6\text{O}_{40}]$ in a mixture of 90 % water (pH 1) and 10 % acetone- d_6 .

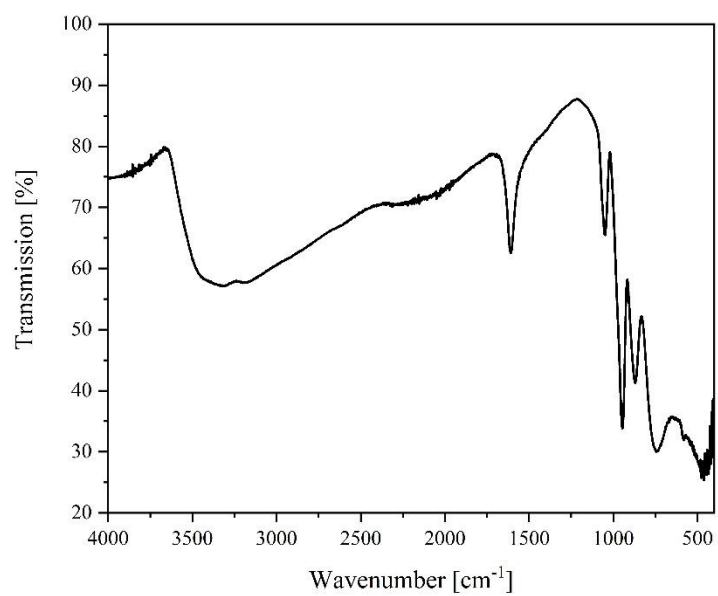


Figure S32. FT-IR (ATR) spectrum of $H_{12}[PV_5MnMo_6O_{40}]$.

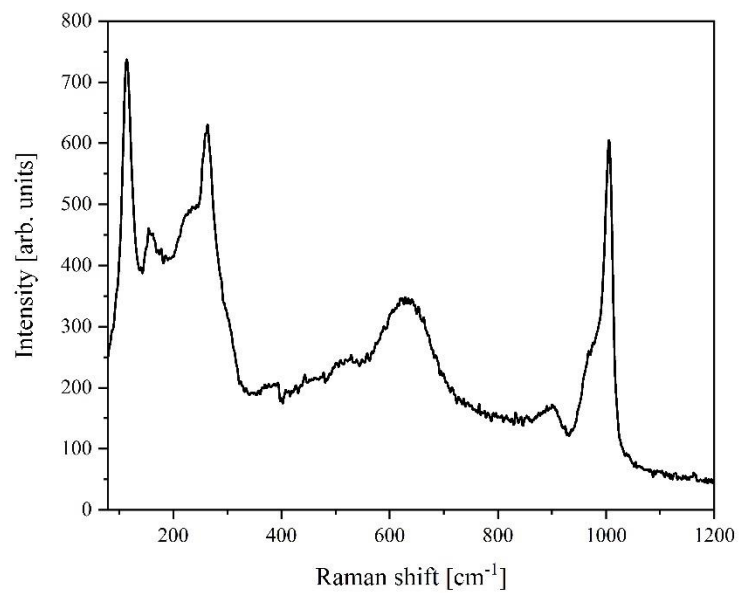


Figure S33. Raman spectrum of $H_{12}[PV_5MnMo_6O_{40}]$.

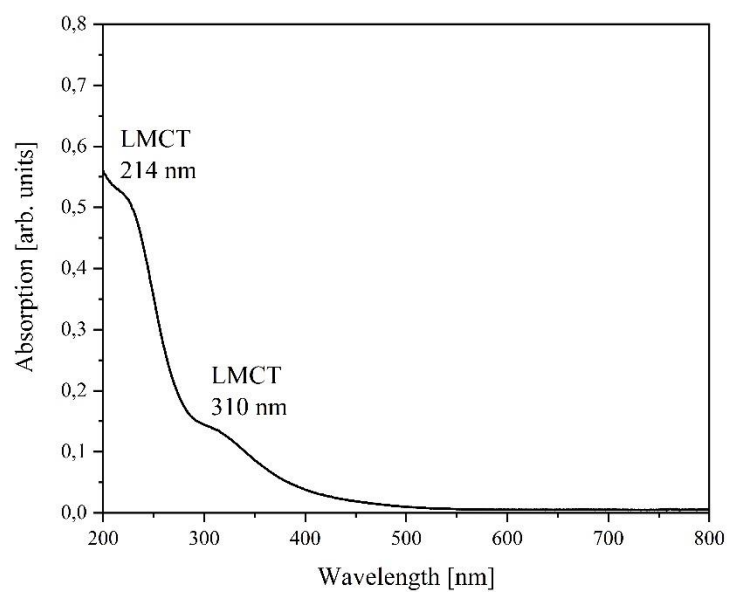


Figure S34. UV-Vis spectrum of $H_{12}[PV_5MnMo_6O_{40}]$ in deionised water.

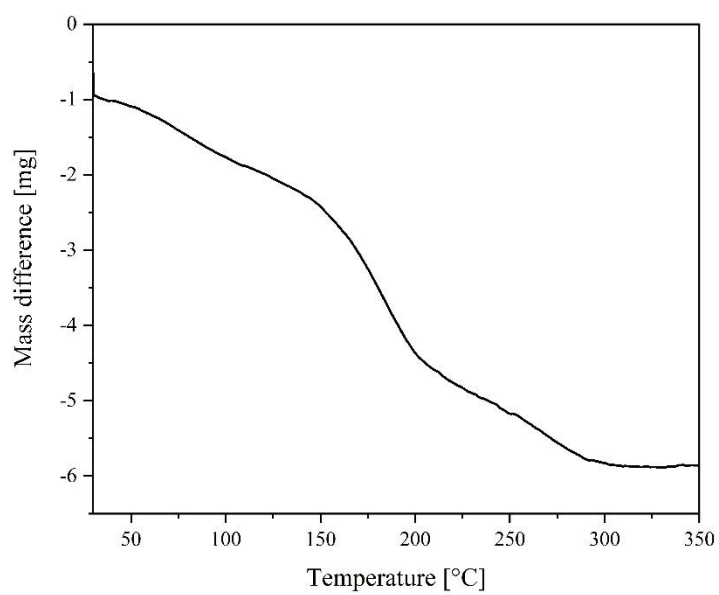


Figure S35. TGA data of $H_{12}[PV_5MnMo_6O_{40}]$.

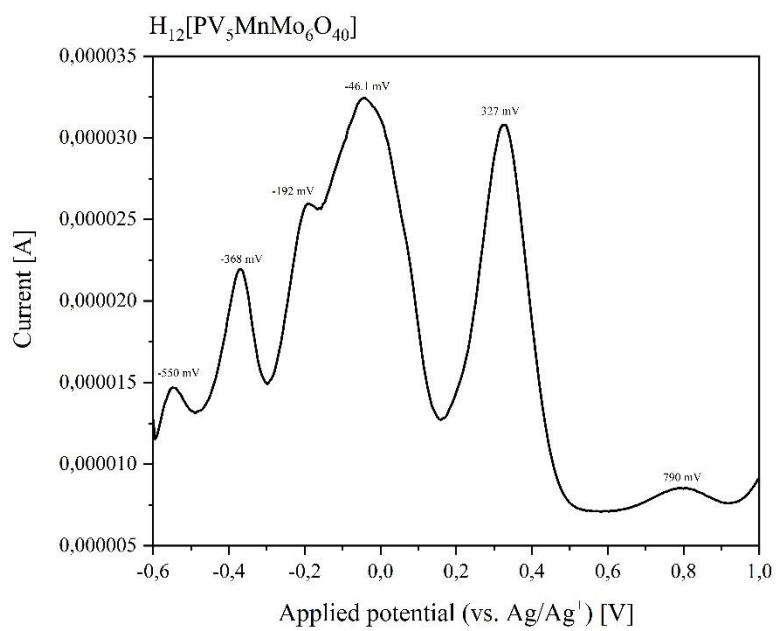
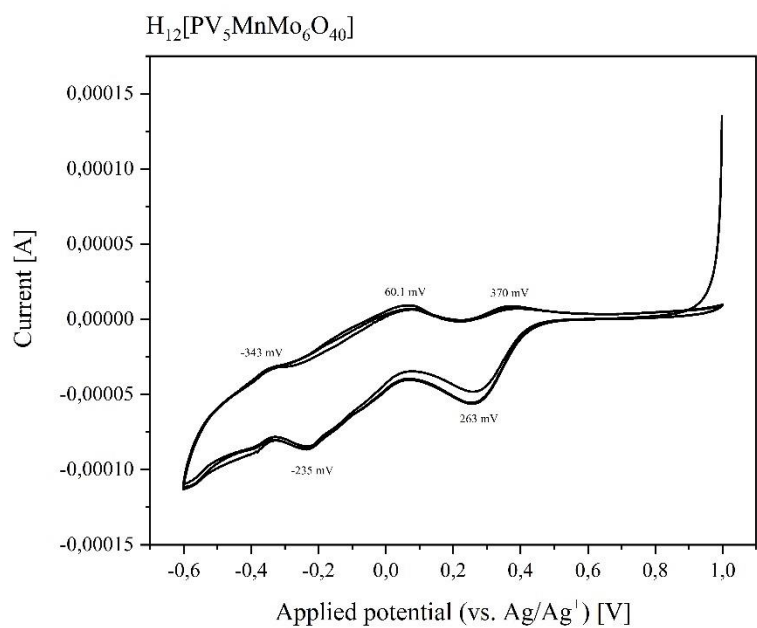


Figure S36. CV (top) and SWV (bottom) data of $H_{12}[PV_5MnMo_6O_{40}]$ in deionised water at pH 1 with a scan rate of 100 mV/s (CV) and 5 mV/s (SWV).

A picture of the cooled $\text{H}_6\text{V}_{10}\text{O}_{28}$ solution in water is shown in figure 37.



Figure S37. Solution of $\text{H}_6\text{V}_{10}\text{O}_{28}$ in water after adding V_2O_5 , hydrogen peroxide and water.

Figure 38 shows the mixture of MoO_3 , H_3PO_4 in water.



Figure S38. A mixture of MoO_3 and H_3PO_4 in water.

At high temperatures it forms a yellow solution (Figure 39).



Figure S39. After the suspension of MoO_3 and H_3PO_4 in water has been heated to boiling point for about one hour, a yellow, clear solution is formed.

After a clear yellow solution has formed, the pre-cooled $\text{H}_6\text{V}_{10}\text{O}_{28}$ solution is dropped into the refluxing solution (Figure 40).



Figure S40. The cooled solution of $\text{H}_9\text{PV}_{14}\text{O}_{42}$ in water is dropped into the boiling solution of MoO_3 and H_3PO_4 in water.

An aqueous manganese(II) acetate solution is dropped to the combined refluxing MoO_3 and $\text{H}_6\text{V}_{10}\text{O}_{28}$ solution (Figure 41 and 42).



Figure S41. An aqueous solution of manganese(II) acetate is added to the boiling solution of $\text{H}_9\text{PV}_{14}\text{O}_{42}$, MoO_3 and H_3PO_4 in water.

During the synthesis of $\text{H}_8\text{PVMnMo}_{10}\text{O}_{40}$ a red colour of the resulting reaction mixture was observed (Figure 42).



Figure S42. During the synthesis of $\text{H}_8[\text{PVMnMo}_{10}\text{O}_{40}]$ a red, clear reaction solution is formed.

2 Vibrational spectroscopy

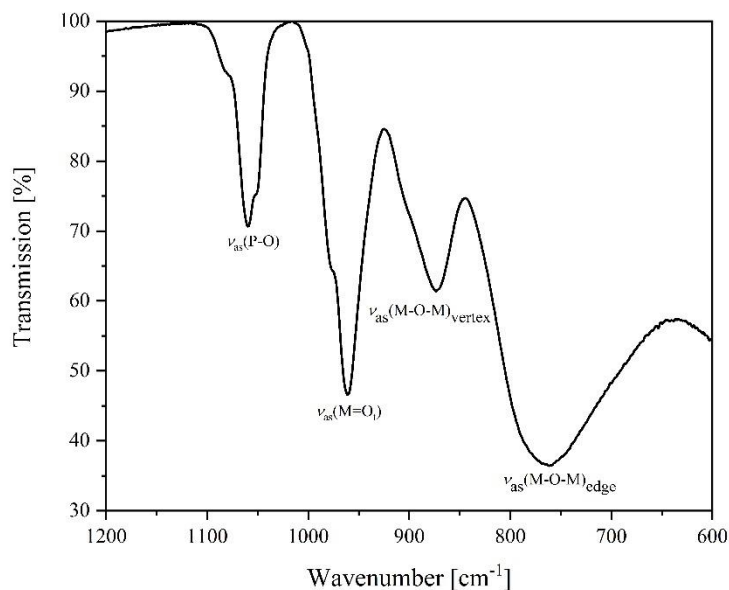


Figure S43. FT-IR spectrum of HPA-0-1 with the characteristic vibration modes: there are three main vibration modes in the IR spectrum of a Keggin POM: 1. The asymmetric P-O vibration between 1100 and 1000 cm^{-1} . 2. The M=O vibration of the terminal oxygen atoms between 950 and 1000 cm^{-1} . 3. The M-O-M vibration of the corner-linked octahedrons (vertex). 4. The M-O-M vibration of the edge-linked octahedrons (edge).^[9-14]

Table 1: Position of the characteristic vibration bands for HPA-X-Y POMs in the IR spectrum.

Vibration type	HPA-0-0	HPA-0-1	HPA-0-2	HPA-1-1	HPA-1-2	HPA-3-2	HPA-5-1
ν_{as} (P=O)	1059	1060	1059	1055	1053	1052	1049
(M=O _t)	962	961	954	959	953	951	945
(M-O-M) _{vertex}	877	874	874	871	869	866	870
(M-O-M) _{edge}	744	762	767	762	757	759	743

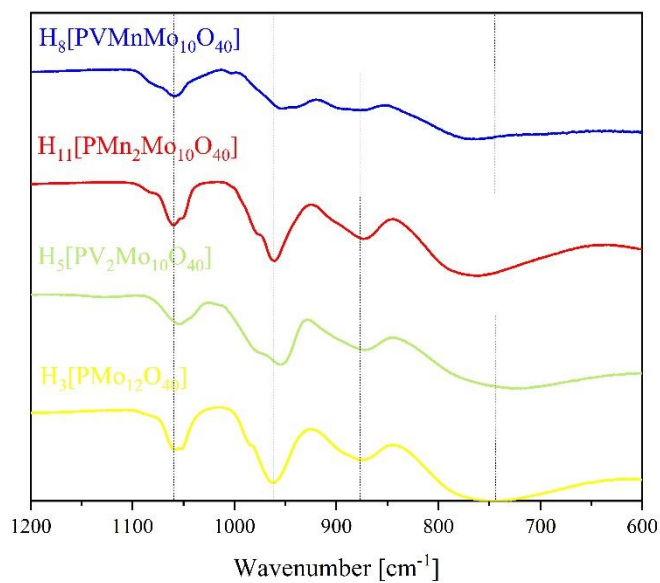


Figure S44. Superimposed IR spectra of the two metal-substituted POMs HPA-1-1, HPA-0-2 and HPA-2-0, compared with the IR spectrum of HPA-0-0.

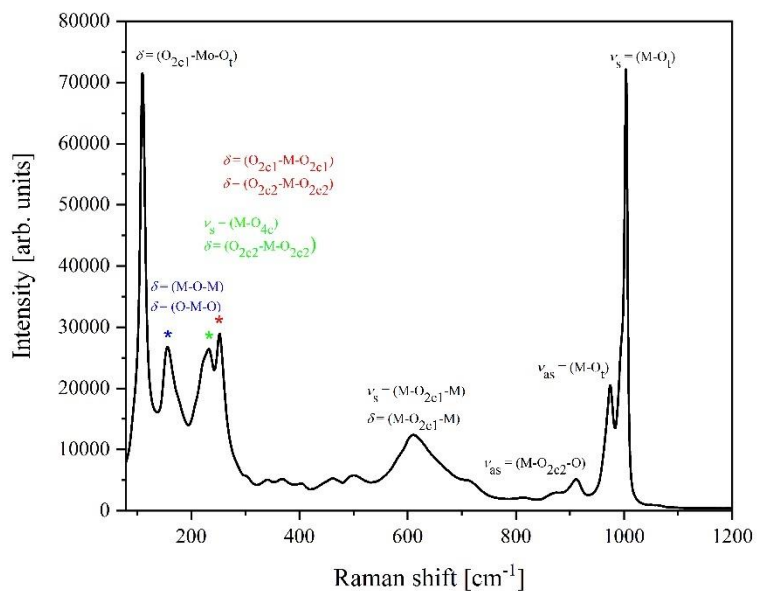


Figure S45. Raman spectrum using the example of HPA-0-1 with the characteristic vibration modes.^[12]

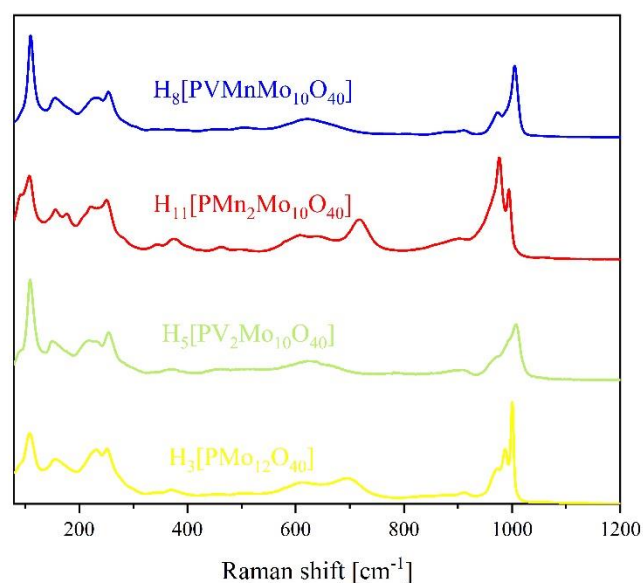


Figure S46. Superimposed Raman spectra of the two metal-substituted POMs HPA-1-1, HPA-0-2 and HPA-2-0, compared with the Raman spectrum of HPA-0-0.

Table 2: Position of the characteristic vibration modes for HPA-X-Y POMs in the Raman spectrum.

Vibration type	HPA-0-0	HPA-0-1	HPA-0-2	HPA-1-1	HPA-1-2	HPA-3-2	HPA-5-1
$\nu_{\text{as}}(\text{M}=\text{O}_t)$	1006	1004	-	-	-	-	1005
$\nu_{\text{as}}(\text{M}=\text{O}_t)$	987	975	969	980	994	956	967
$\nu_{\text{as}}(\text{M}=\text{O}_t)$	972	-	952	949	952	-	-
$\nu_{\text{as}}(\text{M}-\text{O}_{2c2}-\text{M})$	911	912	875	886	-	863	901
$\nu_{\text{as}}(\text{M}-\text{O}_{2c1}-\text{M})$	611	611	693	596	616	637	629
$\delta(\text{M}-\text{O}_{2c1}-\text{M})$							
$\delta(\text{M}-\text{O}_{2c2}-\text{M})$	459	-	439	-	-	493	-
$\delta(\text{M}-\text{O}_{2c1}-\text{M})$	-	-	-	-	-	381	-
$\delta(\text{M}-\text{O}_{2c2}-\text{M})$	369	-	350	-	-	-	-
$\delta(\text{O}_{2c1}-\text{M}-\text{O}_{2c1})$	252	253	226	230	255	249	264
$\delta(\text{O}_{2c2}-\text{M}-\text{O}_{2c2})$							
$\delta(\text{M}-\text{O}_{2c2}-\text{M})$	-	-	-	-	-	-	-
$\nu_{\text{s}}(\text{M}-\text{O}_{4c})$	232	233	198	206	229	-	229
$\delta(\text{M}-\text{O}_{2c2}-\text{M})$							
$\delta(\text{M}-\text{O}_{2c2}-\text{M})$	-	-	153	-	-	-	-
$\delta(\text{O}_{2c1}-\text{M}-\text{O}_t)$	-	-	-	-	-	-	-
$\delta(\text{M}-\text{O}-\text{M})$	156	157	131	130	157	152	155
$\delta(\text{O}-\text{M}-\text{O})$							
$\delta(\text{O}_{2c1}-\text{M}-\text{O}_t)$	109	111	84	86	115	108	115
$\delta(\text{M}-\text{O}-\text{M})$	-	-	-	-	-	-	-
$\delta(\text{O}-\text{M}-\text{O})$							
$\nu_{\text{s}}(\text{M}-\text{O}_t)$	-	-	-	-	-	-	-

Table 3: IR data of Mn(II) substituted POMs compared to the literature IR data of only V(V) substituted HPA-X-0 POMs.^[9]

POM	(P=O)	(M=O) _t	(M-O-M) _{vertex}	(M-O-M) _{edge}
HPA-1-0 H ₄ [PVMo ₁₁ O ₄₀] ^[9]	1052	952	877	740
HPA-0-1 H ₇ [PMnMo ₁₁ O ₄₀]	1060	961	874	762
HPA-2-0 H ₅ [PV ₂ Mo ₁₀ O ₄₀] ^[9]	1051	951	873	740
HPA-0-2 H ₁₁ [PMn ₂ Mo ₁₀ O ₄₀]	1059	954	874	767
HPA-1-1 H ₈ [PVMnMo ₁₀ O ₄₀]	1055	959	871	762
HPA-3-0 H ₆ [PV ₃ Mo ₉ O ₄₀] ^[9]	1048	948	871	735
HPA-1-2 H ₁₂ [PVMn ₂ Mo ₉ O ₄₀]	1053	953	869	757
HPA-5-0 H ₈ [PV ₅ Mo ₇ O ₄₀] ^[9]	1045	948	864	730
HPA-3-2 H ₁₄ [PV ₃ Mn ₂ Mo ₇ O ₄₀]	1052	951	866	759
HPA-6-0 H ₉ [PV ₆ Mo ₆ O ₄₀] ^[9]	1041	948	864	730
HPA-5-1 H ₁₀ [PV ₅ MnMo ₆ O ₄₀]	1049	945	870	743

3 Crystallography

The crystallographic data are provided free of charge by the joint Cambridge Crystallographic Data Centre and Fachinformationszentrum Karlsruhe. Deposition Number(s): 2141261 (for HPA-0-1), 2141263 (for HPA-0-2), 2141259 (for HPA-1-1), 2141262 (for HPA-1-2), 2141260 (for HPA-5-1)

Table 4 shows the lattice parameters (a , b and c) and lattice angles (α , β , γ) of HPA- X - Y compounds obtained from single crystal structure data.

Table 4: Space groups and lattice parameters (lattice constants a , b and c as well as lattice angles α , β and γ) obtained from the single crystal structure data of the POMs.

POM	Space group	a [Å]	b [Å]	c [Å]	α [°]	β [°]	γ [°]
H₇[PMnMo₁₁O₄₀]	Fd-3 (cubic 203)	23.01855(6)			90		
H₁₁[PMn₂Mo₁₀O₄₀]	Fd-3 (cubic 203)	22.98263(8)			90		
H₈[PVMnMo₁₀O₄₀]	Fd-3m (cubic 227)	22.97592(14)			90		
H₁₂[PVMn₂Mo₉O₄₀]	Fd-3m (cubic 227)	23.0200(1)			90		
H₁₂[PV₅MnMo₆O₄₀]	R-3 (trigonal 148)	15.2266(1)	38.8918(3)		90	120	

Table 5 shows characteristic bond lengths of the POMs obtained from single crystal structure data:

Table 5: Characteristic bond lengths of the respective unit cell obtained from the single crystal structure data of the POMs.

POM	Bond P₁-O₁ [Å]	Bond O₂-M₁ [Å]	Bond M₁-O_{2,3} [Å]	Bond M₁-O₄ [Å]
H₇[PMnMo₁₁O₄₀]	1.536	2.433	1.828, 1.849	1.681
H₁₁[PMn₂Mo₁₀O₄₀]	1.539	2.430	1.824, 1.848	1.678
H₈[PVMnMo₁₀O₄₀]	1.537	2.422	1.902, 1.923	1.663
H₁₂[PVMn₂Mo₉O₄₀]	1.532	2.425	1.901, 1.924	1.666
H₁₂[PV₅MnMo₆O₄₀]	1.542, 1.543	2.404	1.798-2.044	1.632, 1.639, 1.644

Note: For H₁₂[PV₅MnMo₆O₄₀] there are four metal atoms in the asymmetric unit.

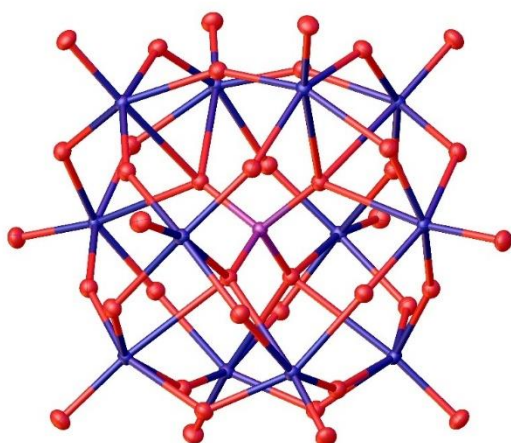


Figure S47. Solid state structure of HPA-0-1. Space group Fd-3 (203). There are six atoms in the asymmetric unit and eight formula units per elementary cell. Residual electron density attributed to hydration water has been refined with a solvent mask (aka SQUEEZE). R_1 : 1.39, wR_2 : 4.21 %, R_{int} : 3.65 %, $Goof$: 1.150. Purple: phosphorous, red: oxygen, and blue: metals (Mo, Mn).

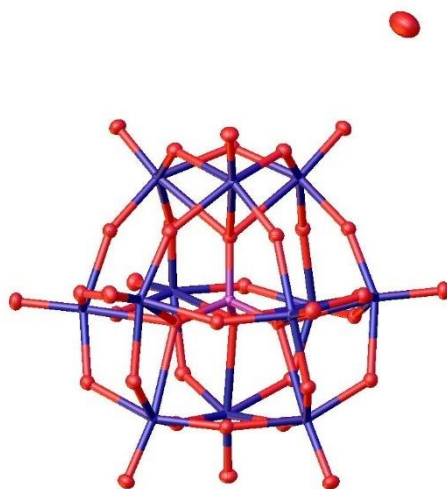


Figure S48. Solid state structure of HPA-0-2. Space group Fd-3 (203). There are six atoms in the asymmetric unit and eight formula units per elementary cell. Residual electron density attributed to hydration water has been refined with a solvent mask (aka SQUEEZE). R_1 : 1.52, wR_2 : 4.25 %, R_{int} : 3.74 %, $Goof$: 1.099. Purple: phosphorous, red: oxygen, and blue: metals (Mo, Mn).

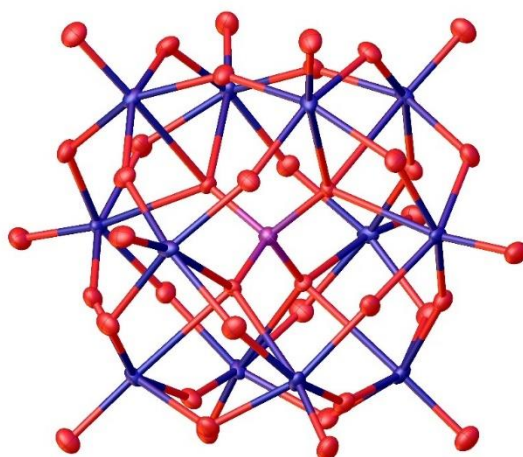


Figure S49. Solid state structure of HPA-1-1. Space group $Fd-3m$ (227). There are six atoms in the asymmetric unit and eight formula units per elementary cell. Residual electron density attributed to hydration water has been refined with a solvent mask (aka SQUEEZE). R_1 : 2.65, wR_2 : 6.03 %, R_{int} : 2.78 %, $Goof$: 1.213. Purple: phosphorous, red: oxygen, and blue: metals (Mo, V, Mn).

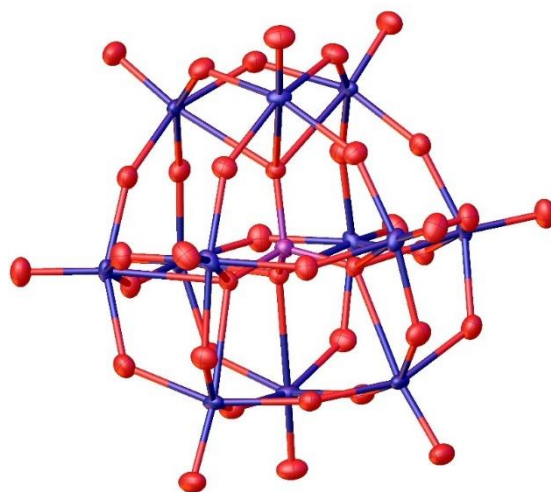


Figure S50. Solid state structure of HPA-1-2. Space group $Fd-3m$ (227). There are six atoms in the asymmetric unit and eight formula units per elementary cell. Residual electron density attributed to hydration water has been refined with a solvent mask (aka SQUEEZE). R_1 : 2.75, wR_2 : 6.83 %, R_{int} : 4.52 %, $Goof$: 1.216. Purple: phosphorous, red: oxygen, and blue: metals (Mo, V, Mn).

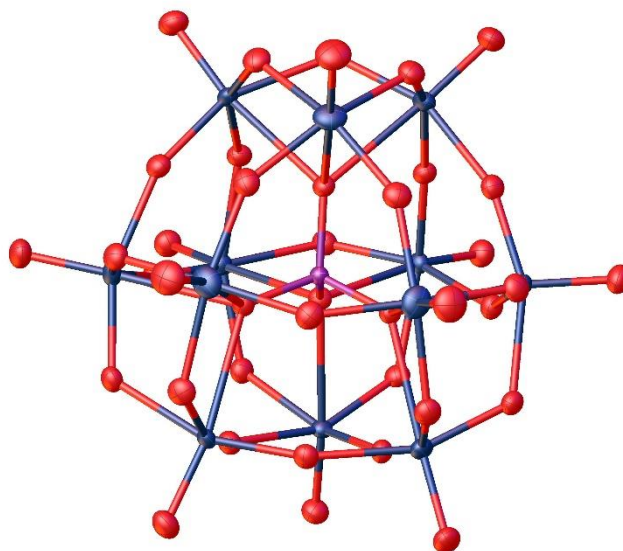


Figure S51. Solid state structure of HPA-5-1. Space group R-3 (148). There are eighteen atoms in the asymmetric unit and six formula units per elementary cell. Residual electron density attributed to hydration water has been refined with a solvent mask (aka SQUEEZE). R_1 : 3.77, wR_2 : 12.03 %, R_{int} : 3.56 %, $Goof$: 1.066. Purple: phosphorous, red: oxygen, and blue: metals (Mo, V, Mn).

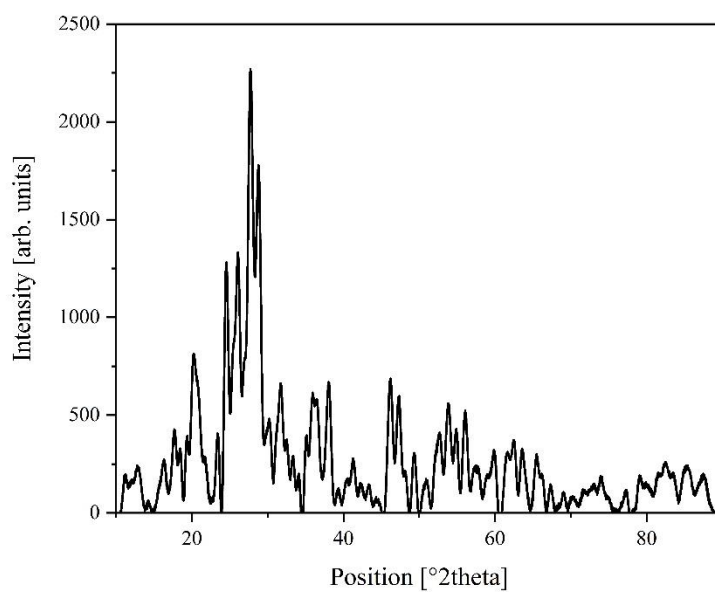


Figure S52. Powder XRD data of H₃[PMo₁₂O₄₀].

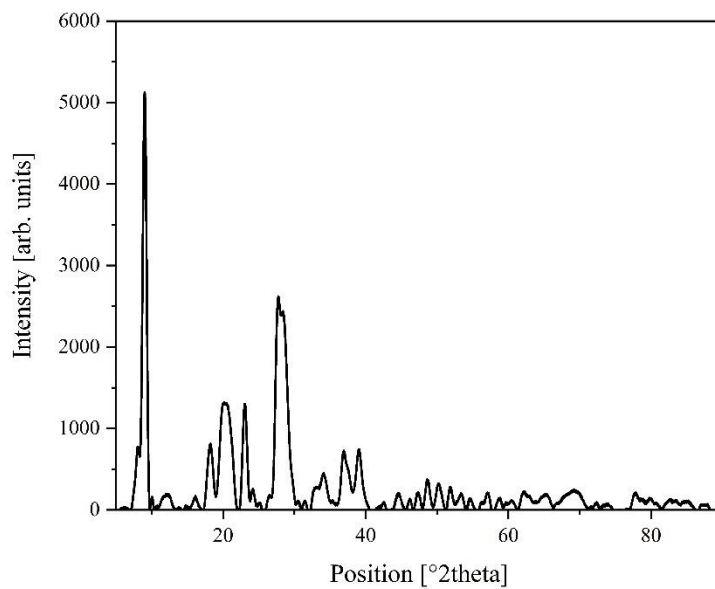


Figure S53. Powder XRD data of H₇[PMnMo₁₁O₄₀].

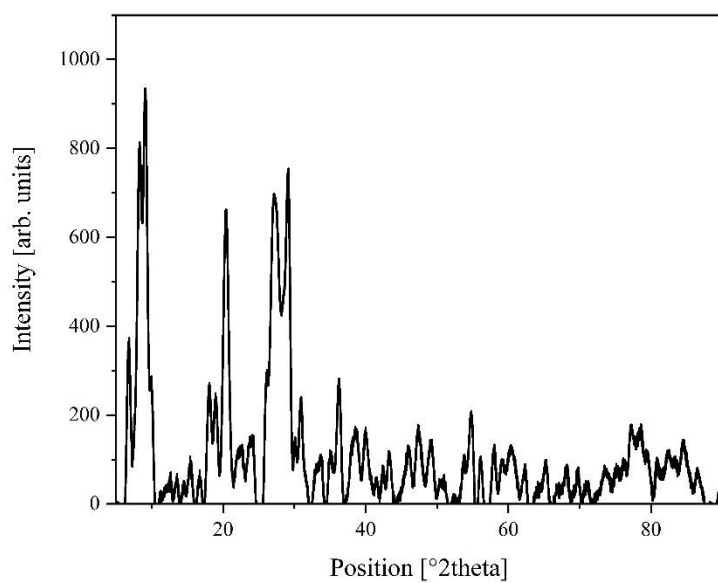


Figure S54. Powder XRD data of $H_{11}[PMn_2Mo_{10}O_{40}]$.

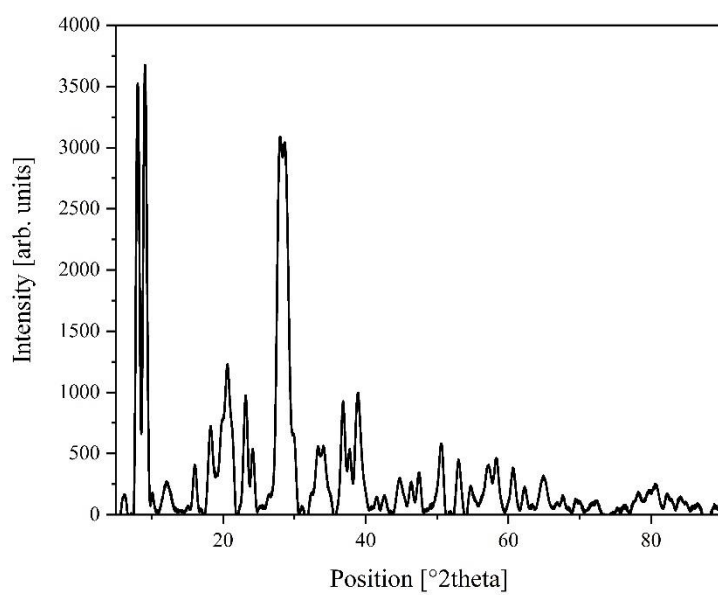


Figure S55. Powder XRD data of $H_8[PVMnMo_{10}O_{40}]$.

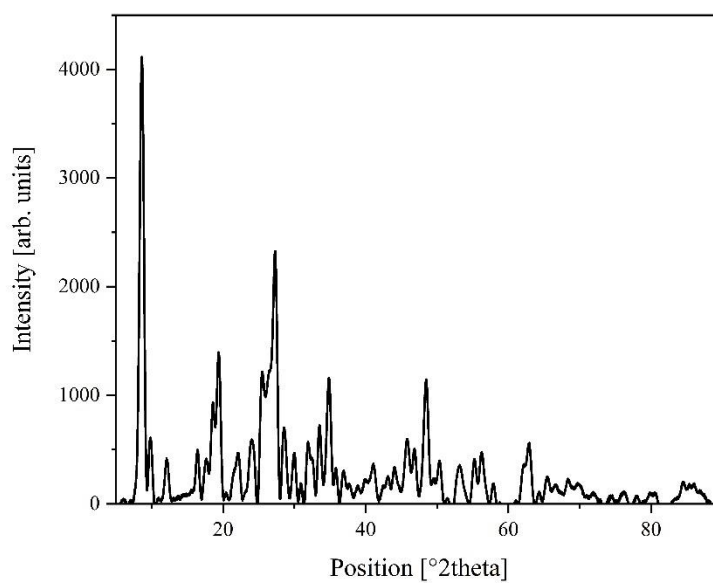


Figure S56. Powder XRD data of $H_{12}[PVMn_2Mo_9O_{40}]$.

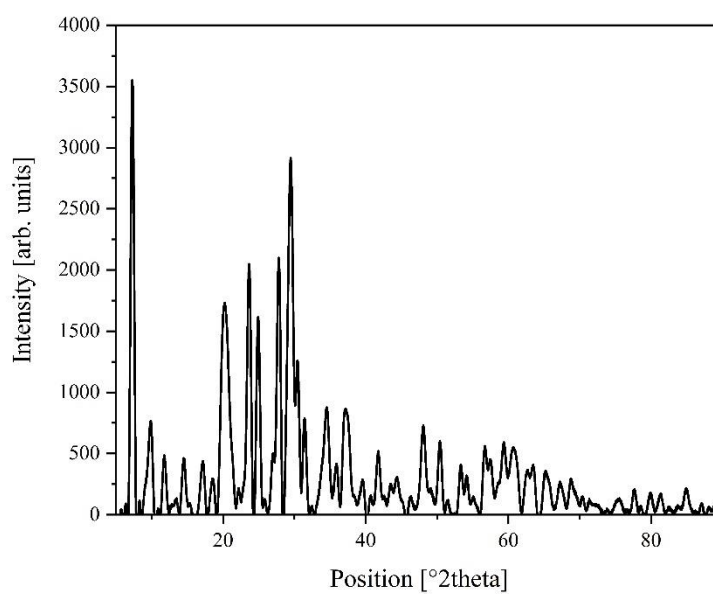


Figure S57. Powder XRD data of $H_{14}[PV_3Mn_2Mo_7O_{40}]$.

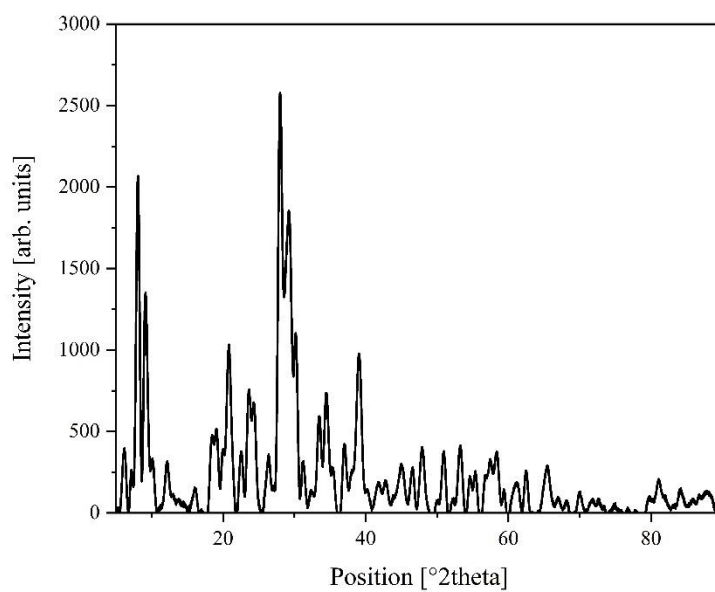


Figure S58. Powder XRD data of $\text{H}_{12}[\text{PV}_5\text{MnMo}_6\text{O}_{40}]$.

4 Nuclear magnetic resonance spectroscopy

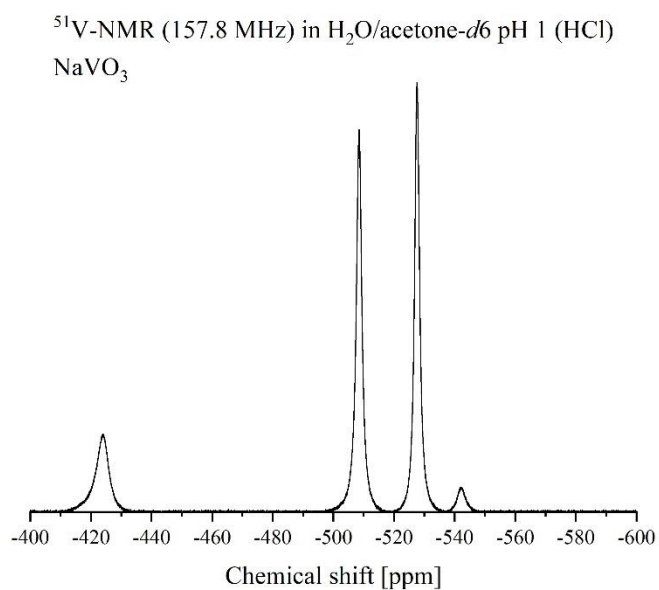
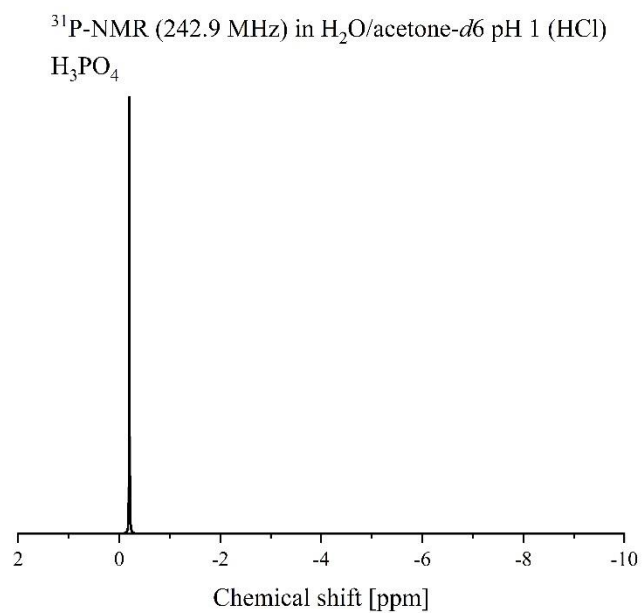


Figure S59. Reference spectra (242.9 MHz and 157.8 MHz): ^{31}P -NMR of phosphoric acid and ^{51}V -NMR of sodium vanadate in a mixture of 90 % water (pH 1) and 10 % acetone- d_6 .

Figure S59 shows the reference spectra of H_3PO_4 and NaVO_3 .

5 UV-Vis spectroscopy

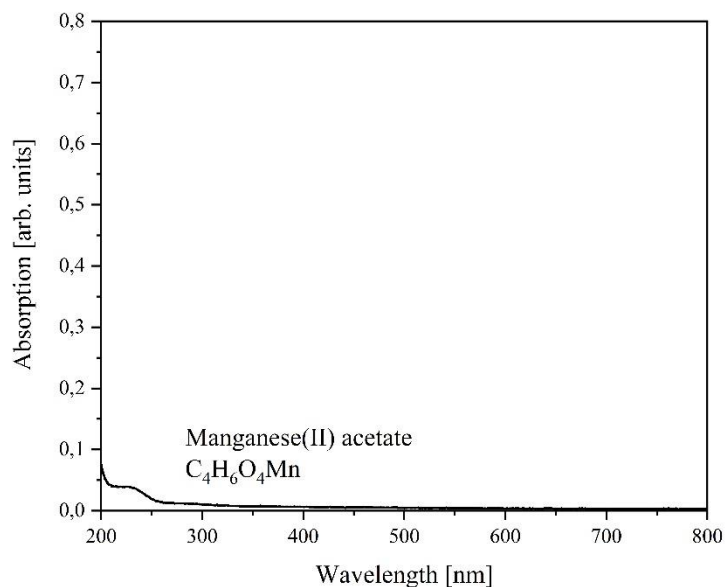


Figure S60. UV-Vis spectrum of manganese(II) acetate in water (range 200-800 nm). There is no significant LMCT peak in the spectrum for Mn(II) (20 $\mu\text{g/mL}$).

The POMs HPA- X -0 with $X = 1$ to 6 were synthesized according to Odyakov *et al.*^[1,2,15] and the UV-Vis spectra were measured under the same conditions and the results are found in Table 6.

Table 6: LMCT (peak maxima) from UV-Vis spectra of all compounds in water. Comparison of the LMCT values from HPA- X - Y to the LMCT values of HPA- X -0 (with $X = 0, 1$ to 6).

Compound	LMCT [nm]	
	O \rightarrow Mo(VI)O ₆	O \rightarrow V(V)O ₆
HPA-0-0 H ₃ [PMo ₁₂ O ₄₀]	218	-
HPA-1-0 H ₄ [PVMo ₁₁ O ₄₀]	219	320
HPA-0-1 H ₇ [PMnMo ₁₁ O ₄₀]	211	-
HPA-2-0 H ₅ [PV ₂ Mo ₁₀ O ₄₀]	213	302
HPA-0-2 H ₁₁ [PMn ₂ Mo ₁₀ O ₄₀]	210	-
HPA-1-1 H ₈ [PVMnMo ₁₀ O ₄₀]	210	311
HPA-3-0 H ₆ [PV ₃ Mo ₉ O ₄₀]	216	311
HPA-1-2	211	309

$H_{12}[PVMn_2Mo_9O_{40}]$		
HPA-5-0		
$H_8[PV_5Mo_7O_{40}]$	216	312
HPA-3-2		
$H_{14}[PV_3Mn_2Mo_7O_{40}]$	215	305
HPA-6-0		
$H_9[PV_6Mo_6O_{40}]$	217	312
HPA-5-1		
$H_{12}[PV_5MnMo_6O_{40}]$	214	310

6 Electrochemistry

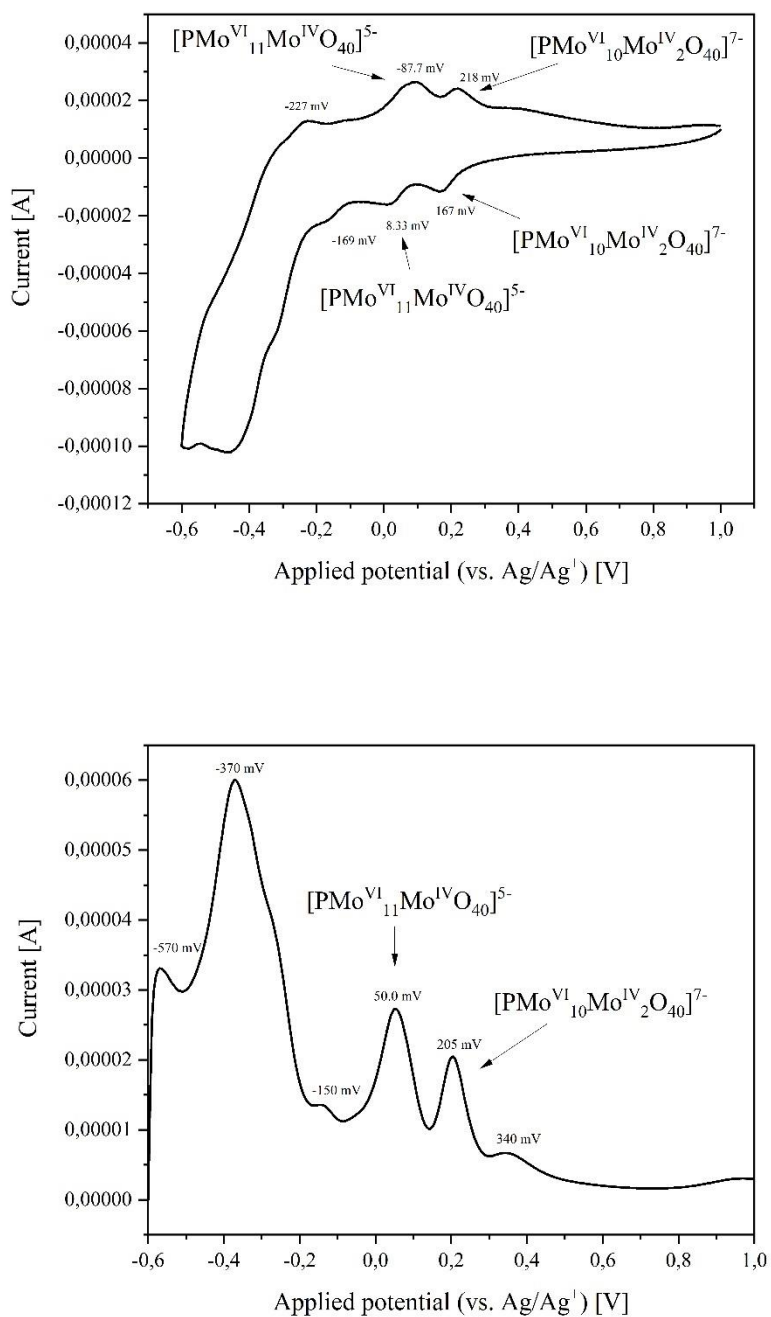


Figure S61. CV (top) and SWV (bottom) data of the POM HPA-0-0 (1 mmol/L) as reference in deionised water at pH 1 with a scan rate of 100 mV/s (CV) and 5 mV/s (SWV).

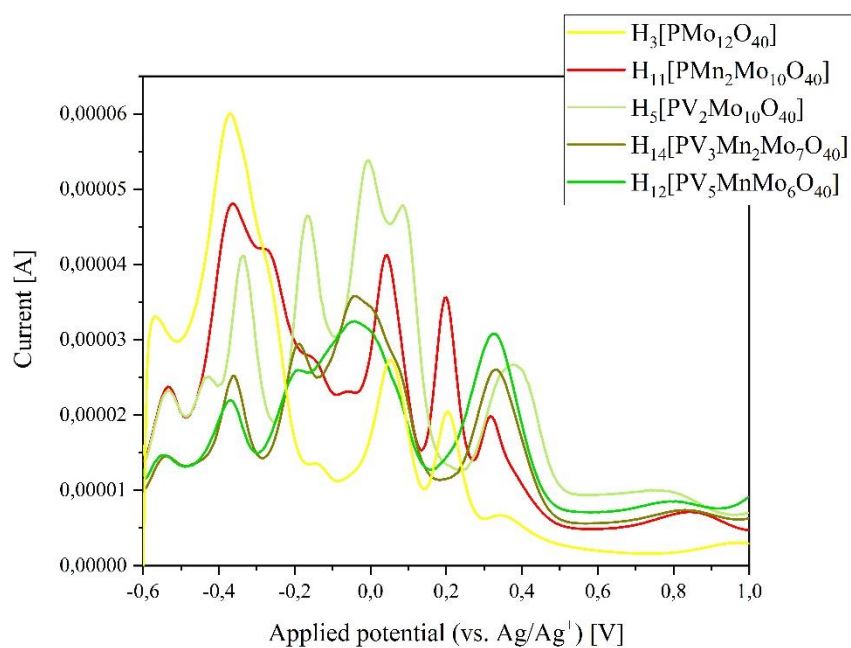
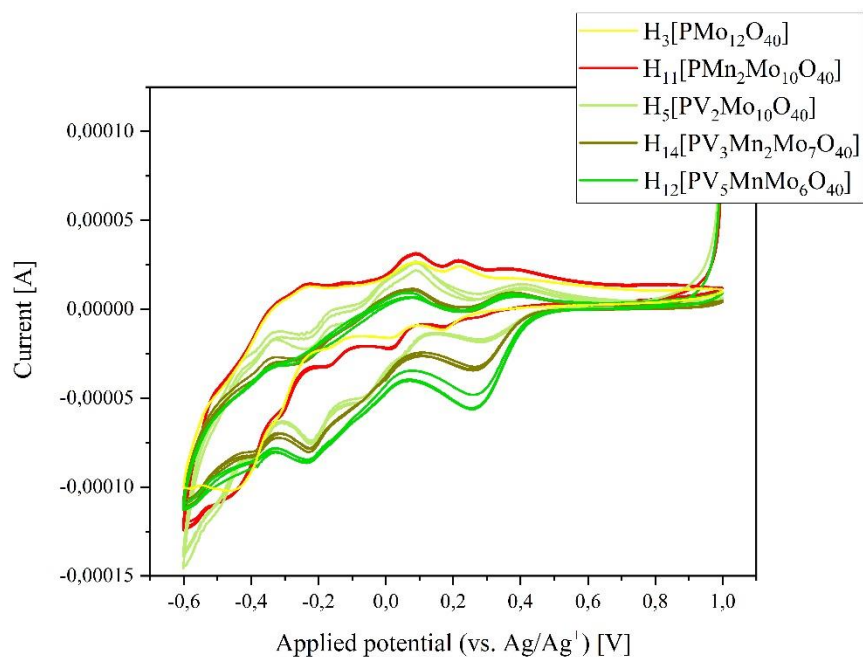


Figure S62. CV (top) and SWV (bottom) data of the POMs HPA-3-2 and HPA-5-1 compared with HPA-2-0, HPA-0-2 and HPA-0-0. The signals between -200 mV and 200 mV merge with increasing V(V) content (1 mmol/L).

The plot in Figure S62 shows the CV/SWV data of the POMs $H_{14}[PV_3Mn_2Mo_7O_{40}]$ and $H_{12}[PV_5MnMo_6O_{40}]$ in comparison with $H_3[PMo_{12}O_{40}]$, $H_5[PV_2Mo_{10}O_{40}]$ and $H_{11}[PMn_2Mo_{10}O_{40}]$ to visualize the significant differences between the low and high substituted POMs.

Table 7: Peak maxima from SWV data, peak maxima (oxidation pathway) and peak minima (reduction pathway) from the CV data of the HPA-X-Y POMs in solution (solvent water) at pH 1 (HCl): concentration 1 mmol/L: scan rate 100 mV/s (CV) and 5 mV/s (SWV).

Peak maxima SWV [mV]	Maximum oxidation pathway [mV]	Minimum reduction pathway [mV]	Mean value [mV]
H₇PMnMo₁₁O₄₀			
-540	-521	-528	-525
-358	-	-365	-
-268	-243	-194	-219
-162	-	-	-
-66.2	-	-	-
39.5	99.2	11.3	55.3
201	214	171	193
342	368	-	-
906	-	-	-
H₁₁PMn₂Mo₁₀O₄₀			
-535	-511	-	-
-363	-	-313	-
-283	-226	-	-
-172	-125	-169	-147
-61.2	-	-	-
46.6	89.4	21.1	55.3
201	216	175	196
316	360	-	-
845	-	-	-
H₈PVMnMo₁₀O₄₀			
-550	-531	-	-
-439	-414	-477	446
-338	-316	-374	345
-172	-152	-199	176
-15.9	6.41	-52.2	-22.9
79.8	99.2	52.8	76.0
392	426	360	393
H₁₂PVMn₂Mo₉O₄₀			
-545	-521	-	-
-439	-432	-489	-461
-338	-316	-372	-344
-172	-152	-199	-176
-15.9	-	-47.3	-
-	1.53	-	-
74.8	96.7	45.5	72.0
397	421	356	389
785	-	-	-
H₁₄PV₃Mn₂Mo₇O₄₀			
-540	-533	-	-
-363	-340	-409	-375
-187	-162	-230	-196

-41.0	-	-	-
-	67.4	-	-
332	370	265	318
830	-	-	-
H₁₂PV₅MnMo₆O₄₀			
-550	-	-	-
-368	-343	-	-
-	-	-235	-
-192	-	-	-
-46.1	-	-	-
-	60.1	-	-
-	-	263	-
327	370	-	-
790	-	-	-

7 References

- [1] V. F. Odyakov, E. G. Zhizhina, R. I. Maksimovskaya, *Appl. Catal. A Gen.* **2008**, *342*, 126–130.
- [2] V. F. Odyakov, E. G. Zhizhina, *Russ. J. Inorg. Chem.* **2009**, *54*, 361–367.
- [3] O. V. Dolomanov, L. J. Bourhis, R. J. Gildea, J. A. K. Howard, H. Puschmann, *J. Appl. Crystallogr.* **2009**, *42*, 339–341.
- [4] C. B. Hübschle, G. M. Sheldrick, B. Dittrich, *J. Appl. Crystallogr.* **2011**, *44*, 1281–1284.
- [5] A. L. Spek, *J. Appl. Crystallogr.* **2003**, *36*, 7–13.
- [6] G. M. Sheldrick, *Acta Crystallogr. Sect. A Found. Crystallogr.* **2008**, *64*, 112–122.
- [7] A. L. Spek, *Acta Crystallogr. Sect. D Biol. Crystallogr.* **2009**, *65*, 148–155.
- [8] A. L. Spek, *Acta Crystallogr. Sect. C Struct. Chem.* **2015**, *71*, 9–18.
- [9] J. Albert, D. Lüders, A. Bösmann, D. M. Guldi, P. Wasserscheid, *Green Chem.* **2014**, *16*, 226–237.
- [10] J. K. Lee, J. Melsheimer, S. Berndt, G. Mestl, R. Schlögl, K. Köhler, *Appl. Catal. A Gen.* **2001**, *214*, 125–148.
- [11] S. Sheshmani, M. A. Fashapoyeh, M. Mirzaei, B. A. Rad, S. N. Ghortolmesh, M. Yousefi, *Indian J. Chem. - Sect. A Inorganic, Phys. Theor. Anal. Chem.* **2011**, *50*, 1725–1729.
- [12] A. J. Bridgeman, *Chem. - A Eur. J.* **2004**, *10*, 2935–2941.
- [13] K. Bruckman, J. Haber, E. M. Serwicka, E. N. Yurchenko, T. P. Lazarenko, *Catal. Letters* **1990**, *4*, 181–189.
- [14] R. Thouvenot, M. Fournier, R. Franck, C. Rocchiccioli-Deltcheff, *Inorg. Chem.* **1984**, *23*, 598–605.
- [15] V. F. Odyakov, E. G. Zhizhina, *React. Kinet. Catal. Lett.* **2008**, *95*, 21–28.

Comparative spectroscopic and electrochemical study of V(V) substituted Keggin-type phosphomolybdates and -tungstates

Supplementary Information

Jan-Christian Raabe ¹, José Aceituno Cruz ¹, Jakob Albert ¹, Maximilian J. Poller ^{1,*}

¹Institute for Technical and Macromolecular Chemistry, Universität Hamburg, Bundesstraße 45, 20146 Hamburg, Germany

*Correspondence: Author

Content

1	Additional data	2
2	Experimental Details	29
2.1	Chemicals	30
2.2	Analytics	31
2.3	Synthesis of Na _{9-x} H _x [PW ₉ O ₃₄] · x H ₂ O according to Domaille <i>et al.</i> ^[1]	35
2.4	Synthesis of Na ₄ [PVW ₁₁ O ₄₀] · 9 H ₂ O according to Domaille <i>et al.</i> ^[1]	37
2.5	Synthesis of Na ₅ [PV ₂ W ₁₀ O ₄₀] · 14 H ₂ O according to a modified procedure of Domaille <i>et al.</i> ^[1]	38
2.6	Synthesis of Na ₆ [PV ₃ W ₉ O ₄₀] · 13 H ₂ O according to Domaille <i>et al.</i> ^[1]	39
2.7	Synthesis of Na _y H _z [PV _x W _{12-x} O ₄₀] with x = 4 to 6 according to a modified procedure of Odyakov <i>et al.</i> ^[2-4]	40
2.8	Etherate method	43
2.9	Crystallography	45
3	References	46

1 Additional data

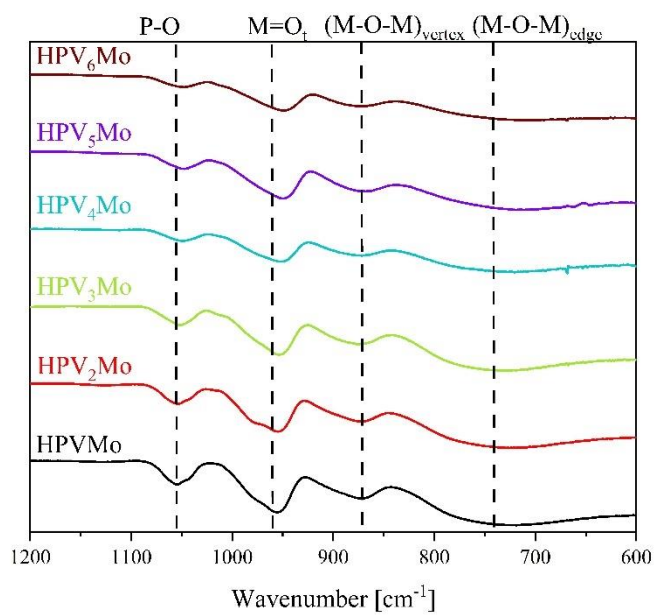


Figure S1: ATR-FT-IR spectra of the POMs HPV_xMo with $x = 1$ to 6.

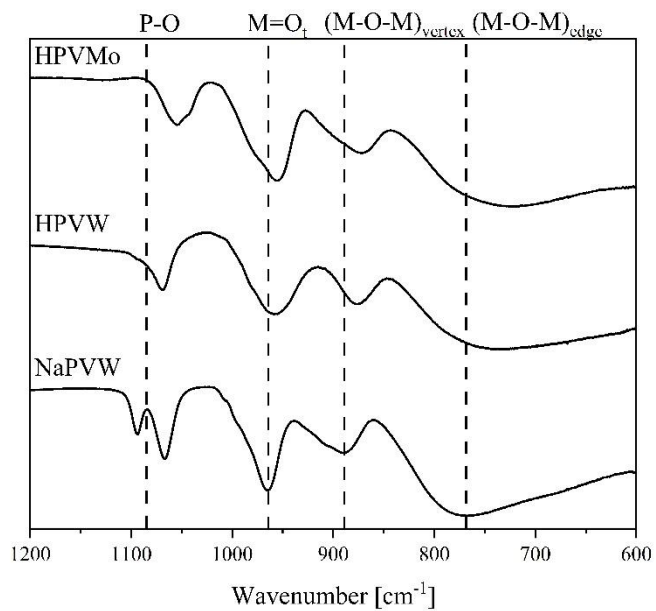


Figure S2: ATR-FT-IR spectra of the POMs NaPVW, HPVW and HPVMo.

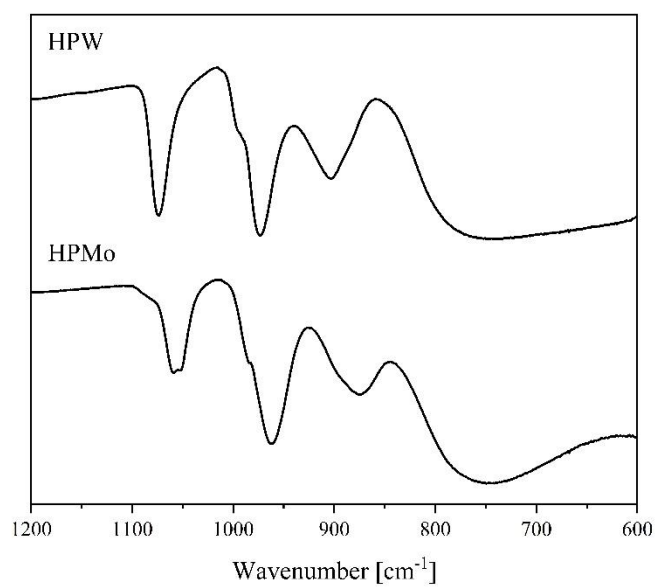


Figure S3: ATR-FT-IR spectra of the POMs HPMo and HPW.

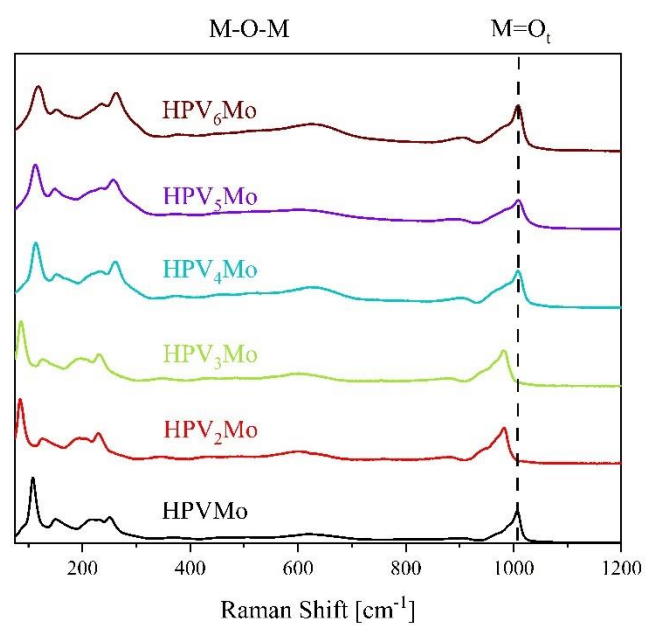


Figure S4: Raman spectra of the POMs HPV_xMo with $x = 1$ to 6.

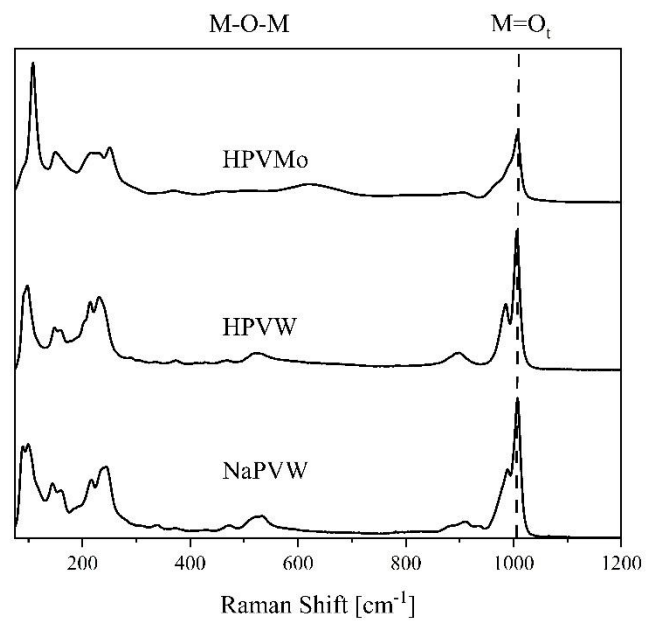


Figure S5: Raman spectra of the POMs NaPVW, HPVW and HPVMo.

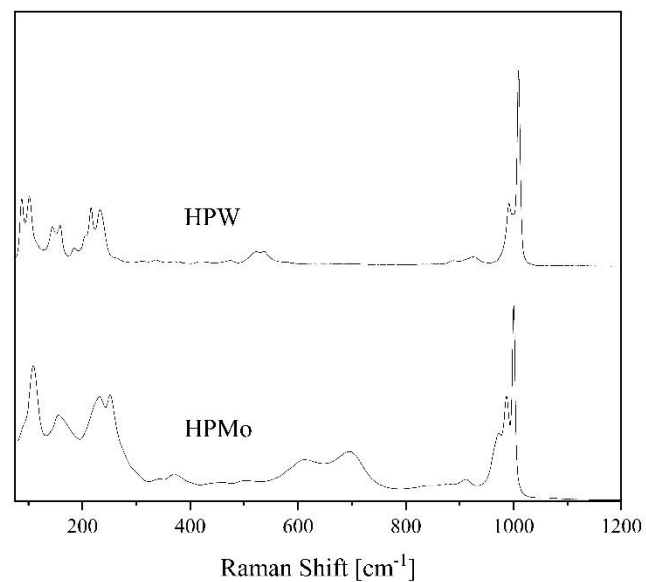


Figure S6: Raman spectra of the POMs HPMo and HPW.

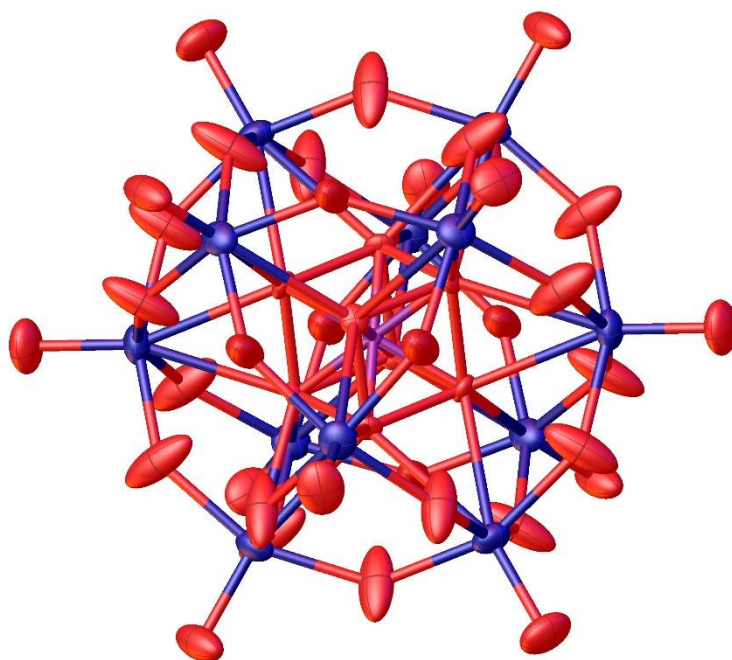


Figure S7: Solid-state structure of compound NaPV_2W determined by X-ray diffraction. The compound was crystallized in the space group $P4/mnc$ (128). Residual electron density attributed to hydration water has been refined with a solvent mask (aka SQUEEZE). R_1 : 2.86 %, wR_2 : 7.35 %, R_{int} : 5.21 %, GooF: 1.061. Colour code: Purple: phosphorous, red: oxygen, and blue: metals (W, V).

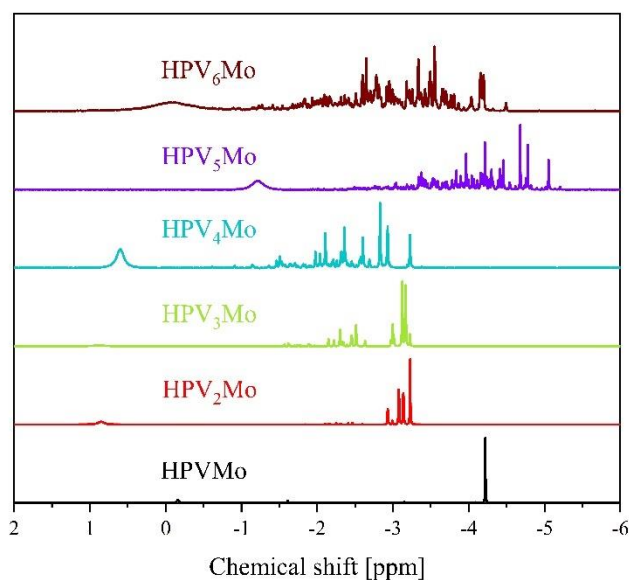


Figure S8: ^{31}P -NMR spectra of the POMs HPV_xMo with $x = 1$ to 6 . All spectra were measured in a mixture of 90 % water (pH 1) and 10 % acetone- d_6 . Measurement frequency: 242.9 MHz. 85 % H_3PO_4 was used as external standard.

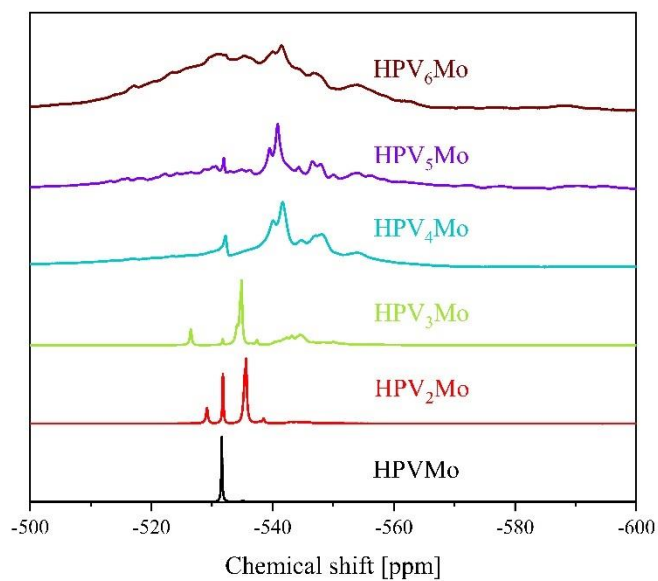


Figure S9: ^{51}V -NMR spectra of the POMs HPV_xMo with $x = 1$ to 6. All spectra were measured in a mixture of 90 % water (pH 1) and 10 % acetone- d_6 . Measurement frequency: 157.8 MHz. NaVO_3 was used as external standard.

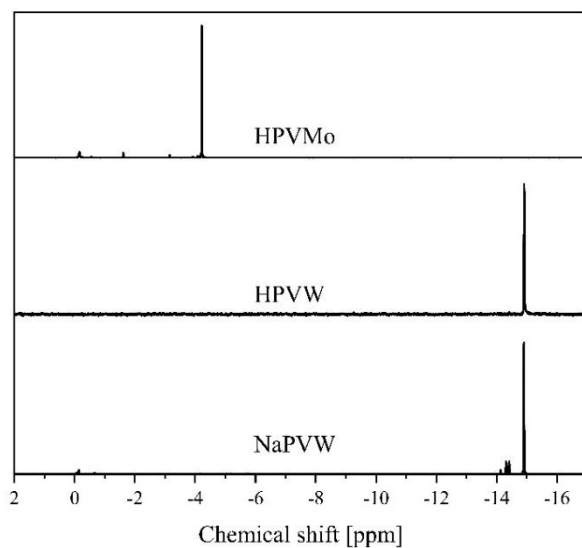


Figure S10: ^{31}P -NMR spectra of the POMs NaPVW, HPVW and HPVMo. Spectra for NaPVW and HPVW were measured in a mixture of 70 % water (pH 1) and 30 % D_2O and spectra for HPV $_2$ Mo were measured in a mixture of 90 % water (pH 1) and 10 % acetone- d_6 . Measurement frequency: 242.9 MHz. 85 % H_3PO_4 was used as external standard.

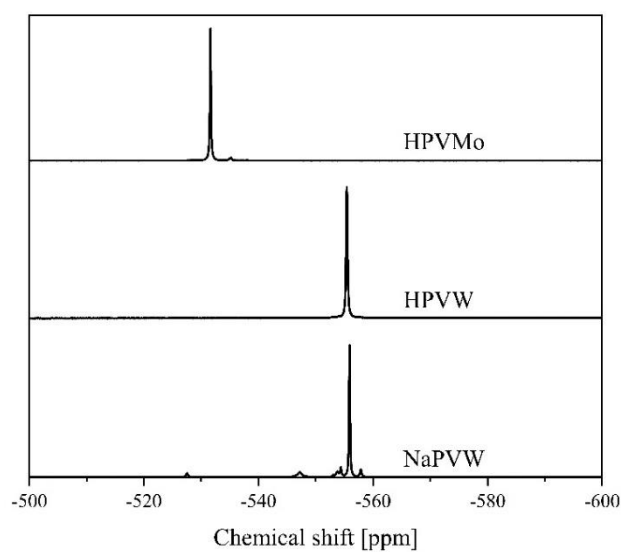


Figure S11: ^{51}V -NMR spectra of the POMs NaPVW, HPVW and HPV₂Mo. Spectra for NaPVW and HPVW were measured in a mixture of 70 % water (pH 1) and 30 % D₂O and spectra for HPV₂Mo were measured in a mixture of 90 % water (pH 1) and 10 % acetone-*d*₆. Measurement frequency: 157.8 MHz. NaVO₃ was used as external standard.

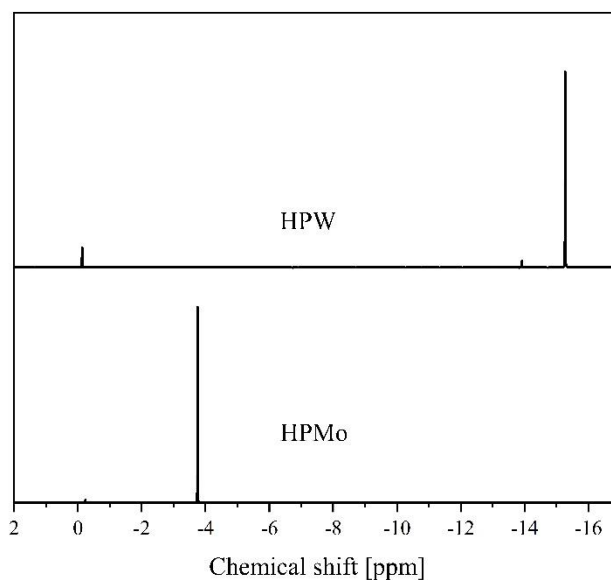


Figure S12: ^{31}P -NMR spectra of the HPMo and HPW. The spectrum for HPW was measured in a mixture of 70 % water (pH 1) and 30 % D₂O and the spectrum for HPMo was measured in a mixture of 90 % water (pH 1) and 10 % acetone-*d*₆. Measurement frequency: 242.9 MHz. 85 % H₃PO₄ was used as external standard.

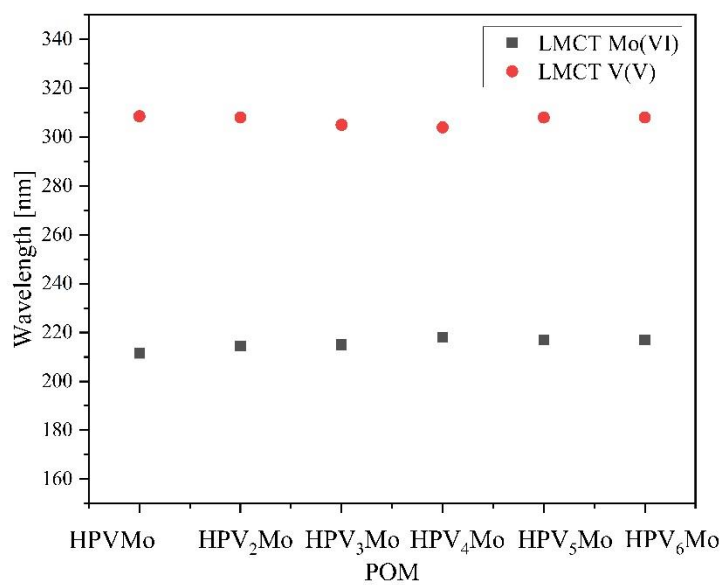


Figure S13: Plot of LMCT maxima vs. HPV_xMo.

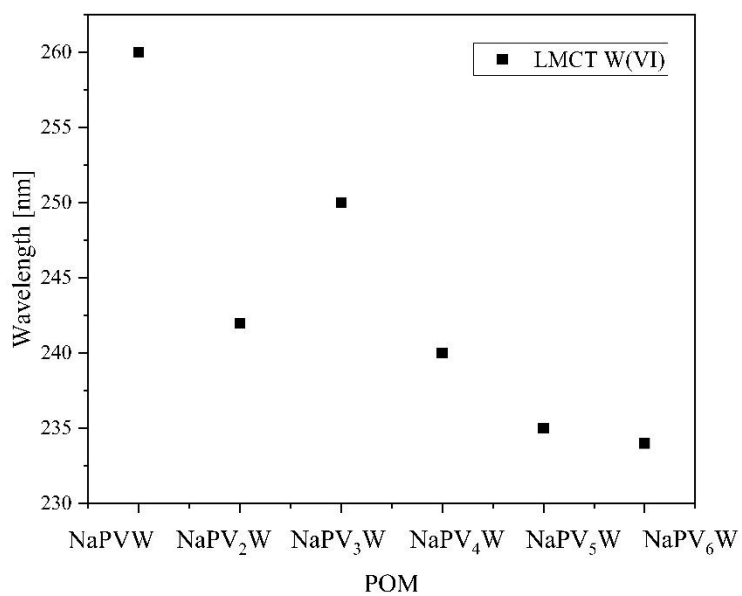


Figure S14: Plot of LMCT maxima vs. degree of substitution in NaPV_xW.

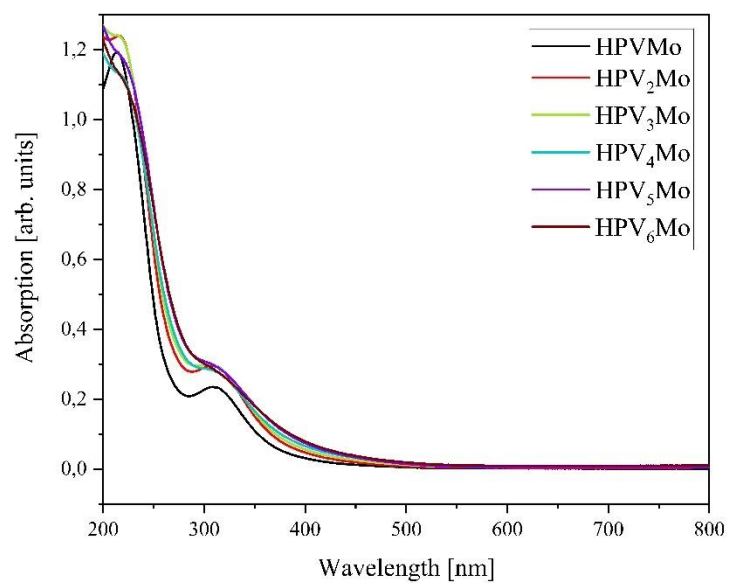


Figure S15: UV-Vis spectra of the POMs HPV_xMo with $x = 1$ to 6.

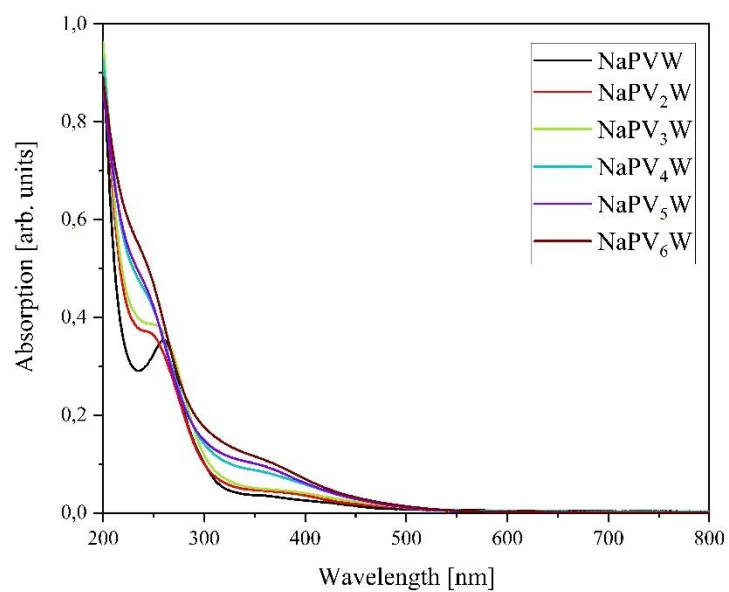


Figure S16: UV-Vis spectra of the POMs NaPV_xW with $x = 1$ to 6.

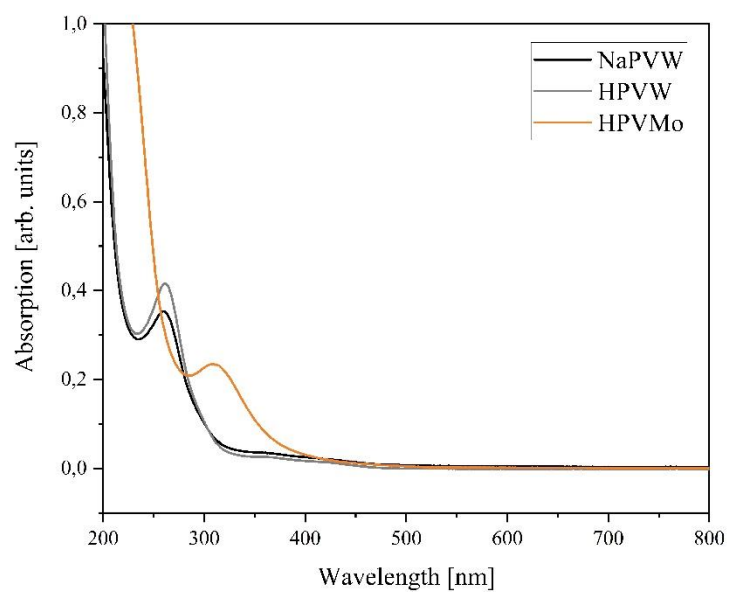


Figure S17: UV-Vis spectra of the POMs NaPVW, HPVW and HPVMo.

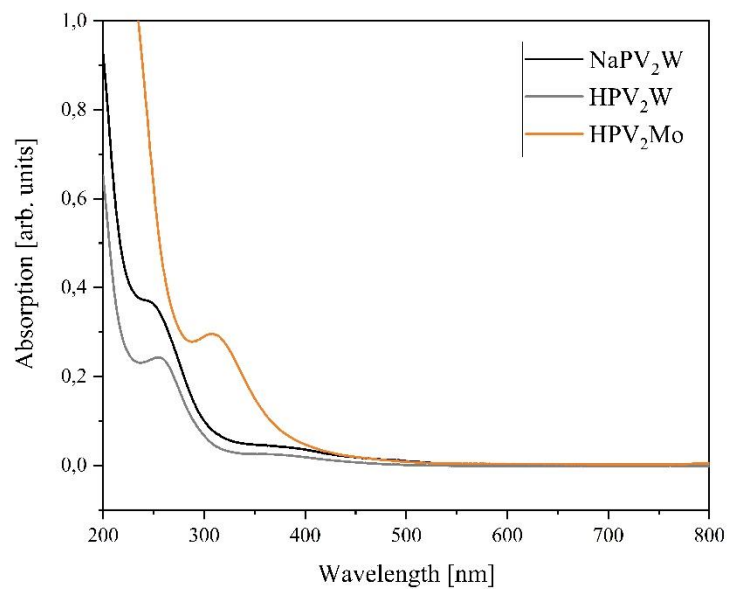


Figure S18: UV-Vis spectra of the POMs NaPV₂W, HPV₂W and HPV₂Mo.

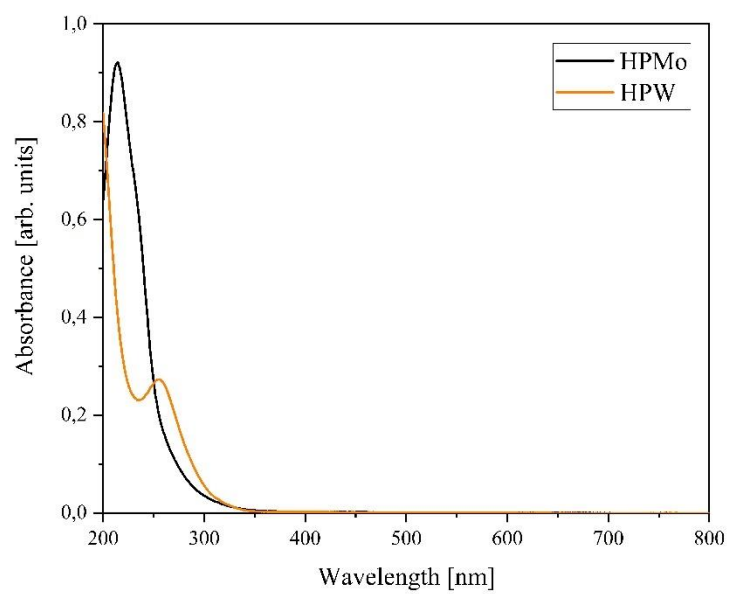


Figure S19: UV-Vis spectra of the POMs HPMo and HPW.

Lambert-Beer's law (equation 1):

$$Abs = \varepsilon_{\lambda} \cdot d \cdot c \quad (1)$$

Abs: Absorption

ε_{λ} : extinction coefficient (wavelength λ dependant) [$\text{l mol}^{-1} \text{cm}^{-1}$]

d: Cuvette layer thickness (1 cm) [cm]

c: concentration [mol/L]

Calibration line (equation 2):

$$Abs = a \cdot c + b \quad (2)$$

a: slope

b: Axis intercept

Determining the extinction coefficient:

$$a = \varepsilon_{\lambda} \cdot d \quad (3)$$

$$\varepsilon_{\lambda} = \frac{a}{d} \quad (4)$$

A detailed description for the measurement procedure can be found under 2.2 UV-Vis spectroscopy, extinction coefficients.

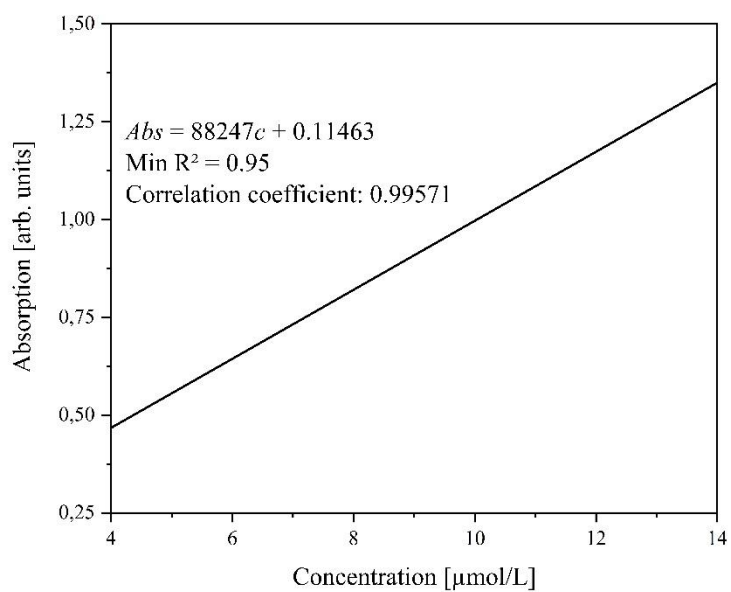


Figure S20: Calibration line for determining the extinction coefficient for HPVMO at 211.5 nm (Mo(VI) LMCT).

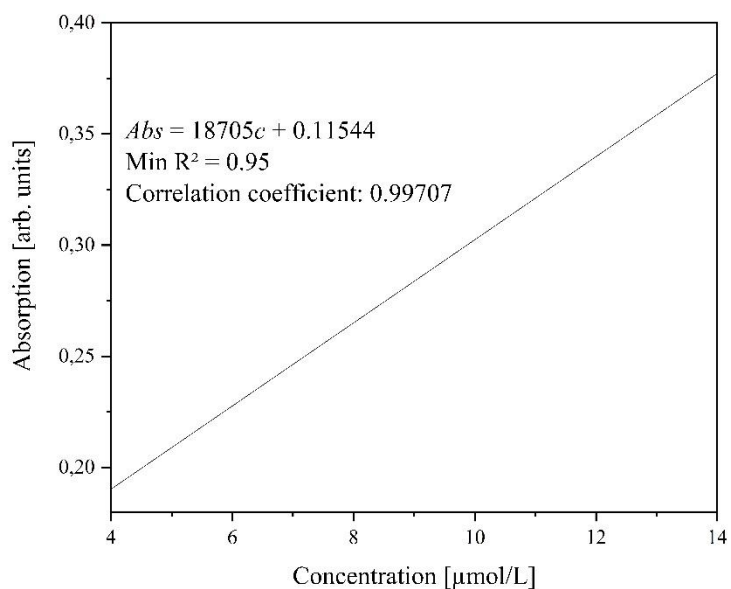


Figure S21: Calibration line for determining the extinction coefficient for HPVMO at 308.5 nm (V(V) LMCT).

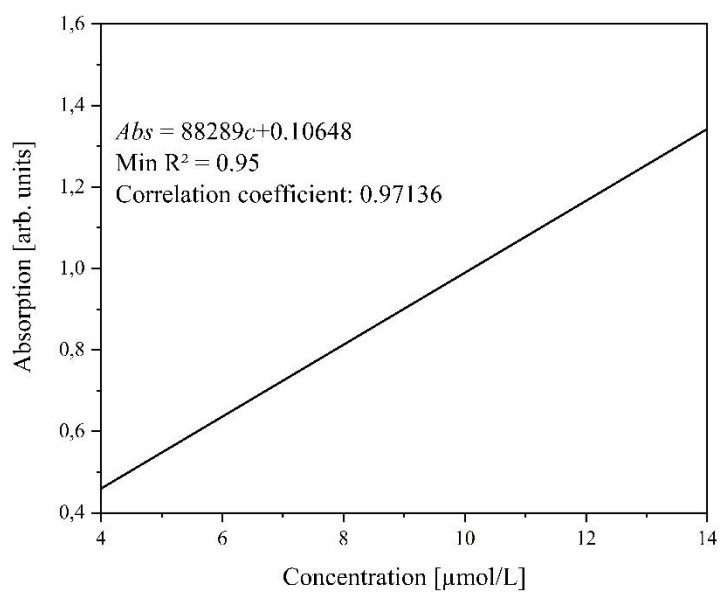


Figure S22: Calibration line for determining the extinction coefficient for HPV₂Mo at 214.5 nm (Mo(VI) LMCT).

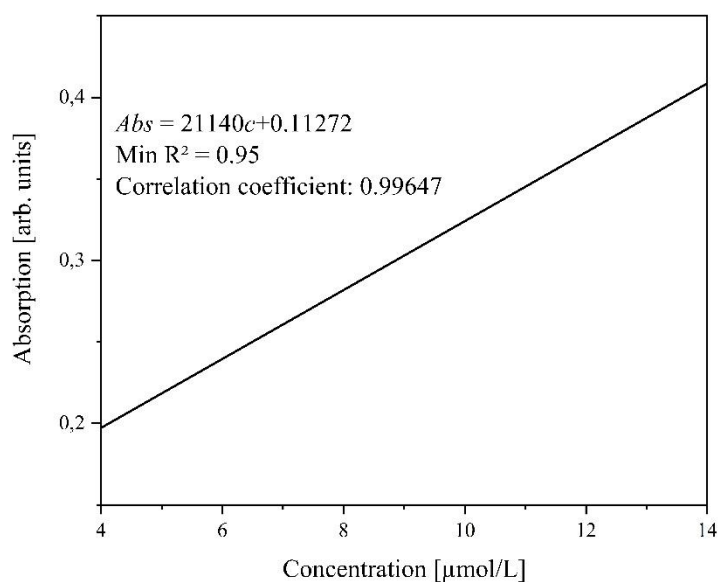


Figure S23: Calibration line for determining the extinction coefficient for HPV₂Mo at 308 nm (V(V) LMCT).

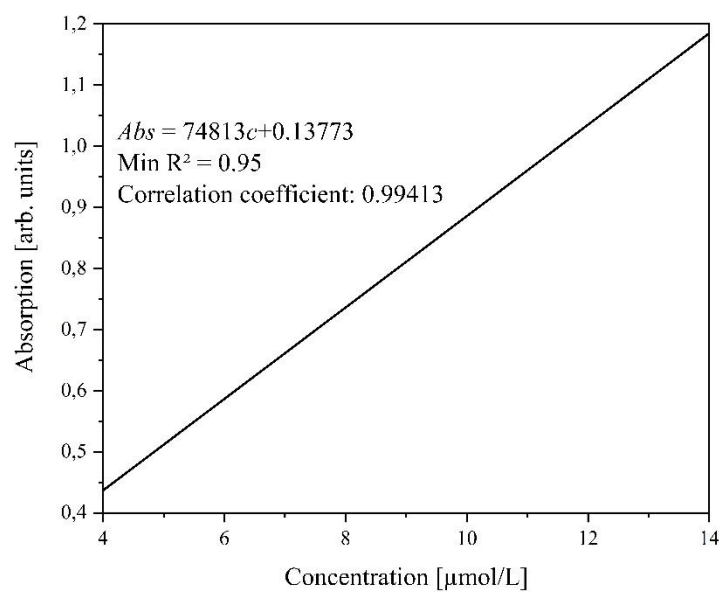


Figure S24: Calibration line for determining the extinction coefficient for HPV₃Mo at 215 nm (Mo(VI) LMCT).

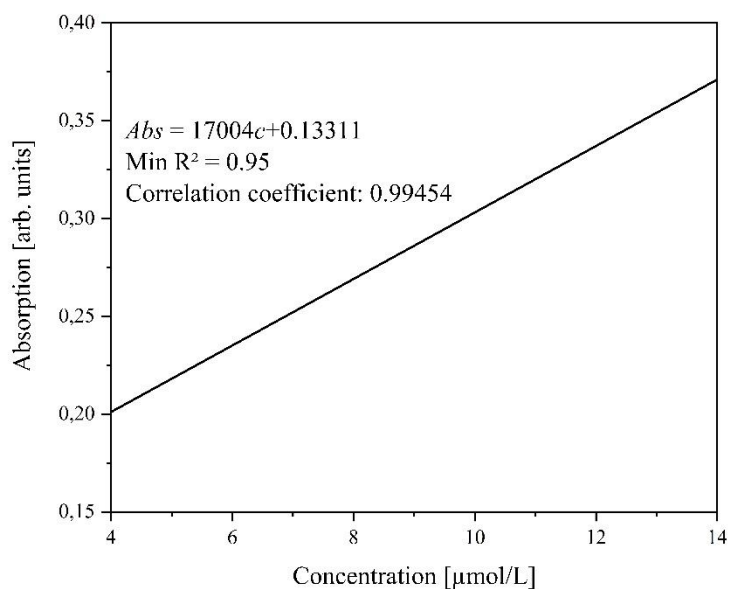


Figure S25: Calibration line for determining the extinction coefficient for HPV₃Mo at 305 nm (V(V) LMCT).

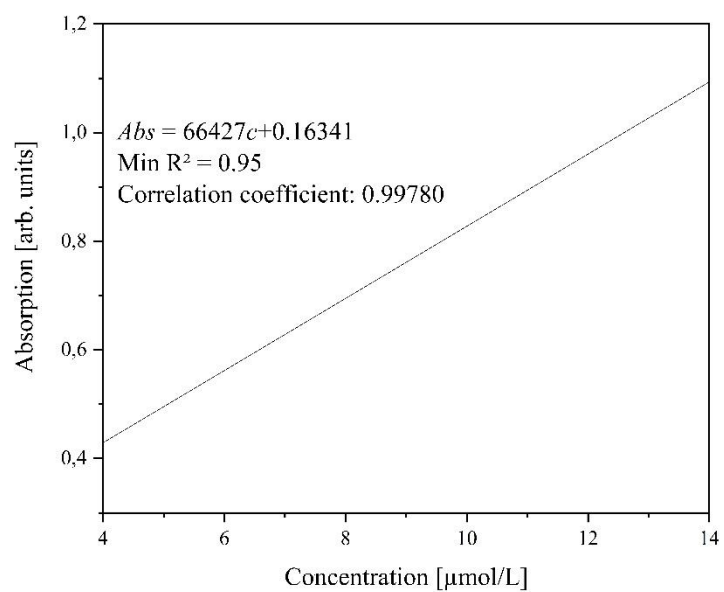


Figure S26: Calibration line for determining the extinction coefficient for HPV₄Mo at 218 nm (Mo(VI) LMCT).

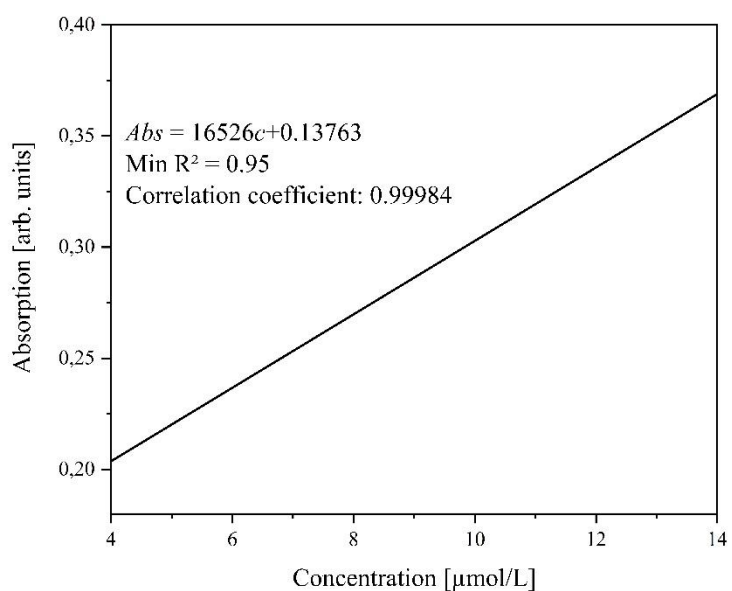


Figure S27: Calibration line for determining the extinction coefficient for HPV₄Mo at 304 nm (V(V) LMCT).

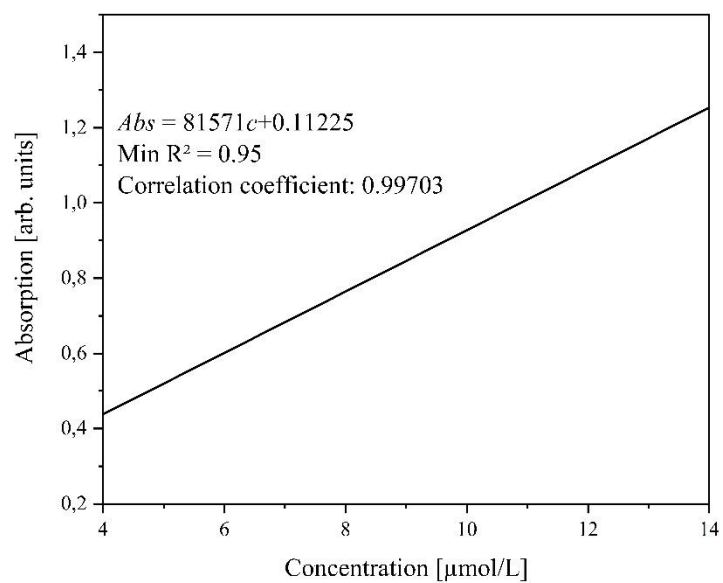


Figure S28: Calibration line for determining the extinction coefficient for HPV₅Mo at 217 nm (Mo(VI) LMCT).

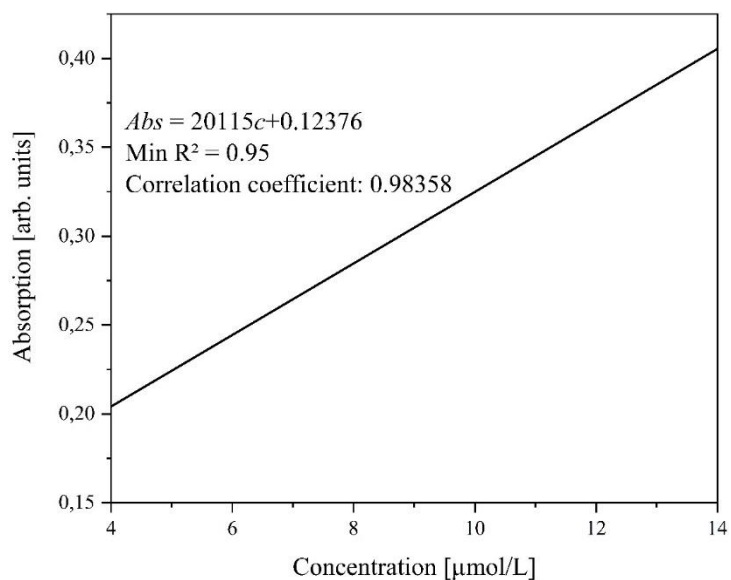


Figure S29: Calibration line for determining the extinction coefficient for HPV₅Mo at 308 nm (V(V) LMCT).

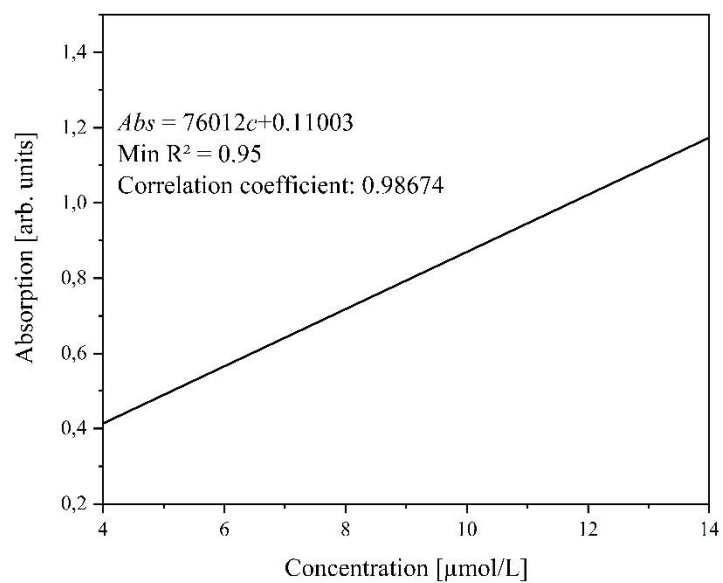


Figure S30: Calibration line for determining the extinction coefficient for HPV₆Mo at 217 nm (Mo(VI) LMCT).

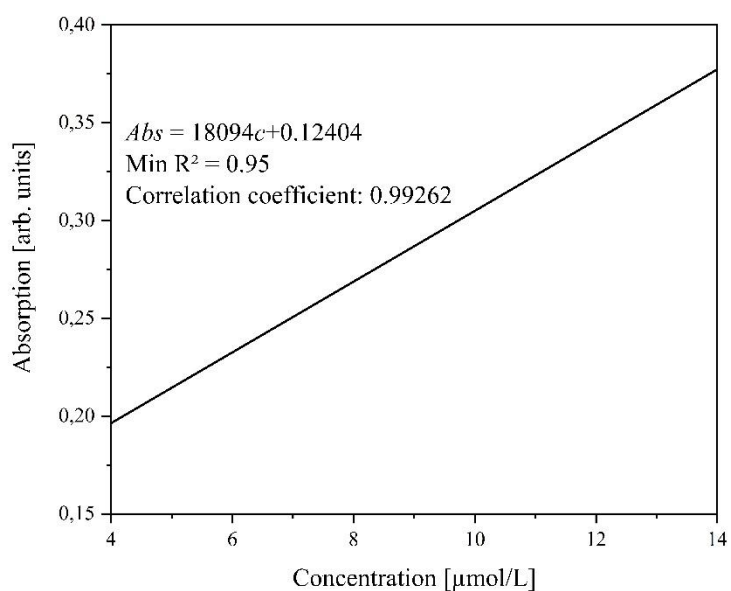


Figure S31: Calibration line for determining the extinction coefficient for HPV₆Mo at 308 nm (V(V) LMCT).

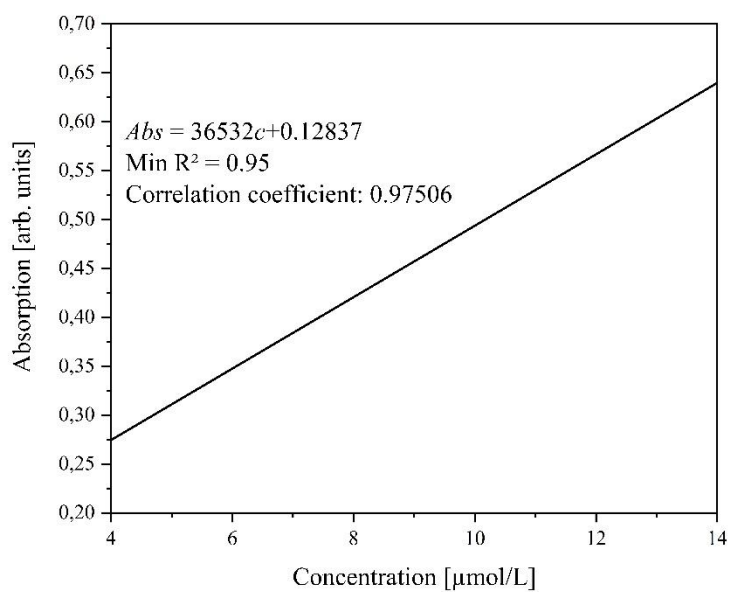


Figure S32: Calibration line for determining the extinction coefficient for NaPVW at 260 nm (W(VI) LMCT).

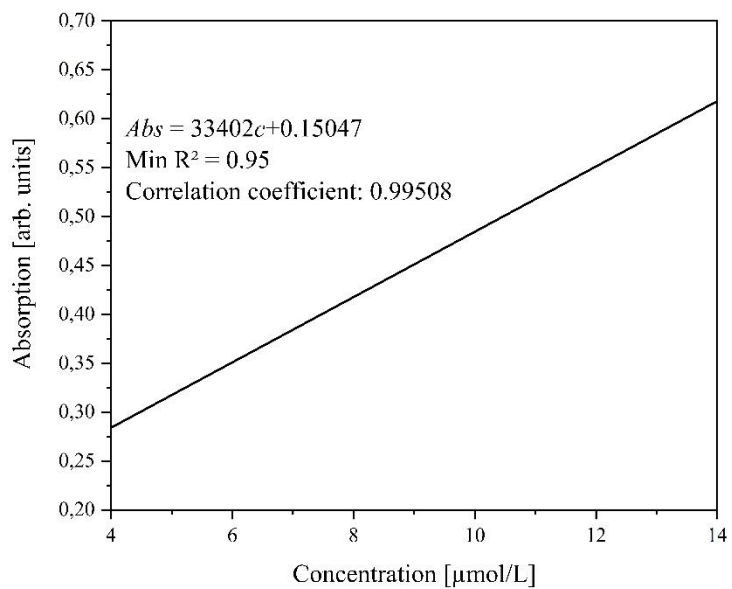


Figure S33: Calibration line for determining the extinction coefficient for NaPV₂W at 242 nm (W(VI) LMCT).

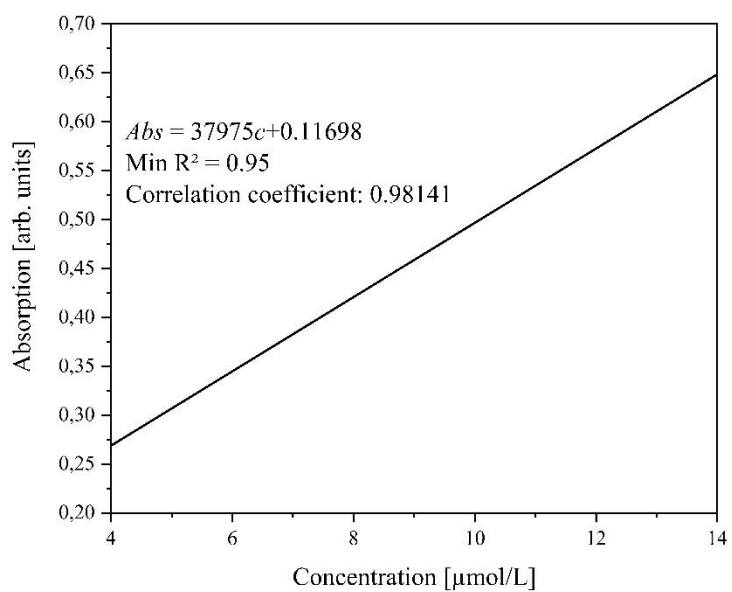


Figure S34: Calibration line for determining the extinction coefficient for NaPV₃W at 250 nm (W(VI) LMCT).

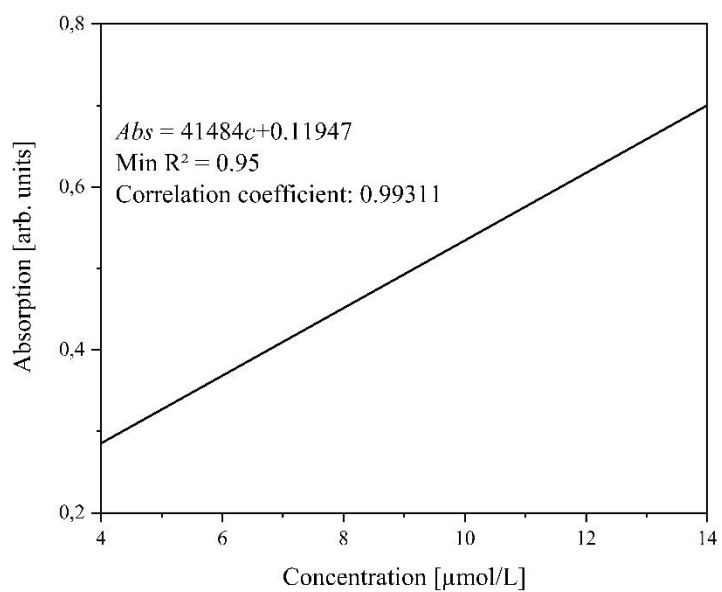


Figure S35: Calibration line for determining the extinction coefficient for NaPV₄W at 240 nm (W(VI) LMCT).

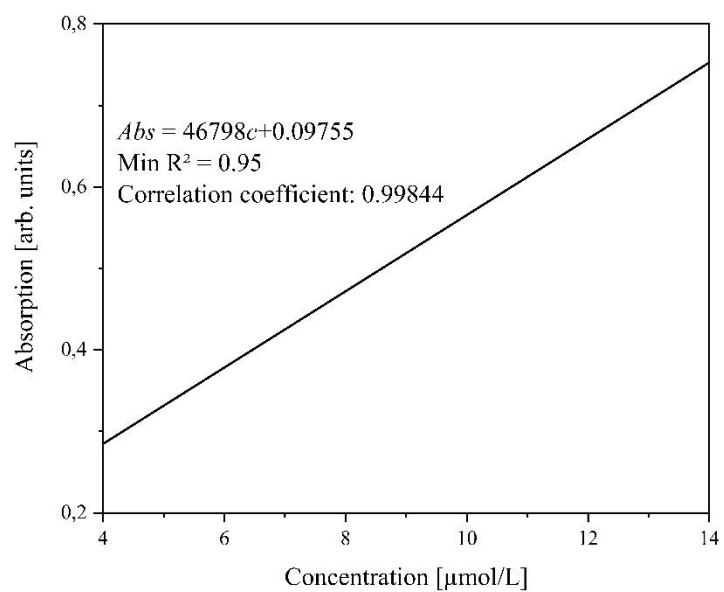


Figure S36: Calibration line for determining the extinction coefficient for NaPV₅W at 235 nm (W(VI) LMCT).

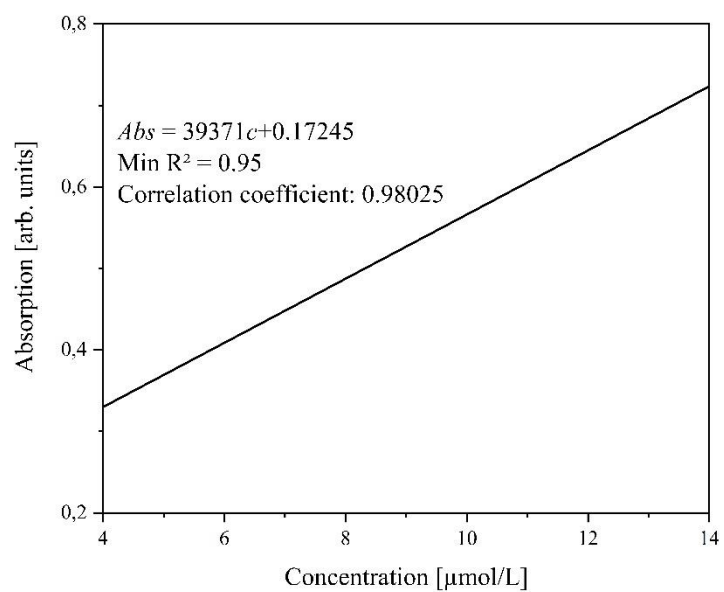


Figure S37: Calibration line for determining the extinction coefficient for NaPV₆W at 234 nm (W(VI) LMCT).

Table 1: Peak maxima (oxidation pathway) and peak minima (reduction pathway) from the CV data and maxima from the SWV data of the POMs in aqueous pH 1 solution (HCl): concentration 1 mmol/L; scan rate 100 mV/s (CV) and 5 mV/s (SWV).

Maximum oxidation pathway CV [mV]	Minimum reduction pathway CV [mV]	Mean value CV [mV]	Peak maxima SWV [mV]
H₃[PMo₁₂O₄₀]			
-	-	-	-570
-277	-	-	-370
-	-169	-	-150
-87.7	8.33	-39.7	-
-	-	-	50
218	167	193	205
-	-	-	340
H₄[PVMo₁₁O₄₀]			
-	-	-	-575
-485	-445	-465	-425
-270	-335	-303	-320
-120	-25	-73	-150
-	-	-	10
120	85	103	70
-	-	-	215
440	340	390	390
H₅[PV₂Mo₁₀O₄₀]			
-	-	-	-555
-	-	-	-425
-	-	-	-325
-275	-185	-230	-
-110	-30/-35	-73	-155
-	-	-	5
125	90	108	90
425	300	363	380
H₆[PV₃Mo₉O₄₀]			
-	-	-	-530
-	-	-	-420
-300	-340	-320	-325
-	-180	-	-150
-	-45	-	10
115	-	-	95
430	305	368	370
H₇[PV₄Mo₈O₄₀]			
-	-	-	-530
-305	-	-	-345
-	-200	-	-155
-	-	-	-55
60	-	-	-
-	270	-	-

410	-	-	350
H₈[PV₅Mo₇O₄₀]			
-	-	-	-525
-350	-	-	-350
-	-220	-	-175
105	-	-	-80
-	-	-	-40
-	285	-	-
400	-	-	340
H₉[PV₆Mo₆O₄₀]			
-	-	-	-535
-300	-	-	-350
-	-200	-	-165
105	-	-	-
-	-	-	-10
-	235	-	-
405	-	-	345
H₃[PW₁₂O₄₀]			
-345	-400	-373	-375
-65	-140	-103	-95
Na₄[PVW₁₁O₄₀]			
-	-	-	-575
525	410	468	475
Na₅[PV₂W₁₀O₄₀]			
-	-	-	-570
330	180	255	250
525	460	493	490
Na₆[PV₃W₉O₄₀]			
-	-	-	-580
-	120	-	150
280	-	-	255
435	-	-	385
Na_{6.6}H_{0.4}[PV₄W₈O₄₀]			
-	-	-	-580
330	180	-	255
Na_{6.8}H_{1.2}[PV₅W₇O₄₀]			
-	-	-	-580
345	180	263	255
Na_{6.7}H_{2.3}[PV₆W₆O₄₀]			
-	-	-	-570
335	160	248	245

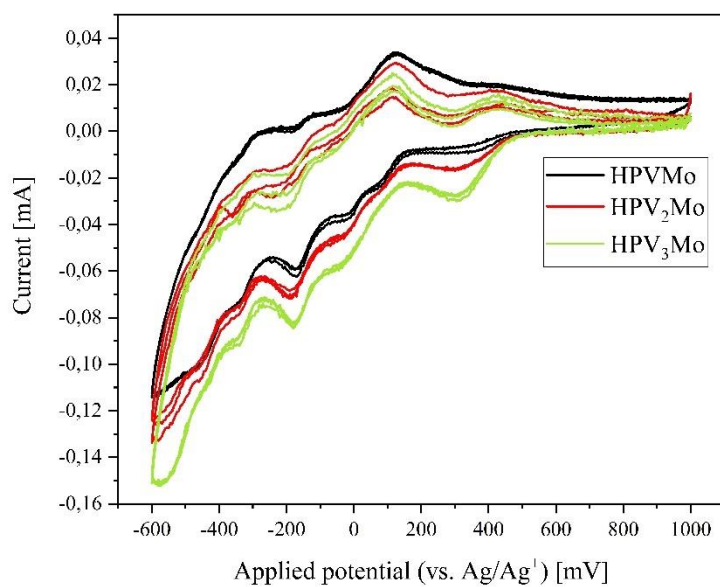


Figure S38: CV data of the POMs HPV_xMo with $x = 1$ to 3 (concentration 1 mmol/L, scan rate 100 mV/s and pH 1 (HCl as supporting electrolyte)).

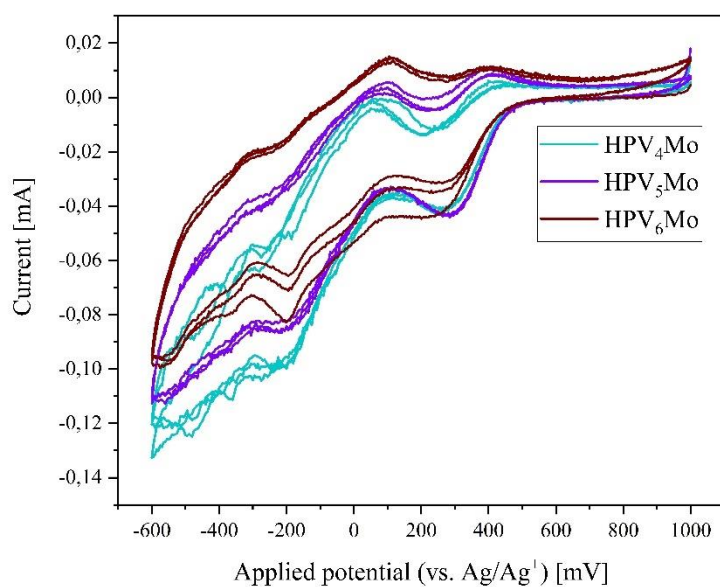


Figure S39: CV data of the POMs HPV_xMo with $x = 4$ to 6 (concentration 1 mmol/L, scan rate 100 mV/s and pH 1 (HCl as supporting electrolyte)).

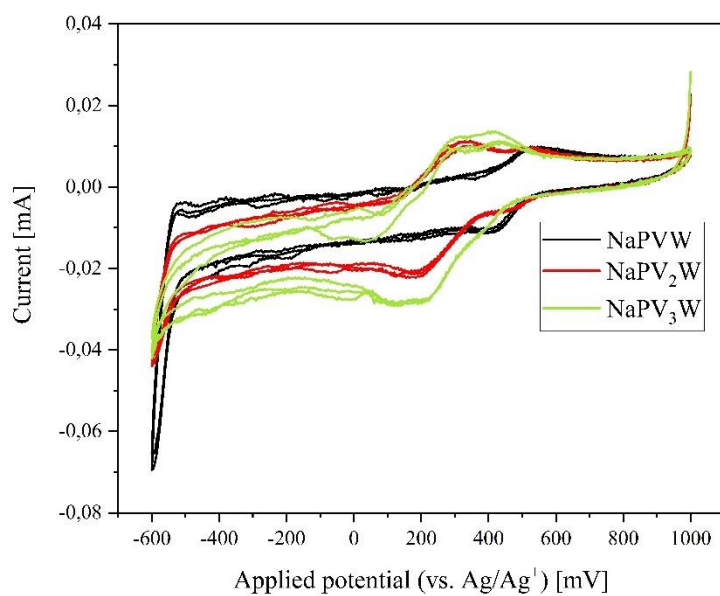


Figure S40: CV data of the POMs NaPV_xW with $x = 1$ to 3 (concentration 1 mmol/L, scan rate 100 mV/s and pH 1 (HCl as supporting electrolyte)).

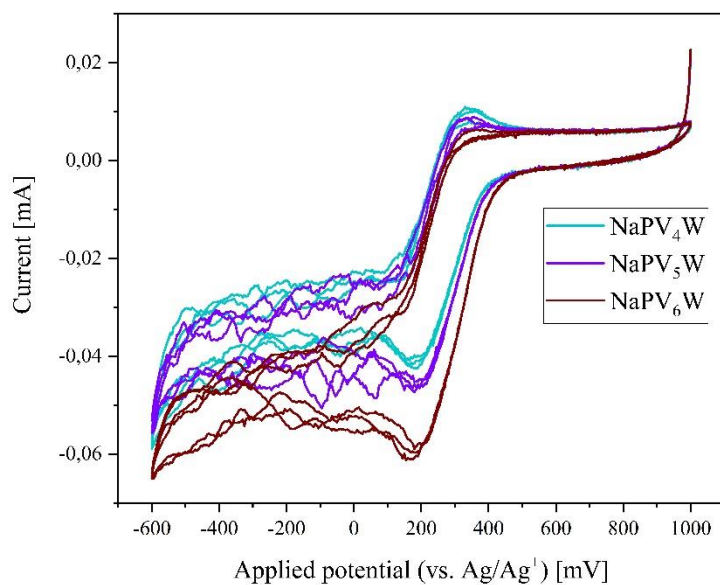


Figure S41: CV data of the POMs NaPV_xW with $x = 4$ to 6 (concentration 1 mmol/L, scan rate 100 mV/s and pH 1 (HCl as supporting electrolyte)).

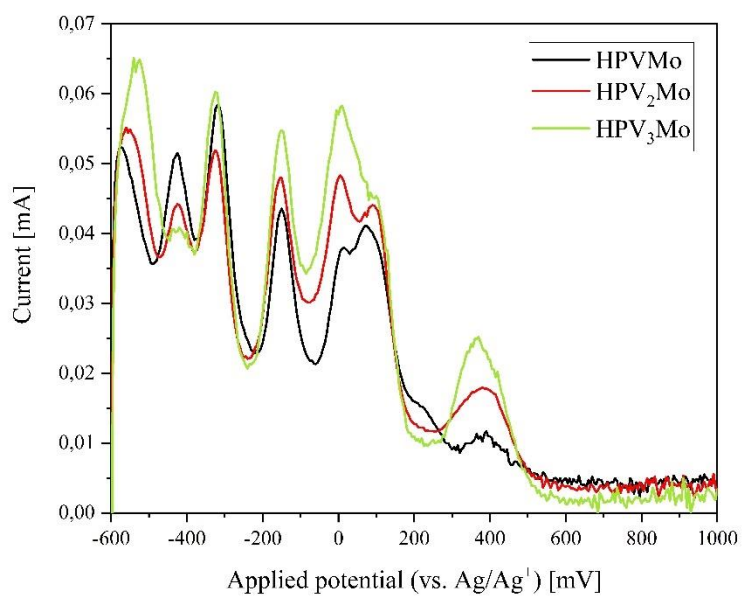


Figure S42: SWV data of the POMs HPV_xMo with $x = 1$ to 3 (concentration 1 mmol/L, scan rate 5 mV and pH 1 (HCl as supporting electrolyte)).

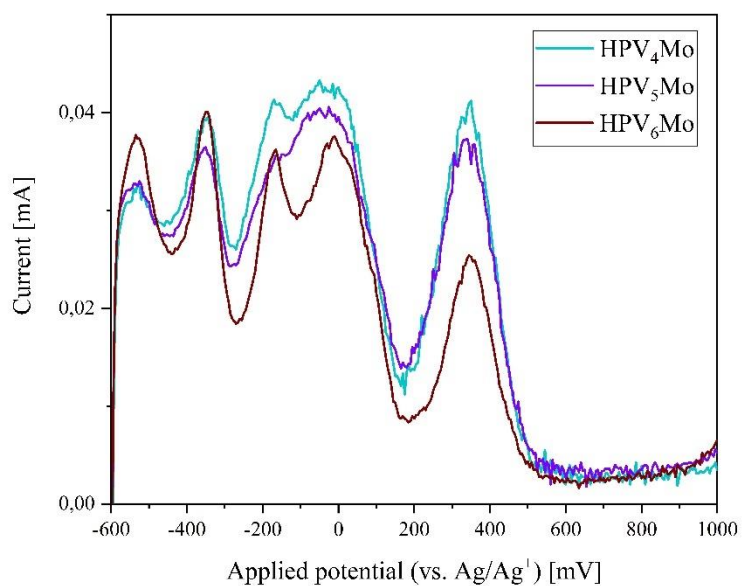


Figure S43: SWV data of the POMs HPV_xMo with $x = 4$ to 6 (concentration 1 mmol/L, scan rate 5 mV and pH 1 (HCl as supporting electrolyte)).

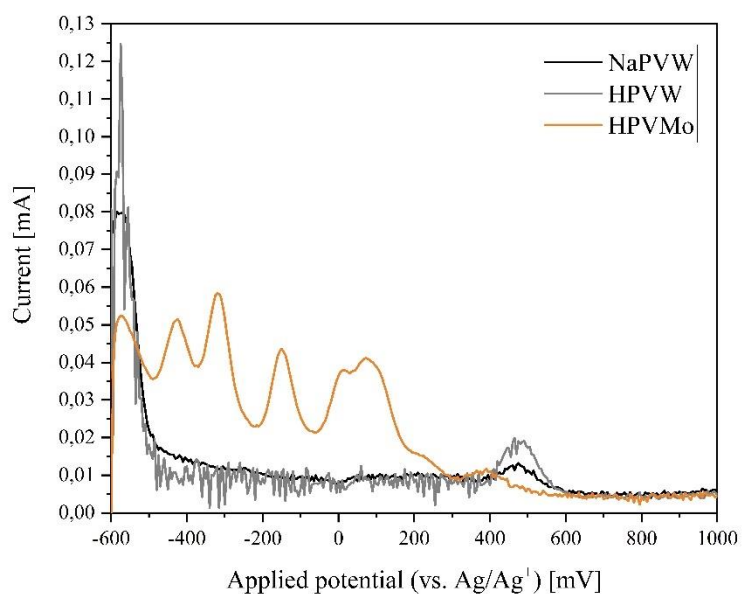


Figure S44: SWV data of the POMs NaPVW, HPVW and HPVMo (concentration 1 mmol/L, scan rate 5 mV and pH 1 (HCl as supporting electrolyte)).

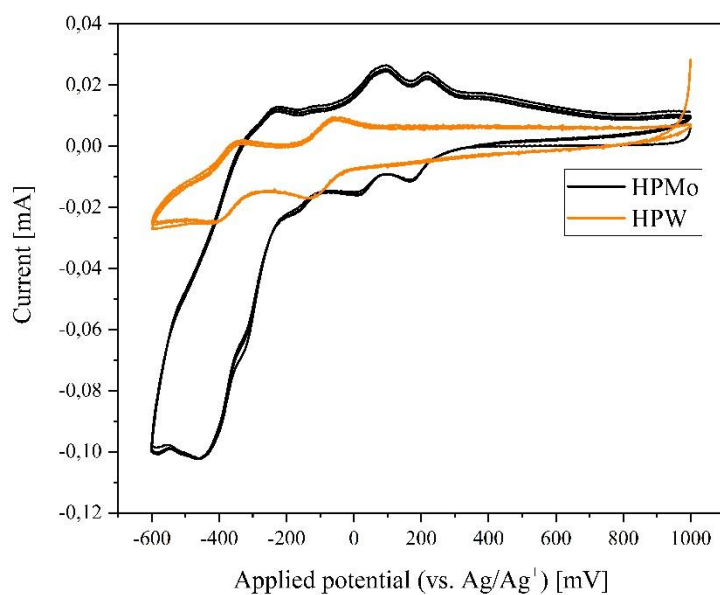


Figure S45: CV data of the POMs HPMo and HPW (concentration 1 mmol/L, scan rate 100 mV/s and pH 1 (HCl as supporting electrolyte)).

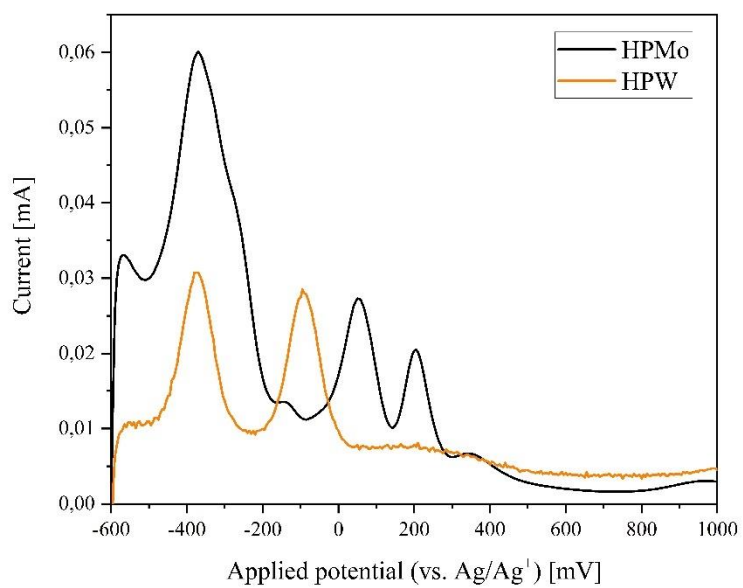


Figure S46: SWV data of the POMs HPMo and HPW (concentration 1 mmol/L, scan rate 5 mV and pH 1 (HCl as supporting electrolyte)).

2 Experimental Details

2.1 Chemicals

- Phosphotungstic acid hydrate: > 99 %, Sigma-Aldrich
- Sodium tungstate dihydrate: 99 %, AlanaR NORMAPUR
- Sodium metavanadate: 96 % Alfa Aesar
- Molybdenum trioxide: 99 %, Alfa Aesar
- Divanadium pentoxide: 99 %, Alfa Aesar
- Phosphoric acid: 85 % in water, Grüssing
- Hydrochloric acid: 37 % in water, VWR chemicals
- Hydrogen peroxide: 30 % in water, VWR chemicals
- Acetic acid glacial: > 99 %, VWR International
- Sodium acetate: 99 %, Merck
- Sodium carbonate: 99 % Grüssing
- Deuterium oxide: 99.9 %, Deutero GmbH

2.2 Analytics

All POMs presented here were characterized for four significantly important properties using selected methods:

1. Composition: Knowledge of the chemical and stoichiometric composition of the POM materials makes it possible to assess the extent to which the desired degree of substitution has been achieved and to estimate the purity of the POM samples. Wet chemical, elemental analytical methods such as AAS or ICP-OES are used for this purpose. Thermogravimetric analyses (TGA) is used in this work to determine the hydrate water content.^[21]
2. Characterization of the POM in the solid-state: Characterization of the POM in the solid-state generates information on the purity, information on the structure type (e.g. Keggin-type) and indirectly information on the degree of substitution, since spectroscopic shifts are known to be generated by mass differences between elements from the periodic table. The methods used for this are essentially vibrational spectroscopic techniques such as attenuated total reflection Fourier transform infrared (ATR-FT-IR) or Raman spectroscopy.^[24]
3. Characterization of the POM in aqueous solution: Spectroscopic analysis of POMs in aqueous solutions allows the behaviour of a POM species in solution to be described. POMs in solutions are known for the pH-dependent formation of numerous dissociation fragments. Likewise, information can be derived about the electronic transitions responsible for the colour of the POM anions. The main methods used for this purpose are nuclear magnetic resonance (NMR) and ultraviolet-visible (UV-Vis) spectroscopy.^[25]

RedOx activity: Electrochemical methods such as cyclic voltammetry (CV) or square wave voltammetry (SWV) are suitable for determining the RedOx activity of a POM species. The information generated from this methods is suitable for estimating the extent to which defined POMs are suitable for RedOx catalytic applications.^[26]

AAS/ICP-OES (elemental analysis)

Samples were analyzed using an ICP-OES-spectrometer for elemental analysis (Fa. Spectro, type ARCOS) for the elements Mo, W, V and P (method ICP-OES). Na was measured with an AAS-F (Fa. Thermo, type Solaar S Series) (method: F-AES without HKL).

TGA analysis:

TGA measurements were performed with a NETZSCH TG 209 F1 220-10-039-K at the Fraunhofer-Zentrum für Angewandte Nanotechnologie CAN. The data were processed with the software Proteus Analysis from NETZSCH. About 20 mg of the sample was weighed into a duran-glas crucible and the change in mass was measured at the following temperature program:

- Tare
- 1 minute waiting time
- Heating to 30 °C with maximum heating rate
- Stay at 30 °C for 15 minutes
- Heating to 350 °C with a heating rate of 10 K/min
- Stay at 350 °C for 30 minute
- The sample was then cooled to room temperature

IR spectroscopy

IR spectra were measured in attenuated total reflection (ATR) measurement mode on a QATR™-S single-reflection ATR (with a diamond prism) from Shimadzu. From the raw data obtained, the baseline was corrected, and the peaks were determined manually. The IR data were then exported as an *x/y* text document.

Raman spectroscopy

Raman spectra were measured on a SENTERRA Raman microscope from Bruker Optik GmbH. The aperture was set to 50 x 1000 µm. A 20 objective was used on the microscope. The excitation laser has a wavelength of 785 nm and the measurement range used was between 75 cm⁻¹ and 1525 cm⁻¹. The integration time was 16 seconds, the number of scans was 8 and the Raman laser power was 10 mW.

NMR-spectroscopy

Samples were measured with a Bruker AVANCEII 600 MHz. Sample preparation: POM (70 mg) was dissolved in deionized water, which had previously been adjusted to the desired pH value using a 2 M hydrochloric acid solution in deionized water. D₂O or acetone-*d*₆ was added. ³¹P spectra: Time Domain Data Sizes (TD) of 32 K, the Number of Scans (NS) were set to 2k (= 2048), the Transmitter Frequency Offset for Channel F1 (O1) and the Spectral Width (SW) were -1 and 40 ppm. The Delay D1 was set to 1 s. ⁵¹V spectra: TD was 32 K, O1 and SW

-520 and 400 ppm, D1 0.5 s and NS was set to 4 K. The NMR analyses were carried out with the software MestReNova®. In MestReNova®, the peaks were first determined, and the data subsequently exported in .csv format.

UV-Vis spectroscopy

Stock solution: The respective POM (0.250 g) was dissolved in deionized water (250 mL) → 1 g/L.

Spectra measurement: All UV-Vis spectra were measured with a Cary 60 UV-Vis spectrometer (Agilent Technologies) in a 3 mL Quartz cuvette (QS). Measurements were carried out using the Cary WinUV software. Measuring range between 200 nm and 800 nm. The absorbance was measured in the slow measurement mode. The data were then exported as a .csv data set. All samples were prepared as follows: Stock solution 1 g/L. From the stock solution 80 µL were filled into the cuvette and 2920 µL were added to reach the final measuring volume of 3 mL.

Extinction coefficients: For determining the extinction coefficients the software Cary concentrations was used. Five calibration standards were prepared from the stock solution (1 g/L) with a final volume of 3 mL for the cuvette:

- 20 µL stock solution + 2980 µL deionized water
- 40 µL stock solution + 2960 µL deionized water
- 50 µL stock solution + 2950 µL deionized water
- 60 µL stock solution + 2940 µL deionized water
- 80 µL stock solution + 2920 µL deionized water

For evaluation equations 1 to 3 were used.

Electrochemistry (CV and SWV):

All CV/SWV measurements were performed in aqueous, hydrochloric acid medium at pH 1 and a concentration of 1 mmol/L on a Metrohm - Autolab PGSTAT101. During the measurement, the solution was purged with nitrogen gas. Working electrode: glassy carbon electrode (diameter: 3 mm); Reference electrode: Ag/Ag⁺ electrode; Counter electrode: platinum electrode. Measurements were taken in the measuring range between -600 and 1000 mV with a scan rate (for CV) of 100 mV/s for 3 scans. All SWV measurements were taken with a scan rate of 5 mV/s, a modulation amplitude of 20 mV and a frequency of 25 Hz. The

measurements were carried out with the software Ivium and the data was subsequently exported as an *x/y* text document.

Origin® 2019b:

All *x/y* files of all analytical data were plotted in Origin® 2019b.

2.3 Synthesis of $\text{Na}_{9-x}\text{H}_x[\text{PW}_9\text{O}_{34}] \cdot x \text{H}_2\text{O}$ according to Domaille *et al.*^[1]

Sodium tungstate dihydrate (20.01 g, 60 mmol, 6 equivalents) was dissolved in deionized water (40 mL) and an 85 % phosphoric acid solution in water (1.17 g, 10 mmol, 1 equivalent) was added. The final pH value was 8.9. Under stirring glacial acetic acid (4.05 g, 70 mmol, 7 equivalents) was added dropwise and during addition a colourless precipitate was formed. The pH changed to 7.4 after complete addition. After two hours of stirring the colourless precipitate was removed by vacuum filtration and was dried in a desiccator for 24 hours. The product was used without further purification. A colourless solid (7.46 g) was obtained.

Characterisation:

Literature hydration water content is seven molecules of water per POM molecule.^[1]

³¹P-NMR (242.9 MHz, $\text{H}_2\text{O}/\text{D}_2\text{O}$, 20 °C): δ [ppm] = -10.82, 2.07.

FT-IR (ATR): $\tilde{\nu}[\text{cm}^{-1}]$ = 3459 (w), 1630 (w, O–H, lattice H_2O), 1056 (s, P–O), 1014 (m, P–O), 932 (s), 882 (m), 812 (s), 760–730 (s, broad).

Elemental analysis calculated for $\text{Na}_9[\text{PW}_9\text{O}_{34}] \cdot 7 \text{H}_2\text{O}$: m/m [%] = Na: 8.07; P: 1.21; W: 64.57. Found: m/m [%] = Na: 7.52; P: 1.32; W: 59.6. Data normalised to tungsten, Na/P/W ratio: 9.06/1.18/9.

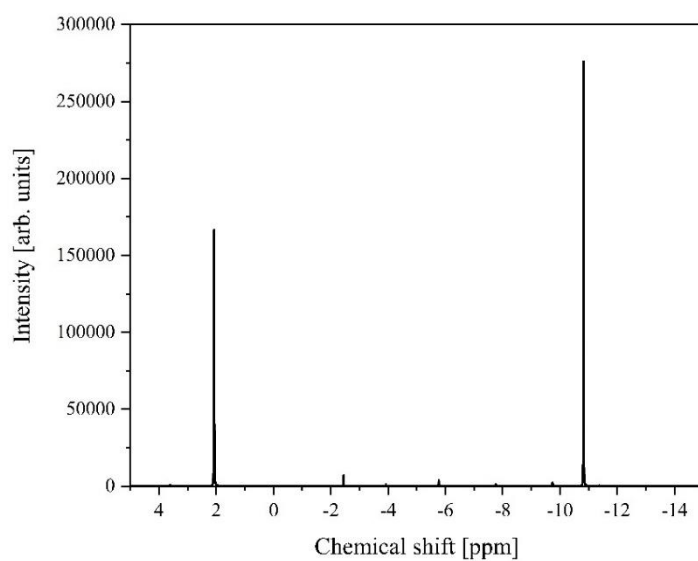


Figure S47: ^{31}P -NMR spectrum of $[\text{PW}_9\text{O}_{34}]^{9-}$ in a mixture of 70 % water (pH 5) and 30 % D_2O . Measurement frequency: 242.9 MHz. 85 % H_3PO_4 was used as external standard.

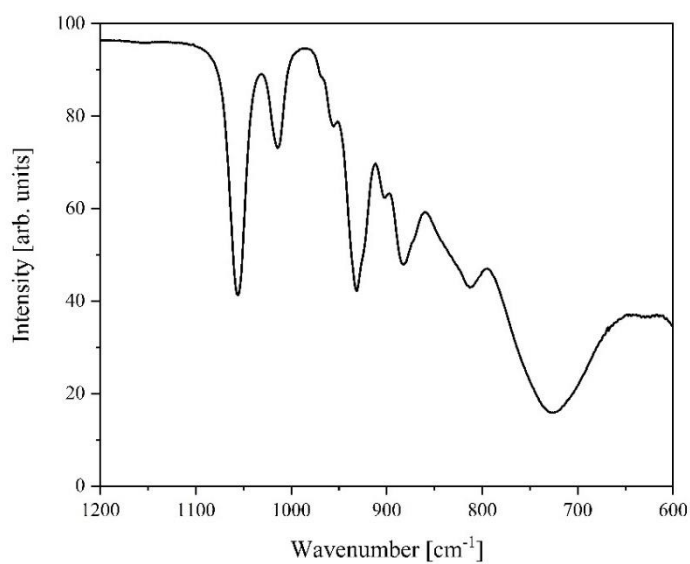


Figure S48: ATR-FT-IR spectrum of $[\text{PW}_9\text{O}_{34}]^{9-}$.

2.4 Synthesis of $\text{Na}_4[\text{PVW}_{11}\text{O}_{40}] \cdot 9 \text{H}_2\text{O}$ according to Domaille *et al.*^[1]

Phosphotungstic acid (11.4 g, 3.6 mmol, 1 equivalent) was dissolved in deionized water (25 mL). The pH value of this solution was 0.5 and was adjusted to 4.8 by addition of small portions sodium carbonate. In parallel sodium metavanadate (0.57 g, 4.5 mmol, 1.25 equivalents) was dissolved in deionized water at 80 °C and added to the $[\text{PW}_{11}\text{O}_{39}]^{7-}$ solution. The pH value of the combined reaction mixture was adjusted to 2.0 by adding a 2 M hydrochloric acid solution in water and then heated up to 60 °C. After cooling to room temperature the pH value was 3.5 and was readjusted to 2.0 using a 2 M hydrochloric acid solution in water. The solution was then reheated to 60 °C. This procedure was repeated once, until upon cooling down to room temperature the pH value remained stable around 2.0. It was filtered and the solution was desalinated using a nanofiltration approach. A yellow solid (9.07 g) was obtained.

Characterisation:

^{31}P -NMR (242.9 MHz, $\text{H}_2\text{O}/\text{D}_2\text{O}$, 20 °C): δ [ppm] = -14.9.

^{51}V -NMR (157.8 MHz, $\text{H}_2\text{O}/\text{D}_2\text{O}$, 20 °C): δ [ppm] = -555.9.

FT-IR (ATR): $\tilde{\nu}$ [cm^{-1}] = 1616 (w, O–H, lattice H_2O), 1094, 1066 (s, P–O), 965 (s, M=O_t), 890 (m, (M–O–M)_{vertex}), 764 (s, broad, (M–O–M)_{edge}).

Elemental analysis calculated for $\text{Na}_4[\text{PVW}_{11}\text{O}_{40}] \cdot 9 \text{H}_2\text{O}$: m/m [%] = Na: 3.07; P: 1.03; V: 1.70; W: 67.45. Found: m/m [%] = Na: 2.96; P: 1.13; V: 1.91; W: 64.2. Data normalised to tungsten, Na/P/V/W ratio: 4.05/1.15/1.18/11.

TGA: 5.45 % weight loss upon drying, this corresponds to 9 mol lattice water per mol of the POM.

2.5 Synthesis of $\text{Na}_5[\text{PV}_2\text{W}_{10}\text{O}_{40}] \cdot 14 \text{H}_2\text{O}$ according to a modified procedure of Domaille *et al.*^[1]

Sodium acetate (2.73 g, 33.3 mmol, 12.2 equivalents) was dissolved in deionized water (30 mL) and after dissolution acetic acid was added until the pH value of the solution reached 4.8. In the next step sodium metavanadate (0.71 g, 5.56 mmol, 2.02 equivalents) and sodium tungstate dihydrate (0.92 g, 2.78 mmol, 1.01 equivalents) were added and after dissolution, $\text{Na}_{9-x}\text{H}_x[\text{PW}_9\text{O}_{34}] \cdot x \text{H}_2\text{O}$ (6.67 g, 2.73 mmol, 1 equivalent) was added and stirred for 48 hours. The colour of the solution changed to dark red. It was filtered and then desalinated using a nanofiltration approach. An orange solid (6.25 g) was obtained.

Characterisation:

³¹P-NMR (242.9 MHz, $\text{H}_2\text{O}/\text{D}_2\text{O}$, 20 °C): δ [ppm] = -12.8 to -14.9.

⁵¹V-NMR (157.8 MHz, $\text{H}_2\text{O}/\text{D}_2\text{O}$, 20 °C): δ [ppm] = -527.0 to -565.0.

FT-IR (ATR): $\tilde{\nu}$ [cm^{-1}] = 3424 (w), 1620 (w, O–H, lattice H_2O), 1083, 1054 (s, P–O), 952 (s, M=O_t), 876 (m, (M–O–M)_{vertex}), 774 (s, broad, (M–O–M)_{edge}).

Elemental analysis calculated for $\text{Na}_5[\text{PV}_2\text{W}_{10}\text{O}_{40}] \cdot 14 \text{H}_2\text{O}$: m/m [%] = Na: 3.86; P: 1.04; V: 3.42; W: 61.73. Found: m/m [%] = Na: 4.71; P: 1.18; V: 3.69; W: 57.7. Data normalised to tungsten, Na/P/V/W ratio: 6.52/1.21/2.31/10.

TGA: 8.53 % weight loss upon drying, this corresponds to 14 mol lattice water per mol of the POM.

2.6 Synthesis of $\text{Na}_6[\text{PV}_3\text{W}_9\text{O}_{40}] \cdot 13 \text{H}_2\text{O}$ according to Domaille *et al.*^[1]

Sodium acetate (2.73 g, 33.3 mmol, 12.2 equivalents) was dissolved in deionized water (30 mL) and after dissolution acetic acid was added until the pH value of the solution reached 4.8. In the next step sodium metavanadate (1.06 g, 8.33 mmol, 3.05 equivalents) and $\text{Na}_{9-x}\text{H}_x[\text{PW}_9\text{O}_{34}] \cdot x \text{H}_2\text{O}$ (6.67 g, 2.73 mmol, 1 equivalent) were added and stirred for 48 hours. The colour of the solution changed to dark red. It was filtered and then desalinated using a nanofiltration approach. A red solid (6.00 g) was obtained.

Characterisation:

³¹P-NMR (242.9 MHz, $\text{H}_2\text{O}/\text{D}_2\text{O}$, 20 °C): δ [ppm] = -12.1 to -14.9.

⁵¹V-NMR (157.8 MHz, $\text{H}_2\text{O}/\text{D}_2\text{O}$, 20 °C): δ [ppm] = -505.0 to -566.0.

FT-IR (ATR): $\tilde{\nu}$ [cm^{-1}] = 3542, 3459, 3361 (w), 1620 (w, O–H, lattice H_2O), 1084, 1053 (s, P–O), 950 (s, M=O_t), 876 (m, (M–O–M)_{vertex}), 765 (s, broad, (M–O–M)_{edge}).

Elemental analysis calculated for $\text{Na}_6[\text{PV}_3\text{W}_9\text{O}_{40}] \cdot 13 \text{H}_2\text{O}$: m/m [%] = Na: 4.84; P: 1.09; V: 5.36; W: 58.1. Found: m/m [%] = Na: 5.22; P: 1.16; V: 5.40; W: 52.8. Data normalised to tungsten, Na/P/V/W ratio: 7.12/1.17/3.32/9.

TGA: 8.16 % weight loss upon drying, this corresponds to 13 mol lattice water per mol of the POM.

2.7 Synthesis of $\text{Na}_y\text{H}_z[\text{PV}_x\text{W}_{12-x}\text{O}_{40}]$ with $x = 4$ to 6 according to a modified procedure of Odyakov *et al.*^[2-4]

Sodium metavanadate was dissolved in deionized water at a temperature of 60 °C. Parallel to this step sodium tungstate dihydrate was dissolved in deionized water and a 85 % solution of phosphoric acid in water was added. The solution was boiled and the aqueous sodium metavanadate solution was added dropwise. After the addition the solution turned into light brown and the final pH value was 7.5 which was adjusted to 1.5 using a 2 M hydrochloric acid solution in water. The dark brown solution was refluxed for 60 min. After cooling to room temperature, the solution was filtered and desalinated using a nanofiltration approach. An intense red coloured solid was obtained.

Characterisation:

NaPV₄W:

³¹P-NMR (242.9 MHz, H₂O/D₂O, 20 °C): δ [ppm] = -10.0 to -13.5.

⁵¹V-NMR (157.8 MHz, H₂O/D₂O, 20 °C): δ [ppm] = -542.0 to -573.0.

FT-IR (ATR): $\tilde{\nu}$ [cm⁻¹] = 3342 (w), 1616 (w, O–H, lattice H₂O), 1072, 1053 (s, P–O), 948 (s, M=O_t), 868 (m, (M–O–M)_{vertex}), 756 (s, broad, (M–O–M)_{edge}).

Elemental analysis calculated for $\text{Na}_7[\text{PV}_4\text{W}_8\text{O}_{40}] \cdot 11 \text{H}_2\text{O}$: m/m [%] = Na: 5.95; P: 1.15; V: 7.53; W: 54.4. Found: m/m [%] = Na: 5.06; P: 1.20; V: 6.95; W: 48.9. Data normalised to tungsten, Na/P/V/W ratio: 6.62/1.17/4.11/8.

TGA: 7.55 % weight loss upon drying, this corresponds to 11 mol lattice water per mol of the POM.

NaPV₅W:

³¹P-NMR (242.9 MHz, H₂O/D₂O, 20 °C): δ [ppm] = -6.18 to -14.4.

⁵¹V-NMR (157.8 MHz, H₂O/D₂O, 20 °C): δ [ppm] = -523.0 to -624.0.

FT-IR (ATR): $\tilde{\nu}$ [cm⁻¹] = 3500 (w), 1600 (w, O–H, lattice H₂O), 1070, 1052 (s, P–O), 945 (s, M=O_t), 865 (m, (M–O–M)_{vertex}), 751 (s, broad, (M–O–M)_{edge}).

Elemental analysis calculated for $\text{Na}_8[\text{PV}_5\text{W}_7\text{O}_{40}] \cdot 11 \text{H}_2\text{O}$: m/m [%] = Na: 7.09; P: 1.19; V: 9.82; W: 49.6. Found: m/m [%] = Na: 5.78; P: 1.26; V: 9.66; W: 47.6. Data normalised to tungsten, Na/P/V/W ratio: 6.79/1.10/5.13/7.

TGA: 7.49 % weight loss upon drying, this corresponds to 11 mol lattice water per mol of the POM.

NaPV₆W:

³¹P-NMR (242.9 MHz, H₂O/D₂O, 20 °C): δ [ppm] = -7.21 to -13.6.

⁵¹V-NMR (157.8 MHz, H₂O/D₂O, 20 °C): δ [ppm] = -525.1 to -621.0.

FT-IR (ATR): $\tilde{\nu}$ [cm⁻¹] = 3500 (w), 1600 (w, O–H, lattice H₂O), 1071, 1059 (s, P–O), 944 (s, M=O_t), 864 (m, (M–O–M)_{vertex}), 748 (s, broad, (M–O–M)_{edge}).

Elemental analysis calculated for $\text{Na}_9[\text{PV}_6\text{W}_6\text{O}_{40}] \cdot 13 \text{H}_2\text{O}$: m/m [%] = Na: 8.21; P: 1.23; V: 12.1; W: 43.8. Found: m/m [%] = Na: 5.69; P: 1.20; V: 11.55; W: 40.68. Data normalised to tungsten, Na/P/V/W ratio: 6.71/1.05/6.15/6.

TGA: 9.65 % weight loss upon drying, this corresponds to 13 mol lattice water per mol of the POM.

See table 2 for details:

Table 2: Experimental details used to synthesize the POMs NaPV_xW with $x = 1$ to 6.

	Sodium metavanadate	Sodium tungstate dihydrate	Phosphoric acid (85 %)	Water for vanadate	Water for tungstate
NaPV₄W	2.03 g 16.6 mmol 4 equivalents	10.53 g 31.9 mmol 8 equivalents	0.51 g 4.4 mmol 1 equivalents	50 mL	50 mL
NaPV₅W	2.65 g 21.7 mmol 5 equivalents	9.64 g 29.2 mmol 7 equivalents	0.54 g 4.68 mmol 1 equivalents	60 mL	50 mL
NaPV₆W	3.33 g 27.3 mmol 6 equivalents	8.66 g 26.3 mmol 6 equivalents	0.57 g 4.94 mmol 1 equivalents	50 mL	50 mL

2.8 Etherate method

The sodium salt NaPV_xW was dissolved in deionized water and a hydrochloric acid solution in water was added. In a separation funnel the acidified solution was mixed with diethyl ether. Upon separation of the phases a third new, oily, and heavy phase with an intense colour was formed at the bottom. The POM ether phase was separated. New acid fractions were added to the aqueous phase and the process was repeated until formation of the third, heavy phase is no longer observed. Combined POM ether phases were dried under reduced pressure to yield a solid product.

See table 3 for details

Table 3: Experimental details for the POM etherate method.

	POM [g]	Water [mL]	Hydrochloric acid (37 %) [mL]	Diethyl ether [mL]
NaPVW → HPVW	2.00	50	20	50
NaPV₂W → HPV₂W	2.01	50	20	50

Characterisation:

HPVW:

³¹P-NMR (242.9 MHz, H₂O/D₂O, 20 °C): δ [ppm] = -14.9.

⁵¹V-NMR (157.8 MHz, H₂O/D₂O, 20 °C): δ [ppm] = -555.9.

FT-IR (ATR): $\tilde{\nu}$ [cm⁻¹] = 1620 (w, O–H, lattice H₂O), 1070 (s, P–O), 959 (s, M=O_t), 876 (m, (M–O–M)_{vertex}), 735 (s, broad, (M–O–M)_{edge}).

Elemental analysis calculated for H₄[PVW₁₁O₄₀] · 18 H₂O: m/m [%] = Na: 0.00; P: 1.01; V: 1.66; W: 65.8. Found: m/m [%] = Na: < 0.02; P: 1.04; V: 1.70; W: 63.0. Data normalised to tungsten, Na/P/V/W ratio: 0.00/1.08/1.07/11.

TGA: 10.33 % weight loss upon drying, this corresponds to 18 mol lattice water per mol of the POM.

HPV₂W:

³¹P-NMR (242.9 MHz, H₂O/D₂O, 20 °C): δ [ppm] = -12.9 to -14.9.

⁵¹V-NMR (157.8 MHz, H₂O/D₂O, 20 °C): δ [ppm] = -528.1, -547.3, -553.3 to -563.9.

FT-IR (ATR): $\tilde{\nu}$ [cm⁻¹] = 1620 (w, O–H, lattice H₂O), 1061.3 (s, P–O), 964 (s, M=O_i), 884 (m, (M–O–M)_{vertex}), 724 (s, broad, (M–O–M)_{edge}).

Elemental analysis calculated for H₄[PVW₁₁O₄₀] · 15 H₂O: m/m [%] = Na: 0.00; P: 1.07; V: 3.53; W: 63.7. Found: m/m [%] = Na: < 0.10; P: 1.15; V: 3.29; W: 66.7. Data normalised to tungsten, Na/P/V/W ratio: 0.00/1.02/1.78/10.

TGA: 9.15 % weight loss upon drying, this corresponds to 15 mol lattice water per mol of the POM.

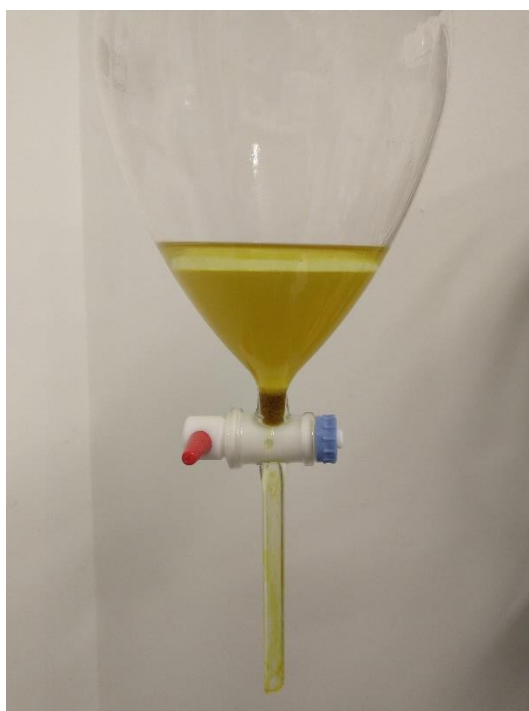


Figure S49: POM etherate method: Extraction of an acidic aqueous POM solution with diethyl ether leads, in the case of low V(V) substituted phosphotungstates, to the formation of a third, etheric POM phase with a higher density than the aqueous phase, from which the POM can be isolated as the corresponding heteropolyacid. Phase above: Diethyl ether, middle: aqueous, acidic POM phase, bottom: oily POM ether phase.

2.9 Crystallography

Both crystals were obtained by slow evaporation of water from an aqueous solution under reduced pressure in a desiccator.

The crystallographic data were solved and refined using Olex2^[5] (ShelX^[6-9]), Shelxtl^[10] and PLATON.^[11] Residual electron density was attributed to hydration water and was refined with a solvent mask (aka SQUEEZE).^[12] The observed disorder of the PO₄ tetrahedron was modelled by assigning a partial occupancy of 0.5 to all four oxygen atoms.

Table 4: Crystal structure data and structure refinement for NaPV₂W and NaPV₅W.

Compound	NaPV ₂ W	NaPV ₅ W
Empirical formula	O ₄₀ PV ₂ W ₁₀	O ₄₀ PV ₅ W ₇
Formula weight	2611.35	2212.62
Temperature/K	99.9(2)	99.97(12)
Crystal system	tetragonal	tetragonal
Space group	P4/mnc	P4/mnc
<i>a</i> [Å]	12.73019(18)	12.67239(15)
<i>b</i> [Å]	12.73019(18)	12.67239(15)
<i>c</i> [Å]	17.9486(4)	17.7115(4)
α [°]	90	90
β [°]	90	90
γ [°]	90	90
Volume [Å ³]	2908.70(10)	2844.28(9)
<i>Z</i>	2	2
ρ_{calc} [g/cm ³]	2.982	2.584
μ [mm ⁻¹]	20.085	14.971
F(000)	2242.0	1936.0
Crystal size [mm ³]	0.24 × 0.22 × 0.1	0.26 × 0.24 × 0.16
Radiation	Mo K α (λ = 0.71073)	Mo K α (λ = 0.71073)
2 θ range for data collection [°]	4.538 to 59.032	4.546 to 58.912
Index ranges	-17 ≤ <i>h</i> ≤ 17, -17 ≤ <i>k</i> ≤ 17, -23 ≤ <i>l</i> ≤ 24	-17 ≤ <i>h</i> ≤ 17, -17 ≤ <i>k</i> ≤ 17, -23 ≤ <i>l</i> ≤ 24
Reflections collected	117752	114121
Independent reflections	2076 [<i>R</i> _{int} = 0.0521, <i>R</i> _{sigma} = 0.0109]	2028 [<i>R</i> _{int} = 0.0586, <i>R</i> _{sigma} = 0.0109]
Data/restraints/parameters	2076/0/69	2028/0/69
Goodness-of-fit on F ²	1.064	1.032
Final <i>R</i> indexes [<i>I</i> >= 2 σ (<i>I</i>)]	<i>R</i> ₁ = 0.0285, <i>wR</i> ₂ = 0.0681	<i>R</i> ₁ = 0.0264, <i>wR</i> ₂ = 0.0616
Final <i>R</i> indexes [all data]	<i>R</i> ₁ = 0.0348, <i>wR</i> ₂ = 0.0734	<i>R</i> ₁ = 0.0298, <i>wR</i> ₂ = 0.0646
Largest diff. peak/hole [e Å ⁻³]	1.45/-1.18	3.22/-0.91
Deposition number	2240685	2240686

3 References

1. Domaille, P.J.; Watunya, G. Synthesis and tungsten-183 NMR characterization of vanadium-substituted polyoxometalates based on B-type tungstophosphate $PW_9O_{34}^{9-}$ -precursors. *Inorg. Chem.* **1986**, *25*, 1239–1242.
2. Odyakov, V.F.; Zhizhina, E.G. A novel method of the synthesis of molybdovanadophosphoric heteropoly acid solutions. *React. Kinet. Catal. Lett.* **2008**, *95*, 21–28.
3. Odyakov, V.F.; Zhizhina, E.G.; Maksimovskaya, R.I. Synthesis of molybdovanadophosphoric heteropoly acid solutions having modified composition. *Appl. Catal. A Gen.* **2008**, *342*, 126–130.
4. Odyakov, V.F.; Zhizhina, E.G. New process for preparing aqueous solutions of Mo-V-phosphoric heteropoly acids. *Russ. J. Inorg. Chem.* **2009**, *54*, 361–367.
5. Dolomanov, O.V.; Bourhis, L.J.; Gildea, R.J.; Howard, J.A.; Puschmann, H. OLEX2: a complete structure solution, refinement and analysis program. *J. Appl. Crystallogr.* **2009**, *42*, 339–341.
6. SHELX. Available online: <https://www.noah-itn.eu/wp-content/uploads/2019/03/shelx-manual.pdf> (accessed on 22 February 2023).
7. Sheldrick, G.M. A short history of SHELX. *Acta Crystallogr. Sec. A: Found. Crystallogr.* **2008**, *64*, 112–122.
8. User Guide to Crystal Structure Refinement with SHELXL. 2008.
9. Hübschle, C.B.; Sheldrick, G.M.; Dittrich, B. ShelXle: a Qt graphical user interface for SHELXL. *J. Appl. Crystallogr.* **2011**, *44*, 1281–1284.
10. Available online: <https://digital-library.theiet.org/content/journals/10.1049/esn.1987.0025?fmt=text> (accessed on 22 February 2023).
11. Spek, A.L.J. Single-crystal structure validation with the program PLATON. *J. Appl. Crystallogr.* **2003**, *36*, 7–13.
12. Spek, A.L. PLATON SQUEEZE: a tool for the calculation of the disordered solvent contribution to the calculated structure factors. *Acta Crystallogr. Sec. C: Struct. Chem.* **2015**, *71*, 9–18.

ChemCatChem

Supporting Information

Synthesis and Characterization of Co(II) Substituted Keggin-Type Polyoxometalates as Novel Catalysts for the Hydroformylation of 1-Hexene in a Thermomorphic Solvent System

Jan-Christian Raabe, Lea Hombach, Maximilian J. Poller, Alberto Collauto, Maxie M. Roessler, Andreas Vorholt, Anna Katharina Beine, and Jakob Albert*

Electronic Supporting Information

1	Catalyst Preparation.....	2
1.1	Chemicals.....	2
1.2	Analytical methods	3
1.3	Synthetic procedures	7
1.3.1	Synthesis of $\text{HPCoMo H}_7[\text{PCoMo}_{11}\text{O}_{40}]$	7
1.3.2	Synthesis of $\text{HPCo}_2\text{Mo H}_{11}[\text{PCo}_2\text{Mo}_{10}\text{O}_{40}]$	7
1.3.3	Synthesis of $\text{HPCo}_3\text{Mo H}_{15}[\text{PCo}_3\text{Mo}_9\text{O}_{40}]$	8
1.4	Elemental analysis	9
1.5	Vibrational spectroscopy	9
1.6	Crystallography	10
1.7	NMR spectroscopy.....	12
1.8	EPR spectroscopy	12
1.9	UV-Vis spectroscopy	13
1.10	Electrochemistry	16
1.11	Reference data for cobalt(II) acetate and HPMo	19
1.12	Incorporation experiments of more than three Co(II) ions	23
2	Hydroformylation	25
2.1	Experimental	25
2.2	Results.....	27
3	References	30

1 Catalyst Preparation

Three Co(II) substituted phosphomolybdates were synthesized in this work. All compounds were characterized as follows:

Compositional analysis:

- Atomic absorption/inductively coupled plasma optical emission spectrometry (AAS/ICP-OES)
- Thermogravimetric analysis (TGA)

Solid-state characterization:

- Vibrational spectroscopy (infrared (IR) and Raman spectroscopy)
- Single X-ray crystal structure analysis (X-ray diffraction, s-XRD)

Characterization in aqueous solution:

- ^{31}P nuclear magnetic resonance (NMR) spectroscopy
- Ultraviolet visible (UV-Vis) spectroscopy
- Continuous-wave (CW) Electromagnetic-spin-resonance (EPR) spectroscopy

RedOx behavior:

- Cyclic voltammetry (CV)
- Square wave voltammetry (SWV)

1.1 Chemicals

The chemicals were obtained from the following suppliers: molybdenum trioxide (MoO_3) from Alfa Aesar and cobalt(II) acetate tetrahydrate from Carl Roth. Phosphoric acid was obtained as a 85 % solution in water from Grüssing and diluted with deionized water to a concentration of 25 %. Deionized water was used as solvent for all synthesis. $\text{H}_3[\text{PMo}_{12}\text{O}_{40}]$ (HPMo) was obtained from Sigma Aldrich. The letter was used as reference for comparing the analytical data.

1.2 Analytical methods

AAS/ICP-OES:

All samples were measured with an ICP-OES-spectrometer for elemental analysis (Fa. Spectro, type ARCOS) for Mo and P (method ICP-OES). The element Co was determined with an AAS-F (Fa. Thermo, type Solaar S Series) (method: F-AES without HKL).

Sample preparation: the initial weight was dissolved in water (5 mL), acidified with a 65 % nitric acid solution in water (100 μ L), and the solution was filled up with water to 25 mL in a volumetric flask.

TGA:

All TGA measurements were measured with a TG 209 F1 Libra of NETZSCH. The data were processed with the software Proteus from NETZSCH. Approximately 20 mg of the sample was weighed into a quartz crucible and the change in mass was measured following a standard temperature program:

- Tare
- Heating to 30 °C with maximum heating rate
- Stay at 30 °C for 15 minutes
- Heating to 350 °C with a heating rate of 10 K/min
- Stay at 350 °C for 30 minutes
- The sample was then cooled to room temperature

The starting temperature was below 30 °C. During the measurement, a nitrogen flow of 60 sccm/min was passed through the instrument. The TGA data show three regions: hygroscopic water (water that comes from the air), lattice water (water from crystal association) and the mass consistency (pure POM without any moisture). The final data were exported as a .x/y text document. With the use of Origin® 2019b the TGA data were plotted as follows: on the y -axis the mass difference measured in mg and on the x -axis the temperature measured in °C.

IR spectroscopy

IR spectra were measured in attenuated total reflection (ATR) measurement mode on a QATR™-S single-reflection ATR (with a diamond prism) from Shimadzu. In the software LabSolutions IR from the raw data obtained, the baseline was corrected, and the peaks were

determined manually. The IR data were then exported as an .x/y text document and plotted in Origin 2019b.

Raman spectroscopy

Raman spectra were measured on a SENTERRA Raman microscope from Bruker Optik GmbH. The aperture was set to 50 x 1000 μm . A 20 objective was used on the microscope. The laser has a wavelength of 785 nm and the measurement range used was between 75 cm^{-1} and 1525 cm^{-1} . The integration time was 16 seconds, the number of scans was 8 and the Raman laser power was 10 mW. Data were exported as .dpt data format from the Opus Software and plotted in Origin 2019b.

Single X-ray crystal structures:

The crystals were obtained by slow evaporation of the solvent under reduced pressure in a desiccator.

All single crystals were measured on a 4-circle single crystal diffractometer SuperNova from Oxford Diffraction (Company: Agilent Technologies, Acquisition: Nov. 2011, using a molybdenum and copper source (dual instrument), Microfocus tubes, cryostream-700 Plus nitrogen steam cooling, 100-500 K (Oxford Cryosystems)). The crystal structure data were solved and refined using Olex2 v1.5 and the ShelX algorithm, as well as the PLATON software.¹⁻⁵ All crystallographic data were saved as .cif file. Some details on the refinement of the individual crystal structure data sets in Olex2 v1.5 are explained below:

- Using Olex2 v1.5 the single-crystal data for HPCoMo were solved and refined as a twinned structure using ShelXS and the method “Direct methods” in the space group Fddd (70). Using the software tool XPREP of Shelxtl the space group Fd-3m (227) was suggested, but a suitable solution in this space group was not found. So, the model was refined using the space group Fddd. Using the “exyz” command the partial occupation of the metals (Mo, Co) was adjusted to 11/12 for Mo (part 1) and 1/12 for Co (part 2). Residual electron density attributed to hydration water has been refined with a solvent mask (aka SQUEEZE). R_1 : 1.40 %, wR_2 : 4.26 %, GooF: 1.194 and R_{int} : 4.86 %.
- Using Olex2 v1.5 the single-crystal data for $\text{H}_{11}[\text{PCo}_2\text{Mo}_{10}\text{O}_{40}]$ were solved and refined as a twinned structure using ShelXS and the method “Direct methods” in the space group Fddd (70). Using the software tool XPREP of Shelxtl⁶ the space group Fd-3m (227) was suggested, but a suitable solution in this space group was not found. So, the model was refined using the space group Fddd. Using the “exyz” command the partial occupation of

the metals (Mo, Co) was adjusted to 5/6 for Mo (part 1) and 1/6 for Co (part 2). Residual electron density attributed to hydration water has been refined with a solvent mask (aka SQUEEZE). R_1 : 1.32 %, wR_2 : 3.80 %, GooF: 1.176 and R_{int} : 3.38 %.

In both datasets hydrogen atoms were not modelled.

NMR spectroscopy

All NMR spectra were measured with a Bruker AVANCEII 600 MHz. The samples were prepared as follows: The respective POM (70 mg) was dissolved in deionized water (0.63 mL), which had previously been adjusted to pH 1 with a 2 M hydrochloric acid solution in deionized water. Acetone- d_6 (0.07 mL) was added as deuterated solvent. All ^{31}P spectra were measured with a Time Domain Data Sizes (TD) of 32 K, the Number of Scans (NS) was set to 2K, the Transmitter Frequency Offset for Channel F1 (O1) and the Spectral Width (SW) were -1 and 40 ppm. The Delay D1 was set to 1 s. The NMR analysis was done with the software MestReNova®. In MestReNova®, the peaks were first determined, and the data subsequently exported in .csv data format. The data were plotted in Origin 2019b. Deuterium oxide (D_2O) should not be used for the NMR measurements because the deuterium atoms are exchanged for the acidic protons of the POMs, so that an automated "NMR-lock" on deuterium oxide fails during the measurement.

EPR spectroscopy

Samples of the $\text{H}_7[\text{PCoMo}_{11}\text{O}_{40}]$ (HPCoMo) and $\text{H}_{11}[\text{PCo}_2\text{Mo}_{10}\text{O}_{40}]$ (HPCo $_2$ Mo) POMs for EPR spectroscopy were prepared by dissolving to a final concentration of 10 mM the corresponding powders in ultrapure water ($\sigma = 0.055 \mu\text{S}/\text{cm}$) acidified to pH 1 with HCl. The solutions were transferred into 3 mm ID, 4 mm OD quartz tubes (Wilmaad-LabGlass) using glass micropipettes; the obtained samples were flash-frozen in cold isopentane immediately after preparation and stored under liquid Nitrogen.

X-band CW-EPR measurements were performed at Imperial College London's PEPR Facility on a Bruker Elexsys E580 spectrometer equipped with an ER4118X-MD5 dielectric resonator; the sample temperature was controlled using a closed-circuit cryostat (Cryogenic Ltd.). The magnetic field was swept in the range from 0 to 1 T with a rate of 33 G/s; for all the measurements the field modulation amplitude was set to 5 G with a 100 kHz modulation frequency. The values of the temperature and microwave power are given for each measurement.^[7,8]

The spectra were processed and simulated using EasySpin 5.2.35 running on MATLAB R2021a.^[9] Owing to the sizeable spin-orbit coupling, high-spin Co(II) ($S = 3/2$) can be treated as an effective $S = 1/2$ spin system characterised by effective g values; these have interpreted in terms of real g values (assumed isotropic) and rhombicity of the zero-field splitting interaction resorting to the theory developed by Pilbrow.^[10] UV-Vis spectroscopy

The UV-Vis spectra were measured with a Cary 60 UV-Vis spectrometer (Agilent Technologies) in a 3 mL Quartz cuvette (QS). Measurements were carried out using the Cary WinUV software. All measurements were taken in the measuring range between 200 nm and 800 nm. The absorption was measured in the slow measurement mode. All data were then exported as a .csv data set and plotted in Origin 2019b. For determining the extinction coefficients the software Cary concentrations was used. The detailed procedure is described in our previous publication.⁷

Electrochemistry (CV and SWV):

The CV/SWV measurements were done in aqueous, hydrochloric acid medium at pH 1 and a concentration of 1 mmol/L on an Ivium potentiostats. During the measurement, the solution was purged with nitrogen. The working electrode was a glassy carbon electrode (diameter: 3 mm), the reference electrode was the Ag/Ag⁺ electrode and the counter electrode was a platinum electrode. Measurements were taken in the measuring range between -0.6 and 1 V with a scan rate (for CV) of 100 mV/s for 3 scans. All SWV measurements were taken with a scan rate of 5 mV/s, a modulation amplitude of 20 mV and a frequency of 25 Hz. Measurements were done with the software Ivium and the data was subsequently exported as an .x/y text document and plotted in Origin 2019b.

1.3 Synthetic procedures

1.3.1 Synthesis of HPCoMo H₇[PCoMo₁₁O₄₀]

Deionized water (200 mL) was introduced, molybdenum trioxide (17.6674 g, 122.7 mmol, 11 equivalents) and a 25 % phosphoric acid solution in water (4.376 g, 11.16 mmol, 1 equivalent) added. The suspension was heated to reflux, forming a yellow clear solution. After 90 minutes, a solution of cobalt (II) acetate tetrahydrate (2.8121 g, 11.29 mmol, 1.011 equivalents) in water (50 mL) was added dropwise to the batch, turning the reaction solution dark brown. It was then cooled to room temperature, filtered, and concentrated under reduced pressure. A light green solid (20.0652 g) was obtained.

Characterization:

³¹P-NMR (242.9 MHz, H₂O/acetone-*d*₆, 20 °C): δ [ppm] = -1.25, -3.02, -3.74.

IR (ATR): $\tilde{\nu}$ [cm⁻¹] = 3464.1 (w, H₂O), 1604.0 (w, H₂O), 1059.8 (me, P-O), 959.3 (st, M=O_t), 873.7 (me, (M-O-M)_{vertex}), 761.7 (st, (M-O-M)_{edge}).

UV-Vis: 212 nm, 230 nm (shoulder).

ICP-OES: Calculated for H₇[PCoMo₁₁O₄₀] · 8 H₂O: 54.5 % Mo, 3.043 % Co, 1.6 % P. Found for H₇[PCoMo₁₁O₄₀] · 8 H₂O: 57.15 % Mo, 3.3 % Co, 1.631 % P. Data normalized to molybdenum. P/Co/Mo ratio: 0.972/1.03/11.

TGA: 7.171 % weight loss upon drying, this corresponds to 8 mol water per mol of the POM.

1.3.2 Synthesis of HPCo₂Mo H₁₁[PCo₂Mo₁₀O₄₀]

Deionized water (185 mL) was introduced, molybdenum trioxide (16.3631 g, 113.7 mmol, 10 equivalents) and a 25 % phosphoric acid solution in water (4.4613 g, 11.38 mmol, 1 equivalent) added. The suspension was heated to reflux, forming a yellow clear solution. After 60 minutes, a solution of cobalt (II) acetate tetrahydrate (5.7274 g, 22.99 mmol, 2.02 equivalents) in water (50 mL) was added dropwise to the batch, turning the reaction solution dark brown. It was then cooled to room temperature, filtered, and concentrated under reduced pressure. A light brown solid (20.0190 g) was obtained.

Characterization:

³¹P-NMR (242.9 MHz, H₂O/acetone-*d*₆, 20 °C): δ [ppm] = 0.96, -0.89, -2.94, -3.72.

IR (ATR): $\tilde{\nu}$ [cm^{-1}] = 3389.2, 3172.4 (me, H_2O), 1607.6 (me, H_2O), 1054.8 (me, P-O), 952.9 (st, M=O_t), 889.4 (st, (M-O-M)_{vertex}), 771.0 (st, (M-O-M)_{edge}).

UV-Vis: 212 nm, 230 nm (shoulder).

ICP-OES: Calculated for $\text{H}_{11}[\text{PCo}_2\text{Mo}_{10}\text{O}_{40}] \cdot 12 \text{H}_2\text{O}$: 48.565 % Mo, 5.966 % Co, 1.568 % P. Found for $\text{H}_{11}[\text{PCo}_2\text{Mo}_{10}\text{O}_{40}] \cdot 12 \text{H}_2\text{O}$: 48.65 % Mo, 6.32 % Co, 1.604 % P. Data normalized to molybdenum. P/Co/Mo ratio: 1.02/2.12/10.

TGA: 11.297 % weight loss upon drying, this corresponds to 12 mol water per mol of the POM.

1.3.3 Synthesis of HPCo_3Mo $\text{H}_{15}[\text{PCo}_3\text{Mo}_9\text{O}_{40}]$

Deionized water (169 mL) was introduced, molybdenum trioxide (15.0084 g, 104.3 mmol, 9 equivalents) and a 25 % phosphoric acid solution in water (4.5610 g, 11.64 mmol, 1 equivalent) added. The suspension was heated to reflux, forming a yellow clear solution. After 60 minutes, a solution of cobalt (II) acetate tetrahydrate (8.7550 g, 35.15 mmol, 3.02 equivalents) in water (75 mL) was added dropwise to the batch, turning the reaction solution dark brown. It was then cooled to room temperature, filtered, and concentrated under reduced pressure. A dark solid (20.4851 g) was obtained.

Characterization:

³¹P-NMR (242.9 MHz, $\text{H}_2\text{O}/\text{acetone-}d_6$, 20 °C): δ [ppm] = 1.19, -0.78, -2.94, -4.01.

IR (ATR): $\tilde{\nu}$ [cm^{-1}] = 3351.4, 3165.2 (me, H_2O), 1615.4 (me, H_2O), 1042.7 (me, P-O), 935.0 (st, M=O_t), 870.1 (st, (M-O-M)_{vertex}), 773.8 (st, (M-O-M)_{edge}).

UV-Vis: 211 nm, 229 nm (shoulder).

ICP-OES: Calculated for $\text{H}_{15}[\text{PCo}_3\text{Mo}_9\text{O}_{40}] \cdot 16 \text{H}_2\text{O}$: 42.861 % Mo, 8.776 % Co, 1.537 % P. Found for $\text{H}_{15}[\text{PCo}_3\text{Mo}_9\text{O}_{40}] \cdot 16 \text{H}_2\text{O}$: 49.4 % Mo, 9.485 % Co, 1.691 % P. Data normalized to molybdenum. P/Co/Mo ratio: 0.955/2.81/9.

TGA: 14.576 % weight loss upon drying, this corresponds to 16 mol water per mol of the POM.

1.4 Elemental analysis

The stoichiometry of the catalysts was verified using ICP-OES and the hydration water content was determined by TGA.

1.5 Vibrational spectroscopy

Table S1: Positions of the different characteristic vibration modes in the FT-IR spectra (measured in cm^{-1}) for all POMs investigated in this work.

POM/vibration mode ν_{as}	(P-O)	(M=O _t)	(M-O-M _{vertex})	(M-O-M _{edge})
HPMo	1059	962	877	744
HPCoMo	1059	960	874	766
HPCo ₂ Mo	1055	953	894	775
HPCo ₃ Mo	1043	935	873	782

Table S2: Position of the characteristic vibration modes for the investigated POMs in the Raman spectra.

Vibration type ν_{as}	HPMo ⁸	HPCoMo	HPCo ₂ Mo	HPCo ₃ Mo
$\nu_{\text{s}}(\text{M}=\text{O}_t)$	1006	1004	993	-
$\nu_{\text{as}}(\text{M}=\text{O}_t)$	987	989	977	980
$\nu_{\text{as}}(\text{M}=\text{O}_t)$	972	973	-	-
$\nu_{\text{as}}(\text{M}-\text{O}_{2\text{c}2}-\text{M})$	911	831	853	893
$\nu_{\text{as}}(\text{M}-\text{O}_{2\text{c}1}-\text{M})$	611	611	609	617
$\delta(\text{M}-\text{O}_{2\text{c}1}-\text{M})$				
$\delta(\text{M}-\text{O}_{2\text{c}2}-\text{M})$	459	-	470	-
$\delta(\text{M}-\text{O}_{2\text{c}1}-\text{M})$	-	-	431	-
$\delta(\text{M}-\text{O}_{2\text{c}2}-\text{M})$	369	363	369	-
$\delta(\text{O}_{2\text{c}1}-\text{M}-\text{O}_{2\text{c}1})$	252	251	251	231
$\delta(\text{O}_{2\text{c}2}-\text{M}-\text{O}_{2\text{c}2})$				
$\delta(\text{M}-\text{O}_{2\text{c}2}-\text{M})$	-	-	226	-
$\nu_{\text{s}}(\text{M}-\text{O}_{4\text{c}})$	232	235	178	-
$\delta(\text{M}-\text{O}_{2\text{c}2}-\text{M})$				
$\delta(\text{M}-\text{O}_{2\text{c}2}-\text{M})$	-	-	158	157
$\delta(\text{O}_{2\text{c}1}-\text{M}-\text{O}_t)$	-	-	-	-
$\delta(\text{M}-\text{O}-\text{M})$	156	157	-	-
$\delta(\text{O}-\text{M}-\text{O})$				
$\delta(\text{O}_{2\text{c}1}-\text{M}-\text{O}_t)$	109	110	-	103
$\delta(\text{M}-\text{O}-\text{M})$				
$\delta(\text{O}-\text{M}-\text{O})$	-	-	78	-
$\nu_{\text{s}}(\text{M}-\text{O}_t)$	-	-	-	-

1.6 Crystallography

Figure S1 shows the asymmetric unit of the HPCo_2Mo structure in the protonated form.

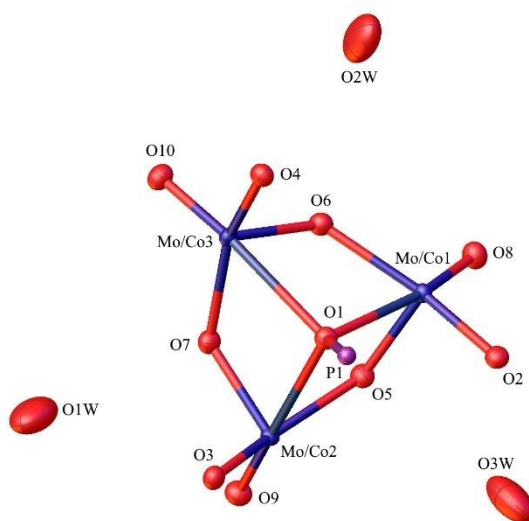


Figure S1: Asymmetric unit of the solid-state structure of HPCo_2Mo with the corresponding numbering of the atoms, hydrogen atoms have not been modeled. Color code: purple: phosphorous, red: oxygen, and blue: metals (Mo, Co).

The space group was originally determined to the cubic space group $Fd\bar{3}m$ (227), but a satisfactory model using this space group for the refinement process was not found. Refining the model in the orthorhombic space group $Fddd$ (70) results in a much better model with a R_1 value of $> 2\%$. Despite the lattice parameters (determined during the measurement and processed by the internal algorithms) $a = b = c = 22.99449(8) \text{ \AA}$ and the lattices angles of $\alpha = \beta = \gamma = 90^\circ$ indicating a cubic system. The same problem occurred for the solid-state structure of HPCoMo . For HPCo_2Mo the real measured lattice parameters are $a = 23.0223(7) \text{ \AA}$, $b = 22.9326(12) \text{ \AA}$, $c = 23.0165(6) \text{ \AA}$, $\alpha = 90.123(3)^\circ$, $\beta = 90.060(2)^\circ$, $\gamma = 90.210(3)^\circ$. Thus, the lattice parameters differ only slightly and are compatible with the orthorhombic crystal system.

The asymmetric unit of HPCo_2Mo in Figure S1 contains three of the metal atoms (blue), ten of the oxygen atoms (red), the phosphorous atom (purple) and three oxygen atoms of hydration water molecules (red). A concrete Co(II) substitution pattern was not found. This means that the Co(II) atoms are distributed over all Mo(VI) positions statistically. The incorporation of Co(II) becomes visible, when comparing the different refinement results of the metal positions with a 12/12 occupancy of Mo(VI) versus the metal ratios determined by elemental analysis

(here for HPCo₂Mo 1/6 Co(II) and 5/6 Mo(VI)), which is resulting in a significantly better model with a smaller R_1 value.

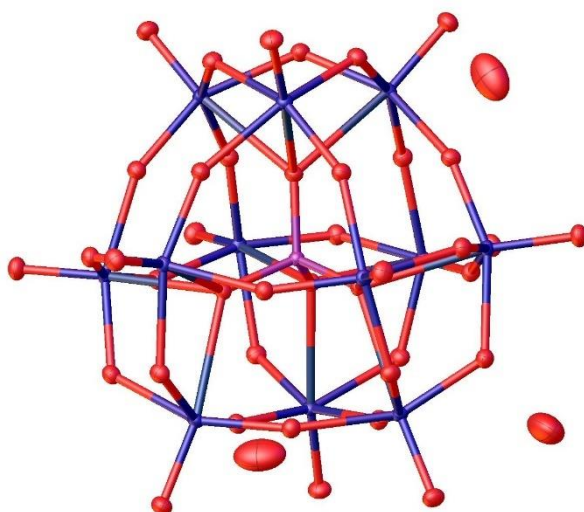


Figure S2: Structure of HPCoMo in the solid-state as determined by s-XRD. Space group: Fddd (70) (orthorhombic). R_1 : 1.40 %, wR_2 : 4.26 %, GooF: 1.194 and R_{int} : 4.86 %. Thermal ellipsoids are drawn at 50 % probability level. Color code: purple: phosphorous, red: oxygen, and blue: metals (Mo, Co). Full .cif file is available through the joint Cambridge Crystallographic Data Centre and Fachinformationszentrum Karlsruhe Access Structures service (deposition number: 2195090).

Table S3: Weighted average of calculated bond lengths (sum of covalent radii) and observed bond lengths of each bond in each POM.⁹

POM	Sum of weighted covalent radii*/observed bond length [Å]			
	P-O _a	O _a -M	M-O _b	M=O _t
HPCoMo	1.74/1.549	1.97/2.422	1.97/1.930	1.97/1.678
HPCo ₂ Mo	1.74/1.555	1.97/2.420	1.97/1.895	1.97/1.679

$$*BL = \frac{a \cdot (r_{Mo} + r_O) + b \cdot (r_{Co} + r_O)}{a + b}$$

With BL the weighted bond length, r_x the covalent radii of the corresponding elements x and a and b the weighting factors (e.g. for HPCo₂Mo-2: $a = 10$ and $b = 2$).

From Table S3 it can be seen that the O_a-M bonds are much longer than the weighted sum of covalent radii of 1.97 Å. This means that this bond is a coordinative-type bond. The bond length between the terminal oxo ligands and the metal atoms is much shorter than the calculated weighted sum of covalent radii, indicating the double bond character. Furthermore the P-O_a bond gets slightly longer with increasing Co(II) content, while the bond length of the two

different M-O bond types shortens. The M=O_t bond length seems not to be affected from the Co(II) substitution in our structures.

1.7 NMR spectroscopy

Table S4: Chemical shifts of the three different HPCo_xMo catalysts in comparison with HPMo.

Compound	HPMo	HPCoMo	HPCo ₂ Mo	HPCo ₃ Mo
³¹ P chemical shift [ppm]	-3.75	-3.62, -3.02, -1.25	-3.72, -2.94, -0.89	-3.72, -2.94, -0.78, 1.19

1.8 EPR spectroscopy

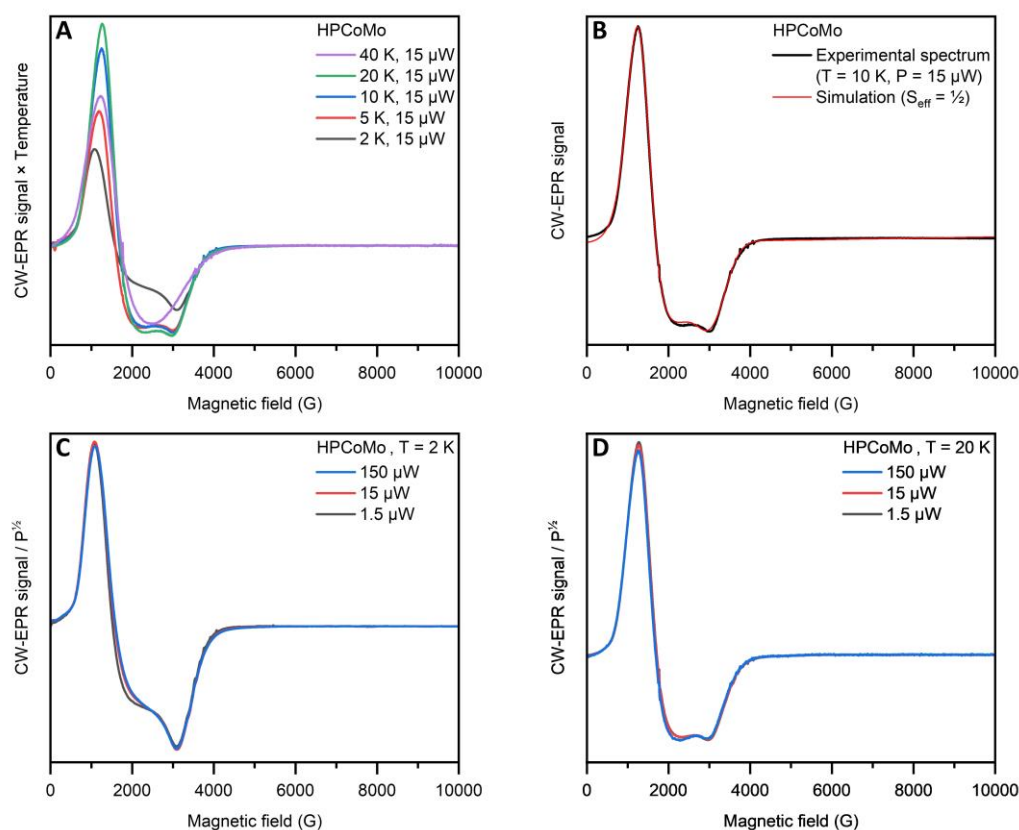


Figure S3: CW-EPR spectra of the HPCoMo POM. **A:** temperature dependence of the spectra recorded under non-saturating conditions in the 2 K – 20 K range. **B:** simulation of the 10 K spectrum as a S = 1/2 effective spin system with g_{eff} values of 5.11 (g strain = 2.08), 4.10 (g strain = 3.13) and 2.27 (g strain = 0.60), corresponding to an $M_S = \pm 1/2$ ground state with $g_{\text{real}} = 2.31$ and $E/D = 0.07$ (see SI 1.2 for further details). **C:** power saturation behaviour at 2 K.

1.9 UV-Vis spectroscopy

Table S5: Position of the different LMCT bands of each catalyst in comparison with HPMo and $\text{Co(OAc)}_2 \cdot 4 \text{H}_2\text{O}$.

POM	HPMo	HPCoMo	HPCo ₂ Mo	HPCo ₃ Mo	Co(OAc) ₂ · 4 H ₂ O
LMCT Mo [nm]	218	212, 230 (shoulder)	210, 231 (shoulder)	210, 230 (shoulder)	-

Figure S4 shows a picture of all three POMs investigated in this work. The mono substituted HPCoMo POM has a yellow/green color and the two- and three-fold substituted POMs show a dark brown color due to the increased Co(II) content.



Figure S4: HPCo_xMo POMs synthesized in this work. From left to the right: $x = 1, 2$ and 3 . The more Co(II) in the Keggin structure the darker the POM.

Lambert-Beer's law (equation 1):

$$Abs = \epsilon_{\lambda} \cdot d \cdot c \quad (1)$$

Abs: Absorption

ϵ_{λ} : extinction coefficient (wavelength λ dependant) [$\text{l mol}^{-1} \text{cm}^{-1}$]

d: Cuvette layer thickness (1 cm) [cm]

c: concentration [mol/L]

Calibration line (equation 2):

$$Abs = a \cdot c + b \quad (2)$$

a : slope

b : Axis intercept

Determining the extinction coefficient:

$$a = \varepsilon_{\lambda} \cdot d \quad (3a)$$

$$\varepsilon_{\lambda} = \frac{a}{d} \quad (3b)$$

The software Cary concentrations was used for determining the calibration curve. Different standards were prepared from a stock solution (1 g/L). The final volume was 3 mL for the cuvette. All calibration curves are shown in Figure S5 to S7:

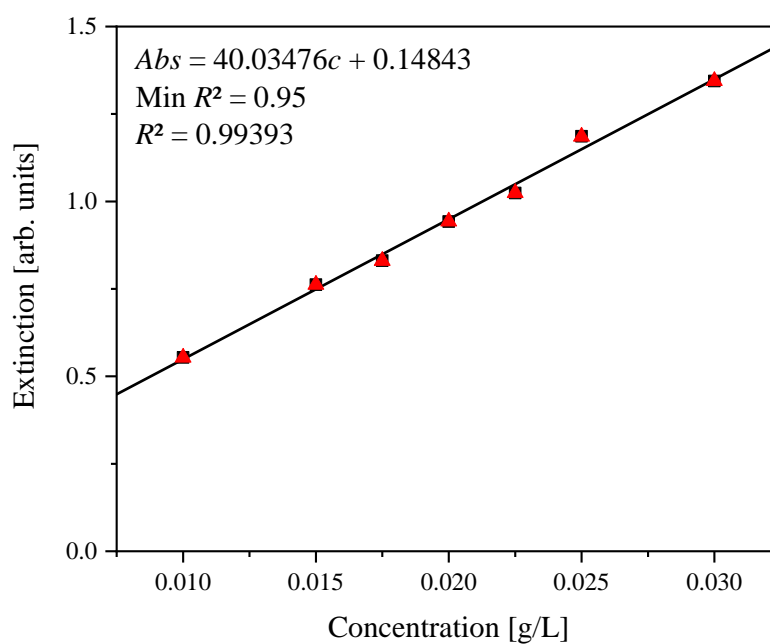


Figure S5: Calibration line for determining the extinction coefficient of HPCoMo at 211.5 nm (Mo(VI) LMCT).

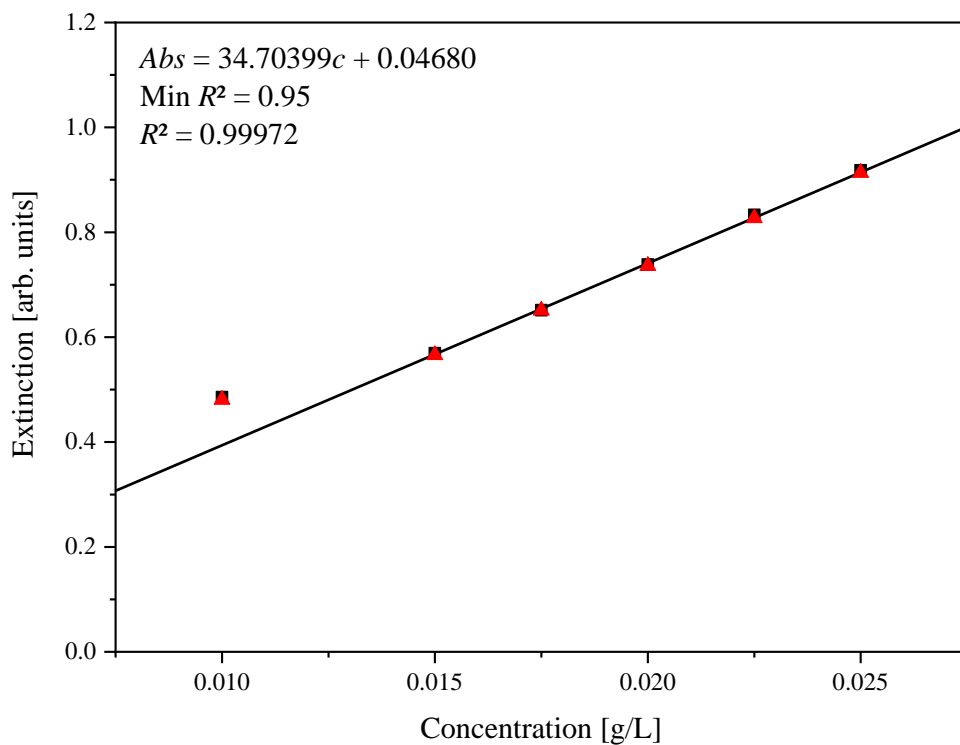


Figure S6: Calibration line for determining the extinction coefficient of HPCo₂Mo at 210.0 nm (Mo(VI) LMCT).

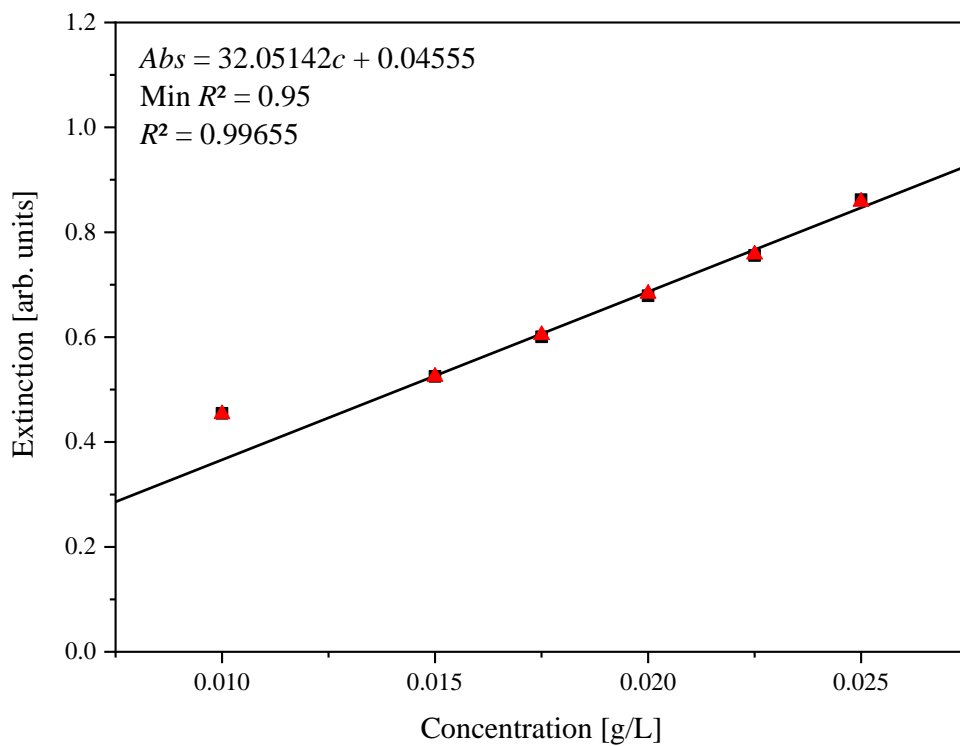


Figure S7: Calibration line for determining the extinction coefficient of HPCo₃Mo at 210.0 nm (Mo(VI) LMCT).

Table S6: Extinction coefficients for the Mo(VI) LMCT band of the HPCo_xMo POMs.

Substitution degree <i>x</i>	HPCo _x Mo	
	Mo(VI)	Mo(V) [$l \text{ mol}^{-1} \text{ cm}^{-1}$]
1		$7.7533 \cdot 10^4$
2		$6.8549 \cdot 10^4$
3		$6.4567 \cdot 10^4$

As expected, the value of the extinction coefficient for the Mo(VI) LMCT decreases with increasing degree of Co(II) substitution, since the Mo(VI) content decreases steadily.

1.10 Electrochemistry

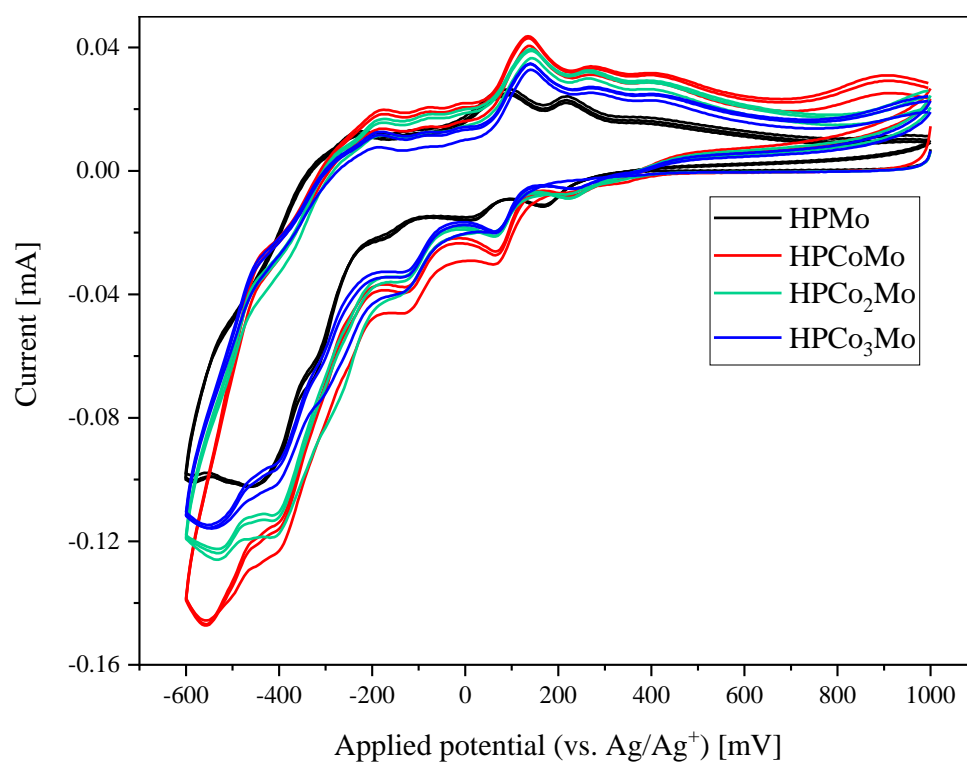


Figure S8: CV measurements of all catalysts in comparison with HPMo using hydrochloric acid (pH 1) as supporting electrolyte (concentration 1 mmol/L, scan rate 100 mV/s).

Table S7 shows an overview of the peak potentials obtained from the SWV and CV (maximum, minimum and mean value) data.

Table S7: Peak maxima from SWV data, peak maxima (oxidation pathway) and peak minima (reduction pathway) from the CV data of the HPCo_rMo POMs in aqueous solution at pH 1 (hydrochloric acid as supporting electrolyte): concentration 1 mmol/L; scan rate 100 mV/s (CV) and 5 mV/s (SWV).

Peak maxima SWV [mV]	Maximum oxidation pathway [mV]	Minimum reduction pathway [mV]	Mean value [mV]
H7[PCoMo₁₁O₄₀]			
-485	-435	-425	-430
-330	-	-	-
-105	-175	-125	-150
-	-75	65	-5
-	-5	-	-
100	135	-	-
255	270	215	243
385	400	-	-
895	900	775	838
H11[PCo₂Mo₁₀O₄₀]			
-500	-440	-	-
-330	-	-	-
-	-170	-140	-155
-105	-70	-	-
-	-0.734	-	-
100	140	65	103
250	270	220	245
380	400	-	-
H15[PCo₃Mo₉O₄₀]			
-495	-435	-410	-423
-330	-	-	-
-285	-	-	-
-	-180	-145	-163
-105	-80	-	-
-	-0.734	-	-
100	140	65	103
260	270	240	255
385	400	-	-

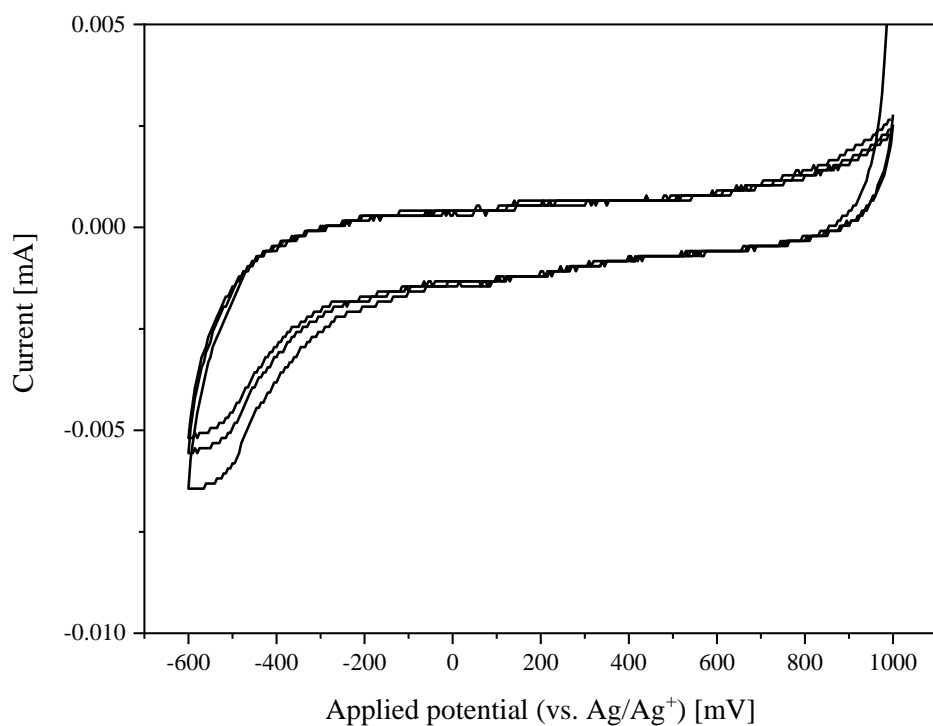


Figure S9: CV measurements of $\text{Co(OAc)}_2 \cdot 4 \text{H}_2\text{O}$ using hydrochloric acid (pH 1) as supporting electrolyte (concentration 1 mmol/L, scan rate 100 mV/s).

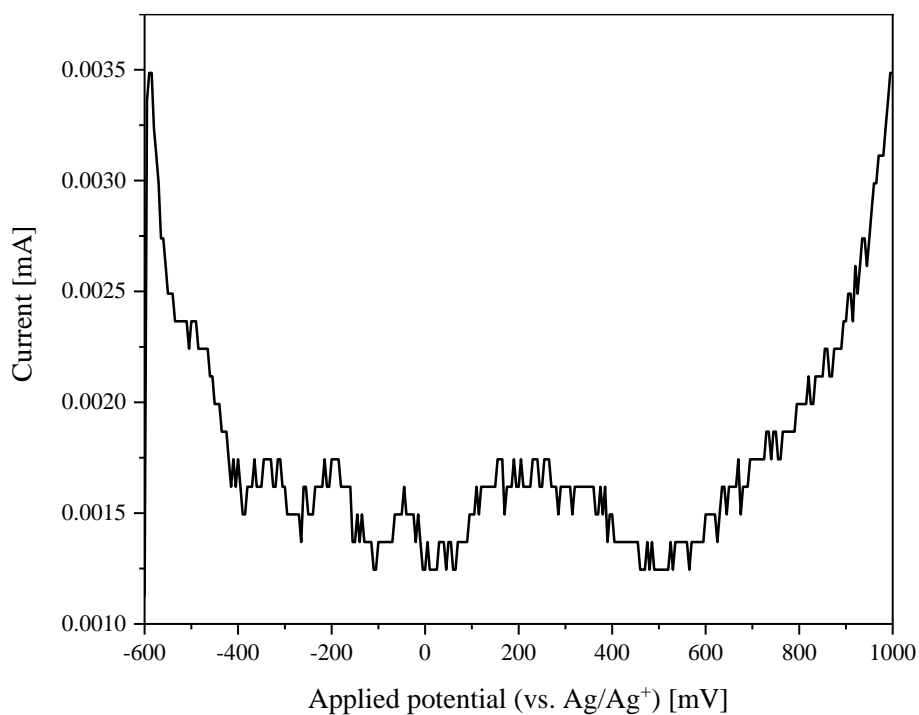


Figure S10: SWV measurements of $\text{Co(OAc)}_2 \cdot 4 \text{H}_2\text{O}$ using hydrochloric acid (pH 1) as supporting electrolyte (concentration 1 mmol/L, scan rate 100 mV/s).

For cobalt(II) acetate there are no RedOx potentials visible in the CV and SWV voltammograms.

1.11 Reference data for cobalt(II) acetate and HPMo

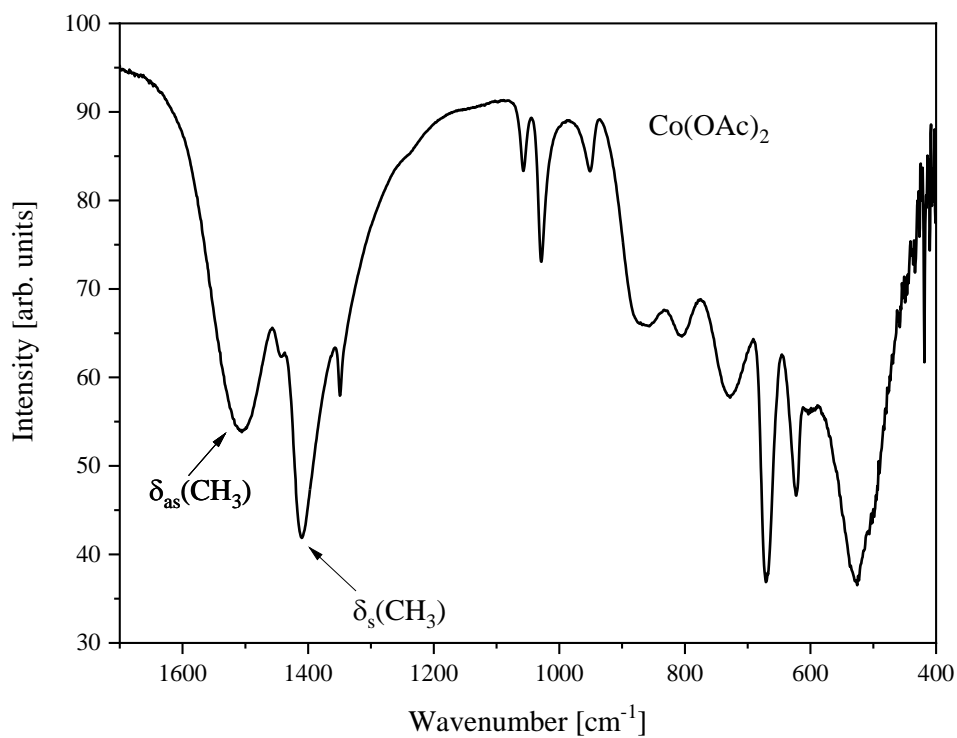


Figure S11: FT-IR data of $\text{Co(OAc)}_2 \cdot 4 \text{H}_2\text{O}$.

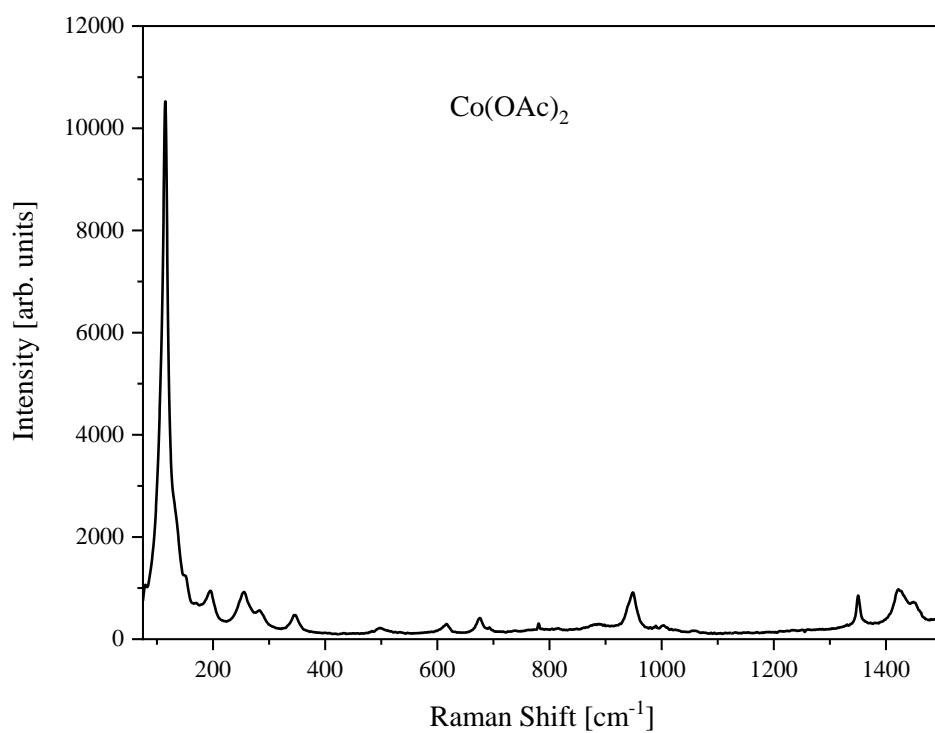


Figure S12: Raman data of $\text{Co(OAc)}_2 \cdot 4 \text{H}_2\text{O}$.

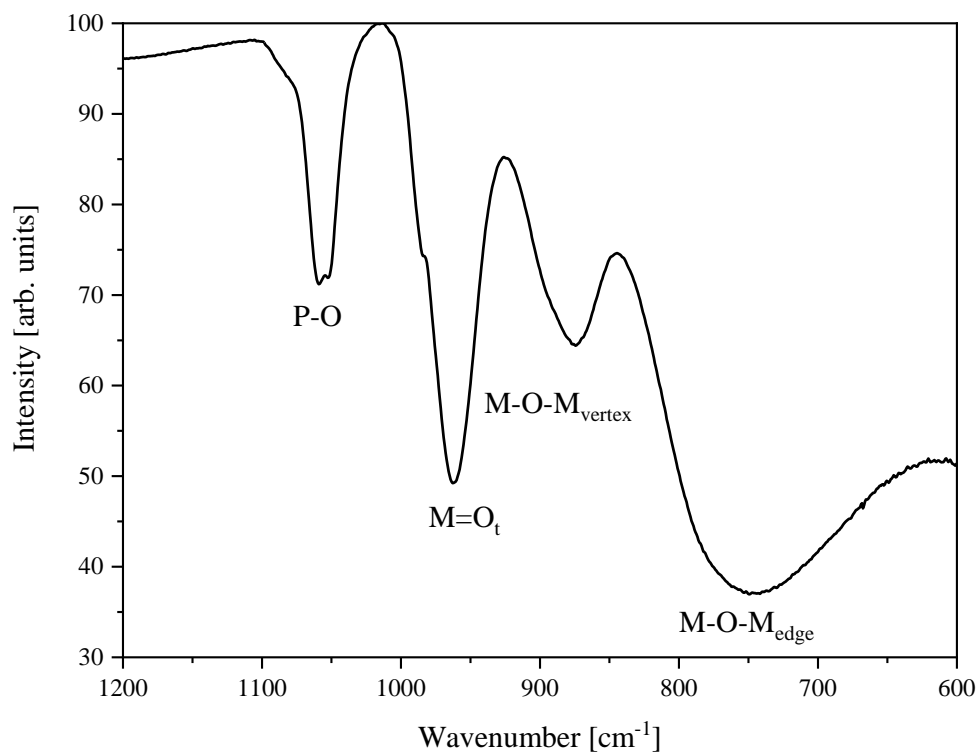


Figure S13: ATR-FT-IR data of HPMo with the characteristic vibrational bands for a typical Keggin structure-type.

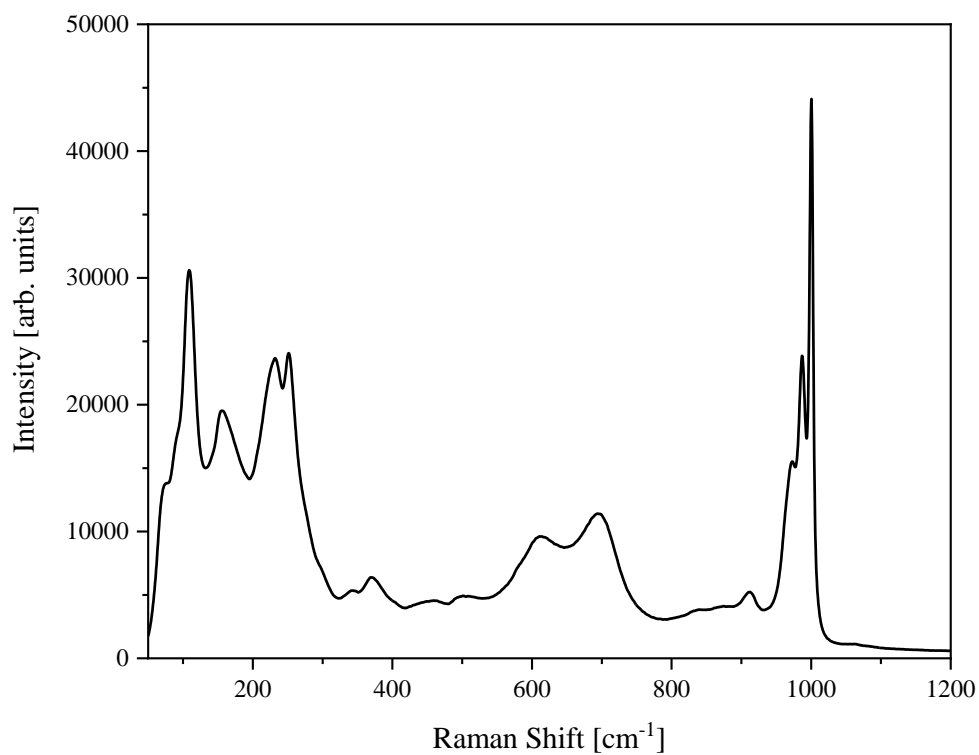


Figure S14: Raman data of HPMo.

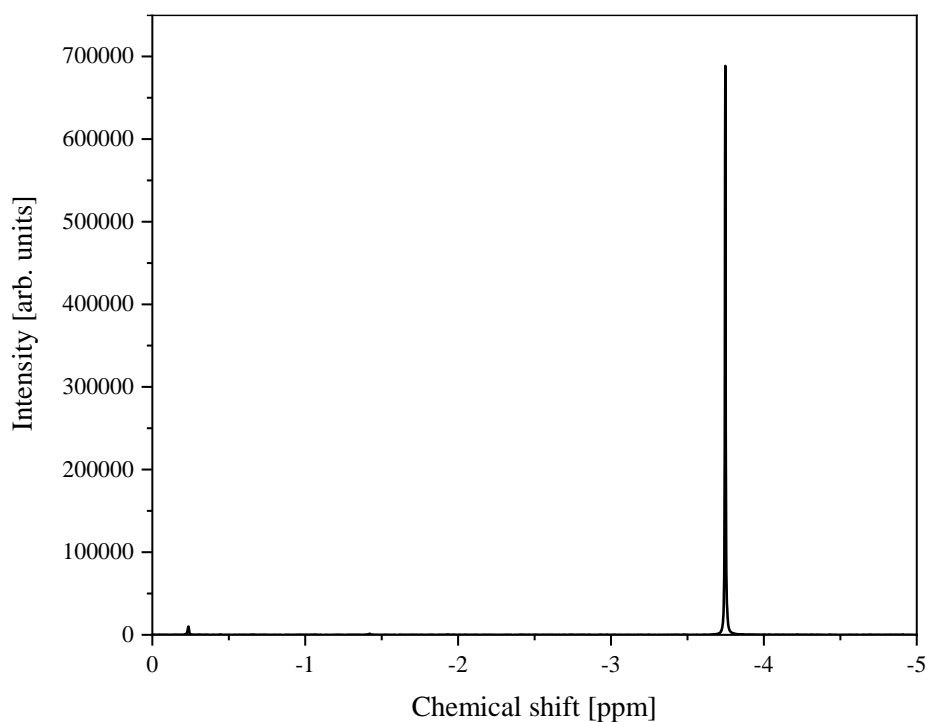


Figure S15: ^{31}P -NMR spectrum of HPMo in a mixture of 90 % water (hydrochloric acid, pH 1) and 10 % acetone- d_6 . The spectrum was measured at 242.9 MHz. 85 % H_3PO_4 was used as external standard.

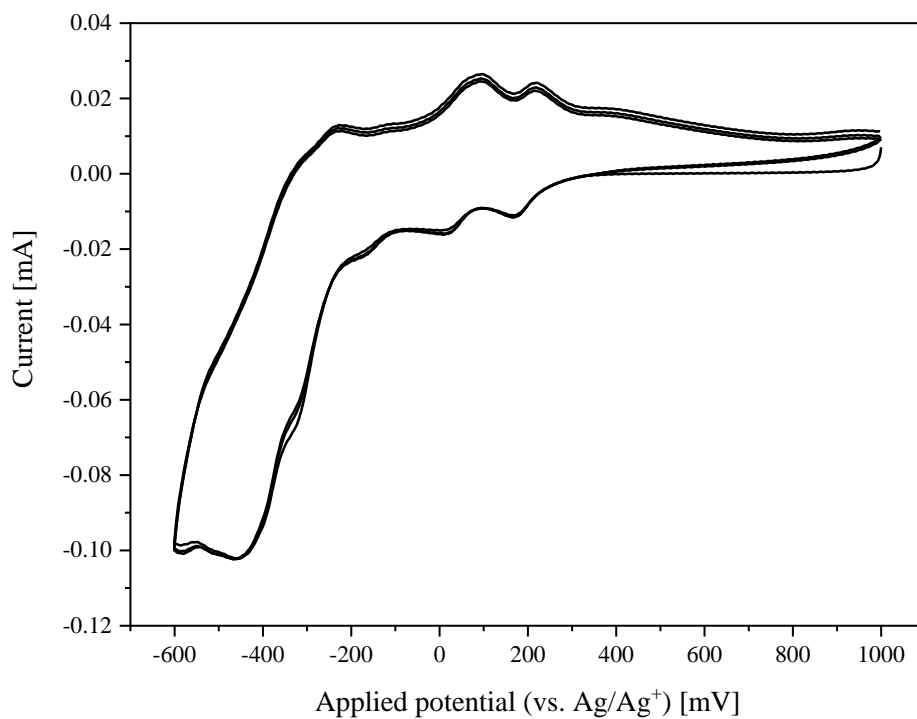


Figure S16: CV measurement of HPMo using hydrochloric acid (pH 1) as supporting electrolyte (concentration 1 mmol/L, scan rate 100 mV/s).

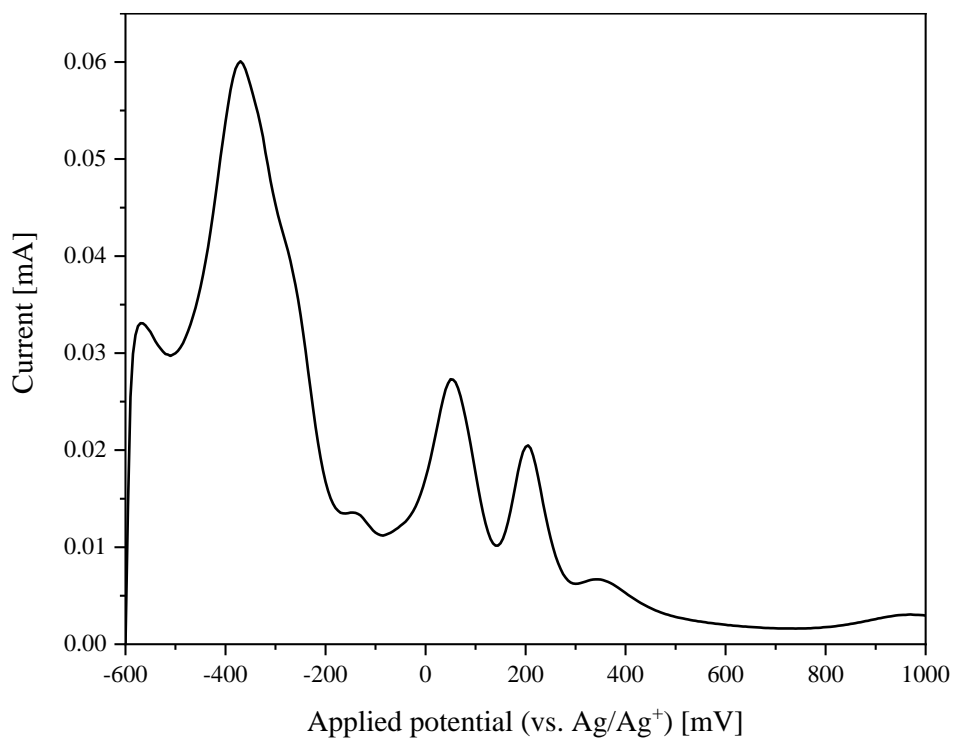


Figure S17: SWV measurement of HPMo using hydrochloric acid (pH 1) as supporting electrolyte (concentration 1 mmol/L, scan rate 100 mV/s).

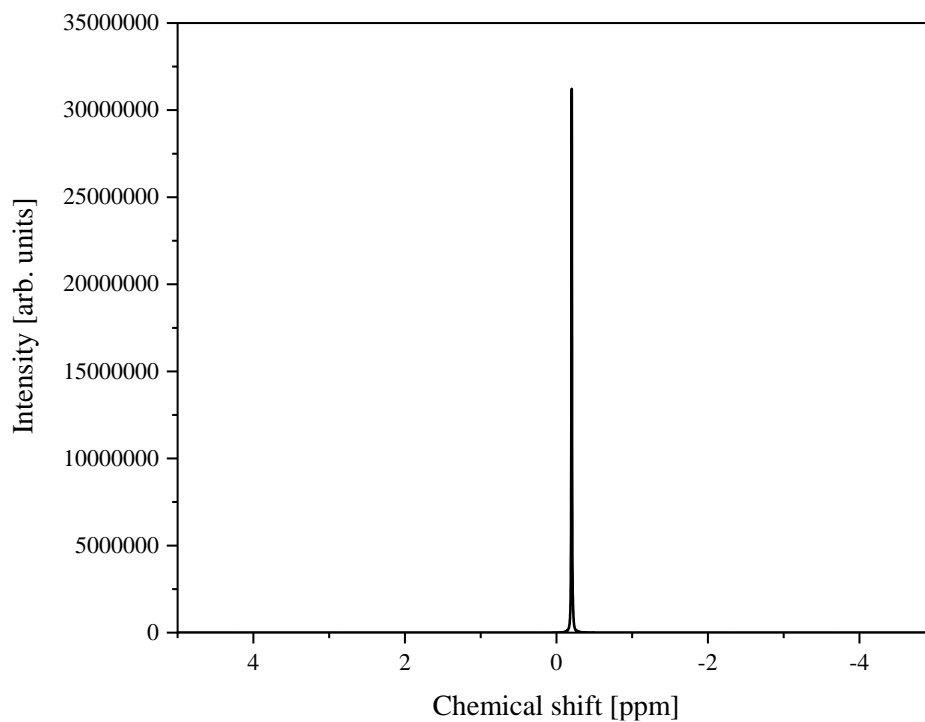


Figure S18: ³¹P-NMR spectrum of 85 % H₃PO₄ in water (90 %) and 10 % acetone-*d*₆. The spectrum was measured at 242.9 MHz. δ [ppm] = -0.20 ppm.

1.12 Incorporation experiments of more than three Co(II) ions

Substituting the POMs with more than three Co(II) results in a precipitation of an insoluble, purple residue, which was identified as cobalt molybdate by AAS/ICP-OES. The aqueous phase contains a mixture of HPCo_3Mo and cobalt(II) acetate. This was verified by the FT-IR spectra showing in addition to the POM bands also acetate bands (see Figure S19).

From the results mentioned above it becomes clear that the maximum substitution degree with Co(II) is three. A possible reason for this observation is the high negative charge resulting, when hexavalent metals such as Mo(VI) are substituted with bivalent metals like Co(II). For the three-fold substitution an anionic charge of 15 results, while for the hypothetically four-fold substituted anion an anionic charge of 19 would be reached. Anionic charges in this range seem not to be compatible for Keggin-type anions. Similar trends were observed for our previous reported incorporation experiments for Mn(II). Here the maximum substitution degree is two.¹⁰

ICP-OES data

Table S8: AAS/ICP-OES results from the experiments of incorporating more than three Co(II) ions into the Keggin-type phosphomolybdate structure.

Compound	P	Co	Mo
Incorporation of four Co(II) [%]	1.748	12.60	45.85
Stoichiometry for $[\text{PCo}_x\text{Mo}_x]^*$	1.063	4.026	9.000
Incorporation of five Co(II) [%]	1.915	14.15	40.60
Stoichiometry for $[\text{PCo}_x\text{Mo}_x]**$	1.315	5.101	9.000
Insoluble residue (cobalt(II) molybdate x hydrate) [%]***	0.9679	23.80	38.15
Calculated values for cobalt(II) molybdate [%]	0	26.93	43.83

*Composition: 1 equiv. HPCo_3Mo + 1 equiv. $\text{Co}(\text{OAc})_2$

**Composition: 1 equiv. HPCo_3Mo + 2 equiv. $\text{Co}(\text{OAc})_2$

***Deviation results from additional hydration water

Vibrational spectroscopy data

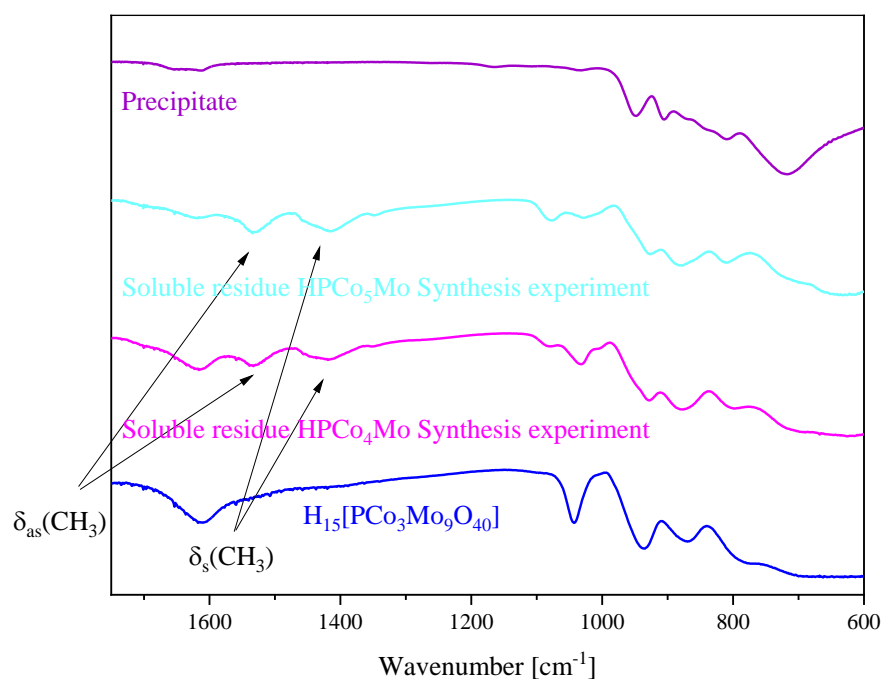


Figure S19: FT-IR results for the incorporation experiments for more than three Co(II) ions into the Keggin-type structure in comparison with HPCo₃Mo. The precipitate was identified as cobalt(II) molybdate.

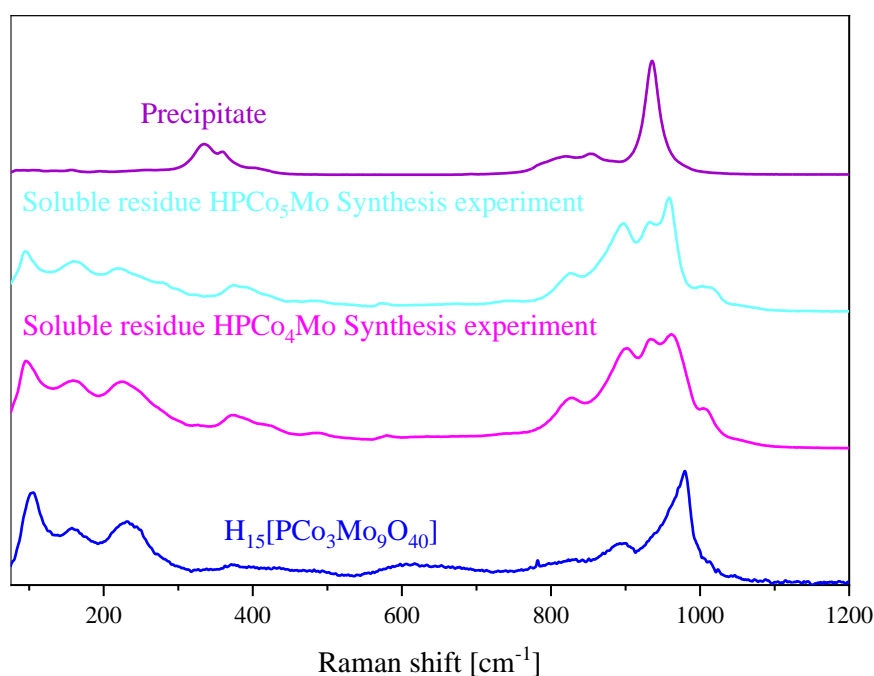


Figure S20: Raman results for the incorporation experiments for more than three Co(II) ions into the Keggin-type structure in comparison with HPCo₃Mo. The precipitate was identified as cobalt(II) molybdate.

2 Hydroformylation

2.1 Experimental

Hydroformylation of 1-hexene: The catalyst (1 mol% Co) was weighed into a glass inlet equipped with a magnetic stirring bar. MilliQ-water (2 mL) were added, followed by of tetradecane (25 mg) as internal standard, 1-hexene (763 mg, 8 mmol) and 1-butanol (2 mL). The inlet was placed in a stainless-steel autoclave, which was pressurized with 150 bar of a 1:1 mixture of CO and H₂. The reaction mixture was then heated at 130 °C and 750 rpm for 4 h. After the autoclave was cooled down, the biphasic reaction mixture was homogenized with 10 mL of *iso*-propanol. Prior to GC-Analysis the sample was filtered through a PFTE-syringe filter.

Standard reaction conditions: $m(1\text{-hexene}) = 0.673 \text{ mg}$, 79 mg HPCo₂Mo (0.04 mmol, 1 mol% Co), $V(\text{H}_2\text{O}/\text{BuOH}) = 4 \text{ mL}$, 130 °C, 150 bar CO/H₂ (1/1), $t = 4 \text{ h}$.

ICP results of violet precipitate: 20.62 wt% Co, 37.14 wt% Mo, 2.66 wt% P. This compound was identified as phosphate contaminated cobalt(II) molybdate x hydrate. Calculated for pure cobalt(II) molybdate 20.93 wt% Co, 43.83 wt% Mo.

Table S9: Reaction conditions for each hydroformylation experiment. Catalysts: HPCoMo **1**, HPCo₂Mo **2**, HPCo₃Mo **3**, HPMo and Co-acetate.

No.	Gas ratio H ₂ /CO	$n(\text{hexene})$ [mmol]	$m(\text{hexene})$ [mg]	$m(\text{Cat})$ [mg]	Cat	$V(\text{solvent})$ [mL]	solvent	T [°C]	Time [h]	$p(\text{H}_2/\text{CO})$ [bar]
1	1:1	8	673.28	79	1	4	H ₂ O/tBuOH	130	4	150
2	1:1	8	673.28	79	2	4	H ₂ O/tBuOH	130	4	150
3	1:1	8	673.28	79	3	4	H ₂ O/tBuOH	130	4	150
4	1:2	8	673.28	79	2	4	H ₂ O/tBuOH	130	4	150
5	2:1	8	673.28	79	2	4	H ₂ O/tBuOH	130	4	150
6	1:1	8	673.28	20	Co-acetate	4	H ₂ O/tBuOH	130	4	150
7	1:1	8	673.28	20+48.7	Co-acetate/HPMo	4	H ₂ O/tBuOH	130	4	150
8	1:1	8	673.28	48.7	HPMo	4	H ₂ O/tBuOH	130	4	150

The experimental procedure in entry 2 was reproduced three times.

Table S10: Weights of the standard tetradecane and the substrate hexene.

No.	Standard tetradecane [mg]	<i>m</i> (hexene) [mg]	<i>n</i> (hexene) [mmol]
1	24.1	679.2	8.070
2.1	25.0	672.3	7.988
2.2	25.2	673.5	8.003
2.3	25.7	667.7	7.934
4	24.0	674.0	8.008
5	24.1	673.5	8.003
6	23.0	678.3	8.060
7	22.4	674.2	8.011
8	21.7	674.5	8.014
9	21.1	676.4	8.037

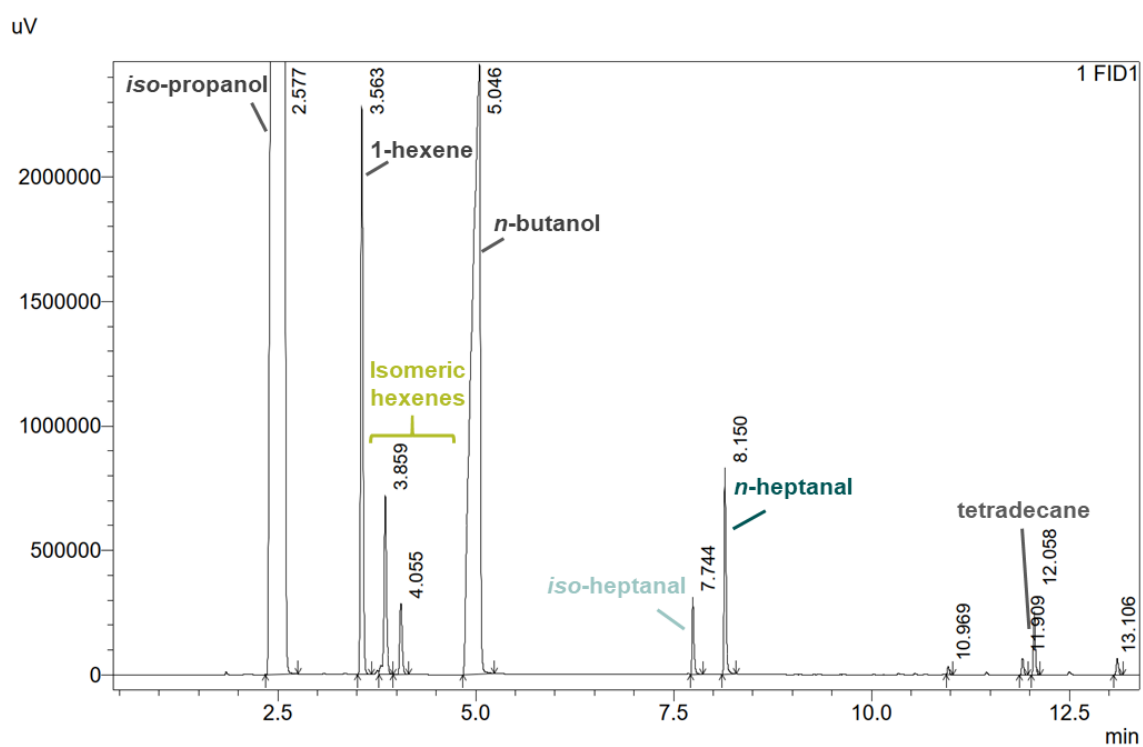


Figure S21: Chromatogram of the reaction solution after homogenisation with *iso*-propanol.

2.2 Results

Figure S22 show the Raman spectra in aqueous solution of the HPCoMo catalyst before and after the catalytic experiment.

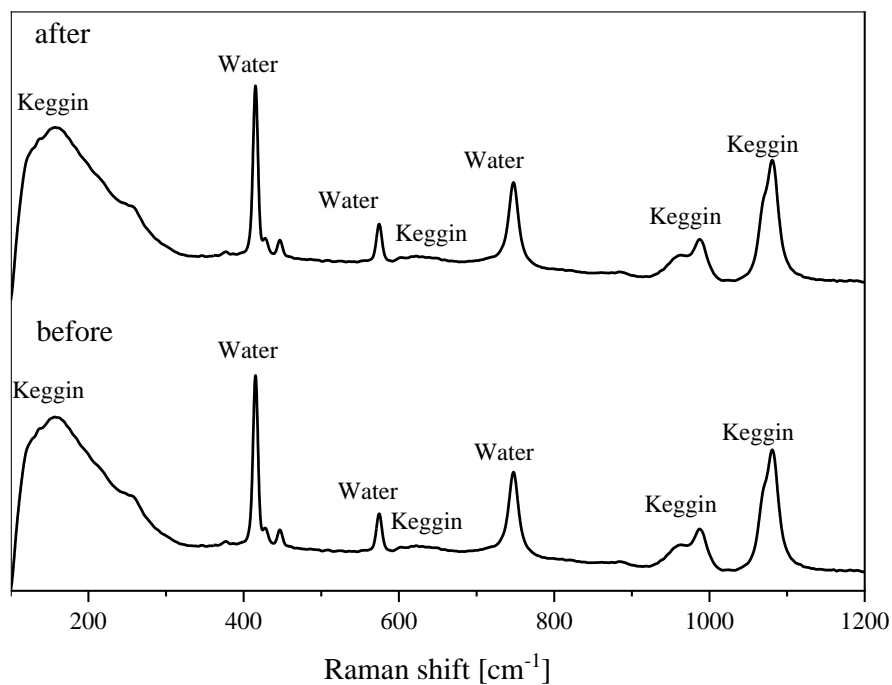


Figure S22: Raman spectroscopic data of HPCoMo in aqueous solution before and after catalytic experiments.

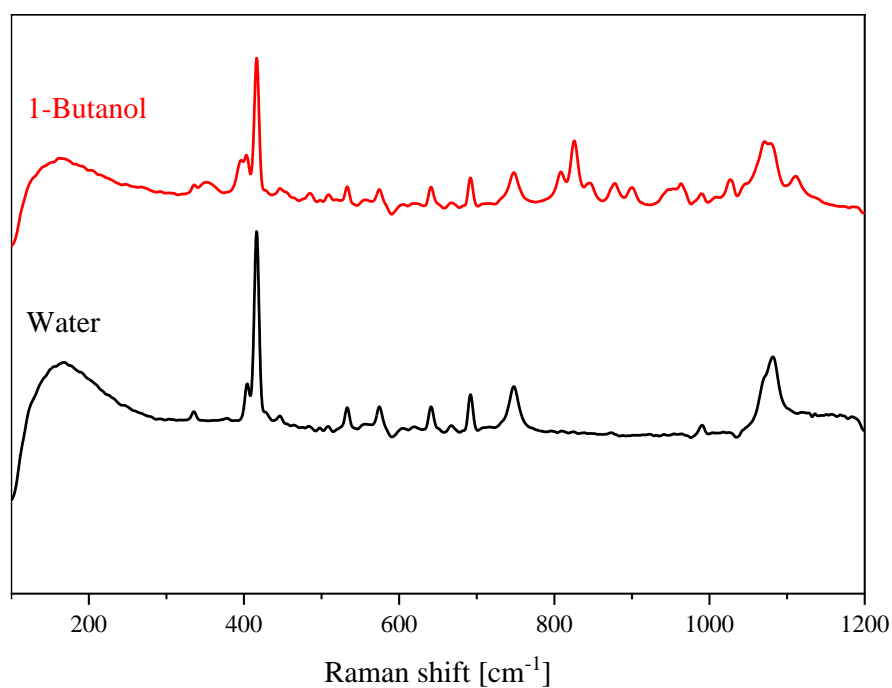


Figure S23: Raman spectroscopic data of an aqueous 1-butanol solution and water.

ICP-OES for recycled catalyst HPCo₂Mo: Calculated for H₁₁[PCo₂Mo₁₀O₄₀] · 12 H₂O: 48.565 % Mo, 5.966 % Co, 1.568 % P. Found: 53.545 % Mo, 6.40 % Co, 1.640 % P.

Table S11: Results of the different hydroformylation experiments using the catalysts HPCoMo **1**, HPCo₂Mo **2**, HPCo₃Mo **3**, HPMo and Co-acetate. Normally the experiments were carried out using a CO/H₂ gas ratio of 1:1 (except of experiments 4 and 5), in 4 mL of a solvent mixture of water/1-butanol over 4 hours at 130 °C and 150 bar pressure. The values for experiment 2 were calculated as average over three experiments.

No.	1	2	3	4	5	6	8
Catalyst	1	2	3	2 CO/H ₂ 1:2	2 CO/H ₂ 2:1	Co- acetate	HPMo
X (hexene)	36.45	63.81 ($\sigma = 6.305$)	18.96	99.13	44.68	59.05	35.98
Y (n-heptanal)	3.410	13.85 ($\sigma = 2.639$)	0.000	31.56	6.314	12.95	3.200
Y (iso-heptanal)	1.460	4.990 ($\sigma = 1.000$)	0.000	14.43	2.710	4.910	2.510
Y (hexane)	0.000	0.000 ($\sigma = 0.000$)	0.000	0.000	0.000	0.000	0.000
Y (iso-hexene)	7.540	21.56 ($\sigma = 3.825$)	2.950	39.40	11.69	22.89	15.78
C-balance	75.96	76.59	83.98	86.26	76.04	81.71	77.51
S (heptanal)	13.37	29.52	0.000	46.39	20.19	30.25	13.88

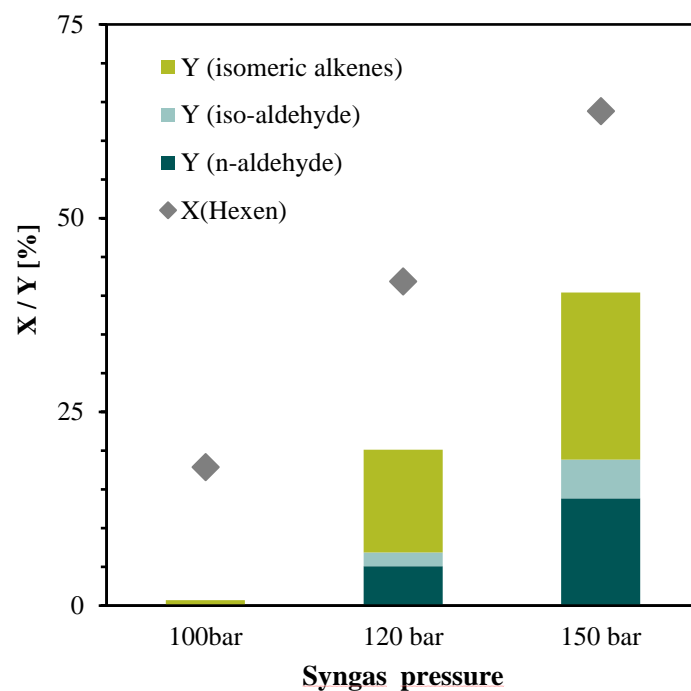


Figure S24: Screening of syngas pressure for catalyst HPCo₂Mo. Conditions: $m(\text{Hexen}) = 0.673 \text{ mg}$, 79 mg HPCo₂Mo (0.04 mmol, 1 mol% Co), $V(\text{H}_2\text{O}/\text{BuOH}) = 4 \text{ mL}$, 130 °C, 100-150 bar CO/H₂ (1/1), 4 h.

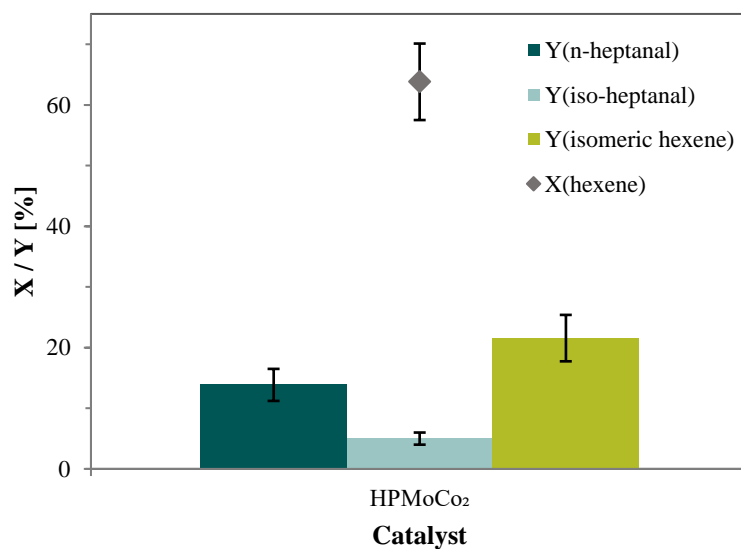


Figure S25: Reproducibility analysis for catalyst HPCo₂Mo. Conditions: $m(\text{Hexen}) = 0.673 \text{ mg}$, 79 mg HPCo₂Mo (0.04 mmol, 1 mol% Co), $V(\text{H}_2\text{O}/\text{BuOH}) = 4 \text{ mL}$, 130 °C, 150 bar CO/H₂ (1/1), 4 h.

3 References

- 1 A. L. Spek, Structure validation in chemical crystallography, *Acta Crystallogr. Sect. D Biol. Crystallogr.*, 2009, **65**, 148–155.
- 2 O. V. Dolomanov, L. J. Bourhis, R. J. Gildea, J. A. K. Howard and H. Puschmann, OLEX2: a complete structure solution, refinement and analysis program, *J. Appl. Crystallogr.*, 2009, **42**, 339–341.
- 3 G. M. Sheldrick, A short history of SHELX, *Acta Crystallogr. Sect. A Found. Crystallogr.*, 2008, **64**, 112–122.
- 4 C. B. Hübschle, G. M. Sheldrick and B. Dittrich, ShelXle: a Qt graphical user interface for SHELXL, *J. Appl. Crystallogr.*, 2011, **44**, 1281–1284.
- 5 A. L. Spek, Single-crystal structure validation with the program PLATON, *J. Appl. Crystallogr.*, 2003, **36**, 7–13.
- 6 I. Lynch, Software Reference Manual, *Electron. Syst. News*, 1987, **1987**, 43.
- 7 J.-C. Raabe, J. Aceituno Cruz, J. Albert and M. J. Poller, Comparative Spectroscopic and Electrochemical Study of V(V)-Substituted Keggin-Type Phosphomolybdates and -Tungstates, *Inorganics*, 2023, **11**, 138.
- 8 A. J. Bridgeman, Computational Study of the Vibrational Spectra of α - and β -Keggin Polyoxometalates, *Chem. - A Eur. J.*, 2004, **10**, 2935–2941.
- 9 P. Pykkö and M. Atsumi, Molecular single-bond covalent radii for elements 1-118, *Chem. - A Eur. J.*, 2009, **15**, 186–197.
- 10 J.-C. Raabe, J. Albert and M. J. Poller, Spectroscopic, Crystallographic, and Electrochemical Study of Different Manganese(II)-Substituted Keggin-Type Phosphomolybdates, *Chem. – A Eur. J.*, 2022, **28**, 1–12.

Electronic supporting information for

**Heteroelements in polyoxometalates: a study on the
influence of different group 15 elements on
polyoxometalate formation**

Jan-Christian Raabe¹, Froze Jameel², Matthias Stein², Jakob Albert¹ and Maximilian J. Poller*¹

¹Institute for Technical and Macromolecular Chemistry, Universität Hamburg, Bundesstraße 45, 20146 Hamburg, Germany

²Max Planck Institute for Dynamics of Complex Technical Systems, Molecular Simulations and Design Group, Sandtorstrasse 1, 39106, Magdeburg, Germany

*Corresponding Author

Content

1	Experimental details	3
1.1	Chemicals	3
1.2	Synthetic procedures.....	3
1.3	Characterization.....	4
1.3.1	Compositional analysis	4
1.3.2	Vibrational Spectroscopy	10
1.3.3	Nuclear magnetic resonance (NMR) spectroscopy	10
1.3.4	Ultraviolet visible spectroscopy (UV-Vis)	12
1.3.5	Crystallography	17
2	Computational data	19
2.1	General information.....	19
2.2	Cartesian coordinates.....	19
3	Literature.....	26

1 Experimental Details

1.1 Chemicals

All chemicals were purchased from the following suppliers:

- Sodium tungstate dihydrate: VWR chemicals
- Nitric acid: was obtained from Merck as 65 % solution in water and was further diluted with deionized water to a concentration of 4 M.
- Phosphoric acid: was purchased as a 85 % solution in water from Grüssing, which was further diluted with demineralized water to a final concentration of 25 %.
- Arsenic(III) oxide: was purchased from Honeywell (ReagentPlus 99.0 %)
- Potassium hexahydroxoantimonate(V): Merck
- Hydrochloric acid: VWR chemicals as a 37 % solution in water
- Hydrogen peroxide: VWR chemicals as a 30 % solution in water
- Deionized water was always used as solvent

1.2 Synthetic procedures

Preparing the As(V) solution: Arsenic(III) oxide was added to a mixture of water (30 mL) and a 30 % solution of hydrogen peroxide in water (30 mL). It was refluxed for two hours, yielding an aqueous, colorless solution of arsenic(V) acid in water.

Preparing the Sb(V) solution: potassium hexahydroxo antimonate(V) was added to water (100 mL) and refluxed for one hour, yielding a colorless solution

General experimental procedure: Sodium tungstate dihydrate was dissolved in water (100 mL) or added to the respective As(V)/Sb(V) solution. The start volume of the reaction mixture was always 100 mL of an aqueous solution. For the experiments with the hetero elements N(V) and P(V) a 4 M solution of nitric acid or 25 % phosphoric acid solution in water was added to the tungstate solution. The pH value was adjusted to 5 or 1 using a 37 % solution of hydrochloric acid in water and the solution was concentrated under reduced pressure (85 °C, 200 to 0 mbar) to yield a white powder in the case of the experiments at pH 5 or a yellow powder in the experiments at pH 1 for N(V) and Sb(V). Purification of the POMs was done by our previous published nanofiltration process.^{1,2}

Table S1 shows an overview of the precise weights of all precursor compounds:

Table S1: Precise weights of all precursor substances used in our experimental procedures.

No.	Precursor	pH 5 experiments			pH 1 experiments		
		Mass	Substance [mmol]	Equivalents	Mass	Amount of substance [mol]	Equivalents
1	Na ₂ WO ₄ · 2 H ₂ O	5.0032 g	15.168	6.02	5.0012 g	15.162	6.02
	4 M HNO ₃	0.63 mL	2.52	1.00	0.63 mL	2.52	1.00
2	Na ₂ WO ₄ · 2 H ₂ O	5.0017 g	15.163	5.97	5.0040	15.170	5.98
	25 % H ₃ PO ₄	0.9954 g	2.5394	1.00	0.9941	2.5361	1.00
3	Na ₂ WO ₄ · 2 H ₂ O	5.0022 g	15.165	11.97	5.0027	15.166	12.00
	As ₂ O ₃	0.2506 g	1.267	1.00	0.2499	1.236	1.00
4	Na ₂ WO ₄ · 2 H ₂ O	5.0031 g	15.168	6.00	5.0012	15.162	6.00
	K[Sb(OH) ₆]	0.6644 g	2.527	1.00	0.6643	2.527	1.00

All precisely measured pH values in our experiments are listed in Table S2:

Table S2: pH values in our experiments.

No.	pH 5 experiments		pH 1 experiments	
	pH value before adjustment	pH value after adjustment	pH value before adjustment	pH value after adjustment
1	7.790	5.040	7.866	1.018
2	7.926	5.066	7.884	0.998
3	5.829	4.984	5.495	0.953
4	9.900	5.180	9.124	1.007

1.3 Characterization

1.3.1 Compositional analysis

Elemental analysis (AAS/ICP-OES):

All samples were analyzed using an ICP-OES-spectrometer for elemental analysis (Fa. Spectro, type ARCOS) for W and P (method ICP-OES). Na, K and Sb were determined with AAS-F (Fa. Thermo, type Solaar S Series), method: F-AAS without HKL). Element As was measured with G-AAS. Nitrate was analyzed with IC.

- Compound $\text{Na}_8[\text{W}_{12}\text{O}_{40}]$ was dissolved in water (25 mL).
- Compound $\text{Na}_{12}[\text{P}_4\text{W}_{14}\text{O}_{58}]$ was dissolved in water (5 mL) and nitric acid (0.1 mL) was added. Then it was filled up to a final volume of 25 mL.
- The As(V) containing sample was dissolved in water (25 mL).
- Compound $\text{Na}_7[\text{SbW}_6\text{O}_{24}]$ was dissolved in water (25 mL).
- The oxides WO_3 and Sb_2O_5 were dissolved in aqua regia invers (5 mL) and hydrofluoric acid (1 mL) was added. Then it was filled up to a final volume of 50 mL.

In our experience, the above described method systematically results in slightly too low values for W, presumably due to partial precipitation of WO_3 during sample preparation.

Thermogravimetric analysis (TGA):

Approximately 20 mg of the sample was weighed into a quart crucible and the change in mass was measured at the following temperature program:

- Tare
- 1 minute waiting time
- Heating to 30 °C with heating rate of 10 K/min
- Stay at 30 °C for 15 minutes
- Heating to 350 °C with a heating rate of 10 K/min
- Stay at 350 °C for 30 minutes
- The sample was then cooled to room temperature

The starting temperature was below 30 °C. During the measurement, a nitrogen flow of 20 mL/min was passed through the instrument. The TGA data show three regions: hygroscopic water (water that comes from the air), lattice water (water from crystal association) and the mass consistency (pure POM without any moisture). The final data were exported as a x/y text document. Using Origin® 2019b the TGA data were plotted.

The results of the ICP-OES analysis for the different compounds are summarized below:

$\text{Na}_8[\text{W}_{12}\text{O}_{40}]$ (hetero element N(V) pH 5):

ICP-OES: Calculated for $\text{Na}_8[\text{W}_{12}\text{O}_{40}] \cdot 11 \text{H}_2\text{O}$: 5.697 % Na, 0.000 % K, 68.339 % W. Found for $\text{Na}_8[\text{W}_{12}\text{O}_{40}] \cdot 9 \text{H}_2\text{O}$: 6.67 % Na, 0.00 % K, 64.92 % W. Data normalized to tungsten. Na/K/W ratio: 9.9/0/12.

TGA: 6.413 % weight loss upon drying, this corresponds to 12 mol lattice water per mol of the POM.

WO₃ (hetero element N(V) pH 1):

ICP-OES: Calculated for WO₃: 79.297 % W. Found for WO₃: 46.23 % W. Nitrate was not determinable, because WO₃ is not soluble in pure water.

The W content deviates because the oxide is contaminated with nitrates.

Na₁₂[P₄W₁₄O₅₈] (hetero element P(V) pH 5):

ICP-OES: Calculated for Na₁₂[P₄W₁₄O₅₈] · 16 H₂O: 16.585 % Na, 0.000 % K, 2.957 % P, 61.43 % W. Found for Na₁₂[P₄W₁₄O₅₈] · 16 H₂O: 0.294 % Na, 0.00986 % K, 2.03 % P, 58.9 % W. Data normalized to tungsten. Na/K/P/W ratio: 0.56/0.01/2.86/14.

The phosphorus content differs due to the loss of PO₄³⁻ during nanofiltration.

TGA: 6.840 % weight loss upon drying, this corresponds to 16 mol lattice water per mol of the POM.

Na₃[PW₁₂O₄₀] (hetero element P(V) pH 1):

ICP-OES: Calculated for Na₃[PW₁₂O₄₀] · 8 H₂O: 2.232 % Na, 0.000 % K, 1.002 % P, 71.391 % W. Found for Na₃[PW₁₂O₄₀] · 8 H₂O: 10.9 % Na, 0.000736 % K, 1.42 % P, 54.7 % W. Data normalized to tungsten. Na/K/P/W ratio: 19.0/0.0007/1.86/12.

The literature known POM Na₃[PW₁₂O₄₀] was not further purified. Therefore, the Na content is increased, which also causes the contents of the other elements to deviate.

TGA: 4.524 % weight loss upon drying, this corresponds to 8 mol lattice water per mol of the POM.

Na₉[AsW₉O₃₄] (hetero element As(V) pH 5):

ICP-OES: Calculated for Na₉[AsW₉O₃₄] · 10 H₂O: 7.777 % Na, 0.000 % K, 2.816 % As, 62.189 % W. Found for Na₉[AsW₉O₃₄] · 10 H₂O: 8.52 % Na, 0.00904 % K, 3.07 % As, 58.3 % W. Data normalized to tungsten. Na/K/As/W ratio: 10.5/0.00656/1.16/9.

TGA: 6.661 % weight loss upon drying, this corresponds to 10 mol lattice water per mol of the POM.

Na₉[AsW₉O₃₄] (hetero element As(V) pH 1):

ICP-OES: Calculated for Na₉[AsW₉O₃₄] · 11 H₂O: 7.725 % Na, 0.000 % K, 2.797 % As, 61.771 % W. Found for Na₉[AsW₉O₃₄] · 11 H₂O: 6.62 % Na, 0.00584 % K, 2.51 % As, 59.3 % W. Data normalized to tungsten. Na/K/As/W ratio: 8.03/0.004/0.93/9.

TGA: 7.605 % weight loss upon drying, this corresponds to 11 mol lattice water per mol of the POM.

Na₇[SbW₆O₂₄] (hetero element Sb(V) pH 5):

ICP-OES: Calculated for Na₇[SbW₆O₂₄] · 14 H₂O: 7.959 % Na, 0.000 % K, 6.022 % Sb, 54.554 % W. Found for Na₇[SbW₆O₂₄] · 14 H₂O: 8.45 % Na, 1.11 % K, 7.18 % Sb, 59.1 % W. Data normalized to tungsten. Na/K/Sb/W ratio: 6.86/0.53/1.10/6.

TGA: 12.12 % weight loss upon drying, this corresponds to 14 mol lattice water per mol of the POM.

WO₃/Sb₂O₅ (hetero element Sb(V) pH 1):

ICP-OES: Calculated for WO₃ and for Sb₂O₅: 79.297 % W, 75.273. Found for WO₃/Sb₂O₅: 42.65 % W, 13.0 % Sb.

The W/Sb content differs because the product was isolated as a mixture of WO₃ and Sb₂O₅.

The stoichiometry of all compounds was verified by ICP-OES analysis and the amount of hydration water was determined using thermogravimetric analysis (TGA) as shown in Table S3.

Table S3: ICP-OES elemental analysis and TGA results of the different synthesized compounds in this work.

Hetero element	Compound	Synthesized at pH value...	Element ratio ^a	Hydration water ^b
N(V)	Na ₈ [W ₁₂ O ₄₀]	5	Na/K/NO ₃ ⁻ /W 9.9/0/0/12	11
	WO ₃	1	W: 46.23 % ^c	-
P(V)	Na ₁₂ [P ₄ W ₁₄ O ₅₈]	5	Na/K/P/W 0.56/0.01/2.86 ^d /14	16
	Na ₃ [PW ₁₂ O ₄₀]	1	Na/K/P/W 19.0/0.0007/1.86/12 ^e	8
As(V)	Na ₉ [AsW ₉ O ₃₄]	5	Na/K/As/W 10.5/0.007/1.16/9	10
	Na ₉ [AsW ₉ O ₃₄]	1	Na/K/As/W 8.03/0.004/0.93/9	11
Sb(V)	Na ₇ [SbW ₆ O ₂₄]	5	Na/K/Sb/W 6.86/0.53/1.10/6	14
	WO ₃ /Sb ₂ O ₅	1	Sb/W 2.76/6	-

^aElement ratios were determined using ICP-OES analysis.

^bHydration water amount was determined by TGA.

^cNO₃⁻ could not be determined because the sample was dissolved in an aqua regia/HF in the microwave. NO₃⁻ determination is only possible in a purely aqueous medium.

^dThe anion [P₄W₁₄O₅₈]¹²⁻ appears to dissociate more strongly in aqueous solution (presumably due to greater instability compared to the other compounds), so that portions of the phosphorus are lost in subsequent purification steps. The identity of the compound was confirmed, especially with IR, Raman, and single crystal structure analysis.

^eThe anion [PW₁₂O₄₀]³⁻ is already known in the literature and was therefore not further purified.

After our dialysis purification^{1,2} for the anion [P₄W₁₄O₅₈]¹²⁻, significant amounts of P were found in the permeate fraction (Table S4), explaining the lowered stoichiometry of 2.86. This indicates a stronger dissociation and thus higher instability of this anion in aqueous solution.

Table S4: Elemental analysis of the permeate fraction after purifying compound Na₁₂[P₄W₁₄O₅₈].

Element	Na	K	P	W
Concentration [g/L]	1.345	0.00046	0.154	0.0551

1.3.2 Vibrational Spectroscopy

ATR-FT-IR spectroscopy:

All IR spectra were measured in attenuated total reflection (ATR) measurement mode on a QATR™-S single-reflection ATR (with a diamond prism) from Shimadzu. From the raw data obtained, the baseline was corrected, and the peaks were determined manually. The IR data were then exported as an x/y text document and plotted in Origin®2019b.

Raman spectroscopy:

All Raman spectra were measured on a SENTERRA Raman microscope from Bruker Optik GmbH. The aperture was set to 50 x 1000 µm. A 20 objective was used on the microscope. The excitation laser has a wavelength of 785 nm and the measurement range used was between 75 cm⁻¹ and 1525 cm⁻¹. The integration time was 16 seconds, the number of scans was 8 and the Raman laser power was 10 mW. All data were exported as .dpt file and plotted in Origin®2019b.

1.3.3 Nuclear magnetic resonance (NMR) spectroscopy

All ³¹P spectra were measured with a Time Domain Data Sizes (TD) of 32 K, the Number of Scans (NS) were set to 2k (= 2048), the Transmitter Frequency Offset for Channel F1 (O1) and the Spectral Width (SW) were -1 and 40 ppm. The Delay D1 was set to 1 s. NMR analysis was done using MestReNova®. All data were exported into .csv data and plotted in Origin®2019b.

The ³¹P-NMR data of compound Na₁₂[P₄W₁₄O₅₈] and Na₃[PW₁₂O₄₀] are shown in Figure S1 and S2.

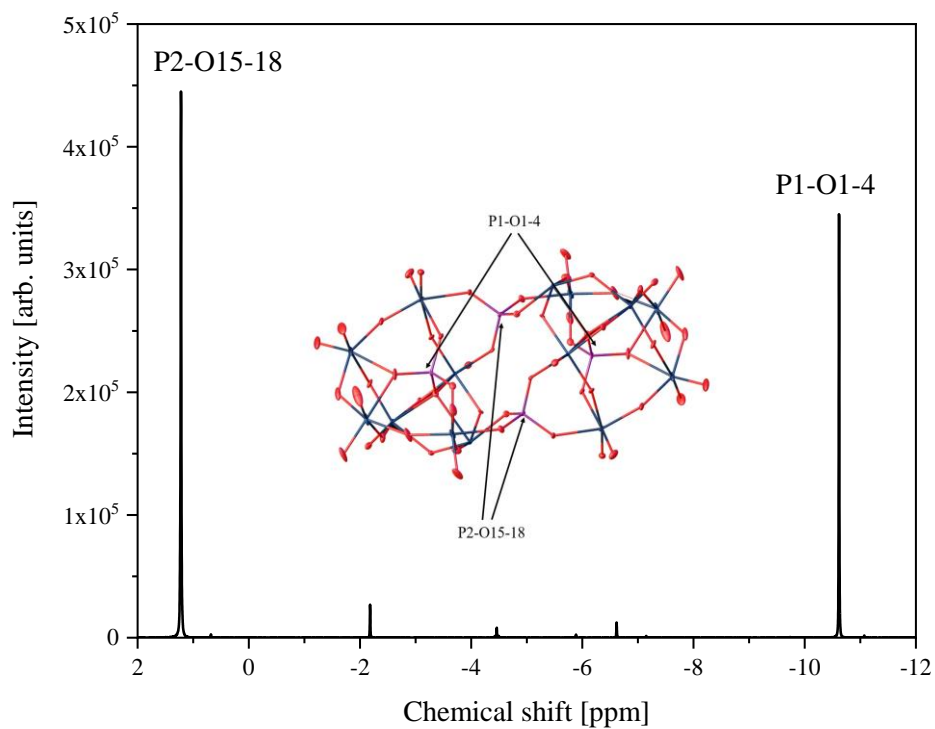


Figure S1: ^{31}P -NMR of $\text{Na}_{12}[\text{P}_4\text{W}_{14}\text{O}_{58}]$ in a mixture of 0.7 mL water (pH 5) and 0.07 mL acetone- d_6 . The spectrum was measured at 242.9 MHz, 85 % H_3PO_4 was used as external standard.

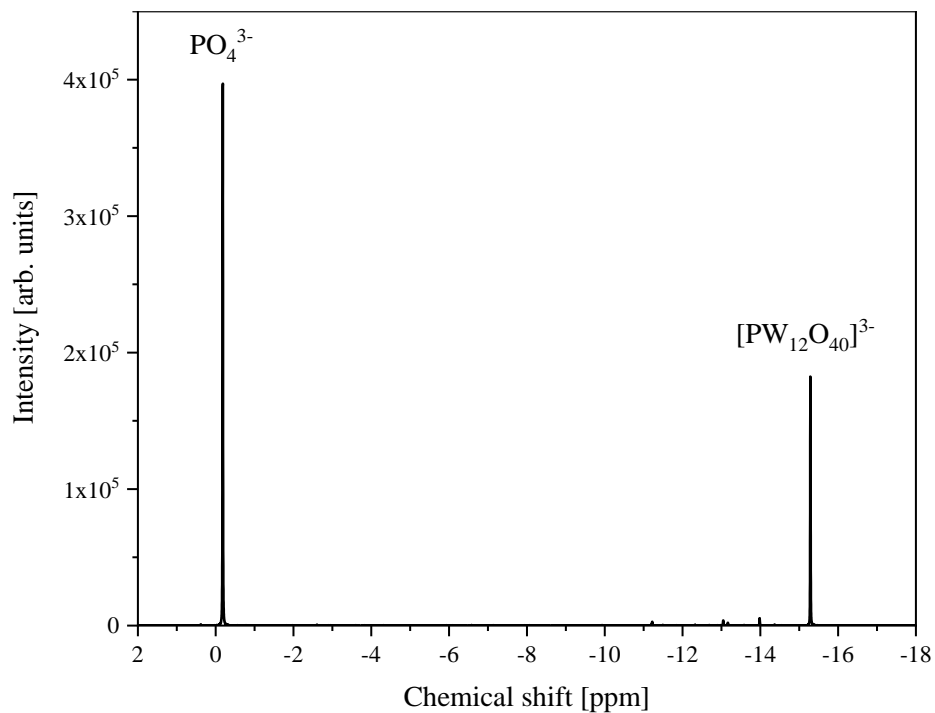


Figure S2: ^{31}P -NMR of $\text{Na}_3[\text{PW}_{12}\text{O}_{40}]^{3-}$ in a mixture of 0.7 mL water (pH 5) and 0.07 mL acetone- d_6 . The spectrum was measured at 242.9 MHz, 85 % H_3PO_4 was used as external standard.

1.3.4 Ultraviolet visible spectroscopy (UV-Vis)

Stock solution: The respective POM (10 mg) was dissolved in deionized water (10 mL) → 1 g/L.

Spectra measurement: All UV-Vis spectra were measured with a Cary 60 UV-Vis spectrometer (Agilent Technologies) in a Quartz cuvette of 3 mL (QS). Measurements were done using the Cary WinUV software. Range: 200 nm and 800 nm. The extinction was measured in the slow measurement mode. Data were then exported as a .csv data set and plotted in Origin®2019b.

For measurement samples were prepared as follows: The stock solution (80 µL) was filled into the cuvette and water (2920 µL) was added to reach the final measuring volume of 3 mL.

The UV-Vis data of all compounds investigated in this work are shown in Figure S3 at a concentration of 26.7 mg/L. All spectra show the ligand-to-metal-charge-transfer bands (LMCT) of W(VI), which are listed in Table 5.^{3,4} The LMCT positions were found in the range of 247 to 259 nm.

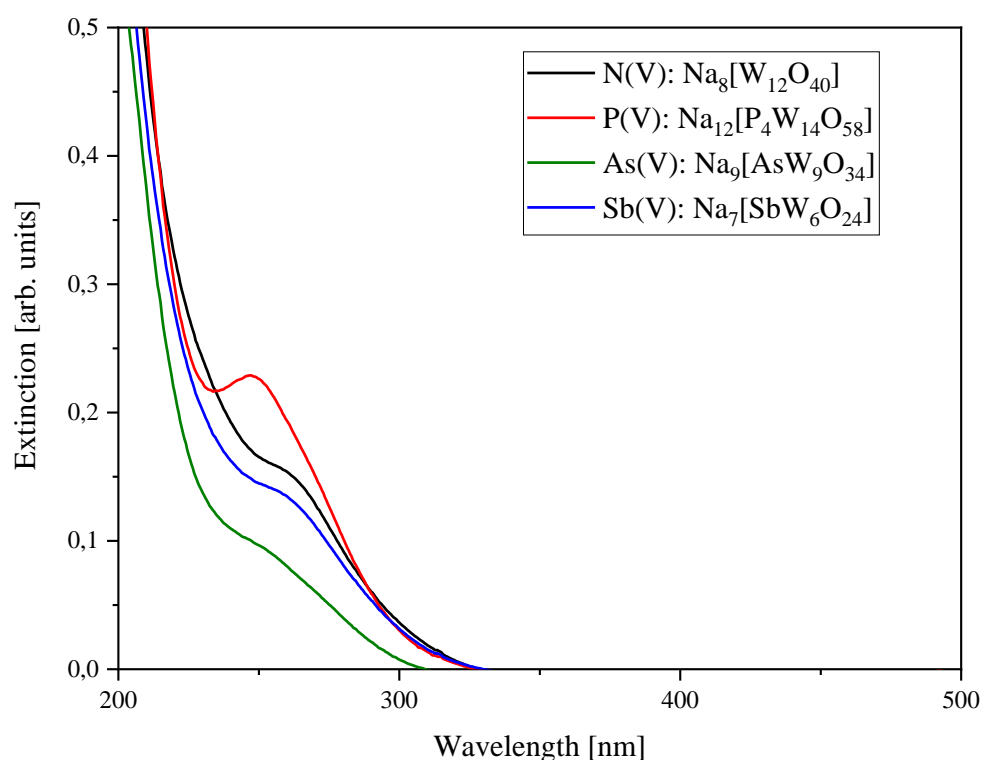


Figure S3: UV-Vis spectra of all POMs (synthesized at pH 5) investigated in this work.

Table S5: LMCT positions for W(VI) of all POMs investigated in this work.

Hetero element involved	N(V)	P(V)	As(V)	Sb(V)
Compound	Na ₈ [W ₁₂ O ₄₀]	Na ₁₂ [P ₄ W ₁₄ O ₅₈]	Na ₉ [AsW ₉ O ₃₄]	Na ₇ [SbW ₆ O ₂₄]
LMCT band [nm]	259.0	247.0	247.0	255.0

Extinction coefficients: Extinction coefficients were determined using the software Cary concentrations. Five calibration standards were prepared from the stock solution (1 g/L) with a final volume of 3 mL for the cuvette:

- 20 μ L stock solution + 2980 μ L deionized water
- 40 μ L stock solution + 2960 μ L deionized water
- 50 μ L stock solution + 2950 μ L deionized water
- 60 μ L stock solution + 2940 μ L deionized water
- 80 μ L stock solution + 2920 μ L deionized water

Extinction coefficients were calculated according to equations 1 to 4:

Lambert-Beer's law (equation 1):

$$Abs = \varepsilon_{\lambda} \cdot d \cdot c \cdot M^{-1} \quad (1)$$

Abs: Absorption

ε_{λ} : extinction coefficient (wavelength λ dependant) [$l \text{ mol}^{-1} \text{ cm}^{-1}$]

d: Cuvette layer thickness (1 cm) [cm]

c: concentration [g/L]

M: molar mass [g/mol]

Calibration line (equation 2):

$$Abs = a \cdot c + b \quad (2)$$

a: slope

b: Axis intercept

Determining the extinction coefficient:

$$a = \varepsilon_{\lambda} \cdot d \cdot M^1 \quad (3)$$

$$\varepsilon_{\lambda} = \frac{a \cdot M}{d} \quad (4)$$

The LMCT peak maxima were analyzed according to the Lambert Beer's law and therefore the extinction coefficients were calculated and listed in Table S6.

Table S6: Extinction coefficients determined according to the Lambert Beer's law.

Hetero element involved	N(V)	P(V)	As(V)	Sb(V)
Compound	Na ₈ [W ₁₂ O ₄₀]	Na ₁₂ [P ₄ W ₁₄ O ₅₈]	Na ₉ [AsW ₉ O ₃₄]	Na ₇ [SbW ₆ O ₂₄]
Extinction coefficient [L mol⁻¹ cm⁻¹]	2.1576 · 10 ⁴	3.5899 · 10 ⁴	0.9380 · 10 ⁴	1.0151 · 10 ⁴

As expected, the POM anion [P₄W₁₄O₅₈]¹²⁻ shows the highest extinction coefficient due to the highest amount of W(VI) per molecule.

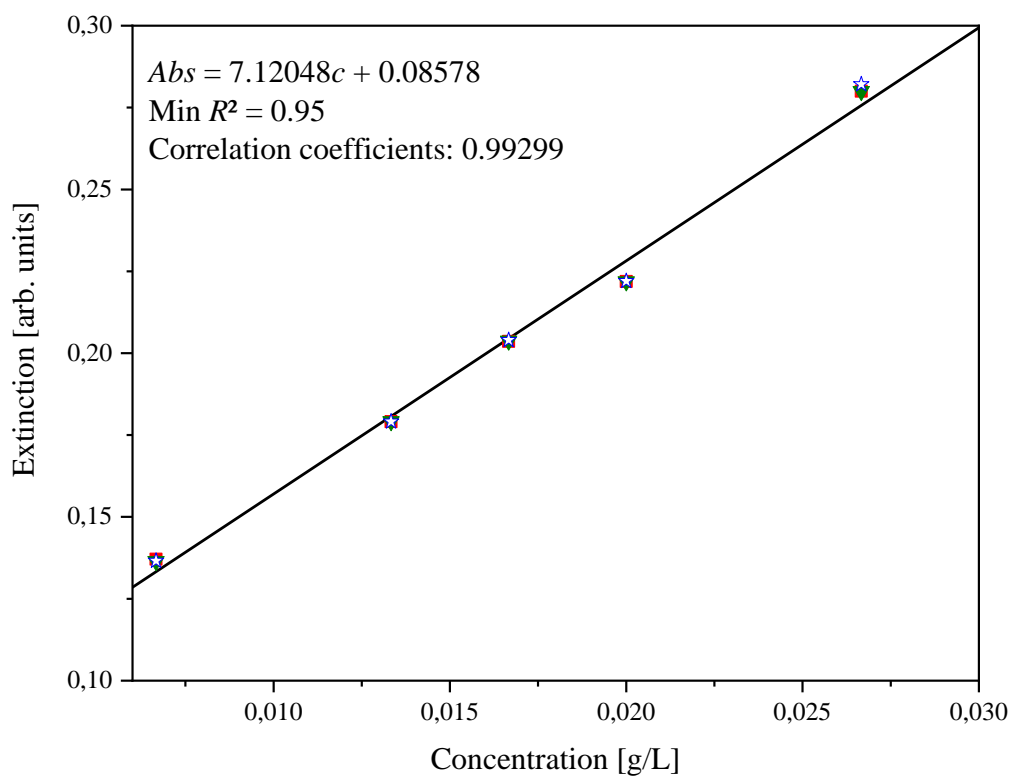


Figure S4: Calibration line for determining the extinction coefficient of the W(VI) LMCT for $[W_{12}O_{40}]^{8-}$.

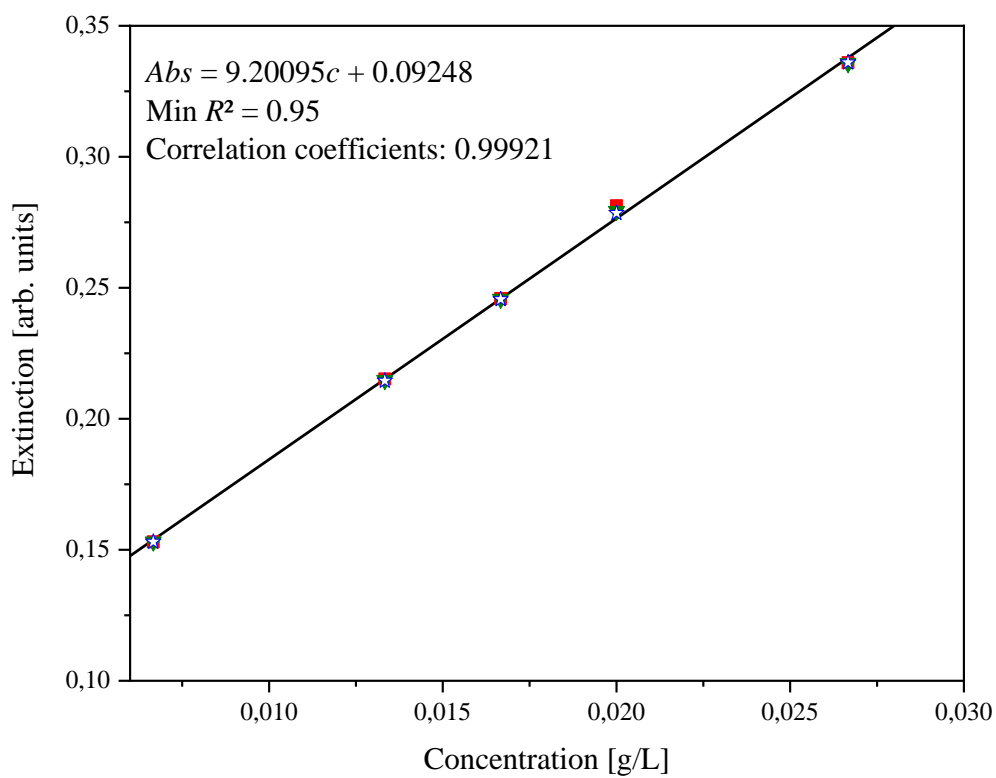


Figure S5: Calibration line for determining the extinction coefficient of the W(VI) LMCT for $[P_4W_{14}O_{58}]^{12-}$.

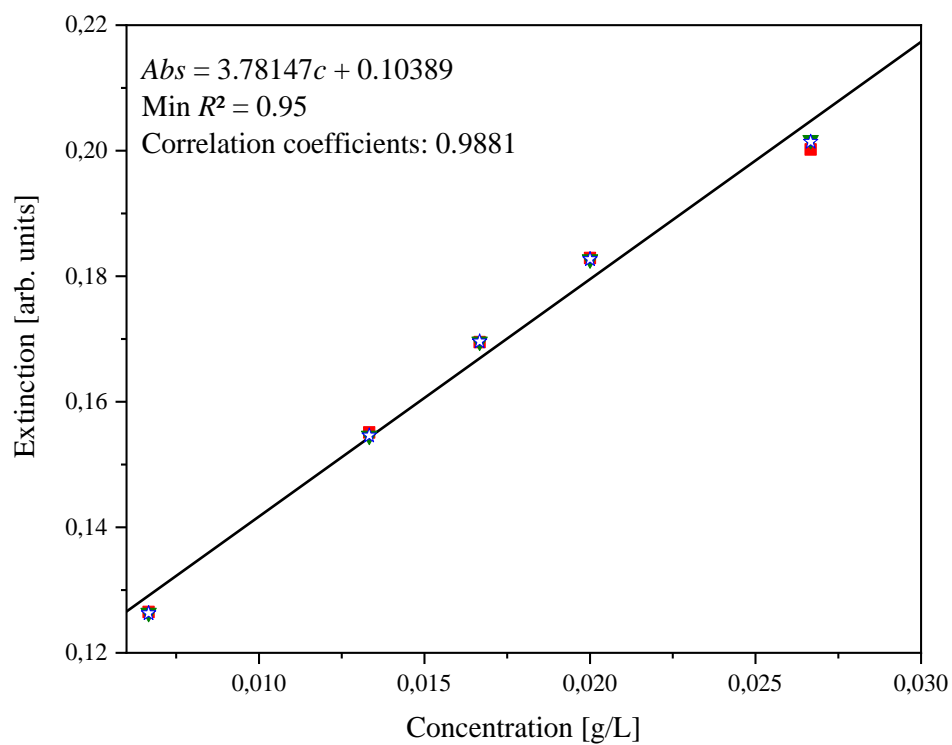


Figure S6: Calibration line for determining the extinction coefficient of the W(VI) LMCT for $[AsW_9O_{34}]^{9-}$.

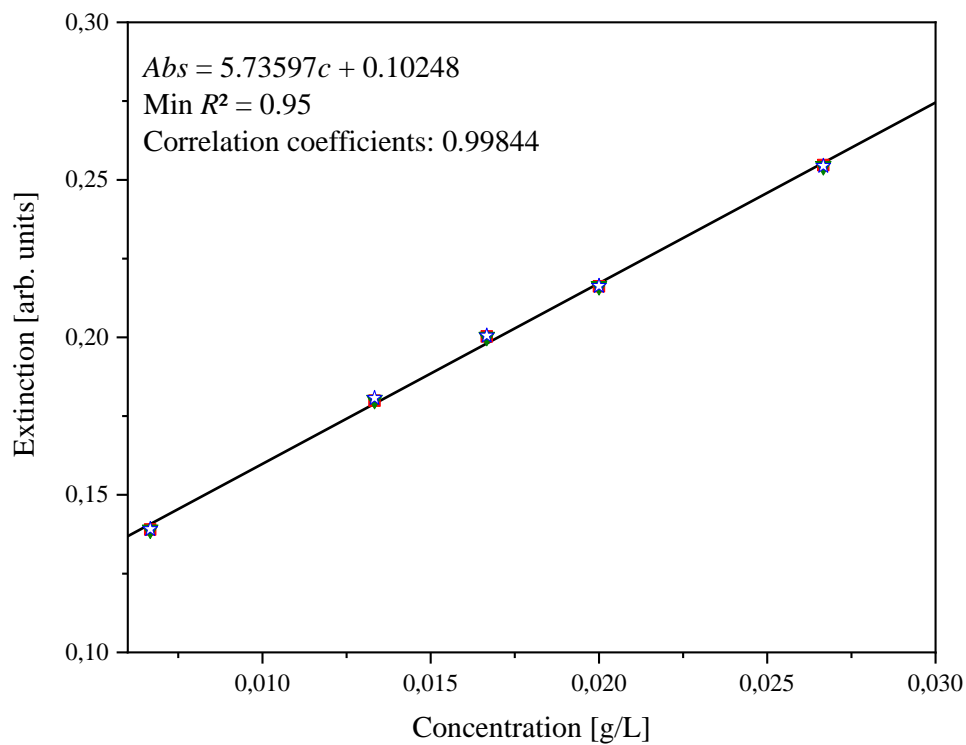


Figure S7: Calibration line for determining the extinction coefficient of the W(VI) LMCT for $[\text{SbW}_6\text{O}_{24}]^{7-}$.

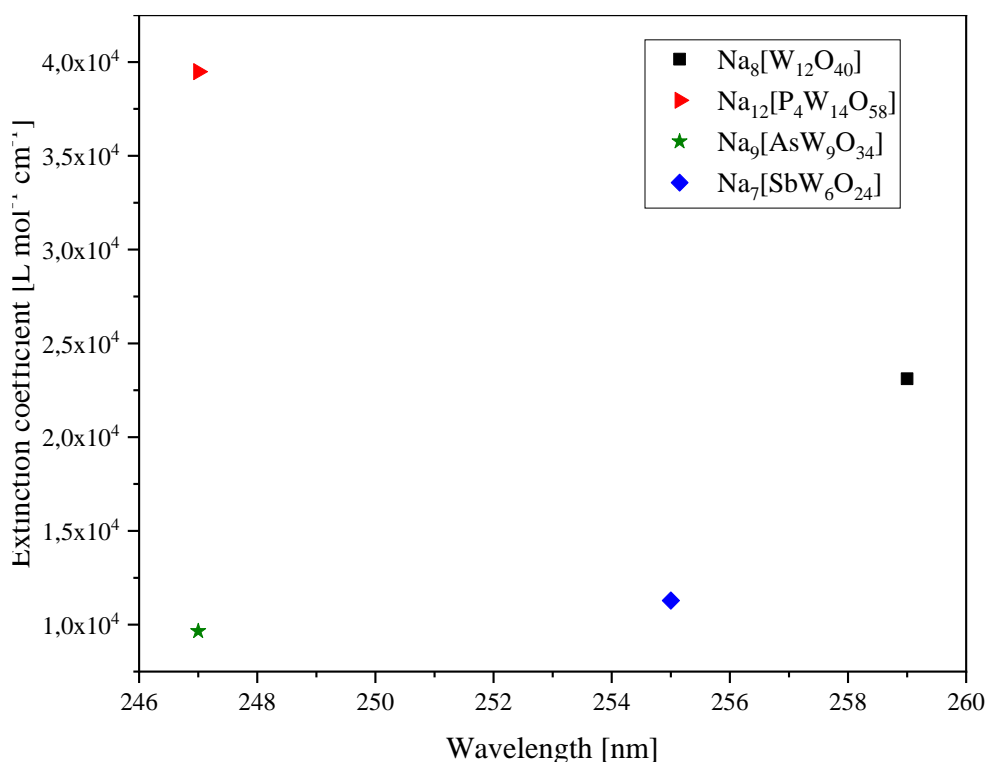


Figure S8: Plot of the extinction coefficient vs. wavelength for each POM.

1.3.5 Crystallography

The crystallographic data set comprising the anion $[\text{W}_{12}\text{O}_{40}]^{8-}$ (deposition number: 2293850) showed some problems during the refinement. Refining the model as $\text{Na}_8[\text{W}_{12}\text{O}_{40}]$ led to a residual electron density with a maximum and minimum peak of 5.6 and -11.5, respectively. This effect might be caused by several factors, including the difficulty to account correctly the absorption effect of the heavy atoms.⁵ However, it turned out that the applied absorption correction scheme (either without face indexing, *i.e.*, empirical, or with face indexing, *i.e.*, numerical sphere, numerical Gaussian grid or analytical according to Clark & Reid⁶) had only a very minor influence on the residual electron/hole density values. Another attempt to fix the problem was the application of the new algorithm "NoSpherA2" as implemented in Olex2 where so-called "non-spherical form factors" are calculated on a quantum mechanical basis.⁷⁻¹⁰ However, this approach did not lead to success, since the wavefunction could not be calculated because the self-consistent field calculation did not converge for unknown reasons. As the Fourier difference map showed a pronounced shashlik-like pattern with too little and too much electron density around the W atoms in alternating fashion (see Figure S9) a

corresponding attempt to model a disorder of the WO_6 octahedra was undertaken. Although this reduced drastically the electron density difference values with a maximum and minimum value of only 3.8 and -3.4, respectively, and the R_1 value could be reduced further down to 3.45 %, some other issues arose as, for instance, atoms with non-positive definite (NPD) values of the displacement parameters and unrealistic W-O bond lengths. Therefore, we believe that the structure altogether is better represented by the non-disordered model. The most important thing is, that due to the low R_1 value of 4.74 %, there is no doubt about the constitution of the $[\text{W}_{12}\text{O}_{40}]^{8-}$ anion and the identity of the paratungstate B, respectively.

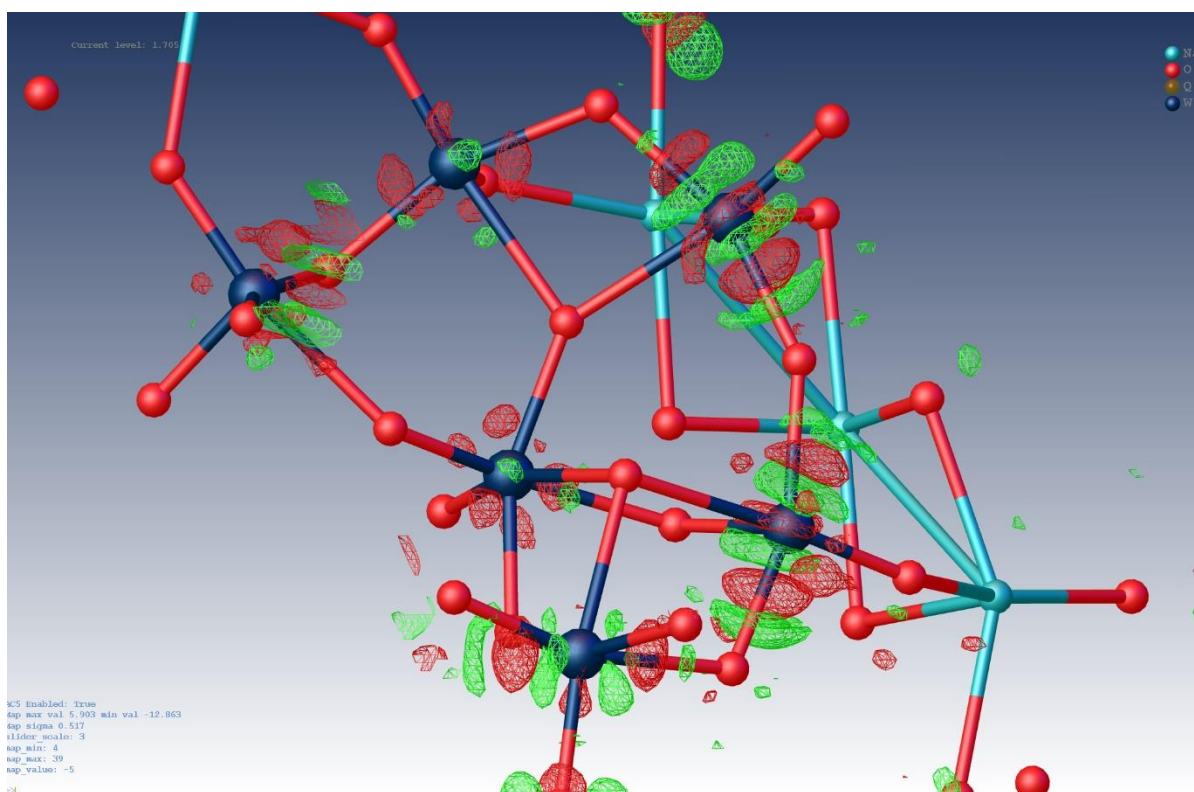


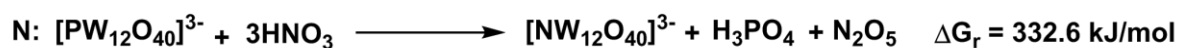
Figure S9: Fourier difference map of $\text{Na}_8[\text{W}_{12}\text{O}_{40}]$ showing a shashlik-like pattern of too high and too low electron density around the W atoms.

2 Computational data

2.1 General information

All DFT calculations were performed using TURBOMOLE V 7.5.1 2021.¹¹ Structures were optimized using the PBE0 hybrid functional¹² using an Ahlrichs' triple- ζ valence polarization (def2-TZVP) basis set for all atoms.¹³ Geometry optimizations were carried out in gas phase with tight SCF convergence (10^{-8} h) criteria using a fine m4 grid. The resolution-of-identity approximation was applied using auxiliary def2-TZVP basis sets to approximate the Coulomb potentials. For each optimized structure, second derivatives were calculated with the same settings used for geometry optimizations. All optimized structures were characterized as minima by absence of any negative frequency. Zero point vibrational energies and thermodynamic corrections were calculated without any scaling factor. The molecular volume of the optimized structures was calculated using MoloVol. The thermodynamic corrections for all species were evaluated at 298 K and 1 bar within the rigid-rotor harmonic-oscillator approximation. The implicit COSMO¹⁴ (Conductor like Solvation MOdel) was used to incorporate solvation effects.

Keggin Heteroelement Substitution



Anderson-Evans Heteroelement Substitution

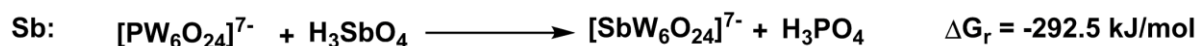
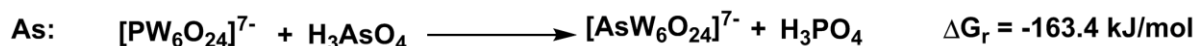


Figure S10: The Gibbs energies of formation from isodesmic reactions of the Keggin and Anderson-Evans complexes with their respective acids.

2.2 Cartesian coordinates

Cartesian coordinates of the optimized structures in Å

[NW₁₂O₄₀]³⁻

O 0.0828607 1.2718738 -3.6874977
O 1.9090346 3.3026590 -0.5793297
O -0.0702244 5.2934969 -0.0172464
O 0.7594919 -3.4953634 1.7905944
O 2.1020083 -0.1178495 2.8850769
O 3.5571844 -0.1061275 -0.3224547
W -1.5610863 1.7300634 -2.7529147
O -0.1403746 -1.4150532 3.3047504
W 1.4505968 -0.0683339 -3.3407307
O 2.4102472 1.2277792 -2.2664785
O -2.4070272 -2.8117048 -3.9572162
O -1.1992073 -0.0778373 0.7045928
W 1.6305185 1.7543414 2.7000795
O -2.7206629 1.2505901 2.4965996
W -1.5592069 -0.0932155 3.2916163
O 0.7290356 -1.2269595 0.3264326
O 2.3914395 -1.3938660 -2.2855004
O -0.2574342 -0.0696717 -1.3679853
O -0.1210995 1.2068305 3.3218640
O -2.8349956 -1.8161490 -1.2940173
O 2.2992216 -2.7246336 4.0822709
O 2.3352074 2.4669614 4.1211675
W 3.1016968 1.7664894 -0.5381587
O -0.6144932 -3.1369512 -1.7300733
O 3.0610654 1.9547432 1.3967842
W 0.0330338 -3.7270042 0.0003287
O -4.5532481 -2.8309000 0.7695888
O 2.3486861 -0.0646067 -4.8293179
W 0.0879328 3.5632223 0.0530029
O 4.5933382 -2.7078862 -0.9776954
O 4.6327901 2.4879746 -0.9394493
W -3.1044817 1.7178383 0.6470592
O -2.3629193 2.7450256 -3.9159121
O -0.1505893 -5.4536191 -0.0933302
O 3.0299180 -2.1831098 1.3665182
O -1.6527000 3.0035141 0.6999533
O -2.1900036 -0.0410772 -3.2596477
W -1.5880930 -1.8284108 -2.7790914
O 1.8574339 -3.4853553 -0.6287880
W 3.0737137 -1.9684843 -0.5654808
O 0.0631184 -1.3837660 -3.7064528
O -2.0939648 -0.0999576 4.9462957
O -2.8086973 1.7152633 -1.2687218
O -3.8919511 -0.0550936 0.5015462
O -4.5129127 2.7250879 0.8112031
O 0.8103679 3.2956131 1.8394081
O -2.7415896 -1.4064968 2.4779626
W 1.6029341 -1.9800536 2.6733685
O 0.7457962 1.0482286 0.3430006

O -0.5666615 3.0065889 -1.6859051
O -1.6979822 -3.1488963 0.6569127
N 0.0062092 -0.0817100 0.0019885
W -3.1304302 -1.8417582 0.6210101

[PW₁₂O₄₀]³⁻

O 0.0771320 1.2620087 -3.7004608
O 1.9172699 3.3137574 -0.5640737
O -0.1375929 5.1685010 -0.0429903
O 0.7764572 -3.5053256 1.7855021
O 2.0357197 -0.1160201 2.7095065
O 3.3812266 -0.1049282 -0.2517354
W -1.5176554 1.6689207 -2.7197447
O -0.1638670 -1.3904775 3.1217433
W 1.3933575 -0.0681712 -3.2932843
O 2.2653519 1.2048424 -2.1682458
O -2.3695528 -2.7996558 -3.8148797
O -1.3183344 -0.0769550 0.7735681
W 1.6073969 1.7426162 2.6231786
O -2.7384238 1.2387780 2.5008883
W -1.5610064 -0.0923859 3.2156795
O 0.7987269 -1.3398184 0.3570135
O 2.2469096 -1.3695827 -2.1870758
O -0.2848815 -0.0683501 -1.5025788
O -0.1443182 1.1852548 3.1403468
O -2.7145879 -1.6781221 -1.2388733
O 2.2210259 -2.6117137 4.0315396
O 2.2583163 2.3578327 4.0677096
W 3.0285137 1.7541911 -0.5068849
O -0.5345745 -2.9807899 -1.6685544
O 3.0595934 1.9740510 1.3959262
W 0.0633367 -3.6560671 0.0142086
O -4.4232760 -2.8164544 0.7116066
O 2.3522337 -0.0649470 -4.6968751
W 0.1173580 3.4914734 0.0661439
O 4.5061028 -2.5920304 -0.9997451
O 4.5434189 2.3747815 -0.9643588
W -3.0512542 1.6558081 0.6578610
O -2.3264566 2.7278063 -3.7752033
O -0.2164199 -5.3273678 -0.1192698
O 3.0280064 -2.2024360 1.3656429
O -1.5546271 2.8400009 0.7187381
O -2.1734149 -0.0412104 -3.2811810
W -1.5441393 -1.7688941 -2.7445368
O 1.8657502 -3.4959222 -0.6137878
W 3.0007556 -1.9548185 -0.5336142
O 0.0573300 -1.3726765 -3.7190414
O -1.9856886 -0.1010446 4.8614644
O -2.6898317 1.5741528 -1.2155541

O	-3.9006332	-0.0556804	0.5224667
O	-4.3816914	2.7096191	0.7507529
O	0.8278539	3.3046360	1.8350184
O	-2.7581809	-1.3953544	2.4818713
W	1.5791276	-1.9664957	2.5961544
O	0.8175047	1.1598609	0.3752015
O	-0.4898691	2.8491915	-1.6263874
O	-1.5987443	-2.9891826	0.6766918
P	0.0031587	-0.0812813	0.0007304
W	-3.0770676	-1.7816420	0.6333617

[AsW₁₂O₄₀]³⁻

O	0.0740751	1.2692053	-3.7368183
O	1.9363986	3.3451042	-0.5627859
O	-0.1563571	5.1686420	-0.0514677
O	0.7898208	-3.5372470	1.7989742
O	2.0268631	-0.1157625	2.6759745
O	3.3494499	-0.1048966	-0.2359695
W	-1.5167277	1.6631645	-2.7325358
O	-0.1690297	-1.3879819	3.0871136
W	1.3841337	-0.0680088	-3.3036284
O	2.2347806	1.2026259	-2.1489173
O	-2.3761620	-2.8143399	-3.8017444
O	-1.4297282	-0.0764622	0.8387233
W	1.6139678	1.7542745	2.6201319
O	-2.7674250	1.2459557	2.5222642
W	-1.5748371	-0.0922301	3.2155284
O	0.8656434	-1.4459747	0.3872307
O	2.2162128	-1.3671368	-2.1676202
O	-0.3089893	-0.0672337	-1.6293703
O	-0.1495403	1.1832829	3.1056358
O	-2.6939212	-1.6508468	-1.2295063
O	2.2154593	-2.5980737	4.0454203
O	2.2524238	2.3436720	4.0815403
W	3.0298700	1.7655387	-0.4995437
O	-0.5174156	-2.9507187	-1.6582220
O	3.0847362	1.9983797	1.4076144
W	0.0747346	-3.6616819	0.0194812
O	-4.4173324	-2.8317118	0.6971602
O	2.3715054	-0.0652236	-4.6879195
W	0.1288674	3.4969734	0.0713113
O	4.5123565	-2.5766144	-1.0136436
O	4.5494814	2.3592967	-0.9781393
W	-3.0599566	1.6500883	0.6664170
O	-2.3329354	2.7423316	-3.7622130
O	-0.2353577	-5.3269439	-0.1278341
O	3.0527038	-2.2272247	1.3769255
O	-1.5360625	2.8099371	0.7245915
O	-2.1882704	-0.0407946	-3.3151385
W	-1.5430673	-1.7627996	-2.7571022

O	1.8845248	-3.5277558	-0.6129083
W	3.0019115	-1.9665098	-0.5265209
O	0.0540812	-1.3791693	-3.7555658
O	-1.9675110	-0.1010707	4.8696889
O	-2.6696264	1.5465241	-1.2066975
O	-3.9359086	-0.0554878	0.5339522
O	-4.3753389	2.7251658	0.7365214
O	0.8414889	3.3357609	1.8487181
O	-2.7872209	-1.4022883	2.5031780
W	1.5854763	-1.9784323	2.5929809
O	0.8863988	1.2642258	0.4069936
O	-0.4734810	2.8191753	-1.6167067
O	-1.5797052	-2.9593624	0.6831434
As	0.0031930	-0.0812895	0.0008475
W	-3.0858068	-1.7757672	0.6420367

[SbW₁₂O₄₀]³⁻

O	0.0705833	1.2817442	-3.7903349
O	1.9650403	3.3924733	-0.5638499
O	-0.1834458	5.1656738	-0.0643435
O	0.8074559	-3.5852251	1.8202570
O	2.0119532	-0.1153896	2.6204307
O	3.2979099	-0.1045882	-0.2106976
W	-1.5141377	1.6523410	-2.7509049
O	-0.1780032	-1.3838162	3.0301256
W	1.3680823	-0.0680469	-3.3178123
O	2.1854379	1.1989516	-2.1178269
O	-2.3847167	-2.8344224	-3.7798720
O	-1.5660517	-0.0759788	0.9186266
W	1.6229486	1.7716871	2.6125440
O	-2.8096645	1.2588486	2.5554073
W	-1.5964900	-0.0918805	3.2131289
O	0.9478822	-1.5759441	0.4241065
O	2.1665718	-1.3634221	-2.1361345
O	-0.3394387	-0.0657872	-1.7847651
O	-0.1584544	1.1800597	3.0484126
O	-2.6602241	-1.6065474	-1.2141031
O	2.2047421	-2.5754467	4.0636510
O	2.2417955	2.3199592	4.0993526
W	3.0299337	1.7830356	-0.4874218
O	-0.4895705	-2.9021007	-1.6415631
O	3.1236769	2.0326657	1.4254455
W	0.0935535	-3.6683542	0.0273746
O	-4.4046348	-2.8528971	0.6757373
O	2.3979268	-0.0658903	-4.6720343
W	0.1478637	3.5032421	0.0796005
O	4.5187870	-2.5529469	-1.0323090
O	4.5557877	2.3360189	-0.9972127
W	-3.0713309	1.6392161	0.6802050
O	-2.3411793	2.7624750	-3.7398768

O	-0.2628857	-5.3233043	-0.1410288
O	3.0912175	-2.2623664	1.3945242
O	-1.5054769	2.7607650	0.7339704
O	-2.2131912	-0.0402430	-3.3651237
W	-1.5406035	-1.7514732	-2.7753443
O	1.9123371	-3.5755944	-0.6142363
W	3.0016584	-1.9839734	-0.5141210
O	0.0503741	-1.3911423	-3.8092353
O	-1.9394348	-0.1009983	4.8792923
O	-2.6366033	1.5012654	-1.1921028
O	-3.9888804	-0.0551341	0.5486922
O	-4.3623322	2.7465990	0.7153737
O	0.8598293	3.3832578	1.8706547
O	-2.8298119	-1.4148816	2.5363330
W	1.5938263	-1.9963393	2.5853295
O	0.9705856	1.3925890	0.4456796
O	-0.4465166	2.7703659	-1.6009741
O	-1.5482510	-2.9107077	0.6936150
Sb	0.0032607	-0.0811744	0.0007145
W	-3.0968468	-1.7649337	0.6562241

[PW₆O₂₄]⁷⁻

W	-2.5642135	1.8624505	0.5788947
W	-1.1661264	0.2528285	2.9937854
W	1.4026744	-1.6043733	2.4146774
P	0.0000025	0.0000032	-0.0000007
O	0.4862797	1.0788202	-1.3119471
O	-1.6256614	0.2269160	-0.6511742
O	-0.4603788	1.2852405	1.1224108
O	-2.7799127	0.5536540	1.9809031
O	-2.6682600	3.3334332	1.5525228
O	-1.8205720	2.7827351	-0.9444943
O	-4.2240308	1.6717523	0.0035534
O	0.6902517	-0.0975132	3.3866840
O	-1.9046384	-0.9961274	4.0025504
O	-1.2297680	1.6733150	4.0431469
O	3.0275070	-1.4002444	3.0781576
O	0.7488619	-2.9102939	3.4100881
W	2.5642029	-1.8624562	-0.5788990
W	1.1661212	-0.2528254	-2.9937827
W	-1.4026793	1.6043687	-2.4146789
O	-0.4862777	-1.0788179	1.3119487
O	1.6256639	-0.2269128	0.6511760
O	0.4603807	-1.2852384	-1.1224090
O	2.7799142	-0.5536623	-1.9809081
O	2.6682705	-3.3334360	-1.5525178
O	1.8205646	-2.7827345	0.9444913
O	4.2240331	-1.6717451	-0.0035439
O	-0.6902541	0.0975072	-3.3866785
O	1.9046332	0.9961308	-4.0025451

O	1.2297673	-1.6733165	-4.0431586
O	-3.0275034	1.4002503	-3.0781668
O	-0.7488522	2.9102916	-3.4100859

[AsW₆O₂₄]⁷⁻

W	-2.6072618	1.8933051	0.5883779
W	-1.1854723	0.2571272	3.0435140
W	1.4264009	-1.6310755	2.4552163
As	-0.0000024	-0.0000008	-0.0000023
O	0.4985775	1.1284192	-1.4157871
O	-1.7230644	0.2742504	-0.6928073
O	-0.5178673	1.3498238	1.1990688
O	-2.7898350	0.5875205	2.0091586
O	-2.7090798	3.3797698	1.5369462
O	-1.8629577	2.7860395	-0.9612160
O	-4.2738828	1.6918663	0.0393533
O	0.6766661	-0.1264079	3.4189719
O	-1.9506556	-0.9808849	4.0444663
O	-1.2249319	1.6669646	4.1069984
O	3.0389675	-1.4114646	3.1412645
O	0.7877288	-2.9562059	3.4332953
W	2.6072593	-1.8933045	-0.5883816
W	1.1854731	-0.2571189	-3.0435108
W	-1.4264035	1.6310732	-2.4552126
O	-0.4985798	-1.1284223	1.4157870
O	1.7230621	-0.2742532	0.6928058
O	0.5178654	-1.3498272	-1.1990708
O	2.7898311	-0.5875228	-2.0091574
O	2.7090901	-3.3797688	-1.5369432
O	1.8629588	-2.7860437	0.9612172
O	4.2738830	-1.6918562	-0.0393479
O	-0.6766683	0.1264055	-3.4189767
O	1.9506539	0.9808829	-4.0444616
O	1.2249341	-1.6669703	-4.1070067
O	-3.0389673	1.4114717	-3.1412691
O	-0.7877217	2.9562080	-3.4332906

[SbW₆O₂₄]⁷⁻

W	-2.6603678	1.9295856	0.5997888
W	-1.2076726	0.2629022	3.1037244
W	1.4547019	-1.6644997	2.5041242
Sb	0.0000035	0.0000033	0.0000017
O	0.5129583	1.1869677	-1.5390145
O	-1.8384483	0.3308736	-0.7423150
O	-0.5865763	1.4260938	1.2899597
O	-2.8043977	0.6231736	2.0418735
O	-2.7632423	3.4343821	1.5158925
O	-1.9102053	2.7939711	-0.9797799
O	-4.3347058	1.7162932	0.0844686

O	0.6647736	-0.1563410	3.4571485
O	-2.0052820	-0.9582719	4.0973006
O	-1.2177835	1.6576219	4.1851224
O	3.0501178	-1.4296264	3.2207661
O	0.8350606	-3.0115776	3.4612700
W	2.6603705	-1.9295727	-0.5997801
W	1.2076768	-0.2628901	-3.1037234
W	-1.4547014	1.6645068	-2.5041299
O	-0.5129588	-1.1869705	1.5390157
O	1.8384451	-0.3308741	0.7423129
O	0.5865775	-1.4260973	-1.2899613
O	2.8043965	-0.6231765	-2.0418747
O	2.7632457	-3.4343905	-1.5158974
O	1.9102055	-2.7939706	0.9797795
O	4.3347034	-1.7162922	-0.0844697
O	-0.6647763	0.1563376	-3.4571491
O	2.0052799	0.9582651	-4.0972998
O	1.2177811	-1.6576285	-4.1851229
O	-3.0501182	1.4296289	-3.2207656
O	-0.8350613	3.0115731	-3.4612658

[W₁₂O₄₀]⁸⁻

O	12.1265246	-0.3516175	10.4116112
W	12.2662838	1.4098398	10.3401221
O	12.5128166	1.9261788	12.0118213
O	13.7058062	1.8432677	9.3307641
O	10.7708477	2.1384711	9.6673147
W	9.1278942	3.0194176	8.6099511
O	8.7513919	3.9709815	10.0109019
O	8.1745098	1.5911181	8.9074635
O	8.0220473	3.8320920	7.3329958
W	14.8162275	3.0239115	7.9926917
O	15.5354086	1.5881206	7.2975151
O	15.9974691	3.4405439	9.2064569
O	15.2566800	4.2929169	6.6911189
O	13.3595189	4.3955197	8.5725299
O	10.1552336	2.0156435	6.9809919
W	11.4433332	2.2754569	5.7514632
O	11.5717734	0.7929265	4.8208609
O	12.9918809	2.5769052	6.5769842
W	12.1283418	5.5623354	7.8894707
O	10.6971270	4.4716057	8.0219960
W	14.8875554	5.6467887	5.3068240
O	15.5463565	4.6078192	4.0711863
O	16.1405662	6.7863072	5.7184602
O	12.1786585	6.7672091	9.1356311
O	10.8789552	6.8971386	6.7110601
W	10.4497283	8.2549919	5.6088011
O	10.3213594	9.7374967	6.5393263
O	8.9011904	7.9535496	4.7832208

O	11.7378382	8.5146876	4.3792106
O	11.0141271	3.6332689	4.6491400
W	9.7646636	4.9680674	3.4707959
O	11.1959792	6.0587816	3.3381853
O	8.5335524	6.1349013	2.7876935
W	7.0055260	4.8836330	6.0534155
O	6.3467336	5.9226356	7.2891423
O	5.7524234	3.7441641	5.6418268
O	9.7144011	3.7631864	2.2245743
O	6.6363600	6.2375478	4.6691628
W	7.0768531	7.5064900	3.3675413
O	6.3576635	8.9423634	4.0627574
O	5.8955789	7.0899268	2.1538214
O	8.1872604	8.6871706	2.0294759
W	9.6267653	9.1204964	1.0200642
O	9.3802033	8.6040639	-0.6515975
O	9.7665784	10.8819335	0.9484840
O	11.1222163	8.3918437	1.6928954
W	12.7651909	7.5109596	2.7502540
O	13.1416670	6.5593279	1.3493418
O	13.7185212	8.9391866	2.4527277
O	13.8709812	6.6982611	4.0272283
O	13.2582475	5.8565484	6.4056831
O	8.6348215	4.6738456	4.954551

[P₄W₁₄O₅₈]¹²⁻

W	0.3091449	11.3546128	11.0651599
W	-1.7772762	8.5723107	9.4859791
W	-2.6172761	5.9395698	11.5782687
W	-1.3326914	6.1828201	15.1663936
W	2.1877367	6.1994594	13.8404375
W	1.0177845	6.2346844	10.5369641
W	3.0249205	8.8420708	11.7434657
P	-0.4965097	8.4848994	12.7638126
P	2.5557275	11.6291350	13.6548606
O	-0.2892002	9.9885931	12.6280276
O	-1.6093626	8.0320309	11.7465102
O	-0.9050447	8.0487755	14.1658865
O	0.8360420	7.7527575	12.3739535
O	-0.7277795	10.0887881	9.9878907
O	-2.4706649	6.7738246	9.8153794
O	-2.1000002	5.7749050	13.4105484
O	0.5302940	5.6829378	14.3598205
O	3.3499972	7.5601683	13.1392228
O	2.0371044	5.4614120	12.1296308
O	2.6658370	7.4435419	10.5569781
O	1.9029264	10.0090897	10.9293268
O	0.1298822	7.4891189	9.5839875
O	-0.5057033	5.4932684	11.1684572
O	2.9103566	10.1610327	13.3423313

O 1.6543677 12.1389223 12.4817900
O 3.8819536 12.4508993 13.7727393
O 1.7925110 11.8164563 14.9820487
O 0.9485955 12.2518157 9.6932003
O -0.9694022 12.4496064 11.5300881
O -1.6533979 8.5394226 7.7175228
O -3.3436086 9.3611547 9.6249091
O -3.0172653 4.2787073 11.1031072
O -4.2473490 6.5259774 11.8833135
O -1.4958372 4.5489223 15.7982119
O -2.7289503 6.9061989 15.9257729
O 3.2623182 5.0118456 14.5134167
O 1.5786849 5.0824831 9.3103117
O 4.6060354 9.2515613 11.1511071
W 3.5523095 7.9597260 19.3729461
W 5.6387252 10.7420301 20.9521262
W 6.4787250 13.3747695 18.8598364
W 5.1941462 13.1315166 15.2717109
W 1.6737191 13.1148770 16.5976673
W 2.8436761 13.0796456 19.9011410
W 0.8365306 10.4722607 18.6946473
P 4.3579636 10.8294340 17.6742913
P 1.3057301 7.6852023 16.7832457
O 4.1506504 9.3257362 17.8100750
O 5.4708185 11.2823026 18.6915951
O 4.7664994 11.2655600 16.2722251
O 3.0254165 11.5615818 18.0641511
O 4.5892350 9.2255485 20.4502116
O 6.3321243 12.5405134 20.6227265
O 5.9614582 13.5394340 17.0275568
O 3.3311586 13.6313982 16.0782810
O 0.5114568 11.7541665 17.2988827
O 1.8243481 13.8529267 18.3084760
O 1.1956207 11.8707930 19.8811260
O 1.9585279 9.3052464 19.5087812
O 3.7315713 11.8252160 20.8541162
O 4.3671580 13.8210704 19.2696524
O 0.9510992 9.1533017 17.0957732
O 2.2070851 7.1754091 17.9563138
O -0.0205006 6.8634366 16.6653658
O 2.0689472 7.4978765 15.4560561
O 2.9128623 7.0625166 20.7449118
O 4.8308628 6.8647265 18.9080176
O 5.5148556 10.7749077 22.7205786
O 7.2050712 9.9531716 20.8131890
O 6.8787262 15.0356252 19.3349999
O 8.1088075 12.7883535 18.5547925
O 5.3572922 14.7654064 14.6398903
O 6.5904014 12.4081316 14.5123296
O 0.5991366 14.3024814 15.9246931
O 2.2827664 14.2318503 21.1277988

O -0.7445745 10.0627724 19.2869992

Na₆[As₂W₁₈O₆₈]¹²⁻

W 5.3694087 2.8978017 27.1859223
W 8.1362933 3.0249838 24.6299776
As 5.4585870 5.4584433 24.6267997
Na 10.1872027 6.2101165 23.8767409
O 4.4783565 4.4774969 25.6068975
O 5.1155477 5.1156660 23.0202568
O 6.5806015 2.4365313 25.8449911
O 3.9359408 2.0572912 26.1491479
O 9.1791569 4.0274575 23.5762072
O 8.8023667 3.8146744 26.2705352
O 6.8486249 2.7543774 23.2367061
O 5.6104386 1.6625829 28.4204770
O 8.9958939 1.4965592 24.6564109
O 5.1150025 7.0646870 24.9704644
O 7.0650903 5.1155400 24.9699508
W 2.8993212 2.8979548 24.7156534
W 3.0245628 5.4548755 21.9495837
Na 6.2090002 6.2104021 19.8983023
O 2.4370808 4.2390387 23.5049965
O 2.0585379 3.9338060 26.1496316
O 4.0262764 6.5095098 20.9068665
O 3.8149973 3.8149632 21.2828172
O 2.7534637 6.8475636 23.2377683
O 1.6647124 1.6628175 24.4744591
O 1.4959754 5.4279279 21.0902688
Na 6.2080016 10.1874280 23.8778016
O 3.9354343 3.9336967 28.0266542
O 6.5079901 9.1784153 26.0601024
O 3.8136647 8.8010316 26.2718121
O 6.8475148 6.8473222 27.3321198
W 3.0238564 8.1350075 24.6312923
O 2.4364462 6.5787251 25.8460703
O 4.0255924 9.1785668 23.5775263
O 1.4950531 8.9939126 24.6583238
W 5.4554614 3.0251422 21.9489571
O 4.2403107 2.4366720 23.5045287
O 6.5093598 4.0276097 20.9062167
O 5.4290007 1.4967577 21.0892656
W 8.1356397 5.4545777 27.0610220
Na 8.8332169 4.8562685 21.2523143
Na 8.8322110 8.8332686 25.2318414
Na 4.8540064 8.8335715 21.2534104
O 6.5801138 4.2387923 27.6483240
O 11.0156080 5.8650932 21.5525062
O 8.5319095 11.0160220 24.2239820
O 5.8627065 8.5345489 19.0707459
O 9.1784750 6.5092070 26.0594301

O	5.8620746	11.0162479	21.5540254	O	10.8009234	12.6069969	21.6256904
O	11.0149592	8.5340836	24.2232310	O	11.2262611	11.2286436	23.8473565
O	8.5331739	5.8653251	19.0699763	O	8.1926080	12.2893158	21.8935424
O	8.9948507	5.4274987	28.5896566	O	13.3765148	13.3808645	20.6557505
W	2.8986397	5.3673955	27.1865633	O	9.6122869	13.5468641	24.0409921
W	5.4540863	8.1348664	27.0616992	O	11.1057262	11.1101082	17.1035192
O	4.2391765	6.5786188	27.6489271	O	6.2388216	11.2290963	18.8597090
O	1.6636224	5.6074999	28.4215097	O	8.1936486	8.1964674	17.7980215
O	5.4269947	8.9936869	28.5905486	W	6.9049231	12.0187452	20.5002776
W	12.1425253	9.6763674	17.9435510	O	8.4605976	12.6072189	19.2852651
W	12.0173298	6.9086961	20.4987498	O	6.0453241	13.5471764	20.4738941
As	9.5826150	9.5852619	20.5033484	W	12.0166719	9.5887488	23.1805336
O	10.5628398	10.5662328	19.5232656	O	12.6041434	10.8046224	21.6251463
O	9.9256795	9.9279975	22.1099004	O	13.5452681	9.6156517	24.0398294
O	12.6047361	8.4650041	19.2840033	W	9.5870681	6.9089149	18.0683913
O	12.9826511	11.1099332	18.9805150	O	10.8019786	8.4651678	17.4811708
O	11.2275001	6.2427151	18.8582221	O	9.6141287	6.0501265	16.5395065
O	12.2877455	8.1960925	21.8923030	W	9.6717719	12.1459779	17.9443004
O	13.3775214	9.4363052	16.7085802	W	6.9055339	9.5892124	18.0691792
O	13.5461382	6.0497777	20.4716705	O	8.4610550	10.8050099	17.4818819
O	7.9761127	9.9281858	20.1602337	O	9.4307259	13.3812397	16.7097900
O	9.9261903	7.9790277	20.1596369	O	6.0462991	9.6163334	16.5405459
W	12.1419010	12.1457389	20.4145330	O	11.1052549	12.9864555	18.9810842
W	9.5857953	12.0185115	23.1812610				

3 Literature

- 1 T. Esser, M. Huber, D. Voß and J. Albert, Development of an efficient downstream process for product separation and catalyst recycling of a homogeneous polyoxometalate catalyst by means of nanofiltration membranes and design of experiments, *Chem. Eng. Res. Des.*, 2022, **185**, 37–50.
- 2 J.-C. Raabe, T. Esser, F. Jameel, M. Stein, J. Albert and M. J. Poller, Study on the incorporation of various elements into the Keggin lacunary-type phosphomolybdate [PMo₉O₃₄]⁹⁻ and subsequent purification of the polyoxometalates by nanofiltration, *Inorg. Chem. Front.*, 2023, **10**, 4854–4868.
- 3 J.-C. Raabe, J. Albert and M. J. Poller, Spectroscopic, Crystallographic, and Electrochemical Study of Different Manganese(II)-Substituted Keggin-Type Phosphomolybdates, *Chem. – A Eur. J.*, 2022, **28**, 1–12.
- 4 J.-C. Raabe, J. Aceituno Cruz, J. Albert and M. J. Poller, Comparative Spectroscopic and Electrochemical Study of V(V)-Substituted Keggin-Type Phosphomolybdates and -Tungstates, *Inorganics*, 2023, **11**, 138.
- 5 F. Demartin, C. M. Gramaccioli and T. Pilati, The importance of accurate crystal structure determination of uranium minerals. II. Sod@Re (UO₂)₂(SiO₄)₂·2H₂O, *Acta Crystallogr. Sect. C Cryst. Struct. Commun.*, 1992, **48**, 1–4.
- 6 R. C. Clark and J. S. Reid, The analytical calculation of absorption in multifaceted crystals, *Acta Crystallogr. Sect. A Found. Crystallogr.*, 1995, **51**, 887–897.
- 7 F. Kleemiss, O. V. Dolomanov, M. Bodensteiner, N. Peyerimhoff, L. Midgley, L. J. Bourhis, A. Genoni, L. A. Malaspina, D. Jayatilaka, J. L. Spencer, F. White, B. Grundkötter-Stock, S. Steinhauer, D. Lentz, H. Puschmann and S. Grabowsky, Accurate crystal structures and chemical properties from NoSpherA2, *Chem. Sci.*, 2021, **12**, 1675–1692.
- 8 S. C. Capelli, H.-B. Bürgi, B. Dittrich, S. Grabowsky and D. Jayatilaka, Hirshfeld atom refinement, *IUCrJ*, 2014, **1**, 361–379.
- 9 D. Jayatilaka and B. Dittrich, X-ray structure refinement using aspherical atomic density functions obtained from quantum-mechanical calculations, *Acta Crystallogr. Sect. A*

Found. Crystallogr., 2008, **64**, 383–393.

- 10 L. Midgley, L. J. Bourhis, O. V. Dolomanov, S. Grabowsky, F. Kleemiss, H. Puschmann and N. Peyrerimhoff, Vanishing of the atomic form factor derivatives in non-spherical structural refinement – a key approximation scrutinized in the case of Hirshfeld atom refinement, *Acta Crystallogr. Sect. A Found. Adv.*, 2021, **77**, 519–533.
- 11 TURBOMOLE, V7.5.1 2021, a development of University of Karlsruhe and Forschungszentrum Karlsruhe GmbH, 1989–2007, TURBOMOLE GmbH, since 2007; available from <http://www.turbomole.com>.
- 12 M. Ernzerhof and G. E. Scuseria, Assessment of the Perdew–Burke–Ernzerhof exchange–correlation functional, *J. Chem. Phys.*, 1999, **110**, 5029–5036.
- 13 A. Schäfer, H. Horn and R. Ahlrichs, Fully optimized contracted Gaussian basis sets for atoms Li to Kr, *J. Chem. Phys.*, 1992, **97**, 2571–2577.
- 14 A. Klamt and G. Schüürmann, COSMO: a new approach to dielectric screening in solvents with explicit expressions for the screening energy and its gradient, *J. Chem. Soc., Perkin Trans. 2*, 1993, 799–805.

Electronic supporting information:

Synthesis and characterization of V substituted Anderson-type telluro-molybdates and tungstates for catalytic oxidation of furan derivatives to formic and maleic acid

Jan-Christian Raabe¹, Tobias Esser¹, Maximilian J. Poller¹ and Jakob Albert^{1*}

¹Institute for Technical and Macromolecular Chemistry, Universität Hamburg, Bundesstraße 45, 20146 Hamburg, Germany

Inhaltsverzeichnis

1	POM synthesis and characterization	3
1.1	Experimental part	3
1.1.1	Chemicals	3
1.1.2	Synthetic procedures	3
1.2	Characterization.....	5
1.2.1	Compositional analysis	5
1.2.2	Vibrational spectroscopy	10
1.2.3	Crystallography	10
1.2.4	NMR-spectroscopy.....	14
1.2.5	UV-Vis spectroscopy	15
1.2.6	Electrochemical analysis	24
2	Catalytic experiments	26
2.1	Experimental part	26
2.1.1	Chemicals	26
2.1.2	Experimental procedures.....	26
2.2	Catalytic results	26
3	Literature	28

1 POM synthesis and characterization

1.1 Experimental part

1.1.1 Chemicals

The chemicals used were purchased from the following suppliers:

- Sodium molybdate dihydrate: Carl Roth with a purity of 99.5 %
- Sodium tungstate dihydrate: VWR chemical with a purity of 99 %
- Telluric acid: Sigma aldrich with a purity of 97 %
- Sodium vanadate: Alfa Aesar with a purity of 96 %
- Molybdenum trioxide from Alfa Aesar with a purity of 99 %
- Hydrochloric acid: VWR chemicals as 37 % solution in water
- Sodium hydroxide
- Demineralized water was always used as solvent.

1.1.2 Synthetic procedures

1.1.2.1 Synthesis of $\text{Na}_6[\text{TeW}_6\text{O}_{24}]$

Sodium tungstate dihydrate (5.0020 g, 15.16 mmol, 5.987 equivalents) and telluric acid (0.5817 g, 2.533 mmol, 1 equivalent) were dissolved in water (100 mL). The pH value was 8.822 and was adjusted to 4.970 by adding a 37 % hydrochloric acid solution in water. In the next step the mixture was purified using our previous published dialysis membrane process.^[1] In the final step the solvent was evaporated under reduced pressure to yield a colorless powder (85 °C oil bath, 200 to 0 mbar).

1.1.2.2 Synthesis of $\text{Na}_6[\text{TeMo}_6\text{O}_{24}]$

Telluric acid (0.8383 g, 3.650 mmol, 1 equiv) was dissolved in water (21 mL), molybdenum trioxide (3.0007 g, 20.85 mmol, 6 equivalents) and sodium hydroxide (0.8377 g, 20.94 mmol, 5.7370 equivalents) were added. A clear colorless solution was formed, which was concentrated under reduced pressure to yield a colorless powder (85 °C oil bath, 200 to 0 mbar).

1.1.2.3 Synthesis of V(+V) substituted Anderson-Evans POMs

Sodium vanadate was added to water (100 mL) and heated to 60 °C for 30 min until a clear, colorless solution was formed. In the next step sodium tungstate/molybdate dihydrate was added followed by the addition of telluric acid. The color of the solution turned from colorless

to red and the pH value was adjusted to 5 using a 37 % hydrochloric acid solution in water, yielding a red solution. The mixture was purified using our previously published dialysis membrane process.^[1] In the final step the solvent was evaporated under reduced pressure to yield an orange, yellow or red powder (85 °C oil bath, 200 to 0 mbar).

1.1.2.4 Alternative procedure for the synthesis of V(+V) substituted Anderson-Evans POMs
Sodium tungstate/molybdate dihydrate, sodium vanadate and telluric acid were added to water (100 mL). A red/orange suspension was formed, and the pH value was adjusted to 5 using a 37 % hydrochloric acid solution in water. It was heated to 60 °C until a clear, orange/red colored solution was formed and the pH value was adjusted to 5 again. The mixture was purified using our previously published dialysis membrane process.^[1] In the final step the solvent was evaporated under reduced pressure to yield an orange, yellow or red powder (85 °C oil bath, 200 to 0 mbar).

All weights and pH values during the experimental procedures are listed in Table S1 and S2.

Table S1: Precise weights of the precursor compounds during the experimental procedures for synthesizing the V(+V) substituted Anderson-Evans-POMs.

No.	Compound	Sodium tungstate dihydrate	Sodium molybdate dihydrate	Sodium vanadate	Telluric acid
1	NaTeVW	5.0033 g 15.17 mmol 4.9900 equiv.	-	0.3713 g 3.045 mmol 1.002 equiv.	0.6981 g 3.040 mmol 1 equiv.
2	NaTeV ₂ W	5.0043 g 15.17 mmol 3.999 equiv.	-	0.9243 g 7.581 mmol 1.999 equiv.	0.8710 g 3.793 mmol 1 equiv.
3	NaTeV ₃ W	5.0028 g 15.17 mmol 2.998 equiv.	-	1.8488 g 15.16 mmol 2.997 equiv.	1.1619 g 5.060 mmol 1 equiv.
4	NaTeVMo	-	5.0020 g 20.67 mmol 5.000 equiv.	0.5056 g 4.147 mmol 1.003 equiv.	0.9495 g 4.134 mmol 1 equiv.
5	NaTeV ₂ Mo	-	5.0032 g 20.68 mmol 4.001 equiv.	1.2613 g 10.34 mmol 2.001 equiv.	1.1869 g 5.168 mmol 1 equiv.
6	NaTeV ₃ Mo	-	5.0019 g 20.67 mmol 3.001 equiv.	2.5233 g 20.69 mmol 3.004 equiv.	1.5818 g 6.888 mmol 1 equiv.

Table S2: pH-values in the experiments for synthesizing the V(+V) substituted Anderson-Evans POMs.

Compound	pH-value before	pH-value after
NaTeVW	8.952	5.078
NaTeV₂W	8.874	5.039
NaTeV₃W	8.969	5.039
NaTeVMo	7.689	5.033
NaTeV₂Mo	7.824	5.063
NaTeV₃Mo	7.830	4.964

1.1.2.5 Decomposition experiment of NaTeVMo

Herefore, an aqueous solution of NaTeVMo was left to stand for several hours at room temperature. A precipitate formation was observed, whereby the precipitate was collected by filtration and was dried in a desiccator under reduced pressure. The precipitate and the solid residue, collected after evaporation of the solvent, were analyzed with AAS/ICP-OES.

1.1.2.6 Procedure for crystallization of the synthesized compounds

For crystallization, an aqueous POM solution (~100 mg in ~100 μ L of water) was concentrated under reduced pressure in a desiccator over orange gel. Single-crystals suitable for X-ray diffraction (XRD) were obtained as an aqueous suspension.

1.2 Characterization

1.2.1 Compositional analysis

Elemental analysis:

POM samples were analyzed using an ICP-OES-spectrometer for elemental analysis (Fa. Spectro, type ARCOS) for W, Mo, V and Te (method ICP-OES). Na and K were analyzed with AAS-F (Fa. Thermo, type Solaar S Series), method: F-AAS without HKL).

- Compound NaTeVW, NaTeV₂W and NaTeW were dissolved in water (25 mL).
- Compound NaTeV₃W, NaTeV₂Mo and NaTeV₃Mo were dissolved in water (5 mL) and nitric acid (0.1 mL) was added. Then it was filled up to a final volume of 25 mL.
- Compound NaTeMo was dissolved in a 3 M hydrochloric acid solution in water (25 mL)
- Compound NaTeVMo was dissolved in water (5 mL) and nitric acid (0.1 mL) was added. Then it was filled up to a final volume of 50 mL.

NaTeW:

ICP-OES: Calculated for $\text{Na}_6[\text{TeW}_6\text{O}_{24}] \cdot 4 \text{H}_2\text{O}$: 7.56 % Na, 6.993 % Te, 60.453 % W. Found for $\text{Na}_6[\text{TeW}_6\text{O}_{24}] \cdot 4 \text{H}_2\text{O}$: 7.20 % Na, 6.92 % Te, 53.89 % W. Data normalized to tungsten. Na/Te/W ratio: 6.41/1.11/6.

TGA: 4.204 % weight loss upon drying, this corresponds to 4 mol hydration water per mol of the POM.

NaTeVW:

ICP-OES: Calculated for $\text{Na}_7[\text{TeVW}_5\text{O}_{24}] \cdot 3 \text{H}_2\text{O}$: 9.485 % Na, 7.52 % Te, 3.002 % V, 54.176 % W. Found for $\text{Na}_7[\text{TeVW}_5\text{O}_{24}] \cdot 3 \text{H}_2\text{O}$: 11.5 % Na, 5.57 % Te, 3.03 % V, 55.63 % W. Data normalized to tungsten. Na/Te/V/W ratio: 8.27/0.722/0.982/5.

The tellurium content is lower than expected because tellurium migrated into the permeate fraction during the nanofiltration process.

TGA: 3.440 % weight loss upon drying, this corresponds to 3 mol hydration water per mol of the POM.

NaTeV₂W:

ICP-OES: Calculated for $\text{Na}_8[\text{TeV}_2\text{W}_4\text{O}_{24}] \cdot 3 \text{H}_2\text{O}$: 11.591 % Na, 8.041 % Te, 6.421 % V, 46.343 % W. Found for $\text{Na}_8[\text{TeV}_2\text{W}_4\text{O}_{24}] \cdot 3 \text{H}_2\text{O}$: 11.4 % Na, 4.38 % Te, 7.01 % V, 51.82 % W. Data normalized to tungsten. Na/Te/V/W ratio: 7.04/0.488/1.95/4.

The tellurium content is lower than expected because tellurium migrated into the permeate fraction during the nanofiltration process.

TGA: 3.854 % weight loss upon drying, this corresponds to 3 mol hydration water per mol of the POM.

NaTeV₃W:

ICP-OES: Calculated for $\text{Na}_9[\text{TeV}_3\text{W}_3\text{O}_{24}] \cdot 5 \text{H}_2\text{O}$: 13.676 % Na, 8.434 % Te, 10.101 % V, 36.454 % W. Found for $\text{Na}_9[\text{TeV}_3\text{W}_3\text{O}_{24}] \cdot 5 \text{H}_2\text{O}$: 10.7 % Na, 6.69 % Te, 12.79 % V, 42.50 % W. Data normalized to tungsten. Na/Te/V/W ratio: 6.04/0.680/3.26/3.

The tellurium content is lower than expected because tellurium migrated into the permeate fraction during the nanofiltration process.

TGA: 5.484 % weight loss upon drying, this corresponds to 5 mol hydration water per mol of the POM.

NaTeMo:

ICP-OES: Calculated for $\text{Na}_6[\text{TeMo}_6\text{O}_{24}] \cdot 4 \text{H}_2\text{O}$: 10.633 % Na, 9.836 % Te, 44.375 % Mo. Found for $\text{Na}_6[\text{TeMo}_6\text{O}_{24}] \cdot 4 \text{H}_2\text{O}$: 10.2 % Na, 9.97 % Te, 41.11 % Mo. Data normalized to molybdenum. Na/Te/Mo ratio: 6.21/1.09/6.

TGA: 6.166 % weight loss upon drying, this corresponds to 4 mol hydration water per mol of the POM.

NaTeVMo:

ICP-OES: Calculated for $\text{Na}_7[\text{TeVMo}_5\text{O}_{24}] \cdot 3 \text{H}_2\text{O}$: 13.376 % Na, 10.605 % Te, 4.234 % V, 39.87 % Mo. Found for $\text{Na}_7[\text{TeVMo}_5\text{O}_{24}] \cdot 3 \text{H}_2\text{O}$: 14.9 % Na, 9.27 % Te, 3.13 % V, 33.67 % Mo. Data normalized to molybdenum. Na/K/Te/V/Mo ratio: 9.23/1.04/0.875/5.

Due to the instability of NaTeVMo, the compound could not be desalinated using the nanofiltration process, so that the sodium content is too high and the content of the framework elements is consequently too low.

TGA: 4.954 % weight loss upon drying, this corresponds to 3 mol hydration water per mol of the POM.

NaTeV₂Mo:

ICP-OES: Calculated for $\text{Na}_8[\text{TeV}_2\text{Mo}_4\text{O}_{24}] \cdot 3 \text{H}_2\text{O}$: 14.89 % Na, 10.33 % Te, 8.248 % V, 31.069 % Mo. Found for $\text{Na}_8[\text{TeV}_2\text{Mo}_4\text{O}_{24}] \cdot 3 \text{H}_2\text{O}$: 15.0 % Na, 10.13 % Te, 7.47 % V, 28.86 % Mo. Data normalized to molybdenum. Na/Te/V/Mo ratio: 8.70/1.06/1.95/4.

Due to the instability of NaTeV₂Mo, the compound could not be desalinated using the nanofiltration process.

TGA: 4.920 % weight loss upon drying, this corresponds to 3 mol hydration water per mol of the POM.

NaTeV₃Mo:

ICP-OES: Calculated for Na₉[TeV₃Mo₃O₂₄] · 4 H₂O: 16.805 % Na, 10.364 % Te, 12.413 % V, 23.377 % Mo. Found for Na₉[TeV₃Mo₃O₂₄] · 4 H₂O: 14.2 % Na, 10.47 % Te, 11.57 % V, 22.4 % Mo. Data normalized to molybdenum. Na/Te/V/Mo ratio: 7.94/1.05/2.92/3.

Due to the instability of NaTeV₃Mo, the compound could not be desalinated using the nanofiltration process.

TGA: 6.234 % weight loss upon drying, this corresponds to 4 mol hydration water per mol of the POM.

Table S3: AAS/ICP-OES results of the decomposition experiment of compound NaTeVMo.

Sample	Na [%]	K [%]	Te [%]	V [%]	Mo [%]
Precipitate	10.0	0.00	9.65	0.00	39.37
Stoichiometry	6.36	0.00	1.11	0.00	6.00
Reference data for pure NaTeMo	11.3	0.00	10.4	0.00	47.0
Stoichiometry	6	0	1	0	6
Residue remained in aqueous solution	14.7	0.00	12.12	7.59	31.77

Data are normalized to Mo.

NaTeMo precipitate:

ICP-OES: Calculated for Na₆[TeMo₆O₂₄] · 4 H₂O: 10.633 % Na, 9.836 % Te, 0.00 % V, 44.375 % Mo. Found for Na₆[TeMo₆O₂₄] · x H₂O precipitate: 10.0 % Na, 9.65 % Te, 0.00 % V, 39.37 % Mo. Data normalized to molybdenum. Na/Te/V/Mo ratio: 6.36/1.11/0/6.

Soluble residue:

ICP-OES: Found: 14.7 % Na, 12.12 % Te, 7.59 % V, 31.77 % Mo.

The precipitate was identified as NaTeMo. Deviations of the obtained AAS/ICP-OES values from the calculated ones are due to the presence of hydration water molecules in the precipitate. The assignment of the values to the compound NaTeMo becomes clearer when the elemental stoichiometry is considered. Here, the expected Na/Te/Mo stoichiometry of 6/1/6 can be verified.

Table S4: Results from the elemental analysis (AAS/ICP-OES) of the dialysis process for desalination of the POMs.

			Na	K	Te	V	W*
NaTeVW	Feed	Concentration [g/L]	9.730	0.43	4.348	1.511	27.610
		Stoichiometry	14.1	$3.66 \cdot 10^{-4}$	1.13	0.987	5.00
	Permeate	Concentration [g/L]	1.288	0.22	0.607	0.00	0.00
		Stoichiometry	1.00	$1.00 \cdot 10^{-4}$	$8.50 \cdot 10^{-2}$	0.00	0.00
	Retentate	Concentration [g/L]	3.018	0.32	2.455	1.331	24.579
		Stoichiometry	4.91	$3.06 \cdot 10^{-4}$	0.720	0.977	5.00
NaTeV₂W	Feed	Concentration [g/L]	6.12	1.47	3.904	2.878	20.665
		Stoichiometry	9.47	1.34	1.09	2.01	4.00
	Permeate	Concentration [g/L]	1.31	0.00	0.860	0.00	0.00
		Stoichiometry	1.00	0.00	0.118	0.00	0.00
	Retentate	Concentration [g/L]	2.225	0.78	1.566	2.478	18.388
		Stoichiometry	3.87	$7.98 \cdot 10^{-4}$	0.491	1.95	4.00
NaTeV₃W	Feed	Concentration [g/L]	9.299	0.63	6.259	6.680	24.379
		Stoichiometry	9.15	$3.65 \cdot 10^{-4}$	1.11	2.97	3.00
	Permeate	Concentration [g/L]	1.648	0.26	1.205	0.00	0.00
		Stoichiometry	1.00	$9.28 \cdot 10^{-5}$	0.132	0.00	0.00
	Retentate	Concentration [g/L]	5.152	0.53	3.651	7.056	26.082
		Stoichiometry	4.74	$2.87 \cdot 10^{-4}$	0.605	2.93	3.00

*Data were normalized to W.

Thermogravimetric analysis (TGA):

TGA measurements were done with a TG 209 F1 Libra of NETZSCH. The data were processed with the software Proteus of NETZSCH (version 8.0.2). Approximately 20 mg of the sample was weighed into a Duran glass crucible and the change in mass was measured.

The starting temperature was below 30 °C. During the measurement, a nitrogen flow of 20 mL/min was passed through the instrument. The TGA data show three regions: hygroscopic water (water that comes from the air), hydration water (water from crystal association) and the mass consistency (pure POM without any moisture). The final data were processed with the software PROTEUS analysis of NETZSCH and exported as a .x/y text document. With the use of Origin® 2019b the TGA data were plotted.

The following temperature program was used:

- Sample was heated to 30 °C with a heating rate of 10 K/min
- Temperature constant at 30 °C for 15 min
- Sample was heated to 350 C with a heating rate of 10 K/min
- Temperature constant at 350 °C for 30 min
- End (Cooling down)

1.2.2 Vibrational spectroscopy

ATR-FT-IR spectroscopy:

IR spectra of all POM samples were measured in attenuated total reflection (ATR) measurement mode on a QATR™-S single-reflection ATR (with a diamond prism) from Shimadzu. In the next step the baseline was corrected and the peaks were determined manually. The data were then exported as an .x/y text document and plotted in Origin 2019b.

Raman spectroscopy:

All Raman spectra were measured on a SENTERRA Raman microscope from Bruker Optik GmbH. The aperture was set to 50 x 1000 μm. A 20 objective was used on the microscope. The excitation laser has a wavelength of 785 nm and the measurement range used was between 75 cm⁻¹ and 1525 cm⁻¹. The integration time was 16 seconds, the number of scans was 8 and the Raman laser power was 10 mW. Raman data were exported as a .DPT file from the Opus software and plotted in Origin 2019b.

Table S5: Wavenumber ranges of the different vibrational modes found for our Anderson-Evans structures.

Vibrational mode	IR [cm ⁻¹]	Raman [cm ⁻¹]
M=O _t	950-850	1000-900
M-O-M/Te-O	700-600	700-550
Te-O/M-O-M		600
O-Te-O/M-O-M	-	400

1.2.3 Crystallography

All powder XRD diffractograms were measured with an X'Pert Pro diffractometer (PANalytical Corp.) using Cu-K_α radiation ($\lambda = 1.5418 \text{ \AA}$). The measurement range was between 5-90 °. With the software X'Pert HighScore Plus the background was determined, and the data were

smoothed. Reflexes were determined. All powder data were exported as .ASC file and plotted in Origin 2019b.

Powder XRD data of the synthesized compounds (Figure S1) compared to those of sodium vanadate and sodium chloride: the presence of sodium vanadate can be ruled out and it can be concluded that the product is indeed the said mixture of POMs and sodium chloride.

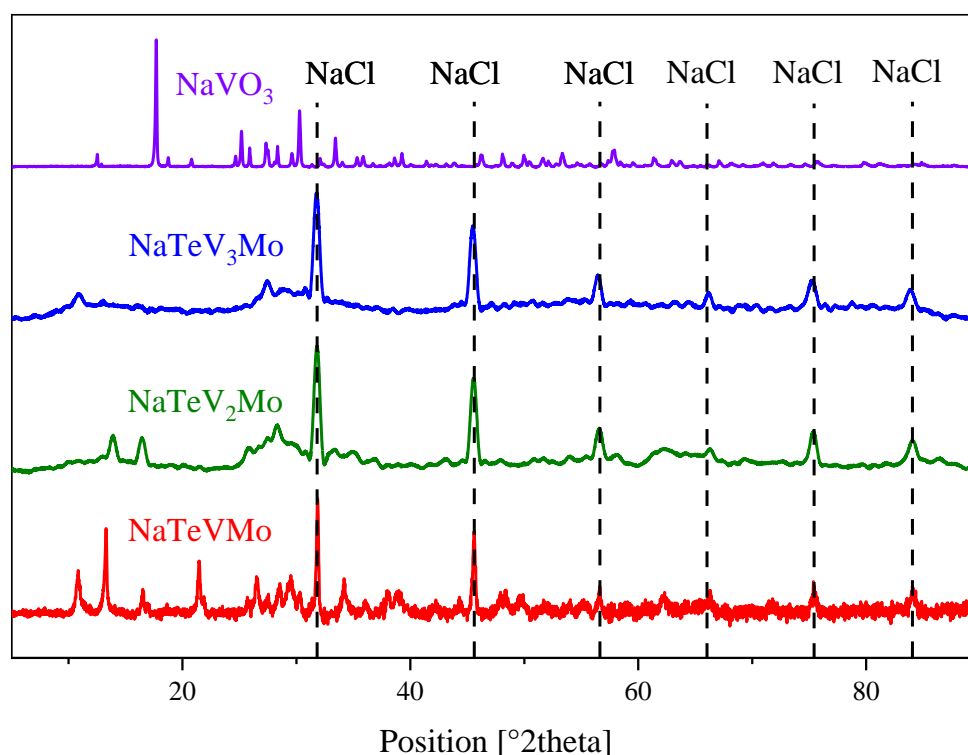


Figure S1: Comparison of the powder XRD data of the POMs NaTeV_xMo with sodium chloride and sodium vanadate.

Single-crystals were measured on a 4-circle single-crystal diffractometer SuperNova from Oxford Diffraction (Company: Agilent Technologies, Acquisition: Nov. 2011, using a molybdenum and copper source (dual instrument), Microfocus tubes, cryostream-700 Plus nitrogen steam cooling, 100-500 K (Oxford Cryosystems)). Data were solved and refined using Olex2 v1.5 and the ShelX algorithm and the PLATON software.^[2-5] Shelxtl XPREP was used for verification of the space group. Before publication the .cif file was checked for publication with the online tool checkcif <https://checkcif.iucr.org/>.

The single-crystals were obtained by slowly evaporating water from aqueous samples of the compounds under reduced pressure. Before the measurement, the crystals were stored in the supersaturated, aqueous solution of the POM and removed from the liquid for measurement.

Figure S2 shows the solid-state structure for compound NaTeVW. The corresponding .cif file is available in the CCDC database with the deposition numbers 2321174 and 2321175.

- NaTeVW: The single-crystals of compound NaTeVW were obtained as aqueous suspension from which suitable crystals were taken for measurements. The phase problem was solved with ShelXS and the Patterson Method. Refinement was done with ShelXS and L.S. The space group is P-1 (2). Hydrogen atoms of the hydration water molecules were not modeled. Final R values: R_1 : 2.75 %, wR_2 : 7.58 %, R_{int} : 4.20 % and Goof: 1.091. The .cif file is available in the CCDC database with the deposition number 2321175.

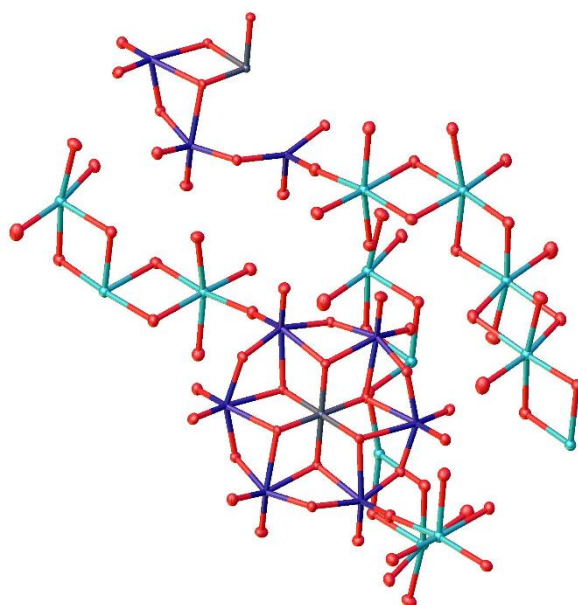


Figure S2: Solid-state structure of compound NaTeVW determined by sc-XRD. The compound was crystallized in the triclinic space group P-1 (2). R_1 : 2.75 %, wR_2 : 7.58, R_{int} : 5.16, GooF: 1.091. Color code: turquoise: sodium, blue: metals (W, V), grey: tellurium and red: oxygen. The full crystallographic information file (.cif) is available through the joint Cambridge Crystallographic Data Centre and Fachinformationszentrum Karlsruhe Access Structures service (deposition number: 2321175).

In the solid-state structure of the anion $[\text{TeVW}_5\text{O}_{24}]^{7-}$, the anions are linked to each other via the terminal oxygen atoms by sodium cations, all of which are in an octahedral coordination geometry. The sodium cations coordinate the hydration water molecules and line up to form long chains of edge-linked NaO_6 octahedra, whereby layer-like structures of POM anions and rows of NaO_6 octahedra are formed. The solid-state structure shown in Figures 6 verifies the Anderson-Evans type of our newly investigated V(+V) substituted tungstates. A specific substitution pattern for the anion was not recognized. This means that all metal atoms are

distributed over all positions statistically. So, we modeled this situation using partial occupation of the metal sites by V and W with the occupancy set according to the results of the elemental analysis. Resulting R_1 value of 2.75 % and the residual electron density map (Figure S3) show that this is a good model.

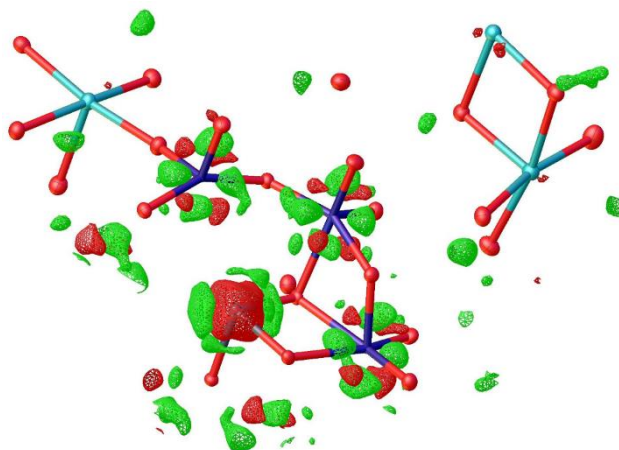


Figure S3: Residual electron density map of the refined crystal structure dataset of compound NaTeVW.

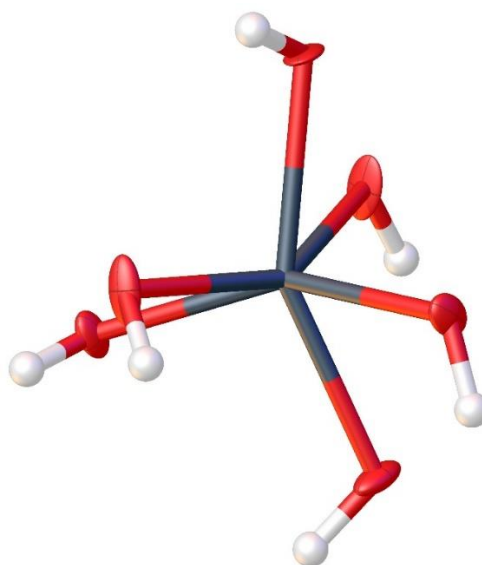


Figure S4: Solid-state structure of telluric acid ($\text{Te}(\text{OH})_6$) determined by sc-XRD. The compound was crystallized in the monoclinic space group $C2 (5)$. R_1 : 2.20 %, wR_2 : 6.28, R_{int} : 4.18, GooF: 1.217. Color code: grey: tellurium, red: oxygen and white: hydrogen. The full crystallographic information file (.cif) is available through the joint Cambridge Crystallographic Data Centre and Fachinformationszentrum Karlsruhe Access Structures service (deposition number: 2321174).

- $\text{Te}(\text{OH})_6$: The single-crystals of $\text{Te}(\text{OH})_6$ were obtained as aqueous suspension from which suitable crystals were taken for measurements. All crystals were obtained by slow

evaporation of an aqueous $\text{Te}(\text{OH})_6$ solution in water. Data were solved with ShelXS and the Patterson Method. Refinement was done with ShelXL and L.S. The space group is C2 (5). The refinement was done as a racemic twin (twin law -1 0 0 0 -1 0 0 0 -1, BASF: 0.410), due to an unusual Flack parameter. Final R values: R_1 : 2.20 %, wR_2 : 6.28 %, R_{int} : 4.18 % and Goof: 1.217. The .cif file is available in the CCDC database with the deposition number 2321174.

The bond angles in telluric acid were found to be in the range of $73.3(5)^\circ$ to $113.0(3)^\circ$ and are distorted in comparison to an ideal bond angle in an octahedron of 90° .^[6,7]

1.2.4 NMR-spectroscopy

Spectra measurement was done using a Bruker AVANCEII 600 MHz. In a typical procedure the samples were prepared as follows: POM (70 mg) was dissolved in diluted aqueous hydrochloric acid solution at pH 5 (0.63 mL) and acetone- d_6 (0.07 mL) was added.

All ^{51}V spectra were measured with a Time Domain Data Size (TD) of 32 K, the Transmitter Frequency Offset for Channel F1 (O1) and the Spectral Width (SW) was set to -520 and 400 ppm. The Delay (D1) was set to 0.5 s and the Number of Scans (NS) was 4 K. NMR analyses was done with the software MestReNova®. In MestReNova®, the peaks were first determined, and the data subsequently exported in .csv format and plotted in Origin 2019b.

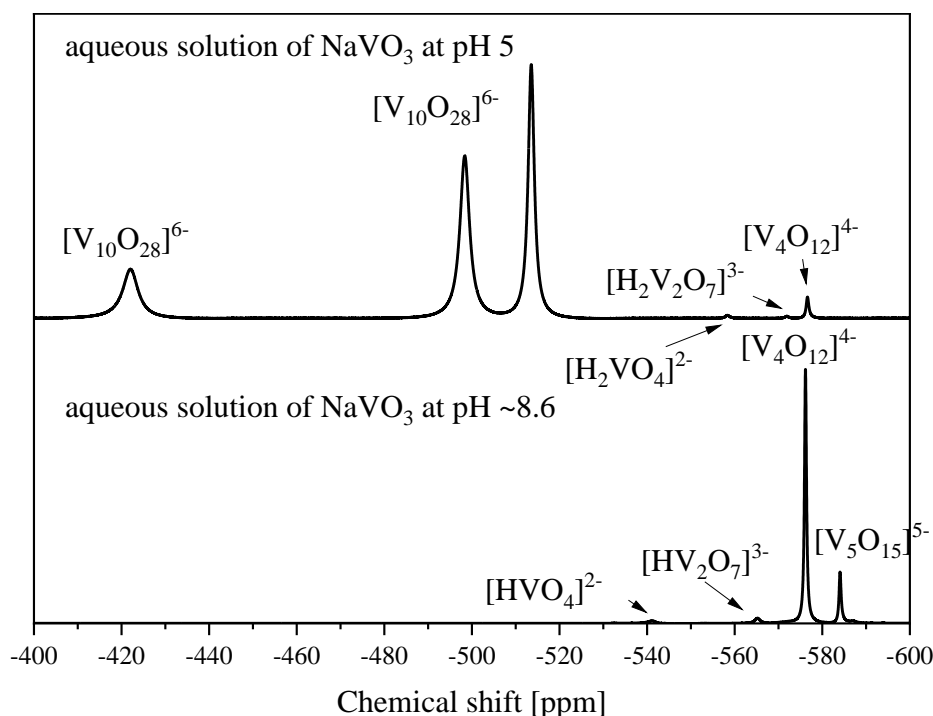


Figure S5: ^{51}V NMR of different vanadate species in aqueous solution compared at two different pH values.

Table S6: ^{51}V peak positions of the different V(+V) substituted Anderson-Evans structures investigated in this work.

Substitution degree x	Tungstates [ppm]	Molybdates [ppm]
1	-508.4	-502.8, -509.9, -520.0
2	-508.5	-485.2, -502.4, -507.0, -509.6, -519.6
3	-508.9	-485.2, -502.4, -507.0, -510.0, -520.0

1.2.5 UV-Vis spectroscopy

Stock solution: The respective POM (10 mg) was dissolved in deionized water (10 mL) \rightarrow 1 g/L.

Spectra measurement: All UV-Vis spectra were measured with a Cary 60 UV-Vis spectrometer (Agilent Technologies) in a Quartz cuvette of 3 mL (QS). Measurements were done using the Cary WinUV software. Measurement range: 200 nm to 800 nm. The absorbance was measured in the slow measurement mode. Data were then exported as a .csv data set and plotted in Origin 2019b.

All samples were prepared as follows: Stock solution 1 g/L. From the stock solution 80 μL were filled into the cuvette and 2920 μL of water were added to reach the final measuring volume of 3 mL.

Table S7: LMCT peak maxima determined for all POMs investigated in this work.

POM	LMCT W(+VI)/Mo(+VI) [nm]	LMCT V(+V) [nm]
NaTeW	< 200	-
NaTeVW	< 200	366
NaTeV ₂ W	< 200	361
NaTeV ₃ W	< 200	358
NaTeMo	203	-
NaTeVMo	205	348
NaTeV ₂ Mo	206	343
NaTeV ₃ Mo	206	343

The accessible LMCT peak maxima were analyzed according to the Beer Lambert's law (Figures S7 to S16) and therefore calculated the extinction coefficients ϵ_{λ} . All values are listed in Table S8.

Extinction coefficients: Extinction coefficients were determined using the software Cary concentrations. Five calibration standards were prepared from the stock solution (1 g/L) with a final volume of 3 mL for the cuvette:

- 20 μL stock solution + 2980 μL deionized water
- 40 μL stock solution + 2960 μL deionized water
- 50 μL stock solution + 2950 μL deionized water
- 60 μL stock solution + 2940 μL deionized water
- 80 μL stock solution + 2920 μL deionized water

Data were exported as .csv file and plotted in Origin 2019b.

Extinction coefficients were calculated according to equations 1 to 4:

Beer-Lambert's law (equation 1):

$$Abs = \varepsilon_{\lambda} \cdot d \cdot c \cdot M^{-1} \quad (1)$$

Abs: Absorption

ε_{λ} : extinction coefficient (wavelength λ dependant) [$\text{l mol}^{-1} \text{cm}^{-1}$]

d: Cuvette layer thickness (1 cm) [cm]

c: concentration [g/L]

M: molar mass [g/mol]

Calibration line (equation 2):

$$Abs = a \cdot c + b \quad (2)$$

a: slope

b: Axis intercept

Determining the extinction coefficient:

$$a = \varepsilon_{\lambda} \cdot d \cdot M^{-1} \quad (3)$$

$$\varepsilon_{\lambda} = \frac{a \cdot M}{d} \quad (4)$$

Table S8: Extinction coefficients determined according to the Beer-Lambert's law.

Substitution degree x	tungstates		Molybdates	
	W(+VI) [L mol ⁻¹ cm ⁻¹]	V(+V) [L mol ⁻¹ cm ⁻¹]	Mo(+VI) [L mol ⁻¹ cm ⁻¹]	V(+V) [L mol ⁻¹ cm ⁻¹]
0	-*	-	$4.4733 \cdot 10^4$	-
1	-*	$1.397 \cdot 10^3$	$3.4330 \cdot 10^4$	$1.050 \cdot 10^3$
2	-*	$2.639 \cdot 10^3$	$3.0654 \cdot 10^4$	$2.241 \cdot 10^3$
3	-*	$3.453 \cdot 10^3$	$2.8771 \cdot 10^4$	$3.516 \cdot 10^3$

-* Extinction coefficients were not calculated, because the peak maxima were not determinable in the measurement range.

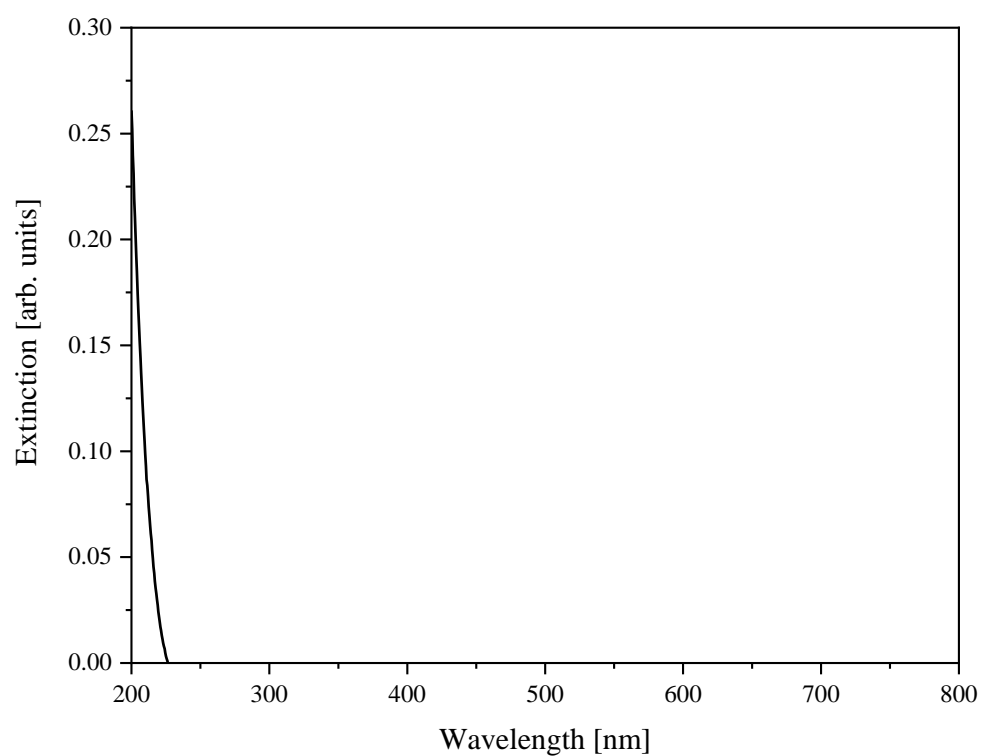


Figure S6: UV-Vis spectrum of telluric acid in aqueous solution.

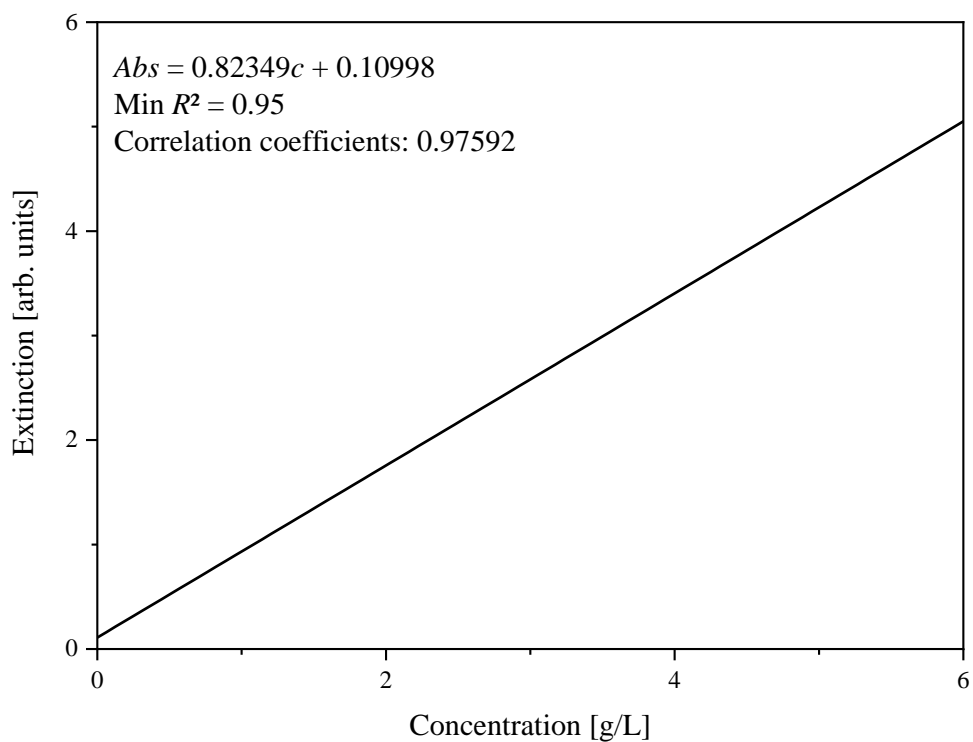


Figure S7: Calibration line for determining the extinction coefficient of the V(+V) LMCT for NaTeVW.

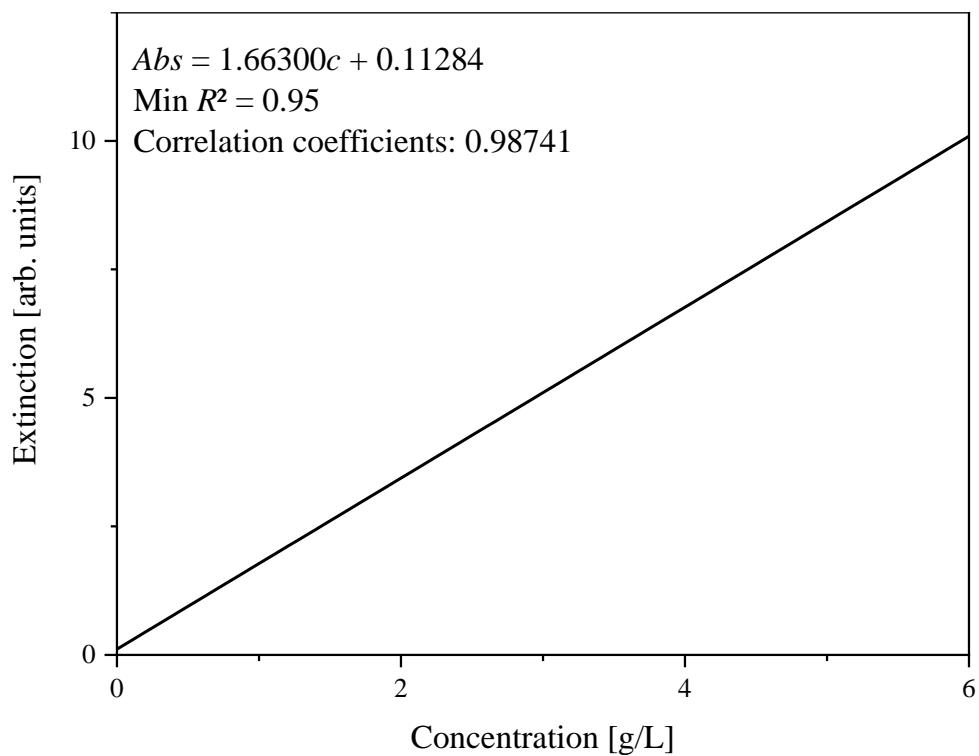


Figure S8: Calibration line for determining the extinction coefficient of the V(+V) LMCT for NaTeV₂W.

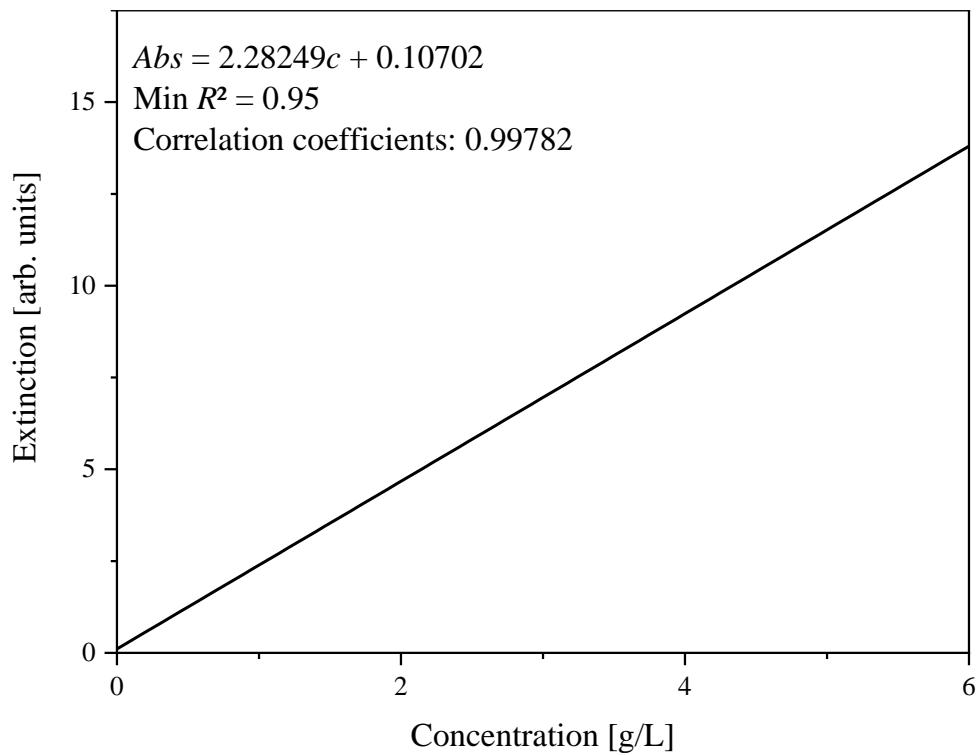


Figure S9: Calibration line for determining the extinction coefficient of the V(+V) LMCT for NaTeV₃W.

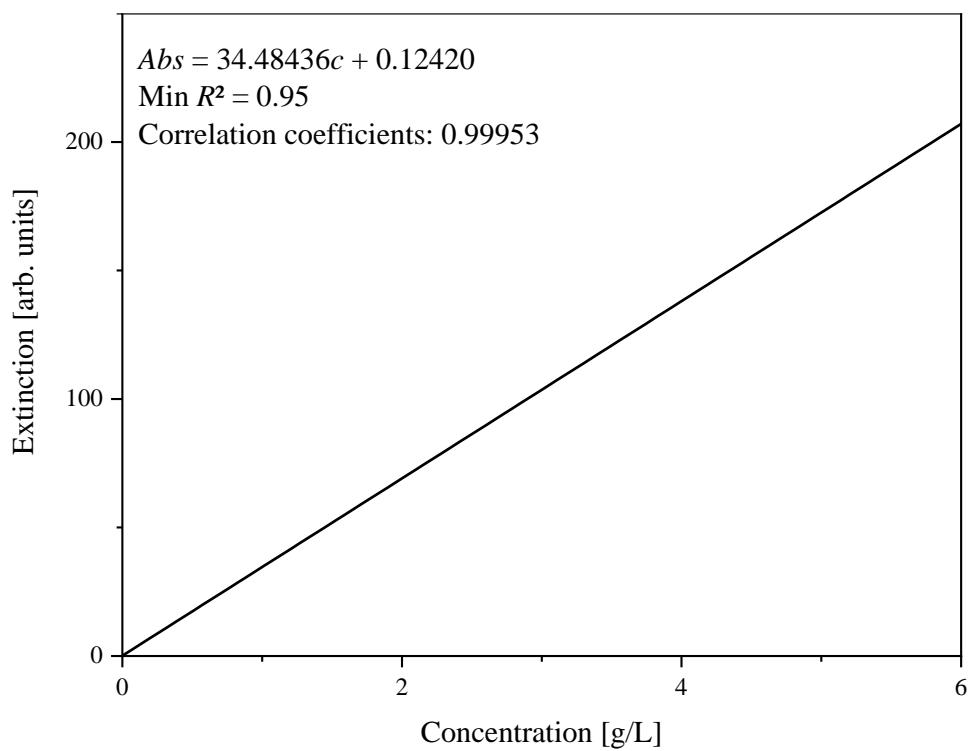


Figure S10: Calibration line for determining the extinction coefficient of the Mo(+VI) LMCT for NaTeMo.

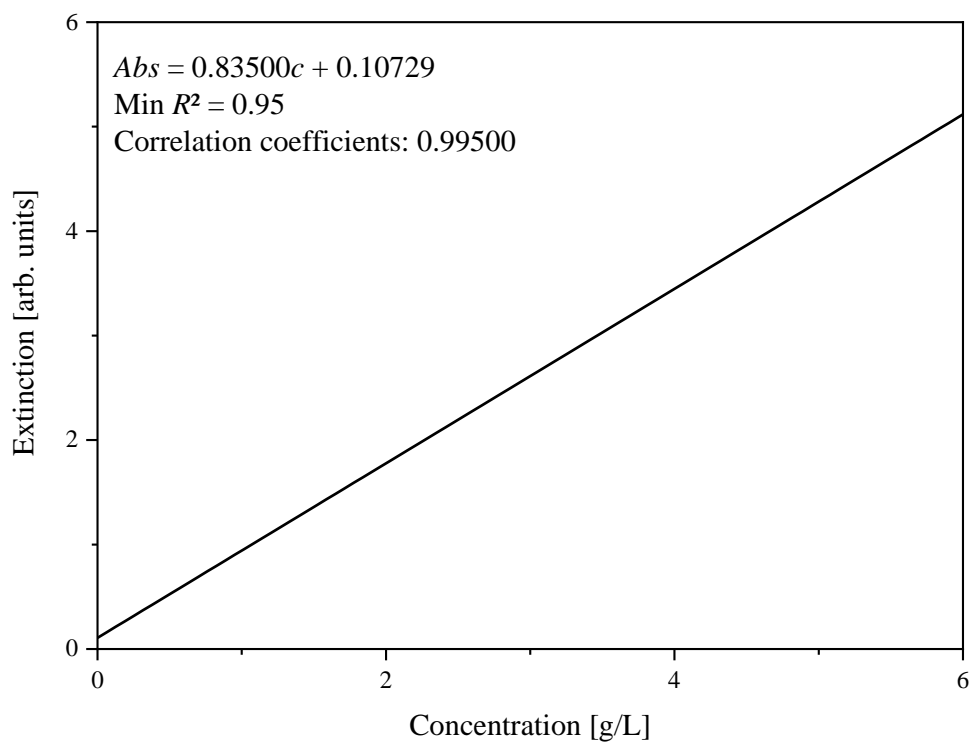


Figure S11: Calibration line for determining the extinction coefficient of the V(+V) LMCT for NaTeVMo.

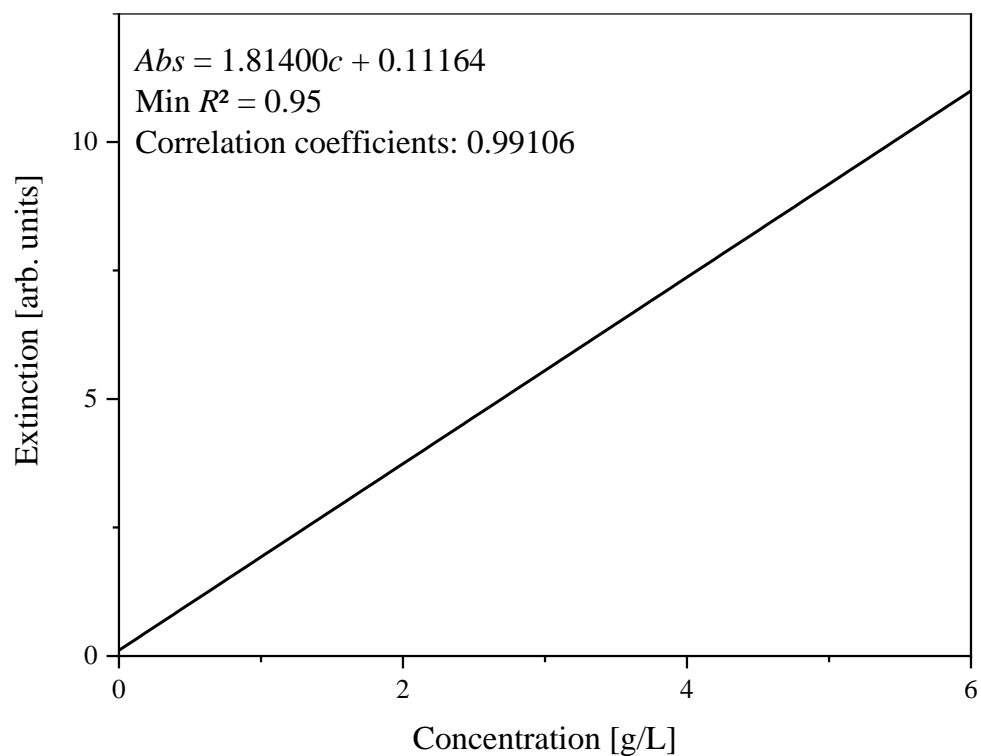


Figure S12: Calibration line for determining the extinction coefficient of the V(+V) LMCT for NaTeV₂Mo.

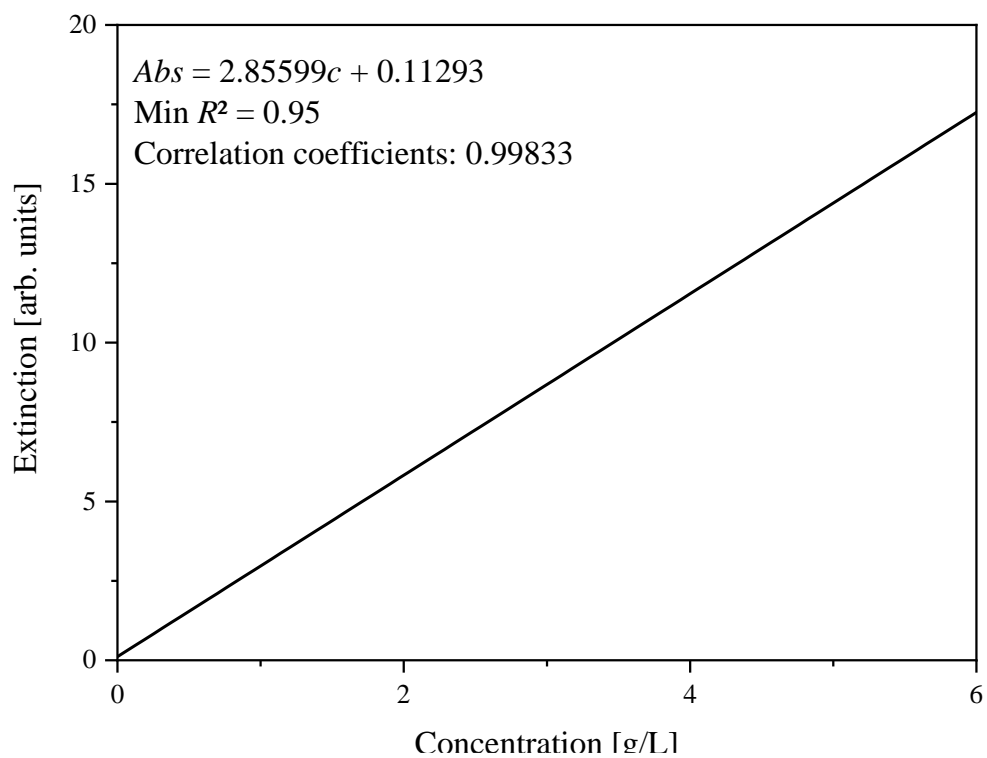


Figure S13: Calibration line for determining the extinction coefficient of the V(+V) LMCT for NaTeV₃Mo.

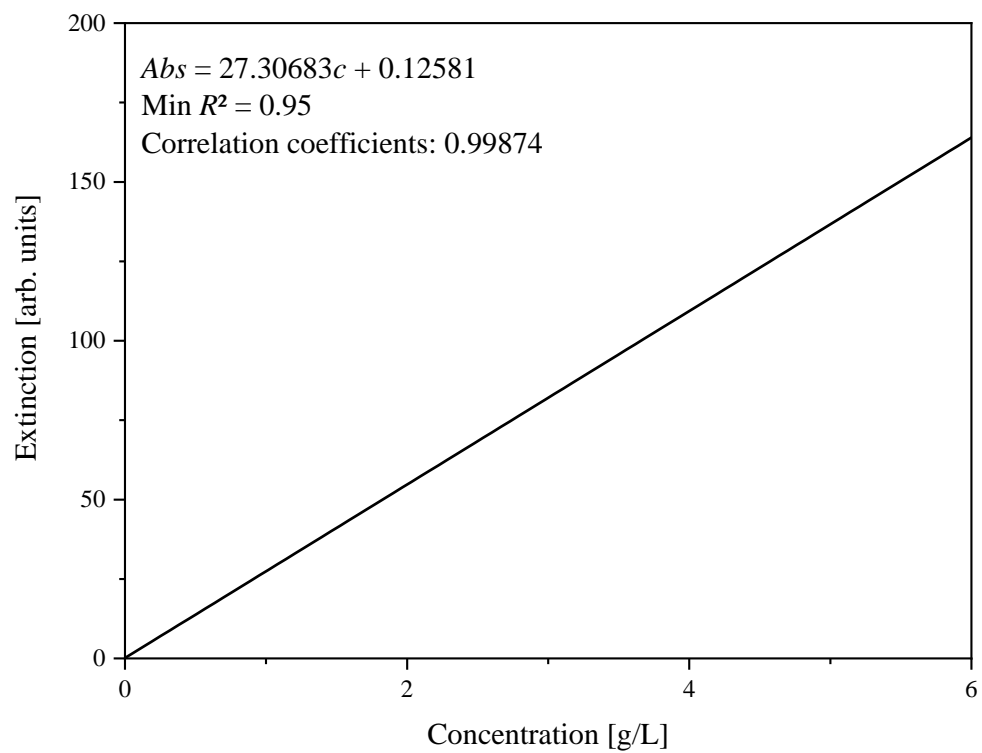


Figure S14: Calibration line for determining the extinction coefficient of the Mo(+VI) LMCT for NaTeVMo.

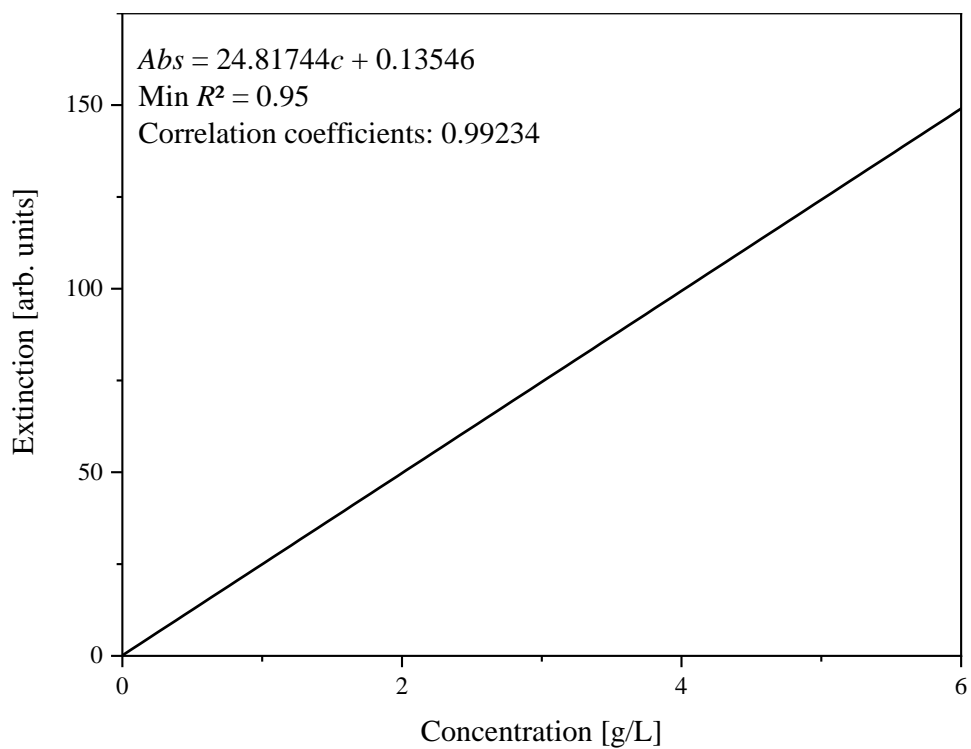


Figure S15: Calibration line for determining the extinction coefficient of the Mo(+VI) LMCT for NaTeV₂Mo.

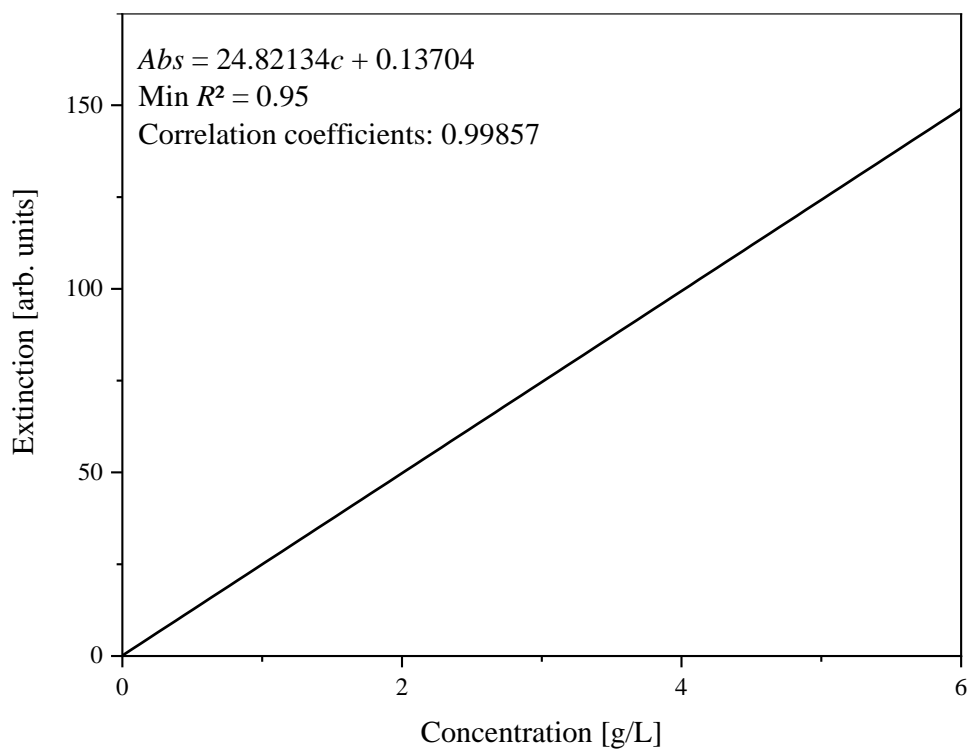


Figure S16: Calibration line for determining the extinction coefficient of the Mo(+VI) LMCT for NaTeV₃Mo.

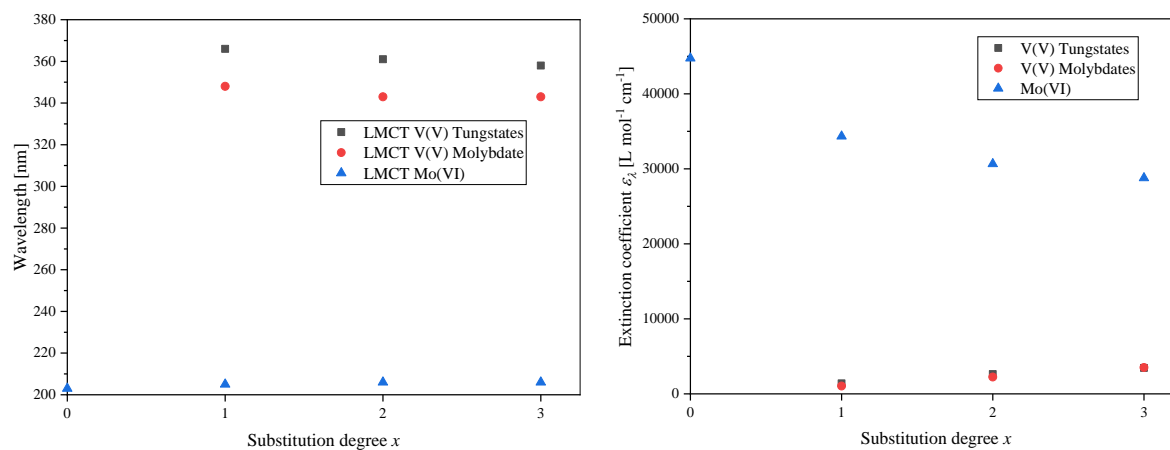


Figure S17: Plot of the extinction wavelength maxima vs. substitution degree x (left) and plot of the extinction coefficients vs. x (right).

As expected, the values of the extinction coefficients for Mo(VI) decrease with increasing degree of substitution, while those of V(V) increase steadily.

1.2.6 Electrochemical analysis

RedOx potentials of the POMs were measured with cyclic voltammetry (CV) and square-wave voltammetry (SWV).

The CV/SWV measurements were done in 10 mL of diluted, aqueous hydrochloric acid solution at pH 5 using sodium chloride as supporting electrolyte. Analyte concentration 1 mmol/L and supporting electrolyte concentration 1 mol/L, resulting in the analyte/supporting electrolyte ratio of 1/1000. Measurements were done on a Ivium (Ivium Technologies). During the measurements the solution was purged with nitrogen gas. Working electrode: glassy carbon electrode (diameter: 3 mm); Reference electrode: Ag/Ag⁺ electrode; Counter electrode: platinum electrode.

The measurement range was set to -600 to 1000 mV with a scan rate (CV) of 100 mV/s for 3 scans and a scan rate (SWV) of 5 mV/s. For the SWV measurements a modulation amplitude of 20 mV and a frequency of 25 Hz was chosen. Measurements were done with the software Ivium and the data were exported as a .x/y text document. Data were then plotted in Origin 2019b.

CV data of all investigated POMs in this work are found in Figure S18.

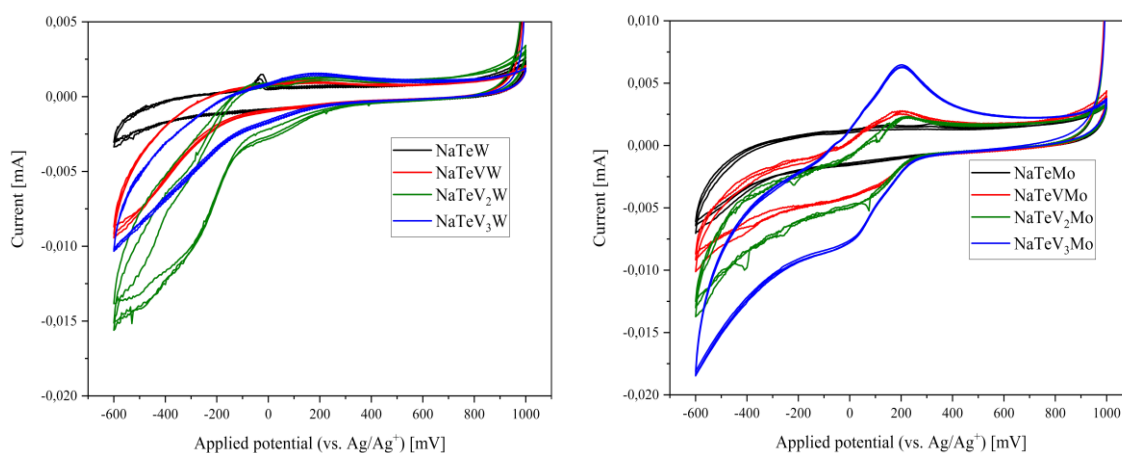


Figure S18: CV data of the V(+V) substituted tungstates (left) and molybdates (right), measured in diluted hydrochloric acid solution at pH 5 (1 mmol/L, 1 equivalent) with sodium chloride as supporting electrolyte (1 mol/L, 1000 equivalents).

Table S9: RedOx potentials of the different POMs measured by using SWV in aqueous, diluted hydrochloric acid solution (pH 5) using sodium chloride as supporting electrolyte.

POM	SWV
	Potential [mV]
NaTeW	-45
	100
NaTeVW	-80
	40
NaTeV₂W	-85
	80
NaTeV₃W	-75
	50
NaTeMo	-135
	80
NaTeVMo	-90
	160
NaTeV₂Mo	-100
	165
NaTeV₃Mo	-90
	145

2 Catalytic experiments

2.1 Experimental part

2.1.1 Chemicals

- Furfuryl alcohol was purchased from VWR chemicals with a purity of 98 %.
- Furfural was purchased from Sigma Adrich with a purity of 98 %.
- Furoic acid was purchased from Sigma Adrich with a purity of 98 %.
- Furanone was purchased from abcr GmbH with a purity of 95 %.
- 2-Methylfuran was purchased from Sigma Aldrich with a purity of 99 %.
- 5-HMF was purchased from Alfa Aesar with a purity of 97 %.
- Demineralized water was always used as solvent.

2.1.2 Experimental procedures

All experimental procedures can be found in the main manuscript.

2.2 Catalytic results

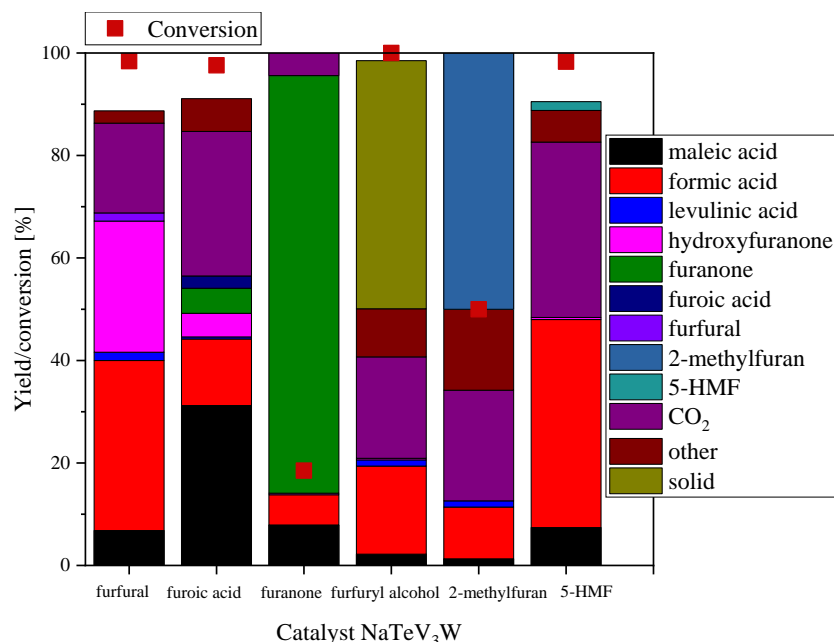


Figure S19: Oxidation experiments of the different monofuran derivatives with NaTeV₃W as a catalyst. Experimental conditions: 10-fold reaction system, 90 °C, 30 bar (O₂), 15 hours, 1000 rpm, 10 mL substrate solution containing 12.5 mmol carbon derived from the respective substrate, 0.14 mmol of vanadium (V) for substitution (90 mol_{Carbon} mol⁻¹_{Vanadium}).

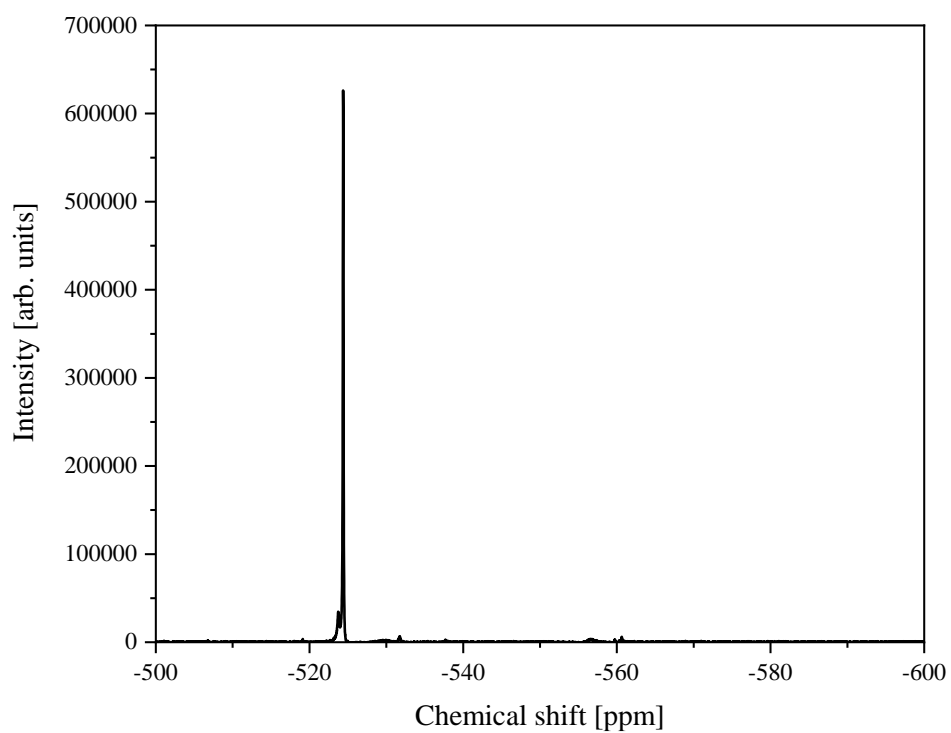


Figure S20: ^{51}V -NMR of the reaction solution containing NaTeV_3W after oxidation of furfural.

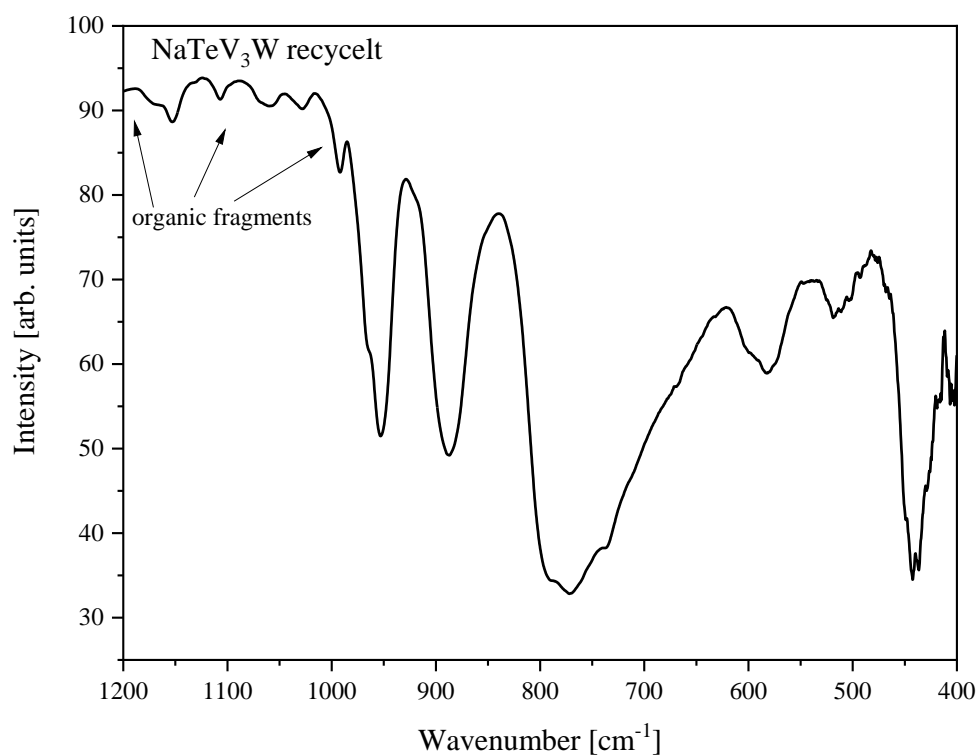


Figure S21: Solid-state IR spectrum of the isolated NaTeV_3W catalyst after reaction oxidation of furfural.

3 Literature

- [1] J.-C. Raabe, T. Esser, F. Jameel, M. Stein, J. Albert, M. J. Poller, *Inorg. Chem. Front.* **2023**, *10*, 4854–4868.
- [2] O. V. Dolomanov, L. J. Bourhis, R. J. Gildea, J. A. K. Howard, H. Puschmann, *J. Appl. Crystallogr.* **2009**, *42*, 339–341.
- [3] G. M. Sheldrick, *Acta Crystallogr. Sect. A Found. Crystallogr.* **2008**, *64*, 112–122.
- [4] C. B. Hübschle, G. M. Sheldrick, B. Dittrich, *J. Appl. Crystallogr.* **2011**, *44*, 1281–1284.
- [5] L. J. Farrugia, *J. Appl. Crystallogr.* **1999**, *32*, 837–838.
- [6] P. Kubáček, R. Hoffmann, *J. Am. Chem. Soc.* **1981**, *103*, 4320–4332.
- [7] M. Darari, A. Francés-Monerris, B. Marekha, A. Doudouh, E. Wenger, A. Monari, S. Haacke, P. C. Gros, *Molecules* **2020**, *25*, 5991–6011.

Verwendete Methoden und Software

Zusammensetzungsanalyse

Elementaranalyse (F-AAS/ICP-OES):

Alle Proben wurden mit einem ICP-OES-Spektrometer für die Elementaranalyse (Fa. Spectro, Typ ARCOS) für die Elemente Mo, W, V, Nb, Mn, In, As, Te und P vermessen (Methode ICP-OES). Die Elemente Na, K, Fe, Co, Ni, Cu, Zn, Sn und Sb wurden mit einem F-AAS (Fa. Thermo, Typ Solaar S Series) vermessen (Methode F-AAS ohne HKL).

Zu den Aufschlüssen: Es wurde eine Lösung (1 mg/10 mL) des (mittels F-AAS/ICP-OES messbaren) Elementes benötigt, dass den niedrigsten Massenprozentwert hat.

- Grundsätzlich wurden alle AAS/ICP-OES-Messungen im wässrigen Medium durchgeführt.
- V(V) und V(V)/Mn(II) gemischt substituierte POMs wurden zusätzlich mit konzentrierter Salzsäure zur Stabilisierung angesäuert (2-5 mL).
- Verbindung NaTeMo wurde in 3 M Salzsäure-Lösung in Wasser gelöst.
- Verbindung KNb wurde in Wasser (1 mL) und einer 30 %igen Wasserstoffperoxid-Lösung in Wasser (1 mL) aufgenommen. Anschließend wurde mit konzentrierter Salzsäure angesäuert.
- Natriumsalze der V(V), In(III), Co(II) und Ni(II) substituierten Phosphormolybdate wurden in Wasser (5 mL) aufgenommen und mit einer 65 %igen Salpetersäure-Lösung in Wasser (100 µL) angesäuert. Dieselbe Prozedur konnte auch für den POM $\text{Na}_{12}[\text{P}_4\text{W}_{14}\text{O}_{58}]$, die Co(II) substituierten Phosphormolybdate, NaTeVMo, NaTeV₃W, NaTeV₂Mo und NaTeV₃Mo angewendet werden.
- Natrium-/Kaliumsalze der Nb(V), der Nb(V)/V(V) gemischt, sowie der Fe(III) und Zn(II) substituierten Phosphormolybdate wurden in Wasser gelöst. Zur vollständigen Löslichkeit der Probe kann erwärmt werden. Die POMs $\text{Na}_8[\text{W}_{12}\text{O}_{40}]$, $\text{Na}_9[\text{AsW}_9\text{O}_{34}]$, $\text{Na}_7[\text{SbW}_6\text{O}_{24}]$, NaTeVW, NaTeV₂W und NaTeW konnten in reinem Wasser gelöst werden.
- Für organisch modifizierte POMs, die sich nicht in Wasser lösten, wurde die Einwaage in inversem Königswasser (3 HNO₃ und 1 HCl) (6 mL) suspendiert und zur vollständigen Löslichkeit wurde eine Flusssäure-Lösung in Wasser (1 mL) hinzugegeben, bevor mit Wasser aufgefüllt wurde (Anton Paar/Organic high).

-
- In Wasser unlösliche Verbindungen, wie Oxide, wurden in Wasser (5 mL) aufgenommen und zur vollständigen Löslichkeit in einer Flusssäure-Lösung in Wasser (1 mL) aufgenommen.

Thermogravimetrische Analyse:

Alle Messungen wurden an einer TG 209 F1 Libra von NETZSCH vermessen (Abbildung 36), die mit einem Massenspektrometrie- (MS)-Detektor gekoppelt wurde. Die Daten wurden mit der Software Proteus (Version 8.0.2) von NETZSCH aufgezeichnet. Ungefähr 20 mg der POM-Probe wurden in einem Duranglastiegel eingewogen und mit folgendem Temperaturprogramm vermessen:

- Probe auf 30 °C mit einer Heizrate von 10 K/min heizen
- Probe konstant bei 30 °C für 15 min halten
- Probe auf 350 °C mit einer Heizrate von 10 K/min heizen
- Probe konstant bei 350 °C für 30 min halten
- Ende (Abkühlung der Probe auf Raumtemperatur)

Es wurde ein Stickstofffluss von 20 mL/min eingestellt. Die Daten wurden mit der Software Proteus Analysis von NETZSCH ausgewertet und als .x/y Textdokument exportiert und in Origin 2019b importiert.

Schwingungsspektroskopie

IR-Spektroskopie:

IR-Daten der POMs wurden im Modus der abgeschwächten Totalreflexion (ATR) an einem QATR™-S von Shimadzu (Abbildung 37) vermessen (mit einem Diamantprisma). Als Auswertsoftware diente die LabSolutions IR Software. Die Basislinie wurde korrigiert und die Peaks manuell bestimmt. IR-Daten wurden als .x/y Textdokument exportiert und in Origin 2019b importiert.

Raman-Spektroskopie:

Alle Raman-Spektren wurden an einem SENTERRA Raman Mikroskop von Bruker Optik GmbH vermessen. Die Apertur wurde auf 50 x 1000 µm eingestellt. Der Anregungslaser hatte eine Wellenlänge von 785 nm und der Messbereich lag zwischen 75 cm⁻¹ und 1525 cm⁻¹. Die

Integrationszeit war 16 Sekunden, die Anzahl der Scans 8 und die Raman Laserleistung 10 mW. Die Raman-Daten wurden mit der Software Opus verarbeitet, als .DPT Datei exportiert und in Origin 2019b geplottet.

Kristallographie

Einkristallstrukturanalyse:

Einkristalle wurden auf einem Einkristalldiffraktometer mit vier Kreisen SuperNova von Oxford Diffraction (Firma: Agilent Technologies, Erwerb: November 2011) vermessen.

- Ausgestattet mit einer Molybdän- und Kupferquelle (dual instrument), Microfocus-Röhren
- Cryostream-700 Plus Stickstoffstromkühlung, 100-500 K (Oxford Cryosystems)

Die Daten wurden gelöst und verfeinert mit der Software Olex2 v1.5, dem ShelX Algorithmus und der PLATON Software.^[211,215,217,218,220] Das Tool XPREP von Shelxtl wurde zur Verifizierung der Raumgruppe herangezogen. Die finalen Daten wurden als .cif Datei gespeichert und mit dem Onlinetool CheckCIF <https://checkcif.iucr.org/> Publikationscheck überprüft.^[210,268] Mit der Software Mercury wurden die p-XRD Diffraktogramme simuliert und als .xye Datei gespeichert. Die Daten wurden zur Visualisierung nach Origin 2019b importiert.

Die .cif Dateien wurden in der Datenbank der *Cambridge Crystallographic Data Centre and Fachinformationszentrum Karlsruhe Access Structures service* veröffentlicht: <https://www.ccdc.cam.ac.uk/>.

Pulverdiffraktometrie:

p-XRD Diffraktogramme wurden an einem X'Pert Pro diffractometer (PANalytical Corp.) mit Cu-K α Strahlung ($\lambda = 1.5418 \text{ \AA}$) im Bereich 2θ 5-90 ° gemessen. Der Untergrund wurde mit der Software X'Pert HighScore Plus bestimmt und die Daten geglättet. Die Diffraktogramme wurden als .ASC Dateiformat exportiert und zur Visualisierung in Origin 2019b importiert.

Kernresonanzpektroskopie

Alle NMR-Spektren wurden an einem Bruker AVANCE III HD 600 MHz Spektrometer (AVIII600) mit einer Basisfrequenz von 600.13 MHz vermessen.

- 5 mm BBFO Probenkopf (Smart Probe) mit ATM und z-Gradient

-
- Probenwechsler: SampleXpress Lite (16 Proben)
 - TOPSPIN 3.6.4

Probenpräparation: Der jeweilige POM (20 bis 70 mg) wurde in deionisiertem Wasser (0.63 mL) gelöst, das zuvor mit konzentrierter Salzsäure auf pH 5 (Anderson-Evans-Strukturen) oder pH 1 (Keggin-Strukturen) eingestellt wurde. Aceton-*d*6 (0.07 mL) wurde als deuteriertes Lösungsmittel hinzugegeben.

³¹P-NMR Spektren wurden mit einer *Time Domain Data Size* (TD) von 32 K vermessen. Die *Number of Scans* (NS) betrug 2K (= 2048), der *Transmitter Frequency Offset* für Kanal F1 (O1) und die *Spectral Width* (SW) betragen -1 and 40 ppm. Der *Delay* D1 betrug 1 s.

⁵¹V-NMR Spektren wurden mit einer TD von 32 K vermessen. O1 und SW betragen -520 and 400 ppm. Der D1 und die NS wurden auf 0.5 s und 4K eingestellt.

Die Spektreninterpretation wurde in der Software MestReNova® durchgeführt und die Daten als .csv Format exportiert. Anschließend wurden die Daten zur Visualisierung in Origin 2019b importiert.

***Ultraviolett-visible-* (UV-Vis-) Spektroskopie**

Vorbereitungen der Stammlösungen: POM (10 mg) wurde in Wasser (10 mL) gelöst. Somit entspricht die Konzentration der Stammlösung 1 g/L.

Spektrenmessung: Alle UV-Vis-Spektren wurden an einem Cary 60 UV-Vis Spektrometer (Agilent Technologies) in einer 3 mL Quartzküvette (QS) gemessen (Abbildung 38). Hierfür wurde die Software Cary WinUV verwendet. Der Messbereich lag zwischen 200 und 800 nm. Die Absorption wurde im langsamen Messmodus gemessen. Die Daten wurden als .csv Format exportiert und in Origin 2019b zur Visualisierung importiert. Die Proben wurden zur Messung wie folgt verdünnt: Von der Stammlösung wurden 80 µL in die Küvette gefüllt und mit 2920 µL Wasser verdünnt, um das Endvolumen von 3 mL zu erreichen.

Extinktionskoeffizienten: Für die Bestimmung der Extinktionskoeffizienten wurde die Software Cary concentrations verwendet. Fünf Kalibrierstandards wurden von der Stammlösung (1 g/L) mit einem Gesamtvolumen von 3 mL in der Küvette angesetzt:

- 20 µL Stammlösung + 2980 µL deionisiertes Wasser

-
- 40 μL Stammlösung + 2960 μL deionisiertes Wasser
 - 50 μL Stammlösung + 2950 μL deionisiertes Wasser
 - 60 μL Stammlösung + 2940 μL deionisiertes Wasser
 - 80 μL Stammlösung + 2920 μL deionisiertes Wasser

Die Daten wurden als .csv Format exportiert und in Origin 2019b zur Auftragung importiert.

Elektrochemie

CV/SWV Messungen wurden in wässrigen, salzsauren Medien bei pH 1 (Keggin) und einer Analytkonzentration von 1 mmol/L an einem Ivium Potentiostaten durchgeführt (Abbildung 39 bis 41). Anderson-Evans-Strukturen wurden in wässrigen, salzsauren Medien bei pH 5 durchgeführt mit Natriumchlorid als Leitelektrolyt. Das optimale Analyt zu Leitsalz Verhältnis betrug 1:1000. Während der Messung wurde die Lösung mit Stickstoffgas gespült. Arbeitselektrode: glassy carbon Elektrode (Durchmesser: 3 mm); Referenzelektrode: Ag/Ag⁺ Elektrode; Gegenelektrode: Platinelektrode (Abbildung 41).

Der Messbereich lag zwischen -600 and 1000 mV mit einer Scanrate (für CV) von 100 mV/s für 3 Scans. Alle SWV Messungen wurden mit einer Scanrate von 5 mV/s, einer Modulationsamplitude von 20 mV und einer Frequenz von 25 Hz durchgeführt. Als Messsoftware wurde die Ivium Software (Ivium Technologies) verwendet und die Daten wurden als .x/y Textdokument exportiert. Zur Visualisierung wurden die Daten in Origin 2019b importiert.



Abb. 36: TG 209 F1 Libra der Firma NETZSCH zur Bestimmung des Hydratwassergehaltes mit gekoppelten Massendetektor (Aelos).



Abb. 37: QATR™-S der Firma Shimadzu für die Messung der IR-Spektren.

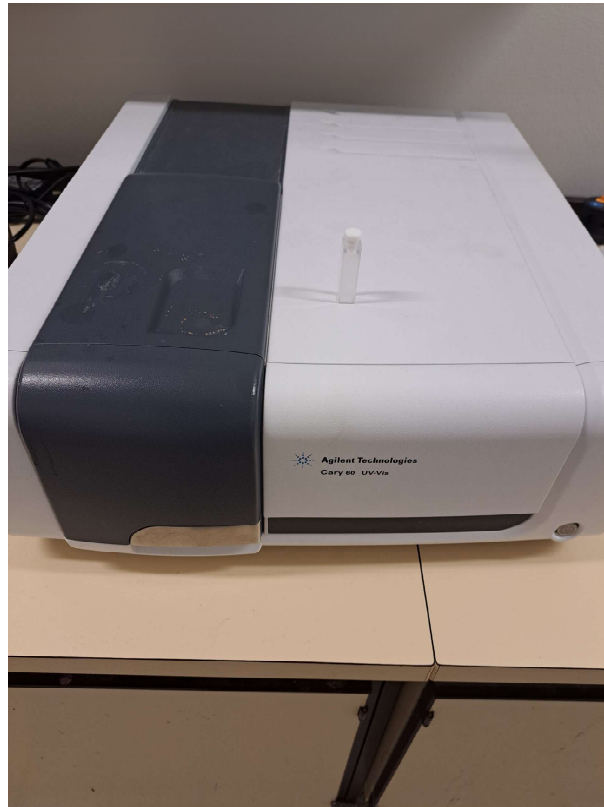


Abb. 38: Cary 60 UV-Vis Spektrometer der Firma Agilent Technologies zur Messung der UV-Vis-Spektren mit Quartz Küvette (QS).



Abb. 39: Messaufbau zur Messung von CV/SWV. Weiße Klemme: Glassy carbon Elektrode; Blaue Klemme: Ag/Ag⁺ Elektrode; Schwarze Klemme: Platinelektrode. Stickstoffspülung erfolgt über die Kanüle.



Abb. 40: Ivium Potentiostat für die CV- und SWV-Messung.



Abb. 41: Elektroden für die CV- und SWV-Messung. Links: Glassy Carbon Elektrode; Mitte: Platinelektrode; Rechts: Ag/Ag⁺ Elektrode.



Abb. 42: 10fach Oxidationssystem mit Rührplatte (komplett).



Abb. 43: Zum 10fach Oxidationssystem gehörender Reaktorkörper mit dem zugehörigen Reaktorkopf (Hastelloy (C-276)).



Abb. 44: Zum 10fach Oxidationssystem gehörendes Reaktorset, bestehend aus insgesamt zehn Reaktorkörpern und -köpfen, die wiederum mit einem digitalen und analogen Druckabnehmer ausgestattet sind.

Bilderanhang

Im folgenden Kapitel wurden einige Bilder einiger (TMS)POMs und experimentellen Prozeduren zusammengestellt (Abbildungen 45 bis 59).

Einkristall von HPA-5



Abb. 45: Einkristall von HPA-5, aufgenommen direkt vor der Messung.



Abb. 46: Farbvielfalt der POMs, hervorgerufen durch die Art und den Substitutionsgrad des entsprechenden Substitutionselementes.



Abb. 47: V(V) substituierte Anderson-Evans Molybdo- (links) und Wolframatotellurate (rechts). Aufsteigender Substitutionsgrad von oben (0) nach unten (3).

Keggin-Typ-POM: $H_3[PMo_{12}O_{40}]$



Abb. 48: Keggin-Typ POM $H_3[PMo_{12}O_{40}]$.

Keggin-Typ-POM: $H_3[PW_{12}O_{40}]$

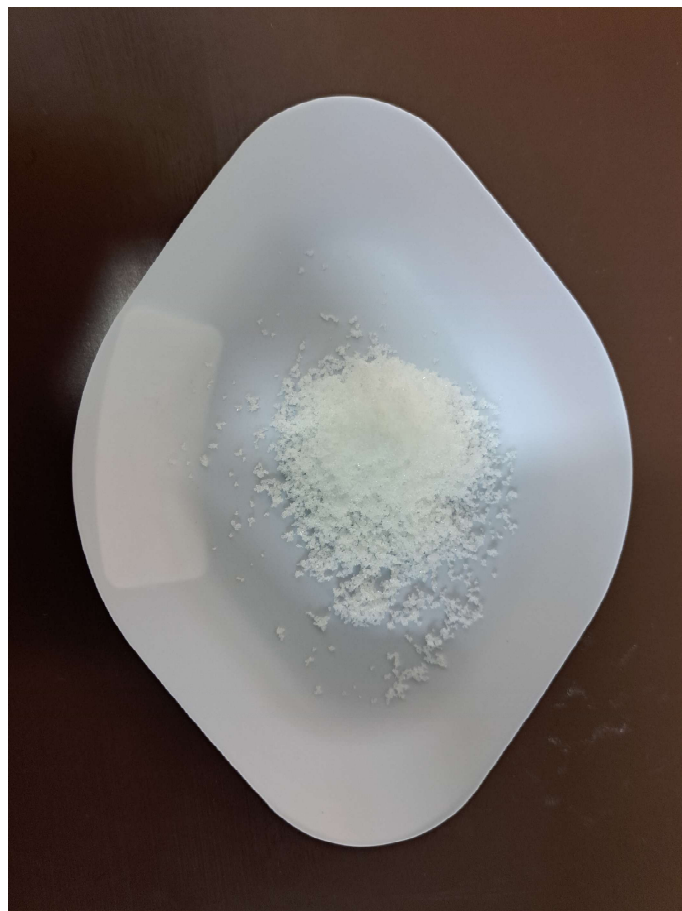


Abb. 49: Keggin-Typ POM $H_3[PW_{12}O_{40}]$.

Wells-Dawson-Typ-POM: $\text{Na}_6[\text{P}_2\text{W}_{18}\text{O}_{62}]$

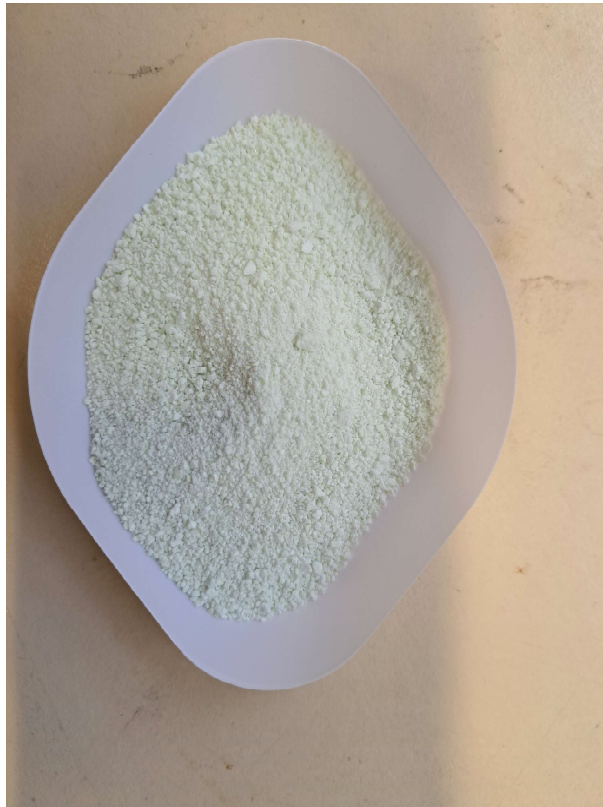


Abb. 50: Wells-Dawson-Typ POM $\text{Na}_6[\text{P}_2\text{W}_{18}\text{O}_{62}]$.

Lindqvist-Typ-POM: $\text{K}_8[\text{Nb}_6\text{O}_{19}]$

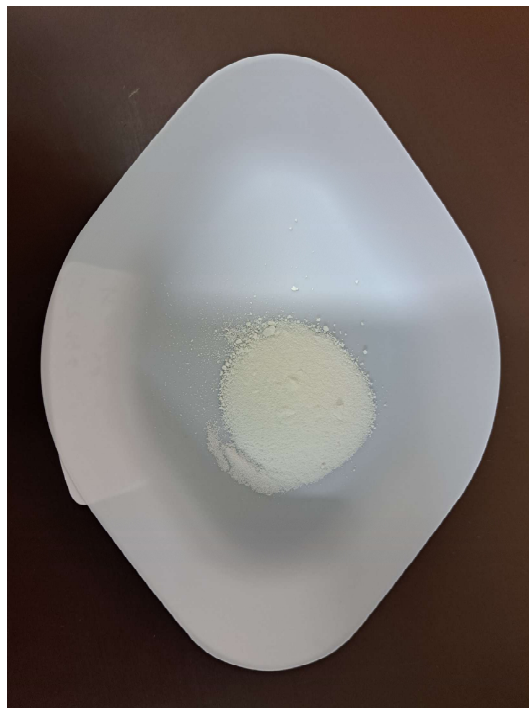


Abb. 51: Lindqvist-Typ POM $\text{K}_8[\text{Nb}_6\text{O}_{19}]$.

Lindqvist-Typ-POM: $K_2[Mo_6O_{19}]$



Abb. 52: Lindqvist-Typ POM $K_2[Mo_6O_{19}]$.

Lindqvist-Typ-POM: $K_2[W_6O_{19}]$

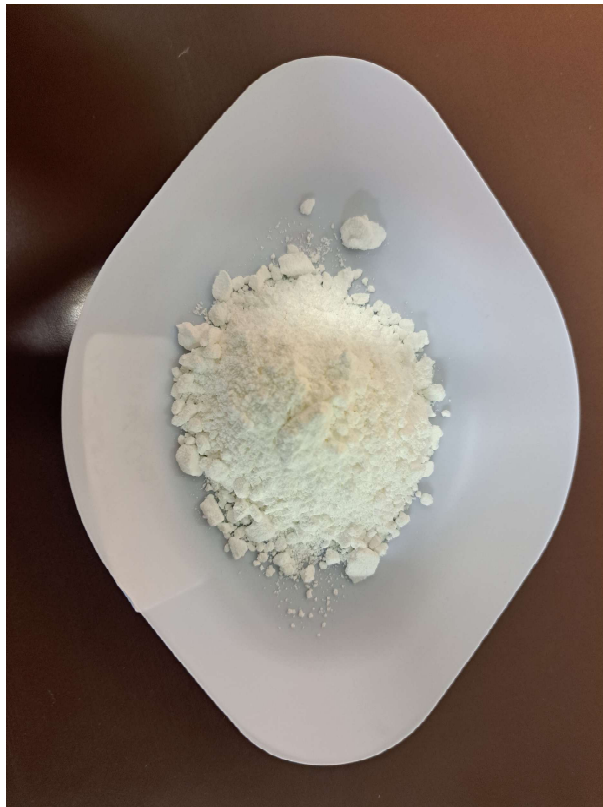


Abb. 53: Lindqvist-Typ POM $K_2[W_6O_{19}]$.

Anderson-Evans-Typ-POM: Na₆[TeMo₆O₂₄]

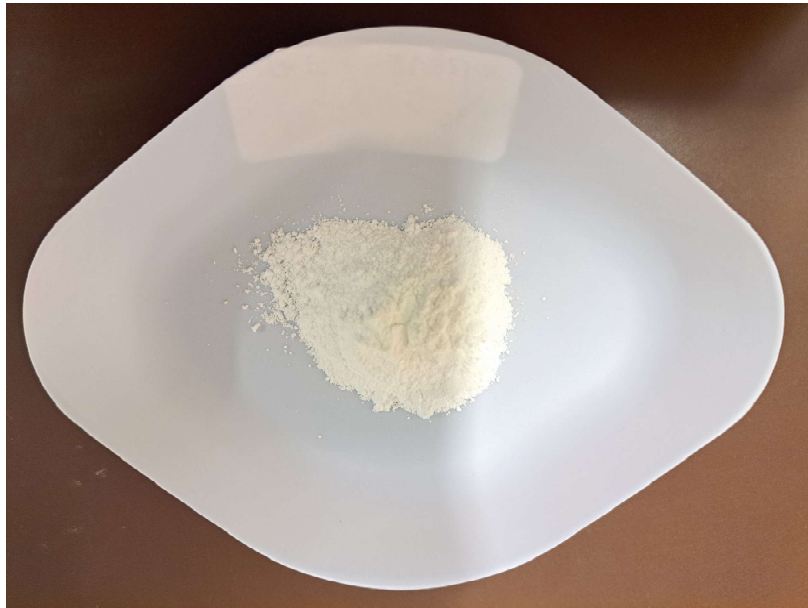


Abb. 54: Anderson-Evans-Typ POM Na₆[TeMo₆O₂₄].

Anderson-Evans-Typ-POM: Na₆[TeW₆O₂₄]

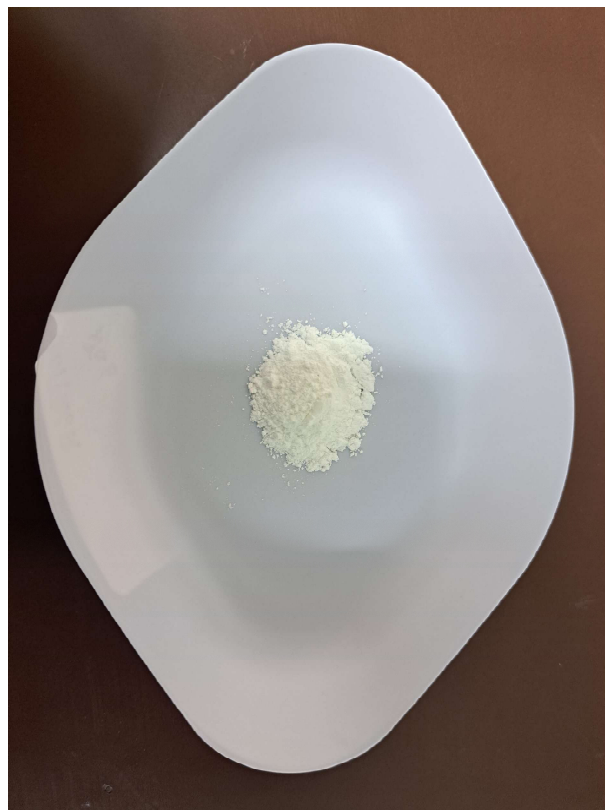


Abb. 55: Anderson-Evans-Typ POM Na₆[TeW₆O₂₄].

Synthese der Co(II) substituierten Phosphormolybdate



Abb. 56: Synthese der Co(II) substituierten Phosphormolybdate: charakteristische Rotfärbung, verursacht durch Co(II).

Synthese der Ni(II) substituierten Phosphormolybdate



Abb. 57: Synthese der Ni(II) substituierten Phosphormolybdate: charakteristische Grünfärbung, verursacht durch Ni(II).

Violettfärbung, induziert durch Co(II)



Abb. 58: Violettfärbung, induziert durch Co(II) Einbau in eine POM-Struktur.

Violettfärbung, induziert durch Co(II) in wässriger Lösung

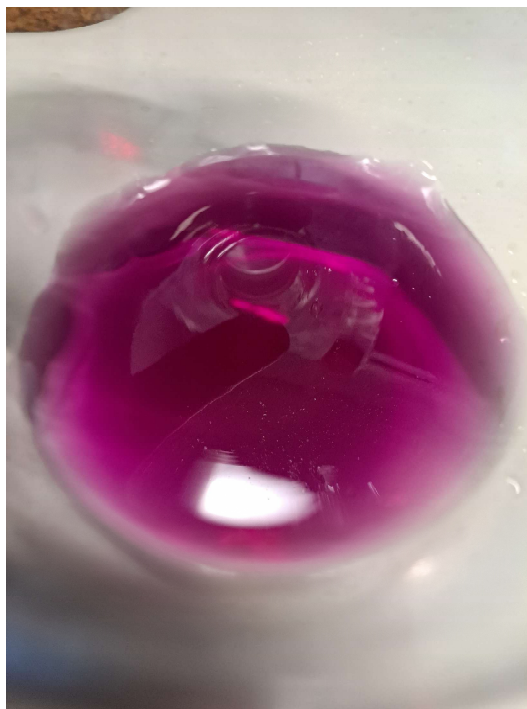


Abb. 59: Violettfärbung, induziert durch Co(II) Einbau in eine POM-Struktur (wässrige Lösung).

Danksagung

Mein Dank gilt meinem ersten Gutachter Prof. Dr.-Ing. Jakob Albert für die Aufnahme in seine Arbeitsgruppe, für die Bereitstellung des spannenden Forschungsthemas und die Betreuung während meinen praktischen Arbeiten. Insbesondere die Möglichkeit meine Forschungsergebnisse in zahlreichen Publikationen und in verschiedenen renommierten Fachzeitschriften unterzubringen und auf verschiedenen Konferenzen zu präsentieren hat mich persönlich und fachlich sehr vorangebracht. An dieser Stelle danke ich auch Herrn Prof. Dr. Michael Steiger für die Übernahme des Gutachtens meiner schriftlichen Arbeit.

Ich danke meinen Prüfern Prof. Dr. Lisa Vondung und Prof. Dr. Wolfgang Maison für die Übernahme der Aufgaben des zweiten und dritten Prüfers.

Weiterhin gilt mein Dank Dr.-Ing. Dorothea Voß für ihre Herzlichkeit und das stets offene Ohr. Insbesondere möchte ich mich hier bedanken für die zahlreichen Tipps und Ratschläge, die mich in vielen Situationen weitergebracht haben. Es war eine großartige Zusammenarbeit. Besonders bedanken möchte ich mich bei meinem Partner Dr. Maximilian J. Poller für die stetige Begleitung meines Forschungsthemas, für die Einbringung zahlreicher Ideen in meinen Projekten, für die zahlreichen fachlichen und privaten Gesprächen nebenbei, für die moralische Unterstützung und die stetige Motivation, sowie für unsere gemeinsamen Publikationen. Es war eine großartige Zusammenarbeit.

An dieser Stelle möchte ich mich auch bei allen Mitgliedern der Arbeitsgruppe Albert bedanken für die Aufnahme in die Gruppe, die stetige Motivation und für die vielen gemeinsamen Momente. Es war eine aufregende und spannende Zeit mit euch, die ich immer in meinen Erinnerungen tragen werde. Mittlerweile habe ich mit dem einen oder anderen von euch gemeinsam zusammengearbeitet und kann rückblickend sagen, dass es eine großartige Zusammenarbeit mit euch war.

Einen herzlichen Dank gilt auch meinen fleißigen Studenten Leon Bacanli (ehemaliger Masterand), José Aceituno Cruz (ehemaliger Masterand), Kelly Tam (DAAD-Forschungspraktikum, dreimonatiger Forschungsaufenthalt) und Hamid Anwari (ehemaliger Bachelorand). Danke für euer Vertrauen in mich und danke, dass ihr euch für meine Forschung interessiert habt. Ihr wart alle sehr fleißig und habt mich und meine Forschung sowohl wissenschaftlich als auch fachlich vorangebracht. Es war eine sehr schöne Zeit mit euch im Labor!

Ich möchte mich bei allen analytischen Abteilungen des Fachbereichs Chemie für die Vermessung zahlreicher Proben von mir bedanken. Hier gilt mein Dank in erster Linie der zentralen Elementanalytik von Dr. Dirk Eifler und seinem Team für das Vermessen zahlreicher AAS/ICP-OES Proben, für die Mühen immer einen geeigneten, nasschemischen Aufschluss für meine komplexen Proben zu finden und für die Meisterung so mancher Herausforderung. Besonders bedanken möchte ich mich beim Service der Röntgenstrukturanalyse von Dr. Frank Hoffmann und Isabelle Nevoigt für das Vermessen und Diskutieren zahlreicher Einkristalle und Pulver-Diffraktogramme. Ich weiß, dass die Lösung und Verfeinerung der Datensätze von meinen Polyoxometallaten herausfordernd war und wir kaum ein kristallographisches Problem ausgelassen haben. Dennoch freue ich mich sehr, dass wir die zahlreichen Herausforderungen und Probleme angehen und in vielen Fällen auch meistern konnten. Daher denke ich, dass wir mit den hieraus gewonnenen Erkenntnissen einen wertvollen Beitrag zum Verständnis der Polyoxometallatchemie leisten konnten. Ich bedanke mich weiterhin bei meinem langjährigen Freund Thomas Marx aus dem Arbeitskreis von Prof. Dr. Peter Burger für die Bereitstellung des Setups und die Unterstützung beim Messen meiner elektrochemischen Proben. Unsere gemeinsamen Mittagspausen bei unserer Stammpizzeria werde ich immer gut in Erinnerung behalten. Bedanken möchte ich mich auch bei Ute Gralla für das Vermessen zahlreicher Raman Proben. Auch möchte ich mich beim NMR-Service von Dr. Thomas Hackl für das Vermessen zahlreicher NMR-Proben bedanken.

Einen herzlichen Dank gilt auch den Kooperationspartnern, Dr. Andreas Vorholt, Dr. Anna Katharina Beine, Lea Hombach, Dr. Alberto Collauto, Dr. Maxie M. Roessler, Nils Kurig, Prof. Dr. Regina Palkovits, Sonja Mürtz, Prof. Dr. Matthias Stein und Froze Jameel für eure wertvollen Beiträge zu unseren gemeinsamen Publikationen.

Ich möchte mich an dieser Stelle herzlich bei meiner Familie und meinem privaten Freundeskreis für die tatkräftige Unterstützung auf meinen Wegen bedanken. Danke, dass ihr alle immer an mich geglaubt habt, mich gestärkt habt und immer für mich da wart, wenn ich euch gebraucht habe. Ohne eure Unterstützung wäre ich heute nicht da, wo ich jetzt bin.

Allen genannten Personen und Personengruppen gilt mein voller und aufrichtiger Dank!

Lebenslauf



Jan-Christian Raabe

Geboren am 09.03.1995 in Hamburg

Persönliche Informationen
Name: Jan-Christian Raabe
Geburtsdatum: 09.03.1995
Geburtsort: Hamburg, Deutschland

Wissenschaftliche Karriere

02/2024 – 05/2024 **Dalhousie University: Gastwissenschaftler in der Arbeitsgruppe von Prof. Dr. Saurabh Chitnis**
in Halifax, Kanada

- Forschungsaufenthalt mit Stipendium finanziert durch einen Mitacs Globalink Research Award
- Titel: *Synthesis and characterization of antimony and bismuth substituted Polyoxometalates*

Schule/Ausbildung

seit 12/2020 **Universität Hamburg: Doktorand und wissenschaftlicher Mitarbeiter in der Arbeitsgruppe von Prof. Dr.-Ing. Jakob Albert**
in Hamburg, Deutschland

- Betreuung chemischer Laborpraktika
- Betreuung von Abschlussarbeiten und Praktika B.Sc. und M.Sc. Chemie
- Forschung an einem Dissertationsprojekt: *Zu Gast bei den Polyoxometallaten: Entwicklung und katalytische Anwendung*
- Anfertigen von wissenschaftlichen Fachpublikationen
- Besuch von Konferenzen

Abschluss: Dr. rer. nat. (geplant bis 2024)

10/2017 - 10/2020 **Universität Hamburg: Studium Chemie M. Sc.**
in Hamburg, Deutschland

- Masterarbeit in der Arbeitsgruppe von Prof. Dr. Wolfgang Maison: *Synthese und Charakterisierung einer Phosphonsäure als polymerisierbare Ankergruppe für Metalloberflächen*

Abschluss: Master of Science
Abschlussnote: sehr gut

10/2014 - 09/2017 **Universität Hamburg: Studium Chemie B. Sc.**
in Hamburg, Deutschland

- Bachelorarbeit in der Arbeitsgruppe von Prof. Dr. Christian Stark und Prof. Dr. Zoya Ignatova: *Synthese und Charakterisierung von nor-Pyochelin*

Abschluss: Bachelor of Science
Abschlussnote: gut

08/2012 - 07/2014 **Marion Dönhoff Gymnasium**
in Hamburg, Deutschland
Abschluss: Abitur (allgemeine deutsche Hochschulreife)

08/2006 - 07/2012 **Gymnasium Rissen**
in Hamburg, Deutschland
Abschluss: Mittlerer Schulabschluss

07/2002 - 07/2006 **Grundschule Marschweg**
in Hamburg, Deutschland

Sonstiges

- Sprachen:** **Englisch** (sehr gute Kenntnisse)
Latein (sehr gute Kenntnisse)
- Qualifikationen:** **Sachkundenachweis nach §11 der Chemikalien-Verbotsverordnung**
Erworben 2017 im Rahmen der Modulprüfung des Moduls Rechtskunde und Toxikologie für Chemiker im Bachelorstudiengang Chemie
- Außerstudentische Aktivitäten:** **International Genetically Engineered Machine competition (iGEM) 2017** (iGEM Foundation)
- **Austragungsort:** Massachusetts Institute of Technology (MIT), Boston
 - Studentisches Forschungsprojekt unter der Mentorenschaft von Prof. Dr. Zoya Ignatova: *Developing A "Trojan Horse" to conquer bacterial resistances*
 - Präsentation der Ergebnisse auf dem iGEM Grand Jamboree Boston, Massachusetts, Vereinigte Staaten von Amerika
- Erste Hilfe** **Erste Hilfettraining (2021)**
- Führerschein:** **Klasse B**
- Mitgliedschaften:** **The Chemical Institute of Canada (2024)**

Stipendien

- 04/2024: 910 € vom "Reisekostenzuschuss aus dem Körperschaftsvermögen der Universität Hamburg" für die CSC 2024 - 107th Canadian Chemistry Conference, Kanada
- 03/2024: 150 € vom "GDCH Tagungsstipendium" für die CSC 2024 - 107th Canadian Chemistry Conference, Kanada
- 11/2023: "Mitacs Globalink Research Award to Canada" für ein Forschungsprojekt in der Arbeitsgruppe von Saurabh Chitnis, Kanada
- 05/2023: 805 € vom DAAD "Kongressreisen 23" für die 6th EuChemS Inorganic Chemistry Conference, Österreich
- 05/2023: 250 € vom "GDCH Tagungsstipendium" für die 6th EuChemS Inorganic Chemistry Conference, Österreich

Hamburg, 23.09.2024

J-C Paabe

Eidesstattliche Versicherung

Hiermit versichere ich an Eides statt, die vorliegende Dissertationsschrift selbst verfasst und keine anderen als die angegebenen Quellen und Hilfsmittel benutzt zu haben. Sofern im Zuge der Erstellung der vorliegenden Dissertationsschrift generative Künstliche Intelligenz (gKI) basierte elektronische Hilfsmittel verwendet wurden, versichere ich, dass meine eigene Leistung im Vordergrund stand und dass eine vollständige Dokumentation aller verwendeten Hilfsmittel gemäß der Guten wissenschaftlichen Praxis vorliegt. Ich trage die Verantwortung für eventuell durch die gKI generierte fehlerhafte oder verzerrte Inhalte, fehlerhafte Referenzen, Verstöße gegen das Datenschutz- und Urheberrecht oder Plagiate.

23.09.2024

Jan-Christian Raabe

